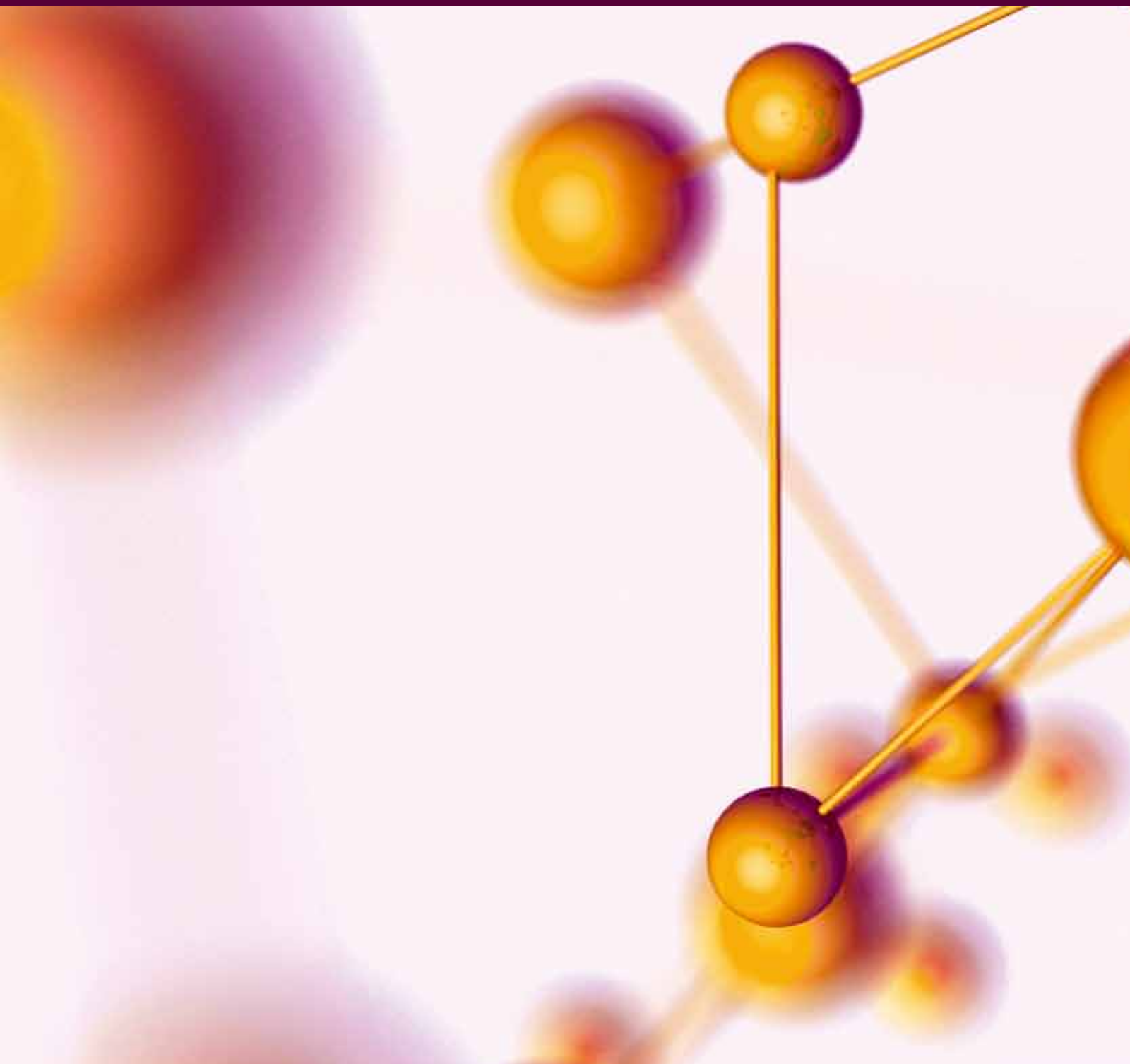


Advances in Physical Chemistry

Advances in Electrocatalysis

Guest Editors: Milan M. Jaksic, Wolfgang Schmickler, and Gianluigi Botton





Advances in Electrocatalysis

Advances in Physical Chemistry

Advances in Electrocatalysis

Guest Editors: Milan M. Jaksic, Wolfgang Schmickler,
and Gianluigi Botton



Copyright © 2012 Hindawi Publishing Corporation. All rights reserved.

This is a special issue published in "Advances in Physical Chemistry." All articles are open access articles distributed under the Creative Commons Attribution License, which permits unrestricted use, distribution, and reproduction in any medium, provided the original work is properly cited.

Editorial Board

- János G. Ángyán, France
M. Sabry Abdel-Mottaleb, Egypt
Taicheng An, China
J. A. Anderson, UK
Panos Argyrakis, Greece
Ricardo Aroca, Canada
Stephen H. Ashworth, UK
Biman Bagchi, India
Hans Bettermann, Germany
Vasudevanpillai Biju, Japan
Joel Bowman, USA
Wybren J. Buma, The Netherlands
Sylvio Canuto, Brazil
Li Ming Dai, USA
Michael Deleuze, Belgium
Michael Dolg, Germany
D. James Donaldson, Canada
Ali Eftekhari, USA
Gregory S. Ezra, USA
Claudio Fontanesi, Italy
Michael J. Frisch, USA
Paul Geerlings, Belgium
Robert Gerber, Israel
Jinlong Gong, China
David Wayne Goodman, USA
Vicki H. Grassian, USA
Lawrence Harding, USA
David Brynn Hibbert, Germany
Kimihiko Hirao, Japan
Paul L. Houston, USA
Jyh-Ping Hsu, Taiwan
- F. Illas, Spain
Kwang S. Kim, Republic of Korea
Bernard Kirtman, USA
Lowell D. Kispert, USA
Marc Koper, The Netherlands
Alexei A. Kornyshev, UK
Yuan Kou, China
David Logan, UK
Clare M. McCabe, USA
James K. McCusker, USA
Michael L. McKee, USA
Robert M. Metzger, USA
Michael V. Mirkin, USA
David Muddiman, USA
Klaus Mullen, Germany
Daniel Neuhauser, USA
Konstantin Neyman, Spain
Minh Tho Nguyen, Belgium
Hiroshi Onishi, Japan
Thomas Oppenlaender, Germany
Samir K. Pal, India
Leonardo Palmisano, Italy
Francesco Paolucci, Italy
Jan Skov Pedersen, Denmark
Piotr Piecuch, USA
M. P. Pileni, France
Simon M. Pimblott, UK
Oleg Prezhdo, USA
Colin Raston, Australia
Benjaram M. Reddy, India
Ranko Richert, USA
- Eli Ruckenstein, USA
Gnther Rupprechter, Austria
Kenneth Ruud, Norway
Viktor A. Safonov, Russia
Dennis Salahub, Canada
Anunay Samanta, USA
Dipankar Das Sarma, India
Joop Schoonman, The Netherlands
Stefan Seeger, Switzerland
Tamar Seideman, USA
Hiroshi Sekiya, Japan
Luis Serrano-Andrés, Spain
Michael D. Sevilla, USA
C. David Sherrill, USA
Kenneth Showalter, USA
Karl Sohlberg, USA
Miquel Solà, Spain
Vasco Teixeira, Portugal
Sergei Tretiak, USA
Thanh N. Truong, USA
Frantisek Turecek, USA
P. Unwin, UK
Eric Vauthey, Switzerland
David Wales, UK
Peter Wolynes, USA
Qiang Xu, Japan
Yigzaw G Yohanis, UK
Jeffrey M. Zaleski, USA
Ruhong Zhou, USA

Contents

Advances in Electrocatalysis, Milan M. Jaksic, Wolfgang Schmickler, and Gianluigi Botton
Volume 2012, Article ID 180604, 4 pages

Fundamental Mechanistic Understanding of Electrocatalysis of Oxygen Reduction on Pt and Non-Pt Surfaces: Acid versus Alkaline Media, Nagappan Ramaswamy and Sanjeev Mukerjee
Volume 2012, Article ID 491604, 17 pages

Multiscale Modeling of Au-Island Ripening on Au(100), Karin Kleiner, Aleix Comas-Vives, Maryam Naderian, Jonathan E. Mueller, Donato Fantauzzi, Mostafa Mesgar, John A. Keith, Josef Anton, and Timo Jacob
Volume 2011, Article ID 252591, 11 pages

Spillover Phenomena and Its Striking Impacts in Electrocatalysis for Hydrogen and Oxygen Electrode Reactions, Georgios D. Papakonstantinou, Jelena M. Jaksic, Diamantoula Labou, Angeliki Siokou, and Milan M. Jaksic
Volume 2011, Article ID 412165, 22 pages

Sequential Electrodeposition of Platinum-Ruthenium at Boron-Doped Diamond Electrodes for Methanol Oxidation, Ileana González-González, Camille Lorenzo-Medrano, and Carlos R. Cabrera
Volume 2011, Article ID 679246, 10 pages

Contrast and Synergy between Electrocatalysis and Heterogeneous Catalysis, Andrzej Wieckowski and Matthew Neurock
Volume 2011, Article ID 907129, 18 pages

Platinum Monolayer Electrocatalysts for the Oxygen Reduction Reaction: Improvements Induced by Surface and Subsurface Modifications of Cores, Yun Cai and Radoslav R. Adzic
Volume 2011, Article ID 530397, 16 pages

Potentiostatic Testing of Oxygen Reduction on Polymer Carbon Electrodes, C. A. C. Sequeira and D. M. F. Santos
Volume 2011, Article ID 414108, 12 pages

Recent Developments of Nanostructured Electrodes for Bioelectrocatalysis of Dioxygen Reduction, Marcin Opallo and Renata Bilewicz
Volume 2011, Article ID 947637, 21 pages

FeCr₂O₄ Nanoparticles as Anode Catalyst for Ethane Proton Conducting Fuel Cell Reactors to Coproduce Ethylene and Electricity, Jian-Hui Li, Xian-Zhu Fu, Gui-Hua Zhou, Jing-Li Luo, Karl T. Chuang, and Alan R. Sanger
Volume 2011, Article ID 407480, 6 pages

Nanoporous PdCo Catalyst for Microfuel Cells: Electrodeposition and Dealloying, Satoshi Tominaka and Tetsuya Osaka
Volume 2011, Article ID 821916, 13 pages

Hydrogen Adsorption on Palladium and Platinum Overlayers: DFT Study, Igor A. Pašti, Nemanja M. Gavrilov, and Slavko V. Mentus
Volume 2011, Article ID 305634, 8 pages



Synthesis, Characterization, and Electrochemical Study of Tetradentate Ruthenium-Schiff Base Complexes: Dioxygen Activation with a Cytochrome P450 Model Using 1- or 2-Methylimidazole as Axial Bases, Ali Ourari, Mostefa Khelafi, Djouhra Aggoun, Gilles Bouet, and Mustayeen A. Khan
Volume 2011, Article ID 157484, 11 pages

Recent Progress in Hydrogen Electrocatalysis, P. Quaino, E. Santos, G. Soldano, and W. Schmickler
Volume 2011, Article ID 851640, 14 pages

Editorial

Advances in Electrocatalysis

Milan M. Jaksic,^{1,2} Wolfgang Schmickler,³ and Gianluigi Botton⁴

¹ Institute of Chemical Engineering and High Temperature Chemical Processes-Patras, FORTH, 26500 Patras, Greece

² Institute of Food Technology, Faculty of Agriculture, University of Belgrade, 11080 Belgrade, Serbia

³ Institute of Theoretical Chemistry, Ulm University, 89081 Ulm, Germany

⁴ Department of Material Science and Engineering and Canadian Centre for Electron Microscopy, McMaster University, Hamilton ON, Canada L8S4M1

Correspondence should be addressed to Milan M. Jaksic, milan@iceht.forth.gr

Received 25 December 2011; Accepted 25 December 2011

Copyright © 2012 Milan M. Jaksic et al. This is an open access article distributed under the Creative Commons Attribution License, which permits unrestricted use, distribution, and reproduction in any medium, provided the original work is properly cited.

“All the ideas that have enormous consequences are always simple ideas.”
(LEV TOLSTOI).

Electrocatalysis and search for promising electrocatalysts effectively started its development after two distinct core reveals in the science: (i) Sir William Grove inventive discovery and theoretical definition of (H₂/O₂) fuel cells and their fundamental structure in 1842 and (ii) Tafel plots in the year 1905, when various metals were distributed and ranged on the $\eta = a - b \log j$ coordination chart, with clear distinction amongst good and bad, or, on more or less *polarizable*, mostly transition elements or their composite electrode materials. In fact, until now the main criterion to characterize electrocatalysts has been primarily based on the Tafel plot assessed polarization and exchange current density, certainly now advanced for the atomic or nanolevel characterization of the actual catalytic surface and theoretical search for their interrelating correlations. There on the first place comes the density functional theory (DFT) and calculations (DFCs), where primarily *d*-band density of states is correlated with electrocatalytic activity.

The most intensive growth of the field of electrocatalysis effectively started in the earliest 1960s and continuously further grows with exponential trend in the number of the highest level published papers and studies. Thus, many authors have been in search to find and reveal the first electrochemist who introduced the term electrocatalysts or electrocatalysis in the electrochemical science, for the priority in creating the field. By this way, we usually find some

almost unknown names, who never enriched electrocatalysis with any substantial theoretical contributions, and it is clear that much earlier electrochemical science named such achievements as—*depolarization*, the term, which almost disappeared after introducing the name electrocatalysis, otherwise the latter being in good relation with the more general field of heterogeneous catalysis, though these have so far never been officially integrated in the science. In other words, these two fields are based on the same fundamental kinetic parameters, both recognize the energy or enthalpy of activation, but the main separation line comes from polarization itself and broad meaning of the electrochemical activation energy. Heterogeneous catalysis is the science for almost a century preceding electrocatalysis, participates with a higher-order number of creative scientists, mostly leads within chemical branches, and we never succeeded to gather together on a meeting to consider two fields: heterogeneous catalysis and electrocatalysis, their common points and specific differences. The point is that polarization is the basic parameter, key variable, and main criterion in electrocatalysis, but not the common point of any significance for catalysis at all, and the state-of-the art still besides the hydrogen electrode reactions and some less significant in metal deposition, electrochemical science, while missing many additional decisive parameters and complementary criteria in electrode kinetics, so far failed to resolve any

decisive and significant mechanism, the first of all but not the most important in aqueous media for the oxygen electrode reactions. In fact, there exists one common point—the electrochemical promotion of catalysts (EPOCs), when by imposed external polarization and negligible Faradaic current flow, one alters work function of heterogeneous catalyst, and in some issues this way dramatically increases the actual proceeding reaction rate and/or the excited catalytic activity. Meanwhile, except some individual issues, these two fields never found any motive to strengthen their creative forces and capacities, and proceed together.

The main imperative guiding aim, challenge, and purpose of electrocatalysis are associated with aqueous media, and founded on hydrogen and oxygen electrode reactions, to substantiate the main target—*hydrogen energy*. Hydrogen as an ideal (sustainable, renewable, inexhaustible, and environmentally clean) fuel might establish the reversible interrelation between the matter and energy in the nature: to return exactly, in the same shape and amounts, what is previously taken from, water to water, and thence make all states and nations in the world equal and independent in energy sources and needs. Since hydrogen does not exist in any significant free state in the Earth, while its water sources are unlimited, to produce hydrogen by electrolysis and subsequently use as a fuel in L&MT PEMFCs, implies remarkable polarization losses in both directions, while in an ideal issue, one tends to approach reversibly balanced input and output. Photovoltaic electrocatalytic solar generation of hydrogen, as being substantially based on the inexhaustible free energy source, certainly could prevailingly and even completely compensate both the polarization inputs for its nominal production by electrolysis and overvoltage in fuel cells. By this way, the overall energy balance even might be effectively brought within the apparent reversible framework between hydrogen evolution and fueling in PEMFC. Unfortunately, although advanced photovoltaic solar electrocatalysis is doubtless still the best promising inexhaustible conversion energy source, it is yet faraway from its economical substantiation. All other aspects in PEMFC energy conversion and generation belong to electrocatalysis. Meanwhile, regardless tremendous fascinating progress in PEMFC electrocatalysts, except for some specific applications, such as in the space program, when the energy losses and profits are of secondary significance, in electrocatalysis for energy conversion we face all the time the same substantial problems and in many aspects still stay on the same positions, where initially was sir William Grove himself.

Mostly, electrochemists use to state that only Pt and its modifications satisfy requirements for electrocatalysts in PEMFCs energy conversion. Amongst so many transition metals this is a rather sad conclusion, and even more so, since even Pt itself prevailingly fails to satisfy the basic electrocatalytic requirements in approaching or establishing the operating reversible potential values. In other words, all energy diagrams so far scanned from LT PEMFCs show the sharp potential drop from almost reversible oxygen electrode value down to a plateau at about 0.6 V versus RHE, or the energy waste for more than a half of theoretically available amount. Cyclic voltammograms, meanwhile, in

addition indicate that the established stable potential range in the energy conversion coincides and corresponds to the reversible adsorption-desorption peaks location of the primary oxide (Pt-OH) so that the polarization determining species (PDS) or the main obstacle is the surface oxide (Pt=O). There has so far practically been done nothing in such a respect to double the converted energy yields of hydrogen feeding fuel cells and/or effectively reduce the number of unit cells for more than a half and still keep the same theoretically available capacity. Some alloying transition metals (Co, Ni, and Fe) succeed to reduce the interatomic Pt-Pt distance, this way weakening Pt=O adsorptive bonds and thereby increasing a little the overall electrocatalytic activity. The externally induced Pt-OH spillover effect and its interference with Pt=O promises to shift the plateau in the conversion energy diagram to the more positive potential range for the ORR, and these both have traced some paths towards the reversible oxygen electrode, so far never attained (accessed) experimentally, just because of the polarization imposed by the surface oxide (Pt=O). Otherwise, instead of two actual contemporary fuel cells running roughly at 0.6 V in energy source, one might theoretically operate with the one unit of about doubled capacity (about 1.2 V), and it has been the main target in electrocatalysis for more than a century. The expectances from such similar and new approaches have been the main purpose and task to initiate the present “*Advances in Physical Chemistry*” (APC) special issue and try to sum up or reveal eventual new trends and new advances in contemporary and forthcoming age in electrocatalytic science. Unfortunately, scientific papers are usually and mostly written on an affirmative and seldom critical manner to reveal and highlight main obstacles and unresolved problems, while the latter when clearly specified, usually impose some stimulant trends and inspirations for new forthcoming generations to substantiate them.

The discouraging fact is that even if electrochemical science succeeds to resolve all just discussed kinetic and electrocatalytic problems and enable us to use the entire theoretically available voltage of the cell composed from hydrogen and oxygen electrodes, Pt nevertheless might effectively impose serious economical problems when employed as the electrocatalyst in PEMFC for massive car traction. In other words, if all vehicles in the actual world would turn on hydrogen fuel and PEMFC driving force, Gordon Conference for such purposes already estimates its annual necessity of hundreds tons. In other words, something that amounts from 20 to even 30 percent of the actual annual production (roughly about 20,000 tons) worldwide. In such circumstances Pt price might be remarkably increased, while Pt still could be employed, in particular with providing more than 85 percent of its recovery and decreasing its loading (the lowest might be about $60 \mu\text{g cm}^{-2}$ of geometric surface). The alternative way would be PEMFC with alkaline membrane and cheaper and more available electrocatalysts (Ni, Co, and Ag), but with relatively higher polarization.

Two main breakthroughs in the preceding century fundamentally advanced and enriched electrochemical science, engineering, and technology: cationic selective membranes (DuPont’s Nafion and/or Asahi Glass Flemion), sustainable

in most severe production conditions (chlorine and chlorate cells), and simplified titanium metal electrowinning, as a cheap and unique constructive material in chemical industry, and ideal carrier for electrocatalysts in most significant and massive industrial electrochemical processes. Initially, one inventive man and his named enterprise (Oronzio de Nora Company, Milan, Italy) developed and granted to the existing world all the leading optimized industrial model cells for unlimited scale-up in electrolysis (chloralkali, classical and membrane type cells, chlorate production, water splitting, hydrochloric acid electrolysis, etc.), and even more so, were the first to launch RuO₂/TiO₂ mixed oxide electrocatalyst on Ti carrying electrodes, today the most massive and most important electrocatalytic production worldwide (more than 30 Mio tons capacity annually). Along with equally efficient electrocatalysts for the HER, membrane cells operate now almost at the reversible hydrogen and chlorine electrode potentials. Meanwhile, De Nora Company successfully introduced electrocatalysts for the ORR, to replace the HER, and succeeded to save for about 0.8 volt for producers who prefer energy savings instead of the industrial hydrogen evolution in hydrochloric acid and chloralkali electrolysis. Such general statements reliably testify for the remarkable progress, tremendous outstanding achievements and unpredictable prospects of electrocatalysis in industrial electrochemical processes, particularly in organic electrosynthesis. Thus, it might be interesting to stress that such significant and massive industrial electrocatalytic processes do not represent electrocatalysts developed or invented by the leading research centers or recognized universities and leading electrochemists in the world of science, but engineers in factories who intensely live with and experience an intimate relation with everyday occurrences in practice.

Main Papers Hints. A unified electrocatalytic (W. Schmickler et al.) model for electrochemical electron transfer reactions, primarily focused on the electrochemical adsorption of a proton from the solution—the Volmer reaction—on a variety of systems, such as bare single crystals and foreign metal on a variety of (111)-substrates, nanostructured surfaces that explicitly account for the electronic structure of the electrode, and provides a framework describing the whole course of bond-breaking electron transfer, enabled to explain catalytic effects caused by the presence of surface *d*-bands, and in application to real systems, the parameters of this model—interaction strengths, densities of states, and energies of reorganization were obtained from density functional theory (DFT) enabling to discuss in details the interaction of the surface metal *d*-band with the valence orbital of the reactant and its effect on the catalytic activity, as well as other aspects that influence the surface-electrode reactivity, such as strain and chemical factors, the hydrogen electrocatalysis thence being substantially founded on the theory and not on a correlations, the entire goal being to combine DFT and new author theory to elucidate the electronic structure, predict and prove the catalytic activity. Consequent and farreaching consequences of the DFT applications are complementarily presented by S. Mentus et al.

Since fundamental information concerning reaction mechanisms, active sites, and catalytic kinetics gleaned from in situ spectroscopy and provided detailed resolution of the molecular transformations of bond making and bond breaking acts that occur at both gas/metal and solvent/metal interfaces, this became the link and great step ahead to allow a more direct comparison, interrelations, and guidance of heterogeneous catalysis and electrocatalysis and crosscut both areas (A. Wieckowski and M. Neurock). In other words, the knowledge of the complex electrified interfaces, the nature of active centers and their environment in electrocatalysis bears a number of common similarities to the aqueous/metal interfaces for catalytic reactions. Advances in spectroscopy allowed opening the common field for more detailed resolution of the molecular transformations that occur in electrocatalytic systems, along with a more detailed introspection of the nature of the active centers and their environment, compared, contrasted, and interrelated them.

Core/shell Pt monolayer (Pt_{ML}) electrocatalysts for the ORR originally developed (R. Adzic et al.) and introduced in electrocatalysis, and further advanced by the modification of surface and subsurface of the core materials, involving the changes on both electronic (ligand) and geometric (strain) properties, primarily use the strain effect (compression on Pd and tensile on Au cores) to induce the shift of *d*-band center as the primary factor to increase the synergy in catalytic activity, while providing each individual Pt atom to be involved in the reaction and keep minimal Pt loading in electrocatalysis. Such an exact monolayer core-shell type of electrocatalysts has dramatically reduced Pt catalyst load relative to the common Pt/C issues and in some inventions increased catalytic activity for more than an order of magnitude.

Complex multielectron transferring mechanism of the ORR as an electrocatalytic innersphere electron transfer process exhibiting strong dependence on the nature of the electrode surface imperatively requires the stability in acidic media and unavoidably imposes the Pt-based limits, in contrast to the involvement of surface-independent outersphere electron transfer component in the overall electrocatalytic process characteristic for alkaline solutions, so that such a surface nonspecificity gives rise to the possibility of employing a wide range of nonnoble metal surfaces as electrocatalytic materials for ORR, while then the whole electrode reaction predominantly leads only to a 2e peroxide intermediate as the final product (N. Ramaswamy and S. Mukerjee). The promoting of the electrocatalytic innersphere electron transfer mechanism by facilitation of direct adsorption of molecular oxygen on the active site has been emphasized with the usage of pyrolyzed biomimetic metal porphyrins as electrocatalysts, while the primary kinetic advantage of performing ORR in alkaline media was found to be the improved stabilization of the peroxide intermediate on the active sites.

Since altermultivalent hypo-d-oxides impose spontaneous dissociative adsorption of water molecules and then pronounced membrane transferring properties, instantaneously resulting with corresponding bronze type (Pt/H_xWO₃) for fast H-adatoms spillover under cathodic, and/or its hydrated state (Pt/W(OH)₆), responsible for Pt-OH effusion,

under anodic polarization, this way establishes instantaneous reversible alterpolar bronze features (or, the specific equilibrium, $\text{Pt}/\text{H}_{0.35}\text{WO}_3 \rightleftharpoons \text{Pt}/\text{W}(\text{OH})_6$), and substantially advanced electrocatalytic properties of these composite interactive electrocatalysts ($\text{Pt}/\text{Nb}_2\text{O}_5, \text{TiO}_2/\text{C}$; $\text{Pt}/\text{WO}_3, \text{TiO}_2/\text{C}$; $\text{Pt}/\text{Ta}_2\text{O}_5, \text{TiO}_2/\text{C}$) for all four hydrogen and oxygen electrode reactions (HER, HOR, ORR, and OER), therefrom consequently resulted mutually interchangeable catalysts for the ideal reversible cell between PEMFC and WE (G. D. Papakonstantinou et al.). Spillover phenomena of interchangeable H-adatoms and the primary oxide ($\text{Pt}-\text{OH}$) have been thoroughly enlightened by various sophisticated contemporary methods and proven as the additional dynamic effect in both electrocatalysis and double-layer charging.

Nanostructured electrodes for bioelectrocatalytic dioxygen reduction catalysed by two copper oxidoreductases: laccase and bilirubin oxidase have recently been developed and introduced as new trend in enzymatic biocatalysis, formerly employed on carbon nanotubes or nanoparticulate carbon carriers, and recently advanced in new nanosized architecture, as conductive metal oxide supports (M. Opallo and R. Bilewicz). Such electrocatalytic nanomaterials are usually adsorbed on the carrying electrode surface or embedded in multicomponent film, and these adsorptive interbonded nanoobjects act as electron shuttles between the enzyme and the electrode substrate providing favourable conditions for mediatorless bioelectrocatalysis. In the latter case, a different mechanism of electron transfer is operative: based on electronic conductivity and not on the redox processes of the mediator, and consequently, nanoparticulate film biocathodes feature mediatorless bioelectrocatalytic effect and current densities competitive with those achieved using osmium polymers (up to 4 mA cm^{-2}).

Nanostructured PdCo alloy electrochemically deposited microelectrodes upon Au substrates, partially dealloyed in the next step to introduce nanopores and produce a rather promising electrocatalyst of highly developed nanointegrated surface, and thereby advanced activity for the ORR, superior relative to Pt/C nanosized issues, has been originally created primarily for the on-chip membraneless microfuel cells, flexible and integratable with other micro-devices in direct methanol fuel cells, suitable because of its nanostructure and therefrom resulting properties of the unique high-catalytic activity and the tolerance to methanol (S. Tominaka and T. Osaka).

Protonic perovskite oxides were introduced as proton conducting ceramic SOFC electrolytes in place of oxide ion conductors so that operating temperature could be reduced from very high to moderate or low levels. At these less stringent conditions, the SOFCs are capable of cogeneration of energy and valuable industrially important chemical products. In particular, ethylene is selectively manufactured from ethane in a fuel cell reactor using on FeCr_2O_4 anode electrocatalyst, $\text{BaCe}_{0.7}\text{Zr}_{0.1}\text{Y}_{0.2}\text{O}_{3-\delta}$ (BCZY) perovskite oxide as the proton conducting ceramic electrolyte, and nanostructured $\text{La}_{0.7}\text{Sr}_{0.3}\text{FeO}_{3-\delta}$ (LSF) as cathode catalyst, with efficient production of DC energy. The power density increases from 70 to 240 mW cm^{-2} , and the ethylene yields from about

14.1% to 39.7% when the operating temperature of the fuel cell reactor increases from 650°C to 750°C (Jingli Luo et al.).

Using a multiscale modeling approach, the ripening of monoatomically high Au islands on Au(100) has been studied (T. Jacob et al.). Starting at the microscopic scale, DFT was used to investigate a limited number of self-diffusion processes on perfect and imperfect Au(100) surfaces. This provided the necessary information to generate a reactive molecular dynamics forcefields that was finally used to create an extended process database for subsequent kinetic Monte Carlo studies. This provides important information on effects such as nucleation, aggregation, fluctuation, and the equilibrium shape structures of these islands on Au(100). Further, this hierarchical approach should also be applicable to address other questions related to the characterization of electrocatalyst surfaces.

Other papers in the present issue deal less with electrocatalytic aspects of general significance, but perfectly resolve some individual and specific aims and tasks, and enrich the overall field.

*Milan M. Jaksic
Wolfgang Schmickler
Gianluigi Botton*

Review Article

Fundamental Mechanistic Understanding of Electrocatalysis of Oxygen Reduction on Pt and Non-Pt Surfaces: Acid versus Alkaline Media

Nagappan Ramaswamy and Sanjeev Mukerjee

Laboratory for Electrochemical Advanced Power, Department of Chemistry and Chemical Biology, Center of Renewable Energy Technology (NUCRET), Northeastern University, 360 Huntington Avenue, Boston, MA 02115, USA

Correspondence should be addressed to Sanjeev Mukerjee, s.mukerjee@neu.edu

Received 2 October 2011; Accepted 22 December 2011

Academic Editor: Milan M. Jaksic

Copyright © 2012 N. Ramaswamy and S. Mukerjee. This is an open access article distributed under the Creative Commons Attribution License, which permits unrestricted use, distribution, and reproduction in any medium, provided the original work is properly cited.

Complex electrochemical reactions such as Oxygen Reduction Reaction (ORR) involving multi-electron transfer is an electrocatalytic inner-sphere electron transfer process that exhibit strong dependence on the nature of the electrode surface. This criterion (along with required stability in acidic electrolytes) has largely limited ORR catalysts to the platinum-based surfaces. New evidence in alkaline media, discussed here, throws light on the involvement of surface-independent outer-sphere electron transfer component in the overall electrocatalytic process. This surface non-specificity gives rise to the possibility of using a wide-range of non-noble metal surfaces as electrode materials for ORR in alkaline media. However, this outer-sphere process predominantly leads only to peroxide intermediate as the final product. The importance of promoting the electrocatalytic inner-sphere electron transfer by facilitation of direct adsorption of molecular oxygen on the active site is emphasized by using pyrolyzed metal porphyrins as electrocatalysts. A comparison of ORR reaction mechanisms between acidic and alkaline conditions is elucidated here. The primary advantage of performing ORR in alkaline media is found to be the enhanced activation of the peroxide intermediate on the active site that enables the complete four-electron transfer. ORR reaction schemes involving both outer- and inner-sphere electron transfer mechanisms are proposed.

1. Introduction

Oxygen reduction reaction (ORR) on noble and nonnoble metal surfaces remains as one of the well-investigated electrochemical processes. While under acidic conditions Pt-based systems remain the mainstay as catalyst materials for ORR, in alkaline electrolyte a wide range of nonnoble metals and their oxides are stable enough for practical applications [1, 2]. *ORR pathway rather than ORR mechanism* has typically been addressed in the literature due to the easy accessibility of the former from rotating ring-disk electrode (RRDE) studies, and the complexity in understanding the latter [3]. ORR pathway is found to be similar in both acid and alkaline media on Pt-based materials [3, 4]. Based on the initial propositions by Damjanovic et al. [4–6], rate determining step (*rds*) on Pt electrodes is widely agreed to

be the first electron transfer step to the adsorbed molecular O₂ with or without rapid proton transfer [4–6]. A major alternative viewpoint to *rds* in ORR was proposed by Yeager et al. [7], wherein it was proposed that ORR on Pt surfaces is likely to involve dissociative chemisorption of molecular O₂ with the initial adsorption of O₂ (with or without an electron transfer) as the *rds*. ORR on Pt-based catalysts is understood to proceed via “parallel” routes with the 4e⁻ “direct” or “series” pathway as the predominant route and a minor route involving 2e⁻ pathway to peroxide. Various kinetic models for ORR have been developed to understand the reaction pathways. The first model was developed by Damjanovic et al. [8] following which Wroblowa et al. [9], and Anastasijević et al. [10, 11], proposed extensive models.

For electrocatalytic reactions proceeding via inner-sphere electron transfer mechanism, it is typically assumed that

either molecular adsorption of reactant species (dissociatively or nondissociatively) or an electron transfer is the first step [12]. For neutral, nonpolar species like molecular O_2 , direct molecular O_2 adsorption is likely to be inhibited relative to, for example, the adsorption of charged superoxide radical anion ($O_2^{\bullet-}$) unless the free energy of adsorption of O_2 molecule is very exothermic on a specific catalyst surface. This is especially true under fuel cell conditions, where the cathodic reaction typically occurs at potentials well positive of the potential of zero charge (pzc). Multistep, multielectron transfer processes like ORR that involves many adsorbed intermediates are undoubtedly classified as an inner-sphere electron transfer reaction. However, among the many elementary reaction steps involved in ORR, there could be a *surface-independent outer-sphere electron transfer component* in the overall electrocatalytic $4e^-$ inner-sphere electron transfer reaction. In that perspective, O_2 reduction by one-electron transfer to superoxide ($O_2^{\bullet-}$) is observed at $E^\circ = -0.3 \pm 0.03$ V versus SHE corresponding to $\Delta G^\circ = 30 \pm 2$ kJ mol $^{-1}$ with both O_2 and $O_2^{\bullet-}$ remaining in the aqueous phase [13, 14]. Given the pH independence of this redox couple ($O_2/O_2^{\bullet-}$), the potential of this reaction does not change as the pH is varied from zero to fourteen [15]. Due to the occurrence of four proton transfer steps in O_2 reduction to H_2O/OH^- , its standard reduction potential changes by 0.828 V from 1.229 V to 0.401 V versus SHE as the pH value changes from zero to fourteen. This causes the overpotential for the first electron transfer step ($O_2/O_2^{\bullet-}$) to decrease from 1.53 V at pH = 0 to 0.7 V at pH = 14 indicating a sharp decrease in overpotential at alkaline pH conditions. Blizanac et al. [15] argued based on a modified Pourbaix diagram approach that the above-mentioned decrease in overpotential is the primary thermodynamic reason for the applicability of a wide range of nonnoble materials in alkaline media. Due to the high overpotential required for $O_2/O_2^{\bullet-}$ redox couple in acidic media, only certain specific catalyst surfaces such as platinum that offer high free energy of adsorption for O_2 can catalyze ORR in acidic media. While the decrease in overpotential for the first electron transfer in alkaline media is certainly significant, this argument is primarily of thermodynamic origin. The concept of involving the possibilities of outer-sphere electron transfer during ORR in alkaline media bears importance, and it was pointed out earlier by Bockris [16] and Appleby [17] that the exchange current density values in alkaline media exhibit near independence on a large number of electrode materials including silver, gold, manganese oxides, perovskites, and various carbon surfaces. So certain steps in the overall ORR process in alkaline media could proceed via a non-electrocatalytic mechanism [17].

The drive to replace expensive and scarce Pt-based catalysts for ORR has led to a class of electrocatalysts composed of first-row transition-metal ions stabilized by surface nitrogen functionalities on graphitic surfaces [2, 18–21]. The nature of the active site (obtained after heat treatment) in terms of its location on the carbon support (edge versus basal plane) [22], coordination number (Fe- N_4 versus non-Fe- N_4 environment) [23], and chemical identity of the nitrogen functional groups (pyridinic, pyrrolic, and quaternary) [24]

have remained a key aspect of intense discussion. Several theories exist to explain the nature of the active site such as those proposed by van Veen et al. [25–27], McBreen et al. [28], Schulenburg et al. [29], Yeager et al. [2, 30], Scherson et al. [31–33], and Dodelet et al. [22, 34–45]. Although some authors observed that ORR is conducted by sites comprised of surface nitrogen groups devoid of any metal ion centers [46, 47], it is now widely accepted that the transition-metal ion centers coordinated to four nitrogen groups (Me- N_4) on graphitic surfaces constitute the active site [22, 23, 30, 48], whereas chelation primarily serves to prevent the metal center from passivation/corrosion under electrochemical conditions [49]. Besides the exact structure of the active site, the low active site density or the metal loading that is obtained in these catalysts eludes clear understanding. A maximum in catalytic activity is obtained at a very low metal loading (~ 5000 ppm by weight for inorganic precursors and ~ 2 wt% for macrocycle precursors) [35]. Dodelet et al. [50] suggested that only the microporosity generated during pyrolysis upon gasification of disordered carbon content acts as a host for active sites. Irrespective of whatever the exact nature of the active site is, this does not necessarily explain the fundamental origin of ORR activity in this class of heat-treated catalysts. It was recently pointed out by Bezerra et al. [51] and Garsuch et al. [52] that most studies on this class of materials have focused on the optimal synthesis conditions and structure necessary for maximum activity, whereas a more fundamental understanding will be of great help in developing innovative routes for new catalyst synthesis.

In this paper, we present a systematic study of ORR reaction mechanisms on Pt and non-Pt surfaces. Fundamental reasons for the so-called kinetic facility of ORR in alkaline media are investigated from the perspectives of the changes in the double-layer structure and the reaction mechanisms in transitioning from acidic to alkaline conditions. New evidence unraveling the influences of inner-sphere and outer-sphere electron transfer mechanisms during ORR is elucidated. Besides the efforts to understand the nature of the active site in heat-treated metal macrocycle-based catalysts, a combination of electrochemical and advanced X-ray absorption spectroscopy techniques has been utilized to understand (1) the fundamental origin of electrocatalytic ORR activity upon heat treatment and (2) the reasons for the low density of active metal sites. To this end, a comparative study of ORR on Pt and non-Pt surfaces in both acid and alkaline media has been performed to (1) analyze the influence of both inner-sphere and outer-sphere electron transfer mechanisms, (2) elucidate the ORR reaction mechanisms, and (3) understand the importance of stabilization of the reaction intermediates on the active site.

2. Experimental

2.1. Electrochemical Characterization. All electrochemical measurements were made at room temperature using a rotating ring-disk electrode (RRDE) setup from Pine Instruments connected to an Autolab (Ecochemie Inc., model-PGSTAT 30) bipotentiostat. Alkaline (0.1 M NaOH) and acidic (0.1 M HClO $_4$) electrolytes were prepared using sodium

hydroxide pellets (semiconductor grade, 99.99%, Sigma-Aldrich) and double-distilled 70% perchloric acid (GFS Chemicals), respectively. 30% Pt/C catalyst from BASF-ETEK (Somerset, NJ) was used as received. Ru/C catalyst was synthesized in-house via aqueous route at a metal loading of 20% by weight [53]. Iron(III) meso-tetraphenylporphyrin chloride (FeTPPCL) was procured from Alfa Aesar. FeTPPCL was mixed with Black Pearl carbon in the mass ratio 1 : 4 and ball milled for 2 hours at 400 rpm followed by pyrolysis at 800°C for 2 hours under argon atmosphere. Catalyst inks were prepared by dispersing 25 mg of the catalyst in 10 mL of 1 : 1 millipore H₂O : isopropyl alcohol mixture along with 100 μ L of 5 wt% Nafion^(R) solution as a binder. 10 μ L aliquot of the catalyst ink was dispensed on Glassy Carbon (GC) disk of 5.61 mm dia. Gold ring electrode was held at 1.1 V versus RHE in alkaline electrolyte and at 1.3 V versus RHE in acidic electrolyte to detect stable peroxide intermediate. Collection efficiency of the disk-ring electrode was 37.5%. All potentials are referred to reversible hydrogen electrode (RHE) scale prepared from the same solution as the bulk electrolyte unless otherwise stated.

2.2. X-Ray Absorption Spectroscopic (XAS) Measurements.

The *in situ* XAS studies at Fe K-edge (7112 eV) were performed at X19A beamline of National Synchrotron Light Source (NSLS, Brookhaven National Laboratory, NY). Detailed information on the spectroelectrochemical cell design are given elsewhere [54]. Spectra at Fe K-edge were collected in fluorescence mode using a PIPS detector. Argon- or oxygen-saturated 0.1 M NaOH was used as the electrolyte. Complete details on data analysis of X-ray absorption near edge structure (XANES) and extended X-ray absorption fine structure (EXAFS) are available elsewhere [54]. Typical k-range window during EXAFS fit was 2.500–12.500 \AA^{-1} (Kaiser-Bessel). Data analysis for Delta-mu ($\Delta\mu$) studies at Fe K-edge involved specific normalization procedures detailed elsewhere [54, 55]. Briefly, this involves careful calibration of edge energy (Fe K-edge 7112 eV), alignment to standard reference scan to account for any drift in the beam energy. A postedge normalization procedure was then applied to the aligned scans via a cubic spline function which normalizes the oscillations over a specific energy range (typically 25 to 200 eV with respect to E_0) on a per-atom basis. Difference spectra were obtained using the equation $\Delta\mu = \mu(V) - \mu(0.1\text{ V})$, where $\mu(V)$ is the XANES spectra of the catalyst at various potentials and $\mu(0.1\text{ V})$ is the reference XANES signal at 0.1 V at which potential no evidence for electrochemical adsorbates (H_{upd} , O_{ads} , OH_{ads}) were found on iron-based catalysts. Theoretical delta-mu curves ($\Delta\mu_t$) were constructed using the FEFF 8.0 code [56]. This was accomplished using the relationship $\Delta\mu_t = \mu(\text{O}_{\text{ads}}\text{-Fe-N}_x\text{-C}) - \mu(\text{Fe-N}_x\text{-C})$, where the oxide species (O_{ads} or OH_{ads}) is in a specific binding site on Fe.

3. Results and Discussions

3.1. ORR on Carbon-Supported Platinum Nanoparticles: Acid versus Alkaline Media. Figure 1 provides a snapshot of the cyclic voltammetry (CV) and ORR on 30% Pt/C in 0.1 M

NaOH and 0.1 M HClO₄ electrolytes. As shown in Figure 1(a), CV of 30% Pt/C catalyst features the typical hydrogen underpotential deposition/stripping region below 0.5 V versus RHE in both of the electrolytes followed by oxide formation on Pt at potentials above 0.7 V versus RHE. Oxide formation on Pt in acidic media is due to oxidation of the solvent water molecules (water activation) [57] and in alkaline media is due to specific adsorption of hydroxide anions from the supporting electrolyte [58, 59]. The onset potential of Pt-OH formation is similar in both electrolytes, although in alkaline media oxide formation current exhibits a characteristic peak shape whereas in acidic media oxide formation current is relatively more flat. Half-wave potential ($E_{1/2}$) of Pt-OH in 0.1 M NaOH is 0.775 V whereas in 0.1 M HClO₄ $E_{1/2}$ of Pt-OH formation is shifted slightly more positive to 0.810 V. Figure 1(b) shows the ring current measured during ORR on Pt/C at 900 rpm in 0.1 M HClO₄ and 0.1 M NaOH. The corresponding ORR polarization curves are shown in the inset of Figure 1(b). The ORR onset potential in both of the electrolytes is \sim 1 V versus RHE which is followed by mixed kinetic-diffusion region between the potentials 0.7 V and 1 V. Well-defined diffusion-limited current density region is observed below 0.6 V versus RHE. The marginally higher Pt-OH coverage in alkaline media (between the potential region of 0.9 V to 0.8 V versus RHE) causes a penalty of \sim 25 mV higher overpotential at a kinetic current density of $i_k = 1\text{ mA cm}^{-2}_{\text{geo}}$ for ORR in 0.1 M NaOH relative to 0.1 M HClO₄. The most interesting observation in this experiment using Pt/C is in the ring currents measured during ORR. As seen in Figure 1(b), in 0.1 M HClO₄ the ring current due to peroxide oxidation is lower in the entire potential region and does not show any significant increase until the disk potential enters the H UPD region. On the contrary, the ring current due to peroxide oxidation in 0.1 M NaOH electrolyte shows a sharp increase at 0.9 V in the cathodic scan. The sharp increase in ring current at 0.9 V during ORR in alkaline media is closely related to Pt-OH formation from specific adsorption of hydroxide anions as seen from the CV in 0.1 M NaOH. As shown in Figure 1(a), in 0.1 M NaOH electrolyte, Pt-OH formation commences at \sim 0.7 V versus RHE and reaches a peak current at 0.81 V and a plateau at \sim 0.9 V. On the cathodic direction, the peak potential for Pt-OH reduction is \sim 0.75 V versus RHE. As seen in Figure 1(b), on the cathodic ORR scan, the increase in ring current commences at 0.9 V and reaches a peak potential of 0.75 V versus RHE. This clearly establishes the interaction between molecular oxygen and the hydroxyl species on the surface. This peroxide formation in the mixed kinetic-diffusion region in alkaline media is more evident at a higher electrolyte concentration of 1.0 M NaOH as shown in Figure 1(c). At a higher concentration of alkaline electrolyte, that is, at 1 M NaOH, peroxide is detected at the ring electrode in both the anodic and the cathodic scan [60].

In order to explain the link between the specifically adsorbed hydroxide anions and the peroxide detected in the mixed kinetic-diffusion region in alkaline media, it is important to understand the double-layer structure of the electrode-electrolyte interface during ORR at high-pH

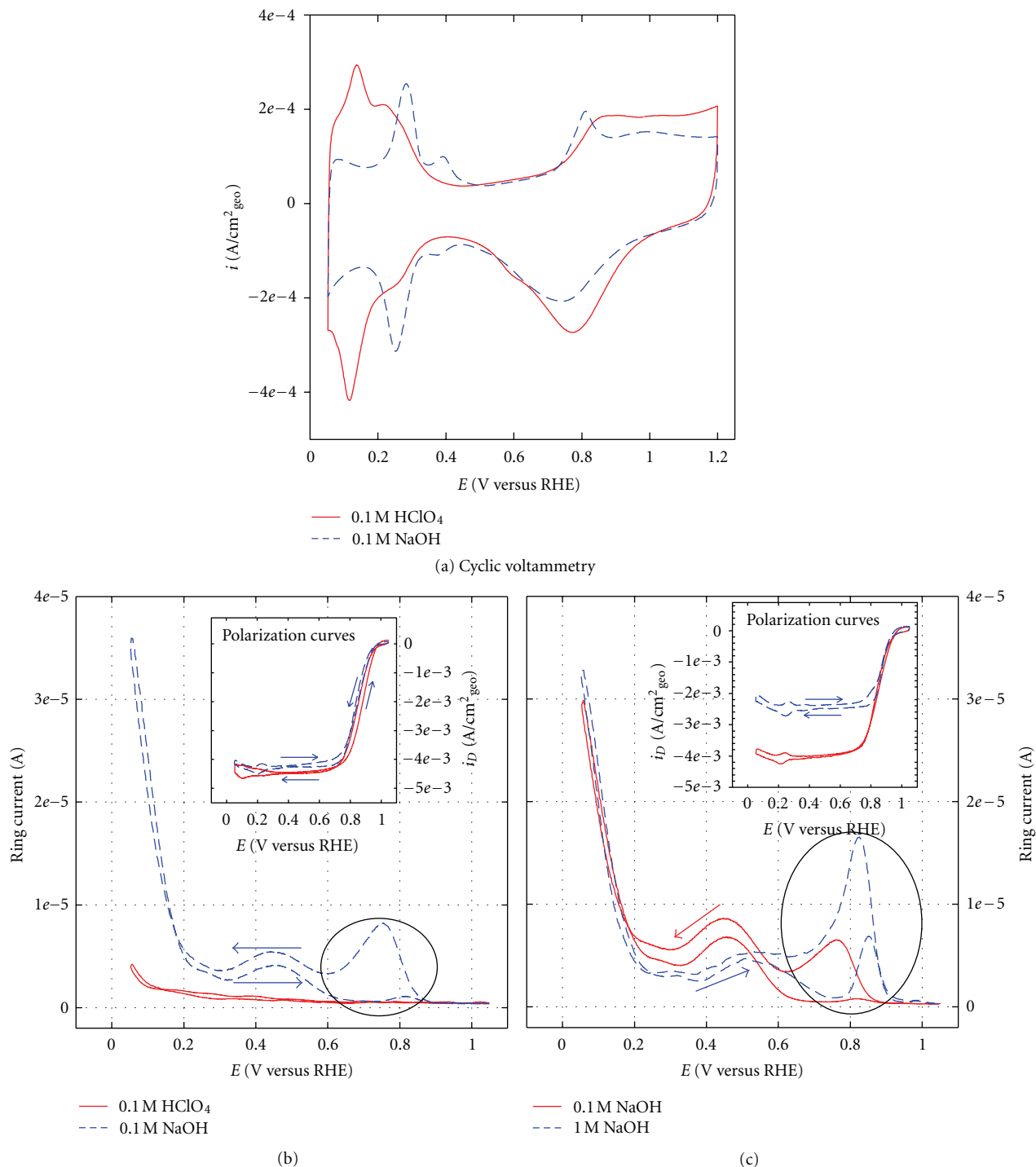


FIGURE 1: Comparison of electrochemical characteristics of BASF-E-TEK 30% Pt/C in 0.1 M HClO₄, 0.1 M NaOH, and 1.0 M NaOH electrolytes. (a) CV in argon-saturated electrolytes, (b, c) Ring currents measured during ORR study at 900 rpm in O₂-saturated electrolytes. Insets in (b, c) show the corresponding ORR polarization curves at 900 rpm. Scan rate: 20 mV/s. $E_{\text{Ring}} = 1.1$ V versus RHE in 0.1 M NaOH and 1.3 V versus RHE in 0.1 M HClO₄. Catalyst loading: 15 $\mu\text{g}_{\text{Pt}}/\text{cm}^2$ on 5.61 mm Glassy Carbon disk electrode.

environments. A schematic illustration of the double-layer structure is shown in Figure 2. In an operating fuel cell, cathodic ORR process typically occurs at potentials well positive of the potential of zero charge (pzc). In alkaline media, water molecules not only act as solvent but also

serve as the source of protons required in ORR. At these conditions in alkaline media, inner Helmholtz plane (IHP) is populated by specifically adsorbed hydroxyl species, solvent water dipoles (oriented with the oxygen atom towards the electrode surface), and chemisorbed O₂. Alkali metal ions

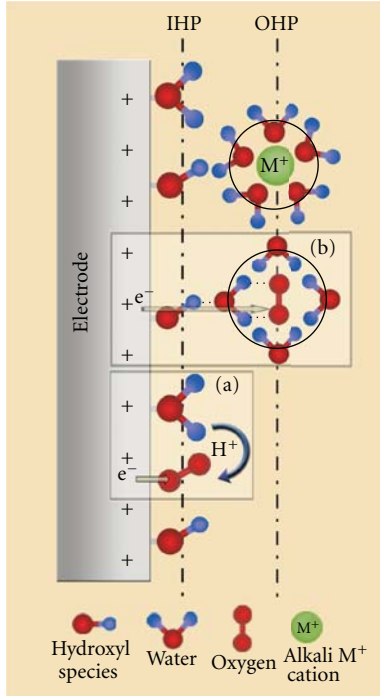


FIGURE 2: Schematic illustration of the double-layer structure during ORR in alkaline media. Insets (a, b) illustrate the inner- and outer-sphere electron transfer processes.

are typically well solvated and are classically expected to populate the outer Helmholtz plane (OHP). In ORR, the case of a typical electrocatalytic inner-sphere electron transfer mechanism involves strong chemisorption of molecular O_2 (with or without bond breaking) on oxide-free Pt active sites followed by $4e^-/4H^+$ transfer. This inner-sphere mechanism depicted in Figure 2 (inset (a)) is common to both acidic and alkaline media, wherein all the reaction intermediates remain adsorbed on the active site until the final product is desorbed into the bulk electrolyte. Also shown in Figure 2 (inset (b)) is the outer-sphere electron transfer mechanism that appears to be unique to the alkaline conditions. The solvated molecular O_2 , represented here as a cluster $O_2 \cdot (H_2O)_n$, could interact with the surface hydroxyl species (OH_{ads}) via a hydrogen bond between H atom in OH_{ads} and O atom in the solvent water molecule. Such hydrogen bond energies ($<35 \text{ kJ mol}^{-1}$) are typically much lower than the energy associated with covalent bond strength such as in the case of direct chemisorption of O_2 on Pt ($>300 \text{ kJ mol}^{-1}$) [61]. This hydrogen bond formation stabilizes the solvated molecular oxygen $O_2 \cdot (H_2O)_n$ cluster in the OHP and promotes an outer-sphere electron transfer to form the superoxide species.

Following this new evidence on the involvement of outer-sphere electron transfer in alkaline media, two ORR mechanisms at high-pH environment are proposed here. The first is the well-known electrocatalytic inner-sphere electron transfer mechanism, where molecular O_2 undergoes direct chemisorption on *oxide-free* Pt site leading to a direct/series $4e^-$ pathway without the desorption of reaction

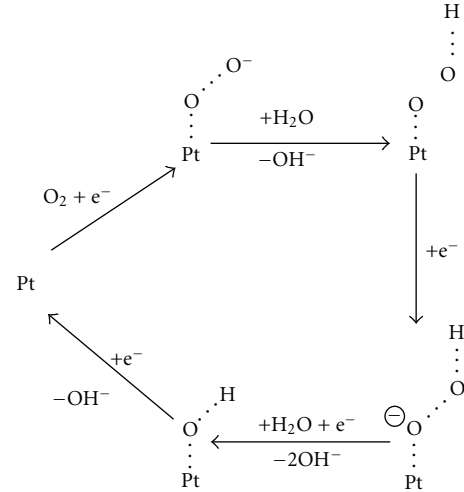
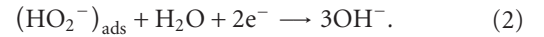
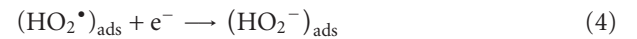
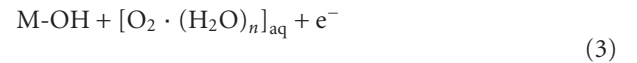


FIGURE 3: Electrocatalytic inner-sphere electron transfer mechanism for ORR on Pt in alkaline media assuming end-on adsorption of O_2 on a single Pt active site.

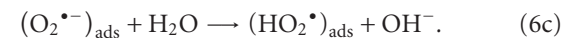
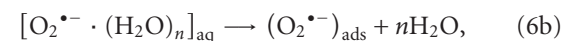
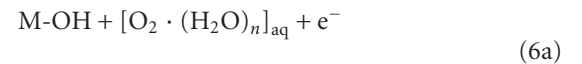
intermediates (such as peroxide) from the surface according to the following well-known reaction scheme (also depicted in Figure 3) [3]:



The second is the outer-sphere electron transfer mechanism, where solvated molecular O_2 cluster $O_2 \cdot (H_2O)_n$ weakly interacts with adsorbed hydroxyl species to promote a $2e^-$ reaction pathway to HO_2^- anion as a reaction product which desorbs from the surface and is eventually detected at the ring electrode. This reaction is formulated as follows:



The first step in the previous reaction shown in (3) involves electron transfer (or tunneling) from the electrode surface across a thin oxide film and at least one layer of solvation shell to solvated O_2 . Equation (3) involves several elementary steps as written in the following:

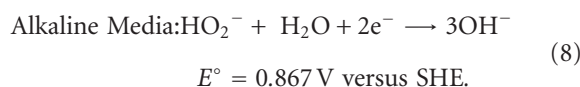
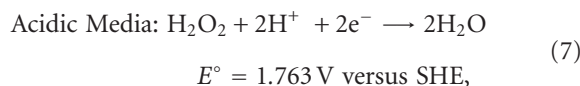


First electron transfer to $O_{2,aq}$ forms $(O_2^{\bullet-})_{aq}$ which then undergoes desolvation and subsequent *adsorption on the oxide substructure* of the Pt surface to form $(O_2^{\bullet-})_{ads}$, followed by proton transfer to form adsorbed hydroperoxyl radical, $(HO_2^{\bullet})_{ads}$. Second electron transfer to $(HO_2^{\bullet})_{ads}$ yields $(HO_2^{\bullet-})_{ads}$. The binding energy of $(HO_2^{\bullet-})_{ads}$ on the oxide substructure of Pt is likely to be lower than that on oxide-free Pt site. This leads to the facile desorption of HO_2^- anion into the electrolyte which is eventually detected at the ring electrode. Also hydrogen peroxide anion formed via the homogeneous chemical disproportionation of superoxide anion would also be detected at the ring electrode. *The interaction between the $O_2 \cdot (H_2O)_n$ cluster and the surface hydroxyl species causes certain nonspecificity to the identity of the underlying electrode metal. This nonspecificity opens the gate to use a wide-range of nonnoble metals and their oxides as electrode materials for ORR in alkaline media.* On noble metals such as Pt, this nonspecificity is observed only in the oxide formation region, and depending on the extent of $-OH$ coverage both inner- and outer-sphere electron transfer mechanisms coexist in alkaline media. On nonnoble metals such as the first-row transition elements that are completely passivated by a layer oxide film upon immersion into the aqueous electrolyte, this outer-sphere electron transfer process is likely to be the dominant mechanism. Furthermore as identified in Figures 1(b) and 1(c), we consider the peak-shaped ring current in the potential range of 0.6 V to 0.9 V in alkaline media to be a characteristic signature of the outer-sphere electron transfer reaction mechanism. In acidic media, the adsorbed OH_{ads} species from water activation primarily serve only to block/inhibit the adsorption of molecular O_2 and other reaction intermediates via the well-known site-blocking effect [62, 63]. However, as shown here in alkaline media, the OH_{ads} species not only block the direct adsorption of O_2 but also serve to promote the $2e^-$ outer-sphere electron transfer reaction to peroxide. There are several precedents for electrochemical reactions which are mediated and/or promoted by specifically adsorbed anions and surface functional groups [64–67]. The anions or the surface groups act as an *outer-sphere bridge* between the reactant and the electrode surface. Furthermore as seen in Figures 1(b) and 1(c), peroxide intermediate is detected at the ring electrode at 0.5 V and also below 0.3 V versus RHE, and the reason for this was explained in detail in an earlier publication [53, 60]. Briefly, in alkaline media, the peak in ring current at 0.50 V is due to the carbon support and the increase in ring current below 0.3 V is due to reorientation of the water molecules at the electrode surface [53, 60].

In light of this new evidence of involvement of outer-sphere electron transfer mechanism during ORR in alkaline media, it is noted that, while this mechanism allows the possibility of nonnoble metals to be used as electrode materials, it predominantly seems to yield the $2e^-$ peroxide intermediate as the final product. So, for efficient $4e^-$ conversion of O_2 , it is important to facilitate direct adsorption of desolvated molecular O_2 on the OH-free active site and avoid the precipitous reaction of solvated molecular O_2 with the OH-covered active site. In agreement with Bard [12], this implies the necessity to promote the electrocatalytic

inner-sphere electron transfer mechanism for efficient $4e^-$ reduction of oxygen.

3.2. ORR on Heat-Treated Carbon-Supported Ru Nanoparticles. Figure 4 shows the ORR on Ru/C catalyst in O_2 -saturated 0.1 M NaOH and 0.1 M $HClO_4$ electrolytes recorded at 900 rpm. The ORR onset potential for Ru/C in 0.1 M $HClO_4$ is 0.78 V versus RHE, whereas in 0.1 M NaOH it is 0.9 V versus RHE. In the alkaline media, mixed kinetic-diffusion region between 0.9 V and 0.5 V is ensued by a well-defined limiting current region below 0.5 V versus RHE. In the acidic electrolyte, ORR is kinetically controlled as indicated by the absence of any clear diffusion-limited current region even at very high overpotentials. As shown in Figure 4(b) at a kinetic current density of $0.1 \text{ mA cm}^{-2}_{geo}$, Ru/C exhibits $\sim 125 \text{ mV}$ lower overpotential in 0.1 M NaOH than in 0.1 M $HClO_4$. Primary reasons to this lower overpotential in alkaline media are delineated here. As seen in Figure 4(c) between the potential regions of 0.7 V to 0.8 V, the shoulder in ring current in 0.1 M NaOH electrolyte is characteristic of the outer-sphere electron transfer mechanism on oxide-covered Ru/C catalyst in alkaline media. This outer-sphere reaction mechanism was depicted in (3)–(5) giving rise to the peroxide intermediate (HO_2^-) as the final product at oxide-covered Ru sites. This $(HO_2^-)_{aq}$ formed is detected at the ring electrode and appears as a shoulder in ring current between 0.7 V and 0.8 V as shown in Figure 4(c). In acidic media, peroxide detected is very minimal and about an order of magnitude lower than that in 0.1 M NaOH. It should be noted that, in 0.1 M NaOH, this outer-sphere electron transfer occurs only at oxide-covered Ru sites, whereas at oxide-free Ru sites direct molecular O_2 adsorption should take place leading to efficient $4e^-$ reduction of O_2 to OH^- via an inner-sphere electrocatalytic pathway. So, in alkaline media, a combination of both inner-sphere and outer-sphere electron transfer mechanisms is operative. The consequence of this outer-sphere electron transfer in alkaline media is that this mechanism leads to higher concentration of HO_2^- to be generated near the electrode surface, that is, the double layer; however, no evidence for such an outer-sphere reaction is observed in acidic media. Higher activity of HO_2^- effectively shifts the potential of the electrode from that of the O_2/HO_2^- couple to that of the HO_2^-/OH^- redox couple by carrying out HO_2^- reduction to OH^- on oxide-free Ru sites. This is shown in Figure 4(d), where ORR and hydrogen peroxide reduction reaction (HPRR) are shown on Ru/C catalyst in both 0.1 M NaOH and 0.1 M $HClO_4$. $2e^-$ reduction of hydrogen peroxide in acidic (H_2O_2/H_2O) and alkaline media (HO_2^-/OH^-) are written as follows [13]:



As is well known, the standard reduction potentials of the above reactions are well positive of the $4e^-$ reduction of

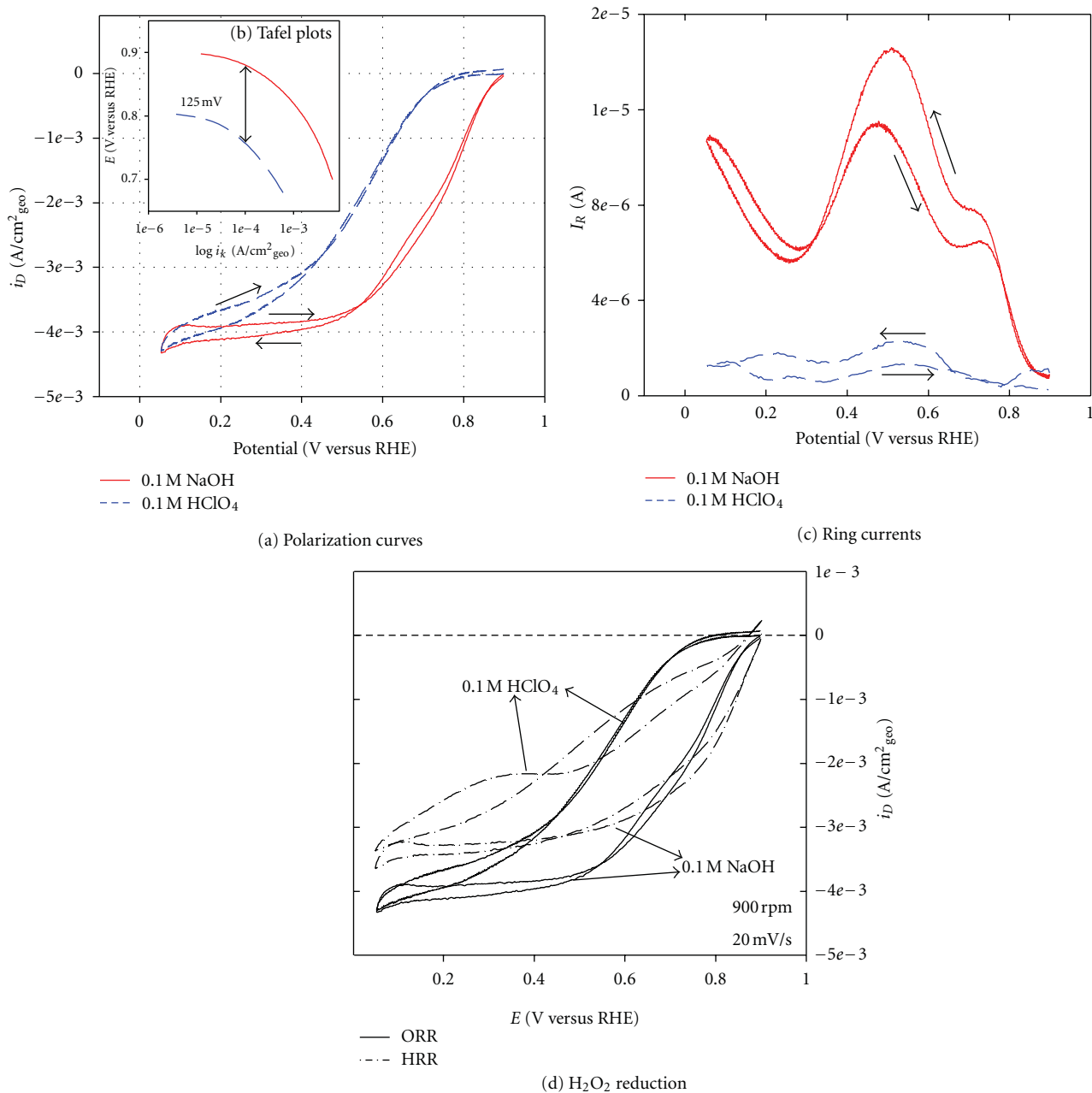


FIGURE 4: Oxygen reduction reaction on Ru/C heat-treated (HT) catalyst in 0.1 M NaOH and 0.1 M HClO_4 electrolytes. (a) ORR polarization curves at 900 rpm and 20 mV/s, (b) mass-transport-corrected Tafel plots, (c) ring current measured during ORR at 900 rpm. $E_{\text{Ring}} = 1.1$ V versus RHE in 0.1 M NaOH and $E_{\text{Ring}} = 1.3$ V versus RHE in 0.1 M HClO_4 , and (d) hydrogen peroxide reduction reaction (HPRR) in comparison to ORR in 0.1 M HClO_4 and 0.1 M NaOH. HPRR is shown in oxygen-free electrolytes containing externally added H_2O_2 at a concentration of 3.5 mM.

molecular O_2 in both acidic and alkaline electrolytes. So, from a thermodynamic perspective, any peroxide intermediate formed should be immediately reduced further. This is also kinetically true on ruthenium as shown in Figure 4(d). Half-wave potential ($E_{1/2}$) of HPRR on Ru/C in 0.1 M NaOH is 40 mV positive compared to that of the $E_{1/2}$ of ORR [68]. So the kinetics of the reaction in alkaline media favors the immediate reduction of any peroxide intermediate generated during ORR. This is also true in acidic media

although the shape of the HPRR profile in acidic media on Ru/C requires more explanation. The onset potential of HPRR on Ru/C in 0.1 M HClO_4 is as high as 0.88 V which is only 20 mV lower than ORR and HPRR onset potentials in 0.1 M NaOH electrolyte. As is known previously [69], H_2O_2 undergoes decomposition to O_2 and H_2O in acidic electrolyte at Ru/C surface. This decomposition reaction that generates O_2 near the electrode surface skews the HPRR profile in acidic media to higher overpotentials characteristic

of ORR in acidic media. However, the aspect of relevance to the discussion here is that the kinetics of the system favors further reduction of hydrogen peroxide intermediate in both acidic and alkaline media. Once the $\text{H}_2\text{O}_2/\text{HO}_2^-$ stable intermediate is generated, this species undergoes adsorption at oxide-free Ru sites and further reduces to $\text{H}_2\text{O}/\text{OH}^-$ according to (7)/(9). So, any *in situ* generation of hydrogen peroxide intermediate should shift the potential to more positive values, and indeed this is what is observed in alkaline media. The *in situ* parallel generation of HO_2^- anion intermediate via the outer-sphere electron transfer reaction scheme shown in (3)–(5) serves to shift the ORR potential to more positive values in alkaline media. On the contrary, this excess parallel generation of H_2O_2 via the outer-sphere reaction mechanism is not observed in acidic media and, hence, the higher overpotential for ORR in acidic media. In general, this can also be further extended to other catalyst systems that exhibit lower ORR overpotential in alkaline media compared to that in acidic electrolytes. The prospects of modifying the carbon-supported ruthenium nanoparticle catalyst by chalcogen groups (S/Se) in order to suppress oxide formation and promote the inner-sphere electrocatalytic process by facilitating direct O_2 adsorption was discussed recently as a separate treatise [70].

3.3. Pyrolyzed Metal Macrocycle for Promoting Inner-Sphere Electron Transfer. Figure 5(a) shows a comparison in dilute acidic and alkaline electrolytes of the ORR activity of FeTPP/C catalyst pyrolyzed at 800°C . As observed in Figure 5(a), the onset potential for ORR in 0.1 M NaOH is 0.95 V versus RHE, whereas in 0.1 M HClO_4 electrolyte it is 0.80 V versus RHE. This 150 mV lower overpotential in alkaline media is clearly reflected over the entire mixed kinetic-diffusion region. In 0.1 M NaOH electrolyte, the mixed kinetic-diffusion region is ensued by a well-defined diffusion-limited region. In 0.1 M HClO_4 , no clear diffusion-limited region could be discerned, which is indicative of kinetic control in acidic media even at high overpotentials. At a potential of 0.80 V versus RHE, the ORR kinetic current density of FeTPP/C (pyrolyzed at 800°C) is clearly four orders of magnitude higher in 0.1 M NaOH electrolyte than that in 0.1 M HClO_4 . For a given catalyst, the four orders of magnitude difference in kinetic activity between acidic and alkaline media are intriguing. Figure 5(b) shows the HPRR activity of FeTPP/C catalyst (pyrolyzed at 800°C) in both acidic and alkaline media in comparison to the corresponding ORR polarization curves. The onset potential for peroxide reduction in 0.1 M HClO_4 is 0.84 V versus RHE, whereas in 0.1 M NaOH it is 1.01 V versus RHE. Besides this onset potential difference, in 0.1 M NaOH electrolyte, the mixed kinetic-diffusion region for peroxide reduction is more anodic compared to that of ORR in the same electrolyte which is then followed by a reasonably discernable diffusion-limited current density region. This clearly indicates that peroxide reduction in alkaline media is kinetically favored such that any peroxide intermediate formed during ORR in 0.1 M NaOH will be immediately reduced to the $4e^-$ product. On the contrary, the reduction of hydrogen peroxide in acidic media is kinetically unfavorable due to weak binding

of H_2O_2 on the active site leading to its desorption into the bulk electrolyte and/or catalytic decomposition to molecular O_2 . *This clearly demonstrates that stabilizing the peroxide intermediate on the active site is important in effectively carrying out $4e^-$ ORR process, and the higher stability of peroxide intermediate on the active site leads to the so-called kinetic facility in alkaline media but not in acidic media.* Given the $\text{p}K_a$ values for the first and second ionization of H_2O_2 at 25°C ($\text{p}K_1 = 11.69$ and $\text{p}K_2 = \sim 20$), the predominant peroxide species for $\text{pH} < 12$ is H_2O_2 whereas at $\text{pH} > 12$ it is HO_2^- [58]. This leads to the formation of a stable Lewis acid-base adduct in alkaline media ($\text{Fe}^{2+}\text{-HO}_2^-$) that enables complete $4e^-$ transfer. On the contrary, the lack of stabilization of ($\text{Fe}^{2+}\text{-H}_2\text{O}_2$) adducts in acidic media leads to desorption of H_2O_2 into the bulk electrolyte.

Figure 5(c) shows the ring current due to peroxide oxidation measured during ORR in both acidic and alkaline electrolytes. Clearly, the peroxide yield during ORR on FeTPP/C (pyrolyzed at 800°C) is higher in acidic media by an order of magnitude compared to that in alkaline media. This observation is opposite to what was observed on the Pt/C and Ru/C catalysts discussed previously. The onset potential for ORR in 0.1 M NaOH is 0.95 V versus RHE, whereas the corresponding peroxide oxidation current does not begin until 0.8 V. In 0.1 M HClO_4 , the onset potential for both ORR and peroxide oxidation is 0.8 V. This is further proof for the instability of peroxide intermediate on the active site in acidic media because the weak binding of the H_2O_2 intermediate on the Fe^{2+} active site facilitates its desorption and/or decomposition into the bulk electrolyte. This desorption of H_2O_2 into the bulk electrolyte due to its weak binding on the active site is the primary source of peroxide detected at the ring in acidic media. At very high overpotentials (< 0.3 V), the ORR process in acidic electrolyte becomes very efficient and consequently the peroxide detected decreases [71, 72]. The ring current profile in 0.1 M NaOH is more complex. Briefly, in alkaline media, the peak in ring current at 0.50 V is due to the carbon support and the increase in ring current below 0.3 V is due to reorientation of the water molecules [60, 73]. More importantly, a weak shoulder in the ring current in 0.1 M NaOH is observed between 0.6 V and 0.7 V. Also shown in Figure 5(c) is the ring current profile of Pt/C for comparison. As discussed previously, the ring current peak due to Pt/C around 0.80 to 0.90 V is the signature for the peroxide formation via outer-sphere electron transfer mechanism at $-\text{OH}$ -covered Pt sites. On Fe-N_x -based catalyst, only a weak shoulder in ring current at more negative potentials of 0.60 to 0.70 V is observed indicating that the outer-sphere electron transfer mechanism is significantly muted. This indicates the facilitation of direct adsorption of O_2 on the Fe^{2+} active site. This is because the specifically adsorbed OH^- species on the Fe^{2+} site acts as a labile ligand that is easily displaced by the molecular O_2 . This is ensued by the successful $4e^-$ reduction of O_2 with minimal occurrence of outer-sphere electron transfer mechanism.

The nature of the active site obtained upon pyrolysis and the fundamental origin of the activity is investigated here in detail. Figure 6(a) shows the square wave voltammetry (SWV) of non-heat-treated Fe(III)TPP/Cl/C in

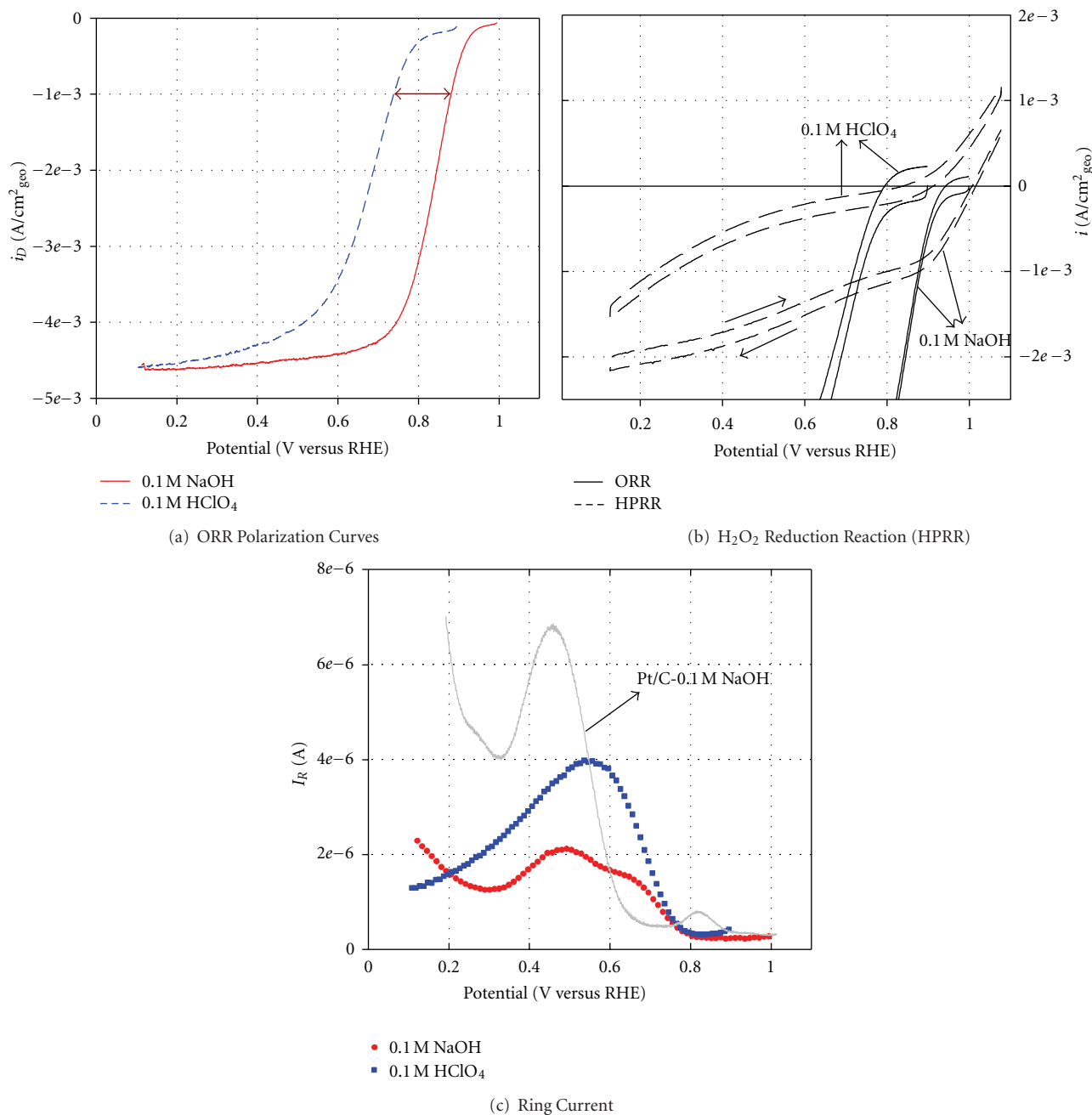


FIGURE 5: ORR activity of FeTPP/C catalyst (pyrolyzed at 800°C) in O_2 saturated acidic and alkaline electrolytes. (a) ORR polarization curves, (b) hydrogen peroxide reduction reaction (HPRR) in comparison to ORR, and (c) ring current. All measurements were performed at 900 rpm rotation rate and 20 mV/s scan rate. $E_{\text{Ring}} = 1.1$ V versus RHE in 0.1 M NaOH and $E_{\text{Ring}} = 1.3$ V versus RHE in 0.1 M HClO_4 . HPRR is shown in oxygen-free electrolytes containing externally added H_2O_2 at a concentration of 3.5 mM. Also shown in (c) is the ring current profile of 30% Pt/C in 0.1 M NaOH for comparison.

argon-saturated 0.1 M NaOH and 0.1 M HClO_4 electrolytes, and Figure 6(b) shows the corresponding CV. As seen in both the SWV and the CV profiles, the redox transition involving the metal center $\text{Fe}^{2+/3+}$ is observed at 0.314 V versus RHE in 0.1 M NaOH and at 0.155 V versus RHE in 0.1 M HClO_4 [30, 31, 74]. As seen in the SWV profile, the peaks at 1.260 V in 0.1 M HClO_4 and 1.508 V in 0.1 M NaOH correspond to the one-electron redox transition involving the delocalized

π -electron system in the macrocycle ligand [74]. As observed in the literature [30], CV of the heat-treated catalysts does not yield useful information, since in most cases after heat treatment the double-layer charging current overwhelms the Faradaic currents. In order to overcome this limitation, SWV was performed as shown in Figure 7 in order to understand the evolution of the active site in these catalysts with increasing heat treatment temperatures. Figures 7(a)

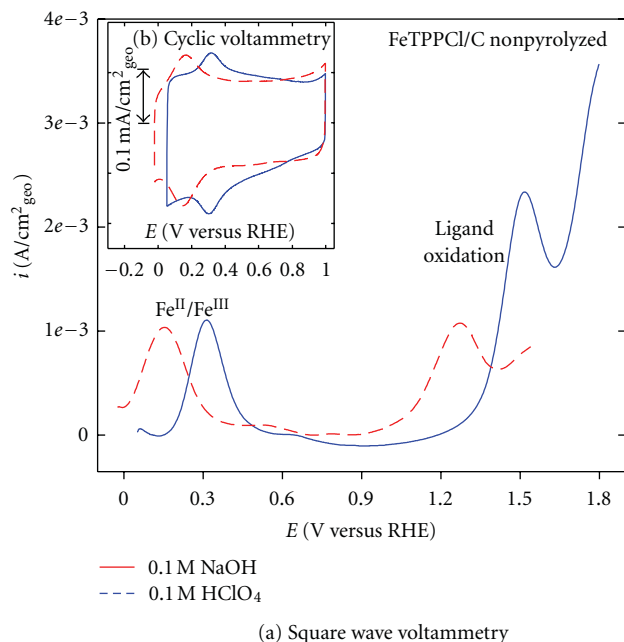


FIGURE 6: (a) Square wave voltammetry (SWV) and (b) cyclic voltammetry (CV) of as-received iron(III) meso-tetraphenylporphyrin chloride (FeTPPCL/C) supported on Black Pearl carbon. Experiments were performed in argon-saturated 0.1 M NaOH and 0.1 M HClO₄ electrolytes. SWV parameters: 5 mV step potential, 20 mV amplitude, and 10 Hz frequency. CV: 20 mV/s.

and 7(b) are divided into two panels each due to different potential ranges that are required for baseline correction of SWV profiles. As seen in Figure 7(a) in alkaline media, after 300°C pyrolysis, the Fe^{2+/3+} redox couple at 0.31 V and the ligand oxidation peak at 1.5 V are similar to the case of non-heat-treated catalyst. After heat treatment at 500°C and 600°C, the magnitude of the peak currents decrease significantly due to the sublimation of some fraction of the metal macrocycle complex. More importantly, the Fe^{2+/3+} peak potentials have shifted to more anodic potentials. As seen in Panel 1 of Figure 7(a), after pyrolysis at 500°C and 600°C, the peak potential (E_p) of the Fe^{2+/3+} couple has shifted to 0.405 V and 0.427 V, respectively. Correspondingly, the ligand oxidation peak at ~1.5 V, shown in Panel 2 of Figure 7(a), decreases in magnitude significantly due to the sublimation and/or destruction of the macrocycle. The ligand oxidation peak is not observed after heat treatment at temperatures greater than 600°C indicating that the delocalized π -electron system of the macrocycle does not survive such high temperatures on the carbon support. After 800°C pyrolysis, Fe^{2+/3+} couple has shifted more anodically to $E_p = 0.48$ V. As shown in Figure 7(a) (Panel 2), the most interesting observation is that after pyrolysis at 600°C a new shoulder begins to emerge at ~1.2 V. This shoulder resolves into a clear peak after 800°C pyrolysis with a peak potential of 1.25 V versus RHE in alkaline media. This new peak is attributed to an anodic shift in the Fe^{2+/3+} redox couple based on the *in situ* XANES experimental results shown later (*vide infra*). This indicates the presence of two Fe^{2+/3+} redox

couples, one at a low potential (~0.48 V) and another at a high potential (1.25 V). The anodic shift in Fe^{2+/3+} redox peak potentials shown in Figure 7(a) (inset) clearly indicates that after 600°C pyrolysis the metal center exists in two redox environments. Qualitatively, similar behavior was observed in acidic media as shown in Figure 7(b). (Note that the ligand oxidation peak in acidic media that occurs above 1 V versus RHE is not shown in Panel 2 of Figure 7(b).) It is interesting to note that after heat treatment at 600°C the Fe^{2+/3+} redox peak potential in 0.1 M HClO₄ was shifted to an anodic potential of only 0.80 V versus RHE compared to the 1.25 V in alkaline media. Thus, there are two reasons for the lower ORR overpotential for FeTPP/C catalyst in alkaline media: (1) the higher redox potential of the Fe^{2+/3+} metal center in alkaline media and (2) the improved stability of the peroxide intermediate on the active site. This translates into efficient 4e⁻ ORR reaction with lower overpotential in alkaline media compared to acidic media.

3.3.1. Delta-Mu ($\Delta\mu$) Studies. Both the extended X-ray absorption fine structure (EXAFS) and X-ray absorption near edge structure (XANES) being bulk averaged techniques overlook the critical electrochemical reactions occurring on the catalyst surface. Delta-mu ($\Delta\mu$) is a surface sensitive, spectral subtraction technique, where the bulk structure of the catalyst is effectively removed leading to information on the nature and site specificity of the surface adsorbates [54, 55, 75, 76]. Figure 8(a) shows the XANES region of FeTPP/C catalyst pyrolyzed at 300°C taken at two different potentials of 0.1 V and 0.9 V versus RHE. At 0.1 V, the metal center exists in the reduced Fe²⁺ state with no adsorbates (neither hydrides nor oxides) at the axial position, and immediate coordination environment is reminiscent of the iron(II) phthalocyanine complex, where the preedge peak is muted. At 0.9 V, the metal center is oxidized to Fe³⁺ state with an oxygen atom at the axial position, and the metal coordination environment is similar to that of the original porphyrin complex, where the preedge Fe(1s \rightarrow 3d) forbidden transition at 7112.5 eV is observed. The delta-mu spectra is obtained by subtracting the XANES regions according to the equation $\Delta\mu = \mu(0.90 \text{ V}) - \mu(0.10 \text{ V})$. In the delta-mu spectra of Figure 8(a), the positive peak feature (boxed portion) indicates the difference in absorption probability at the preedge energy (7112.5 eV). This positive peak feature could be safely assigned as a signature for the existence of the metal center in a centrosymmetric environment undergoing a transition from Fe²⁺-N₄ coordination geometry at 0.10 V to O-Fe³⁺-N₄ coordination geometry at 0.90 V. Ensuing this positive peak is a steep negative dip featuring a split peak below 20 eV. This negative dip characterizes charge transfer from the metal center to the adsorbed oxygen species [77]. As shown in Figure 8(b), the XANES spectra of the 800°C pyrolyzed catalyst is predominantly characteristic of metallic iron at both 0.10 V and 1.10 V that precludes proper analysis of the active site. However, careful analysis of the corresponding delta-mu spectra clearly indicates the positive peak feature at the preedge energy indicative of the fact that the active site is Fe²⁺-N₄ where the metal center is in a centrosymmetric environment which is mildly disrupted by the presence of

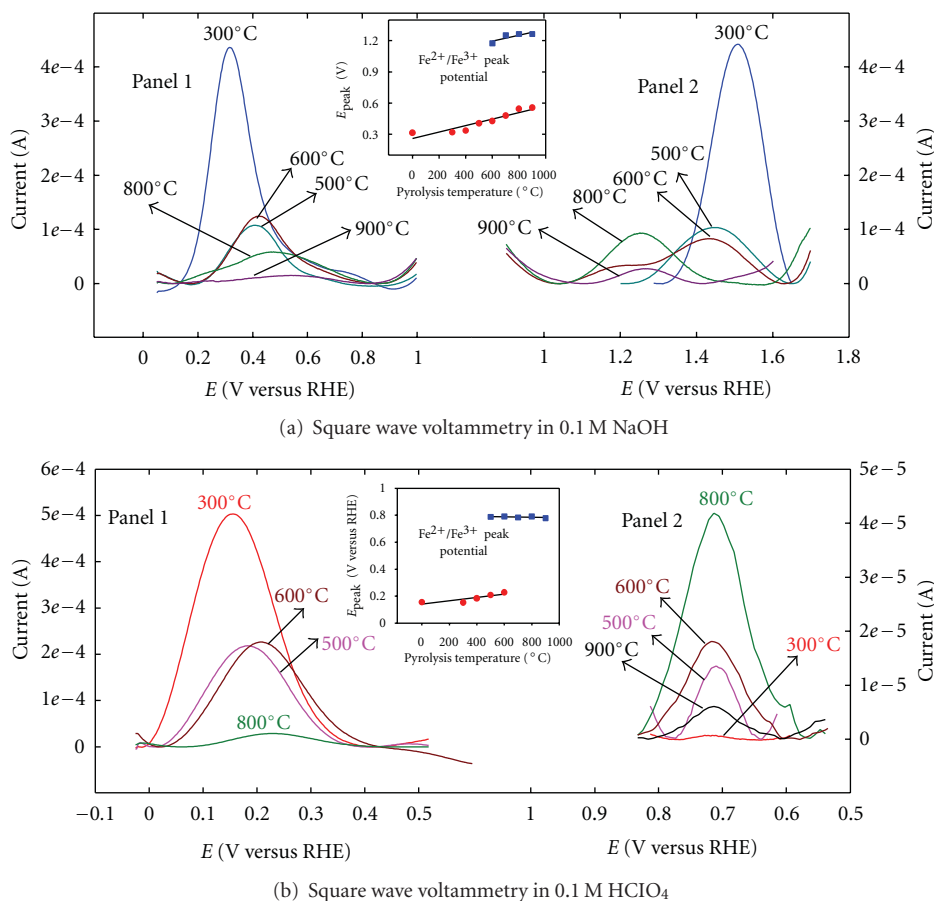


FIGURE 7: SWV profiles of FeTPP/C catalyst as a function of heat treatment temperature in (a) 0.1 M NaOH and (b) 0.1 M HClO₄ electrolytes. Insets show the peak potential of the Fe²⁺/Fe³⁺ redox couple as a function of the heat treatment temperature. SWV experiment parameters: step potential –5 mV, amplitude –20 mV, and scan frequency –10 Hz.

an axial oxygen atom. This clearly indicates that the Fe²⁺ metal center surrounded by four nitrogen atoms is the active site that binds oxygen in the axial position and the redox transition from Fe³⁺ to Fe²⁺ triggers oxygen adsorption according to the redox mechanism [78]. Figure 9 shows the theoretical delta-mu ($\Delta\mu_t$) spectra obtained using FEFF8.0 code [56]. The structural models used are shown in the insets of Figure 9. Only the atoms encircled were used in the theoretical FEFF8.0 modeling. These theoretical spectra were calculated from Fe-N₄-C_x models derived from prior crystallographic data adjusted to the EXAFS fitting results according to the relation $\Delta\mu_t = \mu(\text{O}_{\text{ads}}\text{-Fe-N}_4\text{-C}) - \mu(\text{Fe-N}_4\text{-C})$, where the oxide species (O_{ads} or OH_{ads}) is in a specific binding site. In all cases, the positive peak feature at the preedge energy was observed only when the adsorbed oxygen atom was placed in the axial position of the metal center. No successful theoretical delta-mu fits could be obtained for Fe-N coordination numbers less than four or for oxygen adsorption modes other than at the axial position. As shown in the inset of Figure 9(a), after 300°C pyrolysis the immediate coordination environment of the original precursor porphyrin macrocycle is clearly retained. This corresponds to an FeN₄C₁₂ cluster, where the metal center is coordinated to four nitrogen atoms and each nitrogen

atom in turn bonded to two carbon atoms. Finally, inclusion of the four methine carbon bridges gives a tally of C₁₂. Figure 9(b) shows the theoretical delta-mu spectrum that likely mimics the line shape of the experimental delta-mu shown in Figure 8(b) for the 800°C heat-treated catalyst. As shown in the inset of Figure 9(b), the molecular cluster used to simulate the theoretical delta-mu spectrum consisted of FeN₄C₁₀. While compositionally this cluster is not very different from the 300°C pyrolyzed sample, the immediate coordination environment of the metal active site after 800°C heat treatment is found to be reminiscent of the crystallographic atomic defects such as the divacancy on the graphitic surfaces. This is schematically depicted in Figure 9(c) [79, 80]. Atomic defects such as monovacancy and divacancy on microporous carbon and carbon nanotubes are known to thermodynamically exist or can be induced via various chemical or physical processes [81–85]. The presence of a monovacancy in carbon atom creates three dangling bonds whereas divacancies create four dangling bonds. These dangling bonds give rise to unsaturated valences that then become favorable for nitrogen doping [80]. Consequently, these nitrogen-doped sites constitute defective pockets for metal coordination. Such atomic vacancies are either already present on the graphite surfaces or can be created during the

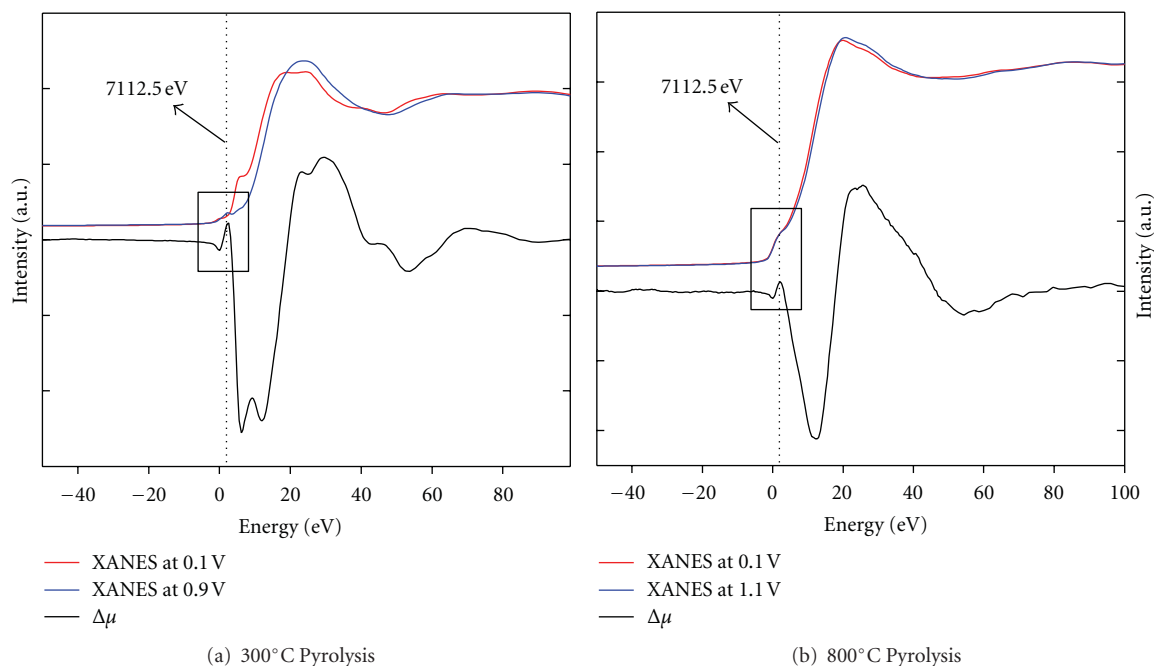
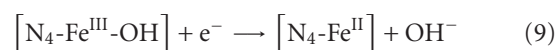


FIGURE 8: Experimental XANES and delta- μ signatures of FeTPP/C catalyst heat treated at (a) 300°C and (b) 800°C. Delta- μ signatures were obtained by subtracting the XANES signatures according to $\Delta\mu = \mu(0.90 \text{ (or) } 1.10 \text{ V}) - \mu(0.10 \text{ V})$. Experiments were conducted at Fe K-edge under *in situ* conditions in argon-saturated 0.1 M NaOH electrolyte. Vertical dotted line indicates the pre-edge position at 7112.5 eV and the boxed region focuses the pre-edge region. Delta- μ spectra have been multiplied by a factor of 5 for visual comparison of the line shapes.

heat treatment step [81, 83]. During heat treatment under inert atmosphere, carbothermic reaction causes desorption of oxygen functional groups along with creation of vacancy defects [83]. It has also been observed earlier that heat-treated Fe-N_x catalysts showed higher activity when supported on carbon that was previously treated in concentrated inorganic acids [52]. Since such acid treatment steps lead to oxygen functional groups on carbon support, it is likely that this yields higher number of defective sites during subsequent heat treatment. These defective pockets are likely the favorable zones for anchoring FeN₄ active sites. Presumably, the low concentration of the defective sites limits the active site density. Therefore, increasing the defect density likely holds key to increasing the metal loading in this class of catalysts.

The following observations are made in an attempt to correlate the SWV and the delta- μ results. The low-potential Fe^{2+/3+} redox couple is characteristic of the original FeN₄ porphyrin moiety, whereas the high-potential Fe^{2+/3+} redox couple is characteristic of the FeN₄ cluster found in the microporous carbon defect sites. At a pyrolysis temperature of 600°C, both of these sites seem to coexist and the higher ORR activity obtained for heat treatment temperatures $\geq 600^\circ\text{C}$ is due to the high-potential Fe^{2+/3+} redox couple seated in the defective pockets. Based on the above experimental results, the following reaction scheme is proposed for ORR in dilute alkaline media on heat-treated FeTPP/C catalyst. Similar set of reactions can be developed, *mutatis mutandis*, for dilute acidic media [22, 71, 72, 86]. Equation

(9) shows the redox reaction involving the metal center that is a prerequisite for adsorption of molecular oxygen on the active site [N₄-Fe^{II}-OH⁻]:



While the Fe^{II} valence state favors a square-planar tetra-coordinate environment, the high potential of this redox reaction causes the OH⁻ species to poison the active site at the axial position. This poisonous OH⁻ species prevents direct molecular adsorption of O₂ on the active site. Further, the adsorbed OH⁻ species mediates the 2e⁻ outer-sphere electron transfer reduction of solvated O₂ molecule as shown in the reaction schemes (3)–(5) although this outer-sphere mechanism appears to be extremely weak in this class of pyrolyzed catalysts as explained previously. It should be noted that the case of outer-sphere mechanism does not arise in acidic media for reasons explained previously.

Finally, the 4e⁻ electrocatalytic inner-sphere electron transfer mechanism is shown in Figure 10, where the molecular O₂ displaces the OH⁻ species and chemisorbs directly on the Fe^{II} active site. Based on our experimental results, the electrocatalytic process in Figure 10 is shown to take place via a redox mechanism involving Fe^{II/III} couple [78]. Once molecular O₂ adsorbs on the Fe^{II} active site, the reaction proceeds to the ferrous-hydroperoxyl adduct via the superoxo and the ferric-hydroperoxyl states. The ferrous-hydroperoxyl adduct is very critical since its stability determines the product distribution. Peroxide anion (HO₂⁻) is a stable intermediate. So, weak binding of HO₂⁻ on the

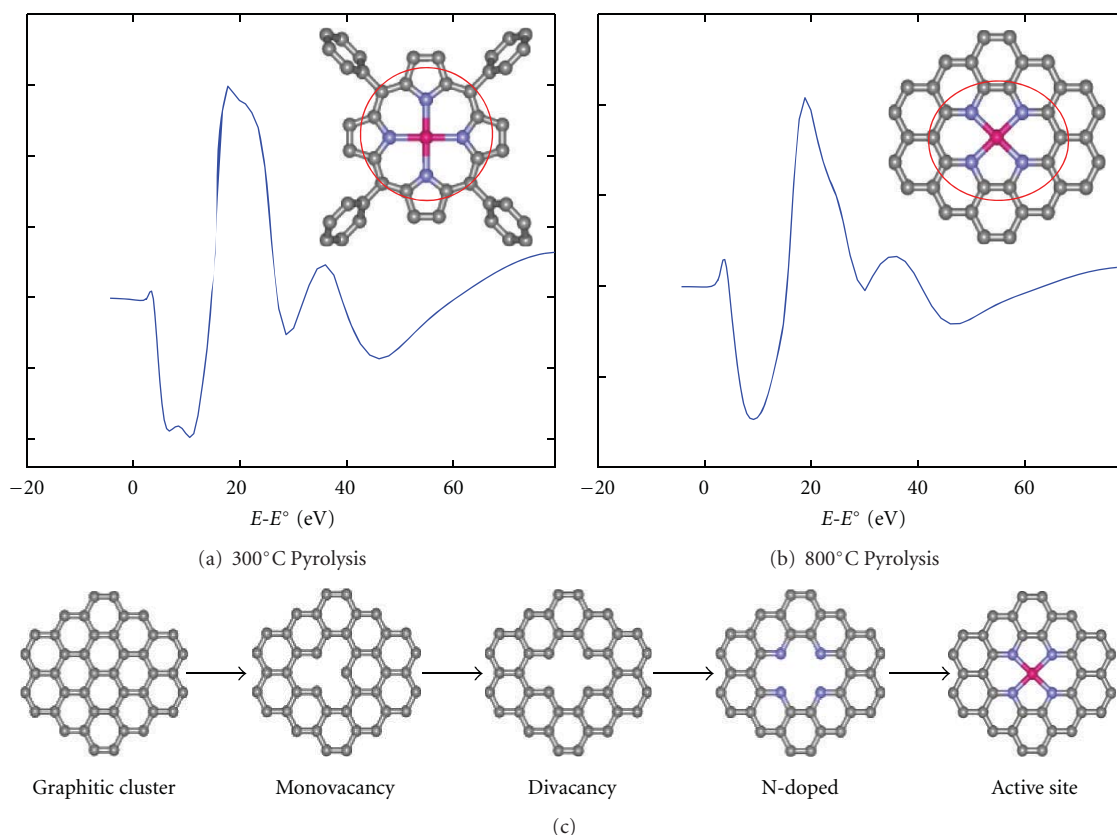


FIGURE 9: Theoretical FEFF8 $\Delta\mu = \mu(\text{Fe-N}_4\text{-C}_x\text{-O}_{\text{ads}}) - \mu(\text{Fe-N}_4\text{-C}_x)$ signatures obtained for (a) 300°C and (b) 800°C pyrolysis conditions. The insets in (a, b) show the corresponding structural models utilized. Only the atoms encircled in these structural models were used for FEFF8 simulation. (c) Schematic illustration of the mono- and divacant defective pockets in amorphous carbon acting as anchors for active site formation during pyrolysis. Color codes: pink: Fe, blue: N, and black: C.

active site will lead to its desorption into the bulk electrolyte. As mentioned previously, the stable acid-base adduct formed in alkaline media stabilizes the ferrous-hydroperoxyl adduct. This ensures that the catalytic cycle shown in Figure 10 regenerates the active site via the formation of ferric-hydroxyl species. However, in acidic media the analogous ferrous-hydrogen peroxide adduct $\text{Fe}^{\text{II}}\text{-(OHOH)}$ is unstable and causes desorption and/or disproportionation of the peroxide intermediate (H_2O_2) into the bulk electrolyte. This leads to higher peroxide yield in acidic media as shown previously.

4. Conclusions

The case of ORR in alkaline media shows interesting mechanistic differences compared to acidic media. In acidic media, the presence of OH_{ad} due to water activation blocks the direct adsorption of molecular O_2 on the active site. In alkaline media, the presence of OH_{ad} due to specific adsorption of hydroxide species not only blocks the O_2 adsorption but also promotes outer-sphere electron transfer mechanism to yield the $2e^-$ peroxide intermediate as the product. The interaction between the $\text{O}_2 \cdot (\text{H}_2\text{O})_n$ cluster and the surface hydroxyl species causes certain nonspecificity to the identity of the underlying electrode metal. This

nonspecificity is a result of kinetic differences in alkaline media that opens the gate to use a wide-range of nonnoble metals and their oxides as electrode materials, while in acidic media the absence of this outer-sphere mechanism necessitates the use of highly catalytic surfaces based on Pt. On noble metals such as Pt, this nonspecificity in alkaline media is observed only in the oxide formation region, and depending on the extent of OH_{ad} coverage both inner- and outer-sphere electron transfer mechanisms coexist in alkaline media. On nonnoble metals such as the first-row transition elements that are completely passivated by a layer oxide film upon immersion into the aqueous electrolyte, this outer-sphere electron transfer process is likely to be the dominant mechanism. While the outer-sphere mechanism primarily seems to yield peroxide intermediate as the final product, this could be beneficial in cases like Ru/C catalyst, where the peroxide intermediate generated in the outer-sphere process could be readsorbed on the oxide-free Ru site to reduce further to form hydroxide as the final product. However, in cases like nonnoble metal surfaces, where the electrode surface is incapable of reducing peroxide intermediate any further, only $2e^-$ reduction products are likely to predominate in alkaline media. So, it is important to promote the inner-sphere electron transfer mechanism in alkaline media by facilitating the direct molecular

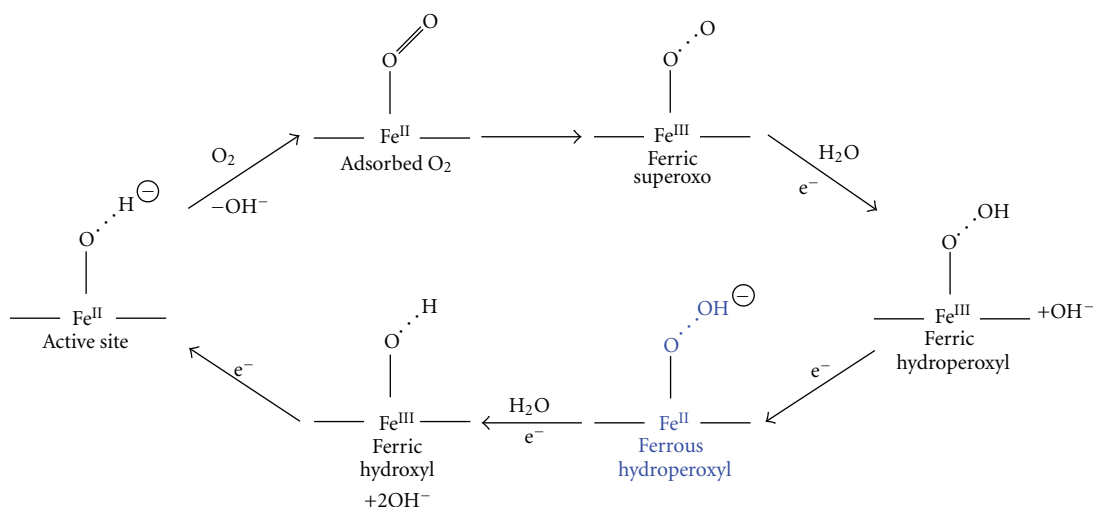


FIGURE 10: Catalytic cycle showing the redox mechanism involved in ORR on heat-treated iron porphyrin macrocycles in dilute alkaline medium. Nitrogen atoms in the square planar positions have been omitted for clarity.

O_2 adsorption and promoting complete $4e^-$ reduction process.

On catalyst surfaces such as the $Fe-N_4$ systems, the operation of redox mechanism allows the direct molecular O_2 adsorption on the $Fe^{2+}-N_4$ active site and prevents the precipitous outer-sphere reaction of solvated O_2 molecule with the OH_{ad} -covered metal site. This is due to the OH_{ad} species acting as a labile ligand in the $Fe-N_4$ -based catalysts that helps to promote the $4e^-$ inner-sphere electron transfer mechanism by efficiently reducing O_2 to OH^- in alkaline media. Further, in the class of $Fe-N_4$ -based catalysts, it is important to perform ORR studies with a thin film of catalyst surface ($\leq 25 \mu m$) rather than thick catalyst films that are typically used in the literature, where the peroxide formed is completely quenched within the catalyst layer and hence not being detected at the ring electrode. This is especially true while Koutecky-Levich plots for calculating the number of electrons transferred since such calculations were derived for smooth electrode surfaces. Also, it is noted that if a catalyst is considered to perform $4e^-$ oxygen reduction, then it is imperative to show the reduction of externally added hydrogen peroxide in the absence of O_2 . Finally, in conclusion, the presence of the outer-sphere electron transfer mechanism in alkaline media is a kinetic effect. The only thermodynamic advantage of performing ORR at high pH is the improved stability of the hydroperoxide anion intermediate on the active site that enables complete $4e^-$ transfer. So, in order to stabilize the H_2O_2 intermediate in acidic media, the use of dimeric active sites that simultaneously bind both oxygen atoms are required.

Acknowledgments

The authors deeply appreciate financial assistance from the Army Research Office under the Single Investigator Grant. The authors also gratefully acknowledge the supply of platinum electrocatalysts from BASF fuel cells (Somerset,

NJ, USA). Use of the National Synchrotron Light Source (NSLS) at Brookhaven National Laboratory (BNL) was supported by the US Department of Energy, Office of Basic Energy Sciences. Support from NSLS beamline personnel Drs. Kaumudi Pandya (X11A), Syed Khalid (X19A), and Nebojsa Marinkovic (X18B) is gratefully acknowledged.

References

- [1] J. S. Spendelow and A. Wieckowski, "Electrocatalysis of oxygen reduction and small alcohol oxidation in alkaline media," *Physical Chemistry Chemical Physics*, vol. 9, no. 21, pp. 2654–2675, 2007.
- [2] E. Yeager, "Electrocatalysts for O_2 reduction," *Electrochimica Acta*, vol. 29, no. 11, pp. 1527–1537, 1984.
- [3] R. Adzic, "Frontiers in electrochemistry," in *Electrocatalysis*, J. Lipkowski and P. N. Ross, Eds., vol. 197, Wiley-VCH, New York, NY, USA, 1998.
- [4] D. B. Sepa, M. V. Vojnovic, and A. Damjanovic, "Kinetics and mechanism of O_2 reduction at Pt in alkaline solutions," *Electrochimica Acta*, vol. 25, no. 11, pp. 1491–1496, 1980.
- [5] D. B. Sepa, M. V. Vojnovic, L. M. Vracar, and A. Damjanovic, "Different views regarding the kinetics and mechanisms of oxygen reduction at Pt and Pd electrodes," *Electrochimica Acta*, vol. 32, no. 1, pp. 129–134, 1987.
- [6] A. Damjanovic, A. Dey, and J. O. M. Bockris, "Kinetics of oxygen evolution and dissolution on platinum electrodes," *Electrochimica Acta*, vol. 11, no. 7, pp. 791–814, 1966.
- [7] E. Yeager, M. Razaq, D. Gervasio, A. Razaq, and D. Tryk, "The electrolyte factor in O_2 reduction electrocatalysis," *Proceedings of the Electrochemical Society*, vol. 92-11, pp. 440–473, 1992.
- [8] A. Damjanovic, M. A. Genshaw, and J. O'M Bockris, "Distinction between intermediates produced in main and side electroic reactions," *The Journal of Chemical Physics*, vol. 45, no. 11, pp. 4057–4059, 1966.
- [9] H. S. Wroblowa, Y.-C. Pan, and G. Razumney, "Electroreduction of oxygen a new mechanistic criterion," *Journal of Electroanalytical Chemistry*, vol. 69, no. 2, pp. 195–201, 1976.

- [10] N. A. Anastasijević, V. Vesović, and R. R. Adžić, "Determination of the kinetic parameters of the oxygen reduction reaction using the rotating ring-disk electrode. Part I. Theory," *Journal of Electroanalytical Chemistry*, vol. 229, no. 1-2, pp. 305–316, 1987.
- [11] N. A. Anastasijević, V. Vesović, and R. R. Adžić, "Determination of the kinetic parameters of the oxygen reduction reaction using the rotating ring-disk electrode. Part II. Applications," *Journal of Electroanalytical Chemistry*, vol. 229, no. 1-2, pp. 317–325, 1987.
- [12] A. J. Bard, "Inner-sphere heterogeneous electrode reactions. Electrocatalysis and photocatalysis: the challenge," *Journal of the American Chemical Society*, vol. 132, no. 22, pp. 7559–7567, 2010.
- [13] A. J. Bard, R. Parsons, and J. Jordan, Eds., *Standard Potentials in Aqueous Solution*, 1985.
- [14] H. H. Yang and R. L. McCreery, "Elucidation of the mechanism of dioxygen reduction on metal-free carbon electrodes," *Journal of the Electrochemical Society*, vol. 147, no. 9, pp. 3420–3428, 2000.
- [15] B. B. Blizanac, P. N. Ross, and N. M. Markovic, "Oxygen electroreduction on Ag(111): the pH effect," *Electrochimica Acta*, vol. 52, no. 6, pp. 2264–2271, 2007.
- [16] J. O. Bockris and J. Appleby, "Alkaline Fuel Cells," in *Assessment of Research Needs for Advanced Fuel Cells*, S. S. Penner, Ed., vol. 11, p. 95, 1986.
- [17] A. J. Appleby, "Electrocatalysis," in *Comprehensive Treatise of Electrochemistry*, B. E. Conway, Ed., vol. 7, pp. 173–239, Plenum, New York, NY, USA, 1983.
- [18] R. Jasinski, "A new fuel cell cathode catalyst," *Nature*, vol. 201, no. 4925, pp. 1212–1213, 1964.
- [19] J. H. Zagal, "Metallophthalocyanines as catalysts in electrochemical reactions," *Coordination Chemistry Reviews*, vol. 119, pp. 89–136, 1992.
- [20] "Macrocycles," in *Handbook of Fuel Cells-Fundamentals*, J. H. Zagal, Ed., pp. 544–554, John Wiley & Sons, Chichester, UK, 2003.
- [21] B. Wang, "Recent development of non-platinum catalysts for oxygen reduction reaction," *Journal of Power Sources*, vol. 152, no. 1-2, pp. 1–15, 2005.
- [22] J.-P. Dodelet, "Oxygen reduction in pem fuel cell conditions: heat-treated non-precious metal-N₄ macrocycles and beyond," in *N₄-Macrocyclic Metal Complexes*, J. H. Zagal, F. Bedioui, and J.-P. Dodelet, Eds., p. 83, Springer, Berlin, Germany, 2006.
- [23] J. M. Ziegelbauer, T. S. Olson, S. Pylypenko et al., "Direct spectroscopic observation of the structural origin of peroxide generation from Co-based pyrolyzed porphyrins for ORR applications," *Journal of Physical Chemistry C*, vol. 112, no. 24, pp. 8839–8849, 2008.
- [24] K. Artyushkova, S. Levandosky, P. Atanassov, and J. Fulghum, "XPS Structural studies of nano-composite non-platinum electrocatalysts for polymer electrolyte fuel cells," *Topics in Catalysis*, vol. 46, no. 3-4, pp. 263–275, 2007.
- [25] A. L. Bouwkamp-Wijnoltz, W. Visscher, and J. A. R. van Veen, "The selectivity of oxygen reduction by pyrolysed iron porphyrin supported on carbon," *Electrochimica Acta*, vol. 43, no. 21-22, pp. 3141–3152, 1998.
- [26] A. L. Bouwkamp-Wijnoltz, W. Visscher, J. A. R. van Veen, E. Boellaard, A. M. van der Kraan, and S. C. Tang, "On active-site heterogeneity in pyrolyzed carbon-supported iron porphyrin catalysts for the electrochemical reduction of oxygen: an in situ mössbauer study," *Journal of Physical Chemistry B*, vol. 106, no. 50, pp. 12993–13001, 2002.
- [27] A. L. Bouwkamp-Wijnoltz, W. Visscher, J. A. R. van Veen, and S. C. Tang, "Electrochemical reduction of oxygen: an alternative method to prepare active CoN₄ catalysts," *Electrochimica Acta*, vol. 45, no. 3, pp. 379–386, 1999.
- [28] J. McBreen, W. E. O'Grady, D. E. Sayers, C. Y. Yang, and K. I. Pandya, "An EXAFS study of pyrolyzed metal macrocyclic electrocatalysts," S. Srinivasan, S. Wagner, and H. Wroblowa, Eds., vol. 87-12, p. 182, The Electrochemical Society, Pennington, NJ, USA.
- [29] H. Schulenburg, S. Stankov, V. Schünemann et al., "Catalysts for the oxygen reduction from heat-treated iron(III) tetramethoxyphenylporphyrin chloride: structure and stability and active sites," *Journal of Physical Chemistry B*, vol. 107, no. 34, pp. 9034–9041, 2003.
- [30] A. A. Tanaka, S. L. Gupta, D. Tryk, C. Fierro, and E. B. Yeager, "Electrochemical and spectroscopic aspects of heat-treated transition metal macrocycles as electrocatalysts for oxygen reduction," in *Structural Effects in Electrocatalysis and Oxygen Electrochemistry*, D. Scherson, D. Tryk, M. Daroux, and X. Xing, Eds., vol. 92-11, p. 555, Proceedings of the Electrochemical Society, 1992.
- [31] I. T. Bae, D. A. Tryk, and D. A. Scherson, "Effect of heat treatment on the redox properties of iron porphyrins adsorbed on high area carbon in acid electrolytes: an in situ Fe K-edge X-ray absorption near-edge structure study," *Journal of Physical Chemistry B*, vol. 102, no. 21, pp. 4114–4117, 1998.
- [32] S. Kim, I. T. Bae, M. Sandifer et al., "In situ XANES of an iron porphyrin irreversibly adsorbed on an electrode surface," *Journal of the American Chemical Society*, vol. 113, no. 24, pp. 9063–9066, 1991.
- [33] S. Kim, D. A. Tryk, I. T. Bae et al., "In situ extended X-ray absorption fine structure of an iron porphyrin irreversibly adsorbed on an electrode surface," *Journal of Physical Chemistry*, vol. 99, no. 25, pp. 10359–10364, 1995.
- [34] M. Lefèvre, J. P. Dodelet, and P. Bertrand, "Molecular oxygen reduction in PEM fuel cells: evidence for the simultaneous presence of two active sites in Fe-based catalysts," *Journal of Physical Chemistry B*, vol. 106, no. 34, pp. 8705–8713, 2002.
- [35] M. Lefèvre, J. P. Dodelet, and P. Bertrand, "O₂ reduction in PEM fuel cells: activity and active site structural information for catalysts obtained by the pyrolysis at high temperature of Fe precursors," *Journal of Physical Chemistry B*, vol. 104, no. 47, pp. 11238–11247, 2000.
- [36] M. Lefèvre and J. P. Dodelet, "Fe-based catalysts for the reduction of oxygen in polymer electrolyte membrane fuel cell conditions: determination of the amount of peroxide released during electroreduction and its influence on the stability of the catalysts," *Electrochimica Acta*, vol. 48, no. 19, pp. 2749–2760, 2003.
- [37] M. Lefèvre, E. Proietti, F. Jaouen, and J. P. Dodelet, "Iron-Based catalysts with improved oxygen reduction activity in polymer electrolyte fuel cells," *Science*, vol. 324, no. 5923, pp. 71–74, 2009.
- [38] G. Lalande, R. Côté, D. Guay, J. P. Dodelet, L. T. Weng, and P. Bertrand, "Is nitrogen important in the formulation of Fe-based catalysts for oxygen reduction in solid polymer fuel cells?" *Electrochimica Acta*, vol. 42, no. 9, pp. 1379–1388, 1997.
- [39] G. Lalande, G. Faubert, R. Côté et al., "Catalytic activity and stability of heat-treated iron phthalocyanines for the electroreduction of oxygen in polymer electrolyte fuel cells," *Journal of Power Sources*, vol. 61, no. 1-2, pp. 227–237, 1996.
- [40] M. C. M. Alves, J. P. Dodelet, D. Guay, M. Ladouceur, and G. Tourillon, "Origin of the electrocatalytic properties for O₂ reduction of some heat-treated polyacrylonitrile and

- phthalocyanine cobalt compounds adsorbed on carbon black as probed by electrochemistry and X-ray absorption spectroscopy," *Journal of Physical Chemistry*, vol. 96, no. 26, pp. 10898–10905, 1992.
- [41] G. Faubert, R. Côté, J. P. Dodelet, M. Lefèvre, and P. Bertrand, "Oxygen reduction catalysts for polymer electrolyte fuel cells from the pyrolysis of FeII acetate adsorbed on 3,4,9,10-perylenetetracarboxylic dianhydride," *Electrochimica Acta*, vol. 44, no. 15, pp. 2589–2603, 1999.
- [42] G. Faubert, G. Lalande, R. Côté et al., "Heat-treated iron and cobalt tetraphenylporphyrins adsorbed on carbon black: physical characterization and catalytic properties of these materials for the reduction of oxygen in polymer electrolyte fuel cells," *Electrochimica Acta*, vol. 41, no. 10, pp. 1689–1701, 1996.
- [43] P. He, M. Lefèvre, G. Faubert, and J. P. Dodelet, "Oxygen reduction catalysts for polymer electrolyte fuel cells from the pyrolysis of various transition metal acetates adsorbed on 3,4,9,10-perylenetetracarboxylic dianhydride," *Journal of New Materials for Electrochemical Systems*, vol. 2, no. 4, pp. 243–251, 1999.
- [44] C. Médard, M. Lefèvre, J. P. Dodelet, F. Jaouen, and G. Lindbergh, "Oxygen reduction by Fe-based catalysts in PEM fuel cell conditions: activity and selectivity of the catalysts obtained with two Fe precursors and various carbon supports," *Electrochimica Acta*, vol. 51, no. 16, pp. 3202–3213, 2006.
- [45] F. Jaouen, E. Proietti, M. Lefèvre et al., "Recent advances in non-precious metal catalysis for oxygen-reduction reaction in polymer electrolyte fuel cells," *Energy and Environmental Science*, vol. 4, no. 1, pp. 114–130, 2011.
- [46] D. P. Amalnerkar, S. Radhakrishnan, H. Minoura, T. Sugiura, and Y. Ueno, "Origin of the photocathodic effect at CdS + CuCl electrodes," *Journal of Electroanalytical Chemistry and Interfacial Electrochemistry*, vol. 260, no. 2, pp. 433–440, 1989.
- [47] G. Gruenig, K. Wiesener, S. Gamburgzev, I. Iliev, and A. Kaisheva, "Investigations of catalysts from the pyrolyzates of cobalt-containing and metal-free dibenzotetraazaannulenes on active carbon for oxygen electrodes in an acid medium," *Journal of Electroanalytical Chemistry*, vol. 159, no. 1, pp. 155–162, 1983.
- [48] J. A. R. van Veen, J. F. van Baar, and K. J. Kroese, "Effect of heat treatment on the performance of carbon-supported transition-metal chelates in the electrochemical reduction of oxygen," *Journal of the Chemical Society, Faraday Transactions 1*, vol. 77, no. 11, pp. 2827–2843, 1981.
- [49] P. Vasudevan, Santosh, N. Mann, and S. Tyagi, "Transition metal complexes of porphyrins and phthalocyanines as electrocatalysts for dioxygen reduction," *Transition Metal Chemistry*, vol. 15, no. 2, pp. 81–90, 1990.
- [50] F. Jaouen, M. Lefèvre, J. P. Dodelet, and M. Cai, "Heat-treated Fe/N/C catalysts for O₂ electroreduction: are active sites hosted in micropores?" *Journal of Physical Chemistry B*, vol. 110, no. 11, pp. 5553–5558, 2006.
- [51] C. W. B. Bezerra, L. Zhang, K. Lee et al., "A review of Fe–N/C and Co–N/C catalysts for the oxygen reduction reaction," *Electrochimica Acta*, vol. 53, no. 15, pp. 4937–4951, 2008.
- [52] A. Garsuch, A. Bonakdarpour, G. Liu, R. Yang, and J. R. Dahn, "Time to move beyond transition metal–N–C catalysts for oxygen reduction," in *Handbook of Fuel Cells*, vol. 5, Springer, New York, NY, USA, 2009.
- [53] N. Ramaswamy, R. J. Allen, and S. Mukerjee, "Electrochemical kinetics and X-ray absorption spectroscopic investigations of oxygen reduction on chalcogen-modified ruthenium catalysts in alkaline media," *Journal of Physical Chemistry C*, vol. 115, no. 25, pp. 12650–12664, 2011.
- [54] T. M. Arruda, B. Shyam, J. S. Lawton et al., "Fundamental aspects of spontaneous cathodic deposition of Ru onto Pt/C electrocatalysts and membranes under direct methanol fuel cell operating conditions: an in situ X-ray absorption spectroscopy and electron spin resonance study," *Journal of Physical Chemistry C*, vol. 114, no. 2, pp. 1028–1040, 2010.
- [55] T. M. Arruda, B. Shyam, J. M. Ziegelbauer, S. Mukerjee, and D. E. Ramaker, "Investigation into the competitive and site-specific nature of anion adsorption on Pt using in situ X-ray absorption spectroscopy," *Journal of Physical Chemistry C*, vol. 112, no. 46, pp. 18087–18097, 2008.
- [56] A. L. Ankudinov, B. Ravel, J. J. Rehr, and S. D. Conradson, "Real-space multiple-scattering calculation and interpretation of x-ray-absorption near-edge structure," *Physical Review B*, vol. 58, no. 12, pp. 7565–7576, 1998.
- [57] V. S. Murthi, R. C. Urian, and S. Mukerjee, "Oxygen reduction kinetics in low and medium temperature acid environment: correlation of water activation and surface properties in supported Pt and Pt alloy electrocatalysts," *Journal of Physical Chemistry B*, vol. 108, no. 30, pp. 11011–11023, 2004.
- [58] M. R. Tarasevich, A. Sadkowski, and E. Yeager, "Kinetics and mechanisms of electrode processes," in *Comprehensive Treatise of Electrochemistry*, B. E. Conway, J. O. M. Bockris, E. Yeager, S. U. M. Khanand, and R. E. White, Eds., vol. 7, pp. 301–398, Plenum Press, New York, NY, USA, 1983.
- [59] N. M. Marković, H. A. Gasteiger, and P. N. Ross, "Oxygen reduction on platinum low-index single-crystal surfaces in alkaline solution: rotating ring diskPt(hkl) studies," *Journal of Physical Chemistry*, vol. 100, no. 16, pp. 6715–6721, 1996.
- [60] N. Ramaswamy and S. Mukerjee, "Influence of inner- and outer-sphere electron transfer mechanisms during electrocatalysis of oxygen reduction in alkaline media," *Journal of Physical Chemistry C*, vol. 115, no. 36, pp. 18015–18026, 2011.
- [61] E. Janin, H. Von Schenck, M. Göthelid, U. O. Karlsson, and M. Svensson, "Bridge-bonded atomic oxygen on Pt(110)," *Physical Review B*, vol. 61, no. 19, pp. 13144–13149, 2000.
- [62] G. Jerkiewicz, G. Vatankhah, J. Lessard, M. P. Soriaga, and Y. S. Park, "Surface-oxide growth at platinum electrodes in aqueous H₂SO₄ Reexamination of its mechanism through combined cyclic-voltammetry, electrochemical quartz-crystal nanobalance, and Auger electron spectroscopy measurements," *Electrochimica Acta*, vol. 49, no. 9–10, pp. 1451–1459, 2004.
- [63] N. M. Marković and P. N. Ross, "Surface science studies of model fuel cell electrocatalysts," *Surface Science Reports*, vol. 45, no. 4–6, pp. 117–229, 2002.
- [64] P. Chen and R. L. McCreery, "Control of electron transfer kinetics at glassy carbon electrodes by specific surface modification," *Analytical Chemistry*, vol. 68, no. 22, pp. 3958–3965, 1996.
- [65] P. Chen, M. A. Fryling, and R. L. McCreery, "Electron transfer kinetics at modified carbon electrode surfaces: the role of specific surface sites," *Analytical Chemistry*, vol. 67, no. 18, pp. 3115–3122, 1995.
- [66] N. Wakabayashi, F. Kitamura, T. Ohsaka, and K. Tokuda, "Effect of adsorbed anions on the outer-sphere electron-transfer reactions of cobalt complexes at platinum single-crystal electrodes," *Journal of Electroanalytical Chemistry*, vol. 499, no. 1, pp. 161–168, 2001.
- [67] T. Wandlowski and R. de Levie, "Double-layer dynamics in the adsorption of tetrabutylammonium ions at the mercury–water interface Part 4. The reduction of hexamine-cobalt

- (III) through tetrabutylammonium films,” *Journal of Electroanalytical Chemistry*, vol. 380, no. 1-2, pp. 201–207, 1995.
- [68] N. A. Anastasijevic, Z. M. Dimitrijevic, and R. R. Adzic, “Oxygen reduction on a ruthenium electrode in alkaline electrolytes,” *Journal of Electroanalytical Chemistry and Interfacial Electrochemistry*, vol. 199, no. 2, pp. 351–364, 1986.
- [69] N. A. Anastasijevic, Z. M. Dimitrijevic, and R. R. Adzic, “Oxygen reduction on a ruthenium electrode in acid electrolytes,” *Electrochimica Acta*, vol. 31, no. 9, pp. 1125–1130, 1986.
- [70] N. Ramaswamy, R. J. Allen, and S. Mukerjee, “Electrochemical kinetics and X-ray absorption spectroscopic investigations of oxygen reduction on chalcogen-modified ruthenium catalysts in alkaline media,” *The Journal of Physical Chemistry C*, vol. 115, no. 25, pp. 12650–12664, 2011.
- [71] R. Boulatov, “Billion-Year-Old Oxygen Cathode that Actually Works: Respiratory Oxygen Reduction and Its Biomimetic Analogs,” in *N4-Macrocyclic Metal Complexes*, J. H. Zagal, F. Bedioui, and J.-P. Dodelet, Eds., p. 1, Springer, Berlin, Germany, 2006.
- [72] R. Boulatov, “Metalloporphyrin Catalysts of Oxygen Reduction,” in *Fuel Cell Catalysis*, M. T. M. Koper, Ed., p. 637, John Wiley & Sons, New York, NY, USA, 2008.
- [73] N. Ramaswamy and S. Mukerjee, “Electrocatalysis of oxygen reduction on nonprecious metallic centers at high pH environments,” *ECS Transactions*, vol. 33, no. 1, pp. 1777–1785, 2010.
- [74] K. M. Kadish, E. van Caemelbecke, and R. Royal, “Electrochemistry of metalloporphyrins in nonaqueous media,” in *The Porphyrin Handbook*, K. M. Kadish, K. M. Smith, and R. Guilard, Eds., vol. 8, chapter 55, pp. 1–97, Academic Press, San Diego, Calif, USA, 2000.
- [75] M. Teliska, V. S. Murthi, S. Mukerjee, and D. E. Ramaker, “Correlation of water activation, surface properties, and oxygen reduction reactivity of supported Pt-M/C bimetallic electrocatalysts using XAS,” *Journal of the Electrochemical Society*, vol. 152, no. 11, pp. A2159–A2169, 2005.
- [76] M. Teliska, W. E. O’Grady, and D. E. Ramaker, “Determination of O and OH adsorption sites and coverage in situ on Pt electrodes from Pt L23 X-ray absorption spectroscopy,” *Journal of Physical Chemistry B*, vol. 109, no. 16, pp. 8076–8084, 2005.
- [77] E. A. Lewis, C. U. Segre, and E. S. Smotkin, “Embedded cluster Δ -XANES modeling of adsorption processes on Pt,” *Electrochimica Acta*, vol. 54, no. 28, pp. 7181–7185, 2009.
- [78] F. Beck, “The redox mechanism of the chelate-catalysed oxygen cathode,” *Journal of Applied Electrochemistry*, vol. 7, no. 3, pp. 239–245, 1977.
- [79] S. R. P. Silva, “Properties of Amorphous Carbon,” in *Properties of Amorphous Carbon*, EMIS Datareviews Series 29, 2003.
- [80] Y. J. Cho, H. S. Kim, S. Y. Baik et al., “Selective nitrogen-doping structure of nanosize graphitic layers,” *Journal of Physical Chemistry C*, vol. 115, no. 9, pp. 3737–3744, 2011.
- [81] J. R. Hahn and H. Kang, “Vacancy and interstitial defects at graphite surfaces: scanning tunneling microscopic study of the structure, electronic property, and yield for ion-induced defect creation,” *Physical Review B*, vol. 60, no. 8, pp. 6007–6017, 1999.
- [82] S. L. Mielke, D. Troya, S. Zhang et al., “The role of vacancy defects and holes in the fracture of carbon nanotubes,” *Chemical Physics Letters*, vol. 390, no. 4–6, pp. 413–420, 2004.
- [83] Y. Luo, Y. Heng, X. Dai, W. Chen, and J. Li, “Preparation and photocatalytic ability of highly defective carbon nanotubes,” *Journal of Solid State Chemistry*, vol. 182, no. 9, pp. 2521–2525, 2009.
- [84] T. Kondo, T. Suzuki, and J. Nakamura, “Nitrogen doping of graphite for enhancement of durability of supported platinum clusters,” *Journal of Physical Chemistry Letters*, vol. 2, no. 6, pp. 577–580, 2011.
- [85] P. Nemes-Incze, Z. Kóinya, I. Kiricsi et al., “Mapping of functionalized regions on carbon nanotubes by scanning tunneling microscopy,” *Journal of Physical Chemistry C*, vol. 115, no. 8, pp. 3229–3235, 2011.
- [86] A. B. Anderson and R. A. Sidik, “Oxygen Electroreduction on FeII and FeIII Coordinated to N4 Chelates. Reversible Potentials for the Intermediate Steps from Quantum Theory,” *Journal of Physical Chemistry B*, vol. 108, no. 16, pp. 5031–5035, 2004.

Research Article

Multiscale Modeling of Au-Island Ripening on Au(100)

Karin Kleiner, Alex Comas-Vives, Maryam Naderian, Jonathan E. Mueller, Donato Fantauzzi, Mostafa Mesgar, John A. Keith, Josef Anton, and Timo Jacob

Institut für Elektrochemie, Universität Ulm, Albert-Einstein-Alle 47, 89069 Ulm, Germany

Correspondence should be addressed to Timo Jacob, timo.jacob@uni-ulm.de

Received 6 June 2011; Revised 31 October 2011; Accepted 14 November 2011

Academic Editor: Gianluigi Botton

Copyright © 2011 Karin Kleiner et al. This is an open access article distributed under the Creative Commons Attribution License, which permits unrestricted use, distribution, and reproduction in any medium, provided the original work is properly cited.

We describe a multiscale modeling hierarchy for the particular case of Au-island ripening on Au(100). Starting at the microscopic scale, density functional theory was used to investigate a limited number of self-diffusion processes on perfect and imperfect Au(100) surfaces. The obtained structural and energetic information served as basis for optimizing a reactive forcefield (here ReaxFF), which afterwards was used to address the mesoscopic scale. Reactive force field simulations were performed to investigate more diffusion possibilities at a lower computational cost but with similar accuracy. Finally, we reached the macroscale by means of kinetic Monte Carlo (kMC) simulations. The reaction rates for the reaction process database used in the kMC simulations were generated using the reactive force field. Using this strategy, we simulated nucleation, aggregation, and fluctuation processes for monoatomic high islands on Au(100) and modeled their equilibrium shape structures. Finally, by calculating the step line tension at different temperatures, we were able to make a direct comparison with available experimental data.

1. Introduction

Surface diffusion plays a key role in dynamical processes occurring on metallic surfaces which involve physical or chemical displacements of atoms or molecules on a particular surface [1], such as adsorption-desorption, crystal growth, coarsening, chemical reactions, wetting, spreading, or capillarity. Hence, a profound understanding of this phenomenon has implications in a great variety of fields such as electrochemistry, microelectronics, tribology, and corrosion protection [2]. Two main pathways can be distinguished for the diffusion of adatoms across a surface. The first one corresponds to the *hopping* of an adatom between different adsorption sites, whereas in the so-called *exchange* mechanism, adatoms replace atoms of the surface layer (or fall into vacancies) while surface atoms are simultaneously pushed onto adsorption sites [3]. The latter pathway was proposed for Al(001) [4] and Au(100) [5] based on theoretical studies (Müller and Ibach stated that the *hopping* mechanism could be also competitive on Au(100)) [6]. While for planar terraces these processes are rather well understood, [7–14] much less is known about diffusion processes on imperfect surfaces with lower coordinated adsorption sites (e.g., kink- and step-sites or vacancies). However, these types

of sites often determine morphological changes of the surface structure, for instance, in Ostwald ripening, metal deposition and dissolution, or island and step fluctuation processes. It should be noted that clean Au(100) shows a quasi-hexagonal reconstruction in the first surface layer [15], however, this reconstruction can be lifted in an electrochemical cell by applying a sufficiently positive potential. Under these conditions, chemisorbed species (e.g., anions) and electric fields are present at the metal interface. Although these parameters are not taken into account in the present work; we reported the influence of these parameters in previous experimental and theoretical studies [16–18]. Moreover, the lifting and the restoration of the reconstruction are slow processes, so that both types of surfaces can be assumed to be present over a sizable range of potentials.

In order to address diffusion phenomena at surfaces theoretically, different approaches are used, which range from experimentally based, semiempirical molecular dynamics up to first principles studies. In the present work, we describe a first principles-based approach for investigating surface dynamics on Au(100). While improvements in experimental techniques have led to considerable progress in the investigation of surface diffusion, there is still a lack on the experimental data for the self-diffusion on Au(100).

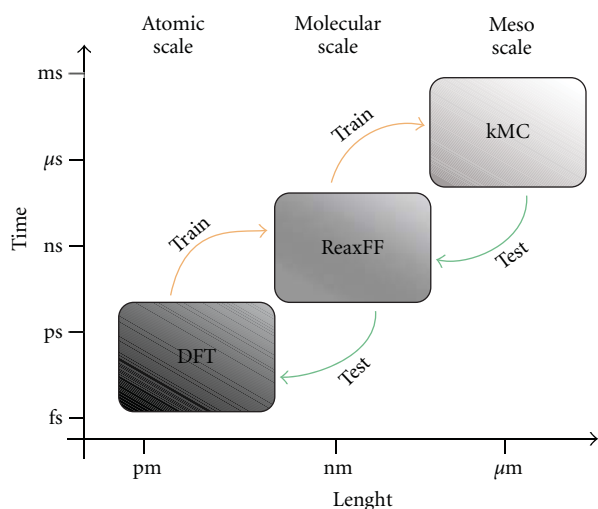


FIGURE 1: Schematic of the hierarchy of computational chemistry used in the present work. Starting on the atomic scale, the information obtained via DFT was used to train a reactive force field (ReaxFF), which addresses the molecular scale. ReaxFF was then used to obtain the relevant data for kinetic Monte Carlo simulations to model the mesoscale. While training was performed upwards, each approach was tested against the next higher-level (more accurate) method.

The basis for the present study is a recent contribution from our group where the most reasonable processes for self-diffusion on Au(100) were studied using quantum mechanics (density functional theory, DFT). This study specifically focused on terraces and imperfect kink- and step-configurations [19]. Since the rate of adatom migration depends mainly on its immediate environment, we concentrated on the nearest neighbor interactions only. Nevertheless, with this restriction, already more than a thousand surface configurations have to be considered [20]. Given the high computational expense of DFT calculations, with the present computing resources, one is rather limited in the number of systems that can be studied from first principles. However, we can use the binding energies and self-diffusion processes previously studied by *ab initio* simulations to construct and optimize a reactive force field (here ReaxFF) that is able to reproduce this behavior. After the mandatory tests related to accuracy and transferability of the force field, ReaxFF has the advantage of being nearly as accurate as QM but with much lower computational demands [21]. Using ReaxFF to investigate all possible diffusion processes (considering only first-nearest neighbors), the obtained process rates were used with kinetic Monte Carlo simulations (kMC) for large-scale simulations that allowed us to analyze island nucleation, aggregation, and fluctuation as well as the equilibrium shapes of adatom islands on Au(100). Figure 1 shows the overall computational procedure, where we started at the *ab initio* level of theory to obtain a reactive molecular dynamics forcefields, which was then used to provide the necessary process rates for macroscopic kinetic Monte Carlo simulations. Similar hierarchical simulation schemes have

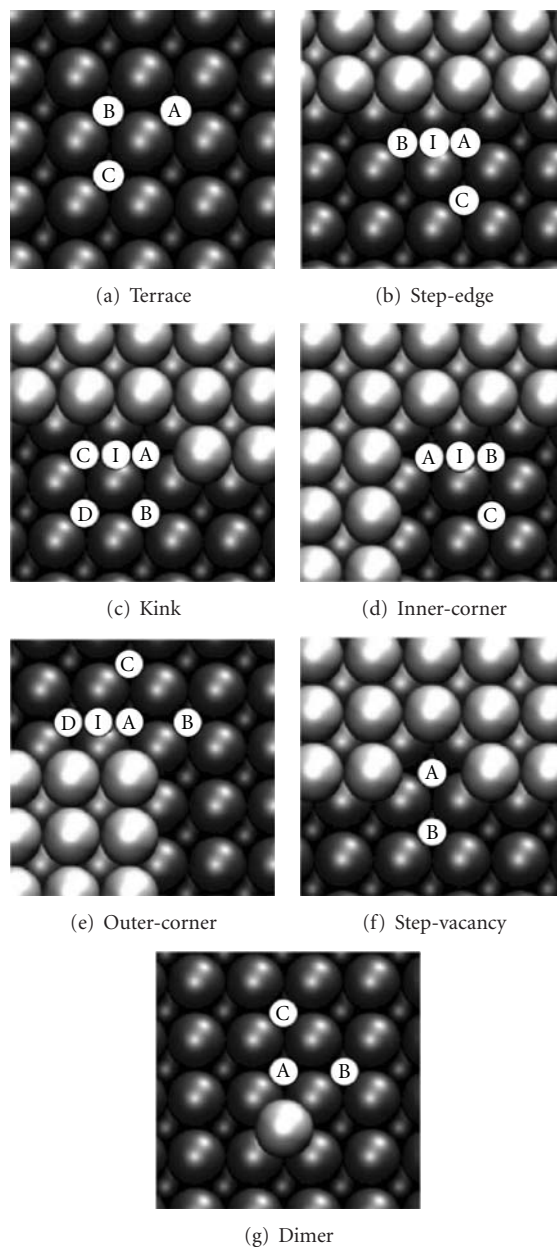


FIGURE 2: Overview of the different diffusion pathways on Au(100) that have been investigated with DFT.

been employed by the groups of Goddard, Neurock, and van Santen, for instance [22–25].

2. First Principles Calculations

We used density functional theory to investigate different self-diffusion mechanisms in the presence or absence of a variety of surface defects on Au(100), for example, kink- and step-edges. Usually, DFT calculations in the gradient generalized approximations (such as the PBE density functional used in this work) are able to achieve a chemical accuracy of ≤ 0.1 eV for reactions [13]. Since the details of these studies are described in [19], here we only give a brief summary.

TABLE 1: Activation energies, prefactors, and calculated rate constants (at 300 K) for the different diffusion pathways.

System		Pathway	E_{act} (eV)	k_0 (10^{12} Hz)	$k^{300\text{K}}$ (Hz)
Terrace	I-1	A \leftrightarrow B (hop)	0.70	1.91	3.34
	I-2	A \leftrightarrow C (hop)	1.39	1.68	7.54×10^{-12}
	I-3	A \leftrightarrow C (exc)	0.55	1.76	1.02×10^3
Step-edge	II-1	A \leftrightarrow B	0.38	1.41	5.83×10^5
	II-2	A \rightarrow C	0.84	1.91	1.48×10^{-2}
	II-3	C \rightarrow A	0.66	1.42	1.17×10^1
Kink-site	III-1	A \rightarrow B	0.86	1.75	6.11×10^{-3}
	III-2	B \rightarrow A	0.46	1.43	2.69×10^4
	III-3	A \rightarrow C	0.62	1.72	6.63
	III-4	C \rightarrow A	0.35	1.45	1.92×10^6
	III-5	C \rightarrow D	0.80	1.67	6.10×10^{-2}
	III-6	D \rightarrow C	0.62	1.42	5.45
Inner-corner	IV-1	A \rightarrow B	0.60	1.70	1.42×10^2
	IV-2	B \rightarrow A	0.34	1.40	2.72×10^6
	IV-3	B \rightarrow C	0.93	1.64	3.91×10^{-4}
	IV-4	C \rightarrow B	0.63	1.50	3.93
Outer-corner	V-1	A \rightarrow B	0.75	1.55	3.90
	V-2	B \rightarrow A	0.56	1.48	5.81×10^2
	V-3	A \rightarrow C	0.89	1.80	2.03×10^{-3}
	V-4	C \rightarrow A	0.66	1.41	1.15
	V-5	A \rightarrow D	0.49	1.55	9.10×10^3
	V-6	D \rightarrow A	0.47	1.45	1.84×10^4

From these first principle studies, we were able to obtain binding energies of the stable intermediates and transition states and to extract rate constants for the diffusion events. An overview of the different pathways that have been studied is given in Figure 2.

On terraced Au(100) surfaces, we found that the lowest energy mechanism was the exchange diffusion pathway from position A to C ($E_{\text{act}} = 0.55$ eV), while hopping diffusion from A to B over a bridge site was less favorable ($E_{\text{act}} = 0.70$ eV). The last evaluated reaction pathway at terraces was the atom hopping over the top position from A to C, being the least favorable with a rather high energy barrier of 1.39 eV.

The presence of step-edges has a tremendous influence on the Au-adatom diffusion, since the energy barrier is even lower for the diffusion along the step-edge (0.38 eV). As expected, diffusion perpendicular to or from the step edge has a much higher barrier of 0.84 eV (detachment) and 0.66 eV (attachment). Comparing the barriers shows that rearrangement of adatoms along the step would be faster than island growth or decay, which would lead to islands that quickly assume their equilibrium shapes before changing their size.

Afterwards, systems involving corners at step-edges were analyzed (see Figure 2). For the inner-corner system, we found that diffusion along long edges is preferred over migration along short edges. This suggests that Au atoms adsorbed at terraces first reach kink-sites or inner-corner

positions at islands by exchange diffusion, followed by a hopping diffusion to the step-edges where they rapidly diffuse along the step-edges. As far as the outer-corner systems are concerned, adatoms, which are located directly next to an island corner, have essentially the same binding energy as an adatom at a step-edge. In addition, we found that detachment from the outer-corner was preferred over detachment away from the step-edge.

Finally, we calculated diffusion pathways for forming Au-dimers, which can be considered the first step of island formation, and for extraction of an adatom out of a step-edge forming a step-vacancy. While the latter process has a relatively high energy barrier of 1.07 eV, dimer diffusion is comparable to the case of a single atom.

In addition to reaction barriers, we calculated vibrational frequencies factors for each reaction. This was accomplished by fitting a frequency to the energy profile of each reactant state to within the harmonic approximation. Using these frequencies, we calculated the rates for the different diffusion events at variable temperatures (see Table 1) by means of the transition-state theory, as given by equation (1):

$$k = k_0 \exp\left(\frac{-E_{\text{act}}}{k_B T}\right), \quad (1)$$

where k_0 is a prefactor, E_{act} is the barrier for diffusion (activation), k_B is the Boltzmann constant, and T is the temperature (all of our mechanisms are first-order kinetic reactions, and so these terms are simply the vibrational frequency of the self-diffusion process in units of Hz). One

of the main limitations of this approach is that it does not account for anharmonicity and thermal expansion, which cause deviations at higher temperatures. Moreover, it also ignores memory effects arising from the surface excitations, which change the effective Arrhenius barrier. Nevertheless, the Arrhenius law’s validity within the limit of $E_{\text{act}}/k_B T \geq 4$ provides reasonable temperature ranges, for which our results are valid [26].

The obtained diffusion rate constants (Table 1) clearly illustrate the importance of the surface structure on cluster formation and island growth. The fastest rate corresponds to the filling of an inner-corner by a diffusing atom (IV-2 pathway), although the same system also yields the slowest rate with pathway IV-3 (not considering the very unfavorable A \rightarrow C hopping diffusion at terraces). Concerning the terraces, the diffusion over the top position is practically negligible while the exchange diffusion rate is around 300 times larger than the bridge diffusion rate. Our calculated activation energies for the A \rightarrow B hopping process and for the A \rightarrow C exchange process on the terrace are 0.70 and 0.55 eV, respectively. These values are in reasonable agreement with the approximated experimental activation barrier of 0.5 eV for the adatom hopping on Au(100) [27]. In addition, they also agree well with previous theoretical studies. For example, Müller and Ibach reported energy barriers of 0.64 eV and 0.60 eV for the hopping and the exchange processes on an Au(100) [6].

Although *ab initio* studies only allow the investigation of a limited set of diffusion possibilities, the studies presented so far already provide useful insights into diffusion events on Au(100) with important implications for Ostwald ripening and island formation. However, the next step is to account for more possibilities, as described subsequently in the list of possible diffusion events section, by means of larger scale reactive forcefield calculations. Therefore, in the next section we will summarize the generation of the corresponding Au-forcefield, which was then used to evaluate the rates for many more diffusion scenarios.

3. Reactive Forcefield (ReaxFF) Simulations

The next step in the multiscale approach presented in this work corresponds to the generation and application of a reactive forcefield within the ReaxFF framework [28–30]. ReaxFF is a reactive molecular dynamics method that uses a bond-order-dependent potential energy formulation, similar to the Tersoff [31] or Brenner [32] potentials. These potentials are all based on Pauling’s idea of mapping bond distances onto bond orders to enable the determination of different quantum chemical states of a molecular structure [33].

The dependence of the energy contributions on the bond order also means that such energy terms implicitly contain multibody contributions. The Au forcefield employed in the present study contains the following three energy terms (2):

$$E_{\text{system}} = E_{\text{bond}} + E_{\text{over}} + E_{\text{vdW}}, \quad (2)$$

where E_{bond} is the energy corresponding to interatomic bonds, E_{over} is a penalty energy that corrects atomic over-

coordinations, and E_{vdW} accounts for van der Waals interactions and interatomic repulsions when atoms are too close to each other. The full expressions for these terms as well as the included parameters can be found in more detail in a previous publication from our group [21].

The formulation of the system energy is more sophisticated than those of nonreactive potentials, for example, EAM [34–37], MEAM [38], UFF [39, 40], CHARMM [41], OPLS [42], or AMBER [43, 44], and therefore computationally more demanding. Reactive forcefields represent a useful tool for overcoming limitations of these empirical potentials as it allows for the description of chemical reactions, that is, bond formation and dissociation, with almost QM accuracy. In contrast to most other forcefields, the ReaxFF potential used in the present work is completely trained against *ab initio* DFT calculations.

The goal of this training process is to optimize the parameters of the forcefield such that the DFT energies and structures are reproduced as accurately as possible. In this specific case, first principles DFT-PBE calculations on the equations of state for several gold bulk phases, as well as binding energies and self-diffusion processes on Au(100) surfaces as described in the previous section, were used in the training procedure. The validity and the transferability of the obtained interaction potential was successfully tested for additional diffusion processes, surface free energies of Au low index surfaces, and cohesive energies of molecular Au clusters. Details concerning these tests as well as a first application to study the morphology of larger Au nanoparticles can be found in [21]. The purpose was to obtain a large database of diffusion processes on Au(100) under a wide range of defects that one might expect to exist on real surfaces, in order to obtain the diffusion barriers which are needed to run kMC simulations. As already mentioned before, the simulation of all the diffusion processes that could occur is a task that cannot be achieved in a reasonable time using DFT or other *ab initio* methods.

Figure 3 shows exemplarily the performance of the ReaxFF Au-forcefield after the optimization procedure. Besides simple terrace (bridge) diffusion, diffusion along step edges, around kink sites, and diffusion forming molecular dimers are compared. The comparison shows that the forcefield is indeed a useful tool for calculating all the remaining diffusion processes required to evaluate the database of diffusion rates required for the kMC approach, and thus for bridging the gap between QM and the macroscopic regime.

4. Kinetic Monte Carlo

Kinetic Monte Carlo (kMC) is a well-known technique for large-scale simulations in various areas of research such as chemical physics or materials design [45–47]. In order to perform such kMC simulations on the dynamic behavior of two-dimensional gold islands on Au(100), we used the previously described ReaxFF forcefield to generate a list of independent (Markov chain) diffusion rates for all possible diffusion scenarios (taking the first-nearest neighbors into account) [48].

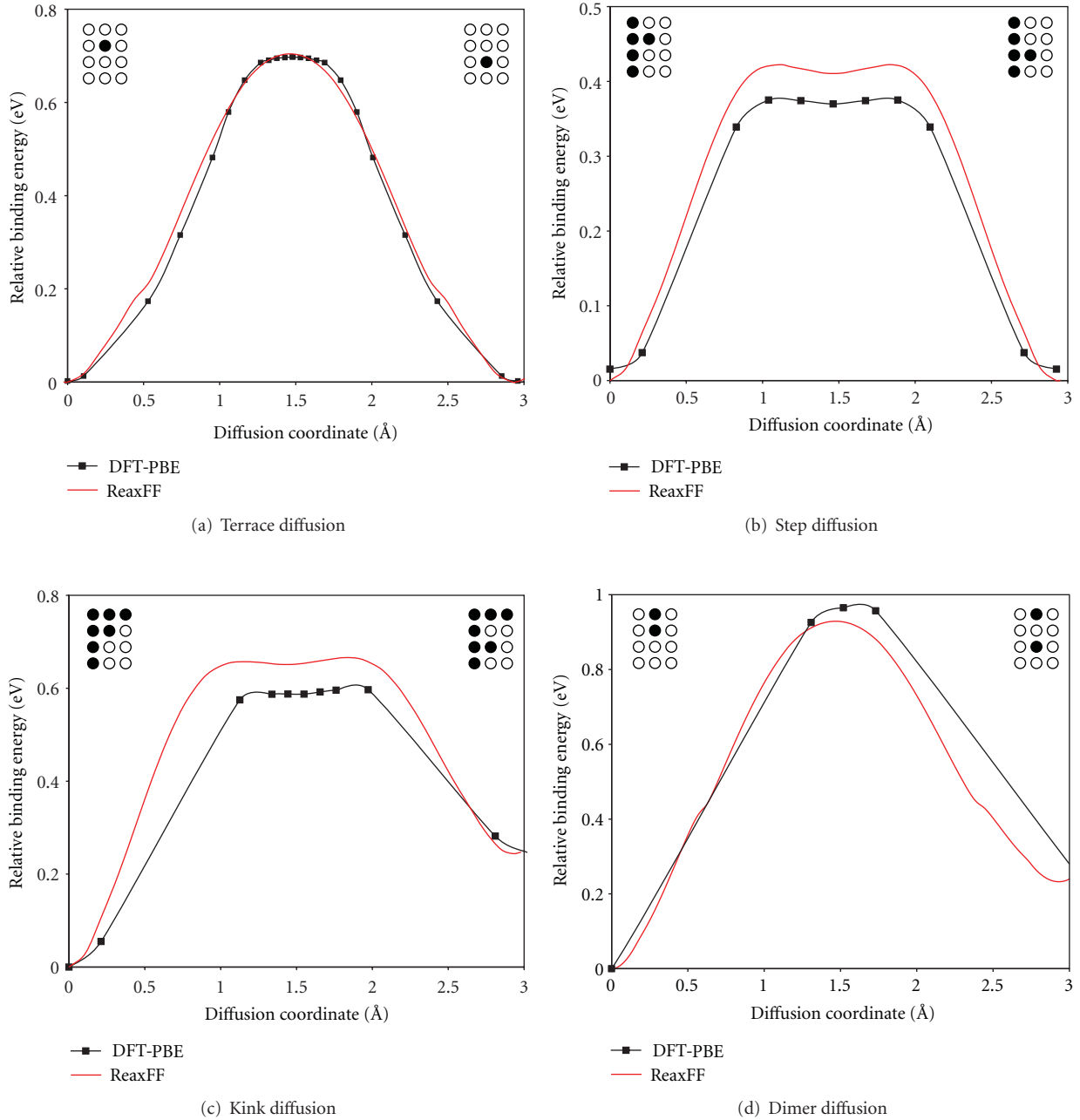


FIGURE 3: Selected Au diffusion pathways on an Au(100) surface (a) bridge diffusion on a terrace, (b) along a step, (c) kink diffusion, and (d) dimer diffusion. Insets in each figure illustrate the diffusion pathways, where filled circles depict adatoms on an Au(100) surface.

Along the kMC simulations, the total rate R (cumulative function) of all diffusion events of a particular system is calculated by means of (3):

$$R = \sum_{i=1}^N k_i. \quad (3)$$

In this function, all possible elementary diffusion processes are taken into account by their individual rates k_i . Then, by using a random number, ρ_1 , between zero and one,

we assign it to a rate out of all the processes described in the cumulative function (R):

$$\sum_{i=0}^{l-1} k_i \leq \rho_1 R \leq \sum_{i=0}^l k_i, \quad (4)$$

where l then specifies the particular process which will be executed. After each diffusion event, the simulation time is propagated by

$$\Delta t = \frac{1}{R}. \quad (5)$$

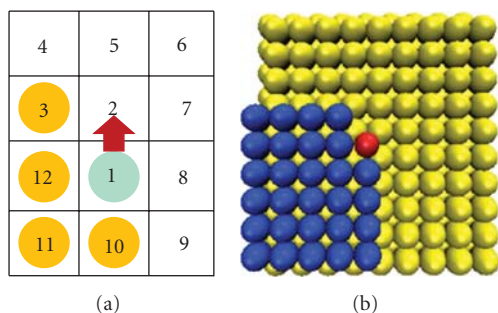


FIGURE 4: (a) Schematic representation of a diffusion event. The adatom of interest (blue) diffuses from position 1 to 2, while the next-nearest neighbor positions 3–12 can be either occupied (yellow) or empty. (b) Hard-sphere model of a possible diffusion process. The red atom would correspond to position 1, while the blue atoms are occupied adsorption sites (yellow spheres in (a)) and yellow atoms are the underlying Au(100) surface.

However, for a realistic value of Δt , we have to allow fluctuations, therefore, a second random number, ρ_2 , is chosen between zero and one and afterwards used in (5) in the following way:

$$\begin{aligned} t &= t + \Delta t, \\ \Delta t &= -\frac{\ln \rho_2}{R}. \end{aligned} \quad (6)$$

After executing the particular diffusion process and propagating the time the iterative simulation proceeds by calculating the cumulative function (R) of the new structure, and so forth. As the kMC approach is based on random numbers, reasonable statistics are required to allow for reliable qualitative and quantitative conclusions.

5. List of Possible Diffusion Events

Given the structure of the Au(100) surface, the number of possible diffusion events, (considering only next-nearest neighbors and neglecting symmetry considerations) is $2^{10} = 1024$, which is the number of reactions required for the rate catalog. The profile of the considered diffusion pathways is depicted in Figure 4. While the atom of interest diffuses from position 1 to 2, the nearest neighbor (NN) sites (labeled from 3 to 12) are either empty or occupied.

Although the classification described in Figure 4 only considers the next-nearest neighbors, when calculating the diffusion events with ReaxFF and afterwards the rates to be used in the following kMC simulations, a slightly modified system has been employed. For the ReaxFF studies, each system was characterized by a four-layer slab for the underlying Au(100) surface with a lateral extension of 10×10 atoms. When occupying the surrounding sites, not only the positions specified by the labels 3–12 have been filled, but always the entire outgoing rows of atoms. Thus, for instance, the diffusion process indicated in Figure 4(a) has been studied with the model shown in Figure 4(b). On the basis of this structure, we used ReaxFF to map the energy profile when moving the diffusion atom (red) successively

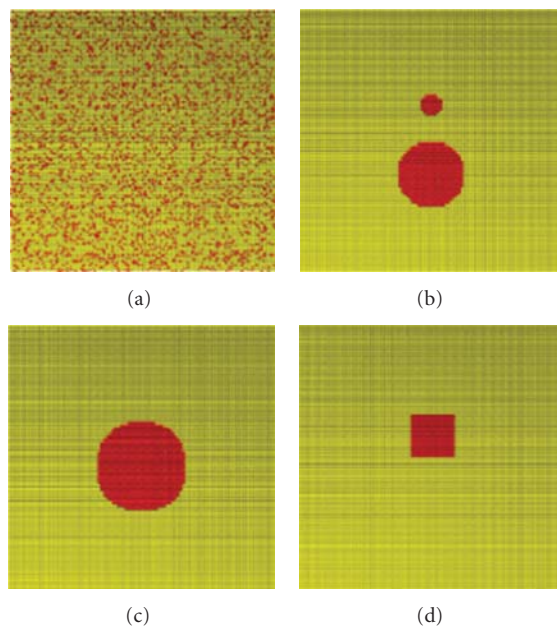


FIGURE 5: Initial input configurations considered in the kMC simulations: (a) random distribution of 3375 adatoms; (b) two islands with 52 and 508 atoms, respectively; (c) round island with 912 Atoms; (d) squared island with 256 Atoms. The Au adatoms are depicted in red while the Au(100) surface atoms are shown in yellow.

from position 1 to 2. The energy profile provided the activation energy and vibrational frequencies, which together with transition state theory (TST) provided all diffusion rates to be included in the event database for the kMC studies.

6. Input Structures

Kinetic Monte Carlo was utilized to study different systems, in which the Au(100) substrate was modeled by a square lattice of 100×100 positions. Periodic boundary conditions were imposed in x - and y -directions (parallel to the substrate) and all atoms were assumed to be uncharged. In this work, we analyzed four different initial input configurations, their evolution are being followed at 850 K. Figure 5 shows (a) a random distribution of adatoms, (b) a two-island structure, (c) a spherical island, and (d) a square island.

It should be noted that although during the kMC simulations the systems were always free to evolve, for simplicity, the exchange mechanism at terraces was not included in the rate catalog.

7. Nucleation and Aggregation

Subsequently, we followed the evolution of the initial input structures (see Figure 5) at 850 K. The first structure (a) starts with a randomly distributed dispersion of adatoms on the Au(100) surface. In Figure 6, we show successive snapshots of the kMC simulation of this structure. Along the structural evolution, particle nucleation is observed, as,

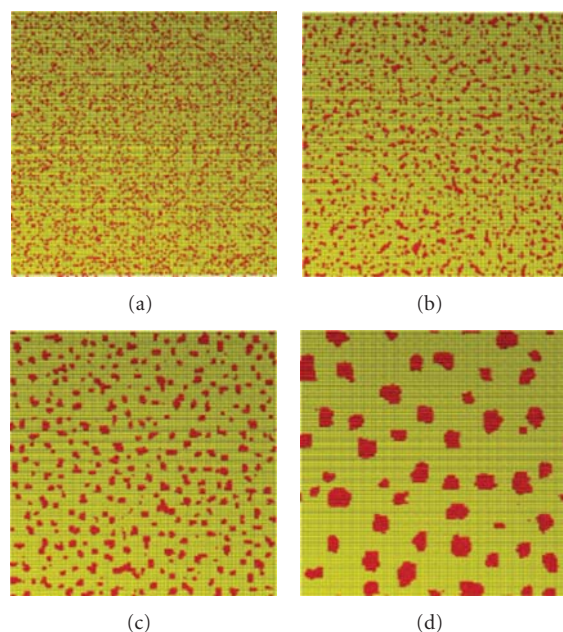


FIGURE 6: Snapshots of the nucleation process at 850 K, starting from randomly dispersed adatoms on the Au(100) surface. (a) Initial structure, (b) after 0.25 ns, (c) after 7.1 ns, and (d) after 4039 ns. After 10^9 iteration steps the average of the island size reaches 180 atoms.

after several hundreds of kMC steps, the randomly dispersed adatoms begin forming nucleation seeds. These nucleation seeds afterwards form small islands that successively grow during the ~ 4000 ns simulation period. Thus, the process indicated in Figure 6 indeed shows the first stages of island formation. As expected, we also found that the nucleation speed increases with temperature and adatom coverage. This can be explained by the fact that with randomly dispersed adatoms at the beginning, the highest rate corresponds to the free hopping of adatoms on the surface. After several simulation steps, adatoms meet each other forming slowly growing islands. This makes the step-edge diffusion possible and avoids the diffusion away from the step (the latter process has a higher energy barrier), therefore, continuously favoring the growth of the islands.

With the second system (Figure 5(b)), we followed the evolution of a pair of disparately sized islands at 850 K (see Figure 7). After several kMC steps, the smaller island starts dissolving, while the detached Au atoms quickly migrate to the larger island where they are assimilated. Hence, this simulation provides insights on how island growth proceeds.

8. Island Shape (Equilibrium and Fluctuation)

Step-edge fluctuation is the dominating process in determining the dynamic shape of islands on the Au(100) surface. Several diffusion processes contribute to step-edge fluctuation: diffusion along the step-edge, along a kink-site, or along an outer-corner. As explained in the DFT section, the rate for step-edge-diffusion is the highest among these

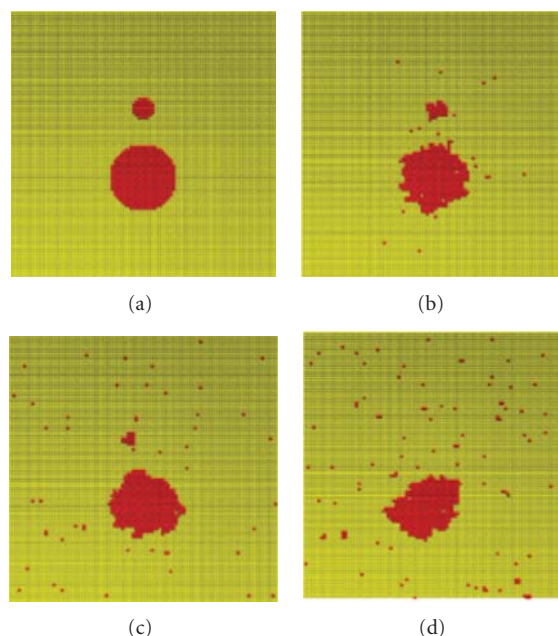


FIGURE 7: Snapshots along the kMC simulation at 850 K of the aggregation of two differently sized islands of 52 and 508 atoms, respectively. (a) Initial structure, (b) after 0.42 ns, (c) after 4.7 ns, and (d) after 95 ns.

processes, followed by the diffusion along the outer-corner and by the diffusion along kink sites.

Figure 8 shows the evolution of an initially spherical island (Figure 5(c)) at 850 K. The snapshots show that after several iterations, the roughness of the island border increases. Qualitatively, this is in good agreement with experimental results obtained by Giesen et al. by means of STM measurements in the case of two-dimensional Cu islands on Cu(100) [14, 49].

Interestingly, starting with a square-shaped island and maintaining a temperature of 850 K (Figure 5(d)) showed no significant deviations from the behavior of the spherical island, and hence the corresponding snapshots are not shown. Every migration step of an adatom out of the square island produces a vacancy. This mechanism has the lowest reaction rate among all the considered ones, and therefore this occurs very rarely. This can be explained by the degrees of freedom. As noted already by Ibach [50] step-atoms can only move in one direction and therefore the binding order on the (100) surface is three. This means that three bonds need to be broken along this process, which results in an increased energy barrier for this diffusion process.

Finally, we analyzed the equilibrium shape of the islands for a fixed number of gold adatoms but at different temperatures. To obtain the equilibrium shape of islands at a given temperature, one needs to average over many individual samples [51]. Therefore, we analyzed the island shapes during the ripening process starting with an initially random adatom distribution Figure 5(a). Islands already begin to show their equilibrium shape during growth, when the effects of island aggregation are averaged out [49, 52, 53]. We

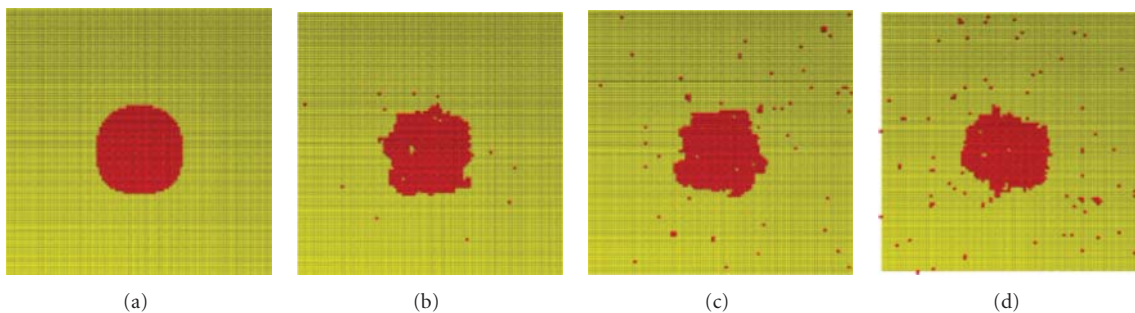


FIGURE 8: Snapshots along the kMC simulation of an initially spherically shaped island of 912 atoms at 850 K. (a) Initial structure, (b) after 0.43 ns, (c) after 4.65 ns, and (d) after 322 ns.

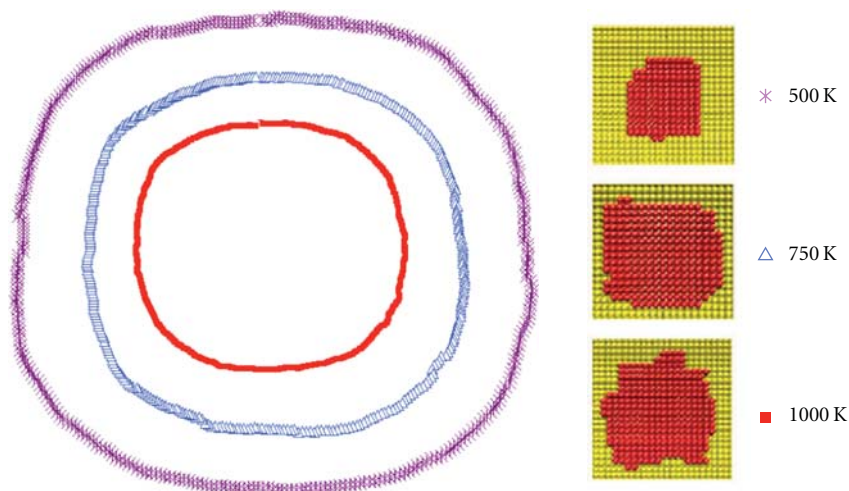


FIGURE 9: Equilibrium island shapes for different temperatures determined by kMC simulations at 500, 750, and 1000 K. Averaging was done over up to 500 individual islands. The right models show snapshots for each temperature, indicating the necessity of a careful averaging.

studied the temperature dependence of equilibrium fluctuations of monatomic high islands on Au(100) by analyzing the obtained island shapes at three different temperatures, 500, 750, and 1000 K. As shown in Figure 9, the equilibrium island shape becomes rougher with increasing temperature, which was also suggested by Giesen et al. [49]. This roughening was found in several STM-studies on Pb and Cu, Ag, Pt, [49, 50, 54], and also for the case of Au(100) [55]. The origin of this temperature dependence of the island shape is connected with the step line tension, which becomes smaller as the temperature increases, causing the island borders to increase their roughness. The step line tension β of a monoatomic step on a solid surface is defined as the work per length required for generating the step. For uncharged surfaces, this work is equal to the Helmholtz step free energy. Bombis and Ibach reported a step line tension of 170 meV per atom length based on STM images in vacuum. This contrasted with the comparative smaller value of $\beta \approx 35\text{--}70$ meV per atom length obtained by Giesen et al. for the unreconstructed Au(100) in an electrolyte solution (sulfuric acid) at higher potentials [56–58]. Also, previous theoretical calculations have estimated step energies on Au(100) between 65 [59] and 180 meV [60] per step atom. Hence, in order to obtain a direct comparison between the available experimental data

and our calculated values, we calculated the step line tension (β_A) for different temperatures ranging from 200–800 K. We calculated the step line tension according to the same procedure used by Bombis and Ibach [55] and described by Schlöber et al. [61] and hence do not describe it in detail here. In this approach, the expectation value $G(R)$ is calculated with (7):

$$\langle G(R) \rangle = \frac{R^2}{N} \sum_{j=1}^N \frac{1}{M} \sum_{i=1}^M \left(\frac{r_i(\theta, j) - R}{R} \right)^2, \quad (7)$$

where R is the middle radius of a circular island, N is the number of islands used in calculating the average value ($N = 40\text{--}80$), M is the number of angles for which $r_i(\theta, j)$ is calculated ($M = 360$), and $r_i(\theta, j)$ is the radius at a given moment. G is proportional to $1/\beta_A$, where β_A depends on the direction of the step relative to the surface. In the particular case of gold clusters, G is obtained by (8):

$$\langle G(R) \rangle = 0.245 \frac{k_B T R}{\beta_A}. \quad (8)$$

From (8), we can calculate β_A at different temperatures. These results are summarized in Table 2. The corresponding

TABLE 2: Calculated step line tension (β_A) and step line tension as function of the gold atom radius ($\beta_{A,a||}$) at different temperatures.

T (K)	β_A (meV/nm)	$\beta_{A,a }$ (meV)
200	399	115
400	453	131
600	557	161
800	650	187

values can also be expressed as a function of the gold atom radius since β_A is proportional to the island radius ($a|| = 288$ pm).

The relation between the temperature T and β_A follows a quadratic dependence. Based on this quadratic dependence and the data reported in Table 2, we obtained a value of 439 meV/nm at 353 K for the step line tension β_A . As function of the gold atom radius ($\beta_{A,a||}$), we obtained a value of 127 meV. At the same temperature (353 K), the value obtained by Bombis and Ibach of 170 meV can be compared to our value [55]. The difference between both values might be due to the rate catalog (exchange processes with the surface have so far not been considered) or the difference in the quotient of the step line tensions (β_B/β_A) along perpendicular steps B and A . This quotient provides information on how far away the islands are from reaching equilibrium conditions (at equilibrium $\beta_B/\beta_A = 1$). The value obtained by Bombis and Ibach for this quotient [55] was 0.96 compared with our value of 0.99 [62].

Ongoing work in our group seeks to include the exchange diffusion process and other processes which could influence the kMC description of the Ostwald ripening on Au(100) in future models.

9. Conclusions

In the present work, we have described a multiscale approach for studying the model case of Au-island ripening on Au(100). Starting with the atomistic level, we performed *ab initio* DFT calculations on a set of selected self-diffusion processes on perfect and imperfect Au(100) surfaces, obtaining both binding and activation energies. Afterwards, this data was used to generate a reactive ReaxFF force field for Au–Au interactions, which provided the basis for investigating many additional diffusion scenarios. Indeed, using ReaxFF, we were able to consider all possible processes involving nearest neighbors. The thus generated database of diffusion rates was finally used to study the system on the macroscopic level by means of kMC simulations.

Using kMC, we evaluated different initial surface configurations, by which we were able to investigate adatom nucleation as well as island aggregation and fluctuation processes on Au(100). Finally, by averaging over island shapes during the simulation runs at different temperatures, we studied the equilibrium shape of monoatomic high islands at different temperatures (here 500, 750, and 1000 K). In good agreement with experimental results for gold islands on Au(100), we found that increasing the temperature leads to island roughening. We explain this temperature

dependence of island roughing in terms of the temperature-dependent behavior of the step line tension. Our step line tensions agree fairly well with the reported experimental values and validate the present multiscale approach, which should be easily adaptable to the study of other systems.

Acknowledgments

The authors gratefully acknowledge financial support from the Deutsche Forschungsgemeinschaft (DFG) within the Emmy Noether Program, and the EU network ELCAT (Proposal no. 214936-2, 2008–2012).

References

- [1] G. Rosenfeld, K. Morgenstern, and G. Comsa, “Diffusion and stability of large clusters on crystal surfaces,” in *Surface Diffusion: Atomistic and Collective Processes*, M. C. Tringides, Ed., pp. 361–377, Plenum Press, New York, NY, USA, 1997.
- [2] A. G. Naumovets and Z. Zhang, “Fidgety particles on surfaces: how do they jump, walk, group, and settle in virgin areas?” *Surface Science*, vol. 500, no. 1–3, pp. 414–436, 2002.
- [3] D. W. Bassett and P. R. Webber, “Diffusion of single adatoms of platinum, iridium and gold on platinum surfaces,” *Surface Science*, vol. 70, no. 1, pp. 520–531, 1978.
- [4] P. J. Feibelman, “Diffusion path for an Al adatom on Al(001),” *Physical Review Letters*, vol. 65, no. 6, pp. 729–732, 1990.
- [5] B. D. Yu and M. Scheffler, “Physical origin of exchange diffusion on fcc(100) metal surfaces,” *Physical Review B*, vol. 56, no. 24, pp. R15569–R15572, 1997.
- [6] J. E. Müller and H. Ibach, “Migration of point defects at charged Cu, Ag, and Au (100) surfaces,” *Physical Review B*, vol. 74, no. 8, article 085408, 2006.
- [7] C. M. Chang and C. M. Wei, “Self-diffusion of adatoms and dimers on fcc(100) surfaces,” *Chinese Journal of Physics*, vol. 43, no. 1 II, pp. 169–175, 2005.
- [8] R. Stumpf and M. Scheffler, “Ab initio calculations of energies and self-diffusion on flat and stepped surfaces of Al and their implications on crystal growth,” *Physical Review B*, vol. 53, no. 8, pp. 4958–4973, 1996.
- [9] H. M. Polatoglou, M. Methfessel, and M. Scheffler, “Vacancy-formation energies at the (111) surface and in bulk Al, Cu, Ag, and Rh,” *Physical Review B*, vol. 48, no. 3, pp. 1877–1883, 1993.
- [10] G. Boisvert, L. J. Lewis, M. J. Puska, and R. M. Nieminen, “Energetics of diffusion on the (100) and (111) surfaces of Ag, Au, and Ir from first principles,” *Physical Review B*, vol. 52, no. 12, pp. 9078–9085, 1995.
- [11] G. Boisvert and L. J. Lewis, “Self-diffusion of adatoms, dimers, and vacancies on Cu(100),” *Physical Review B*, vol. 56, no. 12, pp. 7643–7655, 1997.
- [12] G. Boisvert, L. J. Lewis, and M. Scheffler, “Island morphology and adatom self-diffusion on Pt(111),” *Physical Review B*, vol. 57, no. 3, pp. 1881–1889, 1998.
- [13] C. Lee, G. T. Barkema, M. Breeman, A. Pasquarello, and R. Car, “Diffusion mechanism of Cu adatoms on a Cu(001) surface,” *Surface Science*, vol. 306, no. 3, pp. L575–L578, 1994.
- [14] M. Giesen, “Step and island dynamics at solid/vacuum and solid/liquid interfaces,” *Progress in Surface Science*, vol. 68, no. 1–3, pp. 1–153, 2001.
- [15] G. A. Somorjai and M. A. Van Hove, “Adsorbate-induced restructuring of surfaces,” *Progress in Surface Science*, vol. 30, no. 3–4, pp. 201–231, 1989.

- [16] D. M. Kolb, "Reconstruction phenomena at metal-electrolyte interfaces," *Progress in Surface Science*, vol. 51, no. 2, pp. 109–173, 1996.
- [17] T. Jacob, "Potential-induced lifting of the Au(100)-surface reconstruction studied with DFT," *Electrochimica Acta*, vol. 52, no. 6, pp. 2229–2235, 2007.
- [18] S. Venkatachalam, P. Kaghazchi, L. A. Kibler, D. M. Kolb, and T. Jacob, "First principles studies of the potential-induced lifting of the Au(100) surface reconstruction," *Chemical Physics Letters*, vol. 455, no. 1–3, pp. 47–51, 2008.
- [19] K. Pötting, W. Schmickler, and T. Jacob, "Self-diffusion on Au(100): a density functional theory study," *ChemPhysChem*, vol. 11, no. 7, pp. 1395–1404, 2010.
- [20] G. Rosenfeld, *Habilitation Thesis*, University of Bonn, 1998.
- [21] J. A. Keith, D. Fantauzzi, T. Jacob, and A. C. T. Van Duin, "Reactive forcefield for simulating gold surfaces and nanoparticles," *Physical Review B*, vol. 81, no. 23, Article ID 235404, 2010.
- [22] E. W. Hansen and M. Neurock, "First-principles-based Monte Carlo simulation of ethylene hydrogenation kinetics on Pd," *Journal of Catalysis*, vol. 196, no. 2, pp. 241–252, 2000.
- [23] J. G. O. Ojwang, S. Chaudhuri, A. C. T. Van Duin et al., "Multiscale modeling of interaction of alane clusters on Al(111) surfaces: a reactive force field and infrared absorption spectroscopy approach," *Journal of Chemical Physics*, vol. 132, no. 8, Article ID 084509, 2010.
- [24] T. Verstraelen, B. M. Szyja, D. Lesthaeghe et al., "Multi-level modeling of silica-template interactions during initial stages of zeolite synthesis," *Topics in Catalysis*, vol. 52, no. 9, pp. 1261–1271, 2009.
- [25] W. Goddard, B. Merinov, A. Van Duin et al., "Multi-paradigm multi-scale simulations for fuel cell catalysts and membranes," *Molecular Simulation*, vol. 32, no. 3–4, pp. 251–268, 2006.
- [26] T. Ala-Nissila, R. Ferrando, and S. C. Ying, "Collective and single particle diffusion on surfaces," *Advances in Physics*, vol. 51, no. 3, pp. 949–1078, 2002.
- [27] S. Günther, E. Kopatzki, M. C. Bartelt, J. W. Evans, and R. J. Behm, "Anisotropy in nucleation and growth of two-dimensional islands during homoepitaxy on "hex" Reconstructed Au(100)," *Physical Review Letters*, vol. 73, no. 4, pp. 553–556, 1994.
- [28] A. C. T. Van Duin, S. Dasgupta, F. Lorant, and W. A. Goddard, "ReaxFF: a reactive force field for hydrocarbons," *Journal of Physical Chemistry A*, vol. 105, no. 41, pp. 9396–9409, 2001.
- [29] A. C. T. van Duin, *Computational Methods in Catalysis and Materials Science*, Wiley-VCH, Weinheim, Germany, 2009.
- [30] K. D. Nielson, A. C. T. Van Duin, J. Oxgaard, W. Q. Deng, and W. A. Goddard, "Development of the ReaxFF reactive force field for describing transition metal catalyzed reactions, with application to the initial stages of the catalytic formation of carbon nanotubes," *Journal of Physical Chemistry A*, vol. 109, no. 3, pp. 493–499, 2005.
- [31] J. Tersoff, "Modeling solid-state chemistry: interatomic potentials for multicomponent systems," *Physical Review B*, vol. 39, no. 8, pp. 5566–5568, 1989.
- [32] D. W. Brenner, "Empirical potential for hydrocarbons for use in simulating the chemical vapor deposition of diamond films," *Physical Review B*, vol. 42, no. 15, pp. 9458–9471, 1990.
- [33] L. Pauling, "Atomic radii and interatomic distances in metals," *Journal of the American Chemical Society*, vol. 69, no. 3, pp. 542–553, 1947.
- [34] M. S. Daw and M. I. Baskes, "Semiempirical, quantum mechanical calculation of hydrogen embrittlement in metals," *Physical Review Letters*, vol. 50, no. 17, pp. 1285–1288, 1983.
- [35] M. S. Daw and M. I. Baskes, "Embedded-atom method: derivation and application to impurities, surfaces, and other defects in metals," *Physical Review B*, vol. 29, no. 12, pp. 6443–6453, 1984.
- [36] S. M. Foiles, M. I. Baskes, and M. S. Daw, "Embedded-atom-method functions for the fcc metals Cu, Ag, Au, Ni, Pd, Pt, and their alloys," *Physical Review B*, vol. 33, no. 12, pp. 7983–7991, 1986.
- [37] S. M. Foiles, M. I. Baskes, and M. S. Daw, "Embedded-atom-method functions for the fcc metals Cu, Ag, Au, Ni, Pd, Pt, and their alloys," *Physical Review B*, vol. 37, no. 17, p. 10378, 1988.
- [38] M. I. Baskes, "Modified embedded-atom potentials for cubic materials and impurities," *Physical Review B*, vol. 46, no. 5, pp. 2727–2742, 1992.
- [39] C. J. Casewit, K. S. Colwell, and A. K. Rappé, "Application of a Universal force field to organic molecules," *Journal of the American Chemical Society*, vol. 114, no. 25, pp. 10035–10046, 1992.
- [40] A. K. Rappé, C. J. Casewit, K. S. Colwell, W. A. Goddard, and W. M. Skiff, "UFF, a full periodic table force field for molecular mechanics and molecular dynamics simulations," *Journal of the American Chemical Society*, vol. 114, no. 25, pp. 10024–10035, 1992.
- [41] B. R. Brooks, R. E. Bruccoleri, B. D. Olafson, D. J. States, S. Swaminathan, and M. Karplus, "CHARMM: a program for macromolecular energy, minimization, and dynamics calculations," *Journal of Computational Chemistry*, vol. 4, no. 2, pp. 187–217, 1983.
- [42] W. Damm, A. Frontera, J. Tirado-Rives, and W. L. Jorgensen, "OPLS all-atom force field for carbohydrates," *Journal of Computational Chemistry*, vol. 18, no. 16, pp. 1955–1970, 1997.
- [43] W. D. Cornell, P. Cieplak, C. I. Bayly et al., "A second generation force field for the simulation of proteins, nucleic acids, and organic molecules," *Journal of the American Chemical Society*, vol. 117, no. 19, pp. 5179–5197, 1995.
- [44] W. D. Cornell, P. Cieplak, C. I. Bayly et al., "A second generation force field for the simulation of proteins, nucleic acids, and organic molecules," *Journal of the American Chemical Society*, vol. 118, no. 9, p. 2309, 1996.
- [45] K. Binder and D. P. Landau, *A Guide to Monte Carlo Simulations in Statistical Physics*, Cambridge University Press, Cambridge, UK, 2000.
- [46] A. Gross, *Theoretical Surface Science: A Microscopic Perspective*, Springer, Heidelberg, Germany, 2009.
- [47] K. A. Fichthorn and W. H. Weinberg, "Theoretical foundations of dynamical Monte Carlo simulations," *The Journal of Chemical Physics*, vol. 95, no. 2, pp. 1090–1096, 1991.
- [48] S. P. Meyn and R. L. Tweedee, *Markov Chains and Stochastic Stability*, Springer, 1993.
- [49] M. Giesen, C. Steimer, and H. Ibach, "What does one learn from equilibrium shapes of two-dimensional islands on surfaces?" *Surface Science*, vol. 471, no. 1–3, pp. 80–100, 2001.
- [50] H. Ibach, *Physics of Surfaces and Interfaces*, Springer, Heidelberg, Germany, 2006.
- [51] H. P. Bonzel, "3D equilibrium crystal shapes in the new light of STM and AFM," *Physics Reports*, vol. 385, no. 1–2, pp. 1–67, 2003.

- [52] K. Pötting, N. B. Luque, P. M. Quaino, H. Ibach, and W. Schmickler, "Island dynamics on charged silver electrodes: kinetic Monte-Carlo simulations," *Electrochimica Acta*, vol. 54, no. 19, pp. 4494–4500, 2009.
- [53] M. Giesen and G. Schulze Icking-Konert, "Equilibrium fluctuations and decay of step bumps on vicinal Cu (111) surfaces," *Surface Science*, vol. 412-413, pp. 645–656, 1998.
- [54] J. C. Heyraud and J. J. Métois, "Equilibrium shape and temperature; Lead on graphite," *Surface Science*, vol. 128, no. 2-3, pp. 334–342, 1983.
- [55] C. Bombis and H. Ibach, "Island equilibrium shape and shape fluctuations on the reconstructed Au(100) surface," *Surface Science*, vol. 564, no. 1–3, pp. 201–210, 2004.
- [56] S. Dieluweit, H. Ibach, and M. Giesen, "Potential dependence of step and kink energies on Au(100) electrodes in sulfuric acid," *Faraday Discussions*, vol. 121, pp. 27–42, 2002.
- [57] S. Dieluweit and M. Giesen, "STM studies on the island dynamics on Au(100) electrodes in sulfuric acid," *Journal of Physics Condensed Matter*, vol. 14, no. 16, pp. 4211–4225, 2002.
- [58] S. Baier, S. Dieluweit, and M. Giesen, "Step and island dynamics on Cu(111), Ag(111) and Au(100) electrodes in electrolyte," *Surface Science*, vol. 502-503, pp. 463–473, 2002.
- [59] P. Stoltze, "Simulation of surface defects," *Journal of Physics: Condensed Matter*, vol. 6, no. 45, pp. 9495–9517, 1994.
- [60] L. Vitos, H. L. Skriver, and J. Kollár, "Formation energy for steps and kinks on cubic transition metal surfaces," *Surface Science*, vol. 425, no. 2, pp. 212–223, 1999.
- [61] D. C. Schlößer, L. K. Verheij, G. Rosenfeld, and G. Comsa, "Determination of step free energies from island shape fluctuations on metal surfaces," *Physical Review Letters*, vol. 82, no. 19, pp. 3843–3846, 1999.
- [62] K. Kleiner, *Theoretische modellierung der selbstdiffusion auf Au(100)*, Diploma thesis, University of Ulm, Ulm, Germany, 2010.

Review Article

Spillover Phenomena and Its Striking Impacts in Electrocatalysis for Hydrogen and Oxygen Electrode Reactions

Georgios D. Papakonstantinou,¹ Jelena M. Jaksic,¹ Diamantoula Labou,¹
Angeliki Siokou,¹ and Milan M. Jaksic^{1,2}

¹Institute of Chemical Engineering and High Temperature Chemical Processes, FORTH, 26500 Patras, Greece

²Faculty of Agriculture, University of Belgrade, 11080 Belgrade, Serbia

Correspondence should be addressed to Milan M. Jaksic, milan@iceht.forth.gr

Received 8 May 2011; Accepted 5 September 2011

Academic Editor: Gianluigi Botton

Copyright © 2011 Georgios D. Papakonstantinou et al. This is an open access article distributed under the Creative Commons Attribution License, which permits unrestricted use, distribution, and reproduction in any medium, provided the original work is properly cited.

The core subject of the present paper represents the interrelated spillover (effusion) phenomena both of the primary oxide and the H-adatoms, their theory and practice, causes, appearances and consequences, and evidences of existence, their specific properties, and their alterpolar equilibria and kinetic behavior, structural, and resulting catalytic, and double layer charging features. The aim is to introduce electron conductive and d-d interactive individual and composite (mixed valence) hypo-d-oxide compounds, of increased intervalent capacity, or their suboxides (Magnéli phases), as the interactive catalytic supports and therefrom provide (i) the strong metal-support interaction (SMSI) catalytic effect and (ii) dynamic spillover interactive transfer of primary oxides (M-OH) and free effusional H-adatoms for further electrode reactions and thereby advance the overall electrocatalytic activity. Since hypo-d-oxides feature the exchange membrane properties, the higher the intervalent capacity, the higher the spillover effect. In fact, intervalent hypo-d-oxides impose spontaneous dissociative adsorption of water molecules and then spontaneously pronounced membrane spillover transferring properties instantaneously resulting with corresponding bronze type (Pt/H_xWO₃) under cathodic and/or its hydrated state (Pt/W(OH)₆), responsible for Pt-OH effusion, under anodic polarization, this way establishing instantaneous reversibly revertible alterpolar bronze features (Pt/H_{0.35}WO₃ ⇌ Pt/W(OH)₆) and substantially advanced electrocatalytic properties of these composite interactive electrocatalysts. Such nanostructured-type electrocatalysts, even of mixed-valence hypo-d-oxide structures (Pt/H_{0.35}WO₃/TiO₂/C, Pt/H_xNbO₃/TiO₂/C), have for the first time been synthesized by the sol-gel methods and shown rather high stability, electron conductivity, and nonexchanged initial pure monobronze spillover and catalytic properties. Such a unique electrocatalytic system, as the striking target issue of the present paper, has been shown to be the superior for substantiation of the revertible cell assembly for spontaneous reversible alterpolar interchanges between PEMFC and WE. The main target of the present thorough review study has been to throw some specific insight light on the overall spillover phenomena and their effects in electrocatalysis of oxygen and hydrogen electrode reactions from diverse angles of view and broad contemporary experimental methods and approaches (XPS, FTIR, DRIFT, XRD, potentiodynamic spectra, UHRTEM).

1. Introduction

1.1. Spillover Phenomena: Their Causes, Properties, Consequences, and Uses. Spillover phenomena impose advanced electrocatalytic effects on and play significant kinetic enhancement role in various electrochemical processes, in particular for the oxygen and hydrogen electrode reactions [1–4]. Namely, the fundamental Guldberg-Waage law of mass action (1865–1879) [5, 6] predicts that the faster the

spillover (or effusion) effect of the reacting intermediate species in the RDS (Rate Determining Step), the faster the corresponding electrode reaction becomes.

The first spillover phenomenon in heterogeneous catalysis was observed and defined by Boudart et al. [7, 8] for the interactive supported bronze-type (Pt/WO₃) catalyst, initially at high temperature (above 400°C) for pure solid system. Meanwhile, after the dissociative adsorption of water molecules on hypo-d-oxide support of Pt, the

fast interactive effusion of H-adatoms over its hydrated ($\text{W}(\text{OH})_6$) surface becomes dramatically sped up even at ambient conditions in the ultimate presence of condensed at least monolayered aqueous precipitate [9, 10]. This is significant both for the evidence of the extremely fast spillover widespread migration and thereby resulting with imposed the reversible substrate reduction. The latter finally leads to the corresponding form of electrocatalytically active bronze ($\text{Pt}/\text{H}_{0.35}\text{WO}_3$) for cathodic processes, in which nonstoichiometric incorporated hydrogen obeys the same free reactive properties like adsorptive H-adatoms (Pt-H) and is the main source for the electrode or heterogeneous catalytic reaction. In other words, the point is that spontaneous dissociative adsorption of water molecules imposes much smaller activation energy for transformation of the resulting hydrated $\text{W}(\text{OH})_6$ into corresponding bronze state ($\text{Pt}/\text{H}_{0.35}\text{WO}_3$), even at ambient temperature, than the initial oxide WO_3 and, thereby, dramatically facilitated the overall spillover effect under pronounced wet status.

As the present study is of the same significance to notice and discuss the dissociative hydrogen adsorption followed by fast spillover, establishing in this way the storage capacity of H-adatoms on the wet sol-gel developed surface of carbon current collecting electrocatalysts support (like E-tek Vulcan XC-72), in particular, facilitated by the metallic part of catalyst [11–14] and the hydrated hypo-d-oxide support. *Ab initio* molecular orbital studies have shown that adsorption of H-adatoms on the graphite basal plane [12] is an exothermic process. As the consequence, hydrogen spillover implies the transfer of electrons to acceptors within the support, this way modifying the chemical nature of the latter, activating previously inactive substrate, and inducing H-adatoms spillover sorption like laterally widespread expanding mobile repulsive dipoles [11]. In such a way oxygen functional groups usually facilitate H-adatoms spillover and their reductive interaction (rough value $1,200 \text{ mol}/\text{cm}^2/\text{s}$, with linear velocities of $100 \text{ cm}/\text{s}$ at edges of Pt crystallites, reducing down to a still high value of $5 \text{ cm}/\text{s}$ midway between Pt particles or for about eight to even nine orders of magnitude amounting the transferring distance relative to the radius of spillover dispersing species), so that formation of Mo-bronze is an even faster process relative to tungsten [12]. The fascinating fact is that such spillover transferring rates are obtained within mild pH conditions and even upon mild hydroxide species, far from concentrated phosphoric acid of contemporary PEMs for actual and prospective fuel cells.

The first decisive step towards rather fast spillover expanding phenomena of the primary oxide (M-OH) has been the consequence of a strong first principle thermodynamic confirmed evidence (density functional calculations, DFC) [15] that water molecules undergo prevailing (for more than 50 percent of the entire available surface) spontaneous dissociative adsorption on anatase and even rutile titania and more so on the higher altrivalent oxides [16] of tungsten, tantalum, and/or niobium (Figure 1). In addition, the first-principles molecular-dynamic simulations showed the existence of a mechanism for thermodynamically favored spontaneous dissociation of water molecules even at low

coverage of oxygen vacancies of the anatase (101) surface and consequently to the Magneli phases ($\text{Ti}_n\text{O}_{(2n-1)}$, in average Ti_4O_7), as substantially suboxide structure significant both as highly bulk electronic conductive [2, 3], membrane-type surface transferring hydroxide species and interactive catalyst support [17–19]. In fact, this is the status of reversible open-circuit dissociative adsorption of water molecules at the equilibrium state. Meanwhile, in the presence of the nano-sized metallic part of the catalyst and continuous enough moisture supply, directional electric field (or electrode polarization) further disturbs such an established equilibria and dynamically imposes further continuous forced dissociation of water molecules, and, as the consequence, their membrane transport properties [17–19] and the resulting spillover features [1–4, 20, 21]. Heterogeneous catalysis broadly employs the Tauster [22–25] SMSI (strong metal-support interaction) effect to increase the overall catalytic activity, but so far the additional interactive spillover contribution of the primary oxide (M-OH), in particular for the catalytic oxidation processes, has not been noticed.

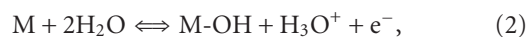
In such a context, the catalytic water-gas shift (WGS) reaction ($\text{H}_2\text{O} + \text{CO} \Rightarrow \text{H}_2 + \text{CO}_2$) has two or even three orders of magnitude higher reaction rate on the same metal catalyst interactive (SMSI) supported on hypo-d- than upon sp-oxides [26, 27] and, by the electrochemical promotion, (EPOC) has already been predestined for further catalytic advances and the efficient separation of final products [28].

In the same respect, Daté and Haruta [29] has pointed out that advanced Au/ TiO_2 interactive supported heterogeneous catalysts feature their pronouncedly high activity for direct CO oxidation *only* when provided with the moisture in the gas stream above some critical content. In fact every SMSI catalytic process, based on the interactive supported hypo-d-oxides and the resulting spillover of the primary oxide, *a priori* implies some decisive threshold in continuous moisture supply below which there is no oxidation of reacting species.

In the same sense Völkening et al. [30] have in addition shown and experimentally proved by HREEL spectra along with STM images that the Doebereiner catalytic reaction of hydrogen oxidation upon Pt surface, even at low temperatures (140 K), proceeds with remarkable amounts of the primary oxide (OH_{ads}), as the decisive and accumulated intermediate, including the auto- or self-catalytic step with adsorbed water molecules:



In fact, Ertl has pointed out the substantial autocatalytic role and the significance of water molecules in heterogeneous catalysis for oxidation processes that in general proceed over the primary oxide generation. The present study in the same sense reveals the increase of the overall reversible reaction rate of the primary oxide generation:



and its further undisturbed spillover both caused by the pronounced and the decisive effect of polarized water dipoles within the double layer [31]. Namely, the latter (2) represents

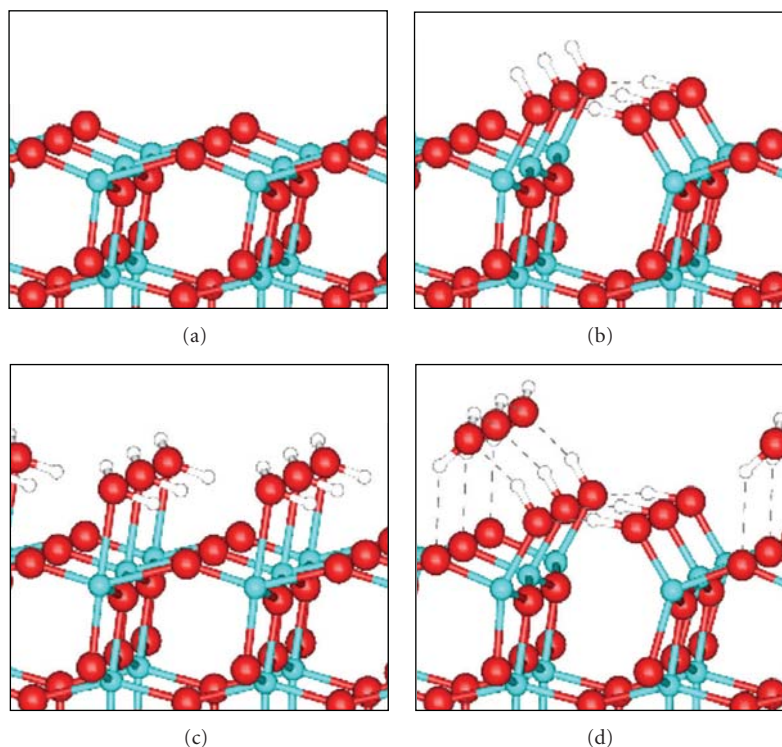


FIGURE 1: The perspective views of DFT-optimized atomic structures for (a) the clean anatase (ADM) ad-molecule model of unreconstructed (001) surface, (b) the dissociated state of water (0.5 monolayer) on (001), (c) the relaxed geometries of molecular state of adsorbed water (1.0 monolayer of hydroxylated anatase) on (001), and (d) the mixed state of water on (001) with a half-dissociated coverage of adsorbed monolayer water molecules (courtesy by Vittadini cf. [15]).

the electrochemical and electrocatalytic equivalent to the Ertl mechanism (1) in heterogeneous catalysis. In fact, it is well known in the electrochemical science from cyclic voltammograms scanned on Pt and Au [32–37] that the anodic adsorptive primary oxide growth and its cathodic desorption proceed as highly reversible and thereby extremely fast electrode processes. In principle, such typical dipoles (M-OH) are 1 : 1 employed within the broader potential range for the double layer capacitor charging and discharging [1, 4], and this is proved by the corresponding symmetric and highly reversible potentiodynamic peaks. What otherwise would dipoles do within double layer except to change the surface potential of an electrode and correspondingly the entire work function [1–4, 20, 21]? Since the heterogeneous reaction of formaldehyde oxidation with Pt-OH, and in particular Au-OH, proceeds as a fast reversible reaction mass transfer limited, and, since HCHO is soluble in all ratios in aqueous media, to prove almost unlimited the primary oxide generation rate cyclic voltammograms have been scanned within the broader concentration range of the latter [4, 38]. Namely, it has then been clearly shown that for the one order of magnitude higher HCHO content correspondingly increased limiting current values of its anodic oxidation, or the corresponding peak values in the present cyclic voltammogram spectra (Figures 2(a) and 2(b)) [1, 4, 20, 21, 38]. Such a fast heterogeneous reaction of anodic HCHO oxidation is apparently able to postpone within an unusually

large potential range the recombination of the primary (Pt-OH) into the more polarizable, more adsorptive, and more stable surface oxide (Pt=O).

1.2. Specific Dipole Properties and Spillover Causes of the Primary Oxide. The reversible fast-reacting primary oxide (M-OH) arises monolayer adsorbed and distinctly marked by a specific potentiodynamic peak, as the first step of water oxidation ((1) and (2)), immediately after the double layer charging range of many metals, first of all on Ru, Au, Pt, Rh, Ag [32–37]. Due to its chemically unstable reactive properties and consequently so fast decomposition recombination, leading to the irreversible and stable surface oxide (M=O) formation, the corresponding reversible peak usually extends in mineral acids and alkaline solutions within a narrow potential range, except when interactively supported on hypo-d-oxides and the latter being continuously supplied by water moisture. Similar behavior is a feature of some other transition metal primary-type oxides of common formulas and structure, like MoO(OH), NiOOH, and WO₂(OH), and can be identified by corresponding peaks within their potentiodynamic and XPS spectra [39, 40]. The point is that all transition metals of any, or in particular high, multivalent capacity, afford the reversible primary-oxide-type states, usually of pronounced catalytic activity and high electronic conductive properties (WO(OH), MoO₂(OH), Pt-OH, Au-OH), but unfortunately, in their oxidation, sequences end up

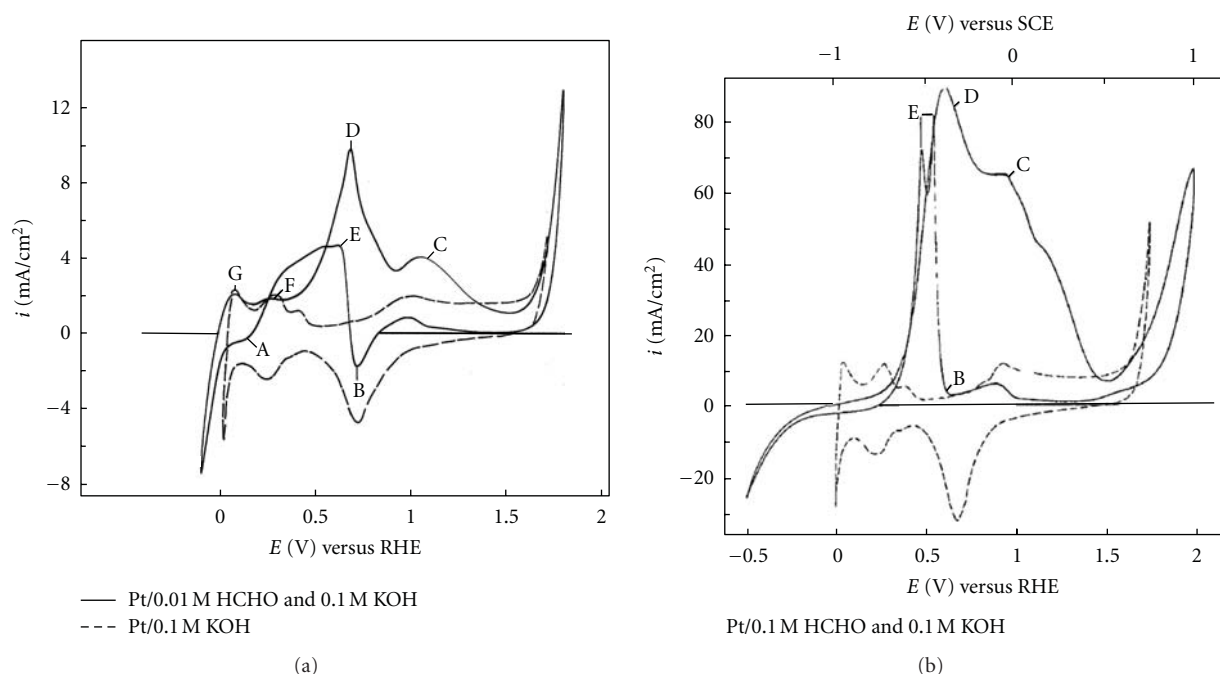


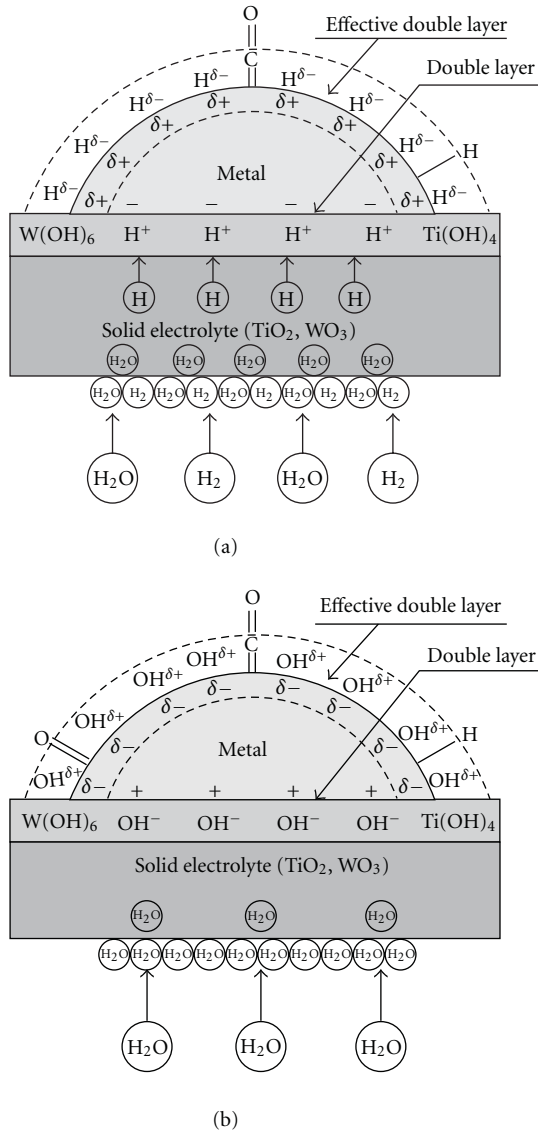
FIGURE 2: Cyclic voltammograms scanned on a polycrystalline Pt wire electrode in alkaline (0.1 M KOH, dashed lines) solution and in admixture of formaldehyde (0.01 M (a) and 0.1 M HCHO (b), full lines) at $200 \text{ mV} \cdot \text{s}^{-1}$ sweep rate between hydrogen and oxygen potential evolving limits. Labels: (A) reversible hydrogen adsorption peak; (B) irreversible Pt surface oxide (Pt=O) desorption peak; (C, D) successive peaks of anodic aldehyde oxidation; (E) sudden sharp current jump and reverse peak of repeated HCHO oxidation; (G, F) reversible H-adatoms oxidation and desorption peaks [38].

with nonconductive and catalytically inactive higher valence oxide states (MoO_3 , WO_3 , $\text{Pt}=\text{O}$, $\text{Au}=\text{O}$, NiO_2); otherwise the whole aqueous electrochemistry would feature another and quite different physiognomy!

The primary oxide species have *dipole properties* with prevailing ionic character of the majority of charge being transferred to the metal catalyst (Scheme 1) and thus appear weakly adsorbed at the interface [31, 41]. Such a state of the adsorptive binding strength varies from the less to the catalytically more active transition metals, from the lower towards the higher d-band electronic filling (density), or from the stronger to the weaker adsorptive bonds decisive for the RDS and substantially defines the overall electrocatalytic activity for both the HOR and ORR. This is the core difference between the reversible and fast-reacting primary oxide relative to the highly polarizable surface oxide, whose polarization difference amounts for more than 600 mV. Meanwhile, this is the reason of a coincidence that reversibly adsorbed H-adatoms and primary oxides feature almost the same enthalpies of adsorptive bonding upon catalytically active transition metal electrode substrates [31, 41].

Although their existence is clearly indicated by XP spectra [39, 40], under electrode polarization primary oxides feature some unique specific fluent (jellium [42] or fluid) structure of dipoles with noticeable Pauli's repulsion (*the spillover precondition*) amongst adjacent M-OH species (Scheme 1). The latter causes their rearrangement into an antiparallel structure (OH-adsorbate being oriented in the upright position, with the O-atoms closest to the metal

plane [31]), and, consequently, there is no surface change monitoring in the course of the *in situ* STM scans, as might be expected along with the corresponding charge transfer for their adsorptive generation within the reversible potentiodynamic peak [41]. In fact, their double-layer charging package imposes such a jellium fluent properties in distinction to the primary oxide free distribution upon simple heterogeneous catalyst surfaces [30]. The M-OH adsorbates are attracted towards and prefer the high coordination three-fold hollow sites on all transition elements, the adsorption energy for *hollow* and *on-top* sites being comparable for all d metals, and; consequently, they donate some electric charge to the surface to establish a dipole state (Scheme 1), in particular when a positive polarization field is imposed, as a substantially distinct example to the nonpolarizable Ertl et al. issue [30] in heterogeneous catalysis. The trends in the bonding of the primary oxide (M-OH, or the "*hydroxyl species*" [43]) have been similar in their nature to the surface oxide (M=O), with the difference that the weaker covalent interaction with the d states is due to the lower degeneracy of the OH^* -species 1π level in comparison with 2p level of M=O and, in addition, the presence of the hydrogen atom, which pools the whole OH-species away from the surface (as confirmed by dipole moment measurements) [31]. Such typical dipole repulsive features stay in the core of the spillover properties of primary oxides. On the contrary, the H-adatoms form a covalent adsorptive bond with transition metals, and, thereby, the effect of exerted electric field upon had a smaller impact. The Pauli repulsion becomes predominant due to the

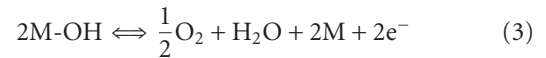


SCHEME 1: Model presentation for the SMSI effect, resulting in the spillover transfer of H-adatoms within the bronze nanostructure ($\text{Pt}/\text{H}_{0.35}\text{WO}_3$, (a)) and/or the primary oxide ($\text{M}-\text{OH}$) effusion, as a dipole along the hydrated counterpart ($\text{Pt}/\text{W}(\text{OH})_6$, (b)), further continuously transferring them upon the metallic part (Pt) of catalyst, otherwise both originating from the hypo-d-oxide continuously fed by moisture stream to such a composite ($\text{M}/\text{TiO}_2, \text{WO}_3$) electrocatalyst structure and maintaining them in the reversible interchangeable equilibrium ($\text{Pt}/\text{H}_{0.35}\text{WO}_3 \rightleftharpoons \text{Pt}/\text{W}(\text{OH})_6$) (constructed by Dimitris Tsipplakides).

increased electron density on the primary oxide adsorptive state with open-shell electronic configuration. The difference in adsorptive bonding upon different d metals is primarily explained by diversities in interaction with the d-band states, since transition metals are characterized by a broad sp band and a much narrower d band, the latter being both the cohesive and adsorptive (and thereby electrocatalytic) orbital, but with much higher density of electronic states. Due to the interactive nature for adsorbing species, in

which the main bonding interaction is covalent, the binding energies at the metal/vacuum and metal/liquid interfaces are comparable, whereas the H-adatoms and M-OH adsorption energies do not exert any significant field dependence [31]. In fact, the main reason why electrode reactions involving various adsorbed hydroxo species are potential dependent is because the electrons are taken from or stored at a different Fermi levels [44], and, consequently, for transition metals the adsorptive bond becomes stronger with a lower d-band filling [31].

Unfortunately, due to a fast-reacting and the short potential range for degenerative recombination transfer of the reversible primary into irreversible surface oxides, with a wider polarization range of the latter, all catalysts so far investigated are deprived from the theoretically possible reversible OER:



while the primary oxide can still be used to speed up and facilitate the overall ORR [1–4] and other fast reactions with aldehydes, monosaccharides, and similar species [20, 21, 38].

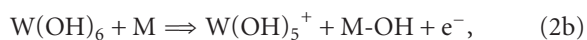
Nguyen van Huong et al. [45] applied electroreflectance spectroscopy for *in situ* interphase characterization but, alike with the STM [41], were unable to identify Au-OH and, therefore, named the later as an invisible jellium state of the “incipient oxidation of gold” to infer on its unique and specific catalytic properties. Conway et al. [32–37] confirmed the primary oxide monolayer coverage, asserted its sublattice intercalation, even the concerted replacement-turnover and thereby arising surface reconstruction, but denied the stoichiometric phase compound state in spite of its pronounced thermal stability [43]. Weaver and Hoflund [46] along with Savinova et al. [43] showed the high thermal stability of primary oxides and their incorporation into the bulk of metals.

In conclusion, the whole dynamic interactive and spillover catalytic properties of primary oxides arise from their unique specific nature and typical dipole behavior.

1.3. Membrane Properties of Hypo-d-oxides and Primary Oxide Spillover. Hypo-d-electronic transition metal ions usually feature several altermultivalent states giving rise even to interactive mixed valence compounds, such as TiO_2/WO_3 , $\text{TiO}_2/\text{Nb}_2\text{O}_5$, or $\text{TiO}_2/\text{Ta}_2\text{O}_5$, and increase the overall spillover effect of both H-adatoms and primary oxides. Such an oxide network, in particular of polyvalent (high altermultivalent capacity) hypo-d-elements, when in hydrous state behaves as an ion exchange membrane [17–20]. In fact, gels (aero- and xerogels) are biphasic systems in which solvent molecules are trapped inside an oxide network, and such a material can be considered as a water-oxide membrane composite [17–20].

Such a membrane transferring mechanism causes the following. (i) Continuous undisturbed reversible anodic transferring membrane mechanism of the altermultivalent changes ($\text{W}^{6+} \rightleftharpoons \text{W}^{5+} \rightleftharpoons \text{W}^{4+} \rightleftharpoons \text{W}^{3+} \rightleftharpoons \text{W}^{2+} \rightleftharpoons \text{W}^{1+}$ and similarly so for Ti^{4+} , Ta^{4+} , and Nb^{5+}) [17–20], as long as enough

moisture supply and catalyst polarization is provided [1–3, 20, 21]:



Such an interchangeable mechanism imposes the anodic OH^- transfer within the ion exchange membrane, yielding the consequent spillover of the interactive primary oxide (M-OH) dipoles over metallic catalyst particles (Scheme 1) [1–4]. Alternatively, (ii) cathodic spillover of H-adatoms exerts spontaneous reduction of hydrous tungsten oxide into corresponding bronze ($\text{Pt}/\text{H}_{0.35}\text{WO}_3$). These two spillover processes are fast and reversible [7–14], so that every change of catalyst polarity imposes instantaneous altering of W-bronze into its hydrated oxide ($\text{W}(\text{OH})_6$) [1–3, 7–14], ($\text{Pt}/\text{H}_{0.35}\text{WO}_3 \rightleftharpoons \text{Pt}/\text{W}(\text{OH})_6$) and *vice versa*, so that such an equilibrium has typical and substantial thermodynamic sense and meaning.

The problem so far was in unattainable *nanostructured* Pt-bronze, the catalytic activity of which exponentially increases with decreased Pt nanosize approaching maximum at monoatomic dispersion [47]. This requirement has now been fulfilled by the grafting implementation of Pt-acac (Pt acetylacetonate) within colloidal particles of peroxopolytungstic acid [1–3, 20, 21], niobia (Nb_2O_5), and tantalum (Ta_2O_5). Concerning the H-adatoms spillover yielding the bronze state out of preceding hydrated species, Tseung et al. [48–50] has achieved the same results with macrostructured Pt electrode in the same polytungstic environment, while the definition of the bronze properties originate from Glemser and Naumann [51].

1.4. Hypo-Hyper-d-d-Interbonding Nature of Electrocatalysis for Hydrogen and Oxygen Electrode Reactions. Where then lies the link between the hypo-hyper-d-d-interelectronic bonding and SMSI synergistic electrocatalytic effects? The whole electrocatalytic theory [52] relies on the Brewer [53] intermetallic bonding model and the Friedel and Sayers [54] hypo-hyper-d-d-electronic correlations. They both infer that the stronger the d-d intermetallic bonding, the more strengthened and exposed d orbitals within the symmetric intermetallic phases, thereby the weaker adsorptive strengths of intermediates (M-H, M-OH) in the RDS, therefore, the easier their cleavage, and, consequently, the higher the reaction rate and the overall catalytic activity [1–6, 20, 21]. The same Brewer- [53] type d-d intermetallic bonding model has been the already anticipated basis for Livage and Guzman [19], Neophytides et al. [20, 21], and Tauster and Fung [22] promotional strong metal-support interaction (SMSI) effect, with the far-reaching consequences in heterogeneous catalysis, electrocatalysis. The latter systematically predetermined interactive grafting [55, 56] and the homogeneous, even uniform distribution

of prevailing hyper-d-metallic catalysts upon hypo-d-oxide supports [1–4, 20, 21]. The same type of hypo-hyper-d-d-interactive bonding between nanostructured metal particles of such composite catalysts and their hypo-d-oxide supports additionally reinforces the entire electrocatalytic activity effect [55, 56]. The pronounced cathodic and anodic interactive spillover (effusion) contributions within the SMSI have been significant for the present theory and its embodiment in electrocatalysis of hydrogen and oxygen electrode reactions for low- and medium-temperature (L&MT) PEMFC and water electrolysis (WE) [1–4, 20, 21]. In aqueous media Pt (Pt/C) features the catalytic surface properties of Pt-H and Pt=O, missing any effusion of other interacting species; a new generation of composite interactive supported (SMSI) electrocatalysts in condensed wet state primarily characterizes extremely fast reversible spillover interplay of either H-adatoms or the primary oxides (Pt-OH, Au-OH) as the significant interactive electrocatalytic ingredients [1–4, 20, 21].

Volcano plots of various physical and chemical properties along transition series reveal the periodicity features of elements based on the d-d electronic correlations, with similar symmetric shape and, consequently, when plotted together yield various linear interdependences. As a consequence, the d band of transition elements has been confirmed to play a crucial role in the bonding, adsorptive, catalytic, and electrocatalytic properties, and, consequently, any search for advances and synergism should be based on the d-d interelectronic correlations and modifications [52, 55, 56]. Such a state of theoretical knowledge and experimental evidence leads to the conclusion that every hypo-hyper-d-d interelectronic phase diagram behaves as the part of the periodic table between the two initial periods of the interacting ingredients. Their intermetallic phases are of the same average d-electronic configuration replacing the missing elements in their energy state and behaviour in between and, consequently, have been used to assess the synergistically active electrocatalysts for the hydrogen electrode reactions (Figure 1, [2]). These theoretical and experimental facts can then be employed to assess the synergistically active electrocatalysts from the peak of corresponding volcano plots along each hypo-hyper-d-d interelectronic phase diagram.

1.5. Miscellaneous Retrospects and Prospects. The present review study represents the theoretical basis of our achievements and advances in electrocatalysis for hydrogen and oxygen electrode reactions, based on individual and hypo-hyper-d-d-interelectronic combinations of intermetallic phases [52], interactively supported upon corresponding hypo-d-oxides and leading to the reversible interrelating composite nanostructured electrocatalysts of bronze $\text{Pt}/\text{H}_{0.35}\text{WO}_3$ versus its hydrated $\text{Pt}/\text{W}(\text{OH})_6$ type [1–4, 20, 21], appearing as the effect of displayed reversible spillover phenomena. In the same context, such bronze type [1, 4] behavior enables the development of reversibly revertible alterpolar cell between PEMFC and water electrolysis (WE), as a target objective for energy conversion, primarily enabling hydrogen production and its immediate straightforward reversal

fueling. Such a system necessarily implies the instantaneous reversible alterpolar properties of the same electrode from hydrogen evolution (HER) to cathodic oxygen reduction (ORR), from oxygen evolution (OER) to anodic hydrogen oxidation (HOR), and *vice versa*. In such a context of longer stepwise development, the need for a thorough review and combination of the main successive sequential data is emphasized in order to get the final version of a specific electrocatalytic theory and discuss it in the light of new prospects and insights.

Based on the present theory, an unusual and specific PEMFC electrode assembly has been created, in which a metallic part of the interactive supported electrocatalyst (Pt) is interconnected with two solid electrolytes: (a) Nafion-117 membrane for proton transfer after hydrogen dissociative adsorption from gas phase (Pt-H) and electrochemical desorptive charging in the subsequent step (Heyrowsky mechanism) and (b) the composite interactive hypo-d-oxide structure (Pt/WO₃ or Pt/Nb₂O₅ and/or their mixed valence compounds with TiO₂, ZrO₂, HfO₂). The latter is capable for simple hydration, originating from continuous dissociative adsorption of moisture [15, 16, 57] supply (2a), followed by the hydroxide ionic migration transport under the anodic polarization field as a driving force ((2b) and (2c)) and resulting in the reversible (back and forth) primary oxide (dipole repulsion homogenized) spillover distribution all over the exposed anodic Pt surface (the overall Equation (2)), available for CO tolerance (even above 600 ppm). Alternatively such a spillover mechanism yields Pt-bronze as the effect of fast H-adatoms reductive effusion at the cathode (Pt/H_{0.35}WO₃) during cathodic polarization [7–14].

Finally, there should be revealed one more critical view in electrocatalysis. Usually student textbooks say that the Tafel plots for the cathodic hydrogen evolution (HER) and its anodic oxidation (HOR) are symmetric and almost equal along two opposite axes. It might be so for some individual metals, but not necessarily, since the metal surface can be covered by oxides during anodic polarization. However, it is not so for the hypo-hyper-d-d-intermetallic phases and alloys. During cathodic polarization, H-adatom intermediates keep the metallic surface free from oxides [47, 58] and feature maximal synergistic electrocatalytic activities [52, 59]. Figure 7 in [40] correspondingly reveals such polarization properties for Pt-Mo intermetallic phases. Meanwhile, since hypo-d-metals are hydrophilic elements and thereby sensitive on water and oxides, hypo-hyper-d-d-intermetallic catalysts feature two different electrode properties. During the cathodic polarization, hypo-d-ingredients are pulled inside the intermetallic phase or alloy, as Mavrikakis et al. [47, 58] have shown by DFT calculations, and H-adatoms provide pure metallic interface. In the course of anodic processes, the strong water molecule interaction draws them backwards on the catalyst's outer boundary, where they undergo the transference into surface oxides and exhibit quite different polarization properties.

The latter can be useful for the CO tolerance, while for the time being only interactive hypo-d-oxide-supported Pt or bronze type satisfies the fast HOR [1–4].

2. Experimental Methods

Experimental methods, in particular concerning novel bronze-type interactive supported electrocatalysts, their synthesis, nanostructured and surface characterization, and kinetic and electrocatalytic activity testing, were described in all necessary details in the preceding papers of the same authors [1, 4].

3. Results and Discussion

3.1. DRIFT Spectra Evidence for the Autocatalytic Water Effect in the Primary Oxide Appearance, Existence, and Spillover.

DRIFT spectra reveal the steady amounts of adsorbed water and the primary oxide upon examined species by the corresponding left and right peaks, respectively. A typical example is shown in Figure 3(a) for Mo/TiO₂ after reduction under hydrogen at 300°C and exposure to He flow at room temperature (RT). Figure 3(b) reveals the same thing for PtMo/TiO₂ at He flow at two different temperatures (300 and 350 K), to investigate the thermal desorption effect. Finally, Figure 3(c) corresponds to the preceding issue, but the thermal effect is investigated under hydrogen flow and at the same temperatures. The striking observation is that regardless of the lack of reaction between hydrogen and water, quite distinctly from and differently to the preceding issue scanned under equal thermal conditions, both peaks disappear during the same time interval at relatively low temperature. Since the initial amount of adsorbed water is fixed, while hydrogen is continuously supplied, the conclusion is very interesting: water molecules undergo spontaneous dissociative adsorption (2a) upon anatase titania [15], and then they become the subject of both the membrane flow, ((2b) and (2c)), and Ertl's [30] autocatalytic (or self-catalytic) mechanism of Pt-OH production (1), the latter being now reduced by H-adatoms (Pt-H). Along with the primary oxide reduction by the hydrogen stream recombined instantaneously and spontaneously in its adatoms (Pt-H), and thereby continuous disturbance of the H₂O/OH* equilibrium (1), the recombination of water molecules into the primary oxide proceeds spontaneously as well, as a driving force to keep the same earlier established equilibria. Thus, the experiment reveals the continuous stepwise consumption both of water and primary oxide due to their interrelating equilibrium and the occurrence of thermodynamically spontaneous reactions. Furthermore, the present DRIFT experiments testify for the existence and spontaneous establishing of the autocatalytic step of water molecules in the primary oxide growth and their equilibrium (1). Such a clear DRIFT spectra sequence seems unequivocal and unique in its sense, meaning, and significance.

3.2. Potentiodynamic Evidence of the Primary Oxide Spillover.

The first experimental evidence for the fast reversible anodic adsorptive growth and corresponding cathodic desorption of the Au-OH and Pt-OH primary oxides, and thereby for their electrochemical spillover confirmation, is primarily owed to the excellent potentiodynamic spectra of Conway et al. [32–37]. The former by their coinciding positions along the

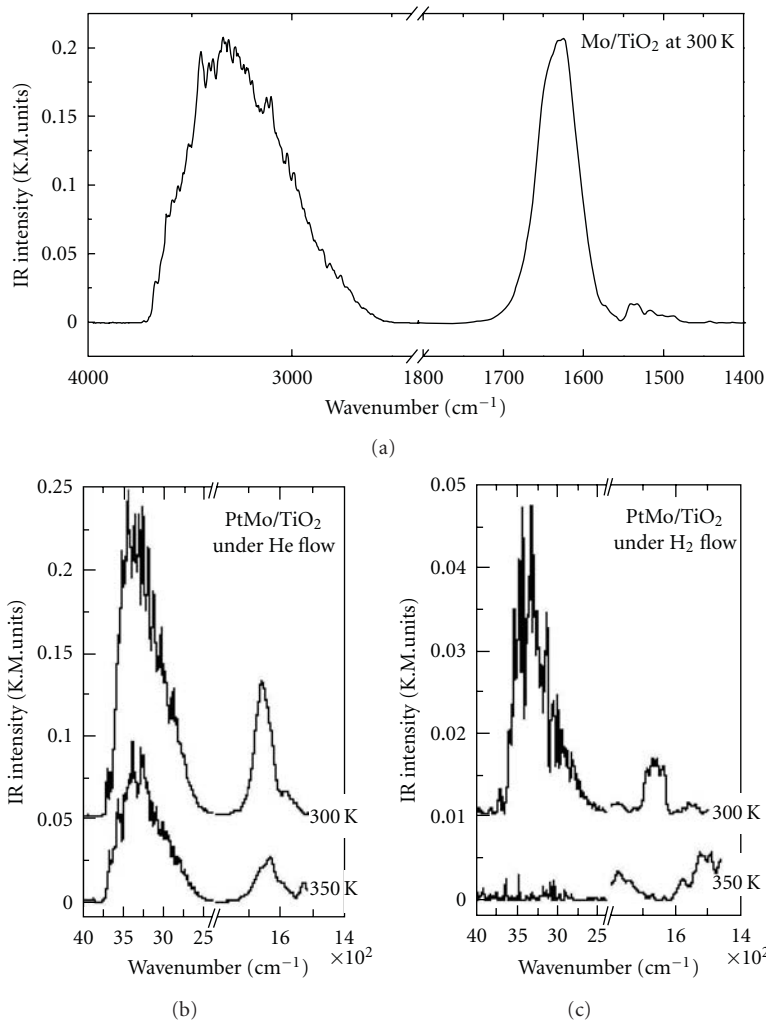


FIGURE 3: DRIFT spectra for H₂O and M-OH: (a) Mo/TiO₂ after reduction under H₂ at 300°C and He flow at RT. (b) As (a) for Pt-Mo/TiO₂ and He flow at 350 K. (c) As (b) under H₂ flow. Since M-OH becomes depleted in hydrogen flow, the same correspondingly occurs with water.

potential axis reveal the typical double layer charging and discharging features of dipolar species upon and from a capacitor. In the same sense, cyclic voltammetry has also been recalled to scan the hydroxide ions' membrane transferring effect, enabled by continuous moisture saturation feeding supply of the hypo-d-oxide support structure for composite nanostructured electrocatalysts, upon the whole reinforced primary oxide both chemisorptive generation and desorptive removal and, consequently, to record its spillover dynamics while charging and discharging of the DL capacity [1–4, 20, 21].

In this respect an intermolecular compatible hypo-d-oxide composite mixed-valence architecture (5.0 mol.% WO₃, 95.0 mol.% TiO₂ = 20 wt.%, along with 10.0 mol.% Nb₂O₅, 90.0 mol.% TiO₂ = 20 wt.%), as the interactive catalytic submonolayer support of rather high altermultivalent capacity, capable of withstanding alkaline media too, has been selected to investigate the primary oxide and H-adatoms spillover properties. In this respect, cyclic voltammograms

scanned upon Pt/WO₃,TiO₂/C (or Pt/Nb₂O₅,TiO₂/C) electrocatalyst at low moisture content of He stream (just enough to enable basic electrode processes to proceed), insufficient for WO₃ (or TiO₂) hydration, (2a), repeatedly reveal similar potentiodynamic spectra characteristic for carbon supported Pt itself (Figure 4), but with high double layer charging capacity, because of the accompanying parallel charging of Vulcan carbon particles beside the metal ($Q_{DL} = 1.07$ C, assessed by the method displayed by Schmidt et al. [60]).

In contrast to such fairly common occurrences, a continuous supply of saturated water vapor in the He stream at higher temperature (80°C), imposing condensation (Boudart spillover precondition [7–10]) and leading to the appearance of wet titania-tungsten mixed altermultivalent oxide composite, as the interactive catalytic support, has been accompanied by the unusual phenomenon of a dramatic expansion of two reversible pairs of peaks of both the primary oxide and H-adatoms chemisorptive deposition and desorption (Figure 4). The latter have both been of

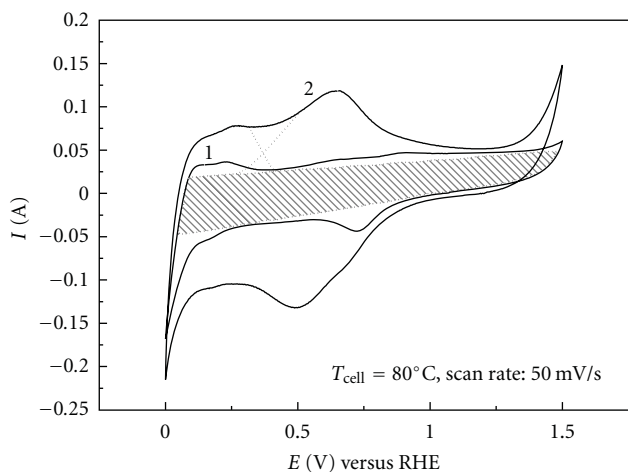


FIGURE 4: Cyclic voltammograms of mixed hypo-d-oxides supported nanostructured Pt electrode (Pt/TiO₂, WO₃), scanned in He stream, ones at negligible moisture content (curve 1) and at water vapor saturation (curve 2).

unusually high spillover charge and discharge capacity values and for Pt-OH (UPD and OPD) shifted towards both much more negative and far positive potential limits. In fact, the latter arises just as the effect of the primary oxide equivalent dipole charging and discharging of the double layer! Namely, just as stated above, nothing else takes place in between. Every cessation in the steam supply instantaneously imposes the sudden reversible shrinkage of both such rather exaggerated pairs of peaks down to the same initial potentiodynamic shape similar to the nanostructured Pt/C voltammogram spectra, but only with less pronounced (UPD and OPD) extensions in the double layer where charging or discharging extends. *Vice versa*, the renewed saturated water vapor feeding immediately leads to their sharp former primary oxide peaks and the same former charge capacities [1–4]. Such an appearance without exception behaves as a typical reversible transient phenomenon by its endless repetition and never appears upon the plain Pt/C electrocatalyst.

Since the two distinctly different cyclic voltammogram shapes (Figure 4) appear only as the result of the difference in water vapor supply, and other parameters being the same, an unequivocal theoretical conclusion, as well as the best heuristic experimental confirmation, has been derived from the interfering interactive character and specific inter-exchangeable double (H-adatoms and Pt-OH) spillover properties of a unique altermultivalent hypo-d-oxide structure under directional electrode features of polarized nanostructured Pt electrocatalyst. The deconvoluted cyclic voltammograms clearly reveal the mutual merging of two otherwise independent spillover peaks for both Pt-H and Pt-OH adsorption and desorption, with farreaching positive consequences in the revertible combination of both PEMFCs and WE [1, 4]. The same conclusion equally concerns the equivalent combinations of Nb₂O₅ and TaO₂ (even MoO₃) with anatase titania, which at some broader ratios, when properly thermally treated, feature very high electron

conductivity (above 300 S cm⁻¹) and corresponding membrane transfer capability with equal dual spillover properties (absent carbon current collector). Meanwhile, the electron conductivity is a bulk property, while the membrane transfer mostly takes place above the rather developed hydrated hypo-d-oxide surface.

As a consequence, the whole phenomenon, in pronouncedly more wet condensation conditions and continuous water vapor supply, is further remarkably more facilitated both in the reversible cathodic H-adatoms spillover yielding Pt-bronze and/or, *vice versa*, its anodic transfer into the hydrated state and sources (W(OH)₆, Ti(OH)₄, Nb(OH)₅, Ta(OH)₄) for Pt-OH effusion, both being fast reversible reactions. Thus, the primary oxide dipole species undertake both the unusually pronounced double layer charging role and/or exaggerated UPD and OPD adsorption and corresponding desorption within much broader potential range. Consequently, the whole system behaves as pronouncedly reversible and smoothly alterpolar both for the primary oxide and H-adatoms spillover and, as a whole, in the reversibly revertible alterpolar coexisting equilibrium interrelation between tungsten bronze and its hydrated state (Pt/H_{0.35}WO₃ ⇌ Pt/W(OH)₆). In other words, two coexisting and mutually interfering reversible pairs of peaks fast altering between H-adatoms (adsorption or desorption) effusion and Pt-OH spillover (and/or its backwards removal) along the potential axis, with all interacting consequences imprinted upon cyclic voltammetry spectra, inherently testify by their exaggerated potentiodynamic features, to the reversible interrelations between two coherent dual alterpolar electrode properties. In addition the extremely fast H-adatoms spillover within the hypo-d-oxide structure highly facilitates their effusion over carbon catalyst support. This experimental evidence implies the equivalence in the endlessly repeatable reversible alterpolar changes and stable electrocatalytic properties of L&M PEMFC in conjunction with equally catalytically advanced WE, in particular important for the impurity (frequent alterpolar interchanging relation) effect of the latter. In this respect, both peaks of Pt-OH adsorption and desorption are equal and of enormous charge capacity ($Q_{\text{Pt-OH(a)}} = Q_{\text{Pt-OH(c)}} = 1.453 \text{ C}$), like a DC capacitance of extremely developed electrode surfaces, and, since they are highly reversible, they keep the same extents even after multiple and repeating number of cycles at any other time. These experimental facts imply conclusive remarks about an already known phenomenon [11–14] that the bipolar primary oxide structure (Pt-OH, Au-OH) establishes the reversible transient adsorption and charging capacity even on usually developed active carbon surface (C-OH), but by no means takes place in its oxidation [1, 4]. The latter statement has been confirmed by *on-line* mass spectrometer, which identifies CO₂ only within the oxygen evolving potential limits. The fast spillover of H-adatoms over also reversibly fast renewing tungsten bronze (Pt/H_{0.35}WO₃) out of its interrelating hydrated state (Pt/W(OH)₆), including its own nonstoichiometric stored H-amounts, along with adsorptive effusional deposition on, and subsequent desorptive removal from exposed carbon surface, in such a way, continuously behaves as its auxiliary

storage [11–14]. The partial participation of moisture in the gas stream supply, along with the available adsorptive surface of the electrode, defines the extent of the charge capacity both for the primary oxide peak itself and double layer extension and growth, the phenomenon that has never been marked on the RDE and any other polished plain Pt-type electrodes in aqueous media. Due to the increased moisture content, now the H-adatoms UPD desorption peaks directly merge with the prevailing broad reversible primary oxide spillover deposition and appear in dramatically expanded charge capacity (247 *versus* 47 mC cm^{-2} or in the ratio of about 5.3:1). In fact, 0.4 mg Pt cm^{-2} effectively corresponds to 200 cm^2 of exposed Pt surface (BET assessed $50 \text{ m}^2 \text{ g}^{-1}$ Pt) or to 42.0 mC cm^{-2} of charge capacity per projected geometric surface of electrode, in good agreement with the UPD H-adatoms determined desorption value under dry conditions. Exactly the same relates to the H-adatoms adsorption and Pt-OH desorption peaks in the equivalence to their corresponding reversible counterparts.

The enriched potentiodynamic experimental evidence, in accordance with the theory of instantaneous reversibly revertible alterpolar properties of the bronze-type electrocatalysts and extremely broad potential range of the primary oxide adsorption and desorption, unambiguously testifies now that the Pt-OH (AuOH, M-OH) in aqueous media both UPD and OPD charges and discharges double layer (2) and thence is available for reaction within broad potential limits. For example, formaldehyde oxidation starts exactly at its reversible potential value (0.32 V *versus* RHE), at the usual lower DL charging potential limits, even merges with the second UPD desorption peak of H-adatoms, and extends as an exaggerated broad twin peak all along the anodic scan until the beginning of OER (Figure 2(a)) [38], similarly and correspondingly to Figure 2(b). A similar cyclic voltammogram, in accordance with the present theoretical model and as the result of the Pt-OH spillover effect, has also been scanned by Tseung et al. [61] for the anodic glucose oxidation on Pt-bronze microelectrode (Figure 1, [61]). In the same sense anodic CO oxidation on composite hypo-d-oxide-supported Pt or Pt and Ru catalysts takes place even within the usual interval of H-adatoms desorption (see further downwards) and can even be brought with the reversible bronze-type Pt electrocatalyst under the conditions of initiation just above the HER (nearly at 0.0 V *versus* RHE). In other words, Pt-OH becomes available for reaction not only within its nominal reversible adsorption and desorption peak limits in regular mineral acid or base aqueous solutions, but depending on the reactant concentration, affinity, and its actual reaction rate, along a broad and extendable potential range.

3.3. Experimental Evidence for the SMSI d-d Effect. Very fine, nanosized Au films deposited by controlled electron beam evaporation of ultra-high-purity gold metal under high vacuum, onto stationary nanocrystalline anatase titania-coated microscopical slides, have been employed to study both the SMSI and the spillover phenomena. The XP spectra of the Au 4f electrons reveal the remarkable binding energy shift (Figure 5), which provides evidence for the d-d-SMSI

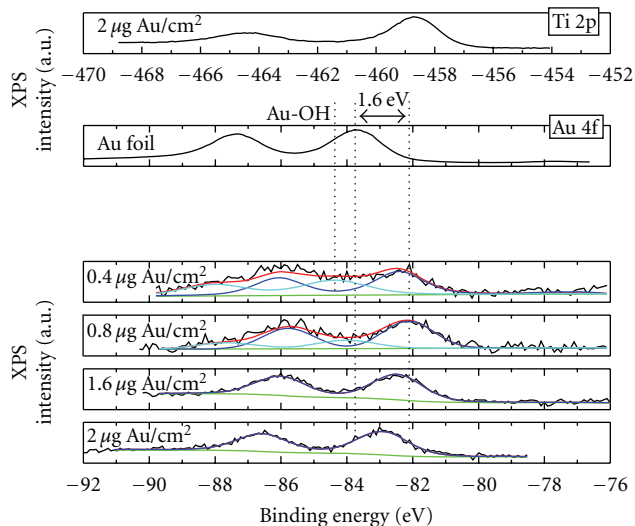


FIGURE 5: XP spectra of Au 4f for vapor-deposited nanolayered Au upon a fine thin film of anatase titania with deconvolution for lower amounts of deposits to reveal the existence of primary oxides (Au-OH and AuOOH) [3].

on the Au/TiO₂ interphase, and this has been one of the first experimental evidences of this kind in heterogeneous catalysis. The smaller the nanoparticle size or the thickness of the Au nanolayer, the larger the binding energy shift in the XP spectra with titania and the more pronounced the d-d SMSI effect, with tendency to its maximal d-d-binding strength at monoatomic dispersion and 1:1 deposition of Au on available Ti atoms, as theoretically predicted in the present and preceding papers [2, 3, 20, 21]. Due to the nanodimensions of the Au layer, the signal, originated mainly from Au/TiO₂ interface, reflects the bonding status within the latter. In other words, the thinner the deposited Au nanolayer, the closer to the interphase itself (Au/TiO₂) penetrate spectral beams and thereby, better and more completely reflect the bonding status within the latter.

The deconvoluted Au 4f peaks with lower Au loadings reveal that Au nanoparticles in interactive bonding contact with titania appear partially oxidized [62, 63]. The peak located at $82.15 \pm 0.1 \text{ eV}$ is attributed to metallic Au, while the peak at $84.05 \pm 0.1 \text{ eV}$ corresponds to the gold primary (Au-OH or AuOOH) oxides. The latter, in accordance with the present theory, appear as the *a priori* naturally provided primary oxide spillover species, associated with and promoted by the wet anatase titania interaction (2) and are, in advance, already available and ready for anodic CO and other oxidation processes.

Haruta et al. [64] have shown that the same reactants (propylene admixture with equimolar amounts of hydrogen and oxygen) yield different products upon different nanosized Au catalysts supported on anatase titania (Au/TiO₂): (i) propane by hydrogenation at nanoparticles <2 nm Au and (ii) propylene oxide by epoxidation or oxygen addition for >2 nm Au. Hydrogenation implies H-adatoms adsorption on Au that should not spontaneously occur on a

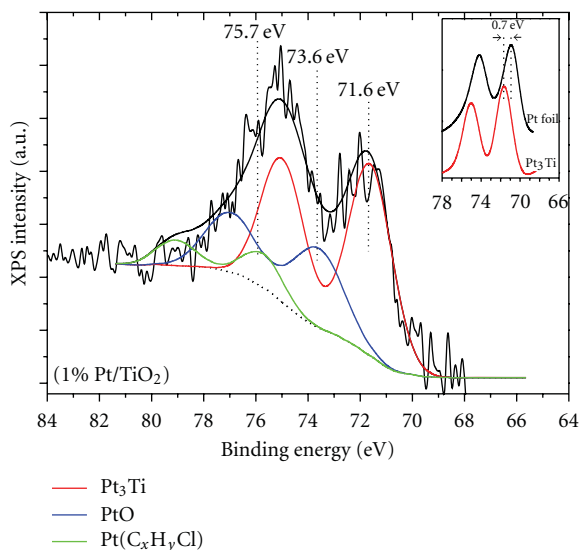


FIGURE 6: XPS 4f spectrascanned at the interphase between Pt catalyst (1.0 wt.%) and interactive anatase TiO_2 support in their d-d-SMSI. Deconvolution exactly reveals the existence of the TiPt_3 intermetallic phase at the interphase Pt/TiO_2 with all identified individual spectral properties, as the prerequisite for the SMSI effect.

pure massive bulky gold surface. Haruta et al. [29, 64–69] ascribes such chemisorptive properties to “forced” or strained Au-*d*-orbitals within smaller (below the critical threshold) nanostructured metal particles, in particular when d-d SMSI deposited on the interactive anatase titania (cf. [52, 53, 59]). In other words, smaller nanostructured Au particles (<2 nm), interactively d-d bonded with anatase titania (Au/ TiO_2), or in particular interactive supported upon mixed valence hypo-d-d-compounds (Au/ Nb_2O_5 , TiO_2 or Au/ WO_3 , TiO_2), thereby being even reinforced in their interbonding effectiveness and thence exposed with the strained d orbitals, are qualitatively different than massive Au. Such highly dispersed nanoparticles consequently behave H-adatoms adsorption, thus feature provided the reversible behavior of hydrogen electrode in the Nernst sense [3], and, finally, are able to carry out the hydrogenation processes. It has been further shown that self-reconstructed Au electrode surface, after multiple potentiodynamic cycles between hydrogen and oxygen evolving limits, features the pronounced H adsorption and even absorption and consequently the reversible electrode properties (Krstajic et al. [3] and references therein). The reconstruction effect has been much more pronounced and faster in heavy water media, because of the stronger interatomic interrelations and deeper penetrating interphase effect of twice larger deuterium than protium ions and atoms [3].

It would be worthwhile to stress the XPS confirmation of the existence of the intermetallic phase TiPt_3 within the interface contact Pt/TiO_2 , Figure 6, as theoretically predicted by Tauster et al. [22, 23], Stevenson [24], and Haller and Resasco [25] for the prerequisite of pronounced interactive bonding (d-d SMSI) and thereby reinforcing of the entire

advanced catalytic effect. In the same sense, one is still missing and looking for the confirmed existence of the TiAu_4 intermetallic phase at the interface of Au/ TiO_2 .

3.4. Broader and Substantial XPS Evidence for the Primary Oxide Presence and Spillover. The link between the basic polycrystalline Pt (85% in (111) crystal structure), as a comparative model issue, and various individual or mixed-valence hypo-d-oxide compounds (Nb_2O_5 , WO_3 , MoO_3 , TaO_2) with anatase titania (TiO_2) itself, interactive supported nanostructured Pt electrocatalysts, imposed the imperative need for surface characterization of the latter, in particular as concerns the primary oxide (Pt-OH) spillover and CO tolerance [1–3, 39]. In order to understand the origin of the oxidation states of Pt deposited on individual and/or mixed-valence hypo-d-oxide supports, *in situ* XP spectra of Pt 4f_(7/2) and O 1s photoelectrons are undertaken before (Figures 7(a) and 8(a)) and after exposure in hydrogen stream at 360°C, followed by continuous heating of the sample under UH vacuum, along with the examination of simple thermal effect relative to room temperature. In other words, both thermal and reactive (Pt-H) effects on the primary oxide reduction or simple desorption have been systematically XPS investigated. Consequently, XPS photoemission experiments were carried out in the specifically constructed and adjusted assembly for the present experimental purposes, which consists of a sample preparation and an analysis chamber within a high-pressure cell attached directly on the fast-entry specimen assembly for *in situ* XP spectra treatment in an ultrahigh vacuum (UHV) system (1×10^{-9} mbar), the whole system being perfectly isolated from the surrounding.

In such a respect, Figures 7(a), 7(b), 8(a), and 8(b) reveal the deconvoluted Pt 4f and O 1s XP spectra, respectively, of the Pt catalyst interactive supported once on the simple $\text{Nb}_2\text{O}_5/\text{C}$ and then on mixed-valence composite ($\text{Pt/Nb}_2\text{O}_5$, TiO_2/C) hypo-d-oxide, scanned at room temperature (RT), distinctly after annealing under UHV conditions at 360°C and after the preceding reduction at the same temperature under 20% H_2 in N_2 flow in the high-pressure cell attached by the fast-entry assembly to the UHV system. The shape Pt 4f spectra indicates the existence of more than one oxide-type Pt species and indeed, in all cases, the photopeak can be analysed into three doublets. For the analysis, the intensity ratio of the Pt 4f doublet components is kept at 3:4 and their splitting energy at 3.3 eV (for a good signal-to-noise ratio, errors in peak positions were assessed to be of about ± 0.05 eV) [70]. The first component at binding energy 71.3 eV is attributed to metallic platinum. The peak at 72.7 eV is assigned to $\text{Pt}(\text{OH})_x$ ($2 \leq x \leq 1$), due to combination of Pt with OH in the primary oxide (M-OH type), or some other congenial O-species, while the third component at 74.9 eV is ascribed to PtO_x [40], finally ending up as the stable surface oxide (PtO_2). The percentage contribution of each Pt-oxy-component to the total peak area is equivalently shown for both specimens in Table 1. As a strong XP spectral evidence for the primary oxide (Pt-OH) interactive transference (2) and existence, it is quantitatively assessed

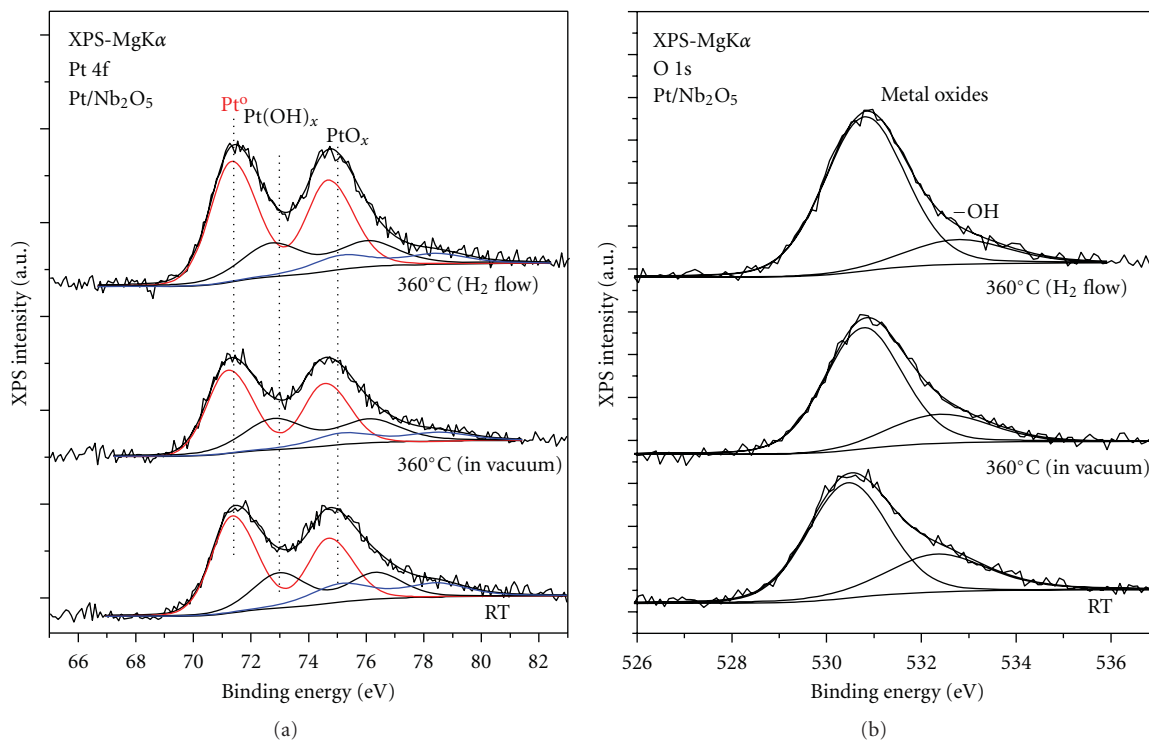


FIGURE 7: Pt 4f (a) and O 1s (b) XPS core level spectra of the Pt catalyst on Nb₂O₅/C support at room temperature (RT), after annealing under UHV conditions at 360°C and after reduction at 360°C under 20% H₂ in N₂ flow.

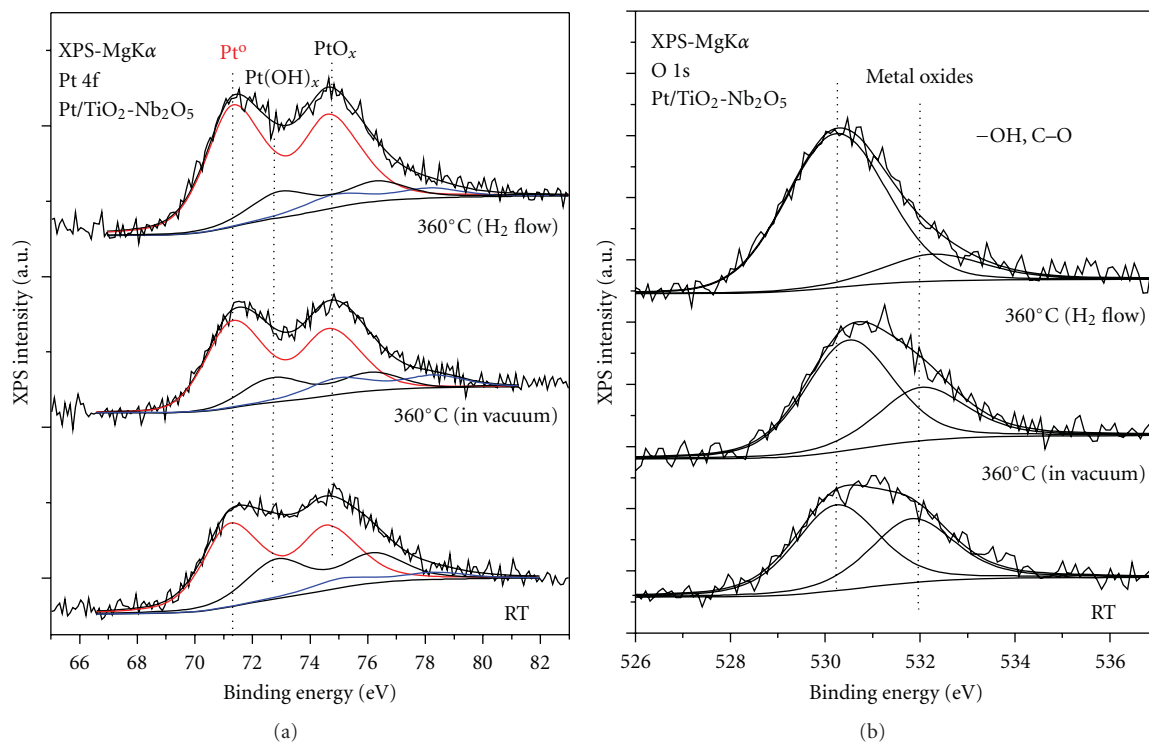


FIGURE 8: Pt 4f (a) and O 1s (b) XPS core level spectra of the Pt catalyst on the mixed Nb₂O₅,TiO₂/C support at room temperature, after annealing under UHV conditions at 360°C and after reduction at 360°C under 20% H₂ in N₂ flow.

TABLE 1: Percentage contribution of each Pt 4f component the total peak area.

	Pt/Nb ₂ O ₅ -TiO ₂			Pt/Nb ₂ O ₅		
	Pt ⁰ (71.3 eV)	Pt(OH) _x (72.7 eV)	PtO ₂ (74.9 eV)	Pt ⁰ (71.3 eV)	Pt(OH) _x (72.7 eV)	PtO ₂ (74.9 eV)
RT	63.6	29.5	6.9	58.3	25.6	16.1
360°C in vacuum	68.8	18.7	12.5	58.5	30.1	11.4
360°C under H ₂ flow	75.9	16	8	71	19.1	9.8

that both the simple thermal and, in particular, the annealing under hydrogen flow cause the corresponding reduction of the Pt oxy-catalyst either as the thermal desorptive effect and even more pronounced by the reactive contribution of Pt-H itself. Similar experimental evidence has already been observed on the simple basic anatase titania (Pt/TiO₂, Figure 4, [2]) interactive supported Pt electrocatalyst [2, 3, 39, 40]. Furthermore, a thorough examination of the O 1s spectra shows a pronounced decrease of the component attributed to the Pt-OH species (BE ~533 eV), which apparently contradicts the enrichment in Pt(OH)_x amounts, observed from the Pt 4f spectrum. In other words, whilst the annealing causes a straight reduction of Pt oxo-species and desorption of the primary oxide (Pt-OH), the intensity decrease of the O 1s component attributed to the same OH* species might be compensated by the spillover from the enriched mixed-valence hypo-d-oxide support. Meanwhile, all XP spectra distinctly indicate the existence, desorptive and/or reactive removal, and compensating spillover of the primary oxide. In any case, the O 1s spectrum reveals a larger initial partial amounts of the primary oxide and similar reactive oxo-species (Pt(OH)_x) for the issues of mixed-valence interactive supported electrocatalysts. As a whole, the annealing in vacuum causes a distinct reduction of platinum oxo-species, in particular the decrease of the primary-type Pt(OH)_x oxides and a slight increase of initially present (long term of the storage nucleation aging effect) PtO_x. At the same time the O 1s component attributed to OH-species correspondingly decreases, indicating the significant desorption of hydroxyl groups in particular pronounced from the mixed valence hypo-d-oxide supports during annealing, as the strong clear evidence for the primary-oxide-enriched presence and spillover.

XP spectral *ex situ* measurements, Figures 9(a) and 9(b), reveal the corresponding Pt 4f deconvoluted spectra of the originally freshly prepared Nb₂O₅, TiO₂-Nb₂O₅, TiO₂-WO₃, and TiO₂ itself, interactive supported Pt electrocatalysts, and for the same specimens after an annual storage. Three distinct components, just as above, participate within the electrocatalytic surface, appearing at three different binding photopeaks, 71.1, 72.7, and 74.8 eV and in this order are correspondingly attributed to the metallic platinum itself, the primary (Pt-(OH)), and nonstoichiometric PtO_x oxides (1 ≤ x ≤ 2), ending with the surface oxide as a final oxidation state [2, 3], respectively, (compare Figure 10, [3]). The latter arises as the minor component amongst others and does not even appear at the Pt 4f spectrum of the freshly prepared Nb₂O₅-TiO₂-supported Pt catalyst after repeating

scans within a longer period (Figure 9(a)). Such a decisive and conclusive remark is of substantial and fundamental significance for the present study: the primary oxide is initially available, in particular, in the condensed wet state of the electrocatalysts. In this respect, one should recall the self-catalytic effect of water molecules on the primary oxide appearance and existence [30].

The percentage contribution of each component to the total peak area is shown in Table 2(a), which has some deeper theoretical significance. The roots and expectancies for the primary oxide spillover are indicated there on an almost quantitative-scale basis. The decisive and pronounced cooperative effect of anatase titania is clearly indicated by its individual rather high initial primary oxide surface percentage, while the Pt/Nb₂O₅,TiO₂ features the most creative synergistic properties for the Pt-OH generation that further reflects on and definitely defines the overall electrocatalytic activity for the ORR [1]. In the same context, one should mention the shrinkage of the same XPS Pt-OH peak capacity both by the thermal and hydrogen reduction effect at higher (360°C) temperature (Figures 7(a), 7(b), 8(a), and 8(b); see also Figure 4, [2]), as the additional experimental evidence for the existence of primary oxide available for further instantaneous spillover distribution under electrode polarization. In the same respect, the complementary DRIFT imprints in Figure 3 in a similar manner reveal the same primary oxide thermal and Pt-H reduction features, but the desorption effect in the present XPS issues arises proportionally smaller since under UHV the examined specimens are deprived from water molecules. Meanwhile, the same specimens after unused storage show the nucleation of PtO_x, ending with PtO₂ (Figure 9(b)), as the common transient in particular pronounced with more active interactive supported electrocatalysts [1–4].

In Figure 10 the deconvoluted Ti 2p spectra of TiO₂-Nb₂O₅- and TiO₂-supported Pt catalysts are comparatively presented. The main doublet in both spectra, at binding energy (Ti 2p_{3/2}) 458.8 eV, is attributed to Ti⁴⁺ species [71, 72]. In the case of the TiO₂-Nb₂O₅ mixed support, a second doublet is apparent at binding energy (Ti2p_{3/2}) 455 eV. This is attributed to the contribution of Ti atoms in the Ti³⁺ state. It should be inferred here that Ti atoms in the other mixed hypo-d-oxide support TiO₂-WO₃ are detected only in the Ti⁴⁺ state [73].

In Figure 11 the deconvoluted Nb 3d XPS core level spectra of TiO₂-Nb₂O₅- and Nb₂O₅-supported Pt catalysts are presented. In both cases only one doublet is apparent at binding energy (Nb 3d_{5/2}) 207.1 eV, which is characteristic

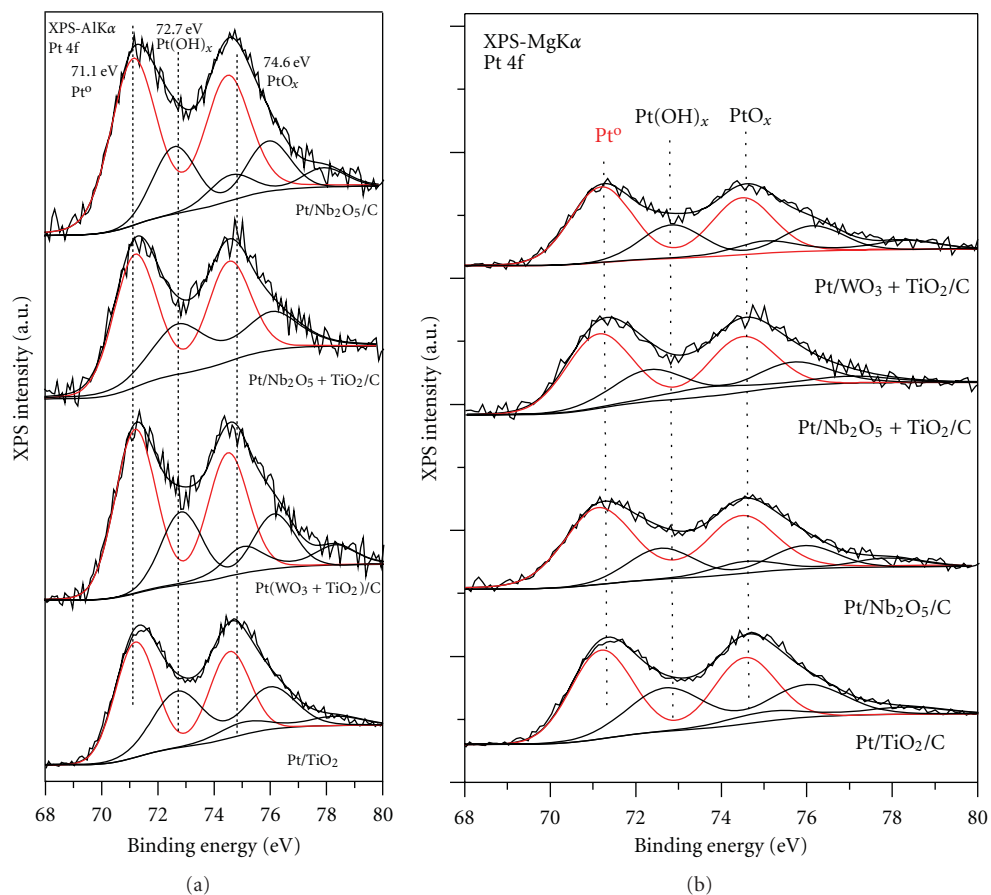


FIGURE 9: Pt 4f XPS core level spectra of Nb₂O₅-, TiO₂-Nb₂O₅-, TiO₂-WO₃-, and TiO₂-supported Pt catalysts at room temperature: (a) scanned fresh and (b) after aging of one year.

for the Nb⁵⁺ state. Namely, it is found in the literature and well known that Nb⁵⁺, when inserted into a titanium dioxide network, usually causes an effect in the charge compensation [74]. The addition of such a charge can be compensated either by creating one vacancy of Ti per four introduced Nb ions or by the reduction of Ti⁴⁺ to Ti³⁺ per each inserted Nb⁵⁺ ion. Both of these effects can occur, with the latter being much more likely at relatively high temperatures [74]. Quantitative analysis of the present results, using the Ti 2p and Nb 3d peak intensities (areas) corrected by the atomic sensitivity factors [75], shows that the appearance of each Ti³⁺ corresponds to one introduced Nb⁵⁺ ion. Thus, in the present case and in agreement with the existing literature, it seems that the introduction of Nb oxide into the composite multivalent mixed compound network with anatase titania causes the partial reduction of Ti⁴⁺ to Ti³⁺ per Nb⁵⁺ ion introduced and perfectly suits the relevant cooperative membrane transferring mechanism (2) [76, 77].

Now, there arises a very interesting situation concerning the most promising electrocatalytic Nb-oxide structure, which at relatively low temperatures of calcination crystallizes as Nb₂O₅. The latter is well confirmed by the XPS analysis, while much more stable NbO₂ appears above 900°C. Such experimental evidence reveals the fifth hydroxide

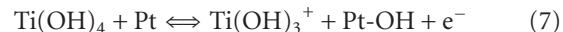
(OH⁻) ion for the most easily transferable within the overall spillover mechanism:



Meanwhile, XPS analysis has also revealed a further interrelating mechanism of similar exchanges with hydrated anatase titania:



or, when summed up,



the entire formalism clears up the equivalence and mutual facilitation between titania and niobia for the primary oxide spillover, as already concluded from Table 2(a).

3.5. FTIR Spectroscopy Evidence of the Primary Oxide Spillover Effect. FTIR spectroscopy has also been employed for the investigation of the primary oxide spillover contribution to CO tolerance [39] from the quantitative study of CO adsorption/desorption properties, as a function of temperature and the type of the interactive hypo-d-oxide-supported

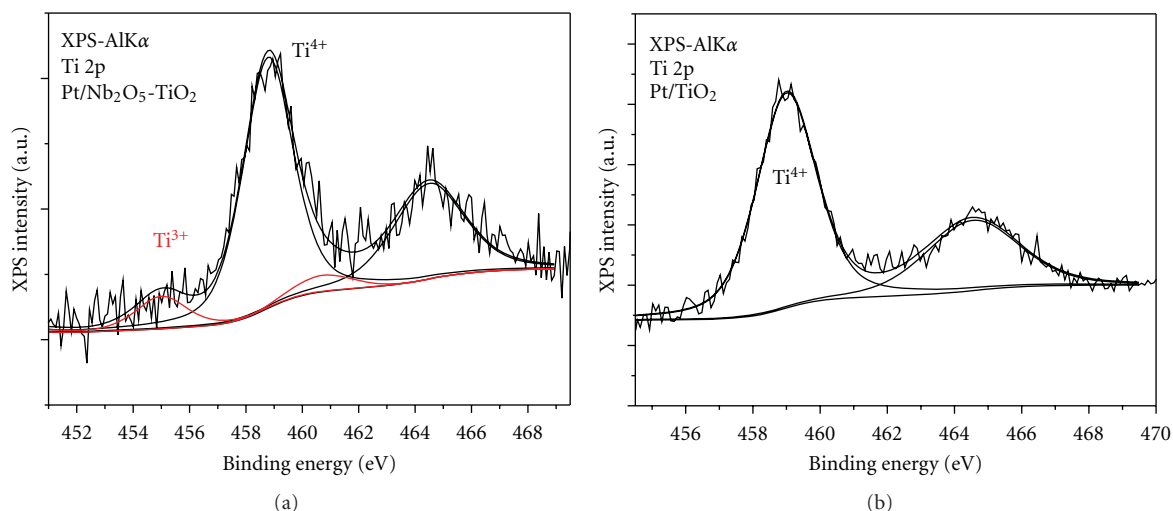


FIGURE 10: Deconvoluted Ti 2p XPS core level spectra of TiO₂-Nb₂O₅- (a) and TiO₂- (b) supported Pt catalysts.

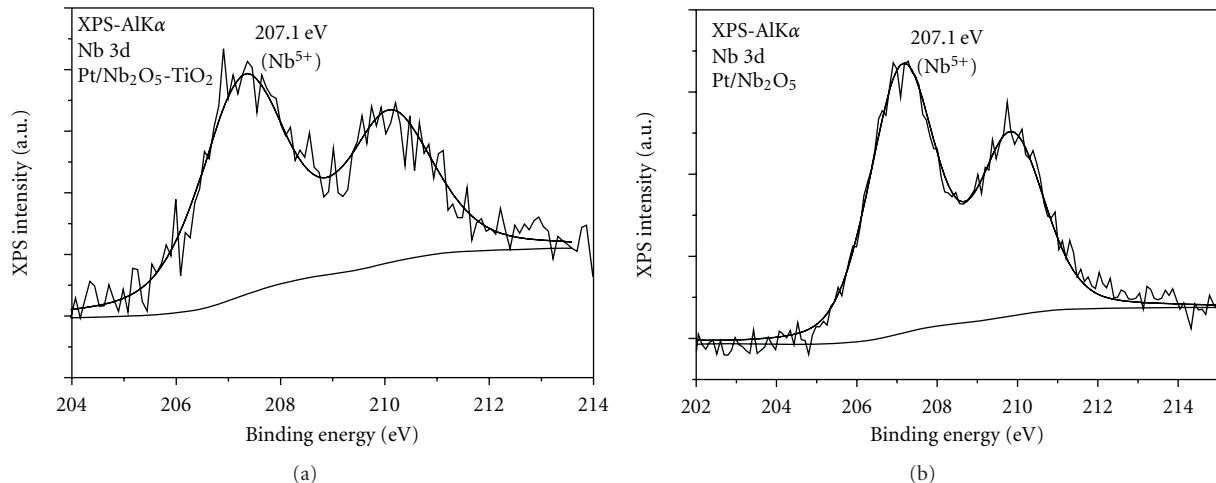


FIGURE 11: Deconvoluted Nb 3d XPS core level spectra of TiO₂-Nb₂O₅- (a) and TiO₂- (b) supported Pt catalysts.

composite electrocatalysts. In other words, the purpose was to get insights about the primary oxide effect indirectly from FTIR investigations of achieved CO tolerance. Namely, to reveal the trends in CO coverage amongst the different electrocatalytic specimens during the linear ramping of temperature in He stream, the ratios of the linearly desorbed CO IR band intensity, at a given temperature to the higher IR band intensity (I_{rel}), are displayed in Figure 12, as a relative coverage of the linearly coordinated CO to Pt sites, labeled as the CO_L species at each temperature. For monometallic supported Pt/TiO₂ catalyst, I_{rel} passes through a maximum at 360 K and declines monotonically thereafter approaching zero in CO adsorption at 500 K, while its derivative of the $(1 - I_{rel})$ curve features maximum in CO_L desorption at 420 K (inset of Figure 12). Contrary to Pt/TiO₂, interactive supported MoPt_x/TiO₂ ($x = 1, 2, 3, 4$) catalysts exhibit significantly different curve profiles, which correspond to much faster CO_L depletion (or much more facilitated oxidation by the primary oxide) rate. In particular, the CO_L area

decreases steadily without featuring any initial increasing stage or any inflection point, while complete desorption of CO is observed already at 370 K. In addition, the profiles obtained from the various catalysts with different Mo/Pt atomic ratios are quite similar, indicating that this factor is not decisive for the CO_L desorption profiles. Meanwhile, it would be noteworthy that, in hydrogen gas stream, the lowest desorption temperature features the sample with the lowest Mo atomic percentage (MoPt₄/TiO₂) [39] or the most active intermetallic phase (MoPt₄) for the HER [40]. As a difference with He atmosphere, H-adatoms consume corresponding amount of the primary oxide (Pt-OH), enabling thereby the higher coverages by CO, and consequently the desorption temperature of the latter increases, while CO tolerance proportionally decreases. Such observations agree quite well with the above-displayed DRIFT spectra obtained under similar conditions, in particular as concerns the interrelating hydrogen reduction effect for the primary oxide removal. In such a context, Figure 12 illustrates adsorptive-desorptive

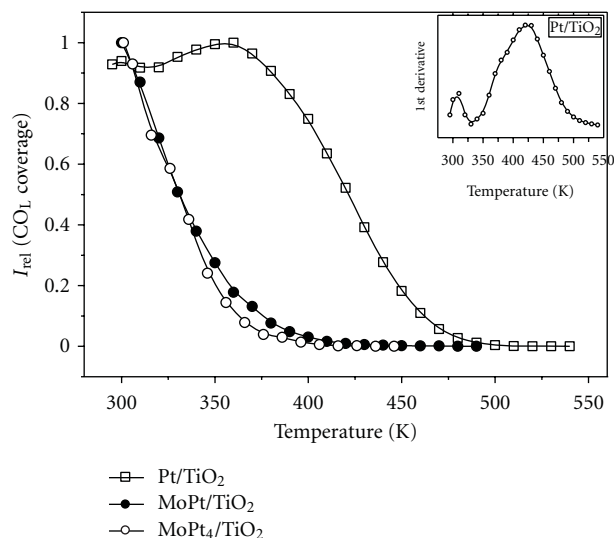


FIGURE 12: The linearly coordinated CO to Pt sites, (CO_L), peak areas normalised to the higher measured intensity as a function of annealing temperature for Pt, MoPt, and MoPt₄ supported on TiO₂ catalysts. Initially the samples were exposed to 7% CO/He for 30 min, and then annealing was carried out under He flow over the catalyst. Inset: peak area derivative of Pt/TiO₂ TPD curve.

TABLE 2: (a) Percentage contribution of each Pt 4f component to the total peak area for freshly prepared specimens. (b) The same for an annual storage of the same specimens.

(a)			
Catalyst support	Percentage contribution of Pt 4f components		
	Pt ⁰ (71.1 eV)	Pt(OH) (72.7 eV)	PtO _x (74.8 eV)
Nb ₂ O ₅	67.2%	23.7%	9.1%
Nb ₂ O ₅ -TiO ₂	65.3%	34.7%	—
WO ₃ -TiO ₂	61.9%	26.7%	11.4%
TiO ₂	56.8%	31.9%	11.3%

(b)			
Catalyst support	Percentage contribution of Pt 4f components		
	Pt ⁰ (71.1 eV)	Pt(OH) _x (72.7 eV)	PtO _x (74.8 eV)
Nb ₂ O ₅	58.3%	25.6%	16.1%
Nb ₂ O ₅ -TiO ₂	63.6%	29.5%	6.9%
WO ₃ -TiO ₂	61.9%	26.7%	11.4%
TiO ₂	56.8%	31.9%	11.3%

properties of various examined catalyst specimens versus CO and thereby reflects a relative measure of their CO tolerance or, *vice versa*, the effect of the primary oxide on the latter. The lower CO desorption temperature has been attributed to its chemical oxidation at the boundaries of the Mo oxide nanoclusters by the OH* species spillover supplied by either Pt-OH or MoO₂OH, the latter being *a priori ex situ* already detected by XPS as the most abundant oxidation state [39, 40].

3.6. *Electrocatalysis and d-Electronic Density of States versus the Fermi Level.* The electrocatalytic reaction mechanism by *ab initio* DFT calculation, both for the HER and ORR, implies that a d band centered near the Fermi level (E_F) can lower the activation energy as the bonding orbital passes E_F , the critical step for reduction processes taking place when the antibonding orbital passes the Fermi level of the metal from above and picks up electrons to become filled [78, 79]. In electrooxidation reactions (HOR, OER), it is the bonding orbital that passes the Fermi level from below and gets emptied. Consequently, a good catalyst for these reactions should have a high density of d states near the Fermi level [44, 80, 81]. Thus, the present concept consists of the proper hypo-hyper-d-d-interelectronic combinations of transition elements both being of rather high densities of d states at the Fermi level (Figure 13), in which hypo-d-oxide components (W, Nb, Ta, Ti), beside the substantially high SMSI bonding effect, as typical oxophilic d metals, in addition involve their pronounced membrane spillover properties for the primary oxide transferring and effusion. In such a state, our aim has been to keep the composite transition element ingredients with their initial high densities of d states, or even to increase the latter by their SMSI interbonding effect, and at the same time to use the benefits of the primary oxide spillover for the overall reaction, in particular for the ORR. In this respect, Figure 13(b) reveals why Nb and Ta, by the position in the periodic table of elements, are electrocatalytically predestined for even higher activity than W, Mo, and Ti.

3.7. *Striping Voltammetry Evidence for the Primary Oxide Spillover Effect.* Interactive hypo-d-oxide-supported and non-supported electrocatalysts (both Pt and RuPt) exhibit dramatically different activity for CO tolerance in LT PEMFC and provide new additional and indirect potentiodynamic evidence for the M-OH spillover effect [2, 3]. Namely, ever since Watanabe and Motoo [82] have shown that Ru even at submonolayer core-shell deposit, or while alloying with Pt, shifts the primary oxide growth to a much more negative potential range and enables CO tolerance, the primary oxide spillover became of substantial significance for PEMFC [83]. Similarly, the hypo-d-oxide-supported Pt and Ru (Pt/TiO₂/C, Ru/TiO₂/C) in their behavior *versus* these two pure metals (Pt/C, Ru/C) themselves or even their alloys, RuPt/C and RuPt/TiO₂/C, have distinctly different catalytic properties, too, the interactive alternatives featuring an even more advanced and much more pronounced primary oxide spillover effect [1–4]. Since hypo-d-oxides, primarily anatase titania, zirconia and hafnia, and even more so tungstenia, niobia and tantalum, facilitate the spillover of M-OH, such facts clearly point to the advanced overall composite effect and advantages of membrane-type OH⁻ transferring within TiO₂, WO₃, Nb₂O₅, and TaO₂ and, in particular, within their mixed networks of altrivalent catalyst support, resulting in the speeded-up primary oxide effusion, relative to the plain carbon (Pt/C).

In other words, while Ru itself facilitates Pt-OH and Ru-OH spillover transfer in RuPt composite electrocatalyst [82, 83], the supporting effusion effect of titania advances the

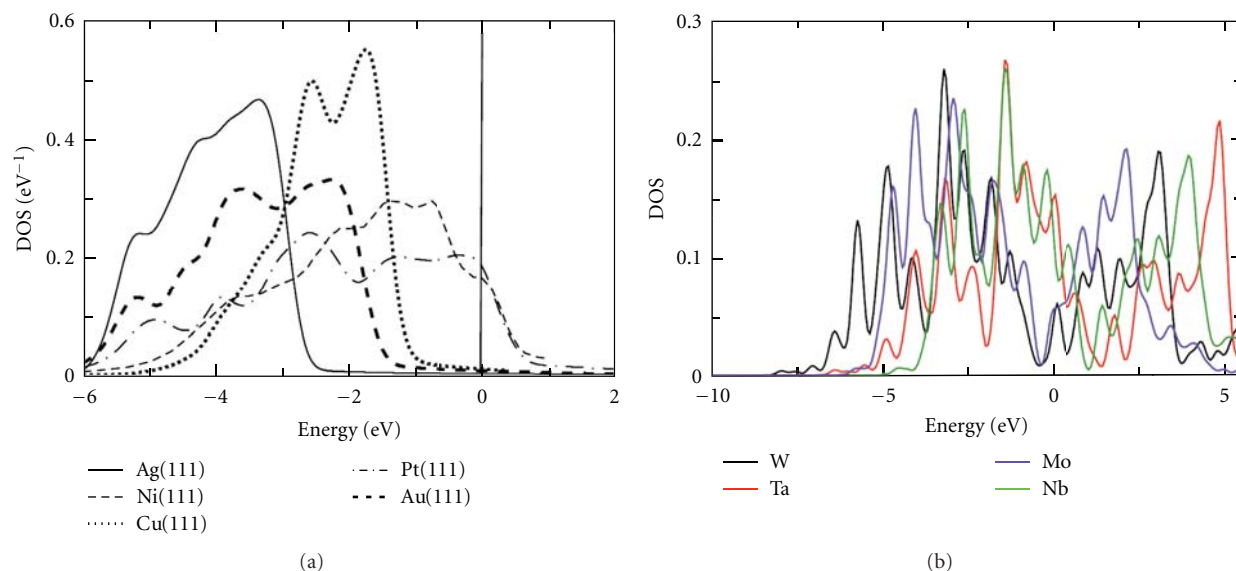


FIGURE 13: (a) Surface densities of d-band states of some selected hyper-d-electronic transition metals. The integral over the densities has been normalized to unity; the vertical line indicates the Fermi level. Indications and labels: dashed-dotted line: Pt (111); thick line: Au (111); thin line: Ag (111); dotted line: Cu (111); dashed line: Ni (111). (b) Lower location: surface densities of d-band states (bulk values differing from exact surface densities for less than 3%) of some selected hypo-d-electronic transition metals (W, Ta, Mo, Nb, color labeled). (Calculated by Professor Wolfgang Schmickler, University of Ulm, Germany.)

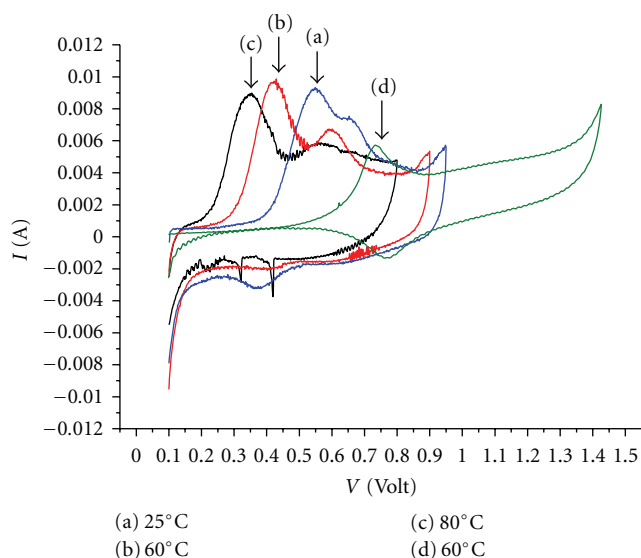


FIGURE 14: The stripping voltammograms for CO desorption from supported 10 wt.% (0.4 mg cm^{-2} , 2 nm in average size, 1 : 1 atomic ratio Ru : Pt) RuPt/TiO₂/C electrocatalyst CO-saturated at three different temperatures: 25 (a), 60 (b), and 80 (c) °C, scanned at the scan rate of 2 mV s^{-1} ; (d) the same stripping scans for CO desorption at 60 °C from unsupported 30 wt.% (0.5 mg cm^{-2} , same average nanosize) E-tek RuPt/C electrocatalyst of the same RuPt nanosize, atomic ratio and load, sweep rate $10 \text{ mV} \cdot \text{s}^{-1}$, and its CO saturation at 55 °C.

same effect for more than 300 mV relative to RuPt/C catalyst (Figure 14). Anodic CO oxidation upon Ru, Pt/TiO₂/C starts even within the potential range of UPD desorption of H-adatoms and becomes much more pronounced in the charge

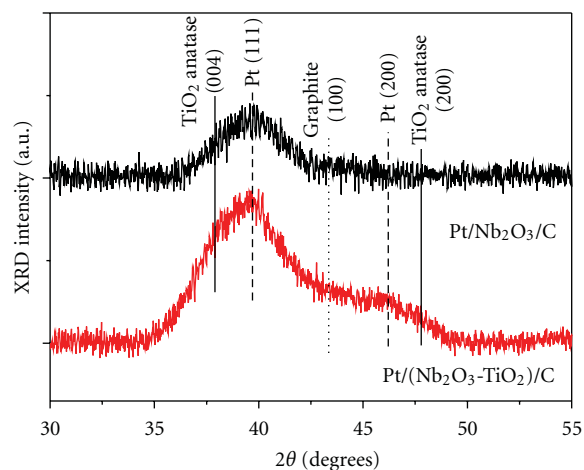


FIGURE 15: XRD spectra of the Pt supported on Nb₂O₃/C and (Nb₂O₃-TiO₂)/C. The lines drawn in the figure show the positions of the respective reflections.

capacity relative to Ru, Pt/C. This important result is one of the most significant confirmations of the present interactive and dynamic spillover catalytic model, as implemented in electrocatalysis for hydrogen and oxygen electrode reactions. In such a context, Figure 3 illustrates the primary role of water (left peaks) versus M-OH (right peaks) by DRIFT relevance, as the *a priori* initial source of primary oxides and supports the just revealed spillover effect and evidence.

It should also be inferred that mixed anatase (and even rutile) titania and, in particular, tungstenia form intermolecular solid oxide solutions of a high altermal

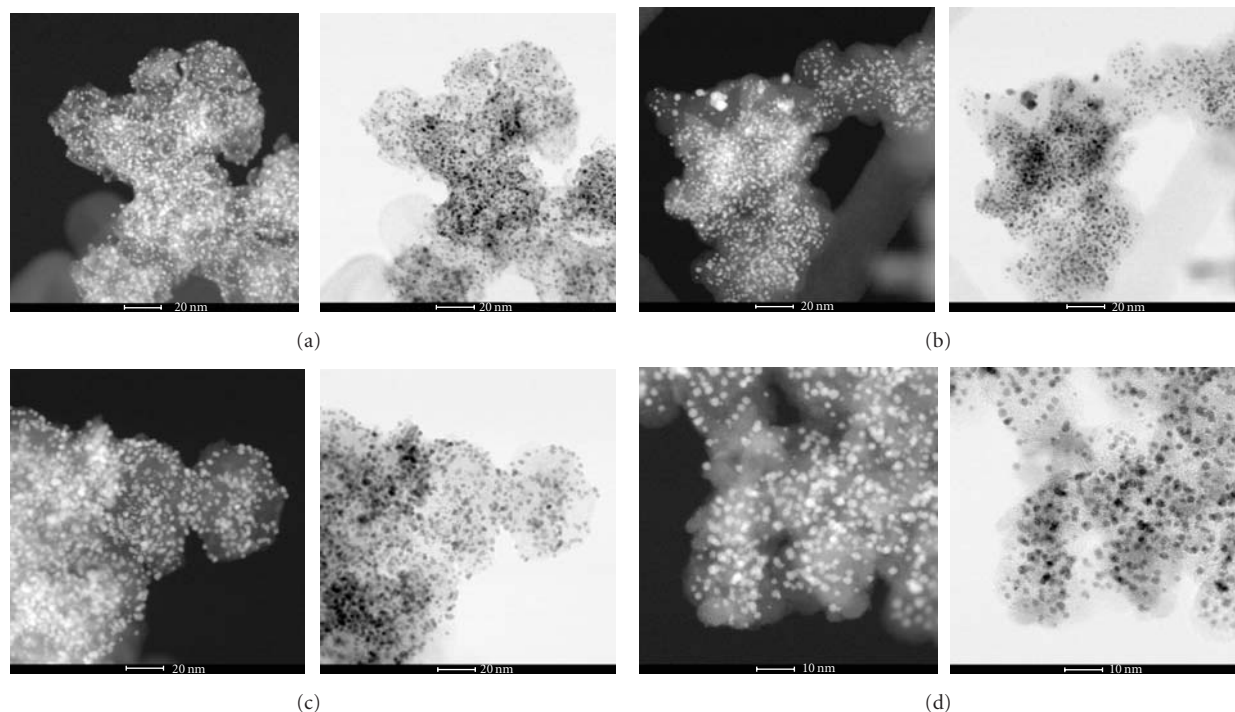


FIGURE 16: Scanning transmission electron nanoimages of TM hypo-d-oxide/carbon support material and nanostructured Pt electrocatalyst nanoparticles: (i) High-resolution high-angle annular dark-field scanning transmission electron micrograph or Z-contrast nanographs (left-hand order) and (ii) Bright-field nanoimages of somewhat higher resolution, but missing the smallest nanoparticles (right-hand order). Labels: (a) Composite simple basic Nb-oxide interactive (SMSI) supported electrocatalyst, {Pt (10 wt.)/20 wt.% Nb₂O₅/C}; (b) Congenial altrivalent supported electrocatalyst, {Pt (10 wt.)/20 wt.% Nb₂O₅, TiO₂/C}; (c) Composite interactive (SMSI) altrivalent supported electrocatalyst of the same hypo-d-oxide structure as in (b), but of triple higher Pt weight percentage, {Pt (30 wt.)/20 wt.% Nb₂O₅, TiO₂/C}, and (d) congenial altrivalent supported electrocatalyst as in (b), but based on mixed W-oxide and anatase titania interactive supported Pt clusters. Courtesy of F. Nan and Professor Gianluigi Botton (McMaster University) for nanoimages.

capacity (Scheme 2, [1]), compatible both in amorphous and crystalline forms of the edge sharing TiO₆ and the corner sharing WO₆ octahedrons, with pronouncedly increased electrochromic features even at high contents of the former [84, 85]. In fact, highly charged W⁶⁺ cations, like Nb⁵⁺, additionally favor the reversible acidic dissociation of water molecules [15, 16, 57], and, thereby, such electrochromic layers exhibit well defined ion exchange and electron conductive properties [2, 3, 15–19, 57]. Thus, one of the fundamental contributions of the present paper is to show that prevailing anatase titania in the form of a composite catalytic support with tungstenia (and/or niobia, tantalum, and even molybdena), which is stable for alkaline media too, also behaves in a compatible way and, regarding the (Pt/H_{0.35}WO₃ ⇌ Pt/W(OH)₆) reversibility, features the same properties as pure tungsten bronze itself!

3.8. XRD and UHRTEM Nanostructured Characterization of Hypo-d-oxide-Supported Electrocatalysts. The spectrum for the Pt/(Nb₂O₃-TiO₂)/C catalyst shows an overlapped region between 35 and 50 degrees (Figure 15). In this region one expects the reflection lines for the Pt (111) and (200), TiO₂ anatase (004) and (200) and as well as the graphitic (100) crystallographic planes, shown with the labeling straight

lines drawn therein. Evidently, all the above mentioned reflections are essentially overlapped. In this respect, it is not possible to estimate exactly the Pt and TiO₂ particle size, while peaks attributable to Nb specimens are at the noise level and absent, due to their very small amount. Nb oxide reflection peaks are also absent from the XRD spectrum of the Pt/Nb₂O₃/C catalyst, though the amount of niobia is now significantly higher as compared to the Pt/(Nb₂O₃-TiO₂)/C sample. The only visible reflection peak in the Pt/Nb₂O₃/C sample is ascribed to the Pt (111) crystallographic plane. By fitting this particular peak with a Gaussian function, it is possible to estimate the average Pt particle size by applying the Scherrer equation. It was found to be approximately 2.2 nm, this way indicating the highly and uniformly dispersed nature of such a catalyst. From H₂ chemisorption measurements [39], the average Pt particle size was estimated to be 3.7 nm (77 m²/gr of Pt assuming spherical particles, while the electrochemically active surface area, UPD H-adatoms estimated by the corresponding potentiodynamic desorption peaks, is even lower, 57.5 m²/gr of Pt). The significantly larger Pt particles estimated by the H₂ chemisorption indicate the interaction between the Pt particles and the oxide support that hinders the H₂ adsorptive properties of Pt crystallites, leading to particle size overestimation. On the other hand, the particle

size determination by XRD is usually overestimated (the overlapping effect), and, since the size is close to the instrument limits, such a state of experimental evidence convincingly suggests that Pt particles are evenly dispersed and strongly bonded on the hypo-d-oxide catalytic support as shown by many XRD measurements with similar interactive hypo-d-oxide supported electrocatalysts. The absence of niobia reflection peaks indicates that Nb oxides are either highly sub- to monolayer dispersed on the carbon particle surface (as essentially the surface species) or less probably in amorphous state. In fact, the present electrocatalyst has been *a priori* planned and calculated by the mass and surface ratio between hypo-d-oxide and Vulcan carbon particles to be deposited as submonolayer (Nb_2O_5 having $170\text{ m}^2\text{ g}^{-1}$, while carbon particles being in higher amount and of much larger surface area, $260\text{ m}^2\text{ g}^{-1}$). Such a unique XRD experimental insight convincingly testifies to the existence of high Pt (111) bronze dispersion upon highly developed hypo-d-oxide support. Such a state relative to the standard Pt/C electrocatalyst, otherwise suffering from agglomeration, characterizes remarkably increased electrocatalytic activity, a much longer-lasting catalyst because of the SMSI bonding effect, while the interactive structure enables Pt metal recovery, which is another high-quality achievement of the novel nanostructured bronze-type electrocatalysts. Meanwhile, the most significant is the control of homogeneous dispersion of grafted nanostructured Pt size magnitude: the ratio of available exposed hypo-d-oxide surface relative to the Pt wt.% defines the latter, and in our issues it is usually fixed between 2.0 and 2.4 nm in average, in particular for Nb-O-, W-O-, and Ti-O- individual and mixed-valence composite hypo-d-supports (SMSI), for Ta-O- not yet optimized. However, UHRTEM (0.7 nm resolution) identifies plenty of about 1.0 nm Pt clusters.

The UHRTEM (ultrahigh resolution transmission electron microscopy, FEI Titan 80–300 cubed, equipped with two aberration correctors (CEOS) and a high-brightness source) nanoimages reveal the strong interactive grafted Pt nanoclusters on hypo-d-oxides supports, with a rather uniform and evenly homogeneous distribution in average of about 2 to 2.5 nm in nanosize on the best issues {Pt (10 wt.%)/20 wt.% $\text{Nb}_2\text{O}_5, \text{TiO}_2/\text{C}$ }, Figure 16(b), {Pt (10 wt.%)/20 wt.% $\text{Nb}_2\text{O}_5/\text{C}$ }, Figure 16(a), and {Pt (10 wt.%)/20 wt.% $\text{WO}_3, \text{TiO}_2/\text{C}$ }, Figure 16(d), obtained so far and already confirmed by XRD scans (resolution 0.7 nm). Even more so, with triple larger Pt amount {Pt (30 wt.%)/20 wt.% $\text{Nb}_2\text{O}_5, \text{TiO}_2/\text{C}$ }, Figure 16(c), the homogeneous nanostructured Pt distribution keeps the same trend and in particular the average nanosize. Such a homogeneous nanosize level of distribution has never so far been achieved and confirms the basis for the rather pronounced spillover effect and the unique electrocatalytic achievements. No single Pt nanostructured cluster has been noticed on the prevailing carbon nanoparticles percentage of their otherwise highly developed exposed surface area and no agglomeration. It would certainly be worthwhile noticing a rather all-over homogeneous widespreading of the interactive hypo-d-oxide support structure and well distinct inter-d-d-bonded and interactive (SMSI) grafted fine Pt nanosized

clusters upon them, as a unique nanostructured Pt-bronze substantiation of advanced electrocatalytic properties, primarily and mostly extended by the pronounced spillover effect.

4. Conclusions

The present paper has shown that, beside the SMSI effect, the interactive grafted and supported hyper-d-elements and their composites, without exception, feature the reversible and thereby fast spillover phenomena both for H-adatoms during the cathodic and the primary oxide (M-OH) in the course of anodic polarization, as an additional dynamic catalytic effect in conjunction with the hypo-hyper-d-d-interelectronic bonding contribution to the overall synergistic electrocatalytic activity. Nanostructured reversibly interchangeable ($\text{Pt}/\text{H}_{0.35}\text{WO}_3 \rightleftharpoons \text{Pt}/\text{W}(\text{OH})_6$) alterpolar bronze-type and its TiO_2 -modified mixed-valence compound-type ($\text{Pt}/\text{Nb}_2\text{O}_5, \text{TiO}_2/\text{C}, \text{Pt}/\text{WO}_3, \text{TiO}_2/\text{C}$) electrocatalyst issues for hydrogen and primarily oxygen electrode reactions (HER, HOR, ORR, OER) have for the first time been developed and produced by a proper sol-gel synthetic method and comprise unpredictable unique advantages in electrocatalysis. Since these four electrode reactions are instantaneously and reversibly interchangeable on the same electrocatalyst (bronze and hydrated state) properties and feature substantially pronounced individual reversible properties for each of them, several significant achievements resulted therein.

- (i) XPS, DRIFT, FTIR, and potentiodynamic spectra have been employed to show the *a priori* existence of the primary oxide species, as predestined for spillover by the membrane transfer through the interactive (SMSI) bonded hypo-d-oxide supports and being available for the double layer charging and discharging. XPS analysis has also confirmed the membrane mechanism in Pt-OH transference and spillover (confirmed surface Ti^{3+} versus Nb^{5+} in the ratio 1:1), as well as the estimated SMSI bonding effect at the Au/ TiO_2 interphase, and indicated the existence of the intermetallic phase (TiPt_3 at Pt/ TiO_2 interface) that enables the entire interactive catalytic synergistic activity. In similar respect, XRD scans in conjunction with UHRTEM contributed to further supportive conclusions concerning the particle size and homogeneous distribution of the metallic phase of such composite electrocatalysts and the interionic interference between titania and niobia, tungstenia, or tantalum. In addition, potentiodynamic spectra scanned under wet and dry PEM proved the whole spillover phenomena of primary oxide and its UPD and OPD double layer charging and discharging, as well as the interchangeable alternating H-adatoms effusion. Cyclic voltammetry in admixture of formaldehyde is cited to reinforce such phenomenological statements, while Ertel⁵⁷ auto- or self-catalytic effect of water molecules, particularly within the double layer structure, was added to

complete the overall phenomenon of effusion and its nature and properties.

- (ii) Since interactive (SMSI) d-d bonded on suitable hypo-d-oxide supports, Pt nanoparticles are first properly grafted upon them, uniformly distributed, and evenly dispersed at the optimal nanosize. The corresponding supported Pt nanoclusters are thereby prevented from agglomeration, thence provide longer lasting of the electrocatalytic activity and even afford possibilities for Pt recovery, otherwise so far missing in LT PEMFC operation and uses.
- (iii) Such reversibly alterpolar and multifunctional electrocatalyst composite enables a still expensive, but functionally, technologically, and catalytically ideal, revertible cell system between PEMFC and WE and opens the way towards cheaper ones. In other words, a proper alkaline membrane might enable the use of the same interchangeable doubled spillover of M-OH and H-adatoms species in a rather mild environment upon nonnoble interactive hypo-d-oxide-supported electrocatalysts, as the main promising system for mobile PEMFC.
- (iv) All proper combinations between higher altervalent capacity hypo-d-oxides (Nb_2O_5 , WO_3 , TaO_2) and anatase TiO_2 , thermally produced, feature high electron conductivity and enable us to avoid the nanosized carbon current collector and as a catalyst support in PEMFC and WE, which is decisive for anodic oxygen evolution.
- (v) Electrocatalytic activity for the ORR has been advanced for more than an order of magnitude [1] relative to the standard nanostructured Pt/C electrocatalyst, enabling us to reduce Pt load for more than four times in L&MT PEMFC and still keep the same activity.
- (vi) The present and former experimental evidence [1–4] have shown that, within the reversible part of Tafel plot, in particular hypo-d-oxide supported Pt electrocatalysts are always partially covered by its oxides, and thereby polarization for the ORR starts at more positive potential values and, consequently, increasingly acquiring the reversible oxygen electrode properties [1–4]. Thus, one of the conclusions is that the present paper has shown the way towards the reversible oxygen electrode, as one of the main goals in aqueous electrochemistry, at least for the ORR.

Acknowledgments

The present study has been the result of several EU research projects (acronyms Apollon, Prometheus) and mostly carried out in the ICEHT/FORTH Laboratories in Patras, Greece, ones of the European leading both in L&MT PEMFC and in particular in electrocatalysis; all authors feel the recognition and gratitudes to their institute.

References

- [1] J. M. Jaksic, D. Labou, G. D. Papakonstantinou, A. Siokou, and M. M. Jaksic, "Novel spillover interrelating reversible electrocatalysts for oxygen and hydrogen electrode reactions," *Journal of Physical Chemistry C*, vol. 114, no. 43, pp. 18298–18312, 2010.
- [2] J. M. Jaksic, N. V. Krstajic, L. M. Vracar et al., "Spillover of primary oxides as a dynamic catalytic effect of interactive hypo-d-oxide supports," *Electrochimica Acta*, vol. 53, no. 2, pp. 349–361, 2007.
- [3] N. V. Krstajic, L. M. Vracar, V. R. Radmilovic et al., "Advances in interactive supported electrocatalysts for hydrogen and oxygen electrode reactions," *Surface Science*, vol. 601, no. 9, pp. 1949–1966, 2007.
- [4] J. M. Jaksic, D. Labou, C. M. Lacnjevac, A. Siokou, and M. M. Jaksic, "Potentiodynamic estimation of key parametric criteria and interrelating reversible spillover effects for electrochemical promotion," *Applied Catalysis A*, vol. 380, no. 1–2, pp. 1–14, 2010.
- [5] C. M. Guldberg and P. Waage, "Concerning chemical affinity," *Erdmann's Journal für Practische Chemie*, vol. 127, pp. 69–114, 1979.
- [6] E. W. Lund, "Guldberg and waage and the law of mass action," *Journal of Chemical Education*, vol. 42, no. 10, pp. 548–550, 1965.
- [7] M. Boudart, M. A. Vannice, and J. E. Benson, "Adlineation, portholes and spillover," *Zeitschrift für Physikalische Chemie*, vol. 64, no. 1–4, pp. 171–177, 1969.
- [8] H. W. Kohn and M. Boudart, "Reaction of hydrogen with oxygen adsorbed on a platinum catalyst," *Science*, vol. 145, no. 3628, pp. 149–150, 1964.
- [9] J. E. Benson, H. W. Kohn, and M. Boudart, "On the reduction of tungsten trioxide accelerated by platinum and water," *Journal of Catalysis*, vol. 5, no. 2, pp. 307–313, 1966.
- [10] M. A. Vannice, M. Boudart, and J. J. Fripiat, "Mobility of hydrogen in hydrogen tungsten bronze," *Journal of Catalysis*, vol. 17, no. 3, pp. 359–365, 1970.
- [11] A. D. Lueking and R. T. Yang, "Hydrogen spillover to enhance hydrogen storage—study of the effect of carbon physicochemical properties," *Applied Catalysis A*, vol. 265, no. 2, pp. 259–268, 2004.
- [12] J. G. Kim and J. R. Regalbuto, "The effect of calcination on H₂ spillover in Pt/MoO₃. II. Kinetic modeling," *Journal of Catalysis*, vol. 139, no. 1, pp. 175–190, 1993.
- [13] R. K. Agarwal, J. S. Noh, J. A. Schwarz, and P. Davini, "Effect of surface acidity of activated carbon on hydrogen storage," *Carbon*, vol. 25, no. 2, pp. 219–226, 1987.
- [14] H. Takagi, H. Hatori, and Y. Yamada, "Reversible adsorption/desorption property of hydrogen on carbon surface," *Carbon*, vol. 43, no. 14, pp. 3037–3039, 2005.
- [15] A. Vittadini, A. Selloni, F. P. Rotzinger, and M. Grätzel, "Structure and energetics of water adsorbed at TiO₂ anatase (101) and (001) surfaces," *Physical Review Letters*, vol. 81, no. 14, pp. 2954–2957, 1998.
- [16] A. Valdes and G. J. Kroes, "First principles study of the photo-oxidation of water on tungsten trioxide (WO₃)," *Journal of Chemical Physics*, vol. 130, no. 11, Article ID 114701, 2009.
- [17] J. Livage, M. Henry, and C. Sanchez, "Sol-gel chemistry of transition metal oxides," *Progress in Solid State Chemistry*, vol. 18, no. 4, pp. 259–341, 1988.
- [18] P. Judeinstein and J. Livage, "Sol-gel synthesis of WO₃ thin films," *Journal of Materials Chemistry*, vol. 1, no. 4, pp. 621–627, 1991.

- [19] J. Livage and G. Guzman, "Aqueous precursors for electrochromic tungsten oxide hydrates," *Solid State Ionics*, vol. 84, no. 3-4, pp. 205-211, 1996.
- [20] S. G. Neophytides, S. H. Zafeiratos, and M. M. Jaksic, "Selective interactive grafting of composite bifunctional electrocatalysts for simultaneous anodic hydrogen and Co oxidation: I. Concepts and embodiment of novel-type composite catalysts," *Journal of the Electrochemical Society*, vol. 150, no. 10, pp. E512-E526, 2003.
- [21] S. G. Neophytides, K. Murase, S. Zafeiratos et al., "Composite hypo-hyper-d-intermetallic and interionic phases as supported interactive electrocatalysts," *Journal of Physical Chemistry B*, vol. 110, no. 7, pp. 3030-3042, 2006.
- [22] S. J. Tauster and S. C. Fung, "Strong metal-support interactions: occurrence among the binary oxides of groups IIA-VB," *Journal of Catalysis*, vol. 55, no. 1, pp. 29-35, 1978.
- [23] S. J. Tauster, S. C. Fung, R. T. K. Baker, and J. A. Horsley, "Strong interactions in supported-metal catalysts," *Science*, vol. 211, no. 4487, pp. 1121-1125, 1981.
- [24] S. A. Stevenson, *Metal-Support Interaction in Catalysis, Sintering and Redispersion*, D. Van Nostrand, New York, NY, USA, 1987.
- [25] G. L. Haller and D. E. Resasco, "Metal-support interaction: group VIII metals and reducible oxides," *Advances in Catalysis*, vol. 36, pp. 173-235, 1989.
- [26] P. Panagiotopoulou and D. I. Kondarides, "Effect of the nature of the support on the catalytic performance of noble metal catalysts for the water-gas shift reaction," *Catalysis Today*, vol. 112, no. 1-4, pp. 49-52, 2006.
- [27] P. Panagiotopoulou and D. I. Kondarides, "A comparative study of the water-gas shift activity of Pt catalysts supported on single (MO_x) and composite ($\text{MO}_x/\text{Al}_2\text{O}_3$, MO_x/TiO_2) metal oxide carriers," *Catalysis Today*, vol. 127, no. 1-4, pp. 319-329, 2007.
- [28] C. Kokkofitis, G. Karagiannakis, and M. Stoukides, "Study of the water gas shift reaction on Fe in a high temperature proton conducting cell," *Catalysis Today*, vol. 127, no. 1-4, pp. 330-336, 2007.
- [29] M. Daté and M. Haruta, "Moisture effect on CO oxidation over Au/TiO₂ catalyst," *Journal of Catalysis*, vol. 201, no. 2, pp. 221-224, 2001.
- [30] S. Völkening, K. Bedürftig, K. Jacobi, J. Wintterlin, and G. Ertl, "Dual-path mechanism for catalytic oxidation of hydrogen on platinum surfaces," *Physical Review Letters*, vol. 83, no. 13, pp. 2672-2675, 1999.
- [31] M. T. M. Koper and R. A. Van Santen, "Interaction of H, O and OH with metal surfaces," *Journal of Electroanalytical Chemistry*, vol. 472, no. 2, pp. 126-136, 1999.
- [32] H. Angerstein-Kozłowska, B. E. Conway, and W. B. A. Sharp, "The real condition of electrochemically oxidized platinum surfaces. Part I. Resolution of component processes," *Journal of Electroanalytical Chemistry*, vol. 43, no. 1, pp. 9-36, 1973.
- [33] H. Angerstein-Kozłowska, B. E. Conway, A. Hamelin, and L. Stoicoviciu, "Elementary steps of electrochemical oxidation of single-crystal planes of Au-I. Chemical basis of processes involving geometry of anions and the electrode surfaces," *Electrochimica Acta*, vol. 31, no. 8, pp. 1051-1061, 1986.
- [34] H. Angerstein-Kozłowska, B. E. Conway, A. Hamelin, and L. Stoicoviciu, "Elementary steps of electrochemical oxidation of single-crystal planes of Au Part II. A chemical and structural basis of oxidation of the (111) plane," *Journal of Electroanalytical Chemistry*, vol. 228, no. 1-2, pp. 429-453, 1987.
- [35] H. Angerstein-Kozłowska, B. E. Conway, K. Tellefsen, and B. Barnett, "Stochastically-gated surface processes involving anions in oxidation of Au: time-resolution of processes down to 0.25% coverages and 50 μs time-scales," *Electrochimica Acta*, vol. 34, no. 8, pp. 1045-1056, 1989.
- [36] B. E. Conway, B. Barnett, H. Angerstein-Kozłowska, and B. V. Tilak, "A surface-electrochemical basis for the direct logarithmic growth law for initial stages of extension of anodic oxide films formed at noble metals," *The Journal of Chemical Physics*, vol. 93, no. 11, pp. 8361-8373, 1990.
- [37] B. E. Conway, "Electrochemical oxide film formation at noble metals as a surface-chemical process," *Progress in Surface Science*, vol. 49, no. 4, pp. 331-452, 1995.
- [38] N. M. Ristic, M. Kotorcevic, C. M. Lacinjevac, A. M. Jokic, and M. M. Jaksic, "Some specific potentiodynamic behaviour of certain aldehydes and monosaccharides: some simple and some specific aldehydes," *Electrochimica Acta*, vol. 45, no. 18, pp. 2973-2989, 2000.
- [39] S. Zafeiratos, G. Papakonstantinou, M. M. Jaksic, and S. G. Neophytides, "The effect of Mo oxides and TiO₂ support on the chemisorption features of linearly adsorbed CO on Pt crystallites: an infrared and photoelectron spectroscopy study," *Journal of Catalysis*, vol. 232, no. 1, pp. 127-136, 2005.
- [40] J. M. Jaksic, L. Vracar, S. G. Neophytides et al., "Structural effects on kinetic properties for hydrogen electrode reactions and CO tolerance along Mo-Pt phase diagram," *Surface Science*, vol. 598, no. 1-3, pp. 156-173, 2005.
- [41] M. Suh, P. S. Bagus, S. Pak, M. P. Rosynek, and J. H. Lunsford, "Reactions of hydroxyl radicals on titania, silica, alumina, and gold surfaces," *Journal of Physical Chemistry B*, vol. 104, no. 12, pp. 2736-2742, 2000.
- [42] N. D. Lang, "Theory of single-atom imaging in the scanning tunneling microscope," *Comments on Condensed Matter Physics*, vol. 14, no. 5, pp. 253-257, 1989.
- [43] D. Y. Zemlyanov, E. Savinova, A. Scheybal, K. Doblhofer, and R. Schlögl, "XPS observation of OH groups incorporated in an Ag(111) electrode," *Surface Science*, vol. 418, no. 2, pp. 441-456, 1998.
- [44] B. Hammer and J. K. Nørskov, "Theoretical surface science and catalysis-calculations and concepts," *Advances in Catalysis*, vol. 45, pp. 71-129, 2000.
- [45] G. Nguyen van Huong, C. Hinnen, and J. Lecoer, "Spectroscopic investigation of single crystal gold electrodes. Part II. The incipient oxidation of gold electrode," *Journal of Electroanalytical Chemistry*, vol. 106, pp. 185-191, 1980.
- [46] J. F. Weaver and G. B. Hoflund, "Surface characterization study of the thermal decomposition of AgO," *Journal of Physical Chemistry*, vol. 98, no. 34, pp. 8519-8524, 1994.
- [47] M. Mavrikakis, P. Stoltze, and J. K. Nørskov, "Making gold less noble," *Catalysis Letters*, vol. 64, no. 2-4, pp. 101-106, 2000.
- [48] A. C. C. Tseung, P. K. Shen, and K. Y. Chen, "Precious metal/hydrogen bronze anode catalysts for the oxidation of small organic molecules and impure hydrogen," *Journal of Power Sources*, vol. 61, no. 1-2, pp. 223-225, 1996.
- [49] A. C. C. Tseung and K. Y. Chen, "Hydrogen spill-over effect on Pt/WO₃ anode catalysts," *Catalysis Today*, vol. 38, no. 4, pp. 439-443, 1997.
- [50] P. K. Shen, K. Y. Chen, and A. C. C. Tseung, "Performance of CO-electrodeposited Pt-Ru/WO₃ electrodes for the electrooxidation of formic acid at room temperature," *Journal of Electroanalytical Chemistry*, vol. 389, no. 1-2, pp. 223-225, 1995.
- [51] O. Glemser and K. Naumann, "Kristallisierte wolframblauerbindungen; wasserstoffanaloga der wolframbronzen

- HxWO₃,” *Zeitschrift für Anorganische Chemie*, vol. 365, no. 4–6, pp. 288–302, 1951.
- [52] M. M. Jaksic, “Advances in electrocatalysis for hydrogen evolution in the light of the Brewer-Engel valence-bond theory,” *Journal of Molecular Catalysis*, vol. 38, no. 1-2, pp. 161–202, 1986.
- [53] L. Brewer, “Bonding and structures of transition metals,” *Science*, vol. 161, no. 3837, pp. 115–122, 1968.
- [54] J. Friedel and C. M. Sayers, “On the role of d-d-electron correlations in the cohesion and ferromagnetism of transition metals,” *Journal de Physique*, vol. 38, pp. 697–705, 1977.
- [55] S. G. Neophytides, S. Zafeiratos, G. D. Papakonstantinou, J. M. Jaksic, F. E. Paloukis, and M. M. Jaksic, “Extended Brewer hypo-hyper-d-interionic bonding theory II. Strong metal-support interaction grafting of composite electrocatalysts,” *International Journal of Hydrogen Energy*, vol. 30, no. 4, pp. 393–410, 2005.
- [56] S. G. Neophytides, S. Zafeiratos, G. D. Papakonstantinou, J. M. Jaksic, F. E. Paloukis, and M. M. Jaksic, “Extended Brewer hypo-hyper-d-interionic bonding theory—I. Theoretical considerations and examples for its experimental confirmation,” *International Journal of Hydrogen Energy*, vol. 30, no. 2, pp. 131–147, 2005.
- [57] A. Tilocca and A. Selloni, “Reaction pathway and free energy barrier for defect-induced water dissociation on the (101) surface of TiO₂-anatase,” *Journal of Chemical Physics*, vol. 119, no. 14, pp. 7445–7450, 2003.
- [58] J. Greeley and M. Mavrikakis, “Alloy catalysts designed from first principles,” *Nature Materials*, vol. 3, no. 11, pp. 810–815, 2004.
- [59] M. M. Jaksic, “Hypo-hyper-d-electronic interactive nature of synergism in catalysis and electrocatalysis for hydrogen reactions,” *Electrochimica Acta*, vol. 45, no. 25-26, pp. 4085–4099, 2000.
- [60] T. J. Schmidt, H. A. Gasteiger, G. D. Stäb, P. M. Urban, D. M. Kolb, and R. J. Behm, “Characterization of high-surface-area electrocatalysts using a rotating disk electrode configuration,” *Journal of the Electrochemical Society*, vol. 145, no. 7, pp. 2354–2358, 1998.
- [61] X. Zhang, K. Y. Chan, and A. C. C. Tseung, “Electrochemical oxidation of glucose by Pt WO₃ electrode,” *Journal of Electroanalytical Chemistry*, vol. 386, no. 1-2, pp. 241–243, 1995.
- [62] M. Peuckert, F. P. Coenen, and H. P. Bonzel, “XPS study of the electrochemical surface oxidation of Platinum in N H₂SO₄ acid electrolyte,” *Electrochimica Acta*, vol. 29, no. 10, pp. 1305–1314, 1984.
- [63] J. E. Drawdy, G. B. Hoflund, S. D. Gardner, E. Yngvadottir, and D. R. Schryer, “Effect of pretreatment on a platinized tin oxide catalyst used for low-temperature CO oxidation,” *Surface and Interface Analysis*, vol. 16, no. 1–12, pp. 369–374, 1990.
- [64] T. Akita, K. Tanaka, S. Tsubota, and M. Haruta, “Analytical high-resolution TEM study of supported gold catalysts: orientation relationship between Au particles and TiO₂ supports,” *Journal of Electron Microscopy*, vol. 49, no. 5, pp. 657–662, 2000.
- [65] M. Haruta, “Size- and support-dependency in the catalysis of gold,” *Catalysis Today*, vol. 36, no. 1, pp. 153–166, 1997.
- [66] F. Boccuzzi, A. Chiorino, S. Tsubota, and M. Haruta, “FTIR study of carbon monoxide oxidation and scrambling at room temperature over gold supported on ZnO and TiO₂. 2,” *Journal of Physical Chemistry*, vol. 100, no. 9, pp. 3625–3631, 1996.
- [67] F. Boccuzzi, A. Chiorino, M. Manzoli et al., “Au/TiO₂ nano-sized samples: a catalytic, TEM, and FTIR study of the effect of calcination temperature on the CO oxidation,” *Journal of Catalysis*, vol. 202, no. 2, pp. 256–267, 2001.
- [68] T. Akita, P. Lu, S. Ichikawa, K. Tanaka, and M. Haruta, *Surface and Interface Analysis*, vol. 31, pp. 73–113, 2001.
- [69] H. Takahashi, I. Harrowfield, C. MacRae, N. Wilson, and K. Tsutsumi, “Analytical TEM study on the dispersion of Au nanoparticles in Au/TiO₂ catalyst prepared under various temperatures,” *Surface and Interface Analysis*, vol. 31, no. 2, pp. 73–78, 2001.
- [70] M. Engelhard, D. Baer, and H. Engelhard, *Surface Science Spectra*, vol. 71, p. 1, 2000.
- [71] M. Engelhard, D. Baer, and H. Engelhard, “Third row transition metals by X-Ray photoelectron spectroscopy,” *Surface Science Spectra*, vol. 7, pp. 1–68, 20030.
- [72] R. E. Fuentes, B. L. Garcia, and J. W. Weidner, “A Nb-doped TiO₂ electrocatalyst for use in direct methanol fuel cells,” *ECS Transactions*, vol. 12, no. 1, pp. 239–248, 2007.
- [73] B. A. Morales, O. Novaro, T. López, E. Sanchez, and R. Gómez, “The effect of hydrolysis catalysts on Ti deficiency and crystallite size of the sol-gel/TiO₂ crystalline phases,” *Journal of Materials Research*, vol. 10, article 2778, 1995.
- [74] J. Arbiol, J. Cerdà, G. Dezanneau et al., “Effects of Nb doping on the TiO₂ anatase-to-rutile phase transition,” *Journal of Applied Physics*, vol. 92, no. 2, p. 853, 2002.
- [75] D. Briggs and M. P. Seah, Eds., *Practical Surface Analysis*, vol. 1, John Wiley & Sons, New York, NY, USA, 2nd edition, 1990.
- [76] J. A. Martinho Simões and J. L. Beauchamp, “Transition metal-hydrogen and metal-carbon bond strengths: the keys to catalysis,” *Chemical Reviews*, vol. 90, no. 4, pp. 629–688, 1990.
- [77] L. C. Anderson, C. E. Mooney, and J. H. Lunsford, “Hydroxyl radical desorption from polycrystalline palladium: evidence for a surface phase transition,” *Chemical Physics Letters*, vol. 196, no. 5, pp. 445–448, 1992.
- [78] E. Santos and W. Schmickler, “Electrocatalysis of hydrogen oxidation—theoretical foundations,” *Angewandte Chemie—International Edition*, vol. 46, no. 43, pp. 8262–8265, 2007.
- [79] W. Schmickler, *Advanced Physical Chemistry*. In press.
- [80] B. Hammer and J. K. Norskov, “Why gold is the noblest of all the metals,” *Nature*, vol. 376, no. 6537, pp. 238–240, 1995.
- [81] E. Christoffersen, P. Liu, A. Ruban, H. L. Skriver, and J. K. Norskov, “Anode materials for low-temperature fuel cells: a density functional theory study,” *Journal of Catalysis*, vol. 199, no. 1, pp. 123–131, 2001.
- [82] M. Watanabe and S. Motoo, “Electrocatalysis by ad-atoms part II. Enhancement of the oxidation of methanol on platinum by ruthenium ad-atoms,” *Journal of Electroanalytical Chemistry*, vol. 60, no. 3, pp. 267–273, 1975.
- [83] J. C. Davies, B. E. Hayden, D. J. Pegg, and M. E. Rendall, “The electro-oxidation of carbon monoxide on ruthenium modified Pt(1 1 1),” *Surface Science*, vol. 496, no. 1-2, pp. 110–120, 2002.
- [84] T. Sonobe, S. Nitta, Y. Katahira et al., “Effect of high frequent vibrating blood flow on the peripheral blood flow distribution using a vibrating electro-magnetic pump (VEMP) in the condition of hypoperfusion,” *Japanese Journal of Artificial Organs*, vol. 21, no. 2, pp. 464–471, 1992.
- [85] S. Hashimoto and H. Matsuoka, “Lifetime of electrochromism of amorphous WO₃-TiO₂ thin films,” *Journal of the Electrochemical Society*, vol. 138, no. 8, pp. 2403–2408, 1991.

Research Article

Sequential Electrodeposition of Platinum-Ruthenium at Boron-Doped Diamond Electrodes for Methanol Oxidation

Ileana González-González,^{1,2} Camille Lorenzo-Medrano,^{1,2} and Carlos R. Cabrera^{1,2}

¹ Department of Chemistry, University of Puerto Rico, Río Piedras Campus, P.O. Box 70377, San Juan, PR 00936-8377, USA

² Center for Advanced Nanoscale Materials, University of Puerto Rico, Río Piedras Campus, P.O. Box 70377, San Juan, PR 00936-8377, USA

Correspondence should be addressed to Carlos R. Cabrera, carlos.cabrera2@upr.edu

Received 5 April 2011; Revised 11 July 2011; Accepted 18 July 2011

Academic Editor: Milan M. Jaksic

Copyright © 2011 Ileana González-González et al. This is an open access article distributed under the Creative Commons Attribution License, which permits unrestricted use, distribution, and reproduction in any medium, provided the original work is properly cited.

Sequential electrodeposition of Pt and Ru on boron-doped diamond (BDD) films, in 0.5 M H₂SO₄ by cyclic voltammetry, has been prepared. The potential cycling, in the aqueous solutions of the respective metals, was between 0.00 and 1.00 V versus Ag/AgCl. The catalyst composites, Pt and PtRu, deposited on BDD film substrates, were tested for methanol oxidation. The modified diamond surfaces were also characterized by scanning electron microscopy-X-ray fluorescence-energy dispersive spectroscopy, X-ray photoelectron spectroscopy, and Auger electron spectroscopy. The scanning Auger electron spectroscopy mapping showed the ruthenium signal only in areas where platinum was electrodeposited. Ruthenium does not deposit on the oxidized diamond surface of the boron-doped diamond. Particles with 5–10% of ruthenium with respect to platinum exhibited better performance for methanol oxidation in terms of methanol oxidation peak current and chronoamperometric current stability. The electrogenerated •OH radicals on BDD may interact with Pt surface, participating in the methanol oxidation as shown in oxidation current and the shift in the peak position. The conductive diamond surface is a good candidate as the support for the platinum electrocatalyst, because it ensures catalytic activity, which compares with the used carbon, and higher stability under severe anodic and cathodic conditions.

1. Introduction

The direct methanol fuel cells (DMFC) are electrochemical cells that convert chemical energy in electrical energy that can be used to power all kinds of appliances. Similar to polymer electrolyte membrane fuel cells (PEMFCs), in the DMFC the anode catalyst draws the hydrogen from the methanol, and both systems use a solid electrolyte, reducing the corrosion of the device and improving the power density. Various catalytic composite systems have been studied, including PtRuOsIr [1], PtRuOs [2], PtMo [3, 4], and PtRu [5, 6]. Electrodes with catalyst nanoparticles have been found to have highly catalytic performance, and the catalytic activity was found to depend on the particle size, the nature of the support, as well as the preparation method [7].

One of the subjects of research on high-efficiency fuel cells is how to minimize the electrocatalytic noble metal loading without losing the high catalytic activity. This is achieved

by dispersing nanoparticles of the catalytic materials (mainly Pt-based alloys) on high surface area materials used as supports. The supports need to, in addition to having high surface, be stable and conductive. The most commonly used particle support is carbon blacks, these undergo irreversible oxidation at positive potentials, and this is a challenge particularly on the oxygen reduction electrode where they undergo high positive potentials (0.7–1.0 versus NHE), but it can occur in the anode during fuel starvation [8–10]. When the carbon blacks support oxidizes their resistance increases, the electrocatalytic particles become loose, and they lose a high number of reaction sites due to agglomeration [10–14]. The development of advanced support materials that are stable at high potentials, low pH, and relatively elevated temperatures is still the subject of much study [15]. Diamond, carbon nanotubes [16], nanoporous supports and highly ordered carbon materials have been studied in order to improve the stability of the electrodes of the cell.

Boron-doped diamond (BDD) films exhibit very high chemical and electrochemical stability. The potential range in which high stability exists is greater than 2.5 V, much greater than conventional carbon-based electrode materials such as glassy carbon and carbon blacks. BDD films exhibit very high stability to vigorous chemical and electrochemical treatments [11, 17]. Diamond films prepared by chemical vapor-deposition have been employed in numerous applications due to their unique characteristics. Various studies on metal particle deposition on BDD have been carried out to examine the catalytic properties of the films [18, 19]. This excellent stability provides a rationale for the use of diamond as a support for metal nanoparticles, because various modified surfaces can be confidently used to enhance the bonding to these nanoparticles.

In the present work, we have used the polished boron-doped microcrystalline diamond film as a model system, in order to study the deposition of noble metal electrocatalysts and to characterize their morphology and electrocatalytic behavior on the diamond surface. As a first step, we have characterized typical BDD films and then have sequentially electrodeposited platinum and ruthenium particles on the surface. The PtRu modified electrodes were used for methanol oxidation.

2. Methodology

2.1. Boron-Doped Diamond Film. BDD films were bought from Element Six, the specifications given by the manufacturer were 10 mm × 10 mm × 1 mm thickness, polished surface finish grown by chemical vapor deposition with a resistivity 0.038–0.105 Ω-cm, and a doping level of [B] > 10²⁰ cm⁻³. Each diamond film was cleaned by using a solution of aqua-regia, followed by cycling from -0.8 V to +1.6 versus Ag/AgCl in sulfuric acid 0.5 M, and tested as clean sample of boron-doped diamond.

2.2. Electrochemistry and Platinum-Ruthenium Electrodeposition. All the experiments were performed in an in-house designed electrochemical cell. The boron-doped diamond (BDD) films were used as working electrodes, Ag/AgCl as reference electrode, and a Pt wire as counter electrode, respectively. Sulfuric acid optima (95–98%, Fisher) was used to prepare a 0.5 M aqueous solution as electrolyte. All the electrochemical measurements were performed using a PARSTAT 2273 potentiostat.

Potassium hexachloroplatinate (IV; 98%, Sigma-Aldrich) and ruthenium (III) chloride (45–55%, Sigma-Aldrich), dissolved in 0.5 M H₂SO₄, were used as metal precursors for the sequential electrodeposition of Pt:Ru. Pt deposition was carried out using K₂PtCl₆ 1 mM cycling between -0.2 V and 1.0 V versus Ag/AgCl at a scan rate of 500 mVs⁻¹. Then the sample was cleaned using cyclic voltammetry between -0.2 V and 1.2 V versus Ag/AgCl at a scan rate of 500 mVs⁻¹ in H₂SO₄ 0.5 M until the voltammogram of polycrystalline platinum was perfectly reproduced. For the Ru sequential deposition, four different concentrations were used 1 mM, 0.5 mM, 0.1 mM, and 0.05 mM of RuCl₃.

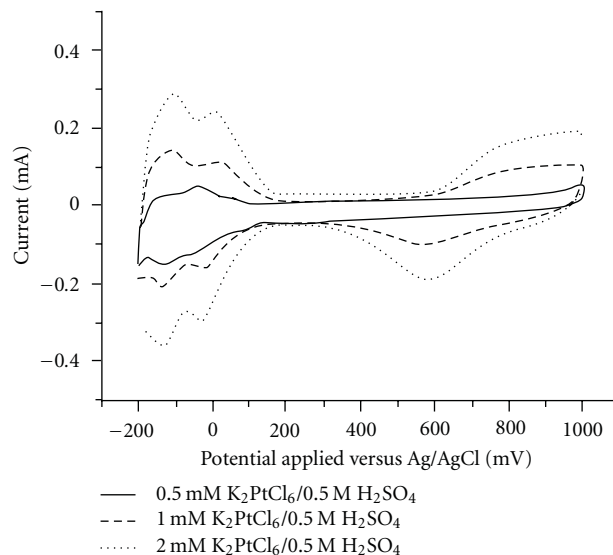


FIGURE 1: Cyclic voltammogram of Pt-BDD films at 50 V/s in a N₂ sparged 0.5 M H₂SO₄ solution. Pt particles deposited by cyclic voltammetry -0.2 V and 1.0 V versus Ag/AgCl at Pt 500 mVs⁻¹ for (a) 0.5, (b) 1.0, and (c) 2.0, x mM K₂PtCl₆.

All the electrodepositions were carried out by cycling the potential between -0.2 V and 0.8 V versus Ag/AgCl at a scan rate of 500 mVs⁻¹. Finally, methanol (99%, Sigma-Aldrich) 1 M in H₂SO₄ 0.5 M was oxidized between -0.2 V and 0.8 V versus Ag/AgCl at a scan rate 50 mVs⁻¹. Chronoamperometry measurements were performed at 0.35 V versus Ag/AgCl. All electrochemical measurements were done at room temperature.

2.3. Particle Characterization. The various electrodeposited catalysts were characterized by scanning electron microscopy-X-ray energy-dispersive analysis (SEM/EDS), X-ray diffraction, and cyclic voltammetry. For the SEM micrographs a JEOL 5800LV microscope was used at 15 kV. Platinum particle size distribution measurements were performed using the UTHSCSA Image Tool program [20], in which the SEM images were imported and the sizes of the white pixels were measured. This was done in the manual mode to avoid incorrect identification of the particles.

X-ray diffraction analyses were performed using a SIEMENS D5000 X-ray diffractometer using a Cu K α polychromatic X-ray source. The Raman spectra were obtained with an ISA-JY T64000 spectrometer. The measurements were performed in the backscattering configuration on a spot of about 3 mm in diameter illuminated with an Ar⁺ laser (514.5 nm, 10-mW).

The XPS analysis data was obtained using a PHI 5600ci spectrometer with an Al K α X-ray source at 15 kV and 350 W. Binding energies were corrected to the C1s sp³ signal at 284.5 eV [21]. Auger electron spectroscopy measurements were done in a Perking Elmer PHI 660 Scanning Auger Multiprobe at 10 keV.

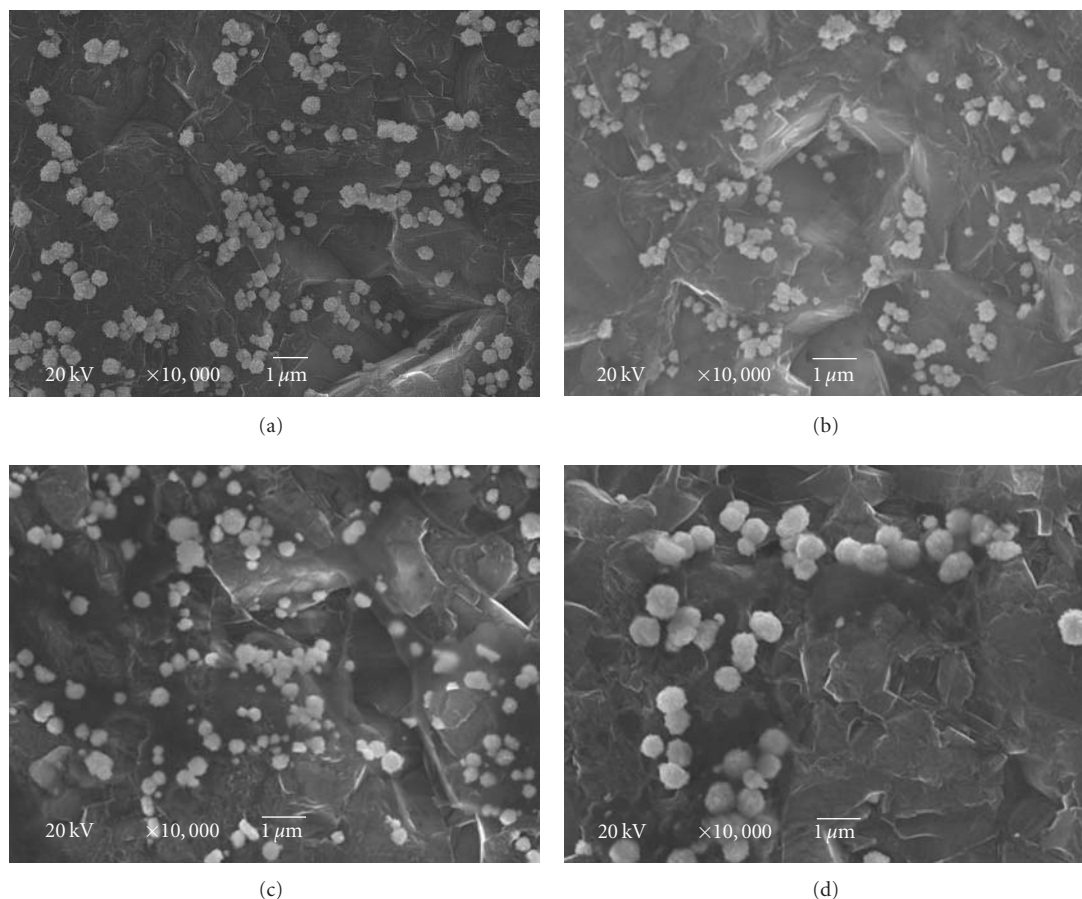


FIGURE 2: SEM images of Pt-Ru sequential deposition on BDD films obtained at 20 kV and magnification of 10,000x, by cyclic voltammetry, between -0.2 V and 1.0 V versus Ag/AgCl for Pt and -0.2 V and 0.8 V versus Ag/AgCl for Ru at sweep rate 500 mVs^{-1} for (a) 1 : 1, (b) 1 : 0.5, (c) 1 : 0.1, and (d) 1 : 0.05, $1 \text{ mM K}_2\text{PtCl}_6$ and $x \text{ mM RuCl}_3$ solution.

3. Results and Discussion

3.1. Boron-Doped Diamond Film Characterization. The BDD films used were of high quality, including predominantly (111-) type and (100-) type grains and facets, as confirmed by X-ray diffraction analysis, which has a peak pattern characteristic for diamond crystals. The first peak, appeared at 44.1° , due to (111) plane, and a second peak, at 75.3° , was characteristic of the (220) plane. The (220) peak were more intense than the (111) peak; this is because the growth process occurred preferentially in the (220) plane. The third peak, at 91.6° , was assigned to the (311) plane.

As a standard characterization of the BDD films bought, Raman spectral analysis was done. From the Raman spectra, the peak at 1332 cm^{-1} confirmed the presence of sp^3 carbons, as expected for diamond materials. A small broad peak in the 1598 cm^{-1} region indicated the presence of sp^2 carbon impurities. The films were of good quality, although sp^2 carbon contamination was present, the width of the 1332 cm^{-1} full width at half-maximum diamond line was $4.7\text{--}7.1 \text{ cm}^{-1}$, compared with 2.6 cm^{-1} and 10.5 cm^{-1} for crystals with best and poorest crystallinity, respectively [22]. The broad peak of the 500 cm^{-1} was used to calculate the

boron concentration using the maximum of the Lorentzian component, $5.6 \times 10^{19}\text{--}3.0 \times 10^{20} \text{ B cm}^{-3}$ in diamond [23].

The cyclic voltammetry measured in $0.5 \text{ M H}_2\text{SO}_4$ showed a wide potential range in which there was relatively small background current, close to 3 V . This contrasts with gold, platinum, glassy carbon, and other commonly used electrodes and is due to the lack of catalytic activity for the hydrogen and oxygen electrolytic gas generation reactions, together with the slow tendency to undergo electrochemically induced surface oxidation [24].

3.2. Platinum Particle Deposition

3.2.1. Particle Analysis. Platinum electrodeposition was carried out by sweeping the potential back and forth (cyclic voltammetry) between -0.2 and 1.0 V in a $\text{K}_2\text{PtCl}_6/0.5 \text{ M H}_2\text{SO}_4$ solution at 500 mV/s , where the platinum concentration was varied from 0.5 mM to 2.0 mM . The particles were observed by scanning electron microscopy (SEM), and their elemental composition was verified by X-ray fluorescence-energy dispersive spectroscopy (EDS; not shown). The average size of the Pt particles was approximately $574 \text{ nm} \pm 200 \text{ nm}$,

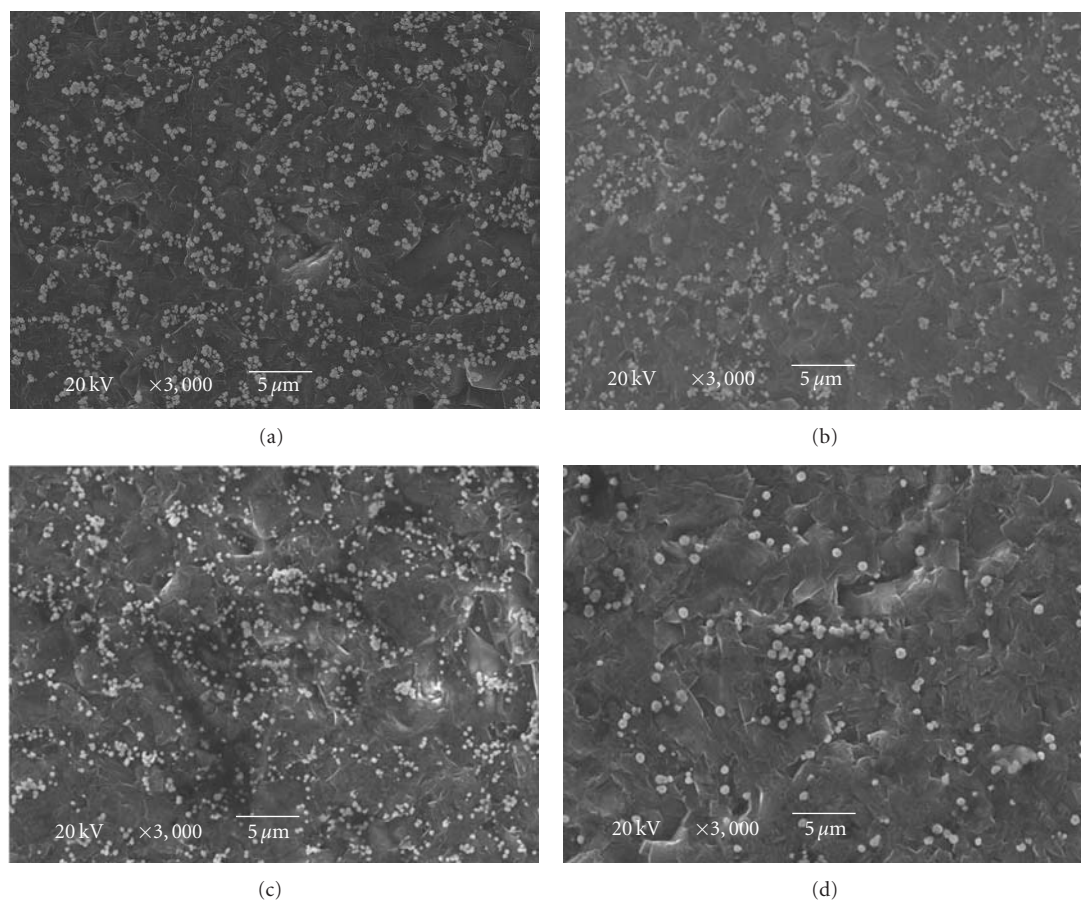


FIGURE 3: Scanning electron microscopy (SEM) images of Pt-Ru sequential deposition on BDD films obtained at 20 kV and magnification of 3,000x, by cyclic voltammetry, between -0.2 V and 1.0 V versus Ag/AgCl for Pt and -0.2 V and 0.8 V versus Ag/AgCl for Ru at sweep rate 500 mVs^{-1} for (a) 1:1, (b) 1:0.5, (c) 1:0.1, and (d) 1:0.05, $1 \text{ mM K}_2\text{PtCl}_6$ and $x \text{ mM RuCl}_3$ solution.

the size of the platinum particles did not change with the platinum solution concentration used during the deposition voltammetry. The particle density was approximately 1.01×10^7 , 1.25×10^7 , and 4.27×10^7 particles- cm^{-2} for 0.5 mM , 1.0 mM , and 2.0 mM , respectively. This value compares with the values obtained by Enea et al. in the $200\text{--}800 \text{ nm}$ range [25], those of Montilla et al. in the 150 to 700 nm range [26] and with those obtained by Bennett et al. prepared by galvanostatic deposition ($20\text{--}45 \text{ nm}$, depending on the type of diamond film) [27], for example, $46 \pm 27 \text{ nm}$ diameter and 1.1×10^9 particles- cm^{-2} .

3.2.2. Electrochemical Characterization. Figure 1 shows the typical cyclic voltammogram for the platinum particles deposited on the boron diamond surface for all the concentrations. Cyclic voltammograms of the platinum particle-decorated BDD film were obtained after cleaning cycles were completed, it showed the characteristic current features for platinum, hydrogen adsorption and desorption (100 to -250 mV), Pt oxide formation ($700\text{--}1000 \text{ mV}$), and Pt oxide reduction (550 mV) [28]. The electrochemically active surface area of the electrode was estimated by integrating the anodic current peak for hydrogen desorption obtained

during the forward sweep (-0.2 V to 0.1 V versus Ag/AgCl) [29]. As shown in Figure 2, the surface area of the platinum particles increases with higher concentration solution used during the depositions cycles; this is because of higher particle distribution, as the particle size remains very close for all the samples. As the concentration of the platinum solution increases the amount of particles formed increases. This tells us that, as expected, the nucleation of a new particle is easier with the proximity of the specie to be reduced to the surface to be modified. For the Pt particles deposited onto bare BDD surface, the Pt seeds firstly appeared and after that grew into large Pt particles. In such cases, the growth process dominates, and finally smaller particles could be formed. These particles that we believed are formed could not be observed in our SEM facilities. Cycle voltammetric analysis for methanol oxidation of the Pt decorated boron-doped diamond films exhibited the characteristic features of methanol oxidation on pure platinum.

3.3. Sequential Platinum-Ruthenium Particle Deposition

3.3.1. Particle Analysis. Platinum and ruthenium were electrochemically deposited sequentially by means of cyclic

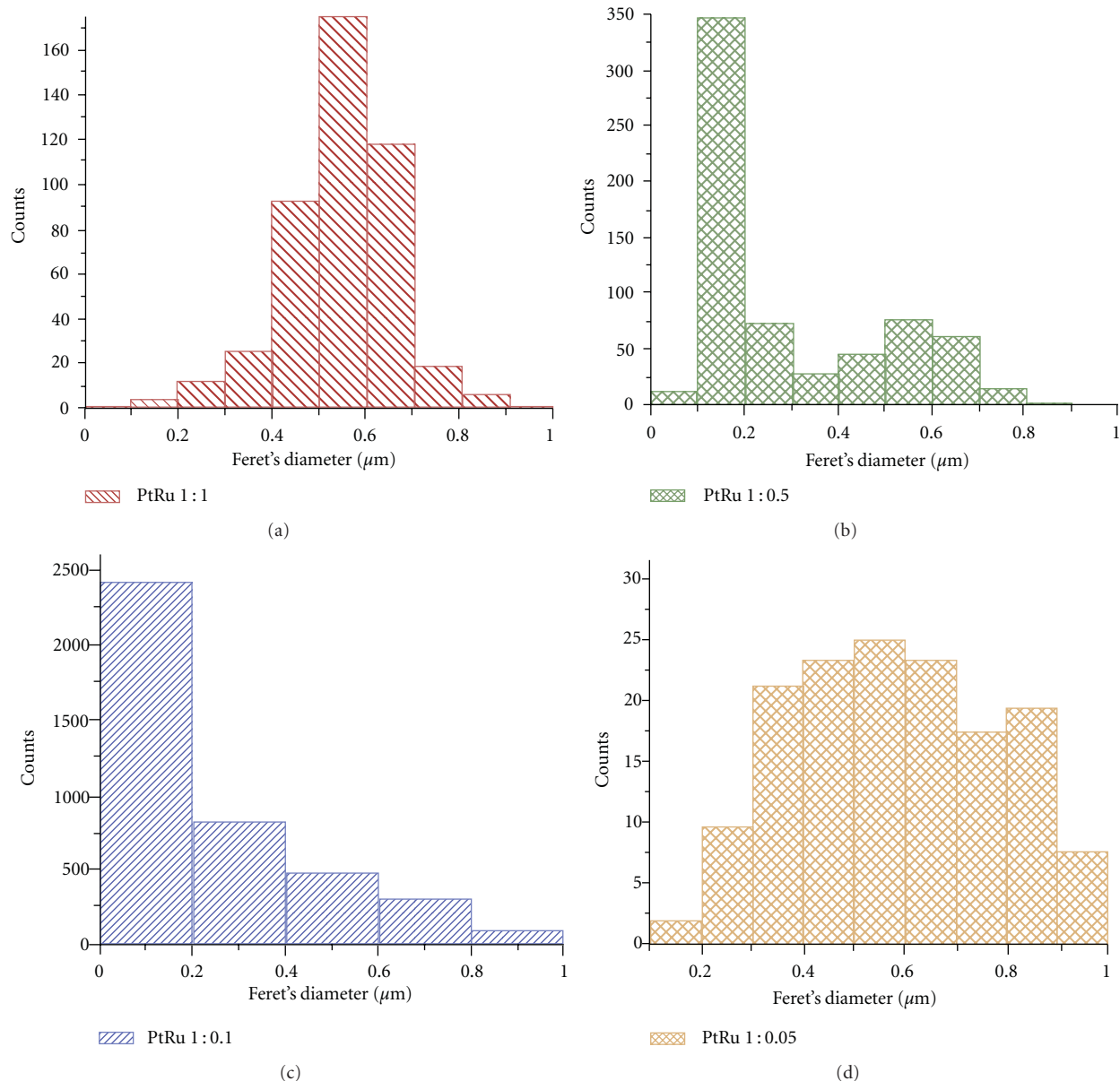


FIGURE 4: Histogram for particle size analysis of Pt-Ru sequential deposition on boron-doped diamond electrodes obtained at 20 kV and magnification of 3,000x, by cyclic voltammetry, between -0.2 V and 1.0 V versus Ag/AgCl for Pt and -0.2 V and 0.8 V versus Ag/AgCl for Ru at sweep rate 500 mVs^{-1} for (a) 1:1, (b) 1:0.5, (c) 1:0.1, and (d) 1:0.05, $1 \text{ mM K}_2\text{PtCl}_6$ and $x \text{ mM RuCl}_3$ solution.

voltammetry, potential sweep between 0.2 and 1.0 V at 50 mVs in $1 \text{ mM K}_2\text{PtCl}_6/0.5 \text{ M H}_2\text{SO}_4$ and $0.05, 0.1, 0.5,$ and $1 \text{ mM RuCl}_3/0.5 \text{ M H}_2\text{SO}_4$ solutions. The particles were observed by SEM, EDS, and Auger electron spectroscopy were used to verify their composition.

The range particle size was approximately 100 – 800 nm for Pt-Ru with particle density of (a) $2.32 \times 10^8 \text{ particles/cm}^2$, (b) $2.02 \times 10^8 \text{ particles/cm}^2$, (c) $1.86 \times 10^8 \text{ particles/cm}^2$ and (d) $5.12 \times 10^7 \text{ particles/cm}^2$. The particles were distributed in a nonhomogenous way throughout the surface of the diamond film, as can be seen in Figures 2 and 3 for all the samples. We see in the micrographs the agglomeration of particles for all the depositions, contrasting

with the results of Montilla et al. [26] and Bennett et al. [27]. We believe this nonhomogenous distribution of the particles is due to the heterogeneous conductivity of diamond films that have been previously observed on doping levels of 10^{20} B/cm^3 and below [30]. Histograms for the particle size distribution are shown in Figure 4, modal sizes are 525 nm , 150 nm , 125 nm , and 625 nm , for deposition done using solutions $0.05, 0.1, 0.5,$ and $1 \text{ mM RuCl}_3/0.5 \text{ M H}_2\text{SO}_4$, respectively.

The chemical composition of the particles was verified with several techniques. Auger spectroscopy and EDS verified the elemental composition of the PtRu particles decorated boron-doped diamond films.

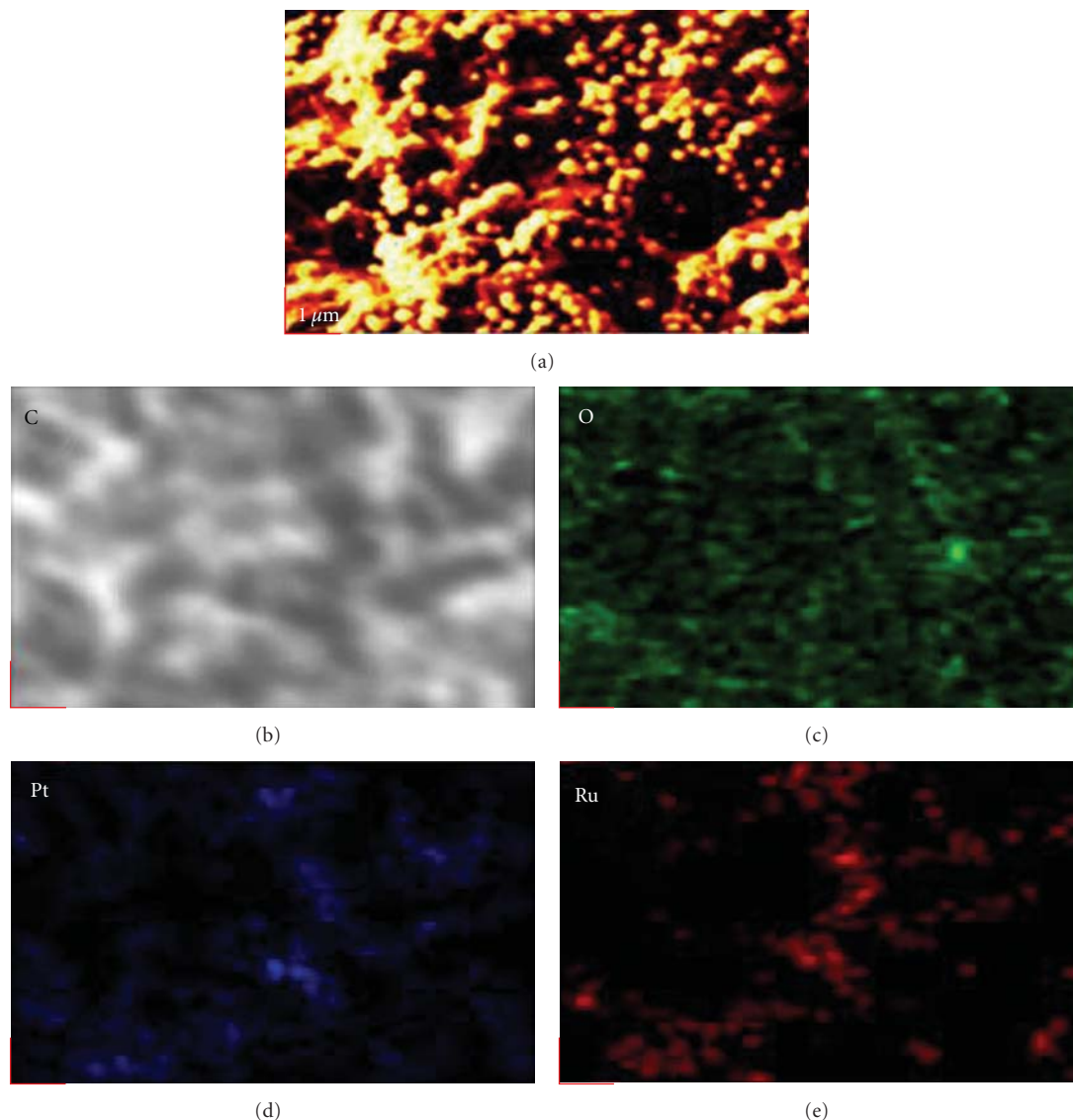


FIGURE 5: Scanning electron microscopy and scanning Auger electron spectroscopy mapping images for the C KLL, O KLL, Pt MNN, and Ru LMM on Pt-Ru particle deposited sequentially on BDD films using 1.0 mM K_2PtCl_6 and 1.0 mM $RuCl_3$ solution.

Figure 5 shows the SEM and Auger electron spectroscopy mapping for signals of the elements: carbon, oxygen, platinum, and ruthenium. Oxygen mapping shows that it is present in the entire surface, boron-doped diamond films surface is oxidized due to the cleaning process and pretreatment done to the films when received. The platinum mapping shows where the platinum particles are deposited on the surface, and the ruthenium signal is only detected in areas where platinum is deposited. Ruthenium, as previously published for other carbon supports, was not deposited on the oxidized diamond surface of the boron-doped diamond [6].

Further chemical characterization was done by high-resolution XPS spectra for the binding energy regions of C 1s, O 1s, Pt 4f, and Ru 3p (Figures 6 and 7). The C1s region has been fitted to three binding energy peaks: one main peak

at 284.5 eV and two additional peaks +1.0 eV and +3.7 eV higher binding energies. The peak at +1.0 eV, attributed to C–O, is correlated [31, 32] to C–OH from (111) facets and C–O–C from (110) facets. The peak +3.7 eV can be attributed to C=O from the (110) facet [33]. Oxygen 1s region shows two main peaks, one attributable to C–O interaction and the second to metal oxides, from both metals, Pt and Ru.

The high-resolution X-ray photoelectron spectrum shows the binding energy peak of Pt^0 4f_{5/2} and Pt^0 4f_{7/2}, and with an increase of +1.2 eV in the binding energy, the signal for platinum dioxide which consist of 20% relative to the Pt^0 signal. Ruthenium 3p_{1/2} region shows two main peaks, ruthenium in its reduced form and ruthenium oxide.

3.3.2. Electrochemical Characterization. The catalytic activity of the electrodeposited metal particles was tested by cyclic

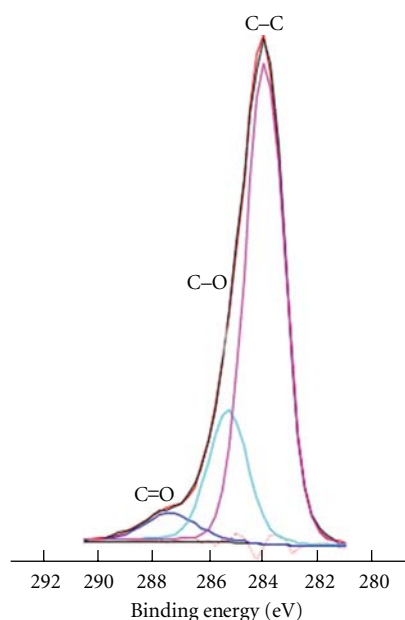
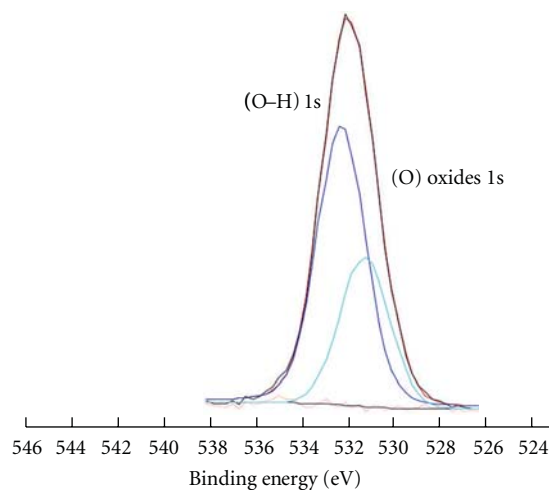


FIGURE 6: High-resolutions X-ray photoelectron spectra of the Pt particle decorated boron-doped diamond film. C 1s binding energy region.

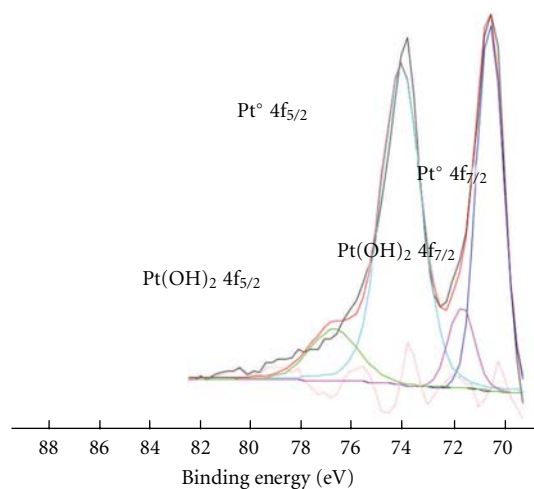
voltammetry (see Figure 8(a)). All the cyclic voltammograms for the electrooxidation of 1 M CH_3OH in 0.5 H_2SO_4 were performed between -0.2 V and 0.8 V versus Ag/AgCl at a sweep rate of 50 mVs^{-1} . The maximum current densities for methanol oxidation were in the range of 190 – 101 mA/cm^2 and 176 – 78 mA/cm^2 , for the Pt-Ru particles deposited on diamond. These results were obtained after the peak currents stabilized after several potential cycles. Thereafter, the peak currents were stable, at least up to 25 total cycles, with no significant loss in activity; only during the first reverse scan we observed smaller currents.

Of greater importance, however, for the fuel cell catalysis is the potential range in which significant anodic current begins to be observed, that is, the oxidation onset potential. Although an arbitrary criterion must be established for this, for example, a given minimum current density, if we take a value of 10 mA/cm^2 , the onset potentials were in the range of 332 – 369 mV versus Ag/AgCl, for Pt-Ru particles deposited on diamond film surface [34]. The fact that Pt-Ru exhibited a lower onset than Pt is certainly expected on the basis of previous literature [5, 35, 36].

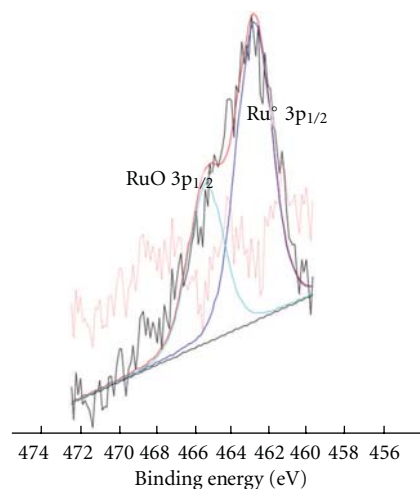
As observed in Figure 8, the reverse current peaks for the oxidation from the platinum surfaces does not correspond to the half the current of the methanol oxidation peak, this observation is consistent with Siné and Chomninellis [37]. This behavior can be explained by the fact that electrogenerated hydroxyl radicals HO^\bullet that are generated on the boron-doped diamond surface at lower pH electrolytes [38] interact with Pt surface and the organic compounds. Depending on the potential applied this specie can intervene on the oxidation of organic compounds. In the region of water stability, the oxidation of methanol would occur only involving direct electron transfer. Methanol oxidation can



(a)



(b)



(c)

FIGURE 7: High-resolutions X ray photoelectron spectra of the Pt particle decorated boron-doped diamond film. (b) Pt 4f region (c) Ru $3p_{1/2}$ energy region (a) O 1s region.

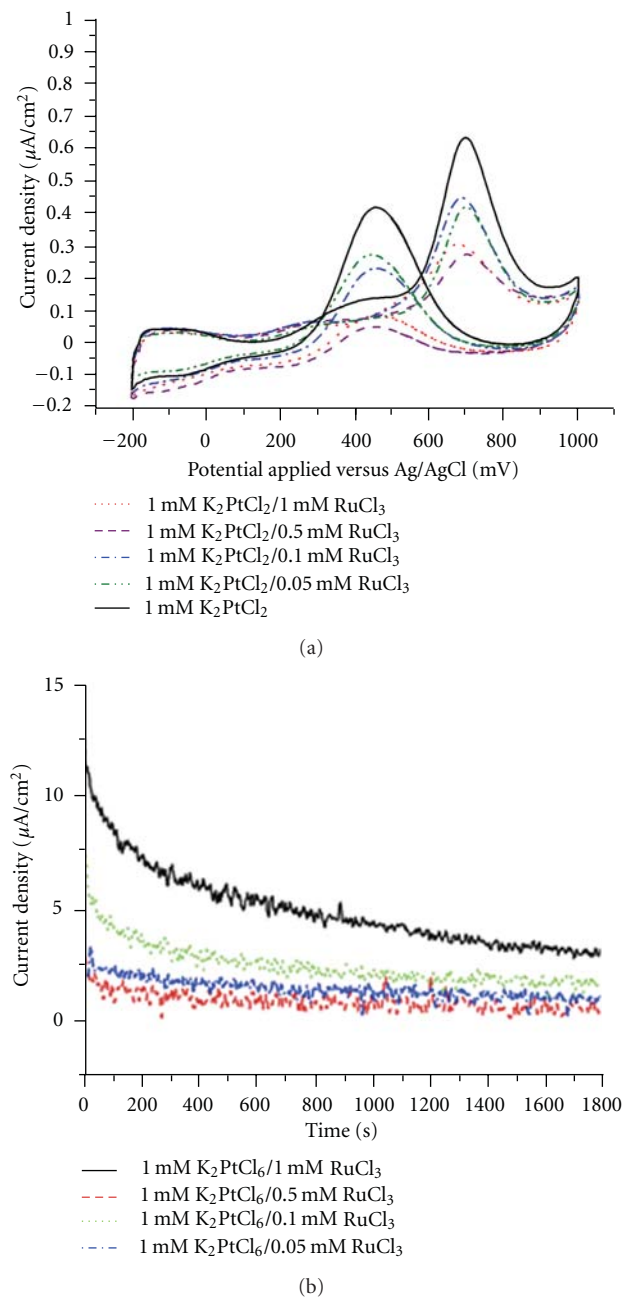


FIGURE 8: Cyclic voltammetry on 0.5 M $\text{CH}_3\text{OH}/0.5$ M H_2SO_4 Pt particles deposited on boron-doped diamond films by cyclic voltammetry. (a) Chronoamperometry at 350 mV versus Ag/AgCl at 24°C of Pt particles deposited on boron-doped diamond films by cyclic voltammetry on 0.5 M $\text{CH}_3\text{OH}/0.5$ M H_2SO_4 (b).

also occur by indirect oxidation, caused by a sequence of chemical and electrochemical steps initiated by the hydroxyl radicals [39].

Also the oxidized surface of diamond that possesses hydroxy ($-\text{OH}$) groups may be involved on the water activation on the platinum surface. Desai and Neurock showed that the presence of surface hydroxyl groups adsorbed to Ru can induce water to adsorb and activate at neighboring Pt

sites [40]. This water activation could also be enhanced on the oxidized diamond surface (111).

Chronoamperometry was performed at 0.350 V versus Ag/AgCl for all the electrodeposited particles for 1800 s, Figures 8(b) and 9. The samples with greater current loss were the ones without ruthenium, as expected, because of the carbon monoxide poisoning of the platinum surface. For the platinum-ruthenium particles the particles with better current stability were the ones with small quantities of ruthenium. It appears that in particles with greater amounts of 20% of ruthenium sequentially deposited the ruthenium covers the platinum and the catalytic property of the particle is lost. Lesser positive methanol oxidation onsets were obtained for samples deposited with 0.1 and 1 mM $\text{RuCl}_3/0.5$ M H_2SO_4 , but in terms of current density stability the sample prepared with 0.1 mM $\text{RuCl}_3/0.5$ M H_2SO_4 had better performance, which is the equivalent to 10% Ru; 90% Pt. Current density for Ru 1 mM in series 2 (\bullet) was taken out of consideration by the q -test with 99% confidence level that is it an outlier.

It is accepted that PtRu is the most promising bimetallic catalyst for methanol oxidation. Its superior activity has been observed for different PtRu materials, such as alloys, codeposits, sequential electrodeposits, and Ru adsorbed on Pt-single-crystal and on Pt carbon-supported electrodes. We have seen that the potential cycling technique yields results that are similar to those of the pulsed galvanostatic technique for platinum itself. For platinum-ruthenium, it is expected that further improvements can be made in reaching higher dispersion, although it has been reported that the dispersion of particles on diamond films is low [41].

4. Conclusion

In this work we have examined the possibility of the use of boron-doped diamond as the support for electrocatalyst particles in a fuel cell. The electrochemical behavior of oxidized boron-doped diamond (BDD) films in 0.5 M H_2SO_4 using cyclic voltammetry showed a very wide electrochemical window. Platinum particles deposited a different platinum concentrations did not show a different particle size; although it did show a difference in the particle distribution. Pt and Pt-Ru particles were deposited on BDD film substrate; the modified diamond surfaces were also characterized by SEM/EDS, XPS, and Auger. High-resolution XPS peak fitting showed that the BDD films were oxidized with C–O, C–OH, and C–O–C. Auger electron spectroscopy mapping showed that a complete oxidized surface of diamond and that ruthenium does not deposit on the oxidized diamond surface of the boron-doped diamond. Particles with 5–10% of ruthenium with respect to platinum exhibited better performance for methanol oxidation in terms of methanol oxidation peak current and current stability. Particles with greater amounts of 20% of ruthenium sequentially deposited the ruthenium covers the platinum, and the catalytic property of the particle is lost. In the case of cyclic voltammogram for methanol oxidation, a current for the reverse peak is higher than what it is usually observed on carbon supports, a possible explanation is that the electrogenerated hydroxyl

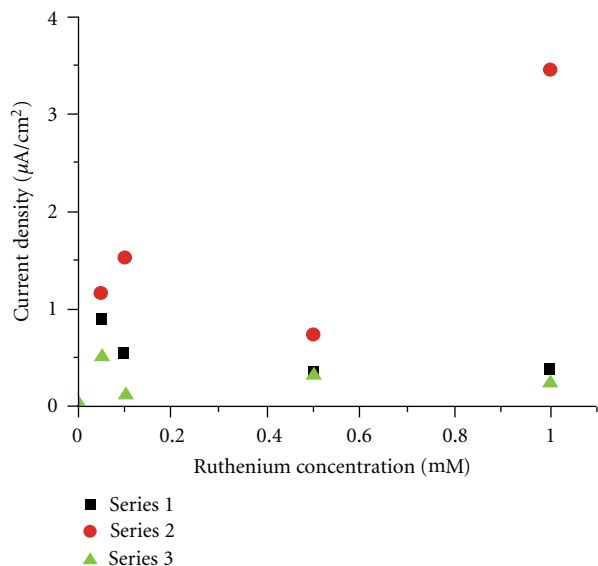


FIGURE 9: Current at the final point of the chronoamperometry at 350 mV versus Ag/AgCl at 24°C of Pt particles deposited on boron-doped diamond films.

radical on BDD may interact with Pt surface, participating in the methanol oxidation as showed in the oxidation current and the shift in the peak position.

Acknowledgments

This paper was supported in part by NASA Grant no. NASA-NNX08BA48A. I. González-González and C. Lorenzo-Medrano gratefully acknowledge support from Center for Advanced Nanoscale Materials and Research Initiative Scientific Enhancement. The authors also thank the UPR Materials Characterization Center for all their help with the surface characterization measurements.

References

- [1] E. Reddington, A. Sapienza, B. Gurau et al., "Combinatorial electrochemistry: a highly parallel, optical screening method for discovery of better electrocatalysts," *Science*, vol. 280, no. 5370, pp. 1735–1737, 1998.
- [2] L. Kevin, R. Liu, C. Pu et al., "Methanol oxidation on single-phase Pt-Ru-Os ternary alloys," *Journal of the Electrochemical Society*, vol. 144, no. 5, pp. 1543–1548, 1997.
- [3] H. Zhang, Y. Wang, E. R. Fachini, and C. R. Cabrera, "Electrochemically codeposited platinum/molybdenum oxide electrode for catalytic oxidation of methanol in acid solution," *Electrochemical and Solid-State Letters*, vol. 2, no. 9, pp. 437–439, 1999.
- [4] S. Mukerjee, S. J. Lee, E. A. Ticianelli et al., "Investigation of enhanced CO tolerance in proton exchange membrane fuel cells by carbon supported PtMo alloy catalyst," *Electrochemical and Solid-State Letters*, vol. 2, no. 1, pp. 12–15, 1999.
- [5] W. F. Lin, M. S. Zei, M. Eiswirth, G. Ertl, T. Iwasita, and W. Vielstich, "Electrocatalytic activity of Ru-modified Pt(111) electrodes toward CO oxidation," *Journal of Physical Chemistry B*, vol. 103, no. 33, pp. 6968–6977, 1999.
- [6] W. Chrzanowski, H. Kim, and A. Wieckowski, "Enhancement in methanol oxidation by spontaneously deposited ruthenium on low-index platinum electrodes," *Catalysis Letters*, vol. 50, pp. 69–75, 1998.
- [7] Y. Takasu, T. Kawaguchi, W. Sugimoto, and Y. Murakami, "Effects of the surface area of carbon support on the characteristics of highly-dispersed Pt-Ru particles as catalysts for methanol oxidation," *Electrochimica Acta*, vol. 48, no. 25-26, pp. 3861–3868, 2003.
- [8] D. Shanna, K. Knights, M. Colbow, J. St-Pierre, and D. Wilkinson, "Aging mechanisms and lifetime of PEMFC and DMFC," *Journal of Power Sources*, vol. 127, no. 1-2, pp. 127–134, 2004.
- [9] J. Wang and G. M. Swain, "Dimensionally stable Pt/diamond composite electrodes in concentrated H₃PO₄ at high temperature," *Electrochemical and Solid-State Letters*, vol. 5, no. 2, pp. E4–E7, 2002.
- [10] M. Hupert, A. Muck, J. Wang et al., "Conductive diamond thin-films in electrochemistry," *Diamond and Related Materials*, vol. 12, no. 10-11, pp. 1940–1949, 2003.
- [11] C. H. Paik, T. D. Jarvi, and W. E. O'Grady, "Extent of PEMFC cathode surface oxidation by oxygen and water measured by CV," *Electrochemical and Solid-State Letters*, vol. 7, no. 4, pp. A82–A84, 2004.
- [12] K. H. Kangasniemi, D. A. Condit, and T. D. Jarvi, "Characterization of vulcan electrochemically oxidized under simulated PEM fuel cell conditions," *Journal of the Electrochemical Society*, vol. 151, no. 4, pp. E125–E132, 2004.
- [13] J. Wang, G. M. Swain, T. Tachibana, and K. Kobashi, "Incorporation of Pt particles in boron-doped diamond thin films. Applications in electrocatalysis," *Electrochemical and Solid-State Letters*, vol. 3, no. 6, pp. 286–289, 2000.
- [14] E. Antolinia, J. R. C. Salgado, R. M. da Silva, and E. R. Gonzalez, "Preparation of carbon supported binary Pt-M alloy catalysts (M = first row transition metals) by low/medium temperature method," *Materials Chemistry and Physics*, vol. 101, no. 2-3, pp. 395–403, 2007.
- [15] H. X. Huang, S. X. Chen, and C. Yuan, "Platinum nanoparticles supported on activated carbon fiber as catalyst for methanol oxidation," *Journal of Power Sources*, vol. 175, no. 1, pp. 166–174, 2008.
- [16] G. Che, B. B. Lakshmi, E. R. Fisher, and C. R. Martin, "Carbon nanotubule membranes for electrochemical energy storage and production," *Nature*, vol. 393, no. 6683, pp. 346–349, 1998.
- [17] Y. V. Pleskov, Y. E. Evstefeeva, M. D. Krotova et al., "Effect of crystal structure on the electrochemical behaviour of synthetic semiconductor diamond: comparison of growth and a nucleation surfaces of a coarse-grained polycrystalline film," *Journal of Applied Electrochemistry*, vol. 33, no. 10, pp. 909–915, 2003.
- [18] J. S. Gao, T. Arunagiri, J. J. Chen, P. Goodwill, and O. Chyan, "Preparation and characterization of metal nanoparticles on a diamond surface," *Chemistry of Materials*, vol. 12, no. 11, pp. 3495–3500, 2000.
- [19] J. A. Bennett and G. M. Swain, "Investigating the nucleation and growth of electrodeposited Pt on polycrystalline diamond electrodes," *Journal of the Electrochemical Society*, vol. 157, no. 8, pp. F89–F95, 2010.
- [20] Developed at the University of Texas Health Science Center at San Antonio, Tex, USA, and available from internet by anonymous FTP from, <http://ddsdx.uthscsa.edu/dig/>.

- [21] J. F. Moulder, W. F. Stickle, P. E. Sobol, and K. D. Bomben, *Handbook of X-Ray Photoelectron Spectroscopy* Perkin-Elmer Corporation, Perkin Elmer Corporation, Eden Prairie, Minn, USA, 1992.
- [22] A. Fujishima, Y. Einaga, T. Narasinga, and D. A. Tryk, Eds., *Diamond Electrochemistry*, Elsevier, Tokyo, Japan, 2005.
- [23] F. Pruvost, E. Bustarret, and A. Deneuve, "Characteristics of homoepitaxial heavily boron-doped diamond films from their Raman spectra," *Diamond and Related Materials*, vol. 9, no. 3, pp. 295–299, 2000.
- [24] N. Vinokur, B. Miller, Y. Avyigal, and R. Kalish, "Electrochemical behavior of boron-doped diamond electrodes," *Journal of the Electrochemical Society*, vol. 143, no. 10, pp. L238–L240, 1996.
- [25] O. Enea, B. Riedo, and G. Dietler, "AFM study of Pt clusters electrochemically deposited onto Boron-doped diamond films," *Nano Letters*, vol. 2, no. 3, pp. 241–244, 2002.
- [26] F. Montilla, E. Morallon, I. Duo, C. Comninellis, and J. L. Vazquez, "Platinum particles deposited on synthetic boron-doped diamond surfaces. Application to methanol oxidation," *Electrochimica Acta*, vol. 48, no. 25–26, pp. 3891–3897, 2003.
- [27] J. A. Bennett, Y. Show, S. Wang, and G. M. Swain, "Pulsed galvanostatic deposition of Pt particles on microcrystalline and nanocrystalline diamond thin-film electrodes I. Characterization of as-deposited metal/diamond surfaces," *Journal of the Electrochemical Society*, vol. 152, no. 5, pp. E184–E192, 2005.
- [28] R. Pattabiraman, "Electrochemical characterisation of platinum catalysts on carbon supports for fuel cell applications," *Indian Journal of Chemical Technology*, vol. 3, no. 5, pp. 269–273, 1996.
- [29] A. M. Feltham and M. Spiro, "Platinized platinum electrodes," *Chemical Reviews*, vol. 71, no. 2, pp. 177–193, 1971.
- [30] N. Tsubouchi, M. Ogura, H. Kato et al., "p-type doping by B ion implantation into diamond at elevated temperatures," *Diamond and Related Materials*, vol. 15, no. 1, pp. 157–159, 2006.
- [31] P. John, N. Polwart, C. E. Troupe, and J. I. B. Wilson, "The oxidation of diamond: the geometry and stretching frequency of carbonyl on the (100) surface," *Journal of the American Chemical Society*, vol. 125, no. 22, pp. 6600–6601, 2003.
- [32] C. D. Wagner, A. V. Naumkin, A. Kraut-Vass, J. W. Allison, C. J. Powell, and J. R. Rumble, "NIST X-Ray Photoelectron Spectroscopy Database, NIST Standard Reference Database 20," Version 3.4, (web version) U.S. Department of Commerce.
- [33] T. Kondo, K. Honda, D. A. Tryk, and A. Fujishima, "Covalent modification of single-crystal diamond electrode surfaces," *Journal of the Electrochemical Society*, vol. 152, no. 1, pp. E18–E23, 2005.
- [34] I. Gonzalez-Gonzalez, E. R. Fachini, M. A. Scibioh et al., "Facet-selective platinum electrodeposition at free-standing polycrystalline boron-doped diamond films," *Langmuir*, vol. 25, no. 17, pp. 10329–10336, 2009.
- [35] W. Chrzanowski and A. Wieckowski, "Surface structure effects in platinum/ruthenium methanol oxidation electrocatalysis," *Langmuir*, vol. 14, no. 8, pp. 1967–1970, 1998.
- [36] H. A. Gasteiger, N. Marković, P. N. Ross, and E. J. Cairns, "Methanol electrooxidation on well-characterized Pt-Ru alloys," *Journal of Physical Chemistry*, vol. 97, no. 46, pp. 12020–12029, 1993.
- [37] G. Siné and C. Comninellis, "Nafion®-assisted deposition of microemulsion-synthesized platinum nanoparticles on BDD: activation by electrogenerated ·OH radicals," *Electrochimica Acta*, vol. 50, no. 11, pp. 2249–2254, 2005.
- [38] T. A. Enache, A. M. Chiorcea-Paquim, O. Fatibello-Filho, and A. M. Oliveira-Brett, "Hydroxyl radicals electrochemically generated in situ on a boron-doped diamond electrode," *Electrochemistry Communications*, vol. 11, no. 7, pp. 1342–1345, 2009.
- [39] B. Marselli, J. Garcia-Gomez, P. A. Michaud, M. A. Rodrigo, and C. Comninellis, "Electrogeneration of hydroxyl radicals on boron-doped diamond electrodes," *Journal of the Electrochemical Society*, vol. 150, no. 3, pp. D79–D83, 2003.
- [40] S. Desai and M. Neurock, "A first principles analysis of CO oxidation over Pt and Pt 66.7%Ru33.3% (111) surfaces," *Electrochimica Acta*, vol. 48, no. 25–26, pp. 3759–3773, 2003.
- [41] J. A. Bennett, Y. Show, S. Wang, and G. M. Swain, "Preparation and characterization of boron-doped diamond powder—a possible dimensionally stable electrocatalyst support material," *Journal of the Electrochemical Society*, vol. 152, no. 5, pp. B369–B375, 2005.

Review Article

Contrast and Synergy between Electrocatalysis and Heterogeneous Catalysis

Andrzej Wieckowski¹ and Matthew Neurock²

¹Department of Chemistry, University of Illinois at Urbana-Champaign, Urbana, IL 61801, USA

²Departments of Chemical Engineering and Chemistry, University of Virginia, Charlottesville, VA 22904-4741, USA

Correspondence should be addressed to Matthew Neurock, mn4n@virginia.edu

Received 27 May 2011; Accepted 27 July 2011

Academic Editor: Wolfgang Schmickler

Copyright © 2011 A. Wieckowski and M. Neurock. This is an open access article distributed under the Creative Commons Attribution License, which permits unrestricted use, distribution, and reproduction in any medium, provided the original work is properly cited.

The advances in spectroscopy and theory that have occurred over the past two decades begin to provide detailed in situ resolution of the molecular transformations that occur at both gas/metal as well as aqueous/metal interfaces. These advances begin to allow for a more direct comparison of heterogeneous catalysis and electrocatalysis. Such comparisons become important, as many of the current energy conversion strategies involve catalytic and electrocatalytic processes that occur at fluid/solid interfaces and display very similar characteristics. Herein, we compare and contrast a few different catalytic and electrocatalytic systems to elucidate the principles that cross-cut both areas and establish characteristic differences between the two with the hope of advancing both areas.

1. Introduction

Electrocatalysis and heterogeneous catalysis are closely related in that they involve well-controlled sequences of elementary bond-breaking and making processes and share many common mechanistic principles in the transformation of molecules over supported metal and metal oxide catalysts. While there are many areas of synergy between the two, including the materials that are used and the available reaction pathways and mechanisms, there are also well-established differences [1–4]. Heterogeneous catalysis has often celebrated more detailed insights into reaction mechanisms than electrocatalysis due to the advances in spectroscopy and theory of the gas/solid interface as compared to the more complex aqueous/solid interface in electrocatalysis. As such electrocatalysis has often followed from the mechanistic advances derived from gas phase heterogeneous catalysis. Many of the current efforts in heterogeneous catalysis, however, are focused on energy conversion strategies involving catalytic transformations which proceed at the fluid/solid interface and, as a consequence, are now closely following the leads from electrocatalysis. A number of common mechanistic principles and features are beginning to emerge between the two fields. Understanding the synergies as well as

the differences between catalysis and electrocatalysis should thus enable advances in the science and application for both areas. Herein, we compare and contrast some of the fundamental mechanistic constructs as well as the practical applications for electrocatalysis and heterogeneous catalysis. More specifically, we focus on metal catalyzed oxidation processes.

2. General Comparisons between Catalysis and Electrocatalysis

At the macroscopic level, many of the catalytic materials that are used in catalysis and electrocatalysis are very similar in that they involve supported metal particles, where the interaction between the metal and support is critical to catalyst performance as well as catalyst stability. The metal or metal oxide/support interface can result in sites with unique structural or electronic characteristics, novel bifunctional sites, and/or sites that promote proton and electron transfer. The nature and the strength of the bonds between the metal and the support control the stability of these materials and their resilience to harsh reaction environments.

The characterization of the electronic and atomic structure of the metal and the support in both catalysis as well

as electrocatalysis is typically carried out through the use of extended X-ray absorption spectroscopy (XAFS), electron microscopy, X-ray (XPS) and ultraviolet photoelectron spectroscopy (UPS). In addition, many of the most active metals used in electrocatalysis are very often the same as those used in heterogeneous catalysis. For example, Pt and other group VIII metals are known to be very active in the electrocatalytic oxidation of alcohols and the reduction of oxygen in fuel cells, automotive exhaust catalysis and hydrogenolysis, and hydrogenation catalysis in the conversion of petroleum and renewable resources. This is predominantly the result of the well-established Sabatier's Principle which suggests that the metals in middle of the periodic table demonstrate an optimal metal-adsorbate bond strengths necessary to balance surface reaction steps and product desorption steps [5–9].

In addition to similarities, there are well-established differences between traditional gas phase heterogeneous catalysis and electrocatalysis. Perhaps the greatest difference between the two relates to the unique reaction environments in which they are carried out. The gas phase catalytic environment is far less complex than that of the electrified water/metal interface for electrocatalytic systems, thus allowing for more detailed spectroscopic characterization of the working surface intermediates, application of ultrahigh vacuum experiments as well as direct comparisons with theoretical simulations on model surfaces. The presence of solution, ions, charged interfaces, complex surface potentials, and electric fields present in electrocatalytic systems can all act to significantly change the surface chemistry and catalysis that occurs in these environments. These interfaces tend to significantly promote polar reactions and direct heterolytic bond activation steps which would otherwise be unstable and not occur in gas phase catalytic systems. The electrochemical environment, however, is typically much harsher and deleterious to catalyst stability than that found in gas phase catalysis. The dissolution of the metal and the support are thus important concerns for electrocatalytic processes as these steps are enhanced under electrochemical conditions. In addition, the presence of electrolyte often enhances or impedes catalytic kinetics and within certain potential regions can result in poisoning of the surface.

While there are important differences between electrocatalysis and catalysis that result from the presence of solution, counter ions, and electric fields, Nørskov [8–12], Anderson [13–18], and others [1, 6] have been able to model the electrochemical systems by simply carrying out gas phase calculations on well-defined model clusters and surfaces and adding in the critical features that influence the surface chemistry such as local water molecules as well as the influence of potential. This is an important step in that one has the ability to not only understand but begin to tune the reaction chemistry. Understanding the similarities and differences of the molecular transformations that occur at ultrahigh vacuum conditions and electrochemical conditions will undoubtedly drive advances in the development of catalytic and electrocatalytic materials and processes.

In addition to the scientific issues, there are also a number of important technological differences in the “infrastructure” that supports the heterogeneous and electrocatalysis

communities. Most of electrocatalysis appears to be centered around fuel cells and more specifically proton exchange membrane (PEM) fuel cells carry out the oxidation of hydrogen, oxygenates, or hydrocarbon molecules to CO₂ and the reduction oxygen to water [19]. This is in clear contrast to heterogeneous catalysis, which spans a wide and diverse range of different molecules with very rich chemistry and stands behind extensive chemical, automotive, petroleum, and pharmaceutical industries. In addition, there have been significant research and development investments in heterogeneous catalysis from the government as well as industry. Methane reforming, methane combustion, ammonia synthesis NO_x conversion, and Fischer Tropsch synthesis, for example, are very large-scale processes which have no analogue in electrocatalysis. Furthermore, the future directions for PEM fuel cell catalysis is very specific with a strong focused effort on resolving the issues related to durability and maintaining catalytic activity for many years. This is quite different than the shorter lifetimes involved in most heterogeneous catalytic processes with the exception of automotive emission catalysis. In electrocatalysis, catalyst must be able to withstand the harsh operating conditions and operate effectively over the lifetime of the vehicle. Catalyst loss and deactivation tend to be quite severe in electrocatalysis due to the presence of solution, ions, and electric fields which not only lead to catalyst poisoning but also catalyst dissolution. This significantly limits the choice of catalytic materials to specific supported metals/alloys, metal oxides, and other stable inorganic materials such as chalcogenides or carbides. This is a very narrow range of possibilities as compared to what is typically practiced in the gas phase heterogeneous catalysis community. The long term durability, aggressive solution conditions (both high and low pH), as well as the cost tend to prevent other avenues available to gas phase catalysis to be applied in the field of electrocatalysis.

Despite the complexity and the challenges of the electrochemical environment and the differences outlined above, many of the fundamental constructs that govern gas phase catalysis are also integral to electrocatalysis. There have been a number of pioneering developments in spectroscopy, kinetic analyses, theory, and synthesis that have occurred over the past few decades that have clearly shown how traditional concepts from heterogeneous catalysis apply directly to electrocatalysis. This includes the elucidation of nature of the active site, competitive adsorption phenomena, the influence of alloys, promoters and poisons, structure sensitivity, surface oxidation state, particle size effects, and metal support interactions. A schematic representation of the complex metal solution interface that would exist in either the catalytic or electrocatalytic oxidation of glucose over a carbon-supported PtRu alloy cluster is shown in Figure 1. In a review that is now over ten years old, Jarvi and Stuve [20] elegantly described the direct link between some of the fundamental principles that control heterogeneous catalysis and electrocatalysis. This included the specific accounting of active sites, the identification of reaction intermediates in elucidating reaction mechanisms, and the role of poisons and modifiers and their influence on catalytic kinetics and aging. The authors nicely showed that the kinetics for catalysis and

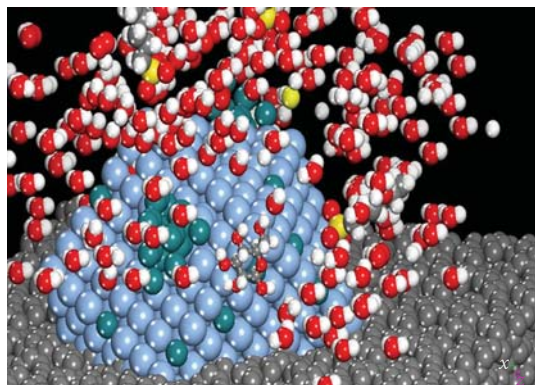


FIGURE 1: Schematic representation of the complex aqueous/metal interface involved in the catalytic and electrocatalytic oxidation of glucose over a PtRu alloy particle supported on carbon in the presence of electrolyte.

electrocatalysis were essentially the same and shared a common framework.

The complexity of the aqueous/metal interface and the inability to spectroscopically resolve molecular intermediates at this interface limited early electrocatalytic studies to measurements of macroscopic kinetics with little understanding of the elementary molecular transformations, the active sites or the influence the atomic and the electronic structure. This put electrocatalysis at a distinct disadvantage over traditional gas phase heterogeneous catalysis. The tremendous breakthroughs that have occurred over the past two decades in the ability to characterize the atomic structure of the working surface and reaction intermediates on the surface within the electrochemical environments have made it possible to begin to discuss elementary mechanisms and the influence of specific structural and composition parameters. Breakthroughs in broad-band spectroscopy [21], in situ electrochemical NMR [22–24], EXAFS [25–29], and surface-enhanced infrared spectroscopy [30, 31] are helping to significantly advance our understanding of electrocatalysis and in some cases begin to rival that in gas phase catalysis. These methods now allow for the direct insights into the nature of the active sites as well as surface intermediates under actual working conditions. Such insight has led to an exponential growth in the literature in the identification of active sites, reaction mechanisms, and rigorous structure-property relationships. Despite these important advances, the molecular resolution of intermediates under working conditions still presents a significant challenge and as such has been limited to only a few different intermediates and systems. In addition, these methods provide information on model systems that lack the complexity of the actual catalytic environment and often provide only a limited understanding.

In addition to these advances in spectroscopy, the past two decades have witnessed exponential increases in computational power and tremendous advances in theory and simulation methods. The development of density functional theory along with higher level *ab initio* wave function methods, and novel embedding methods, for example, has revolutionized our understanding adsorbate bonding and reactivity

on well-defined surfaces and organometallic clusters. Due to limited computational resources, methods, and knowledge, most of these initial theoretical studies were focused on modeling ideal single-crystal surfaces under vacuum conditions. The insights and confidence gained from these initial efforts together with further increases in computational methods and nurturing from the experimental electrocatalysis community have helped to “seed” the exponential growth that has occurred in the development and the application of theory in electrocatalysis over the past ten years. Many of the initial developments were based on important insights into the electronic factors that controlled electrocatalytic reactivity. Anderson pioneered the development of reaction center model [13, 15, 18, 32–35], whereas Nørkov and colleagues [11, 12] developed a simple but elegant method that directly relates gas phase surface reaction energies to reaction energies at applied potentials. Schmickler et al. [36–38] developed a model Hamiltonian that appropriately captures bond-breaking and bond-making processes that occur over metal surfaces in electrochemical systems by combining fundamental electron transfer and solvent reorganization principles derived from Marcus theory, Newns Anderson theory on surface reactivity, and a tight binding theory.

These initial efforts were subsequently followed by *ab initio*-based simulation methods to follow chemistry within the aqueous metal interface and the direct relationship to electrocatalysis at applied potentials. There are now a number of rather sophisticated models that include the presence of solution, electrochemical potentials, applied fields, and actual electrolyte in modeling the electrocatalysis. Filhol, Taylor, and Neurock used explicit electrolyte or charge to establish the double layer at the surface [39–43]. The charged surfaces were then referenced to vacuum in order to establish the working potential. Otani et al. used DFT to describe the water metal interface and coupled this with an effective screening medium to represent to polarizable continuum [44, 45]. Jionnouchi and Anderson developed a similar approach by combined density functional theory and modified Poisson-Boltzmann theory [46]. Rossmesl et al. [47] used explicit protons at the water/metal interface to establish the double-layer interface. While the models by Neurock, Otani, Anderson, and Nørkov differ in how they treat the double layer, they are providing more rigorous solutions to the electrochemical transformations that occur on electrode surfaces. It is important, however, to note that these approaches are at best semiquantitative due to limitations of fundamental accuracy of the quantum mechanical methods, modeling electron transfer reactions and simulating long time dynamics, the full reaction environment, or the millions of configurations needed for accurate statistical treatments. Vapor phase density functional calculations of bond energies and activation barriers are typically within the range of 0.1–0.2 eV accuracies but can have outliers [2, 48]. The simulation of electrochemical systems would at best only be 0.3 V. Despite these issues, theory has plaid and will likely continue to play a very valuable role in understanding and establishing trends.

The discussions that follow will look to theory only to provide insights rather than quantitative predictions. All of

the simulations reported were carried out gradient corrected periodic DFT calculations using the Vienna Ab Initio Simulation Program (VASP) [49, 50] with four-layer metal slabs in the presence of solution, where the bottom two layers in the metal were held fixed to the bulk lattice positions of the metal. The coordinates of the metal atoms in the top two layers along with all of the atoms in the adsorbates as well as in the solution layer were fully optimized. Transition states were isolated using the nudged elastic band method with climbing [51, 52] followed by the dimer method [53]. The specific details are reported in the previous papers [39–43].

Rather than continue to discuss the obvious connections between electrocatalysis and gas phase heterogeneous catalysis, it is perhaps more interesting to discuss the growing efforts for carrying out heterogeneous catalysis in solution and new and emerging results that connect heterogeneous catalysis to well-established principles and phenomena in electrocatalysis. There has been an exponential growth over the past few years in carrying out heterogeneous catalytic reactions in solvents or aqueous media. This has been the result of the significant efforts to convert biomass into chemicals and fuels [54–59]. The carbohydrates that result from the breakdown of biomass are soluble in aqueous media and in addition can be catalytically converted at lower temperatures and much milder conditions than traditional gas phase processes. Similarly, many of the processes used in the selective hydrogenation and selective oxidation of fine chemical and pharmaceutical intermediates are also carried out in aqueous or solvent media that operate at lower temperatures to control both chemical as well as enantiomeric selectivities. Many of the catalyst performance and durability issues found in these systems have strong parallels to those found in electrocatalysis. Despite the similarities, there have been very few attempts to connect or compare the two.

3. Specific Comparisons between Catalysis and Electrocatalysis: Example Systems

3.1. Metal Support Interface. Before discussing specific chemistry, we will first focus the metal-support interface in aqueous phase heterogeneous catalysis and electrocatalysis. While the lower temperatures used in aqueous phase catalysis help to control the reaction selectivity, the presence of water often leads to the hydrolysis of metal support bonds which can significantly limit the supports that can be used due to issues related to metal sintering and dissolution. Much of the initial work in the area of conversion of biorenewables was carried out over traditional transition metal catalysts (Pd, Ru, Pt, and Ni) and their supports including SiO_2 , Al_2O_3 , TiO_2 , and high surface area carbons in order to identify active and selective materials [54–57, 60]. There was little emphasis on the fundamental surface chemistry that occurred in the solution phase or the stability of these materials. Maris et al. [61, 62] were some of the first to identify the potential issues related to metal-support interactions under aqueous phase catalytic conditions. They showed that while Ru supported on SiO_2 leads to 100% selective hydrogenation of glucose to

the sugar alcohol, the catalyst used was inherently unstable in aqueous media and resulted in the significant metal particle growth. Subsequent studies by Ketchie et al. [63] used in situ X-ray absorption spectroscopy to monitor the oxidation state of the Ru and follow the metal stability over a range of traditional supports including SiO_2 , $\gamma\text{-Al}_2\text{O}_3$, carbon, and TiO_2 . Significant sintering of Ru on both SiO_2 and Al_2O_3 supports occurred at the mild conditions associated with the conversion of biorenewables. Both the high surface area activated carbon and titania, on the other hand, were found to be stable supports for aqueous phase catalysis over a range of operating conditions. They showed that different carbons may behave differently and that great care must be taken to elucidate the nature of the metal-support interactions under actual process conditions. Most of the recent studies on the conversion of renewables as well as the hydrogenation of pharmaceutical intermediates are now carried out on activated high surface area carbon due to the stability issues.

Interestingly, many of these issues were resolved in the electrocatalysis community many years earlier as metal dissolution is one of the key issues that limit fuel cell durability. Carbon has been the preferred support throughout electrocatalysis as a result of the stability, durability, conductivity, and reactivity of the metal/carbon interface. More recent efforts have demonstrated that the introduction of titania can help to stabilize the metal/support interactions at the cathode for oxygen reduction.

Despite the advances in both catalysis and electrocatalysis towards stabilizing the metal/support interface, it is clear that this is an important area which will require mechanistic insights into the fundamental processes that lead to dissolution and loss of metal and practical advances to solve the issues of durability.

3.2. Oxidation of CO

3.2.1. Catalytic Oxidation of CO. A second example in which heterogeneous catalysis and electrocatalysis are related is the recent discoveries concerning the unique catalytic activity of supported metal particles in the presence of an aqueous medium. Perhaps most evident is the work that has been carried out over supported Au. Up until 1987, gold was considered to be inert and inactive for catalysis. In a pioneering discovery, Haruta et al. [64, 65] demonstrated that nanometer-sized Au particles supported on TiO_2 were highly active for low-temperature CO oxidation in the gas phase. This work led to a tremendous number of follow-up studies aimed at understanding the mechanism by which this reaction proceeds and demonstrates the unique behavior of nanometer and subnanometer-sized Au particles in catalyzing a range of different reactions over TiO_2 as well as other supports [66, 67]. A number of possible explanations for the unique reactivity of Au have been presented in the literature [67] including quantum-size effects [68], increased coordinatively unsaturated edge and corner sites [69], the presence of cationic or anionic Au centers [70, 71], and unique sites at the Au/ TiO_2 interface [72]. While the mechanism is still openly debated, much of the literature suggests that sites along the interface are responsible for the high

catalytic activity. Some have speculated that the Au-Ti site pairs that result at the Au/TiO₂ interface stabilize the adsorption and activation of O₂ or the formation of hydroxyl intermediates both of which can catalyze these reactions [67]. The later idea is supported by the fact that the introduction of small amounts of water or base significantly promotes CO oxidation over Au/TiO₂ [73, 74]. Catalysis on these active 2–4 nm-sized Au clusters is thought to be quite different than that found in the electrocatalysis, as the former is carried out in the gas phase at low temperatures over small Au clusters without an applied potential or the presence of promoters. In addition, O₂ is the active oxidant in gas phase heterogeneous catalysis, whereas activated water or hydroxyl intermediates are thought to oxidize CO in electrocatalysis.

Kim et al. [75] and Sanchez-Castillo et al. [76] and Ketchie et al. [77, 78] later demonstrated that bulk Au as well as Au nanotubes were also very active in catalyzing CO oxidation if the reactions were carried out in an aqueous media. The rates over bulk Au were found to be over an order of magnitude higher in water than those in gas phase. While CO oxidation can proceed readily in the gas phase for nanometer clusters of Au on TiO₂, water is necessary for carrying the reactions out over bulk Au as well as Au supported on carbon.

These same aqueous phase CO oxidation rates were increased by up to 50 times upon increasing the pH of solution from neutral conditions (pH = 7) to basic conditions (pH = 14) and by over an order of magnitude from those in neutral solutions when the reactions were carried out in the presence of 0.5% H₂O₂ [76].

Dumesic et al. suggested that mechanism for CO oxidation in water may proceed via the formation of surface hydroxyl intermediates that can catalyze CO oxidation similar to the classic bifunctional mechanism suggested in electrocatalysis [79–82] and shown previously from theoretical calculations by Desai and Neurock [83, 84]. In this mechanism, water is activated on Ru sites within a PtRu surface alloy, whereas CO binds/blocks the Pt sites as is shown in Figure 2. CO oxidation proceeds via a nucleophilic attack of the OH (bound to Ru) on a neighboring CO (bound to Pt) coupled with the heterolytic splitting of O–H to form CO₂ as well as an electron and a proton. This mechanism would also help to explain the significant promotional effects that occur when the reaction is carried out in the presence of base both catalytically [76, 78] as well as electrocatalytically [85, 86].

3.2.2. Electrocatalytic Oxidation of CO over Au. The anodic oxidation of CO over Au/C was actually established in 1965, over two decades before the pioneering work of Haruta [87, 88]. The reaction readily proceeds over single crystal as well as polycrystalline Au electrodes at low temperature in alkaline media at potentials which are 0.5 V lower than those found with Pt which is used in most fuel cells. While CO oxidation readily occurs over single-crystal electrodes in acidic media, the rate is significantly enhanced when carried out in alkaline media. CO oxidation proceeds over Au(111) and Au(110) at potentials of 0.1 and 0.2 V RHE, respectively, which is 0.5 V lower than those recorded in acid media [88]. Similar differences for CO oxidation in acidic and alkaline

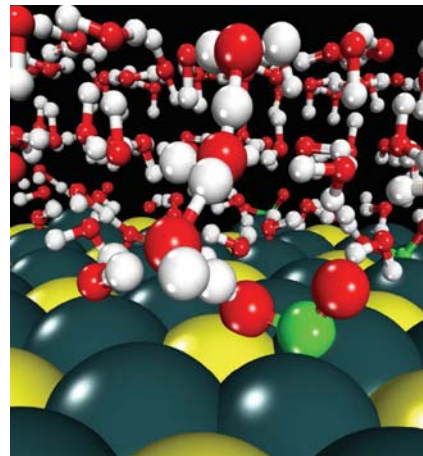


FIGURE 2: DFT-calculated transition state for the electrocatalytic oxidation of CO on Pt (green spheres) by hydroxyls formed via the dissociation of water over Ru (yellow spheres). The resulting electron is transferred to the metal whereas the proton shuttles away from the surface via the water network (copyright Science [83]).

media also exist for polycrystalline Au. The reaction is thought to proceed via the coupling of CO* and OH* in a mechanism that is similar to that presented above in Figure 2. While the reaction proceeds in acidic media, the activation of water to form OH* on Au at lower potentials is difficult. The reaction is significantly faster in alkaline media as a result of increased formation of OH* at lower potentials and the stronger adsorption of CO at these lower potentials. The higher coverages of CO* and OH* in alkaline media further enhance the rate of reaction at the lower potentials. This shift in potential results in an increase in electron density at the metal surface which further enhances backdonation. Rodriguez et al. [88, 89] suggested that the increased CO adsorption further enhances the adsorption of OH and self-promotes the reaction.

Nearly all of the early electrocatalytic studies were carried out over bulk polycrystalline Au electrodes. The exceptional findings by Haruta et al. [64, 65] and the suggestions of the unique interface for nanoparticles of Au supported on TiO₂ prompted Hayden et al. [85, 86] to examine the electrocatalytic oxidation of CO over nanoparticles of Au on TiO₂. They demonstrated considerable enhancements in the electrocatalytic rates of CO oxidation for Au nanoparticles supported on TiO₂ even when the reaction is carried out in acidic media. The enhancement was attributed to the substrate-induced reactivity of Au as discussed below [85, 86].

3.2.3. Particle Size Effects on CO Oxidation. The results from gas phase catalysis carried out over supported Au clusters indicate that the reaction is structure sensitive where the highest catalytic activity occurs for 2–4 nm sized particles supported on TiO₂ [66, 67]. The results in aqueous media, however, are not as clear. Ketchie et al. show a significant increase in the activity in moving from 42 nm down to 5 nm [77]. The activity on 2–3 nm-sized clusters, however, was

more difficult to quantify as a result of difficulties in the synthesis of monodisperse particles [64, 65, 67]. Under electrochemical conditions, Hayden et al. [85, 86] showed that while polycrystalline Au electrodes readily oxidize CO to CO₂, they require overpotentials greater than 0.7 V as AuO forms and inhibits the reaction. They demonstrated significant structure sensitivity in the reaction, whereby 3 nm Au particles were much more active even at potentials as low as 0.3 V. Au particles smaller than 2.5 nm showed a significant decrease in activity as did particles larger than 3.5 nm. They speculate that the loss in activity below 3 nm is the result of quantum size effects rather than from irreversibly adsorbed oxygen. There appears to be clear similarities for particle size effects in comparing the results for CO oxidation under electrocatalytic conditions with those found for Au/TiO₂ in the gas phase heterogeneous catalysis. The reactions over Au/C in solution, however, were less conclusive.

3.2.4. CO Oxidation Mechanisms. As was suggested earlier, the heterogeneous catalytic and the electrocatalytic oxidation of CO may proceed by common mechanisms or at least common features in the mechanism. We compare the mechanistic ideas for the catalytic and electrocatalytic oxidation of CO over both TiO₂ and carbon supports.

(1) Catalytic and Electrocatalytic Oxidation of CO over TiO₂.

The unique reactivity of nanometer-sized Au particles on TiO₂ used in both catalysis as well as electrocatalysis is thought to be dictated by sites at the Au/TiO₂ interface. We have recently shown that the Ti cations in direct proximity to the adsorbed Au become positively charged as a result of local charge transfer from Au to local Ti⁵⁺ cations as is shown in Figure 3 [90]. This increase in charge along with the direct involvement of both Au and Ti⁵⁺ atoms stabilize the bidentate adsorption of O₂. This increases the O₂ adsorption strength by nearly 60 kJ/mol and promotes its activation at these dual interface sites. This subsequently catalyzes the reaction between O₂ coadsorbed CO. While O₂ is not present in the electrocatalytic oxidation of CO, water can adsorb and activate at these same perimeter sites. DFT calculations indicate that the adsorption of water at this same charged interfacial Ti⁵⁺ site is -104 kJ/mol, whereas water on a Ti⁵⁺ site removed from Au and on a Au site near the support are significantly weaker at -77 kJ/mol and -8 kJ/mol, respectively. These Au-Ti perimeter sites likely attenuate the activation of water. The resulting intermediate (either activated water or surface hydroxyl groups) can then react with coadsorbed CO to form CO₂. This is consistent with the results from Hayden et al. [85, 86] who showed a direct relationship between electrocatalytic activity and the perimeter of the particle and was able to rule out the influence of low coordinate Au atoms and quantum size effects.

The differences between the gas phase reactions and the electrocatalytic reactions may simply be the nature of the active oxidant that forms. In the presence of water, the oxidant involved in catalysis and electrocatalysis is likely the same.

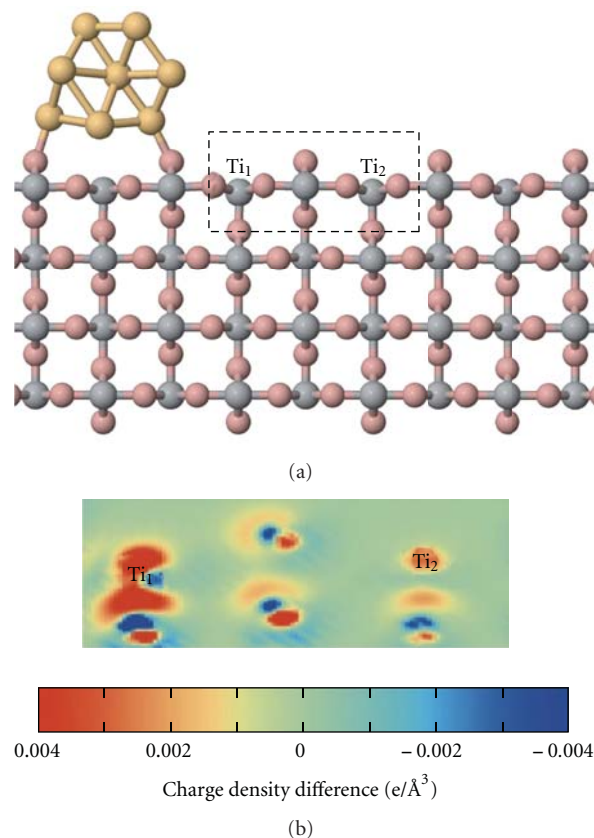
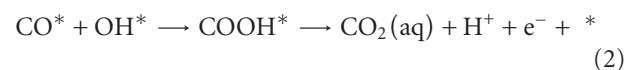
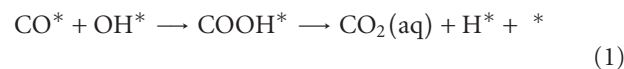


FIGURE 3: Charge density difference that results at Ti⁵⁺ centers of TiO₂ adjacent to Au upon the adsorption of Au nanorods or clusters. (Copyright Science [90]).

(2) Au/C The Effects of Water and Base. The heterogeneous oxidation of CO over bulk Au/C in water appears to proceed via a mechanism that involves the nucleophilic addition of OH groups present in solution or on the surface formed under reaction conditions to adsorbed CO*. This results in the formation of CO₂ and either adsorbed hydrogen or a proton and an electron.



The latter is identical to the mechanism typically proposed in electrocatalysis. The results for the heterogeneous CO oxidation in water over Au/C indicate that the reaction can proceed solely by the presence of H₂O₂ and water without oxygen [76]. In the presence of oxygen, small amounts of H₂ are formed possibly as the result of the water gas shift reaction [76]. Both of these results strongly suggest that OH groups are formed and directly participate in the oxidation mechanism [76]. Similar reactions occur in the electrocatalytic oxidation of CO over Au/C in both acid as well as alkaline media.

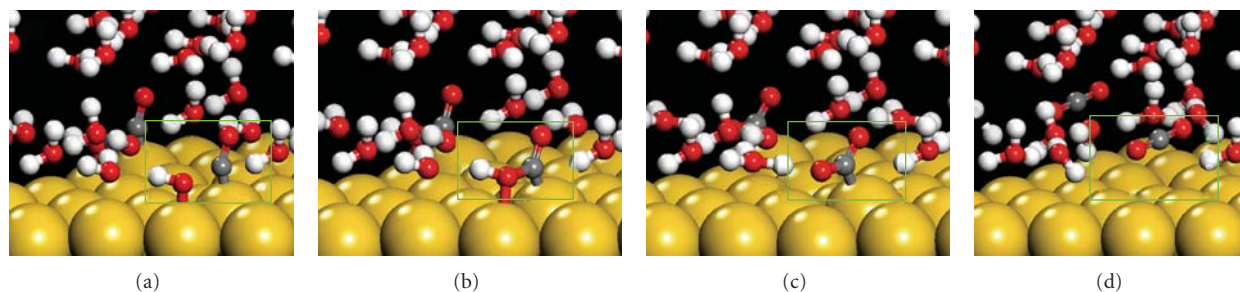


FIGURE 4: DFT-calculated reaction coordinate for the oxidation of CO via adsorbed OH* over Au. The reaction proceeds via: (a) the coadsorption of CO* and OH*, (b) the nucleophilic attack of OH* on CO* to form the HO*-CO surface intermediate, (c) cleavage of O-H bond in the transition state, and (d) formation of CO₂ and H₃O⁺ products. The active CO* and OH* surface species are highlighted in green as they proceed through the reaction.

In order to model the oxidation of CO over bulk Au in solution, we have carried out detailed density functional theory calculations with CO and OH or H₂O adsorbed on a Au(111) surface immersed in water [91]. The resulting activation barrier for the reaction (2) above was calculated to be negligible, whereas the overall reaction energy was calculated to be exothermic by -231 kJ/mol. Various structures along the reaction coordinate are shown in Figure 4. The reaction proceeds via the formation of the OC-OH bond combined with the heterolytic splitting of the O-H bond to form an H₃O⁺ intermediate which subsequently undergoes a second proton transfer to another water molecule.

The overall mechanism for the heterogeneous catalyzed oxidation of CO may proceed via the formation of local electrochemical cell or circuit, where CO is oxidized by OH resulting in the formation of proton and an electron which subsequently catalyzes the reduction of O₂ to the active OH intermediates or to H₂O₂. This is discussed in somewhat more detail in Section 3.3.2(1). These same ideas on the oxidation of CO can readily be extended to methanol as well as other alcohols.

3.3. Alcohol Oxidation. The increasing demand to shift from petroleum-based fuels and chemical to those derived from biomass has significantly increased efforts in both the electrocatalytic and catalytic oxidation of carbohydrates feedstocks. Significant efforts have been focused on the selective oxidation of methanol, ethanol, glycerol, and other C₂-C₆ polyols into chemical intermediates via heterogeneous catalysis [92-98] as well as the total oxidation of these fuels to electrical energy via electrocatalysis [99-107]. In the next few sections, we compare some of the similarities and differences involved in the catalytic and electrocatalytic oxidation of these alcohols in acidic as well as alkaline media.

3.3.1. Alcohol Oxidation in Acidic Media

(1) Catalytic. The catalytic oxidation of glycerol as well as ethanol is rather low when carried out in neutral solution over Pd and Pt with reported turnover frequencies of 0.05 and 0.06 s⁻¹, respectively [98]. The products that form over these metals are predominantly intermediate aldehydes and

ketones that result from dehydrogenation with only 25% selectivity to form the acid product. Glycerol oxidation, for example, leads to the formation of glyceraldehyde as well as dihydroxyacetone without further oxidation to C₁ or C₂ acids or CO₂. Supported Au clusters under neutral and acidic conditions were found to be completely inactive [98].

The dehydrogenation reactivity that results over Pd and Pt can proceed via C-H and O-H activation over the metal or by adsorbed oxygen or hydroxyl intermediates that form upon O₂ dissociation or by the subsequent reaction of adsorbed oxygen with water. DFT-calculated activation barriers suggest that O-H activation of ethanol occurs via the reaction of adsorbed ethanol with OH*, whereas the C-H activation of ethanol preferentially occurs via metal sites on the Pt and Pd surfaces [98]. Both reactions, however, are limited on Pt and Pd, as the high surface coverages on these metals result in barriers for both C-H and O-O activation that are significantly greater than 100 kJ/mol. The oxidation of alcohols over Au does not proceed over Au alone under neutral or acidic conditions as gold cannot activate water, O₂, or alcohol [98].

(2) Electrocatalytic. The oxidation of methanol, ethanol, glycerol, and other alcohols occurs in acidic media but requires significantly higher overpotentials than reactions carried out in alkaline media [79, 100, 108-119]. The oxidation of methanol proceeds over most transition metals through a sequence of elementary C-H and O-H bond activation steps which occur on the metal, and ultimately result in the formation of CO [79, 109, 110]. Through the combination of cyclic voltammetry, chronoamperometry, and DFT studies, we demonstrated that the methanol decomposition occurs via a dual path mechanism [1, 120]. At potentials below 0.35 V, the mechanism proceeds predominantly through a sequence of C-H activation steps to form the hydroxyl methylene (CHOH*) intermediate that subsequent breaks the O-H and C-H bonds to form CO*. At potentials above 0.35 V, the O-H bond of methanol can also be activated, resulting in the formation of formaldehyde which can desorb or continue on to form CO. The onset potential was found to be a function of the Pt surface structure. The dual paths for the oxidation of methanol to CO over Pt(111) along with their

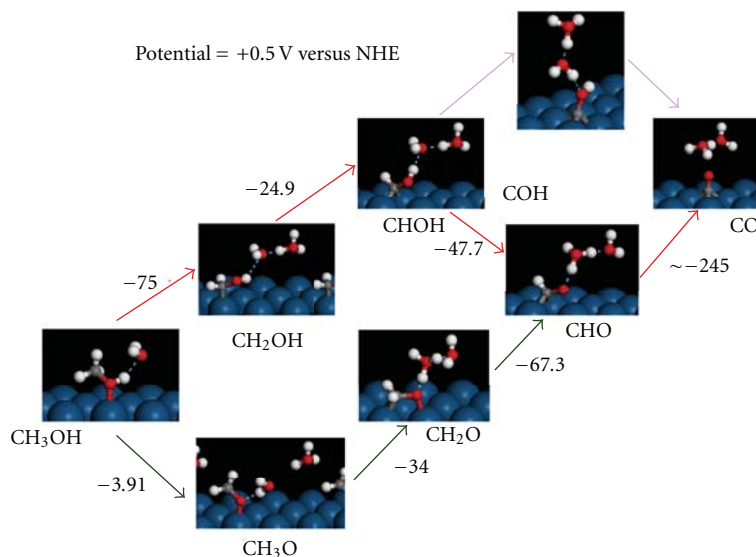


FIGURE 5: DFT-calculated potential-dependent reaction paths for the oxidation of methanol to CO over Pt(111) [1]. At 0.5 V, both experiments and theory point to the onset of dual paths. The primary path, available over a wide range potentials, is shown in red. It proceeds via a sequence of C–H bond activation steps ultimately forming the hydroxyl methylene intermediate (CHOH) before activating the final O–H bond to form CO. The minor path begins between 0.4–0.5 V RHE proceeds via the initial activation of O–H bond of methanol to form a surface methoxy intermediate which subsequently reacts to form formaldehyde consistent with previous speculations [122].

corresponding reaction energies calculated at 0.5 V RHE are shown in Figure 5 [1, 120]. While CO is an intermediate to CO₂, it readily builds up on the surface and poisons more active metals such as Pt. As such, Pt is typically alloyed with a more oxophilic metal such as Ru to promote the adsorption and dissociation of water thus creating bifunctional sites on the surface [79, 109, 110]. The OH groups that result interrupt the CO adlayer and readily oxidize CO to CO₂. The addition of Ru also helps to weaken the Pt–CO bond thus enhancing CO desorption. The addition of Ru to Pt lowers the overpotential for CO oxidation by ~0.25 V [80–82, 121] as it prevents CO poisoning.

The oxidation of ethanol, glycerol and other larger alcohols in acidic media result in dehydrogenation which forms the corresponding aldehyde [114–117]. The subsequent activation of the C–C bond, however, is very difficult over typical metals such as Pt, Pd, or Au, and as such, very limited CO₂ is formed. The dehydrogenation routes are identical to those presented above for the catalytic oxidation of the same alcohols. The higher potentials used electrochemically can activate water at higher potentials, and thus result in the formation of surface hydroxyl intermediates that can subsequently oxidize the aldehyde and ketone intermediates [115]. This leads to the formation of acids as well as carboxylate intermediates which inhibit the surface under acidic conditions and prevent the formation of CH_x intermediates on closed-packed crystal surfaces. Feliu et al. have shown that steps on specific Pt surfaces Pt(554) and Pt(110) can begin to enhance C–C bond breaking and CO₂ formation, but rate is still very limited [111, 114].

The electrooxidation of ethanol over Pt in acidic media has two major limitations which prevent its viability as was

discussed by Lia et al. [115]. The first relates to the fact that reaction predominantly produces acetate and acetic acid intermediates, thus resulting in only 2 and 4 electrons, respectively, which are only very minor contributions to total possible current. Both are thus unwanted side products for fuel cell applications. The second limitation is that the path to CO₂ is rather difficult in that it requires the activation of C–C bond as well as the oxidation of both the CH_x and CO intermediates that form. Both of these intermediates tend to inhibit or poison metal surfaces at lower potentials [48].

The characteristic difference between the catalytic oxidation and electrocatalytic oxidation of alcohols in acidic media lies in the generation of the active surface intermediate. In heterogeneous catalysis, the metal plays an important role in activating oxygen. The surface oxygen can directly activate the alcohol or adsorbed water to generate hydroxyl intermediates that aid in activating and oxidizing the alcohol. Under electrocatalytic conditions, the O–H and C–H bonds of the alcohol can be activated on the metal directly as a result of higher potentials or via adsorbed hydroxyl intermediates that form by the activation of water.

3.3.2. Alcohol Oxidation in Alkaline Media

(1) *Catalytic.* The catalytic oxidation of polyols over Pd, Pt, and Au is much more favorable when carried out in alkaline media [78, 98, 123]. The TOF increases by over an order of magnitude on Pt and over two orders of magnitude on Pd upon the addition of a 2/1 ratio of NaOH to glycerol [98]. Remarkably, the TOF over gold in base is over 6 s⁻¹, whereas the rate over Au in acidic media is negligible [98]. In addition to these increases in TOF, there are also significant

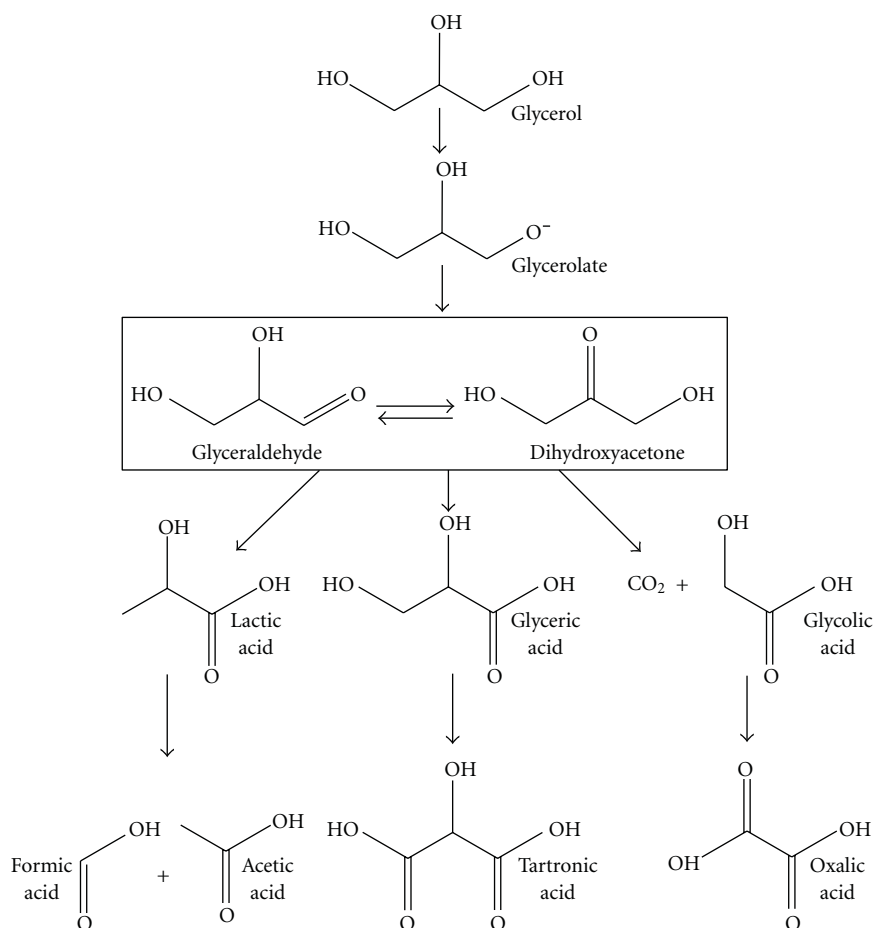


FIGURE 6: Reaction pathways speculated in the catalytic and electrocatalytic oxidation of glycerol over Au and Pt. Arrows in red depict paths observed over Au and Pt whereas the paths in black are only observed over Pt. Adapted from [123].

improvements in the overall selectivity to form the acid from the alcohol. For glycerol, the selectivity to glyceric acid was found to be 83% over Pd, 70%–78% over Pt, and 67% over Au [98]. The predominant side products are glycolic and tartronic acid which are shown in the paths outlined in Figure 6. In the presence of base, the second terminal hydroxyl group can be oxidized to form tartronic acid, but this only occurs over Pt and Pd. The oxidation over Au results only in the monofunctional glyceric acid product. In addition to the selective oxygen addition, Pd and Pt can also promote C–C activation resulting in the formation of glycolic, oxalic, lactic, formic, and acetic acids. These C–C activation paths appear to coincide with the formation of hydrogen peroxide [123]. The activation of the C–C bonds have been speculated to occur either through a retroaldol reaction which would be catalyzed by the OH⁻ base, or via oxidation catalyzed by the hydrogen peroxide that forms [78, 123].

Through detailed labeling studies along with DFT simulations, we established a plausible mechanism for the oxidation of alcohols over Au in basic media [98]. The mechanism also helps to explain the unique promotional effects of OH on Au. We discuss here the energetics involved in the reaction over the model Au(111) surface. The first step involves

the dehydrogenation of the alcohol to form the corresponding aldehyde. This can proceed via the activation of the O–H and C–H bonds of the alcohol by the metal, adsorbed oxygen, or adsorbed OH intermediates. As one might expect, Au atoms alone cannot activate the O–H bond of the alcohol. The calculated barrier to activate ethanol to ethoxy over Au(111) in the presence of solution was calculated to be 204 kJ/mol (the transition state is shown in Figure 7(a)). The O–H bonds are much more readily activated by the weakly adsorbed OH^{δ-} intermediates via a mechanism which involves a proton abstraction by the OH^{δ-} surface intermediate (the transition state is shown in Figure 7(b)). The inability of Au(111) to activate the O–H and C–H bonds is well established, as bulk Au is quite noble. The binding energy of OH^{δ-} on Au(111) in water is only –216 kJ/mol (versus –274 kJ/mol on Pt(111)), thus making it quite basic. The weak interaction promotes its ability to readily abstract a proton from a neighboring O–H on the alcohol. Similarly, the activation of the C–H bond of the ethoxy intermediate to form acetaldehyde does not occur over Au(111) alone (see the transition state in Figure 7(c)) but instead proceeds by the reaction of OH^{δ-} with the adsorbed ethoxy intermediate with a barrier of only 12 kJ/mol (see the transition state in

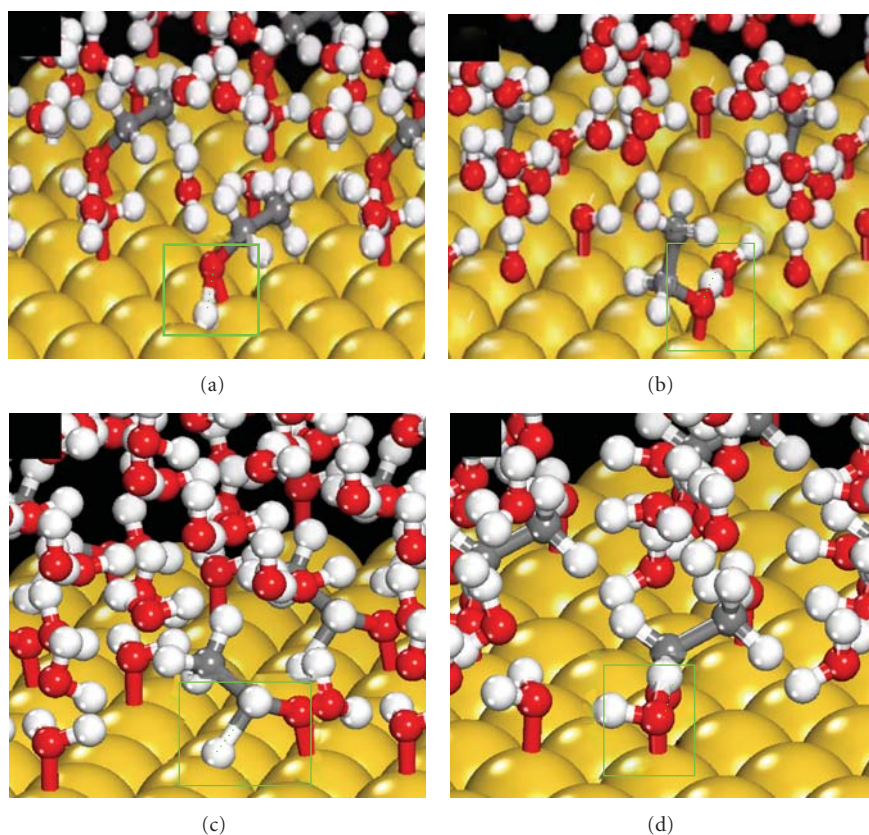


FIGURE 7: DFT-calculated transition states for the activation of the O–H bond of ethanol adsorbed to Au by (a) metal surface atom or (b) a coadsorbed hydroxyl intermediate on Au(111). The activation of the C–H bonds of the adsorbed ethoxy are activated similarly via (c) Au atoms in the Au(111) surface or (d) via the bound OH groups on the Au(111) surface. The active bond breaking and forming sites are highlighted in green.

Figure 7(d)). The aldehyde that results is a key reaction intermediate to form the acid in alkaline media over Au.

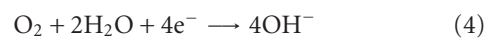
Most of the initial studies in the aqueous phase catalytic oxidation of alcohols assumed that O_2 was responsible for carrying out the oxidation. By carrying out the reaction with ^{18}O -labeled O_2 and H_2O , however, we showed that only labeled water found its way into the resulting acid product that forms [98]. DFT results for Au in an aqueous medium showed that this reaction proceeds via a classic nucleophilic attack of $OH^{*\delta-}$ on the adsorbed aldehyde quite similar to thought found for the oxidation of CO. The barrier to form the geminal diol intermediate shown in Figure 8(a) was only 5 kJ/mol when carried out over Au and 42 kJ/mol for reactions in the solution phase Figure 8(b). The final C–H activation of the geminal diol to form the acid can proceed over the Au itself (21 kJ/mol) or via reaction with adsorbed $OH^{*\delta-}$ (29 kJ/mol). A schematic representation of the mechanism which involves the unique reactivity of OH^- intermediates at the aqueous/Au interface for the selective oxidation of the alcohol to the acid is depicted in Figure 9, whereas the corresponding potential energy surface is shown in Figure 10. This oxidation path proceeds without the activation or incorporation of oxygen from O_2 .

While O_2 is not directly involved in any of the steps depicted in the mechanism for alcohol oxidation shown in

Figure 10, it is critical as the reaction does not occur without it. Oxygen must somehow be intimately coupled with the overall catalytic process which requires the balance of charge and the regeneration of OH^- . As the result of theoretical calculations, we showed that oxygen is necessary to remove the electrons that are generated as result of the oxidation of the alcohol. The measured rate for the oxidation reaction is 6.1 turnovers per second per site [98]. As the steps outlined in the cycle presented in Figure 10 consume 4 hydroxyl ions, they generate 4 electrons per every turnover.



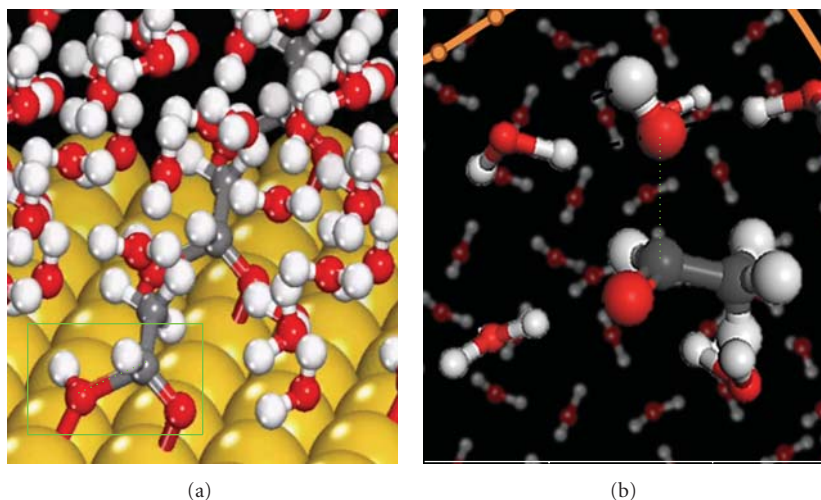
In order for the reaction to occur catalytically, the electrons that are produced per turnover must be consumed. Each oxygen molecule can effectively remove 4 electrons via the oxygen reduction reaction (ORR).



The oxygen reduction reaction is known to occur quite readily over single crystal Au electrodes. DFT calculations were used to determine the reaction energies and the activation barriers for the most relevant steps for ORR. The results reported in Table 1 indicate that the direct dissociation of O_2 (reaction 5) does not take place over Au as is well established

TABLE 1: DFT-calculated reaction energies and activation barriers for possible steps involved in the reduction of O_2 to OH over $Au(111)$ in aqueous media [98].

	ΔE_{rxn} (kJ/mol)	ΔE^* (kJ/mol)	Reaction
$O_2^* + * \rightarrow O^* + O^*$	41	105	(5)
$O_2^* + H_2O^* \rightarrow OOH^* + OH^*$	-4	16	(6)
$OOH^* + * \rightarrow OH^* + O^*$	-56	83	(7)
$OOH^* + H_2O^* \rightarrow HOOH^* + OH^*$	37	48	(8)
$HOOH^* + * \rightarrow OH^* + OH^*$	-86	71	(9)

FIGURE 8: DFT-calculated transition states and their activation barriers for the oxidation of acetaldehyde on (a) the $Au(111)$ surface or (b) in the presence of solution. The active bond breaking and forming sites are highlighted in green.

experimentally. Oxygen instead is reduced by the protons from water and the electrons in the metal to form a peroxo intermediate along with OH^- (reaction 6). The peroxo intermediate is subsequently reduced to hydrogen peroxide (reaction 7) which can subsequently dissociate and result in the formation $2OH^-(aq)$. The intermediate formation of hydrogen peroxide is consistent with observed experimental results and suggestions that peroxide is responsible for C–C bond breaking and formation of shorter acids.

This overall ORR cycle removes the 4 electrons from the metal produced via the oxidation, and thus allows the reaction to continue catalytically. The cycle also regenerates $OH^-(aq)$. The overall catalytic reaction then involves the direct coupling of both alcohol oxidation and oxygen reduction cycles in one system. This can thus be considered a local, short-circuited, electrochemical cell, where the oxidation and reduction occur simultaneously at the metal/surface interface. The role of O_2 then is to simply to remove the electrons from the metal at a rate fast enough to maintain the optimal surface potential of the local electrochemical cell.

(2) *Electrocatalytic.* The development and application of carbonate as well as anion-exchange membrane electrolytes have significantly renewed interest in the development of alkaline-based direct alcohol fuel cells [100]. Many of the reaction intermediates, products, and paths discussed above for the catalytic oxidation of alcohols in alkaline media

have also been identified or speculated to take part in the electrocatalytic oxidation of these same alcohols. As such, the mechanistic insights established from catalytic oxidation should be important in understanding the chemistry and the mechanisms that control electrocatalytic oxidation. Similarly, the detailed insights established from electrochemical methods such as cyclic voltammetry should provide new insights into heterogeneous catalytic oxidation.

The oxidation of methanol, ethanol, as well as other polyols in alkaline media is thought to proceed either by $4e^-$ or $6e^-$ processes thus resulting in the formation of either formate and carbonate intermediates by reactions (5), or (6) [100]



For methanol, the later reaction is speculated to occur through the formation of CO . In the presence of base, surface OH^- groups readily catalyze the oxidation of methanol to CO_2 or carbonate as shown in reactions (5) and (6), respectively. At higher potentials, however, OH binds very strongly to the metal surface and inhibits the reaction. The selectivity to formate or carbonate depends upon the metal, metal surface structure, potential pH, and alcohol concentration present during the reaction. We discuss here the difference in the electrocatalytic oxidation over Pt and Au and compare

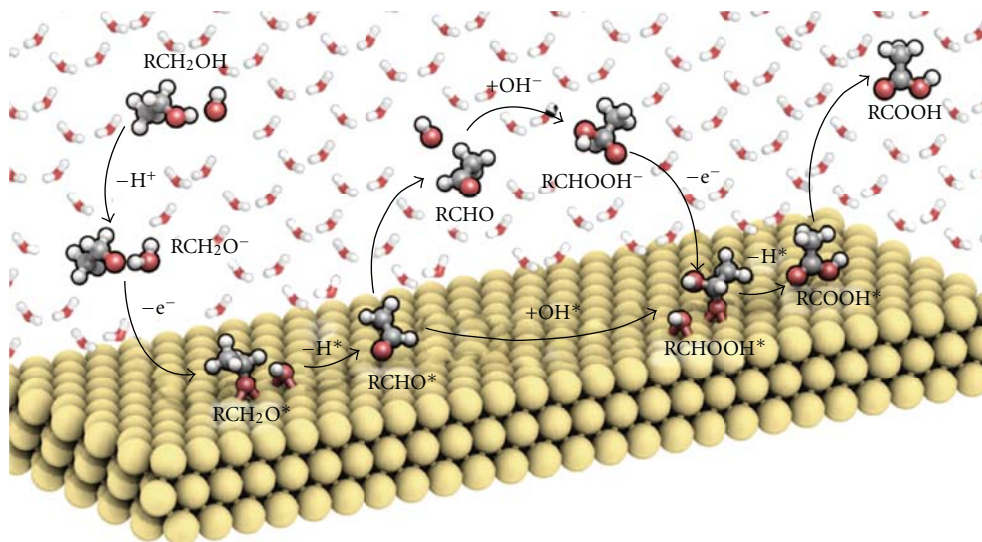


FIGURE 9: Schematic representation of the reaction paths for ethanol and other polyol oxidation to acids over Au and Pt in alkaline media based on DFT results and isotopic kinetic labeling experiments. (Copyright Science [98]).

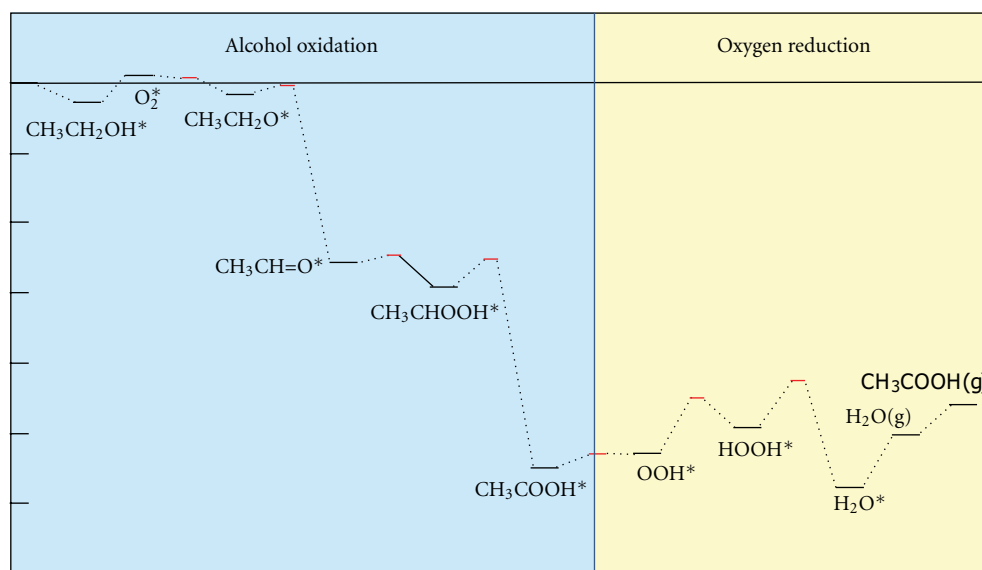


FIGURE 10: DFT-calculated potential energy surface for the catalytic oxidation of ethanol to acetic acid over Au(111) in the presence of base (OH^-) and in water. Both the OH^- as well as the metal are involved in the mechanism. In order to establish an overall cycle, O_2 is reduced via the electrons that form as a result of the oxidation of the alcohol as well as by the reaction protons that form upon the activation of water. Red lines refer to transition states, whereas the black lines refer to reaction intermediates.

the changes that result upon changing the pH and concentration.

While the oxidation of methanol as well as other alcohols can be carried out in acid media as was discussed above, the activity is rather low. The rates and currents increase significantly with increasing the pH of solution. The electrocatalytic oxidation of methanol as well as other alcohols over Au is quite high in alkaline media [100, 101, 104–108, 110, 118, 124–126]. The higher rates and current densities found in alkaline media are the result of the high reactivity of OH^- anions that are weakly bound to the Au substrate at moderate

potentials. The weakly bound hydroxyls are quite basic and will readily activate C–H and O–H bonds (on adsorbed species) as was presented above in the catalytic oxidation of alcohols over Au in basic media. The electrocatalytic activity over different Au substrates including polycrystalline Au, Au(111), and Au(210) all show increases in activity with increases in the solution pH [101]. The adsorption of OH^- anions onto Au is thought to significantly enhance the reactivity of the surface over a range of potentials. Electrocatalytic oxidation can, therefore, proceed at much lower potentials where Au is not oxidized.

The anodic oxidation of methanol begins to occur with the adsorption of OH^- . In general, there are two very different regimes that result for methanol oxidation over Au [101]. In the first regime, methanol is actively oxidized by adsorbed OH^- intermediates on Au at potentials as low as 0.6 V RHE. The second regime which occurs at much more positive potentials and results in the formation of Au–O monolayers which are much less active for carrying out oxidation.

Chen and Lipkowski [127] and Yan et al. [107] provided more details in terms of the changes that take place at the surface as a result of these changes in potential and suggest that there are actually three regimes that result upon increasing the potential. The initial oxidation of methanol and other alcohols proceeds quite readily from 0.07–0.13 V versus Hg/HgO. The current increases linearly with the adsorption of OH^- in this regime. There appears to be a weak amount of charge transfer between the OH^- and the metal surface. The second regime appears between 0.13–0.3 V versus Hg/HgO and results in a higher degree of charge transfer of OH and the Au sites in the surface. Regime 3 which appears at potentials greater than 0.3 V Hg/HgO is the inactive monolayer Au oxide that results. The oxidation of methanol is thought to proceed via the weakly held OH^- intermediates found in both regimes 1 and 2. The more strongly held oxygen intermediates which begin to form in regime 2 are less active. Regime 3 leads to the formation of monolayer Au oxide coverages and thus the loss of the active OH^- sites. For methanol oxidation, the reaction is 0.75 order in methanol and 0.55 order in OH [107]. There is a clear negative shift in the potential and an increase in the current density with an increase in the concentration of weakly adsorbed $\text{OH}^{\delta-}$ and methanol coverage.

3.3.3. Ethanol Oxidation over Au. Ethanol oxidation is similar to methanol oxidation in that there is a significant shift to lower potentials and increased current that results upon increasing pH. Ethanol oxidation proceeds at a potential of 0.6 V versus RHE in alkaline solution which is 0.3 V lower than that reported in acid [115]. In addition there is a shift of -0.1 V in the maximum from 1.35 V to 1.25 V. The current density in alkaline media is found to be over an order of magnitude higher than that in neutral or acid conditions [115]. Regardless of the potential or pH there is negligible C–C bond breaking that occurs on Au, and as such, there is very little to no CO_2 formation. The mechanism is thought to be very similar to the path outlined in Figure 10 and presented above for the catalytic oxidation of ethanol. The main path involves the oxidation of ethanol to acetaldehyde through the activation of the acidic O–H and C–H bonds by weakly adsorbed hydroxyl intermediates on the Au surface. Acetaldehyde subsequently reacts with weakly held $\text{OH}^{\delta-}$ intermediates via simple nucleophilic attack depending of $\text{OH}^{\delta-}$ on the C=O bond of the aldehyde to form the geminal diol intermediate which can further react with OH^- to form acetic acid or adsorbed acetate in alkaline media.

3.3.4. Extension to Polyols. These same ideas have been further extended to larger polyols such as glycerol and glucose in alkaline media [104–106, 125]. Glycerol, for example, reacts

via a $4e^-$ transfer process to form glyceric acid on both Au as well as Pt electrodes. At higher potentials, the C–C bond of glyceric acid can further oxidize via a two electron transfer step to form glycolic and formic acids [125]. While this occurs over both Au and Pt, the selectivity to the over-oxidized glycolic state is much higher on Au. This was thought to be due to the fact that Pt deactivates by the formation of a surface oxide intermediate at much lower potential (0.9 V) than that found on Au (~ 1.3 V) [125]. This results in much lower oxidation potentials and a much narrower window for the subsequent oxidation to proceed. Glyceric acid as well as glycolic acid can both undergo further oxidation on Pt to form tartronic as well as oxalic acid, respectively. The subsequent OH^- addition steps, however, only appear to proceed over Pt as neither of the di-substituted products appear over Au. The results reported by Kwon and Koper [125] for the electrocatalytic oxidation of glycerol discussed here are very similar to those reported by Ketchie et al. [78] for the catalytic oxidation of glycerol. Both show that C–C bond breaking steps can readily take place in the presence of OH^- to form glycolic, formic, and oxalic acids on Au as well as on Pt. Both also reveal that Au will only oxidize one of the terminal $-\text{CH}_2\text{OH}$ bonds of the polyol, whereas Pt can oxidize both. It is very likely that the detailed mechanism for the formation of glyceric acid established for catalytic systems holds also for the electrocatalytic oxidation. The elementary steps involved in C–C bond breaking are not known for either the catalytic or the electrocatalytic paths. The catalytic routes have been speculated to occur via oxidation with hydrogen peroxide or by base catalyzed paths. There is no evidence, however, for the formation of hydrogen peroxide electrocatalytically and more likely the reaction proceeds solely via the reaction with base.

The similarities and differences between the catalytic and electrocatalytic oxidation of alcohols is very informative. A closer analysis between the two suggests that the two are nearly equivalent with the exception that oxidation of the alcohol which occurs at the anode is decoupled from the oxygen reduction which occurs at the cathode. The two electrodes communicate via charge and ion transfer. In the heterogeneous catalytic system, the alcohol is oxidized where the electrons are directly used at the same aqueous metal interface to reduce O_2 . The rate of oxidation is thus directed by the rate at which O_2 can be reduced by electrons. This is directly analogous to that which happens in the PEM alcohol fuel cells.

CO and alcohol oxidation make up just two reaction systems. One can readily draw analogies to other catalytic reaction systems carried out in aqueous media. Desai and Neurock for example carried out first principles DFT calculations to show that an aqueous medium could readily facilitate the catalytic hydrogenation of adsorbed oxygenates [83, 84, 128]. They showed that adsorbed hydrogen could undergo an electron transfer coupled with proton transfer at the metal interface to form a local proton in the form of a hydronium ion that could readily transfer through solution and attach itself with the negatively charged adsorbed surface intermediate. The solution phase here acts as a cocatalyst. As such, the solution provides for a short-circuited electrocatalytic cell

which allows for electron and proton generation transfer and facile recombination. The ability carry out this heterolytic proton transfer process is controlled by the work function or “electron affinity” of the metal. Metals such as Pd and Pt should have the ability to convert adsorbed hydrogen into protons that reside in solution and electrons which remain in the metal. This was demonstrated by both Wagner and Moylan [129] and Kizhakevariam and Struve [130] who both showed that adsorbed hydrogen on ideal Pt substrates in the presence of water in UHV (at low temperature) forms hydronium ions in solution near the surface. These results are consistent with the results from theory. More generally the results suggest that the presence of protic media along with high work function metals can carry out hydrogenation reactions much more efficiently through proton coupled electron transfer processes that mimic electrocatalysis.

4. Summary

While fundamental information concerning reaction mechanisms, active sites and catalytic kinetics gleaned from in situ spectroscopy, detailed theoretical simulations and rigorous kinetic studies for gas phase heterogeneous catalysis has helped guide the development of electrocatalytic systems, the complexity of the reaction environment has often precluded more in-depth or quantitative analyses. The tremendous advances in spectroscopy along with theory, that have taken place over the past few decades, however, have allowed for more detailed resolution of the molecular transformations that occur in electrocatalytic systems along with a more detailed following of the nature of the active centers and their environment. There appears to be an important and growing trend where this knowledge and guiding principles from electrocatalysis are being used to guide heterogeneous the complex aqueous and solvent-based catalytic processes. The knowledge of the complex electrified interface in electrocatalysis bears a number of common similarities to the aqueous/metal interface for catalytic reactions carried out the presence of solution. More detailed fundamental studies which attempt to rigorously compare heterogeneous catalysis in solution with electrocatalysis will continue and will likely be crucial in establishing the links between the two.

Acknowledgments

A. Wieckowski gratefully acknowledges support from the National Science Foundation under Grant no. NSF CHE06-51083 A. Wieckowski and ARO under Grant no. W911NF-08-1-0309. M. Neurock gratefully acknowledges support from the Office of Basic Energy Sciences under Award no. ERKCC61 for the work on metal/solution interfaces. (This work is part of the Fluid Interface Reactions, Structures and Transport (FIRST) Center, an Energy Frontier Research Center funded by the U.S. Department of Energy, Office of Science, Office of Basic Energy Sciences), U.S. Department of Energy, Division of Chemical Sciences, Office of Basic Energy Sciences (DE-FG02-07ER15894) for the work on oxygen reduction, the National Science Foundation Research

Center for Biorenewable Chemicals (EEC-0813570), and the National Science Foundation PIRE (NSF OISE-0730277) for the work on alcohol oxidation. M. Neurock would also kindly acknowledge the computational time at the Environmental Molecular Science Laboratory, a national scientific user facility sponsored by the Department of Energy's Office of Biological and Environmental Research and located at Pacific Northwest National Laboratory, the National Center for Computational Sciences at Oak Ridge National Laboratory and the National Energy Research Scientific Computing Center, which is supported by the Office of Science of the U.S. Department of Energy which was used to carry out the work. Lastly, the authors would like to thank Professor Robert J. Davis, David Hibbitts, and Craig Plaisance for helpful discussions.

References

- [1] D. Cao, G. Q. Lu, A. Wieckowski, S. A. Wasileski, and M. Neurock, “Mechanisms of methanol decomposition on platinum: a combined experimental and ab initio approach,” *Journal of Physical Chemistry B*, vol. 109, no. 23, pp. 11622–11633, 2005.
- [2] M. J. Janik, S. A. Wasileski, C. D. Taylor, and M. Neurock, “First principles simulation of the active sites and reaction environment in electrocatalysis,” in *Fuel Cell Catalysis: A Surface Science Approach*, M. Koper, Ed., John Wiley and Sons, 2008.
- [3] M. Koper, Ed., *Fuel Cell Catalysis: A Surface Science Approach*, John Wiley and Sons, 2008.
- [4] A. Wieckowski and J. K. Nørskov, *Fuel Cell Science: Theory, Fundamentals, and Bio-Catalysis*, John Wiley and Sons, 2010.
- [5] R. A. van Santen and M. Neurock, “Theory of surface chemical reactivity,” in *Handbook of Catalysis*, H. K. G. Ertl and J. Weitcamp, Eds., pp. 942–958, Springer, 1997.
- [6] R. A. van Santen and M. Neurock, *Molecular Heterogeneous Catalysis: A Mechanistic and Computational Approach*, VCH-Wiley, 2006.
- [7] R. A. van Santen, M. Neurock, and S. G. Shetty, “Reactivity theory of transition-metal surfaces: a brønsted-evans-polanyi linear activation energy-free-energy analysis,” *Chemical Reviews*, vol. 110, no. 4, pp. 2005–2048, 2010.
- [8] T. Bligaard and J. K. Nørskov, “Ligand effects in heterogeneous catalysis and electrochemistry,” *Electrochimica Acta*, vol. 52, no. 18, pp. 5512–5516, 2007.
- [9] J. Greeley, T. F. Jaramillo, J. Bonde, I. B. Chorkendorff, and J. K. Nørskov, “Computational high-throughput screening of electrocatalytic materials for hydrogen evolution,” *Nature Materials*, vol. 5, no. 11, pp. 909–913, 2006.
- [10] P. Liu, A. Logadottir, and J. K. Nørskov, “Modeling the electro-oxidation of CO and H₂/CO on Pt, Ru, PtRu and Pt₃Sn,” *Electrochimica Acta*, vol. 48, no. 25-26, pp. 3731–3742, 2003.
- [11] J. K. Nørskov, J. Rossmeisl, A. Logadottir et al., “Origin of the overpotential for oxygen reduction at a fuel-cell cathode,” *Journal of Physical Chemistry B*, vol. 108, no. 46, pp. 17886–17892, 2004.
- [12] J. Rossmeisl, J. K. Nørskov, C. D. Taylor, M. J. Janik, and M. Neurock, “Calculated phase diagrams for the electrochemical oxidation and reduction of water over Pt(111),” *Journal of Physical Chemistry B*, vol. 110, no. 43, pp. 21833–21839, 2006.
- [13] A. B. Anderson, “O₂ reduction and CO oxidation at the Pt-electrolyte interface. The role of H₂O and OH adsorption

- bond strengths,” *Electrochimica Acta*, vol. 47, no. 22-23, pp. 3759–3763, 2002.
- [14] A. B. Anderson and Y. Cai, “Calculation of the Tafel plot for H₂ oxidation on Pt(100) from potential-dependent activation energies,” *Journal of Physical Chemistry B*, vol. 108, no. 52, pp. 19917–19920, 2004.
- [15] A. B. Anderson, J. Roques, S. Mukerjee, V. S. Murthi, N. M. Markovic, and V. Stamenkovic, “Activation energies for oxygen reduction on platinum alloys: theory and experiment,” *Journal of Physical Chemistry B*, vol. 109, no. 3, pp. 1198–1203, 2005.
- [16] J. Roques and A. B. Anderson, “Electrode potential-dependent stages in OH_{ads} formation on the Pt₃Cr alloy (111) surface,” *Journal of the Electrochemical Society*, vol. 151, no. 11, pp. E340–E347, 2004.
- [17] J. Roques, A. B. Anderson, V. S. Murthi, and S. Mukerjee, “Potential shift for OH(ads) formation on the Pt skin on Pt₃Co(111) electrodes in acid theory and experiment,” *Journal of the Electrochemical Society*, vol. 152, no. 6, pp. E193–E199, 2005.
- [18] R. A. Sidik and A. B. Anderson, “Density functional theory study of O₂ electroreduction when bonded to a Pt dual site,” *Journal of Electroanalytical Chemistry*, vol. 528, no. 1-2, pp. 69–76, 2002.
- [19] A. Lamm, H. Gasteiger, and W. Vielstich, Eds., *Fuel Cell Handbook, Vol. 2, Electrocatalysis*, Wiley-VCH, 2003.
- [20] T. D. Jarvi and E. M. Stuve, “Fundamental aspects of vacuum and electrocatalytic reactions of methanol and formic acid on platinum surfaces,” in *Electrocatalysis*, J. Lipkowski and P. N. Ross, Eds., Wiley-VCH, 1998.
- [21] G. Q. Lu, A. Lagutchev, D. D. Dlott, and A. Wieckowski, “Quantitative vibrational sum-frequency generation spectroscopy of thin layer electrochemistry: CO on a Pt electrode,” *Surface Science*, vol. 585, no. 1-2, pp. 3–16, 2005.
- [22] P. K. Babu, H. S. Kim, S. T. Kuk et al., “Activation of nanoparticle Pt-Ru fuel cell catalysts by heat treatment: A195Pt NMR and electrochemical study,” *Journal of Physical Chemistry B*, vol. 109, no. 36, pp. 17192–17196, 2005.
- [23] H. Yano, J. Inukai, H. Uchida et al., “Particle-size effect of nanoscale platinum catalysts in oxygen reduction reaction: an electrochemical and ¹⁹⁵Pt EC-NMR study,” *Physical Chemistry Chemical Physics*, vol. 8, no. 42, pp. 4932–4939, 2006.
- [24] T. Kobayashi, P. K. Babu, J. H. Chung, E. Oldfield, and A. Wieckowski, “Coverage dependence of CO surface diffusion on Pt nanoparticles: an EC-NMR study,” *Journal of Physical Chemistry C*, vol. 111, no. 19, pp. 7078–7083, 2007.
- [25] S. Maniguet, R. J. Mathew, and A. E. Russell, “EXAFS of carbon monoxide oxidation on supported Pt fuel cell electrocatalysts,” *Journal of Physical Chemistry B*, vol. 104, no. 9, pp. 1998–2004, 2000.
- [26] J. McBreen and S. Mukerjee, “In situ X-ray absorption studies of a Pt-Ru electrocatalyst,” *Journal of the Electrochemical Society*, vol. 142, no. 10, pp. 3399–3404, 1995.
- [27] F. J. Scott, C. Roth, and D. E. Ramaker, “Kinetics of CO poisoning in simulated reformat and effect of Ru island morphology on PtRu fuel cell catalysts as determined by operando X-ray absorption near edge spectroscopy,” *Journal of Physical Chemistry C*, vol. 111, no. 30, pp. 11403–11413, 2007.
- [28] F. J. Scott, S. Mukerjee, and D. E. Ramaker, “CO coverage/oxidation correlated with PtRu electrocatalyst particle morphology in 0.3 M methanol by in situ XAS,” *Journal of the Electrochemical Society*, vol. 154, no. 5, pp. A396–A406, 2007.
- [29] C. Roth, N. Benker, T. Buhrmester et al., “Determination of O[H] and CO coverage and adsorption sites on PtRu electrodes in an operating PEM fuel cell,” *Journal of the American Chemical Society*, vol. 127, no. 42, pp. 14607–14615, 2005.
- [30] G. Samjeske, A. Miki, S. Ye, and M. Osawa, “Mechanistic study of electrocatalytic oxidation of formic acid at platinum in acidic solution by time-resolved surface-enhanced infrared absorption spectroscopy,” *Journal of Physical Chemistry B*, vol. 110, no. 33, pp. 16559–16566, 2006.
- [31] G. Samjeske, A. Miki, and M. Osawa, “Electrocatalytic oxidation of formaldehyde on platinum under galvanostatic and potential sweep conditions studied by time-resolved surface-enhanced infrared spectroscopy,” *Journal of Physical Chemistry C*, vol. 111, no. 41, pp. 15074–15083, 2007.
- [32] A. B. Anderson, “Theory at the electrochemical interface: reversible potentials and potential-dependent activation energies,” *Electrochimica Acta*, vol. 48, no. 25-26, pp. 3743–3749, 2003.
- [33] A. B. Anderson, Y. Cai, R. A. Sidik, and D. B. Kang, “Advancements in the local reaction center electron transfer theory and the transition state structure in the first step of oxygen reduction over platinum,” *Journal of Electroanalytical Chemistry*, vol. 580, no. 1, pp. 17–22, 2005.
- [34] A. B. Anderson, N. M. Neshev, R. A. Sidik, and P. Shiller, “Mechanism for the electrooxidation of water to OH and O bonded to platinum: quantum chemical theory,” *Electrochimica Acta*, vol. 47, no. 18, pp. 2999–3008, 2002.
- [35] Y. Cai and A. B. Anderson, “The reversible hydrogen electrode: potential-dependent activation energies over platinum from quantum theory,” *Journal of Physical Chemistry B*, vol. 108, no. 28, pp. 9829–9833, 2004.
- [36] E. Santos, A. Lundin, K. Potting, P. Quaino, and W. Schmickler, “Model for the electrocatalysis of hydrogen evolution,” *Physical Review B*, vol. 79, no. 23, Article ID 235436, 2009.
- [37] E. Santos and W. Schmickler, “Electronic interactions decreasing the activation barrier for the hydrogen electrooxidation reaction,” *Electrochimica Acta*, vol. 53, no. 21, pp. 6149–6156, 2008.
- [38] F. Wilhelm, W. Schmickler, R. R. Nazmutdinov, and E. Spohr, “A model for proton transfer to metal electrodes,” *Journal of Physical Chemistry C*, vol. 112, no. 29, pp. 10814–10826, 2008.
- [39] J. S. Filhol and M. Neurock, “Elucidation of the electrochemical activation of water over Pd by first principles,” *Angewandte Chemie*, vol. 45, no. 3, pp. 403–406, 2006.
- [40] C. Taylor, R. G. Kelly, and M. Neurock, “First-principles calculations of the electrochemical reactions of water at an immersed Ni(111)/H₂O interface,” *Journal of the Electrochemical Society*, vol. 153, no. 12, pp. E207–E214, 2006.
- [41] C. D. Taylor and M. Neurock, “Theoretical insights into the structure and reactivity of the aqueous/metal interface,” *Current Opinion in Solid State and Materials Science*, vol. 9, no. 1-2, pp. 49–65, 2005.
- [42] C. D. Taylor, M. Neurock, and J. R. Scully, “First-principles investigation of the fundamental corrosion properties of a model Cu₃₈ nanoparticle and the (111), (113) surfaces,” *Journal of the Electrochemical Society*, vol. 155, no. 8, pp. C407–C414, 2008.
- [43] C. D. Taylor, S. A. Wasileski, J. S. Filhol, and M. Neurock, “First principles reaction modeling of the electrochemical interface: consideration and calculation of a tunable surface potential from atomic and electronic structure,” *Physical Review B*, vol. 73, no. 16, Article ID 165402, pp. 1–16, 2006.

- [44] M. Otani, I. Hamada, O. Sugino, Y. Morikawa, Y. Okamoto, and T. Ikeshoji, "Structure of the water/platinum interface—a first principles simulation under bias potential," *Physical Chemistry Chemical Physics*, vol. 10, no. 25, pp. 3609–3612, 2008.
- [45] M. Otani, I. Hamada, O. Sugino, Y. Morikawa, Y. Okamoto, and T. Ikeshoji, "Electrode dynamics from first principles," *Journal of the Physical Society of Japan*, vol. 77, no. 2, Article ID 024802, 2008.
- [46] R. Jinnouchi and A. B. Anderson, "Electronic structure calculations of liquid-solid interfaces: combination of density functional theory and modified Poisson-Boltzmann theory," *Physical Review B*, vol. 77, no. 24, Article ID 245417, 2008.
- [47] J. Rossmeis, E. Skulason, M. E. Bjorketun, V. Tripkovic, and J. K. Nørskov, "Modeling the electrified solid-liquid interface," *Chemical Physics Letters*, vol. 466, no. 1–3, pp. 68–71, 2008.
- [48] M. Neurock, W. Vielstich, H. A. Gasteiger, and H. Yokokawa, "First principles modeling for the electrooxidation of small molecules," in *Handbook of Fuel Cells*, W. Vielstich, H. A. Gasteiger, and H. Yokokawa, Eds., John Wiley and Sons, 2009.
- [49] G. Kresse and J. Furthmuller, "Efficiency of ab-initio total energy calculations for metals and semiconductors using a plane-wave basis set," *Computational Materials Science*, vol. 6, no. 1, pp. 15–50, 1996.
- [50] G. Kresse and J. Furthmuller, "Efficient iterative schemes for ab initio total-energy calculations using a plane-wave basis set," *Physical Review B*, vol. 54, no. 16, pp. 11169–11186, 1996.
- [51] G. Henkelman and H. Jónsson, "Improved tangent estimate in the nudged elastic band method for finding minimum energy paths and saddle points," *Journal of Chemical Physics*, vol. 113, no. 22, pp. 9978–9985, 2000.
- [52] G. Henkelman, B. P. Uberuaga, and H. Jónsson, "Climbing image nudged elastic band method for finding saddle points and minimum energy paths," *Journal of Chemical Physics*, vol. 113, no. 22, pp. 9901–9904, 2000.
- [53] G. Henkelman and H. Jónsson, "A dimer method for finding saddle points on high dimensional potential surfaces using only first derivatives," *Journal of Chemical Physics*, vol. 111, no. 15, pp. 7010–7022, 1999.
- [54] R. R. Davda, J. W. Shabaker, G. W. Huber, R. D. Cortright, and J. A. Dumesic, "Aqueous-phase reforming of ethylene glycol on silica-supported metal catalysts," *Applied Catalysis B*, vol. 43, no. 1, pp. 13–26, 2003.
- [55] P. Gallezot, N. Nicolaus, G. Fleche, and A. Perrard, "Glucose hydrogenation on ruthenium catalysts in a trickle-bed reactor," *Journal of Catalysis*, vol. 180, no. 1, pp. 51–55, 1998.
- [56] D. K. Sohounloue, C. Montassier, and J. Barbier, "Catalytic hydrogenolysis of sorbitol," *Reaction Kinetics and Catalysis Letters*, vol. 22, no. 3–4, pp. 391–397, 1983.
- [57] M. B. Valenzuela, C. W. Jones, and P. K. Agrawal, "Batch aqueous-phase reforming of woody biomass," *Energy and Fuels*, vol. 20, no. 4, pp. 1744–1752, 2006.
- [58] N. Dimitratos, C. Messi, F. Porta, L. Prati, and A. Villa, "Investigation on the behaviour of Pt(0)/carbon and Pt(0), Au(0)/carbon catalysts employed in the oxidation of glycerol with molecular oxygen in water," *Journal of Molecular Catalysis A*, vol. 256, no. 1–2, pp. 21–28, 2006.
- [59] R. D. Cortright, R. R. Davda, and J. A. Dumesic, "Hydrogen from catalytic reforming of biomass-derived hydrocarbons in liquid water," *Nature*, vol. 418, no. 6901, pp. 964–967, 2002.
- [60] J. W. Shabaker, G. W. Huber, R. R. Davda, R. D. Cortright, and J. A. Dumesic, "Aqueous-phase reforming of ethylene glycol over supported platinum catalysts," *Catalysis Letters*, vol. 88, no. 1–2, pp. 1–8, 2003.
- [61] E. P. Maris, W. C. Ketchie, V. Oleshko, and R. J. Davis, "Metal particle growth during glucose hydrogenation over Ru/SiO₂ evaluated by X-ray absorption spectroscopy and electron microscopy," *Journal of Physical Chemistry B*, vol. 110, no. 15, pp. 7869–7876, 2006.
- [62] E. P. Maris, W. C. Ketchie, M. Murayama, and R. J. Davis, "Glycerol hydrogenolysis on carbon-supported PtRu and AuRu bimetallic catalysts," *Journal of Catalysis*, vol. 251, no. 2, pp. 281–294, 2007.
- [63] W. C. Ketchie, E. P. Maris, and R. J. Davis, "In-situ X-ray absorption spectroscopy of supported Ru catalysts in the aqueous phase," *Chemistry of Materials*, vol. 19, no. 14, pp. 3406–3411, 2007.
- [64] M. Haruta, T. Kobayashi, H. Sano, and N. Yamada, "Novel gold catalysts for the oxidation of carbon monoxide at a temperature far below 0.DEG.C," *Chemistry Letters*, vol. 16, no. 2, pp. 405–408, 1987.
- [65] M. Haruta, N. Yamada, T. Kobayashi, and S. Iijima, "Gold catalysts prepared by coprecipitation for low-temperature oxidation of hydrogen and of carbon monoxide," *Journal of Catalysis*, vol. 115, no. 2, pp. 301–309, 1989.
- [66] G. C. Bond, C. Louis, and D. T. Thompson, *Catalysis by Gold*, Imperial College Press, London, UK, 2006.
- [67] R. Meyer, C. Lemire, S. K. Shaikhutdinov, and H. Freund, "Surface chemistry of catalysis by gold," *Gold Bulletin*, vol. 37, no. 1–2, pp. 72–124, 2004.
- [68] M. Valden, X. Lai, and D. W. Goodman, "Onset of catalytic activity of gold clusters on titania with the appearance of nonmetallic properties," *Science*, vol. 281, no. 5383, pp. 1647–1650, 1998.
- [69] N. Lopez, T. V. W. Janssens, B. S. Clausen et al., "On the origin of the catalytic activity of gold nanoparticles for low-temperature CO oxidation," *Journal of Catalysis*, vol. 223, no. 1, pp. 232–235, 2004.
- [70] Q. Fu, H. Saltsburg, and M. Flytzani-Stephanopoulos, "Active nonmetallic Au and Pt species on ceria-based water-gas shift catalysts," *Science*, vol. 301, no. 5635, pp. 935–938, 2003.
- [71] J. Guzman and B. C. Gates, "Simultaneous presence of cationic and reduced gold in functioning MgO-supported CO oxidation catalysts: evidence from X-ray absorption spectroscopy," *Journal of Physical Chemistry B*, vol. 106, no. 31, pp. 7659–7665, 2002.
- [72] L. M. Molina and B. Hammer, "Active role of oxide support during CO oxidation at Au/MgO," *Physical Review Letters*, vol. 90, no. 20, 4 pages, 2003.
- [73] C. K. Costello, M. C. Kung, H. S. Oh, Y. Wang, and H. H. Kung, "Nature of the active site for CO oxidation on highly active Au/ γ -Al₂O₃," *Applied Catalysis A*, vol. 232, no. 1–2, pp. 159–168, 2002.
- [74] H. H. Kung, M. C. Kung, and C. K. Costello, "Supported Au catalysts for low temperature CO oxidation," *Journal of Catalysis*, vol. 216, no. 1–2, pp. 425–432, 2003.
- [75] W. B. Kim, T. Voitl, G. J. Rodriguez-Rivera, and J. A. Dumesic, "Powering fuel cells with CO via aqueous polyoxometalates and gold catalysts," *Science*, vol. 305, no. 5688, pp. 1280–1283, 2004.
- [76] M. A. Sanchez-Castillo, C. Couto, W. B. Kim, and J. A. Dumesic, "Gold-nanotube membranes for the oxidation of CO at gas-water interfaces," *Angewandte Chemie*, vol. 43, no. 9, pp. 1140–1142, 2004.

- [77] W. C. Ketchie, Y. L. Fang, M. S. Wong, M. Murayama, and R. J. Davis, "Influence of gold particle size on the aqueous-phase oxidation of carbon monoxide and glycerol," *Journal of Catalysis*, vol. 250, no. 1, pp. 94–101, 2007.
- [78] W. C. Ketchie, M. Murayama, and R. J. Davis, "Promotional effect of hydroxyl on the aqueous phase oxidation of carbon monoxide and glycerol over supported Au catalysts," *Topics in Catalysis*, vol. 44, no. 1-2, pp. 307–317, 2007.
- [79] N. M. Marković and P. N. Ross, "Surface science studies of model fuel cell electrocatalysts," *Surface Science Reports*, vol. 45, no. 4–6, pp. 117–229, 2002.
- [80] F. B. de Mongeot, M. Scherer, B. Gleich, E. Kopatzki, and R. J. Behm, "CO adsorption and oxidation on bimetallic Pt/Ru(0001) surfaces—a combined STM and TPD/TPR study," *Surface Science*, vol. 411, no. 3, pp. 249–262, 1998.
- [81] H. A. Gasteiger, N. Markovic, P. N. Ross, and E. J. Cairns, "Electro-oxidation of small organic molecules on well-characterized PtRu alloys," *Electrochimica Acta*, vol. 39, no. 11-12, pp. 1825–1832, 1994.
- [82] N. M. Markovic, H. A. Gasteiger, P. N. Ross, X. Jiang, I. Villegas, and M. J. Weaver, "Electro-oxidation mechanisms of methanol and formic acid on Pt-Ru alloy surfaces," *Electrochimica Acta*, vol. 40, no. 1, pp. 91–98, 1995.
- [83] S. Desai and M. Neurock, "A first principles analysis of CO oxidation over Pt and Pt 66.7%Ru33.3% (111) surfaces," *Electrochimica Acta*, vol. 48, no. 25-26, pp. 3759–3773, 2003.
- [84] S. K. Desai and M. Neurock, "First-principles study of the role of solvent in the dissociation of water over a Pt-Ru alloy," *Physical Review B*, vol. 68, no. 7, Article ID 075420, pp. 754201–754207, 2003.
- [85] B. E. Hayden, D. Pletcher, M. E. Rendall, and J. P. Suchsland, "CO oxidation on gold in acidic environments: particle size and substrate effects," *Journal of Physical Chemistry C*, vol. 111, no. 45, pp. 17044–17051, 2007.
- [86] B. E. Hayden, D. Pletcher, and J. P. Suchsland, "Enhanced activity for electrocatalytic oxidation of carbon monoxide on titania-supported gold nanoparticles," *Angewandte Chemie*, vol. 46, no. 19, pp. 3530–3532, 2007.
- [87] J. L. Roberts and D. T. Sawyer, "Electrochemical oxidation of carbon monoxide at gold electrodes," *Electrochimica Acta*, vol. 10, no. 10, pp. 989–1000, 1965.
- [88] P. Rodriguez, N. Garcia-Araez, and M. T. M. Koper, "Self-promotion mechanism for CO electrooxidation on gold," *Physical Chemistry Chemical Physics*, vol. 12, no. 32, pp. 9373–9380, 2010.
- [89] P. Rodriguez, N. Garcia-Araez, A. Koverga, S. Frank, and M. T. M. Koper, "CO electrooxidation on gold in alkaline media: a combined electrochemical, spectroscopic, and DFT study," *Langmuir*, vol. 26, no. 14, pp. 12425–12432, 2010.
- [90] I. X. Green, W. Tang, M. Neurock, and J. T. Yates Jr., "Spectroscopic observation of dual catalytic sites during oxidation of CO on a Au/TiO₂ catalyst," *Science*, vol. 333, no. 6043, pp. 736–739, 2011.
- [91] M. Neurock, D. Hibbitts, and J. A. Dumesic, "Mechanistic insights into the role of water on the oxidation of CO over Au," to be submitted, 2011.
- [92] N. Dimitratos, J. A. Lopez-Sanchez, J. M. Anthonykutty et al., "Oxidation of glycerol using gold-palladium alloy-supported nanocrystals," *Physical Chemistry Chemical Physics*, vol. 11, no. 25, pp. 4952–4961, 2009.
- [93] N. Dimitratos, J. A. Lopez-Sanchez, S. Meenakshisundaram et al., "Selective formation of lactate by oxidation of 1,2-propanediol using gold palladium alloy supported nanocrystals," *Green Chemistry*, vol. 11, no. 8, pp. 1209–1216, 2009.
- [94] M. D. Hughes, Y. J. Xu, P. Jenkins et al., "Tunable gold catalysts for selective hydrocarbon oxidation under mild conditions," *Nature*, vol. 437, no. 7062, pp. 1132–1135, 2005.
- [95] G. J. Hutchings, S. Carrettin, P. Landon et al., "New approaches to designing selective oxidation catalysts: Au/C a versatile catalyst," *Topics in Catalysis*, vol. 38, no. 4, pp. 223–230, 2006.
- [96] M. Sankar, N. Dimitratos, D. W. Knight et al., "Oxidation of glycerol to glycolate by using supported gold and palladium nanoparticles," *ChemSusChem*, vol. 2, no. 12, pp. 1145–1151, 2009.
- [97] B. N. Zope and R. J. Davis, "Influence of reactor configuration on the selective oxidation of glycerol over Au/TiO₂," *Topics in Catalysis*, vol. 52, no. 3, pp. 269–277, 2009.
- [98] B. N. Zope, D. D. Hibbitts, M. Neurock, and R. J. Davis, "Reactivity of the gold/water interface during selective oxidation catalysis," *Science*, vol. 330, no. 6000, pp. 74–78, 2010.
- [99] J. S. Spendelow, P. K. Babu, and A. Wieckowski, "Electrocatalytic oxidation of carbon monoxide and methanol on platinum surfaces decorated with ruthenium," *Current Opinion in Solid State and Materials Science*, vol. 9, no. 1-2, pp. 37–48, 2005.
- [100] J. S. Spendelow and A. Wieckowski, "Electrocatalysis of oxygen reduction and small alcohol oxidation in alkaline media," *Physical Chemistry Chemical Physics*, vol. 9, no. 21, pp. 2654–2675, 2007.
- [101] Z. Borkowska, A. Tymosiak-Zielinska, and G. Shul, "Electrooxidation of methanol on polycrystalline and single crystal gold electrodes," *Electrochimica Acta*, vol. 49, no. 8, pp. 1209–1220, 2004.
- [102] P. Parpot, A. P. Bettencourt, A. M. Carvalho, and E. M. Belgsir, "Biomass conversion: attempted electrooxidation of lignin for vanillin production," *Journal of Applied Electrochemistry*, vol. 30, no. 6, pp. 727–731, 2000.
- [103] P. Parpot, A. P. Bettencourt, G. Chamoulaud, K. B. Kokoh, and E. M. Belgsir, "Electrochemical investigations of the oxidation-reduction of furfural in aqueous medium—application to electrosynthesis," *Electrochimica Acta*, vol. 49, no. 3, pp. 397–403, 2004.
- [104] P. Parpot, N. Nunes, and A. P. Bettencourt, "Electrocatalytic oxidation of monosaccharides on gold electrode in alkaline medium: structure-reactivity relationship," *Journal of Electroanalytical Chemistry*, vol. 596, no. 1, pp. 65–73, 2006.
- [105] P. Parpot, S. G. Pires, and A. P. Bettencourt, "Electrocatalytic oxidation of D-galactose in alkaline medium," *Journal of Electroanalytical Chemistry*, vol. 566, no. 2, pp. 401–408, 2004.
- [106] P. Parpot, P. R. B. Santos, and A. P. Bettencourt, "Electrooxidation of d-mannose on platinum, gold and nickel electrodes in aqueous medium," *Journal of Electroanalytical Chemistry*, vol. 610, no. 2, pp. 154–162, 2007.
- [107] S. H. Yan, S. C. Zhang, Y. Lin, and G. R. Liu, "Electrocatalytic performance of gold nanoparticles supported on activated carbon for methanol oxidation in alkaline solution," *Journal of Physical Chemistry C*, vol. 115, no. 14, pp. 6986–6993, 2011.
- [108] P. A. Christensen, A. Hamnett, and D. Linares-Moya, "Oxygen reduction and fuel oxidation in alkaline solution," *Physical Chemistry Chemical Physics*, vol. 13, no. 12, pp. 5206–5214, 2011.
- [109] D. Kardash, C. Korzeniewski, and N. Markovic, "Effects of thermal activation on the oxidation pathways of methanol at bulk Pt-Ru alloy electrodes," *Journal of Electroanalytical Chemistry*, vol. 500, no. 1-2, pp. 518–523, 2001.

- [110] A. V. Tripkovi, K. D. Popovi, B. N. Grgur, B. Blizanac, P. N. Ross, and N. M. Markovi, "Methanol electrooxidation on supported Pt and PtRu catalysts in acid and alkaline solutions," *Electrochimica Acta*, vol. 47, no. 22-23, pp. 3707–3714, 2002.
- [111] F. Colmati, G. Tremiliosi-Filho, E. R. Gonzalez, A. Berna, E. Herrero, and J. M. Feliu, "The role of the steps in the cleavage of the C-C bond during ethanol oxidation on platinum electrodes," *Physical Chemistry Chemical Physics*, vol. 11, no. 40, pp. 9114–9123, 2009.
- [112] F. Colmati, G. Tremiliosi-Filho, E. R. Gonzalez, A. Berna, E. Herrero, and J. M. Feliu, "Surface structure effects on the electrochemical oxidation of ethanol on platinum single crystal electrodes," *Faraday Discussions*, vol. 140, pp. 379–397, 2008.
- [113] V. Del Colle, A. Berna, G. Tremiliosi-Filho, E. Herrero, and J. M. Feliu, "Ethanol electrooxidation onto stepped surfaces modified by Ru deposition: electrochemical and spectroscopic studies," *Physical Chemistry Chemical Physics*, vol. 10, no. 25, pp. 3766–3773, 2008.
- [114] J. Souza-Garcia, E. Herrero, and J. M. Feliu, "Breaking the C-C bond in the ethanol oxidation reaction on platinum electrodes: effect of steps and ruthenium adatoms," *ChemPhysChem*, vol. 11, no. 7, pp. 1391–1394, 2010.
- [115] S. C. S. Lai, S. E. F. Kleijn, F. T. Z. Ozturk et al., "Effects of electrolyte pH and composition on the ethanol electro-oxidation reaction," *Catalysis Today*, vol. 154, no. 1-2, pp. 92–104, 2010.
- [116] S. C. S. Lai, S. E. F. Kleyn, V. Rosca, and M. T. M. Koper, "Mechanism of the dissociation and electrooxidation of ethanol and acetaldehyde on platinum as studied by SERS," *Journal of Physical Chemistry C*, vol. 112, no. 48, pp. 19080–19087, 2008.
- [117] S. C. S. Lai and M. T. M. Koper, "Electro-oxidation of ethanol and acetaldehyde on platinum single-crystal electrodes," *Faraday Discussions*, vol. 140, pp. 399–416, 2008.
- [118] S. C. S. Lai and M. T. M. Koper, "Ethanol electro-oxidation on platinum in alkaline media," *Physical Chemistry Chemical Physics*, vol. 11, no. 44, pp. 10446–10456, 2009.
- [119] S. C. S. Lai and M. T. M. Koper, "The influence of surface structure on selectivity in the ethanol electro-oxidation reaction on platinum," *Journal of Physical Chemistry Letters*, vol. 1, no. 7, pp. 1122–1125, 2010.
- [120] M. Neurock, M. Janik, and A. Wieckowski, "A first principles comparison of the mechanism and site requirements for the electrocatalytic oxidation of methanol and formic acid over Pt," *Faraday Discussions*, vol. 140, no. 1, pp. 363–378, 2008.
- [121] S. R. Brankovic, J. X. Wang, Y. Zhu, R. Sabatini, J. McBreen, and R. R. Adzic, "Electrosorption and catalytic properties of bare and Pt modified single crystal and nanostructured Ru surfaces," *Journal of Electroanalytical Chemistry*, vol. 524-525, pp. 231–241, 2002.
- [122] T. Iwasita, "Electrocatalysis of methanol oxidation," *Electrochimica Acta*, vol. 47, no. 22-23, pp. 3663–3674, 2002.
- [123] W. C. Ketchie, M. Murayama, and R. J. Davis, "Selective oxidation of glycerol over carbon-supported AuPd catalysts," *Journal of Catalysis*, vol. 250, no. 2, pp. 264–273, 2007.
- [124] A. T. Governo, L. Proenca, P. Parpot, M. I. S. Lopes, and I. T. E. Fonseca, "Electro-oxidation of D-xylose on platinum and gold electrodes in alkaline medium," *Electrochimica Acta*, vol. 49, no. 9-10, pp. 1535–1545, 2004.
- [125] Y. Kwon and M. T. M. Koper, "Combining voltammetry with HPLC: application to electro-oxidation of glycerol," *Analytical Chemistry*, vol. 82, no. 13, pp. 5420–5424, 2010.
- [126] Z. W. Liu, F. Peng, H. J. Wang, H. Yu, W. X. Zheng, and J. A. Yang, "Phosphorus-doped graphite layers with high electrocatalytic activity for the O₂ reduction in an alkaline medium," *Angewandte Chemie*, vol. 50, no. 14, pp. 3257–3261, 2011.
- [127] A. C. Chen and J. Lipkowsky, "Electrochemical and spectroscopic studies of hydroxide adsorption at the Au(111) electrode," *Journal of Physical Chemistry B*, vol. 103, no. 4, pp. 682–691, 1999.
- [128] S. Desai, "Theoretical investigation of solution effects on metal catalyzed hydrogenation and oxidation processes," in *Department of Chemical Engineering*, University of Virginia, 2002.
- [129] F. T. Wagner and T. E. Moylan, "Generation of surface hydronium from water and hydrogen coadsorbed on Pt(111)," *Surface Science*, vol. 206, no. 1-2, pp. 187–202, 1988.
- [130] N. Kizhakevariam and E. M. Stuve, "Coadsorption of water and hydrogen on Pt(100): formation of adsorbed hydronium ions," *Surface Science*, vol. 275, no. 3, pp. 223–236, 1992.

Review Article

Platinum Monolayer Electrocatalysts for the Oxygen Reduction Reaction: Improvements Induced by Surface and Subsurface Modifications of Cores

Yun Cai and Radoslav R. Adzic

Department of Chemistry, Brookhaven National Laboratory, Upton, NY 11973, USA

Correspondence should be addressed to Radoslav R. Adzic, adzic@bnl.gov

Received 18 May 2011; Accepted 22 August 2011

Academic Editor: Wolfgang Schmickler

Copyright © 2011 Y. Cai and R. R. Adzic. This is an open access article distributed under the Creative Commons Attribution License, which permits unrestricted use, distribution, and reproduction in any medium, provided the original work is properly cited.

This paper demonstrates that the ORR activity of Pt_{ML} electrocatalysts can be further improved by the modification of surface and subsurface of the core materials. The removal of surface low-coordination sites, generation (via addition or segregation) of an interlayer between Pt_{ML} and the core, or the introduction of a second metal component to the subsurface layer of the core can further improve the ORR activity and/or stability of Pt_{ML} electrocatalysts. These modifications generate the alternation of the interactions between the substrate and the Pt_{ML}, involving the changes on both electronic (ligand) and geometric (strain) properties of the substrates. The improvements resulted from the application of these approaches provide a new perspective to designing of the new generation Pt_{ML} electrocatalysts.

1. Introduction

Fuel cells are considered to be one of the most promising clean energy technologies that can help resolve the energy crisis and problems of environmental pollution. However, the promise of their widespread application is seriously hindered by the necessarily high content of Pt in the cathode catalysts and the slow kinetics of oxygen reduction reaction on the best available Pt-based catalysts. New catalysts are needed that reduce considerably the Pt content while affording the possibility of enhanced catalytic activity. In recent years, we developed a new approach for designing and synthesizing electrocatalysts that significantly reduce the Pt content and surpass the oxygen reduction reaction (ORR) activity of the state-of-the-art carbon-supported Pt electrocatalysts [1]. These electrocatalysts consist of a monolayer of Pt on carbon-supported metal or metal-alloy nanoparticles and has the highest utilization of Pt since almost every Pt atom are present on the surface and participate in the electrocatalytic reactions. These electrocatalysts are referred as platinum monolayer (Pt_{ML}) electrocatalysts.

The Pt monolayer deposition process involves the galvanic displacement of an underpotentially deposited Cu monolayer on a suitable substrate by Pt [2].

Since the first development, Pt_{ML} electrocatalysts with various core materials were designed and synthesized for assorted reactions in fuel-cell applications [1, 3–10]. Many of them exhibit excellent activities and stabilities. The interaction between the Pt monolayer and the substrate material has been demonstrated to induce a synergistic effect for ORR kinetics [6, 11–13]. When Pt atoms deposit on a foreign metal, due to the difference in atomic radius, the Pt surface will undergo compressive or tensile strain. As illustrated in Figure 1 [1], Pt atoms deposited on a Ru substrate would have a large compressive strain, but they would have only a small compressive strain on Pd and a tensile strain when deposited on Au. Santos et al. also observed such strain effect and demonstrated a strong correlation between the strain and electrocatalytic activities [14]. D-band center shift induced by the surface strain has been demonstrated to be a major factor determining the catalysts' activity [15]. Moreover, electronic (ligand) effect from the electronic

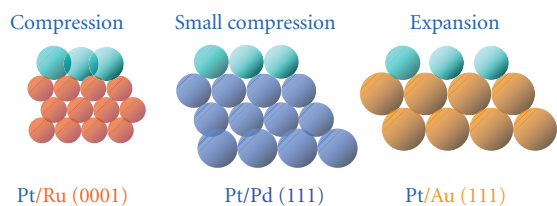


FIGURE 1: Models of pseudomorphic monolayers of Pt on three different substrates inducing compressive strain (Ru(0001) and Pd(111)) and expansive strain (Au(111)) [1].

coupling between Pt_{ML} and its supporting substrate play an additional role in determining the catalytic activity [16]. Density functional theory (DFT) calculations have shown that the binding energies and reactivity of small adsorbates have a great correlation with the position of d-band center on strained surfaces and metal overlayers [17, 18]. The interaction with the proper substrate can also decrease the oxidation of Pt monolayer and thus enhance the stability of the catalyst.

In our earlier study (Figure 2) [6], we demonstrated that the electrocatalytic activity for ORR of Pt monolayer on six different single crystal surfaces has a volcano-type dependence on the position of their d-band center from DFT calculations. On the top of the “volcano” plot is the Pt monolayer on a Pd(111) surface, that is, the most active electrocatalyst among six Pt monolayer-substrate couples, plus the single Pt(111) surface. Our experiments on various Pt monolayer nanoparticles also demonstrated that the variation of the core materials significantly affect the performance of the catalyst [1, 3–10]. Among the Pt_{ML} electrocatalysts we studied for the ORR, the palladium and palladium alloy cores outperform the rest in terms of both activity and stability [6, 19].

Several unique features of Pt_{ML} electrocatalysts open various possibilities for designing electrocatalysts with specific catalytic properties by choosing appropriate substrates. The strong dependence of the catalytic activity on the interaction between Pt monolayer and its substrate suggests that the electrocatalytic activity of Pt monolayer catalysts may be further improved via the modification of substrate materials. Since palladium and palladium alloy are the best candidates as a substrate to support Pt_{ML} , they will be our major focus in the efforts of achieving further enhanced activity and stability. In the ORR kinetics, the reaction rate is either limited by the dissociation of O_2 or the protonation of O_2 for metal surface that binds oxygen too weakly, or by the removal of adsorbed O and OH species if the metal binds oxygen too strong [21]. In the case of Pd, the oxygen binding energy is still slightly higher than the optimum value for the ORR kinetics [16], therefore in the design of the new generation Pt_{ML} electrocatalysts, we are targeting at fine-tuning the core materials to further weaken the oxygen binding on Pd substrate. In this review, we will describe several examples demonstrating the improvements of the Pt monolayer electrocatalysts for the ORR via the modifications of surface and subsurface of the core materials.

2. Direct Modification of the Surface of the Core [22]

Although the Pd(111) substrate for Pt monolayer has been demonstrated possessing an oxygen binding energy close to the optimum value, the nanoparticle Pd, however, exhibits much more difficulty in the removing of OH species due to the existence of considerable amount of low-coordination sites, edges, defects, adatoms, and so forth, which bind oxygen much stronger than that on terrace sites [23]. To obtain a smoother Pd nanoparticle surface, we developed a strategy, referred to as bromide treatment, to successfully remove significant amount of low-coordination sites on Pd/C and Pd_3Co/C and produce more (111) facets while maintaining the particle size.

The schematic in Figure 3 illustrates how the bromide solution removes the atoms on low-coordination sites during the potential cycles. In brief, the process starts from the chemisorption of a bromine layer in an alkaline solution, followed by the reductive desorption of bromine. After immersing the electrode in the bromide-containing solution, Br^- immediately is adsorbed on the surface, preferentially on the low-coordination sites, since the atoms on those sites bind with Br more strongly than those on terrace sites. In the cathodic scan, the reductive desorption of the bromine triggers the migration of low-coordinated Pd to terrace sites to minimize the total surface-free energy. Moreover, the reduction of Br to Br^- introduces a positive charge in the adjacent Pd, and the low-coordinated atoms have a looser structure than the high-coordinated ones. Hence, it is likely that the low-coordinated Pd forms a Pd- Br_2 pair in solution, that is, redeposited onto the surface in the following anodic scan, accompanied by the oxidative adsorption of bromide. Meanwhile, during the cycling, the adsorbed bromine layer undergoes rearrangement to attain the stable adlayer structure on a given surface, for example, $(\sqrt{3} \times \sqrt{3}) R30^\circ$ -Br on Pd(111), (2×2) -Br on Pd(100) [24]. Therefore, during this Br-rearrangement on the surface, the adsorbed-Br may draw the dangling atoms to fill the defect sites to form a large terrace patches containing an ordered Br-adlayer if the original terrace size is large enough to stabilize it.

Figure 4 shows the TEM images of palladium nanoparticles before and after bromide treatment. Various shapes of particles with obtruding edges are present in the commercial E-TEK sample. In contrast, the Br-treated Pd/C nanoparticles are rounded, and their size distribution is narrow.

The formation of a well-ordered 2D metal overlayer via UPD is known to depend on the substrate’s crystallographic orientation and density of imperfection [25]. The less the amount of imperfections at the surface the better the formation of more ordered commensurate 2D phases is, provided that the atomic sizes are not too dissimilar. In this case, more Pt(111) 2D patches instead of 3D clusters would form on the bromide-treated surface, which in turn, should benefit the oxygen-reduction reaction.

Figure 5 shows the polarization curves for the ORR. The sample with Pt_{ML} on Br-treated-Pd/C nanoparticles shows significant enhancement of kinetics of the ORR, compared

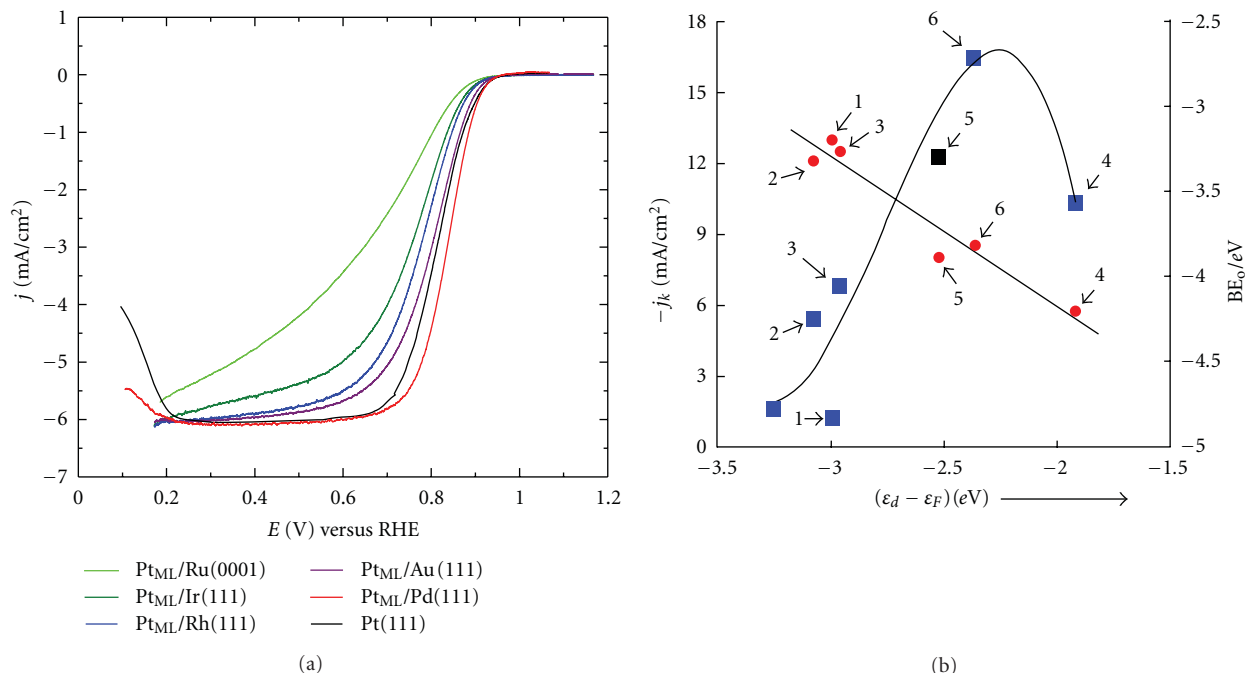


FIGURE 2: (a) Polarization curves for O₂ reduction on platinum monolayers (Pt_{ML}) on Ru(0001), Ir(111), Rh(111), Au(111), and Pd(111) in a 0.1 M HClO₄ solution on a disk electrode. The curve for Pt(111) is taken from [19, 20] and included for comparison. The rotation rate is 1600 rpm, and the sweep rate is 20 mV s⁻¹ (50 mV s⁻¹ for Pt(111)); j = current density, RHE = reversible hydrogen electrode [6]. (b) Kinetic currents (j_K , square symbols) at 0.8 V for O₂ reduction on the platinum monolayers supported on different single-crystal surfaces in a 0.1 M HClO₄ solution and calculated binding energies of atomic oxygen (BE_o , filled circles) as functions of calculated d-band center ($\epsilon_d - \epsilon_F$); relative to the Fermi level) of the respective clean platinum monolayers. The current data for Pt(111) is taken from [19, 20] and included for comparison. Labels: (1) Pt_{ML}/Ru(0001), (2) Pt_{ML}/Ir(111), (3) Pt_{ML}/Rh(111), (4) Pt_{ML}/Au(111), (5) Pt(111), and (6) Pt_{ML}/Pd(111) [6].

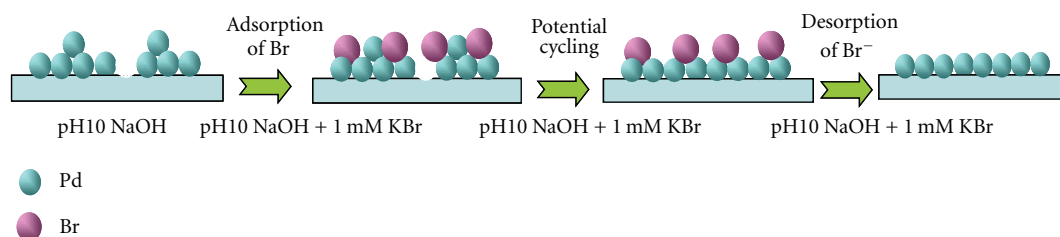


FIGURE 3: Illustration of the removal of surface low-coordination sites via the oxidative adsorption and reductive desorption of a bromine layer [22].

with the untreated nanoparticles, especially at potentials more negative than the half-wave potential (marked by a circle), the so-called combined diffusion-kinetic control region. In this region, the adsorption and dissociation of molecular oxygen competes with strongly adsorbed hydroxyl species (OH_{ads}) for the same sites [20, 23, 26]. Furthermore, OH_{ads} does not only block the active sites on Pt, but also changes the adsorption energy of intermediates adjacent to it formed during the reaction [20]. On a smooth surface, OH binding is less strong with respect to that on edge sites, and thus, the inhibition of the ORR kinetics decreases. We summarize the corresponding mass activity and specific activity for the ORR in the inset of Figure 5; 0.25-fold and 0.5-fold enhancements were found, respectively.

2.1. Br-Treatment of Pd₃Co/C. The oxygen-reduction reaction on Pt_{ML}/Pd₃Co/C attained a Pt mass activity 2~3-fold that of commercial Pt/C [7]. However, its poor stability due to the dissolution of Co hampered its industrial applications. Because the surface Co leaches during the reaction, more low-coordination sites are generated, thereby accelerating further dissolution of the Co, and degrading the catalyst. Our bromide-treatments of Pd/C nanoparticles demonstrated an excellent method of removing the low-coordination sites by having a bromine-adlayer and the resulting advantages for the ORR.

Figure 6 shows the morphologies of the original Pd₃Co/C nanoparticles, and of Pt_{ML} on Pd₃Co/C after the Br-treatment. The particles in the original Pd₃Co/C have average

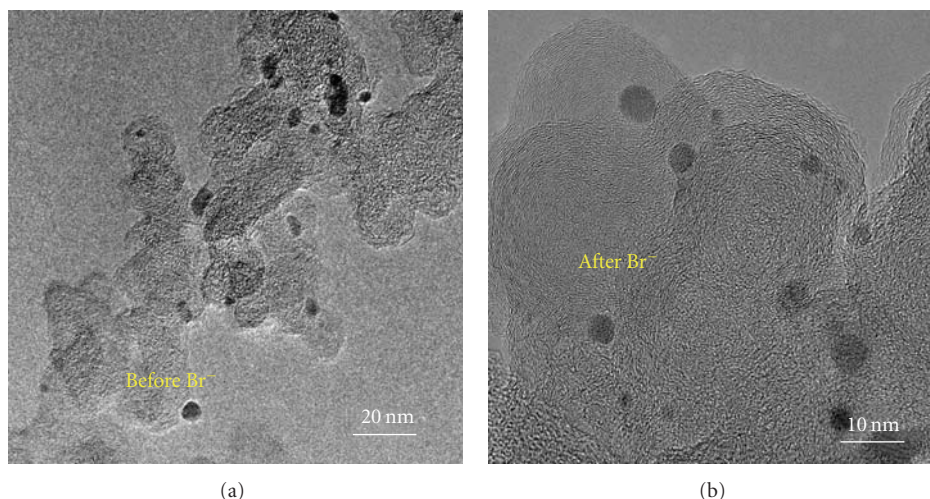


FIGURE 4: High-resolution TEM images of Pd/C before (a) and after (b) Br-treatment [22].

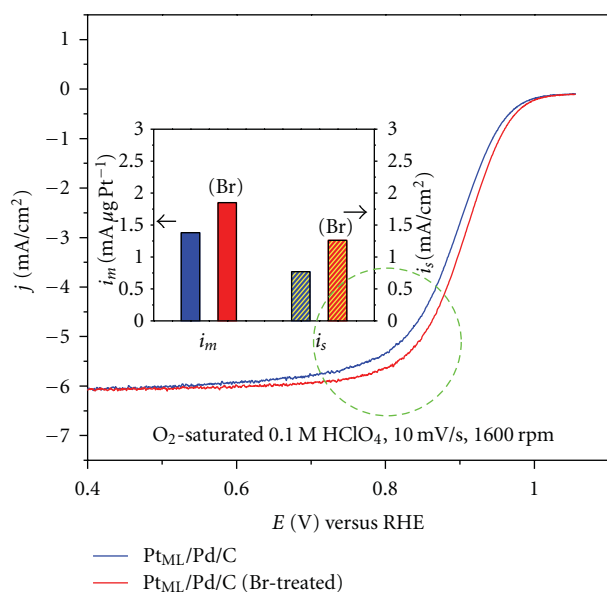


FIGURE 5: Polarization curves of oxygen reduction at Pt_{ML} on Br-treated and -untreated Pd/C. Inset: comparison of mass activity and specific activity on Pt_{ML}/Pd/C [22].

diameter of 4.25 nm, but a wide size distribution, from 1.1 to 10 nm. Many small particles with a diameter of 3 nm were present and considerable number of defects and edges on the particles are observed. The Pt monolayer catalysts supported on Br-treated Pd₃Co/C nanoparticles show a much more uniform particle size, averaging 5.8 nm. Considering this size includes the thickness of a Pt monolayer, the average Br-treated Pd₃Co/C nanoparticles should be around 5.5 nm at most. The Br-treated nanoparticles exhibit a large area of well-defined (111)-crystalline structure, even after the deposition of the platinum monolayer while the untreated-Pd₃Co/C particles have much smaller patches with poorly defined crystalline structures. Seemingly, after bromide

treatment, most particles with diameters less than 3 nm dissolved and were redeposited on larger particles, suggesting the occurrence of Ostwald ripening [27] during the Br-treatment.

Figure 7 shows the CV and polarization curves for ORR on Pt_{ML} catalysts supported on Br-treated Pd₃Co/C after various potential cycles. The activity and surface area remains unchanged after 25,000 potential cycles between 0.6 and 1.0 V. It is a significant improvement of the stability since the same test with Johnson Matthey's Pt_{ML}/Pd₃Co/C resulted in a negative shift of the half-wave potential of more than 30 mV in the first 5000 cycles.

The above examples of surface modifications of Pd and Pd₃Co core demonstrated that the removal of surface low-coordination sites via bromide-treatment enables to obtain nanoparticles with smooth surfaces having a high density of (111)-oriented facets and a slightly contracted structure. The after-treated cores become excellent substrate for Pt monolayer and significant enhancements were realized of the mass activity and specific activity for the ORR.

3. Addition of an Interlayer between the Pt Monolayer and the Core

3.1. Pt_{ML}/Pd/IrCo/C [28]. Iridium is one of the most stable transition metals; its dissolution potential is comparable with platinum [29]. Its particular activity for the ORR is enhanced by alloying it with cobalt or platinum [30, 31]. However, Ir is not a good support for a Pt monolayer because it causes the Pt lattice to contract too strongly, and consequently, significantly decreases the d-band center; that is, it lowers the reactivity of Pt, entailing a very weak adsorption of O₂ on Pt and a slow ORR kinetics [1, 6, 32]. Moreover, the relatively low ORR activity on Ir alone and its alloys, confirmed experimentally and theoretically, results from the disproportionately strong binding energy of oxygen at the surface [6]. Thus, it is a challenge to design an electrocatalytic system containing a highly stable and less expensive core,

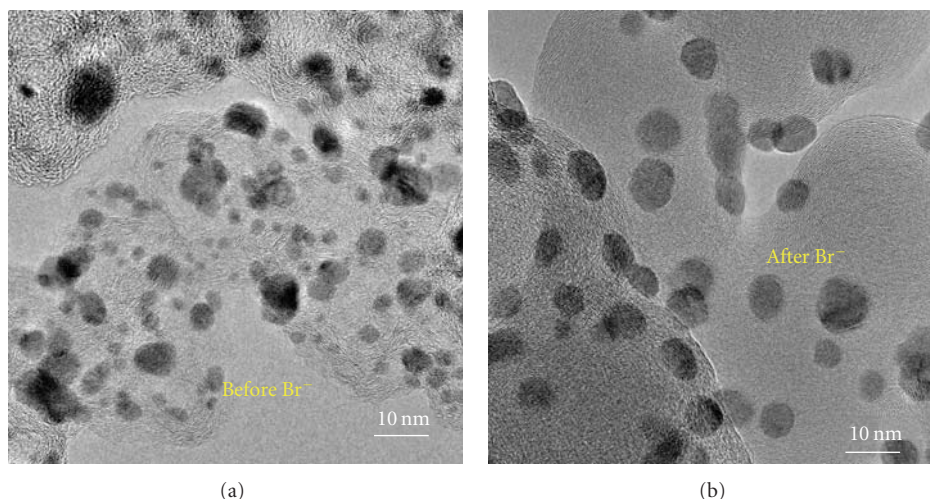


FIGURE 6: High-resolution TEM images of the original Pd₃Co/C and of Pt_{ML} on Br-treated Pd₃Co/C [22].

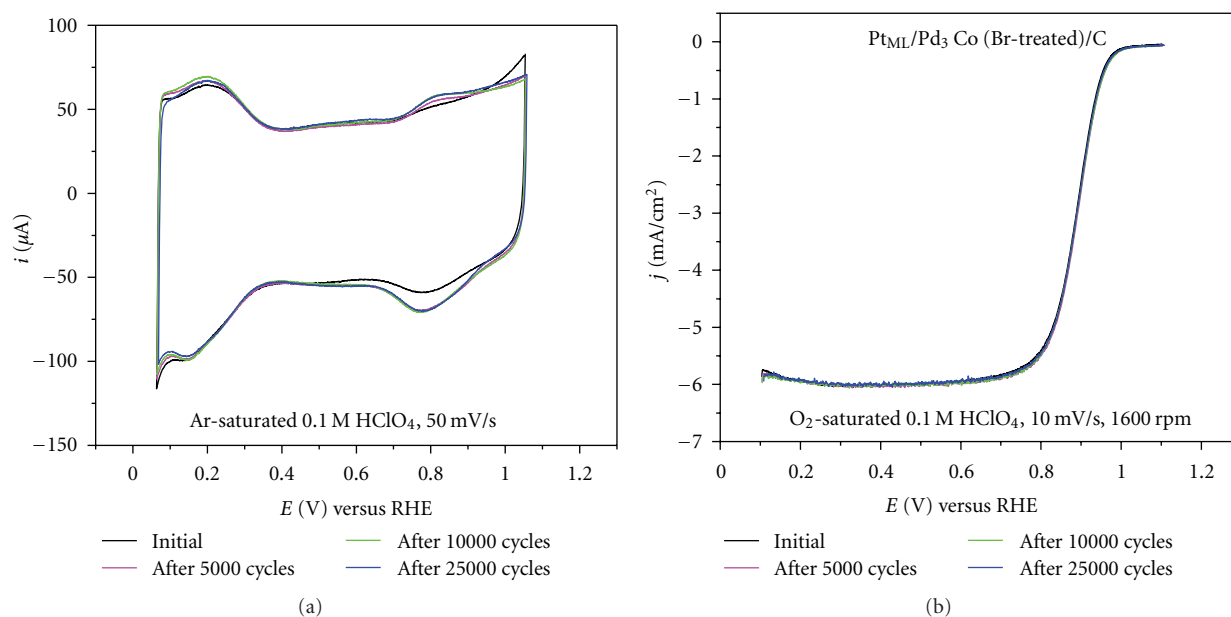


FIGURE 7: Voltammetry curves for the Pt_{ML}/Br-treated-Pd₃Co/C (a), and polarization curves for the ORR (b) in a stability test involving 25,000 potential cycles [22].

such as iridium or its alloys, to support a Pt monolayer yielding an efficient catalyst. Oxygen binding of Pd, contract to Ir, located in the other side of the volcano plot, is much stronger. Therefore, to reduce the effect of Ir on the d-band center of a Pt monolayer, and to assure it can make a moderately strong bond with diatomic oxygen at the surface platinum, we placed a Pd monolayer (interlayer) between the Pt monolayer and the IrCo core. Thus, while Ir causes the Pt lattice to contract too strongly, and consequently entails low activity, a Pd support entails only a small contraction that suffices to increase the ORR kinetics on platinum.

Figure 8 depicts the voltammetry curves in the absence of O₂ for the Pt_{ML}/IrCo with and without a palladium interlayer. The effects of the Pd interlayer on the properties

of a Pt monolayer are reflected in the shift of Pt oxidation in comparison with the curve without it. These effects are more pronounced on the ORR kinetics as shown in Figure 9. For both the as-prepared IrCo and the Ir₃Co cores, the palladium interlayer engenders a positive shift of about 50 mV and 150 mV, respectively, in the half-wave potential compared to the corresponding electrocatalysts lacking a palladium interlayer, clearly demonstrating that this interlayer significantly increases the electrocatalytic activity for the ORR.

For comparison, the mass activities for oxygen reduction at 0.9 V (RHE) of the Pt_{ML}/IrCo/C and Pt_{ML}/Pd_{ML}/IrCo/C were calculated and summarized in Figure 10; the activity on commercial Pt/C is included as a reference. The Pt

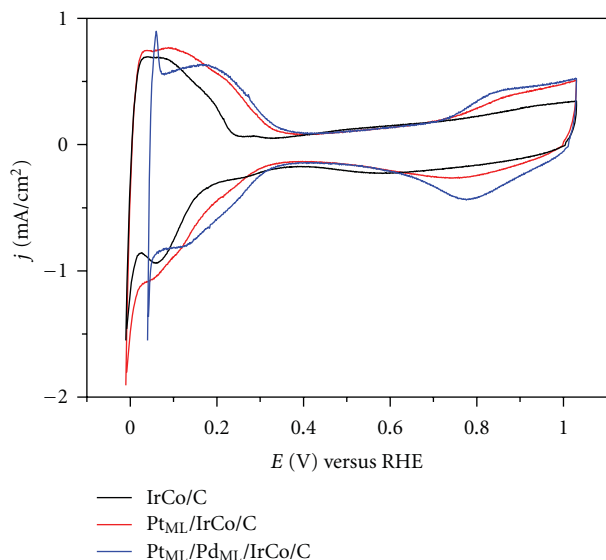


FIGURE 8: Cyclic voltammograms of IrCo/C (black), Pt_{ML}/IrCo/C (red), and Pt_{ML}/Pd_{ML}/IrCo/C (blue) in argon-blanketed 0.1 M HClO₄ at the scan rate of 50 mV s⁻¹ [28].

loadings were calculated from the coulombic charge for the underpotential deposition of copper monolayer. It is exciting to find that the mass activity of the Pt_{ML}/Pd_{ML}/IrCo/C in terms of platinum mass and the platinum-group-metals' mass is, respectively, seven-times and four-times higher than that obtained with Pt_{ML}/IrCo/C (without palladium interlayer). These substantial enhancements in the specific activities again highlight the essential role of the palladium monolayer in improving the overall kinetics for the ORR.

To further explore these observations, we investigated the ORR activity on these surfaces using density functional theory, within the plane-wave approach, using the program VASP [33, 34], with the Perdew-Burke-Ernzerhof exchange-correlation functional [35] within the generalized gradient approximation. For further analysis and comparison of the relative reactivity of all surfaces at 0.9 V, we constructed an activity measure based on a microkinetic model that is detailed elsewhere [36]. In brief, the maximal activity A can be expressed as $A = kT \min_i(\log(k_i/k_0))$, where k_i is the rate constant of each elementary step [36]. The DFT-based activities at 1 bar, 300 K, and 0.9 V shown in Figure 11 indicate that the ORR activity on all surfaces studied is limited by the OH removal step. These values closely follow the trend in OH adsorption; therefore, OH adsorption energy is a descriptor of ORR activity of these surfaces. Both catalysts, IrCo and Ir₃Co, with a Pd interlayer have a weaker OH binding than those without the interlayer, which is in agreement with the experimental results, that is, higher activity was observed on the catalysts with a Pd interlayer. Moreover, we note that the effect of the reduced lattice constant of the Ir-Co cores by the Pd interlayer clearly is reflected in the adsorption energies of the adsorbates. Ramírez-Caballero et al. [37] recently reported adsorption energies of O and OH, respectively, on Pt/Pd (bulk) as -4.21

and -2.33 eV; the values of O and OH, correspondingly, for Pt/PdIr₃Co are -3.62 and -2.47 eV, and for Pt/Pd/IrCo are -3.48 and -2.10 eV.

To summarize, this section describes a simple method of improving Pt monolayer core-shell catalysts that have an inadequate Pt-core interaction causing their relatively low ORR activity. Using a Pd monolayer as an interlayer between Pt and the core modifies their interaction and improves their ORR activity significantly. Employing the IrCo and Ir₃Co alloy cores as supports, we demonstrated the essential role of a palladium interlayer in developing excellent platinum monolayer electrocatalysts for the ORR. Incorporating a palladium interlayer in the Pt_{ML}/IrCo/C catalyst realized a sevenfold- and a fourfold-higher specific activity, respectively, in terms of platinum mass and platinum-group-metals' mass. Our results reveal that the right choice of an interlayer, such as Pd, can facilitate the use of stable and relatively inexpensive core, such as IrCo, and tune the electrocatalytic properties of the surface platinum monolayer to achieve an efficient ORR electrocatalyst. Our DFT calculations corroborated these findings. Therefore, improved, low-cost ORR electrocatalysts with high activity, and increased potential for commercialization, can be obtained based on this approach.

3.2. Pt_{ML}/(PdAu)_{ML}/Pd/C [38]. The above example evidently demonstrated the meditation effect of the interlayer for the interaction between Pt monolayer and the metal core. The state-of-the-art Pt_{ML}/Pd/C has been shown to be one of the electrocatalysts that is close to the optimum design for the ORR in terms of the value of oxygen binding energy and the position of d-band center. To further perfect this electrocatalyst, we modified the Pd core by the addition of a PdAu layer with only a small content of Au included, forming a new substrate for Pt monolayer.

The deposition of the PdAu alloy layer on the Pd/C surface was carried out via Cu UPD method. The detail of the structure for this modified Pt_{ML} electrocatalyst is illustrated in Figure 12. Three compositions of the PdAu alloy layer were studied, namely, Pd₉₅Au₅, Pd₉₀Au₁₀, and Pd₈₀Au₂₀. Their polarization curves for ORR are displayed in Figure 13. All of the catalysts show improved ORR activities over those without an alloy sublayer. The activities can be ranked in a decreasing order as Pd₉₀Au₁₀ > Pd₉₅Au₅ > Pd₈₀Au₂₀ > Pd₁₀₀, where Pd₁₀₀ represents the catalyst without an alloy layer. The Pt_{ML} catalyst with 10 at% Au sublayer exhibits the highest activity.

The enhanced ORR activities can be attributed to the surface strain and the d-band center shift of the Pt_{ML} induced by the alloy layer. The lattice constants of Pt, Pd, and Au are 3.920, 3.890, and 4.080 Å, respectively. The mismatch between Pt and Pd produces a lateral compressive strain when a Pt_{ML} is deposited on Pd (extended surfaces): $\epsilon_{Pt/Pd} = (\alpha_{Pt} - \alpha_{Pd})/\alpha_{Pd} = 0.8\%$, where ϵ is the lateral strain and α is the lattice constant. This is for flat surfaces. For nanoparticles, surface curvature also contributes to producing a strain [39, 40]. For a 7.8 nm particle, this

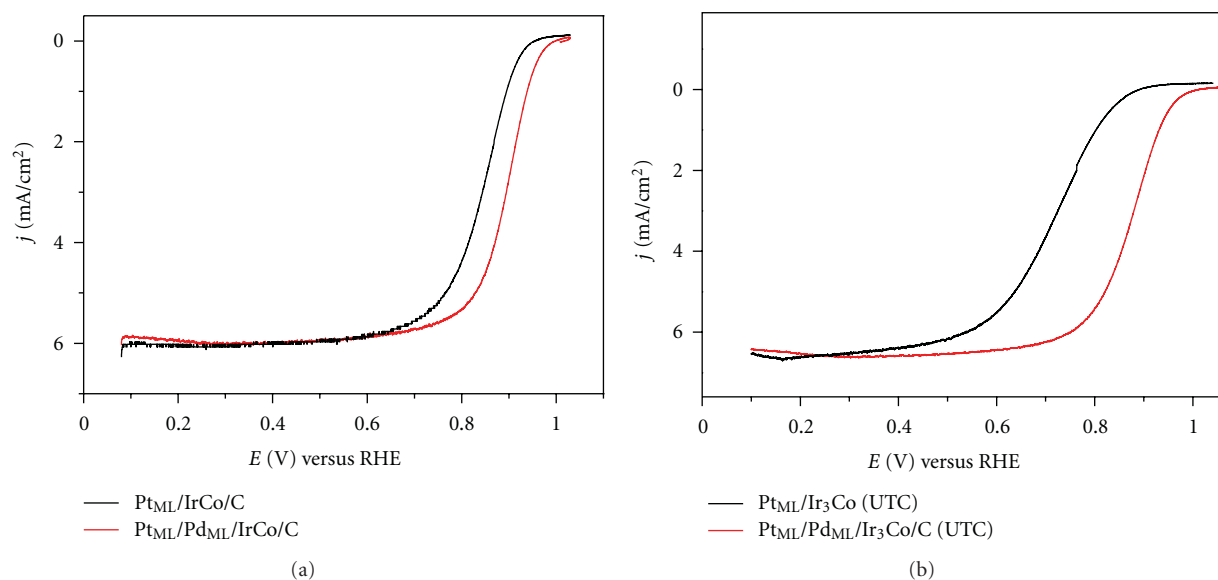


FIGURE 9: Polarization curves of $\text{Pt}_{\text{ML}}/\text{IrCo}/\text{C}$ (a) and $\text{Pt}_{\text{ML}}/\text{Ir}_3\text{Co}/\text{C}$ (b) with (red curves) and without (black curves) a palladium interlayer in oxygen-saturated 0.1 M HClO_4 . Scan rate: 10 mV s^{-1} ; rotation speed: 1600 rpm [28].

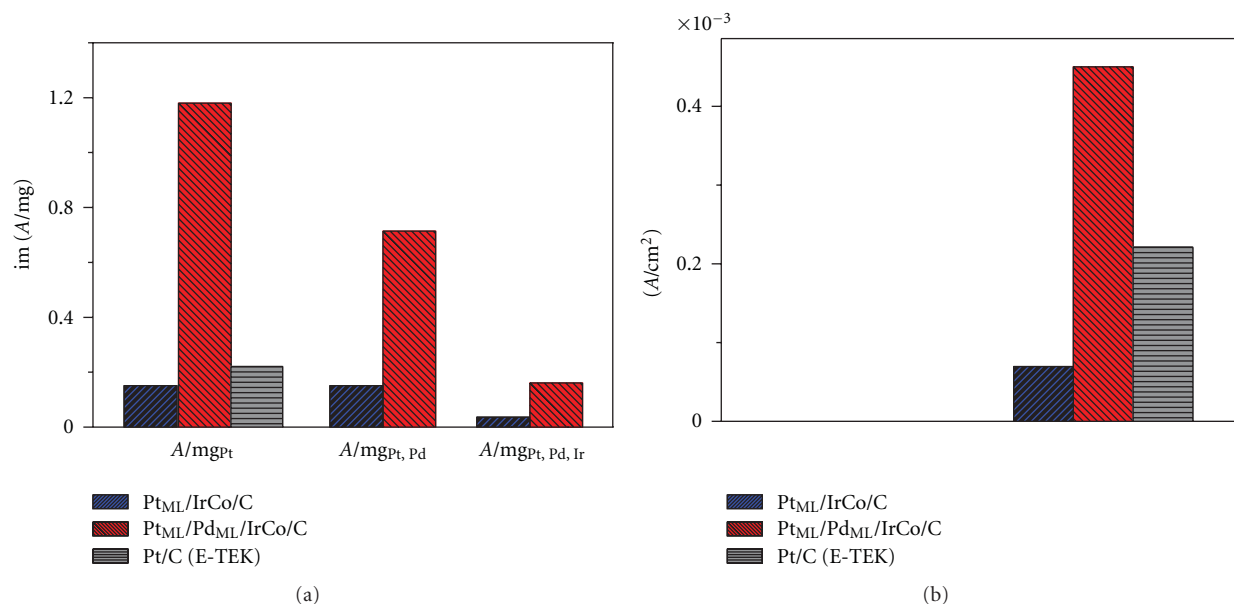


FIGURE 10: Comparison of the mass activity in terms of Pt mass, (Pt + Pd) mass and the platinum-group-metal's mass (a) and the surface-area activity (b) at 0.9 V (RHE) of $\text{Pt}_{\text{ML}}/\text{IrCo}/\text{C}$ (blue) and $\text{Pt}_{\text{ML}}/\text{Pd}_{\text{ML}}/\text{IrCo}/\text{C}$ for oxygen reduction. The activity of Pt/C, the commercial catalyst, is shown in black [28].

contribution is estimated to be about $\sim 0.4\%$. Although the total surface strain of $\sim 1.2\%$ is still small, contraction in surface atoms in the radial direction can make a significant contribution. The enhancement in ORR activity due to the lattice contraction has been demonstrated in experiments and density functional theory calculations [18]. Huang et al. [41] have recently reported that up to 8% reduction in bond length was found in 4 nm Au nanoparticles.

When a Pt_{ML} is deposited on Au, a lateral tensile strain can be generated in Pt_{ML} at 3.92% that will expand Pt in the surface layer. Contraction due to the decreasing coordination

numbers of surface atoms will act in the opposite direction. Therefore, when Pd-Au alloys are used as the sublayer for mediation, the interplay of lateral strain (compressive and tensile) and radial contraction (compressive strain) can lead to activity improvement of the ORR catalysts, as observed in the experiments. There should be an optimal alloy composition, that is, both too little and too much Au would decrease the ORR activity. For the results reported here, the 10 at% Au, which is estimated using the atomic radii to have about 10.5% surface coverage by Au atoms in the alloy sublayer, seems to produce the highest ORR activity.

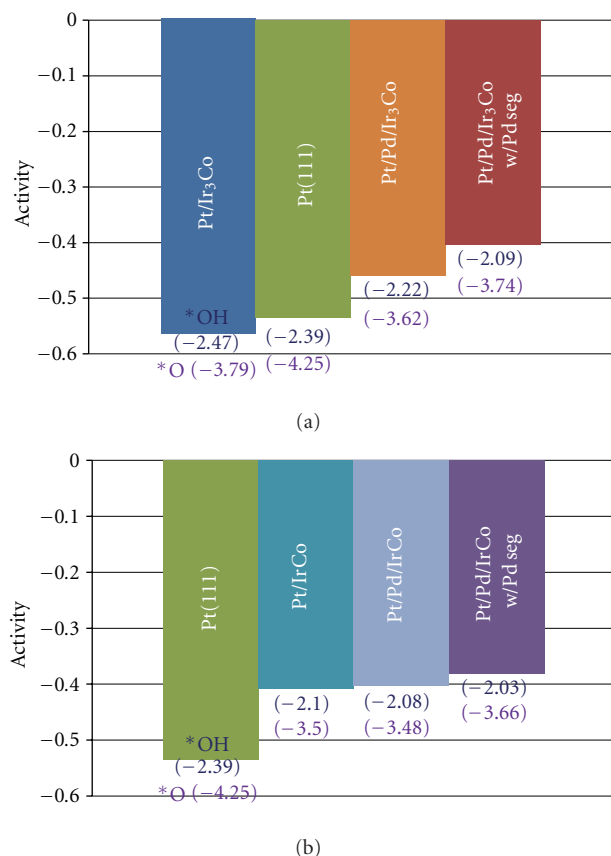


FIGURE 11: Oxygen reduction activity at 0.9 V plotted in the order of strongest to weakest OH binding energy, and the binding energy of O is also given; both are shown in parenthesis in eV. (a) Ir₃Co, (b) Ir-Co cores. The Pt-skin surfaces with an interlayer of Pd show the highest activities in both cases [28].

While lattice contraction may be important, the interaction of the substrate with Pt_{ML} could result in an electronic effect on the ORR activity through charge redistribution [18, 42]. As demonstrated previously, [42] the formation of PtOH is significantly prohibited for the Pt_{ML} on Pd nanoparticles when compared with Pt nanoparticles. Hydroxyl formation is considered as a major factor affecting ORR activity because of site blockage by OH [26]. Au may play an important role in protecting low-coordination sites on Pt from being oxidized. Wang et al. [43] recently reported that Au coated with FePt₃ stabilizes the oxidation of the surface atoms in certain facets of the nanoparticles. Likewise, the Au in the sublayer of our catalysts also has contributed to the reduction of surface oxidation, leading to the improved ORR activity of the catalysts.

The polarization curves of Pt_{ML}/Pd/C with a Pd₉₀Au₁₀ interlayer before and after 5000 potential cycles are shown in Figure 14. Less than 1% loss in ORR activity was observed, demonstrating the excellent stability of the catalyst. The stabilization of the catalyst can be attributed to the reduction of surface oxidation from Au in the sublayer, therefore inhibiting the dissolution of metal. The stabilizing effects of Au on Pt nanoparticles have been reported by Zhang et al.

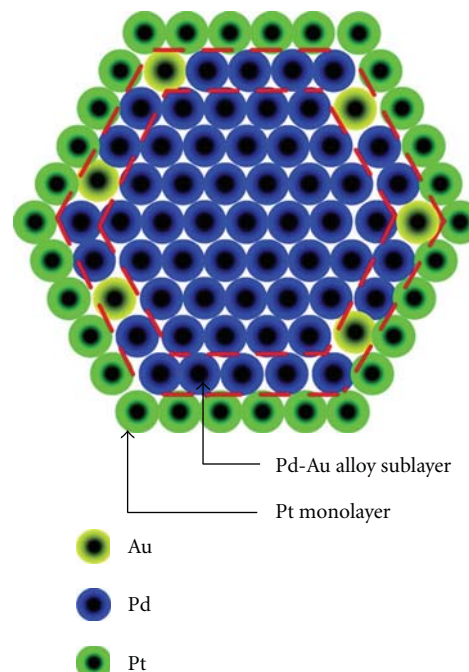


FIGURE 12: Illustration of the core-shell structure of PdAu alloy sublayer nanoparticles [38].

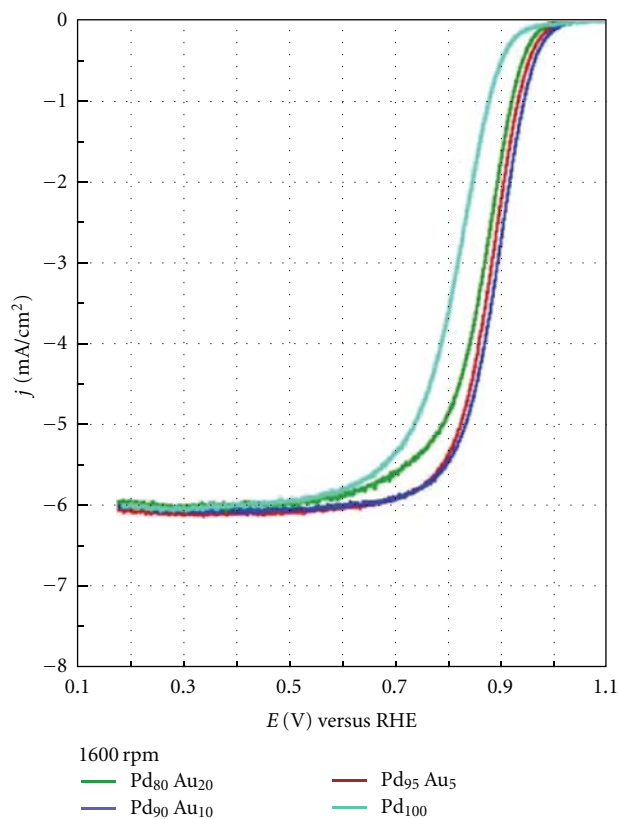


FIGURE 13: ORR activities of Pt_{ML} catalysts with different contents of Pd-Au interlayer on a Pd/C core obtained with electrode rotating speed at 1600 rpm in an oxygen-saturated 0.1 M HClO₄ [38].

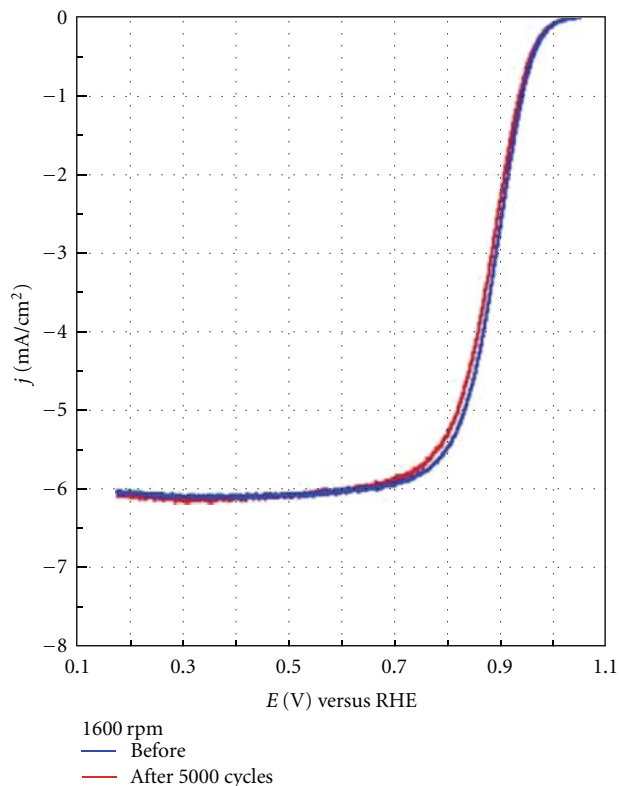


FIGURE 14: Polarization curves for the ORR of the catalyst with Pd₉₀Au₁₀ alloy sublayer before and after 5000 potential cycles [38].

[44] and other studies [43, 45, 46] have also demonstrated the same effect of Au. The addition of a Pd-Au alloy between Pt_{ML} and Pd/C core enhance both the activity and stability for ORR from the induced lattice contraction (both lateral and radial). The fact that the sublayer alloy can be of different metals and compositions may open up various opportunities in tailoring catalysts for best ORR activity.

4. A Core for Pt_{ML} with a Segregated Pd Layer on Pd₃Fe(111) [47]

Pd-M alloys (M) (M = Co, Fe, or Ti) [19, 48] have shown comparable or even slightly better ORR activity than commercial Pt catalysts. The high ORR kinetics and significantly decreased cost of materials along with their satisfactory stability make some Pd-M alloys very promising candidates to replace conventional Pt catalysts for the ORR. The enhanced ORR activity observed with bulk and high-surface-area Pd-M alloys was ascribed either to the modification of the electronic property of Pd on the segregated surface layer [16, 48, 49] or to the synergistic effect between Pd and the second metal [49, 50]. This segregated Pd surface layer that has different electronic properties from pure Pd [16] was considered to be the key factor responsible for the enhanced ORR activity on Pd-M alloys [51]. Our work on Pd₃Fe(111) demonstrated that the segregated Pd layer from high-temperature annealing exhibits the same surface structure but different electronic properties. As shown in

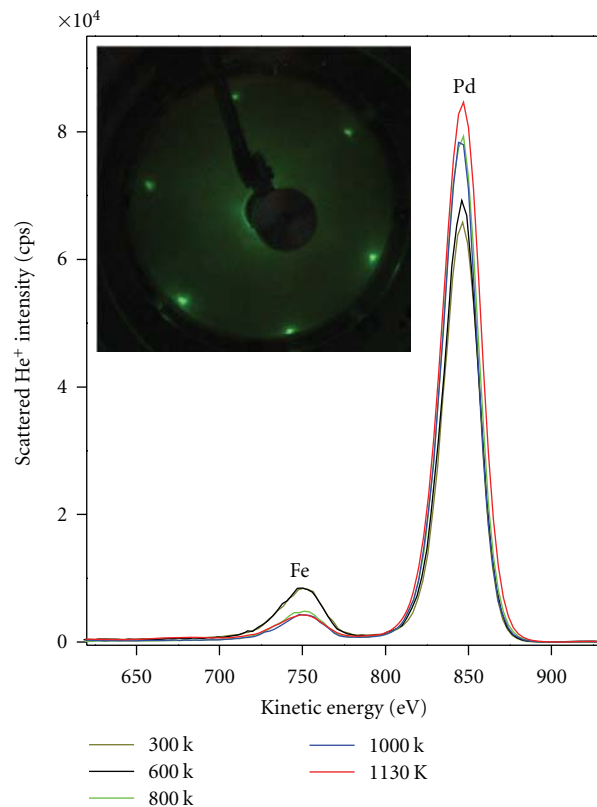


FIGURE 15: LEIS spectra (1 keV He⁺) for a Pd₃Fe(111) surface annealed to various temperatures. Inset shows a (1 × 1) LEED pattern for a Pd₃Fe(111) surface annealed to 1200 K. The electron beam energy was 55 eV [47].

Figure 15 upon annealing to 1200 K, surface Pd signal increases and a sharp (1 × 1) LEED pattern was observed, suggesting that Pd segregates to the surface and forms a well-ordered layer. This segregated Pd layer modified the interaction of Pt_{ML} and its substrate, and an enhancement of the ORR activity was observed.

When the annealed Pd₃Fe(111) electrode was treated with 0.1 M HClO₄, only a small amount, if any, of Fe in the topmost layer immediately dissolved since no voltammetric features related to Fe dissolution were observed, leaving a pure Pd skin-like layer on the surface (referred to hereafter as Pd/annealed-Pd₃Fe(111)) and verifying the migration of Pd to the surface during annealing.

Figure 16(a) shows the cyclic voltammetry scans for a Pd/annealed-Pd₃Fe(111) surface immersed in 0.1 M HClO₄ at 0.05 V and subsequently cycled between 0.05 V and various positive potential limits at a scan rate of 20 mV s⁻¹. A reversible process is observed between +0.05 and +0.40 V, a finding that has not been observed on a Pd(111) electrode (Figure 16(b)) [52, 53]. Baldauf and Kolb [54] reported that H absorption (H_{abs}) occurs only for Pd films thicker than 2 ML. This reversible process that is very similar to the $H_{\text{ads/des}}$ occurred on a Pd_{ML}/Pt(111) electrode [55] and therefore is tentatively assigned to $H_{\text{ads/des}}$ on a segregated Pd layer on a Pd₃Fe(111) surface. The surface oxidation of

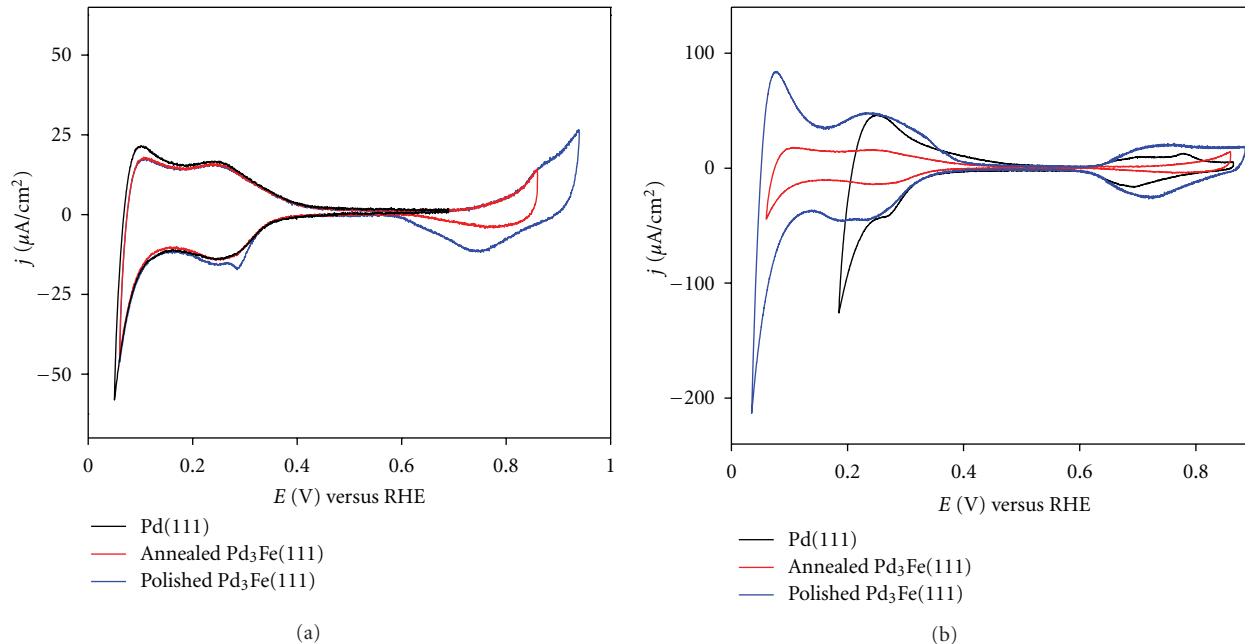


FIGURE 16: (a) Voltammetry curves for an annealed Pd₃Fe(111) in 0.1 M HClO₄ solution with different positive potential windows. (b) Voltammetry curves for an annealed (red line) and a polished Pd₃Fe(111) (blue line), and Pd(111) (black line) in 0.1 M HClO₄ solution. Scan rate: 20 mV s⁻¹ [47].

a Pd/annealed-Pd₃Fe(111) electrode does not occur until the positive potential limit extends beyond 0.73 V (red and blue line in Figure 16(a)); this indicates the positively shifted onset of oxidation of ~ 0.1 V relative to that of Pd(111). The charge density under the cathodic peak at ~ 0.73 V, reflecting the surface coverage of oxygen-containing species, is considerably smaller for the Pd/annealed-Pd₃Fe(111) electrode than for the Pd(111) one (Figure 16(b)). These important new properties of the alloy's surface play a role in determining the kinetics of the ORR. A similar electrochemical phenomenon occurred on a Pt skin surface on Pt₃Ni alloys [56]. The voltammetry curves stayed unchanged, even after driving the positive potential limit very high (i.e., 0.95 V).

To assess the role of Fe in determining the electrochemical and catalytic properties of the Pd layer on the Pd₃Fe(111) surface, the Fe atoms in several topmost layers were removed almost completely by polishing and exposing such surface to acid. The remaining Pd layers on the Pd₃Fe(111) electrode have some similarity to the Pt₃Ni skeleton surface described by Stamenkovic et al. [57] except this pure Pd surface layer likely was thicker. This electrode showed very similar electrochemical behavior to that of a Pd(111) electrode, which verifies the role of Fe in this catalyst.

Figure 17(a) provides a set of polarization curves for the ORR on the Pt_{ML}-covered surfaces of Pd/annealed-Pd₃Fe(111) and Pd(111), and Pt(111) obtained in 0.1 M HClO₄ at room temperature. Figure 17(b) shows their corresponding specific activities at 0.9 V. A Pt monolayer supported on Pd/annealed-Pd₃Fe(111) shows the highest ORR kinetics among these three surfaces, by a factor of at least 2 compared with that of the Pt(111) surface, and

TABLE 1: Binding energies of OH on the surfaces of Pt(111), Pt_{ML}/Pd(111) and Pt_{ML}/Pd/Pd₃Fe(111).

	Pt(111)	Pt _{ML} /Pd(111)	Pt _{ML} /Pd/Pd ₃ Fe(111)
BE _{OH} (eV)	-2.09	-2.07	-1.93

Data from [46].

also demonstrates significantly increased ORR activity in comparison with that of the Pt_{ML}/Pd(111) surface.

To elucidate the fundamental aspects of the ORR activity of composite core-shell structures, DFT calculations were conducted for model systems composed of a single Pt_{ML} on a Pd monolayer supported on the close-packed surfaces of several different substrates. On the basis of this analysis, the binding energy of OH on Pt_{ML}/Pd(111) is weaker than that of OH on Pt(111) and OH removal is easier on Pt_{ML}/Pd(111) than it is on Pt(111) (Table 1). As a result, the ORR activity is increased on Pt_{ML}/Pd(111) compared to that on Pt(111).

As shown in Table 1, Pt_{ML}/Pd/Pd₃Fe(111), an appropriate model for the Pt_{ML} on the annealed-Pd₃Fe(111) surface, the binding of OH on which is destabilized much more than on the Pt_{ML}/Pd(111) and Pt(111). This leads to Pt_{ML}/Pd/Pd₃Fe(111) having more OH-free sites for O₂ adsorption and reactions than the Pt_{ML}/Pd(111) and Pt(111) surfaces. Interestingly, we are finding that the activity of Pt_{ML}/Pd(111) and Pt(111) is limited by OH removal (left side of the ORR activity volcano plotted against BE_{OH}) whereas the activity of Pt_{ML}/Pd/Pd₃Fe(111) is limited by the O–O bond scission in the OOH intermediate, placing this surface on the other side of the volcano plot. Yet, a

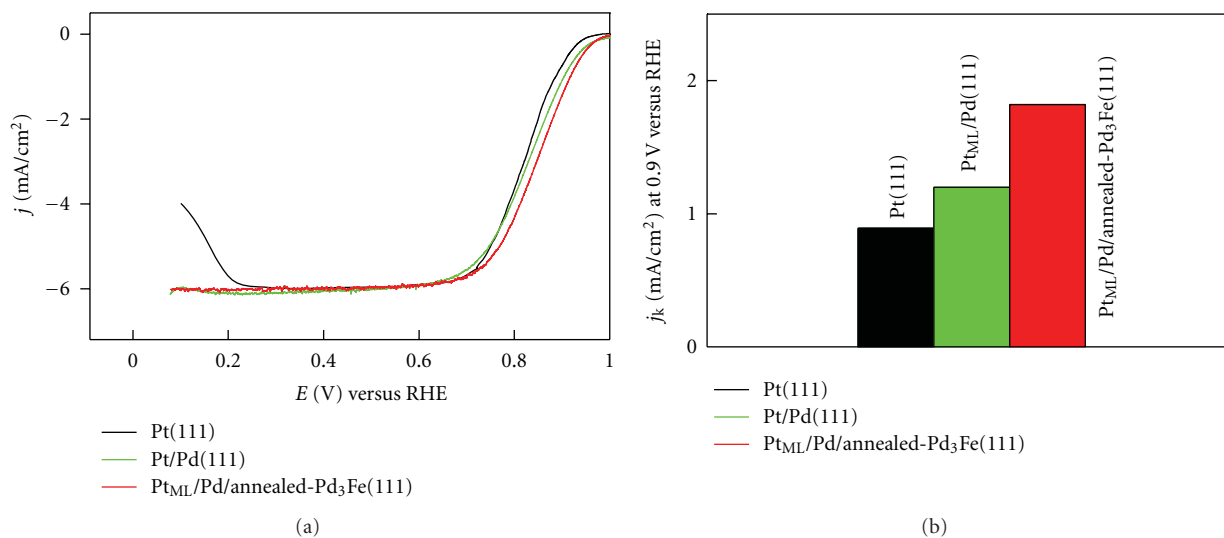


FIGURE 17: (a) Polarization curves for the ORR on a Pt monolayer covered annealed-Pd₃Fe(111) (red), annealed-Pd(111) (green), and Pt(111) surfaces (black) at 1600 rpm in oxygen-saturated 0.1 M HClO₄ at room temperature; scan rate: 20 mV s⁻¹. (b) The bar plot for the comparison of ORR-specific activities of the corresponding three surfaces at 0.9 V (RHE) [47].

direct comparison between the BE_{OH} and the calculated ORR activities on Pt_{ML}/Pd(111) and Pt_{ML}/Pd/Pd₃Fe(111) at the relevant bias voltage suggests that the enhanced activity of the latter surface originates mainly from the destabilization of OH on that surface, compared to that on the former surface.

The segregated Pd layer further weakens the Pt–OH bonding, and is proven to be an excellent substrate for a Pt monolayer for the ORR, as indicated by the enhanced ORR kinetics on Pt_{ML}/Pd/annealed-Pd₃Fe(111) compared to that of Pt_{ML}/Pd(111) and Pt(111).

5. Subsurface Modification of the Core: Introduction of Iridium to the Pd Subsurface [58]

This approach introduces a second metal to the subsurface of Pd core and thus generates a Pd-interlayer which alters both the electronic and geometric properties of the core and also affects the catalytic activity of the Pt monolayer.

The purpose of submerging Ir under the Pd surface is to influence the Pt–Pd interaction in order to improve the ORR activity of the already established highly active Pt_{ML}Pd/C [42]. Also, since Ir has a much higher dissolution potential than Pd (1.16 V for Ir and 0.99 V for Pd), [29] the addition of subsurface Ir can enhance Pd stability under fuel cell operating conditions.

Figure 18 depicts the process of introducing Ir to the subsurface of Pd core for Pt monolayer. In brief, an Ir layer was first placed on Pd/C via the Cu UPD method and then was subsequently annealed at elevated temperatures to enable a thin layer of Pd to segregate to the surface. After that, a Pt monolayer was deposited via the Cu UPD. The Ir loading in IrPd/C is estimated to be 4.1 wt% and there is 11 at% of Ir in IrPd.

In Figure 19(a), the voltammetry curve of Pt_{ML}PdIr/C (red line) is compared to Pt_{ML}Pd/C (blue line) and Pt/C (black line) in de-aerated 0.1 M HClO₄ while Figure 19(b) illustrates a set of polarization curves for the ORR on the same samples with the addition of the notannealed sample (Pt_{ML}/IrPd/C, green line) at 1,600 rpm in oxygenated 0.1 M HClO₄. From the above CVs, the segregated Pd surface layer on PdIr nanoparticles exhibits different electrochemical behavior compared to that of Pd/C electrodes. The influence of Ir is revealed in the oxidation region. The oxidation of Pt_{ML} on PdIr/C is delayed compared to that of Pt_{ML}/Pd/C and Pt/C. This is in qualitative agreement with DFT calculations predicting weaker Pd–O interaction on Pd/Ir(111) than on Pd(111) [19].

As shown in Figure 19(b) the Pt_{ML}PdIr/C has higher ORR activity than Pt/C and Pt_{ML}Pd/C even though it has a smaller surface area. The Pt-specific activity (a) and Pt-mass activity (b) at 0.9 V of Pt/C, Pt_{ML}Pd/C, and Pt_{ML}PdIr/C are summarized in Figure 20. The Pt-specific activity for Pt_{ML}PdIr/C is three-times and 25% higher than that of Pt/C and Pt_{ML}Pd/C, respectively; the Pt-mass activity of Pt_{ML}PdIr/C is more than 20-times and 25% higher than that of Pt/C and Pt_{ML}Pd/C, respectively.

The influence of the Ir sublayer on the ORR activity could be explained by the position of the Pt_{ML} d-band center (ϵ_d). Previous DFT calculations have shown that the ϵ_d of the metal monolayer under compressive strain tends to downshift in energy whereas tensile strain has the opposite effect [6, 15]. A surface characterized by a higher-lying ϵ_d tends to bind adsorbates more strongly, thereby enhancing the kinetics of dissociation reactions producing these adsorbates. On the other hand, a surface with a lower-lying ϵ_d tends to bind adsorbates more weakly and facilitates the formation of bonds towards larger intermediates. The

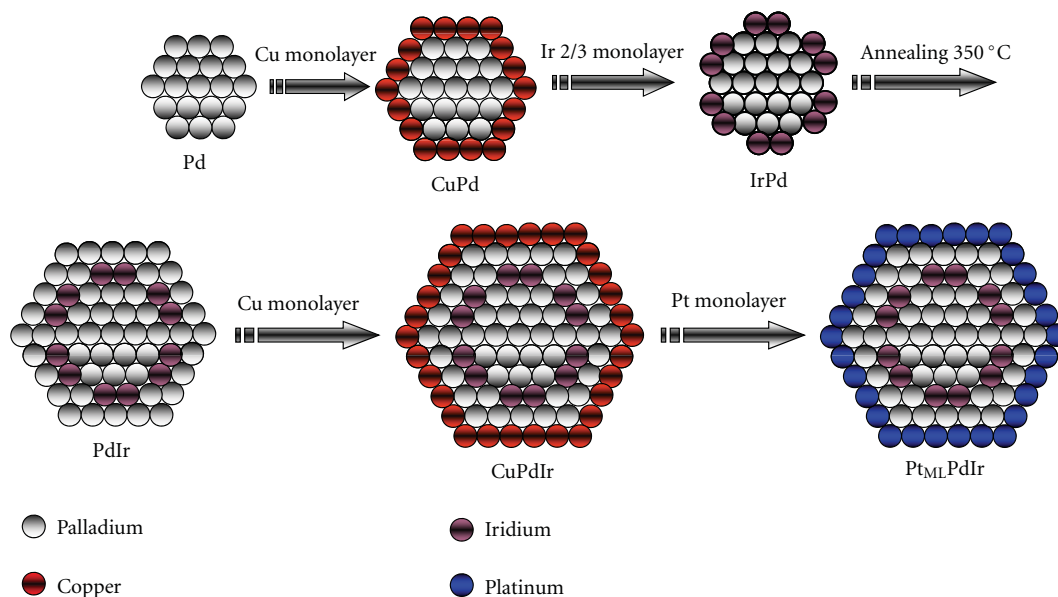


FIGURE 18: Depiction showing the catalyst preparation (see text) [58].

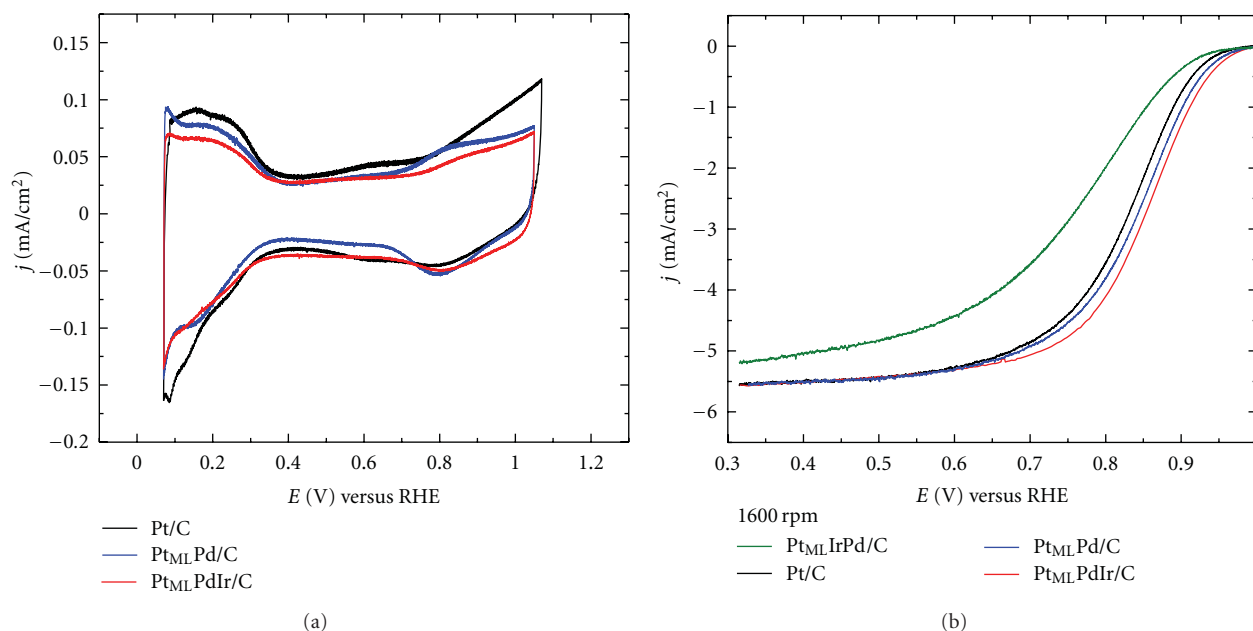


FIGURE 19: Voltammetry curves for Pt_{ML}Pd/C (blue), Pt_{ML}PdIr/C (red), and Pt/C (black) in deaerated 0.1 M HClO₄ solution. Scan rate, 20 mV s⁻¹. (b) Polarization curves for the ORR on Pt_{ML}IrPd/C (green), Pt_{ML}Pd/C (blue), Pt_{ML}PdIr/C (red), and Pt/C (black) at 1,600 rpm in oxygen-saturated 0.1 M HClO₄ solution. Scan rate, 10 mV s⁻¹ [58].

Pt_{ML} on Pd is compressed but the position of the ϵ_d for the Pt_{ML} depends both on the strain (geometric effects) and on the electronic interaction between the Pt_{ML} and its substrate (ligand effect) [6]. Introducing subsurface Ir causes a small contraction of the Pd surface layer due to the smaller atomic

size of Ir compared to Pd. As a consequence, the Pt_{ML} put on top of the Pd surface covering the PdIr subsurface will be further compressed causing additional downshift in ϵ_d which is manifested by weaker Pt–OH interaction leading to the reduced oxidation of this ternary system. Since the intrinsic

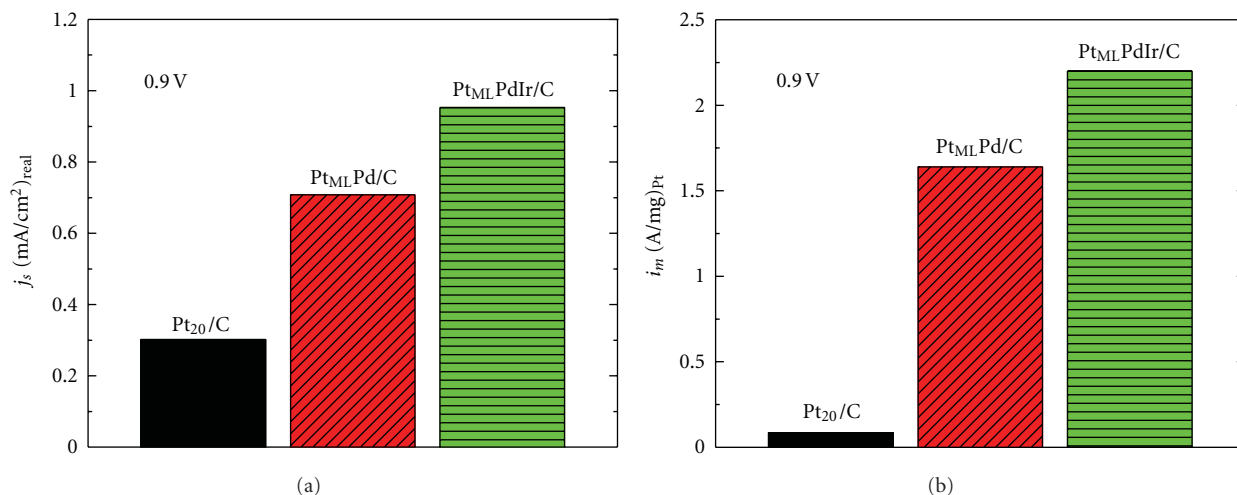


FIGURE 20: (a) Pt-surface specific activity, (b) Pt-mass activities of Pt/C, Pt_{ML}Pd/C, and Pt_{ML}PdIr/C at 0.9 V versus RHE [58].

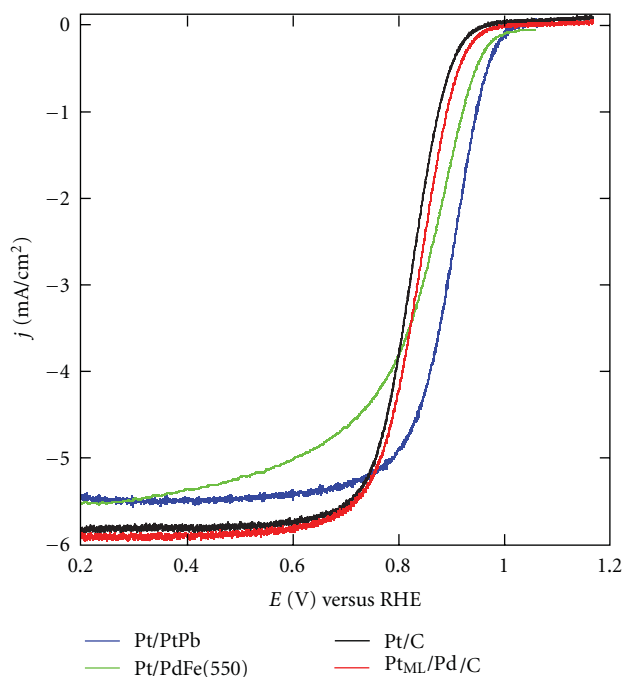


FIGURE 21: Comparison of the activities for the ORR of Pt/C, core-shell Pt_{ML}/Pd/C, and Pt/PtPb and Pt/PdFe in 0.1 M HClO₄; 1600 rpm; 10 mV/s [59].

ORR activity is largely determined by the binding energy of OH, weaker Pt–OH interaction should result in enhanced ORR activity.

To directly demonstrate the destabilization of OH on Pt_{ML}PdIr (as compared to Pt_{ML}Pd or Pt), density functional theory calculations were performed on representative close packed (111) facets of the appropriate model systems. The results of these calculations are shown in Table 2. The calculations show that depositing a monolayer of Pt on a Pd substrate destabilizes OH binding ($BE_{OH} = -2.07$ eV) as compared to pure Pt ($BE_{OH} = -2.17$ eV) or Pd ($BE_{OH} =$

-2.29 eV). Since the lattice constant for Pt and Pd are quite similar, this difference is mostly a manifestation of the ligand effect. Introducing Ir into the second sublayer below a Pt_{ML} and a Pd_{ML} sublayer further reduces binding of OH on the Pt surface ($BE_{OH} = -2.00$ eV). In the case that the catalysts were not annealed prior to depositing the Pt overlayer, OH binding is enhanced ($BE_{OH} = -2.21$ eV), translating into ORR performance of the notannealed Pt_{ML}/IrPd inferior to that of pure Pt, as one can see in Figure 20(b). Therefore, according to our calculations, the annealed Pt_{ML}/PdIr catalyst possesses the weakest binding of OH of all systems studied here. Weaker binding of OH leads to lower OH coverage, less poisoning for ORR, and thereby higher ORR activity. Our calculations provide support to the reported distribution of Ir within the sublayers. In particular, the total energies of the two Pt_{ML}/PdIr model slabs employed suggest that Pd is more stable in the first sublayer (right below the Pt_{ML}) than Ir is. Therefore, upon annealing, Pd atoms are pulled from the bulk to form a Pd-rich first sublayer right below the Pt surface monolayer, with an Ir-rich second sublayer found right below the first Pd sublayer.

This work suggests that the introduction of Ir to the subsurface of the Pd core successfully modified the electronic and geometric properties of the substrate for the Pt_{ML}, which in turns benefit the ORR kinetics.

6. Other Modifications of Cores to Improve Pt_{ML} Electrocatalysts

In addition to the above approaches, some of our efforts were also put on the study of unconventional core materials for Pt_{ML}. Two examples will be briefly shown here.

In addition to the conventional carbon-supported metallic nanoparticles, we found that intermetallic compound can be a great alternative as the substrate for Pt monolayer [59]. Some intermetallic compound nanoparticles are stable and highly active catalysts for small organic molecular oxidation [60, 61]. Figure 21 shows the comparison of the

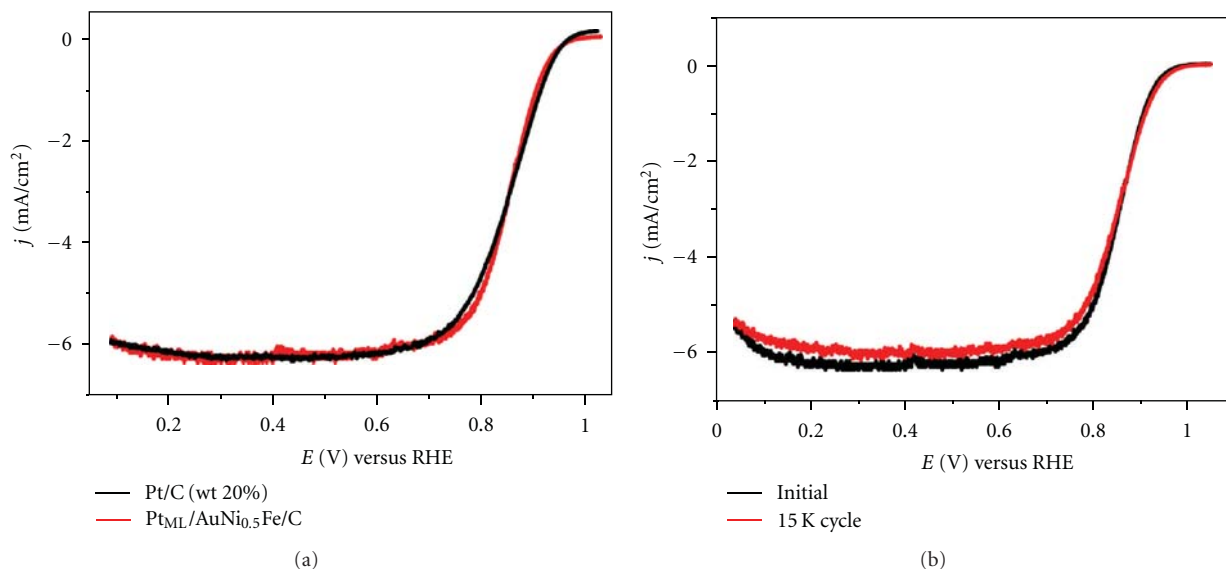


FIGURE 22: (a) Polarization curves of $\text{Pt}_{\text{ML}}/\text{AuNi}_{0.5}\text{Fe}/\text{C}$ and Pt/C in an oxygen-saturated 0.1 M HClO_4 ; (b) polarization curves for $\text{Pt}_{\text{ML}}/\text{AuNi}_{0.5}\text{Fe}/\text{C}$ before and after 15000 cycles of sweeping potentials between 0.6 and 1.0 V at 50 mV/s. Conditions: scan rate, 10 mV/s; rotation speed, 1600 rpm [62].

TABLE 2: Binding energy (BE) of OH (in eV) on several close-packed (111) model surfaces at 1/6 ML coverage.

	Pd	Pt	$\text{Pt}_{\text{ML}}/\text{Pd}$	$\text{Pt}_{\text{ML}}/\text{Pd}/\text{PdIr}_2/\text{Pd}$	$\text{Pt}_{\text{ML}}/\text{PdIr}_2/\text{Pd}$
BE_{OH} (eV)	-2.29	-2.17	-2.07	-2.00	-2.21

Zero of the energy scale corresponds to $\text{OH}(\text{g})$ and the respective metal slab at infinite separation from each other. $\text{Pt}_{\text{ML}}/\text{Pd}/\text{PdIr}_2/\text{Pd}$ represents the synthesized annealed catalyst ($\text{Pt}_{\text{ML}}\text{PdIr}$) whereas $\text{Pt}_{\text{ML}}/\text{PdIr}_2/\text{Pd}$ would be the expected catalyst without annealing ($\text{Pt}_{\text{ML}}\text{IrPd}$). The BE of OH on other relevant model systems is provided for comparison [58].

ORR activity of the Pt_{ML} electrocatalysts with intermetallic compound PtPb and PdFe cores with the standard Pt/C . The activity of the Pt/C is inferior to those Pt_{ML} intermetallics. It demonstrated that the combination of highly stable, inexpensive intermetallics with Pt monolayer is promising in the design of electrocatalysts with high activity, low metal content, and high stability.

Another example is using multimetallic nanoparticles as the substrate for Pt monolayer. Our study on $\text{Pt}_{\text{ML}}/\text{AuNi}_{0.5}\text{Fe}/\text{C}$ [62] demonstrated that by choosing proper combination of metals, the multimetallic core materials can be a promising substrate for Pt_{ML} for the ORR from the synergetic contribution from each metal component. Figure 22 shows the ORR activity (a) and stability (b) of this catalyst. 5- and 7-fold increase in the Pt mass and specific activities, respectively, compared with Pt/C and an insignificant loss in the electrochemical surface area and almost unchanged activity were achieved.

7. Summary

This review demonstrates that the ORR activity of Pt_{ML} electrocatalysts can be further improved by the modification of surface and subsurface of the core materials. The removal of surface low-coordination sites, generation (via addition or segregation) of an interlayer between Pt_{ML} and the core, or the introduction of a second metal component to

the subsurface layer of the core can further improve the ORR activity and/or stability of Pt_{ML} electrocatalysts. These modifications generate the alternation of the interactions between the substrate and the Pt_{ML} , involving the changes on both electronic (ligand) and geometric (strain) properties of the substrates. The improvements resulted from the application of these approaches provide a new perspective to designing of the new generation Pt_{ML} electrocatalysts.

Acknowledgment

This paper is supported by US Department of Energy (DOE), Divisions of Chemical and Material Sciences, under Contract no. DE-AC02-98CH10886.

References

- [1] R. R. Adzic, J. Zhang, K. Sasaki et al., "Platinum monolayer fuel cell electrocatalysts," *Topics in Catalysis*, vol. 46, no. 3-4, pp. 249-262, 2007.
- [2] S. R. Brankovic, J. X. Wang, and R. R. Adžić, "Metal monolayer deposition by replacement of metal adlayers on electrode surfaces," *Surface Science*, vol. 474, no. 1-3, pp. L173-L179, 2001.
- [3] J. Zhang, F. H. B. Lima, M. H. Shao et al., "Platinum monolayer on nonnoble metal-noble metal core-shell nanoparticle electrocatalysts for O_2 reduction," *Journal of Physical Chemistry B*, vol. 109, no. 48, pp. 22701-22704, 2005.

- [4] J. Zhang, M. B. Vukmirovic, K. Sasaki, A. U. Nilekar, M. Mavrikakis, and R. R. Adzic, "Mixed-metal Pt monolayer electrocatalysts for enhanced oxygen reduction kinetics," *Journal of the American Chemical Society*, vol. 127, no. 36, pp. 12480–12481, 2005.
- [5] J. Zhang, M. B. Vukmirović, K. Sasaki, F. Uribe, and R. R. Adžić, "Platinum monolayer electrocatalysts for oxygen reduction: effect of substrates, and long-term stability," *Journal of the Serbian Chemical Society*, vol. 70, no. 3, pp. 513–525, 2005.
- [6] J. Zhang, M. B. Vukmirovic, Y. Xu, M. Mavrikakis, and R. R. Adzic, "Controlling the catalytic activity of platinum-monolayer electrocatalysts for oxygen reduction with different substrates," *Angewandte Chemie International Edition*, vol. 44, no. 14, pp. 2132–2135, 2005.
- [7] M. Shao, K. Sasaki, N. S. Marinkovic, L. Zhang, and R. R. Adzic, "Synthesis and characterization of platinum monolayer oxygen-reduction electrocatalysts with Co-Pd core-shell nanoparticle supports," *Electrochemistry Communications*, vol. 9, no. 12, pp. 2848–2853, 2007.
- [8] M. H. Shao, K. Sasaki, P. Liu, and R. R. Adzic, "Pd3Fe and Pt monolayer-modified Pd3Fe electrocatalysts for oxygen reduction," *Zeitschrift für Physikalische Chemie*, vol. 221, no. 9-10, pp. 1175–1190, 2007.
- [9] M. B. Vukmirovic, J. Zhang, K. Sasaki et al., "Platinum monolayer electrocatalysts for oxygen reduction," *Electrochimica Acta*, vol. 52, no. 6, pp. 2257–2263, 2007.
- [10] K. Sasaki, L. Zhang, and R. R. Adzic, "Niobium oxide-supported platinum ultra-low amount electrocatalysts for oxygen reduction," *Physical Chemistry Chemical Physics*, vol. 10, no. 1, pp. 159–167, 2008.
- [11] A. U. Nilekar, Y. Xu, J. Zhang et al., "Bimetallic and ternary alloys for improved oxygen reduction catalysis," *Topics in Catalysis*, vol. 46, pp. 276–284, 2007.
- [12] Y. Xu, A. V. Ruban, and M. Mavrikakis, "Adsorption and dissociation of O₂ on Pt-Co and Pt-Fe alloys," *Journal of the American Chemical Society*, vol. 126, no. 14, pp. 4717–4725, 2004.
- [13] J. X. Wang, H. Inada, L. Wu et al., "Oxygen reduction on well-defined core-shell nanocatalysts: particle size, facet, and Pt shell thickness effects," *Journal of the American Chemical Society*, vol. 131, no. 47, pp. 17299–17302, 2009.
- [14] E. Santos, P. Quaino, and W. Schmickler, "On the electrocatalysis of nanostructures: monolayers of a foreign atom (Pd) on different substrates M(1 1 1)," *Electrochimica Acta*, vol. 55, no. 14, pp. 4346–4352, 2010.
- [15] B. Hammer and J. K. Nørskov, "Theoretical surface science and catalysis—calculations and concepts," in *Advances in Catalysis*, C. G. Bruce and K. Helmut, Eds., vol. 45, pp. 71–129, Academic Press, 2000.
- [16] M. Shao, P. Liu, J. Zhang, and R. Adzic, "Origin of enhanced activity in palladium alloy electrocatalysts for oxygen reduction reaction," *Journal of Physical Chemistry B*, vol. 111, no. 24, pp. 6772–6775, 2007.
- [17] J. Greeley and M. Mavrikakis, "Alloy catalysts designed from first principles," *Nature Materials*, vol. 3, pp. 810–815, 2004.
- [18] J. Greeley, J. K. Nørskov, and M. Mavrikakis, "Electronic structure and catalysis on metal surfaces," *Annual Review of Physical Chemistry*, vol. 53, pp. 319–348, 2002.
- [19] M. H. Shao, T. Huang, P. Liu et al., "Palladium monolayer and palladium alloy electrocatalysts for oxygen reduction," *Langmuir*, vol. 22, no. 25, pp. 10409–10415, 2006.
- [20] N. M. Marković, H. A. Gasteiger, B. N. Grgur, and P. N. Ross, "Oxygen reduction reaction on Pt(111): effects of bromide," *Journal of Electroanalytical Chemistry*, vol. 467, no. 1, pp. 157–163, 1999.
- [21] V. Stamenkovic, B. S. Mun, K. J. J. Mayrhofer et al., "Changing the activity of electrocatalysts for oxygen reduction by tuning the surface electronic structure," *Angewandte Chemie International Edition*, vol. 45, no. 18, pp. 2897–2901, 2006.
- [22] Y. Cai, C. Ma, Y. Zhu, J. X. Wang, and R. R. Adzic, "Low-coordination sites in oxygen-reduction electrocatalysis: their roles and methods for removal," *Langmuir*, vol. 27, no. 13, pp. 8540–8547, 2011.
- [23] K. J. J. Mayrhofer, B. B. Blizanac, M. Arenz, V. R. Stamenkovic, P. N. Ross, and N. M. Markovic, "The impact of geometric and surface electronic properties of Pt-catalysts on the particle size effect in electrocatalysis," *Journal of Physical Chemistry B*, vol. 109, no. 30, pp. 14433–14440, 2005.
- [24] A. Carrasquillo, J. J. Jeng, R. J. Barriga, W. F. Temesghen, and M. P. Soriaga, "Electrode-surface coordination chemistry: ligand substitution and competitive coordination of halides at well-defined Pd(100) and Pd(111) single crystals," *Inorganica Chimica Acta*, vol. 255, no. 2, pp. 249–254, 1997.
- [25] E. Budevski, G. Staikov, and W. J. Lorenz, *Electrochemical Phase Formation and Growth—An Introduction to the Initial Stages of Metal Deposition*, VCH Verlagsgesellschaft mbH, Weinheim, Germany, 1996.
- [26] J. X. Wang, N. M. Markovic, and R. R. Adzic, "Kinetic analysis of oxygen reduction on Pt(111) in acid solutions: intrinsic kinetic parameters and anion adsorption effects," *Journal of Physical Chemistry B*, vol. 108, no. 13, pp. 4127–4133, 2004.
- [27] P. W. Voorhees, "The theory of Ostwald ripening," *Journal of Statistical Physics*, vol. 38, no. 1-2, pp. 231–252, 1985.
- [28] K. Gong, W. F. Chen, K. Sasaki et al., "Platinum-monolayer electrocatalysts: palladium interlayer on IrCo alloy core improves activity in oxygen-reduction reaction," *Journal of Electroanalytical Chemistry*, 2010.
- [29] D. A. J. Rand and R. Woods, "Cyclic voltammetric studies on Iridium electrodes in sulfuric acid solutions—nature of oxygen layer and metal dissolution," *Journal of Electroanalytical Chemistry*, vol. 55, pp. 375–381, 1974.
- [30] F. J. Vidal-Iglesias, J. Solla-Gullón, V. Montiel, J. M. Feliu, and A. Aldaz, "Screening of electrocatalysts for direct ammonia fuel cell: ammonia oxidation on PtMe (Me: Ir, Rh, Pd, Ru) and preferentially oriented Pt(1 0 0) nanoparticles," *Journal of Power Sources*, vol. 171, no. 2, pp. 448–456, 2007.
- [31] K. Lee, L. Zhang, and J. Zhang, "IrxCo_{1-x} (x = 0.3 – 1.0) alloy electrocatalysts, catalytic activities, and methanol tolerance in oxygen reduction reaction," *Journal of Power Sources*, vol. 170, no. 2, pp. 291–296, 2007.
- [32] J. Greeley, I. E. L. Stephens, A. S. Bondarenko et al., "Alloys of platinum and early transition metals as oxygen reduction electrocatalysts," *Nature Chemistry*, vol. 1, no. 7, pp. 552–556, 2009.
- [33] G. Kresse and J. Furthmüller, "Efficient iterative schemes for ab initio total-energy calculations using a plane-wave basis set," *Physical Review B*, vol. 54, no. 16, pp. 11169–11186, 1996.
- [34] G. Kresse and J. Furthmüller, "Efficiency of ab-initio total energy calculations for metals and semiconductors using a plane-wave basis set," *Computational Materials Science*, vol. 6, pp. 15–50, 1996.
- [35] J. P. Perdew, K. Burke, and M. Ernzerhof, "Generalized gradient approximation made simple," *Physical Review Letters*, vol. 77, no. 18, pp. 3865–3868, 1996.
- [36] J. K. Nørskov, J. Rossmeisl, A. Logadottir et al., "Origin of the overpotential for oxygen reduction at a fuel-cell cathode,"

- Journal of Physical Chemistry B*, vol. 108, no. 46, pp. 17886–17892, 2004.
- [37] G. E. Ramírez-Caballero, Y. Ma, R. Callejas-Tovar, and P. B. Balbuena, “Surface segregation and stability of core-shell alloy catalysts for oxygen reduction in acid medium,” *Physical Chemistry Chemical Physics*, vol. 12, no. 9, pp. 2209–2218, 2010.
- [38] Y. Xing, Y. Cai, M. B. Vukmirovic et al., “Enhancing oxygen reduction reaction activity via Pd-Au alloy sublayer mediation of Pt monolayer electrocatalysts,” *Journal of Physical Chemistry Letters*, vol. 1, no. 21, pp. 3238–3242, 2010.
- [39] L. Wang, A. Roudgar, and M. Eikerling, “Ab initio study of stability and site-specific oxygen adsorption energies of Pt nanoparticles,” *Journal of Physical Chemistry C*, vol. 113, no. 42, pp. 17989–17996, 2009.
- [40] Q. Jiang, L. H. Liang, and D. S. Zhao, “Lattice contraction and surface stress of fcc nanocrystals,” *Journal of Physical Chemistry B*, vol. 105, no. 27, pp. 6275–6277, 2001.
- [41] W. J. Huang, R. Sun, J. Tao, L. D. Menard, R. G. Nuzzo, and J. M. Zuo, “Coordination-dependent surface atomic contraction in nanocrystals revealed by coherent diffraction,” *Nature Materials*, vol. 7, no. 4, pp. 308–313, 2008.
- [42] J. Zhang, Y. Mo, M. B. Vukmirovic, R. Klie, K. Sasaki, and R. R. Adzic, “Platinum monolayer electrocatalysts for O₂ reduction: Pt monolayer on Pd(111) and on carbon-supported Pd nanoparticles,” *Journal of Physical Chemistry B*, vol. 108, no. 30, pp. 10955–10964, 2004.
- [43] C. Wang, D. Van Der Vliet, K. L. More et al., “Multimetallic Au/FePt₃ nanoparticles as highly durable electrocatalyst,” *Nano Letters*, vol. 11, no. 3, pp. 919–926, 2011.
- [44] J. Zhang, K. Sasaki, E. Sutter, and R. R. Adzic, “Stabilization of platinum oxygen-reduction electrocatalysts using gold clusters,” *Science*, vol. 315, no. 5809, pp. 220–222, 2007.
- [45] W. Tang, S. Jayaraman, T. F. Jaramillo, G. D. Stucky, and E. W. McFarland, “Electrocatalytic activity of gold-platinum clusters for low temperature fuel cell applications,” *Journal of Physical Chemistry C*, vol. 113, no. 12, pp. 5014–5024, 2009.
- [46] J. B. Xu, T. S. Zhao, S. Y. Shen, and Y. S. Li, “Stabilization of the palladium electrocatalyst with alloyed gold for ethanol oxidation,” *International Journal of Hydrogen Energy*, vol. 35, no. 13, pp. 6490–6500, 2010.
- [47] W. P. Zhou, X. Yang, M. B. Vukmirovic et al., “Improving electrocatalysts for O₂ reduction by fine-tuning the Pt-support interaction: Pt monolayer on the surfaces of a Pd₃Fe(111) single-crystal alloy,” *Journal of the American Chemical Society*, vol. 131, no. 35, pp. 12755–12762, 2009.
- [48] M. H. Shao, K. Sasaki, and R. R. Adzic, “Pd-Fe nanoparticles as electrocatalysts for oxygen reduction,” *Journal of the American Chemical Society*, vol. 128, no. 11, pp. 3526–3527, 2006.
- [49] J. L. Fernández, J. Michael White, Y. Sun, W. Tang, G. Henkelman, and A. J. Bard, “Characterization and theory of electrocatalysts based on scanning electrochemical microscopy screening methods,” *Langmuir*, vol. 22, no. 25, pp. 10426–10431, 2006.
- [50] J. L. Fernández, V. Raghuvier, A. Manthiram, and A. J. Bard, “Pd-Ti and Pd-Co-Au electrocatalysts as a replacement for platinum for oxygen reduction in proton exchange membrane fuel cells,” *Journal of the American Chemical Society*, vol. 127, no. 38, pp. 13100–13101, 2005.
- [51] M. H. Shao, P. Liu, and R. R. Adzic, “Superoxide anion is the intermediate in the oxygen reduction reaction on platinum electrodes,” *Journal of the American Chemical Society*, vol. 128, no. 23, pp. 7408–7409, 2006.
- [52] N. Hoshi, K. Kagaya, and Y. Hori, “Voltammograms of the single-crystal electrodes of palladium in aqueous sulfuric acid electrolyte: Pd(S)-[n(111)×(111)] and Pd(S)-[n(100)×(111)],” *Journal of Electroanalytical Chemistry*, vol. 485, no. 1, pp. 55–60, 2000.
- [53] N. Hoshi, M. Kuroda, and Y. Hori, “Voltammograms of stepped and kinked stepped surfaces of palladium: Pd(S)-[n(111)×(100)] and Pd(S)-[n(100)×(110)],” *Journal of Electroanalytical Chemistry*, vol. 521, no. 1-2, pp. 155–160, 2002.
- [54] M. Baldauf and D. M. Kolb, “A hydrogen adsorption and absorption study with ultrathin Pd overlayers on Au(111) and Au(100),” *Electrochimica Acta*, vol. 38, no. 15, pp. 2145–2153, 1993.
- [55] M. Arenz, V. Stamenkovic, T. J. Schmidt, K. Wandelt, P. N. Ross, and N. M. Markovic, “CO adsorption and kinetics on well-characterized Pd films on Pt(1 1 1) in alkaline solutions,” *Surface Science*, vol. 506, no. 3, pp. 287–296, 2002.
- [56] V. R. Stamenkovic, B. Fowler, B. S. Mun et al., “Improved oxygen reduction activity on Pt₃Ni(111) via increased surface site availability,” *Science*, vol. 315, no. 5811, pp. 493–497, 2007.
- [57] V. R. Stamenkovic, B. S. Mun, K. J. J. Mayrhofer, P. N. Ross, and N. M. Markovic, “Effect of surface composition on electronic structure, stability, and electrocatalytic properties of Pt-transition metal alloys: Pt-skin versus Pt-skeleton surfaces,” *Journal of the American Chemical Society*, vol. 128, no. 27, pp. 8813–8819, 2006.
- [58] S. L. Knupp, M. B. Vukmirovic, P. Haldar, J. A. Herron, M. Mavrikakis, and R. R. Adzic, “Platinum monolayer electrocatalysts for O₂ reduction: Pt monolayer on carbon-supported PdIr nanoparticles,” *Electrocatalysis*, pp. 1–11, 2010.
- [59] T. Ghosh, M. B. Vukmirovic, F. J. DiSalvo, and R. R. Adzic, “Intermetallics as novel supports for Pt monolayer O₂ reduction electrocatalysts: potential for significantly improving properties,” *Journal of the American Chemical Society*, vol. 132, no. 3, pp. 906–907, 2010.
- [60] L. R. Alden, C. Roychowdhury, F. Matsumoto et al., “Synthesis, characterization, and electrocatalytic activity of PtPb nanoparticles prepared by two synthetic approaches,” *Langmuir*, vol. 22, no. 25, pp. 10465–10471, 2006.
- [61] C. Roychowdhury, F. Matsumoto, V. B. Zeldovich et al., “Synthesis, characterization, and electrocatalytic activity of PtBi and PtPb nanoparticles prepared by borohydride reduction in methanol,” *Chemistry of Materials*, vol. 18, no. 14, pp. 3365–3372, 2006.
- [62] K. Gong, D. Su, and R. R. Adzic, “Platinum-monolayer shell on AuNi_{0.5}Fe nanoparticle core electrocatalyst with high activity and stability for the oxygen reduction reaction,” *Journal of the American Chemical Society*, vol. 132, no. 41, pp. 14364–14366, 2010.

Research Article

Potentiostatic Testing of Oxygen Reduction on Polymer Carbon Electrodes

C. A. C. Sequeira and D. M. F. Santos

ICEMS and Instituto Superior Técnico, TU Lisbon, Av. Rovisco Pais, 1049-001 Lisboa, Portugal

Correspondence should be addressed to C. A. C. Sequeira, cesarsequeira@ist.utl.pt

Received 16 May 2011; Revised 2 August 2011; Accepted 4 August 2011

Academic Editor: Milan M. Jaksic

Copyright © 2011 C. A. C. Sequeira and D. M. F. Santos. This is an open access article distributed under the Creative Commons Attribution License, which permits unrestricted use, distribution, and reproduction in any medium, provided the original work is properly cited.

The preparation of polymer carbon electrocatalysts by the controlled pyrolysis of polyfurfuryl alcohol polymer is described. Potentiostatic testing in oxygen-saturated KOH electrolytes is performed, and electrokinetic properties of the electrodes prepared from the electrocatalysts are presented and discussed. It is revealed that a pure polymer carbon electrode pyrolysed in powder form possesses a very high active area, displaying higher catalytic activity than a polymer pyrolysed in bulk. Suitable reduction mechanisms are proposed.

1. Introduction

The four-electron reduction of oxygen in either acid or alkaline solution is of primary concern due to its possible use in fuel cells and metal-air batteries on the basis of its high theoretical equilibrium potential of 1.229 V versus a hydrogen electrode in the same solution.

The majority of research on this reaction has centred on the use of noble metal electrodes, due to their relative stability in acidic or alkaline solutions [1–9]. Emphasis has also been placed on the study of oxygen reduction on simple carbon electrodes [10–12] and carbon electrodes containing catalysts to aid in the decomposition of the peroxide intermediates to yield the four-electron reduction process [13–18]. Early research on metal chelates [19–22] has also shown that both the stability and the activity of these metal chelates could be greatly enhanced by adsorption onto a graphite or glassy carbon surface followed by a partial pyrolysis at 900°C. It was suggested that this heat treatment resulted in the partial pyrolysis and polymerisation of the adsorbed metal chelates enhancing the activity as a result of increased stability and increased electrical conductivity. Other workers reached practically similar conclusions.

The research for this series of works was based in part on the previously observed behaviour of oxygen reduction on pure and modified carbon electrodes and on the established

structure and properties of polymer (glassy) carbons [23–29]. Accordingly, the oxygen reduction kinetics and mechanism determination on pure and doped polymer carbon electrodes are being conducted in our laboratory. In this paper, results and subsequent analysis of the oxygen reduction reaction on two similar polymer carbon (PC) electrodes, differing in their preparation procedure, is presented. The activity of these electrodes in comparison to that of a Pt electrode is also illustrated.

2. Experimental

2.1. Electrode Synthesis. In this study, three electrodes were used: a Pt electrode and two PC electrodes (PCA and PCB). The following procedure was developed to synthesise the PCA electrode: 40.0 mL of furfuryl alcohol (NR Grade) was added to a 250 mL vacuum flask connected to an aspirator and sitting on a stirring/heating mantle. The flask was insulated with glass wool: 0.01 mL of 5 M HCl was added, and the flask stoppered with a thermometer to determine the temperature of the solution. Low heat was applied under stirring until the temperature reached 55°C. The heating was controlled so that the temperature was not allowed to rise higher than 75°C, due to the polymerization of the liquid that releases heat. The liquid was kept at 75°C for at least

one hour under constant stirring. Afterwards, a vacuum was applied by the aspirator to remove the water vapour. During evacuation, no heat was applied, and the temperature dropped below 40°C. Then, low heat was applied to maintain the temperature at 70°C for 30 min. Thereafter, the vacuum was discontinued and the polyfurfuryl alcohol resin poured into 20 mL test tubes with 1.25 cm diameter. The test tubes were then heated in an oven at a temperature of 85°C for 48 h followed by heating at 110°C for 24 h. After cooling, the polymer rod could be easily removed and sliced into 1-2 mm thick discs with a band saw. The discs were then polished on silicon carbide papers and acetone-soaked paper. After drying, weight and area measurements were made on each disc. The polymer discs were then placed on a porcelain disc of the same diameter and placed in a small porcelain boat. The boat was then placed into a tube furnace, designed to allow thermal treatment in the temperature range of 25°C to 1200°C. The heating rate was $15 \pm 1^\circ\text{C}/\text{hour}$ with the maximum temperature set for two hours. The pyrolysis was conducted under a nitrogen flow and atmospheric pressure. Thereafter, the furnace was allowed to cool naturally to room temperature. The polymer carbon discs were then removed and area and weight measurements conducted. It was observed that the percentage of weight loss of the discs after the pyrolysis at 1200°C was about 30%. The density, thickness, exposed area, and DC three-point conductivity of the prepared discs were about 1.53 g cm^{-3} , 0.15 cm, 0.75 cm^2 , and over $4 \times 10^{-2} \text{ mho cm}^{-1}$, respectively. Each disc was then stored in a separate corked test tube.

To largely increase the area of the PC electrodes, some of the prepared polymer discs were pyrolysed to 300°C. At this temperature, the polymer was practically pyrolysed, but was very brittle and could be powdered. Then, the pyrolysis was followed to the desired temperature, as in the procedure outlined for the PCA discs. The resulting electrocatalyst possessed a much higher active area than the polymer pyrolysed in bulk, allowing the construction of PCB electrodes from this material by compressing the electrocatalyst with a PVDF binder and baking.

2.2. Potentiostatic Testing. The electrochemical measurements were taken in a conventional three-compartment cell with PAR equipment. Each specially mounted PC served as the working electrode. The counter electrode was a Pt gauge, and a saturated calomel electrode served as the reference electrode. Before inserting the electrodes, the cell was pre-cleaned by soaking in a Chromerge bath followed by washing with bidistilled water and oven dried. Then a fresh electrolyte solution (200 mL KOH pH 13.9 and KOH + KCl solutions of decreasing pH) was added for each particular test. Oxygen and oxygen-nitrogen mixtures flowed continually for 4 hours to allow the solution to saturate with the gas and the working electrode to reach a stable rest potential. The potential was slowly polarized negatively until a limiting current density of about 0.1 mA cm^{-2} was approached.

It should be noted that the reported current densities are referred to the apparent surface area (75 mm^2) of the PC electrodes; the real surface area, as determined from static

volumetric methods, was $120 \text{ m}^2 \text{ g}^{-1}$ (PCB) and $1 \text{ m}^2 \text{ g}^{-1}$ (PCA). All experiments were conducted at $298 \pm 2 \text{ K}$.

3. Results and Discussion

3.1. Determination of α , i_0 , and i_l . The general method of dealing with a net reaction rate, in which a limiting rate can occur, uses the following equation to derive a relation for the current density, (i)

$$\left(\frac{1}{i}\right) = \left(\frac{1}{i_{ab}}\right) + \left(\frac{1}{i_l}\right). \quad (1)$$

The term i_{ab} is the current density in the absence of any limiting current density, i_l . Equation (1) provides the basis for the following logical steps, since it takes into account charge transfer and diffusion steps, which commonly occur in many electrochemical processes [30, 31]. Rearranging (1) gives

$$i = i_{ab} \left[1 - \left(\frac{i}{i_l}\right)\right]. \quad (2)$$

The current density i_{ab} can be expressed as a function of the exchange current density, i_0 , and the overpotential, η , by the following expression:

$$i_{ab} = i_0 \exp\left(\frac{\alpha F \eta}{RT}\right), \quad (3)$$

where α is the cathodic transfer coefficient. In oxygen reduction, the observed rest potentials [10, 32, 33] are over 100 mV cathodic to the true equilibrium potential, E_r^0 . For this reason, the applied overpotential is large enough so that the anodic current density can be neglected in relation to the cathodic current density, as represented by (3). The overpotential, η , represents the difference between the standard equilibrium for oxygen reduction, E_r^0 , and the potential set by the potentiostat with reference to an hydrogen electrode in the same solution (E_{he}):

$$\eta = E_r^0 - E_{he}. \quad (4)$$

Here, η will always refer to a cathodic overpotential. Insertion of (3) into (2) followed by rearrangement yields

$$\eta = \left(\frac{RT}{\alpha F}\right) \ln\left[\frac{i}{i_l - i}\right] + \left(\frac{RT}{\alpha F}\right) \ln\left[\frac{i_l}{i_0}\right]. \quad (5)$$

Thus, it can be seen from (5) that a plot of η as a function of $\ln[i/(i_l - i)]$ will give a linear relationship, with a slope of $(RT/\alpha F)$ and an intercept of $(RT/\alpha F) \ln(i_l/i_0)$.

This allowed for the maximum number of data points to be used in the analysis. In the normal Tafel plot of η as a function of $\ln i$, as the current density increased to more than 10% of the limiting current density, the points would fall off the linear Tafel plot. Equation (5) allows these points to be used effectively in the analysis.

In order to use (5), it was necessary to know the limiting current density. With the potentiostatic technique employed, the limiting current density was approached but

never actually reached experimentally. At each potential, the current was allowed to come to a steady value, but, at the point of the limiting current density (which should be constant), a steady current density was never achieved. Instead, current oscillations were observed because at i_l the oxygen concentration drops to zero, and then there is no ionic charge to counterbalance the electronic charge imposed by the potentiostatic technique. The limiting current density was calculated in another manner using all the potentiostatic data up to the point at which oscillations were observed. These points were all steady values. With this method, the limiting current density did not have to be estimated from the graphs of the potential as a function of $\ln i$. As a starting point in this determination, an arbitrary current density slightly greater than the largest value observed experimentally was used to calculate a least squares fit of η as a function of $\ln[i/(i_l - i)]$ and a corresponding correlation coefficient, R_c . R_c is merely a measure of the fit of the calculated line to the data points. It could vary from -1 to $+1$ depending on whether the slope was negative or positive and how well the fit was. A perfect correlation would be ± 1 . The $\ln i_l$ was then decreased by a small increment and another least squares fit calculated for η as a function of $\ln[i/(i_l - i)]$ using the new value of i_l . If the correlation coefficient indicated a better fit, then the value of $\ln i_l$ was decreased again and the identical procedure followed. The R_c value would reach a maximum absolute value of 0.97 and then begin to decrease with the decrease in $\ln i_l$. The value of $\ln i_l$ which gave the maximum absolute value for R_c was interpreted to be the most accurate value for the actual $\ln i_l$ and was used to give the optimum and the most accurate value for the diffusion current density. This procedure was written into a noncommercial computer program so that the data could be analysed quickly and efficiently.

Using this optimum limiting diffusion current density, the transfer coefficient and the exchange current density could be determined from the slope (S) and the y -intercept (Y) of η as a function of $\ln[i/(i_l - i)]$, also calculated by this computer program,

$$\alpha = \left(\frac{RT}{SF} \right), \quad (6)$$

$$i_0 = i_l \exp\left(\frac{-\alpha FY}{RT} \right).$$

This computer analysis was completed for the data obtained from each potentiostatic run made for all electrodes tested.

3.2. Reaction Order with respect to $[\text{OH}^-]$. In order to calculate the reaction orders, it was necessary to know the current density, i , as a function of the potential with respect to a standard hydrogen electrode E [34, 35] as shown by the following relation for the possible O_2 reduction on the PC electrodes, yielding OH^- ions:

$$i = k[\text{OH}^-]^m [\text{O}_2]^p \exp\left[\frac{-\alpha FE}{RT} \right]. \quad (7)$$

The value of k refers to the rate constant for the reaction. By taking the log of both sides of (7), the reaction order

with respect to $[\text{OH}^-]$, m , can be expressed by the following derivative at constant potential, E , and constant $[\text{O}_2]$:

$$m = \left(\frac{\partial \log i}{\partial \log [\text{OH}^-]} \right)_E. \quad (8)$$

This value of m can also be determined from the derivative of $\log i$ with respect to pH at constant potential, E , as shown in the following equations:

$$\text{pH} = 14 + \log [\text{OH}^-],$$

$$\left(\frac{\partial \text{pH}}{\partial \log [\text{OH}^-]} \right)_E = 1,$$

$$m = \left(\frac{\partial \log i}{\partial \log [\text{OH}^-]} \right)_E \quad (9)$$

$$= \left(\frac{\partial \log i}{\partial \text{pH}} \right)_E \times \left(\frac{\partial \text{pH}}{\partial \log [\text{OH}^-]} \right)_E$$

$$= \left(\frac{\partial \log i}{\partial \text{pH}} \right)_E.$$

Thus, from a least squares analysis of $\log i$ as a function of pH at constant potential, E , and constant $[\text{O}_2]$, the reaction order m can be determined from the slope. It should be noted that one usually considers the inward and outward O_2/OH^- reactions to more correctly define the reaction order, m , with respect to $[\text{OH}^-]$.

Experimentally it was difficult to determine the values of the current density at the exact same potential values, E , for each different electrolyte pH. It was much simpler to use the procedure outlined earlier to determine the values of α and i_0 by the least squares computer analysis for oxygen reduction on these electrodes in oxygen-saturated electrolytes of differing pH. Using these parameters, the values of $\log i$ as a function of the electrolyte pH in which these parameters were determined could be calculated at a constant value of potential, E . A least squares analysis of these data would yield a value of m at each potential E . The potential values were in increments of 5 to 10 mV and were chosen to give the same range of current densities as observed experimentally in the potentiostatic analysis. The average of the orders m calculated at each potential E was reported as the most probable reaction order with respect to $[\text{OH}^-]$. Calculated in this manner, most of the experimentally determined data points could be used. This varied from 40 to 120 data points, depending on the electrode being tested.

The relation necessary to calculate $\log i$ as a function of pH for a set potential E with reference to a standard hydrogen electrode can be derived from (3) and (4). The potential with respect to a hydrogen electrode in the same electrolyte can be expressed by the following relation under constant oxygen saturation:

$$E_{\text{he}} = E + 0.0591 \text{pH}. \quad (10)$$

Substitution of (10) into (4) yields

$$\eta = E_r^0 - E - 0.0591 \text{pH}. \quad (11)$$

Substitution of (11) into (3) followed by taking the log of both sides yields (letting i represent i_{ab})

$$\log i = \left[\frac{\alpha F}{2.30 RT} \right] \left[E_r^0 - E - 0.0591 \text{pH} + \left(\frac{RT}{\alpha F} \right) \ln i_0 \right]. \quad (12)$$

Thus, from the potentiostatic data for oxygen reduction at each electrolyte pH, analysis values for α and i_0 are calculated via the least squares computer analysis at the particular pH. These can be fed into (12) for each corresponding value of pH and used to generate $\log i$ as a function of the pH for set values of potential. The value used for E_r^0 , for oxygen reduction in an electrolyte saturated with oxygen at 1 atm. measured with respect to a hydrogen electrode in the same electrolyte, was 1.229 V. Any change due to the lower atmospheric pressure is accounted for by the experimental value of i_0 used in (12). This was the case since the value of the overpotential calculated from (4) used the value of 1.229 for E_r^0 also.

3.3. Reaction Order with respect to $[O_2]$. This calculation was completed in much the same manner as the calculation of the reaction order with respect to $[OH^-]$. By taking the log of both sides of (7), the reaction order with respect to $[O_2]$, p , can be expressed by the following derivative at constant potential E and constant pH:

$$p = \left(\frac{\partial \log i}{\partial \log [O_2]} \right)_{E, \text{pH}}. \quad (13)$$

Since the oxygen concentration in the electrode is directly proportional to the oxygen partial pressure, the oxygen concentration was varied by dilution with nitrogen. This was controlled by measuring the flow rate of each gas before mixing. The potentiostatic analysis was performed in the pH range of 13.9 to 10.9.

From the potentiostatic data at each oxygen partial pressure, the values of α and i_0 for each oxygen partial pressure were determined via the least squares computer analysis outlined previously. These values could then be inserted into (12) in order to calculate $\log i$ as a function of the log of the oxygen partial pressure, $\log [O_2]$ for each set potential E . For each value of potential E , a least squares analysis was performed on the data which yielded the order of the reaction with respect to $[O_2]$ from the slope of the function (13). The average of the orders calculated at all potential values E was taken as the most probable order of the reaction with respect to $[O_2]$.

3.4. Analysis of the Observed Rest Potentials. A limited analysis of the observed rest potentials (open-circuit potentials) for oxygen reduction on these electrodes was conducted from the data used to determine the reaction orders. This should be considered to be a rough determination of dependence of the rest potentials on $[OH^-]$ and $[O_2]$ due to the small number of data points available. They were sufficient to indicate the dependencies though.

The observed rest potential, E_r , can be expressed as a function of the observed standard potential, E_r^0 , the total

number of electrons transferred in the reaction, n , the concentration $[OH^-]$, and the oxygen partial pressure, $[O_2]$, by the following relation, assuming that the activity coefficients are 1:

$$E_r = E_r^0 - \left(\frac{RT}{nF} \right) \ln \left([OH^-]^{m'} [O_2]^{-p'} \right). \quad (14)$$

Equation (14) can be rearranged to yield

$$E_r = E_r^0 - \left(\frac{2.3RTm'}{nF} \right) \log [OH^-] + \left(\frac{2.3RTp'}{nF} \right) \log [O_2]. \quad (15)$$

From (15) and (9), it can be seen that the value of m' can be determined from the derivative of the potential, E_r , with respect to the pH, and the value of p' from the derivative of the potential E_r , with respect to the $\log [O_2]$ values:

$$m' = \left(\frac{nF}{2.3RT} \right) \left(\frac{\partial E_r}{\partial \text{pH}} \right)_{[O_2]}, \quad (16)$$

$$p' = \left(\frac{nF}{2.3RT} \right) \left(\frac{\partial E_r}{\partial \log [O_2]} \right)_{\text{pH}}.$$

These values should not be confused with the reaction orders m and p . A least squares analysis is performed on the values of E_r as a function of pH and the $\log [O_2]$ in which m' and p' are determined from (16) for possible values of n ranging from 1 to 4. This value is unknown since the equilibrium potential may or may not be due to the 4 electron transfer reduction of oxygen. The possibilities are discussed below.

3.5. Calculated Mechanistic Criteria. Figure 1 shows representative oxygen reduction kinetics on the two pure polymer carbon electrodes developed in this study relative to the kinetics on a Pt metal electrode. The maximum pyrolysis temperature of the synthesised PCs was 1200°C. The Pt electrode was obtained commercially and mounted in an arrangement similar to the PCs such that the test conditions of all the electrodes were equivalent. The kinetic analysis of oxygen reduction on this Pt electrode was not conducted since numerous studies have appeared in the general literature for this electrode [2]. However, the authors are aware that it would be informative for the limiting current estimation. From the analysis of the obtained potentiostatic data, it could be seen that there exists a limiting current density, i_l , of approximately 0.1 mA cm⁻² for oxygen reduction on the PC electrodes in oxygen-saturated electrolyte. This was also the case for oxygen reduction on the shielded Pt electrode under the same conditions of oxygen saturation and pH (see Figure 1).

This was due to the limited diffusion of reactants to the surface. For most of the tests, the hydroxyl anion concentration was 0.83 M, decreasing to 8.3×10^{-4} M in some tests. The solubility of oxygen in a KOH electrolyte of 0.13 M is approximately 9.0×10^{-4} M [36]. The reactant which is the probable cause of the limiting diffusion current density is then oxygen since the i_l did not change as $[OH^-]$ decreased. Then, the depletion of oxygen at the surface as

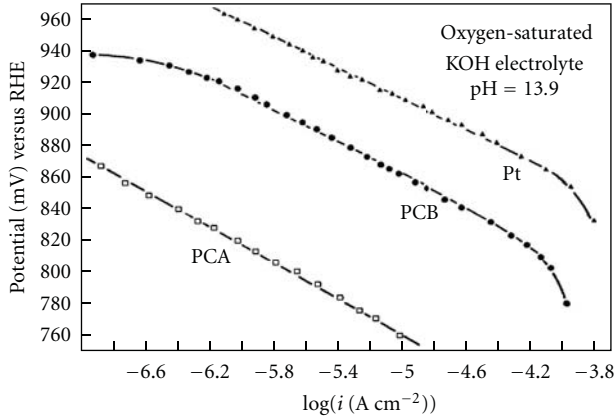


FIGURE 1: A comparison of the oxygen reduction kinetics on the prepared polymer carbon electrodes with that of a Pt metal electrode.

the rate of reduction increases results in a diffusion overpotential [34].

Plots of the applied potential as a function of $\ln[i/(i_l - i)]$, as shown in Figure 2, gave linear relationships for the oxygen reduction on the studied PCs in oxygen-saturated KOH electrolytes of pH ranging from 13.9 to 10.9.

The use of these plots, combined with (6), enabled the calculation of α , i_0 , and i_l . The average values for these kinetic parameters are as follows: 1.0 ± 0.08 for α , $(1.0 \pm 0.4) \times 10^{-8}$ A cm $^{-2}$ (PCA) and $(1.0 \pm 0.2) \times 10^{-6.5}$ A cm $^{-2}$ (PCB) for i_0 , and $(4.9 \pm 0.4) \times 10^{-5}$ A cm $^{-2}$ (PCA) and $(1.3 \pm 0.2) \times 10^{-4}$ A cm $^{-2}$ (PCB) for i_l . We recall that the transfer coefficient α is an experimental parameter obtained from the current-potential relationship, allowing us to evaluate the mechanism of electrode reactions or to distinguish between different plausible mechanisms. In the present case the fitted parameter $\alpha = 1$ could suggest that if the anodic transfer coefficient, β (the factor in the anodic direction), is equal to α , then $\alpha + \beta = 2$; that is, our reduction mechanism could be seen as a multistep electrode process involving the transfer of two electrons (see below). The fitted parameter $\alpha = 1$ has been found by many workers as cited in [2].

Figure 3 shows the dependence of the oxygen reduction kinetics on the electrolyte pH for the prepared PC electrodes, and Figure 4 shows the dependence of the oxygen reduction kinetics on the oxygen partial pressure for the prepared PC electrodes in KOH electrolyte of pH = 13.9. In these figures, i is the measured current density.

From these figures, (9) and (13), the values for m and p could be calculated. The results indicate that for the pH range of 13.9 to 10.9, the rate kinetics for oxygen reduction on the PC electrodes can be represented by the following equation:

$$\begin{aligned} \text{PCA, pH 13.9-10.9: } i &= K[\text{O}_2] \exp\left(\frac{-FE}{RT}\right), \\ \text{PCB, pH 13.9-11.9: } i &= K[\text{OH}^-]^{-1/2}[\text{O}_2]^p \exp\left(\frac{-FE}{RT}\right). \end{aligned} \quad (17)$$

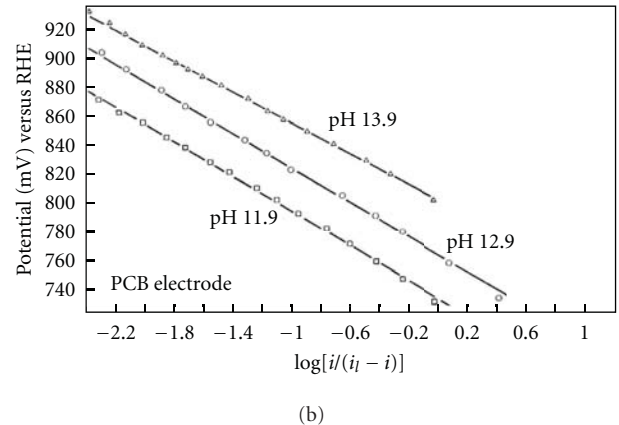
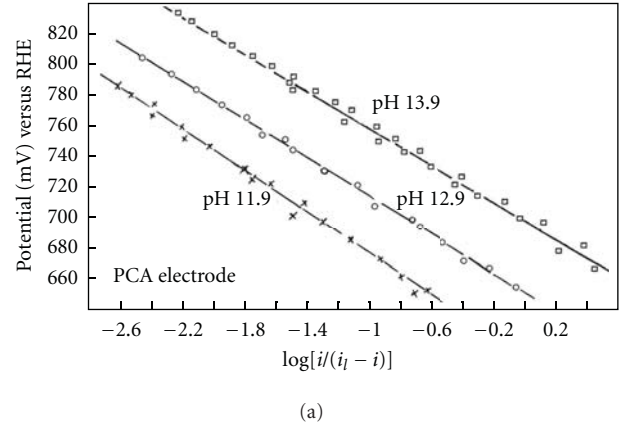
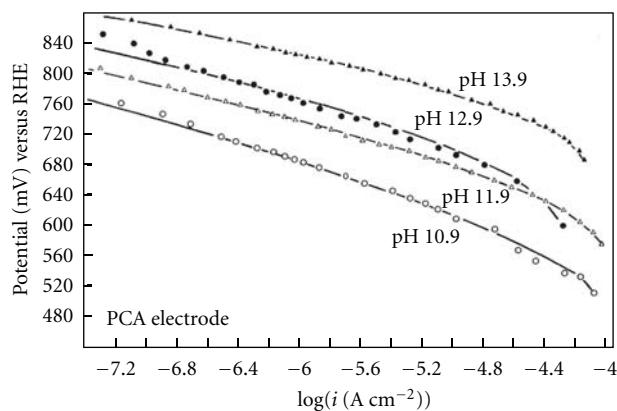


FIGURE 2: Plots of the potential as a function of $\log[i/(i_l - i)]$ as calculated from the oxygen reduction kinetic data for the PC electrodes. Oxygen-saturated KOH electrolyte. Constant ionic strength maintained by dilution with 1 M KCl.

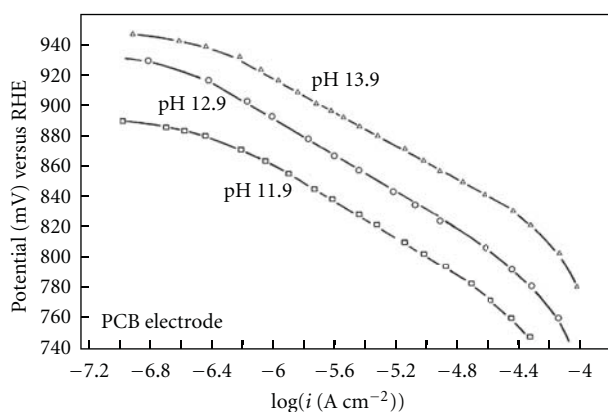
The value of m of -0.14 is interpreted to be a reaction order of 0. The value of p was determined to be 0.28 ± 0.06 which can indicate an order of $1/3$. In other words, it was determined that on the PCA electrodes in the pH range of 10.9 to 13.9 and on the PCB electrodes in the pH range of 11.9 to 13.9, the average values for the order of reaction with respect to $[\text{OH}^-]$ and $[\text{O}_2]$ were 0 and 1, respectively, for the PCA and $-1/2$ and $1/3$, respectively, for the PCB, at constant potential with respect to the SHE.

The data used to calculate the values m' and p' are plotted in Figures 5 and 6, and possible experimental values for m' and p' are tabulated in Table 1. In this table, the values for the rest potential, used in the calculations of p' for the PCA electrode, were obtained by extrapolating the potentiostatic data to an approximate current density of $10^{-8.4}$ A cm $^{-2}$, since the rest potentials were somewhat unsteady. This close-to-zero value was the minimum current density above which steady potentials could be measured.

3.6. Discussion of Equilibrium Potentials. To derive what is considered to be the most probable reduction mechanism that can, at least partially, explain the oxygen reduction kinetics on the polymer carbon electrodes tested in this work,



(a)



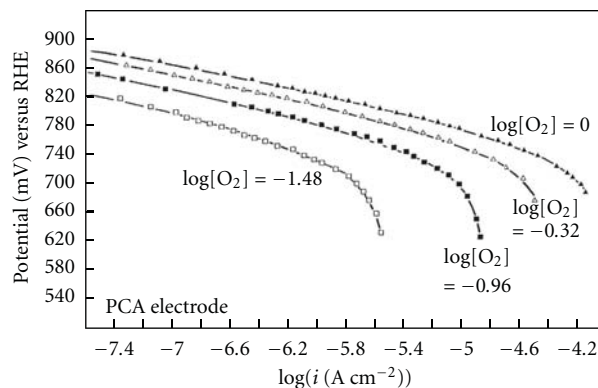
(b)

FIGURE 3: The dependence of the oxygen reduction kinetics on the electrolyte pH for the prepared PC electrodes in oxygen-saturated KOH electrolyte of constant ionic strength maintained by dilution with 1 M KCl.

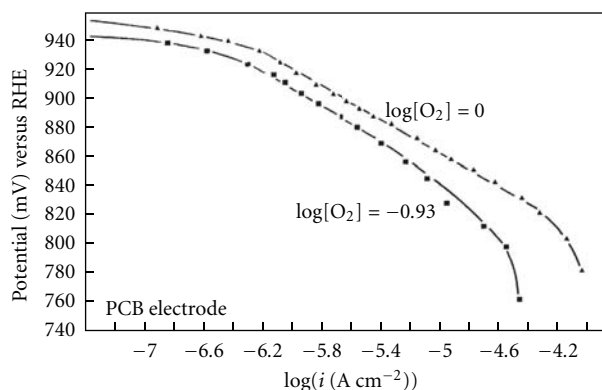
a comparison had to be performed on the experimental data and calculated parameters presented in the previous subsections with the calculated mechanistic criteria determined from all the possible mechanistic paths examined, as tabulated in a previous paper [2]. In that paper, 18 common mechanisms from the literature, with additional modifications, are analysed on the assumption that the Langmuir conditions of adsorption are obeyed. But, it should be noted that by far many other mechanisms could be postulated, namely, those which use catalysis by adsorbed hydroxyl groups under the Langmuir conditions and those using the Temkin conditions of adsorption.

In order to narrow the number of possible mechanisms, it is beneficial to examine the results concerning the equilibrium potentials for oxygen reduction on the PC electrodes in light of information from the general literature. The analysis of the equilibrium potentials was presented in Section 3.4, and the experimental results are listed in Table 1.

The first equilibrium potentials to be examined are those produced by oxygen on the least active electrode, the PCA pyrolysed in bulk. The observed equilibrium potentials could be attributed to three possible oxygen reduction reactions.



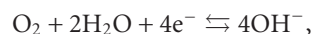
(a)



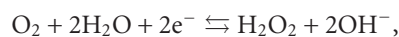
(b)

FIGURE 4: The dependence of the oxygen reduction kinetics on the oxygen partial pressure, $[O_2]$, for the prepared PC electrodes in KOH electrolyte, pH 13.9.

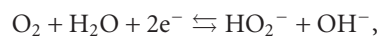
These, in addition to the equations for the concentration dependence of the equilibrium potentials, are given by the following reactions:



$$E_r = 0.401 - \left(\frac{RT}{4F}\right) \ln\left(\frac{[OH^-]^4}{[O_2]}\right); \quad (18)$$



$$E_r = -0.146 - \left(\frac{RT}{2F}\right) \ln\left(\frac{[H_2O_2][OH^-]^2}{[O_2]}\right); \quad (19)$$



$$E_r = E_r^0 - \left(\frac{RT}{2F}\right) \ln\left(\frac{[HO_2^-][OH^-]}{[O_2]}\right). \quad (20)$$

The results listed in Table 1 show that for (15), if $n = 2$, then $m' \cong 1$ and $p' \cong 1$, and, if $n = 4$, then $m' \cong 2$ and $p' \cong 2$. Comparison of these results with (18), (19), and (20) shows that only (20) agrees with the experimental values for n , m' , and p' . Even though the experimental values should only be considered to be approximate due to the small number

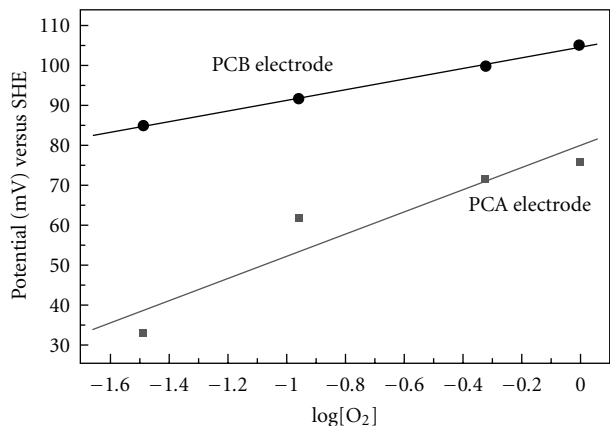


FIGURE 5: Plots of the oxygen reduction rest potentials as a function of the log of the oxygen partial pressure in KOH electrolyte at pH 13.9.

of data points, they were considered sufficient to distinguish between the three probable equilibrium reactions. Equation (20), based on the suggested net oxygen reduction reaction on the PCA electrode, is in agreement with the results of an earlier study by Taylor and Humffray [37], who used a rotating ring-disc electrode for analysis of oxygen reduction on a polymer carbon electrode. Much earlier studies by Yeager et al. [38] on oxygen reduction in alkaline electrolyte containing peroxide showed that the equilibrium could be attributed to this reaction. The only oddity here is that Yeager et al. [38] and Berl [39] found that the experimental value for E_r^0 was -0.048 V/SHE at a pH of 14.0 whereas the value calculated from thermodynamic data by Latimer [40] and Berl [39] was -0.076 V/SHE at a pH of 14.0.

Since no added peroxide was present in the alkaline solutions used in this study, it is interesting to calculate the equilibrium concentration of HO_2^- necessary to yield the observed equilibrium potential on the pure polymer carbon. Thus, some idea of the surface coverage of the peroxide anion can be obtained. From the previous data, the observed equilibrium potential which would occur at the pH of 14.0 is 0.082 V/SHE. Assuming activity coefficients of unity, the use of (20) gives

$$\begin{aligned} 0.082 &= -0.048 - (0.030) \log [\text{HO}_2^-] \therefore [\text{HO}_2^-] \\ &= 4 \times 10^{-5} \text{ M.} \end{aligned} \quad (21)$$

This bulk concentration could then ideally correspond to a planar surface concentration of 8×10^{10} molecules $\text{HO}_2^-/\text{cm}^2$ if no concentration gradient of peroxide anions is present between the bulk solution and the surface. On the assumption of 10^{15} sites/ cm^2 [41–44] and one HO_2^- anion per site, a surface coverage of 8×10^{-5} is calculated for adsorbed HO_2^- . Even if a concentration gradient of 10 to 100 times the bulk concentration exists at the surface, the coverage due to HO_2^- would be less than 10^{-2} . Thus, it is at least safe to say that the surface blockage due to this reaction intermediate would be insignificant.

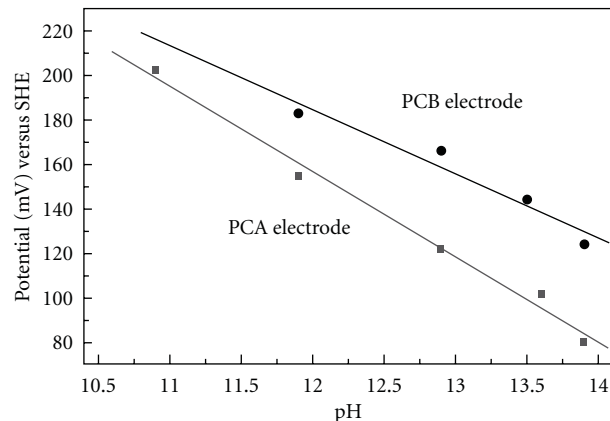


FIGURE 6: Plots of the oxygen reduction rest potentials as a function of electrolyte pH for the PC electrodes in oxygen-saturated KOH electrolyte of constant ionic strength maintained by dilution with 1 M KCl.

TABLE 1: Calculated dependence of the rest potential (open-circuit potential) on the hydroxyl anion concentration, and the oxygen partial pressure for oxygen reduction for the PC electrodes in KOH electrolyte.

Electrode	n	$m' (\pm 0.1)$	$p' (\pm 0.1)$
PCA $E_r^0 = 80$ mV versus SHE	1	0.6	0.5
	2	1.3	0.9
	3	1.9	1.4
	4	2.6	1.9
PCB $E_r^0 = 130$ mV versus SHE	1	0.5	0.2
	2	0.9	0.4
	3	1.4	0.5
	4	1.9	0.7

See (15); E_r is the rest potential, and E_r^0 is the standard rest potential; n refers to the possible number of electrons transferred for the proposed equilibrium reaction.

It is also beneficial to examine the data on the observed equilibrium potentials for oxygen reduction on the PCB electrode, the activated electrode, before discussing the probable reaction mechanisms. As determined in Section 3.4 and Table 1, the results indicate that the equilibrium is a two-electron process and of the equilibrium reactions discussed, only (20) gives the correct dependence of the equilibrium potential on pH and $[\text{O}_2]$ for these electrodes. Independent of the kinetic data, these results would indicate that oxygen reduction on the PCB electrode is a two-electron process, yielding one OH^- and the peroxide anion HO_2^- instead of the four-electron reduction of oxygen to four OH^- anions. However, the kinetic data dispute this conclusion since the reaction order with respect to oxygen was determined to be approximately 1/3 for oxygen reduction on this electrode. No two electron mechanism yielding the peroxide anion or molecule and a reaction order with respect to oxygen of 1/3 can be written unless a totally illogical assumption is made. One would have to assume that the oxygen to oxygen bond in the diatomic molecule is broken in a step preceding the

rate-determining step and then reformed to yield a peroxide anion in the rate-determining step (RDS) or a subsequent step. Such a possibility is considered improbable due to the large irreversibility of oxygen reduction which is generally attributed in the literature to the low exchange current density and the difficulty of breaking the oxygen to oxygen bond. Isotopic investigations of the peroxide oxygen couple, which yields (20) by Davies et al. [45], proved that all the peroxide anion oxygen originated from gaseous oxygen and that the oxygen to oxygen bond is not actually broken in the formation of the peroxide anion. It has also proved to be impossible to write a two-electron mechanism which also yields the correct transfer coefficient and the correct order of the reaction with respect to $[\text{OH}^-]$, in addition to the correct reaction order with respect to $[\text{O}_2]$.

The only way to account for both the observed equilibrium potential dependence and the kinetics is to assume that the equilibrium potential for oxygen reduction on the PCB electrode is a mixed potential. If two separate reactions are occurring on an electrode surface, one cathodic and one anodic, then the potential at which the currents are equal and cancel each other, to yield a net current of zero, is called a mixed potential.

Here, it is suggested that the most probable cause for the anodic reaction is the oxidation of peroxide anions at the inactive PCA sites. The rest potentials for oxygen reduction on the PCB electrodes were approximately 50 mV to 60 mV anodic to the equilibrium potential for oxygen reduction established on the PCA electrodes. The equilibrium reaction on the pure polymer carbon sites was attributed to reaction (20). If the inactive PC sites on the PCB electrodes are considered to be equivalent in oxygen reduction activity to the carbon sites on the PCA electrodes, then this equilibrium could be considered as representing the reaction occurring on the inactive sites of the PCB electrodes. Since the potentials established on these active electrodes by the oxygen reduction kinetics could be anodic to the established equilibrium potentials of the inactive pure PC sites (established from the PCA electrodes), then a net anodic overpotential could exist at these inactive sites. In summary, the O_2/HO_2^- redox reactions occur at the inactive sites; the O_2/OH^- reduction and the HO_2^-/O_2 oxidation occur at the active sites. In other words, the inactive sites have a key role for the anodic peroxide oxidation, and the active sites have a key role for the cathodic oxygen reduction. Thus, if any peroxide anions adsorbed at these inactive sites, they would be preferentially oxidised to O_2 by reaction with OH^- . If HO_2^- intermediates are produced by the reduction of oxygen at the active sites, then the possibility exists for the surface migration of at least a portion of these intermediates to the inactive sites. Alternatively, it could be more probable that the peroxide anions are formed on similar to PCA electrode sites and that their decomposition would preferably be occurring on the excessive active sites of the PCB electrode surface. Depending on the overall potential of the electrode, these intermediates could then be oxidised at the inactive sites. At the potential at which this oxidation of surface-migrated intermediates at the inactive sites is equal in rate to the complete oxygen reduction occurring at the active sites,

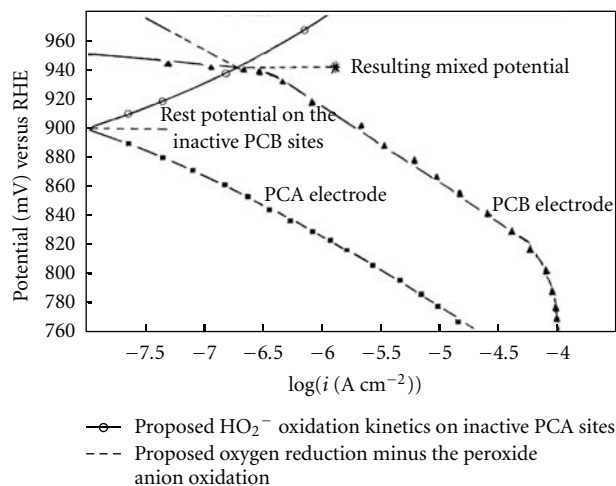


FIGURE 7: The creation of the oxygen reduction rest potential at PCB electrodes by a mixed potential in oxygen-saturated KOH electrolyte at pH 13.9.

the net current density would drop to zero. This would be the established rest potential. Such a possibility is illustrated by the data presented in Figure 7. The cathodic reduction data for an active (PCB) and an inactive (PCA) electrode is plotted in the form of potential, E_{he} , as a function of $\log i$. In addition, the expected oxidation curve for the peroxide anion on the electrode (or the inactive PC sites) is drawn as calculated from the reduction data and the equilibrium responsible for the oxygen reduction on the PCA electrodes.

The expected transfer coefficient (α_a) for the oxidation of the peroxide anion $[\text{HO}_2^-]$ by OH^- can be calculated from the following equation derived by Bockris and Reddy [46]:

$$\alpha_a + \alpha_c = \left(\frac{n}{\nu} \right). \quad (22)$$

In this equation, the number of electrons transferred in the net equilibrium reaction, n , is 2, the number of times the expected RDS is expected to occur for the complete 2 electron transfer (ν , the stoichiometric number) will be found to be 1 once the proposed mechanism is discussed, and the transfer coefficient for the oxygen, α_c , on these inactive carbon sites was found to be 1. This data gives an expected α_a of 1 using (20). Since the anodic and cathodic functions should intersect at the equilibrium potential, then the proposed anodic oxidation of the peroxide anion is drawn in Figure 7. If the inactive sites on the PCB electrodes are assumed to be equivalent to the sites on the PCA electrodes, then the potential at which the oxidation current density of the peroxide anions on the inactive sites is equal but opposite in sign to the reduction current density of the oxygen at the active sites, the net observable current density, would be expected to drop to zero. As illustrated in Figure 7, this predicted behaviour was exactly what occurred experimentally.

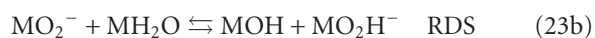
4. Conclusions

Before drawing conclusions regarding possible mechanistic paths, it should be noted that only a partial kinetic analysis was performed on two-polymer carbon electrodes, both being interrelated with strong basic similarities. Both differed only in the preparative procedure used, with the alteration of surface sites and the creation of pure electrode surfaces (PCAs) and mixed electrode surfaces (PCBs). For this reason, it was useful to propose a comprehensive reduction mechanism to account for oxygen reduction on these more active and less active electrodes rather than two separate mechanisms totally unrelated to each other. In this manner, it may be possible to account for the differing kinetics as due to minor changes in one or two reaction steps. The possible mechanistic paths were chosen from those presented in paper [2], which lists the kinetic equations and the mechanistic criteria.

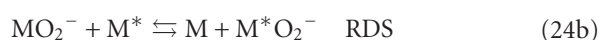
The kinetics of oxygen reduction on the PCA electrodes were found in Section 3.5 to obey the ideal rate law (17), in the pH range 13.9 to 10.9, KOH electrolyte. The resulting overall equilibrium responsible for the equilibrium potential was found to be (20) (Section 3.6).

The kinetics are indicative of a nonelectrochemical RDS in which an electron transfer step precedes it and is in equilibrium or in a steady state. The determination of the Tafel slope would also be indicative on this issue. The overall mechanism has to yield the net two-electron reduction previously discussed. In order to give the observed kinetics, it is necessary that the first electron transfer step involves the formation of an adsorbed O_2^- intermediate either during or following the adsorption of an O_2 molecule. The probable mechanisms which obey these restrictions are presented. The RDS which yields the correct reaction kinetics is indicated for each mechanism.

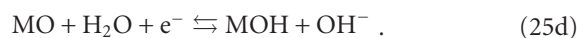
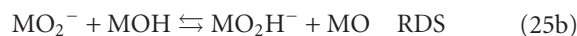
Mechanism A:



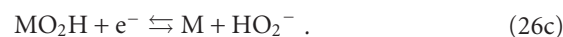
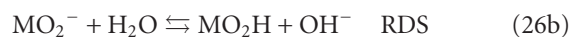
Mechanism B, where M^ refers to an active site:*



Mechanism C:



Mechanism D:



Mechanism B was suggested by Taylor and Humffray [37] who also postulated the RDS to be the surface diffusion of adsorbed O_2^- intermediates to active sites. This mechanism would seem to be unlikely since step (24c) represents a trimolecular process. However, the surface diffusion step from an inactive site to an active site is a plausible RDS and could be inserted into mechanisms A, C, or D. Yet such a RDS would be expected to produce a dependence of the current density on agitation of the electrolyte, but such a dependence was not observed in this research nor in other results in the literature [12, 38, 47]. Mechanism C is proposed by the authors but is considered to be unlikely since the qualitative analysis of the voltammograms (not shown here) indicated a low coverage of oxygen-containing redox groups on the surface (such as MOH). Mechanisms A and D have been suggested by Apple and Appleby et al. [12, 47] from extensive studies of oxygen reduction on carbon materials in alkaline electrolyte [2]. Mechanism A has also been proposed by many other workers (see [2]) in their extensive studies on oxygen reduction on Pt, Rh, Ag, and so forth, in acid or alkaline electrolytes whenever peroxide was the reaction product. However, studies by Damjanovic et al. [48–50] contradict those studies favouring a coupled-electron proton transfer rather than a separated electron transfer as given in (23a). Thus, it is clear that there is an urgent need to resolve such contradictions in order to understand the charge transfer sequence of electrochemical oxygen reduction. The first three steps of mechanism D were suggested by Hurlen et al. [51] to account for oxygen reduction to peroxide anion on silver electrodes in alkaline electrolytes. It is then impossible to positively distinguish between mechanisms A or D as responsible for the kinetics. It should be noted, however, that Damjanovic et al. [50] proposed in their rotating ring-disc studies of oxygen reduction on Pt in acid or alkaline electrolytes that the HO_2^- -adsorbed intermediate does not result in the formation of peroxide anion. Such an intermediate was used in the mechanisms to explain the kinetics of oxygen reduction in which no peroxide anions at all were detected by the ring-disc technique, and the overall reduction was a four-electron process. If this assumption is correct, then step (26c) in mechanism D would be improbable since it proposes the formation of an HO_2^-

from an adsorbed HO₂ intermediate. For this reason and the fact that mechanism A has received more general support by previous investigators, mechanism A is assumed to be more correct, that is, the more probable to explain present results, followed by mechanism D, to explain oxygen reduction on the electrode in alkaline electrolyte. Mechanism A with step (23b) as the RDS gives the following predicted kinetics:

$$i = k_2 K_1 [\text{O}_2] \exp\left[-\frac{FE}{RT}\right]. \quad (27)$$

The concentration of vacant sites [M] and adsorbed water [MH₂O] are assumed to be constant and included in k_2 .

Using the mechanisms described in paper [2] and the conclusions presented previously on the observed open-circuit potentials, it was tried to establish a reduction mechanism to account for the kinetics of oxygen reduction on the PCB electrode.

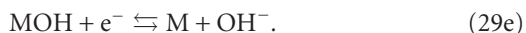
In the open literature, there are essentially three classes of proposed mechanisms for oxygen reduction. Some mechanistic paths use only oxide intermediates. Other paths use peroxide intermediates with no aid from adsorbed OH groups while some paths use peroxide intermediate in addition to catalysis by adsorbed OH groups.

As presented in Section 3, the following ideal rate law holds for oxygen reduction on the PCB electrode in the pH range of 13.9 to 11.9 (KOH electrolyte, constant ionic strength):

$$i = K [\text{OH}^-]^{-1/2} [\text{O}_2]^{1/3} \exp\left[-\frac{FE}{RT}\right]. \quad (28)$$

No pH-induced change was detected for oxygen reduction on this electrode.

Of the mechanisms presented, only the calculated kinetics for the following mechanism (see Table 18 of [2]) approximates simultaneously the observed kinetics represented by (27) and (28) for oxygen reduction on the PCA and PCB electrodes; respectively,



If step (29b) is considered the RDS, the calculated rate equation is

$$i = k_2 K_1 [\text{MH}_2\text{O}] [\text{M}] [\text{O}_2] \exp\left[-\frac{FE}{RT}\right], \quad (30)$$

which agrees with (27) for the PCA electrode. If step (29e) is considered the RDS, then the calculated rate equation can be written:

$$i = K_5 \left\{ K_4 K_3 K_2 K_1 [\text{M}] [\text{MH}_2\text{O}]^2 \right\}^{1/3} [\text{OH}^-]^{-1/3} [\text{O}_2]^{1/3} \times \exp\left[-\frac{5FE}{6RT}\right]. \quad (31)$$

This equation gives $\alpha = 5/6$ (0.83) and $m = -1/3$ (-0.33), which do not agree with the observed kinetics ($\alpha = 1.02 \pm 0.08$, $m = -0.50 \pm 0.04$) represented by (28) for oxygen reduction on the PCB electrode in the pH range of 13.9 to 11.9. It was also concluded earlier in this paper that the observed open-circuit potential was a mixed potential formed by the anodic oxidation of peroxide anion intermediates and the overall four-electron reduction of oxygen, but it is clear that mechanism (29a)–(29e) is not a likely explanation for the observed open-circuit potential (see Table 1). In fact, the observed m' and p' values were 0.9 ± 0.1 and 0.4 ± 0.1 , respectively, and the calculated values based on mechanism (29a)–(29e) are 2 and 1, respectively. These reasons effectively lower the probability that the reduction mechanism (29a)–(29e) can explain the observed mechanistic criteria. Equation (29a) as well as (23a), is also contradicted on a recent article by Qi et al. [52], where these authors performed density functional theory simulations of O₂ on Pt(111) surface finding that all oxygen adsorbates are charge neutral, so the 4 electron transfers always occur concurrently with the 4 proton (hydronium) transfers from the aqueous electrolyte; that is, all electron transfers are proton-coupled, rather than separated transfers. In summary, it is certain that the kinetics cannot be easily studied on the PC electrodes. But, that is a fact that the PCB electrode shows an enhanced activity for oxygen reduction in comparison to the PCA electrode. Extensive elemental surface analysis and determination of any induced structural alteration by the preparation procedure was beyond the scope of this research. Such analysis, complemented by further electrochemical studies, would be necessary to help elucidate the nature of the inactive and active surface sites, and this is being more easily accomplished with further research in progress at the moment, which will be published in the near future. A short and qualitative discussion on the surface sites of the two catalysts, that is, ordered or disordered, and their link to the adsorption and reaction mechanisms would also be beneficial in such a publication.

References

- [1] M. Paucirova, D. M. Drazic, and A. Damjanovic, "The effect of surface coverage by adsorbed oxygen on the kinetics of oxygen reduction at oxide free platinum," *Electrochimica Acta*, vol. 18, no. 12, pp. 945–951, 1973.
- [2] P. S. D. Brito and C. A. C. Sequeira, "Cathodic oxygen reduction on noble metal and carbon electrodes," *Journal of Power Sources*, vol. 52, no. 1, pp. 1–16, 1994.
- [3] L. Liu, J. W. Lee, and B. N. Popov, "Development of ruthenium-based bimetallic electrocatalysts for oxygen reduction reaction," *Journal of Power Sources*, vol. 162, no. 2, pp. 1099–1103, 2006.
- [4] M. Van Brussel, G. Kokkinidis, A. Hubin, and C. Buess-Herman, "Oxygen reduction at platinum modified gold electrodes," *Electrochimica Acta*, vol. 48, no. 25–26, pp. 3909–3919, 2003.
- [5] V. Tripković, E. Skúlason, S. Siahrostami, J. K. Nørskov, and J. Rossmeisl, "The oxygen reduction reaction mechanism on Pt(1 1 1) from density functional theory calculations," *Electrochimica Acta*, vol. 55, no. 27, pp. 7975–7981, 2010.

- [6] S. Walch, A. Dhanda, M. Aryanpour, and H. Pitsch, "Mechanism of molecular oxygen reduction at the cathode of a PEM fuel cell: non-electrochemical reactions on catalytic Pt particles," *Journal of Physical Chemistry C*, vol. 112, no. 22, pp. 8464–8475, 2008.
- [7] T. Jacob, "The mechanism of forming H₂O from H₂ and O₂ over a Pt catalyst via direct oxygen reduction," *Fuel Cells*, vol. 6, no. 3-4, pp. 159–181, 2006.
- [8] E. B. Yeager, "Dioxygen electrocatalysis: mechanisms in relation to catalyst structure," *Journal of Molecular Catalysis*, vol. 38, pp. 5–25, 1986.
- [9] N. M. Marković, R. R. Adžić, B. D. Cahan, and E. B. Yeager, "Structural effects in electrocatalysis: oxygen reduction on platinum low index single-crystal surfaces in perchloric acid solutions," *Journal of Electroanalytical Chemistry*, vol. 377, no. 1-2, pp. 249–259, 1994.
- [10] D. Qu, "Investigation of oxygen reduction on activated carbon electrodes in alkaline solution," *Carbon*, vol. 45, no. 6, pp. 1296–1301, 2007.
- [11] T. Nagaoka and T. Sakai, "Oxygen reduction at electrochemically treated glassy carbon electrodes," *Analytical Chemistry*, vol. 58, no. 9, pp. 1953–1955, 1986.
- [12] M. Appel and A. J. Appleby, "A ring-disk electrode study of the reduction of oxygen on active carbon in alkaline solution," *Electrochimica Acta*, vol. 23, no. 11, pp. 1243–1246, 1978.
- [13] I. Iliev, J. Mrha, A. Kaisheva, and S. Gamburgzev, "Influence of the electrolyte content of oxygen carbon gas-diffusion electrodes on their electro-chemical performance in acid solutions," *Journal of Power Sources*, vol. 3, no. 3, pp. 245–255, 1978.
- [14] I. Kruusenberg, J. Leis, M. Arulepp, and K. Tammeveski, "Oxygen reduction on carbon nanomaterial-modified glassy carbon electrodes in alkaline solution," *Journal of Solid State Electrochemistry*, vol. 14, no. 7, pp. 1269–1277, 2010.
- [15] L. Elbaz, E. Korin, L. Soifer, and A. Bettelheim, "Electrocatalytic oxygen reduction by Co(III) porphyrins incorporated in aerogel carbon electrodes," *Journal of Electroanalytical Chemistry*, vol. 621, no. 1, pp. 91–96, 2008.
- [16] P. Manisankar and A. Gomathi, "Mediated oxygen reduction at a glassy carbon electrode modified with riboflavin and 9,10-anthraquinones," *Journal of Power Sources*, vol. 150, no. 1-2, pp. 240–246, 2005.
- [17] P. Manisankar and A. Gomathi, "Electrocatalysis of oxygen reduction at polypyrrole modified glassy carbon electrode in anthraquinone solutions," *Journal of Molecular Catalysis A*, vol. 232, no. 1-2, pp. 45–52, 2005.
- [18] K. Vaik, A. Sarapuu, K. Tammeveski, F. Mirkhalaf, and D. J. Schiffrin, "Oxygen reduction on phenanthrenequinone-modified glassy carbon electrodes in 0.1 M KOH," *Journal of Electroanalytical Chemistry*, vol. 564, pp. 159–166, 2004.
- [19] R. Jasinski, "Cobalt phthalocyanine as a fuel cell cathode," *Journal of The Electrochemical Society*, vol. 112, pp. 526–528, 1965.
- [20] V. S. Bagotzky, M. R. Tarasevich, K. A. Radyushkina, O. A. Levina, and S. I. Andrusyova, "Electrocatalysis of the oxygen reduction process on metal chelates in acid electrolyte," *Journal of Power Sources*, vol. 2, pp. 233–240, 1977.
- [21] C. Z. Deng and M. J. Dignam, "Sputtered cobalt-carbon-nitrogen thin films as oxygen reduction electrocatalysts: II. Electrochemical stability and proposed mechanism," *Journal of the Electrochemical Society*, vol. 145, no. 10, pp. 3513–3520, 1998.
- [22] A. Van Der Putten, A. Elzing, W. Visscher, and E. Barendrecht, "Oxygen reduction on pyrolysed carbon-supported transition metal chelates," *Journal of Electroanalytical Chemistry*, vol. 205, no. 1-2, pp. 233–244, 1986.
- [23] Q. L. Zhao, Z. L. Zhang, L. Bao, and D. W. Pang, "Surface structure-related electrochemical behaviors of glassy carbon electrodes," *Electrochemistry Communications*, vol. 10, no. 2, pp. 181–185, 2008.
- [24] P. J. F. Harris, "Fullerene-related structure of commercial glassy carbons," *Philosophical Magazine*, vol. 84, no. 29, pp. 3159–3167, 2004.
- [25] K. Shi and K.-K. Shiu, "Scanning tunneling microscopic and voltammetric studies of the surface structures of an electrochemically activated glassy carbon electrode," *Analytical Chemistry*, vol. 74, pp. 879–885, 2002.
- [26] A. J. Downard and M. J. Prince, "Barrier properties of organic monolayers on glassy carbon electrodes," *Langmuir*, vol. 17, no. 18, pp. 5581–5586, 2001.
- [27] A. A. Mikhaylova, O. A. Khazova, and V. S. Bagotzky, "Electrocatalytic and adsorption properties of platinum microparticles electrodeposited onto glassy carbon and into Nafion films," *Journal of Electroanalytical Chemistry*, vol. 480, no. 1-2, pp. 225–232, 2000.
- [28] J. S. Field and M. V. Swain, "The indentation characterisation of the mechanical properties of various carbon materials: glassy carbon, coke and pyrolytic graphite," *Carbon*, vol. 34, no. 11, pp. 1357–1366, 1996.
- [29] K. R. Kneten and R. L. McCreery, "Effects of redox system structure on electron-transfer kinetics at ordered graphite and glassy carbon electrodes," *Analytical Chemistry*, vol. 64, no. 21, pp. 2518–2524, 1992.
- [30] R. J. Taylor and A. A. Humffray, "Electrochemical studies on glassy carbon electrodes—II. Oxygen reduction in solutions of high pH (pH>10)," *Journal of Electroanalytical Chemistry*, vol. 64, pp. 63–84, 1975.
- [31] J. O. M. Bockris, "Kinetics of activation controlled consecutive electrochemical reactions: anodic evolution of oxygen," *The Journal of Chemical Physics*, vol. 24, no. 4, pp. 817–827, 1956.
- [32] D. S. Gnanamuthu and J. V. Petrocelli, *Journal of The Electrochemical Society*, vol. 114, p. 1036, 1967.
- [33] O. E. Mouahid, C. Coutanceau, E. M. Belgsir, P. Crouigneau, J. M. Léger, and C. Lamy, "Electrocatalytic reduction of dioxygen at macrocycle conducting polymer electrodes in acid media," *Journal of Electroanalytical Chemistry*, vol. 426, no. 1-2, pp. 117–123, 1997.
- [34] K. J. Vetter, *Electrochemical Kinetics*, Academic Press, New York, NY, USA, 1967.
- [35] E. Gileadi, *Physical Electrochemistry*, Wiley-VCH, Weinheim, Germany, 2011.
- [36] R. E. Davis, G. L. Horvath, and C. W. Tobias, "The solubility and diffusion coefficient of oxygen in potassium hydroxide solutions," *Electrochimica Acta*, vol. 12, no. 3, pp. 287–297, 1967.
- [37] R. J. Taylor and A. A. Humffray, "Electrochemical studies on glassy carbon electrodes—III. Oxygen reduction in solutions of low pH (pH<10)," *Journal of Electroanalytical Chemistry*, vol. 64, no. 1, pp. 85–94, 1975.
- [38] E. Yeager, P. Krouse, and K. V. Rao, "The Kinetics of the oxygen-peroxide couple on carbon," *Electrochimica Acta*, vol. 9, pp. 1057–1070, 1964.
- [39] W. G. Berl, "A reversible oxygen electrode," *Transactions of the Electrochemical Society*, vol. 83, pp. 253–270, 1943.

- [40] W. M. Latimer, *The Oxidation States of the Elements and Their Potentials in Aqueous Solutions*, Prentice-Hall, New York, NY, USA, 2nd edition, 1952.
- [41] S. Basu, Ed., *Recent Trends in Fuel Cell Science and Technology*, Springer, New York, NY, USA, 1st edition, 2007.
- [42] A. J. Appleby, in *Modern Aspects of Electrochemistry*, B. E. Conway and J. O'M. Bockris, Eds., vol. 9, pp. 369–378, Plenum Press, New York, NY, USA, 1974.
- [43] J. Bett, J. Lundquist, E. Washington, and P. Stonehart, "Platinum crystallite size considerations for electrocatalytic oxygen reduction-I," *Electrochimica Acta*, vol. 18, no. 5, pp. 343–348, 1973.
- [44] J. T. Lundquist and P. Stonehart, "Platinum crystallite size effects on oxide formation and reduction parameters-II," *Electrochimica Acta*, vol. 18, no. 5, pp. 349–354, 1973.
- [45] M. O. Davies, M. Clark, E. Yeager, and F. Hovorka, "The oxygen electrode-I. Isotopic investigation of electrode mechanisms," *Journal of The Electrochemical Society*, vol. 106, pp. 56–61, 1959.
- [46] J. O'M. Bockris and A. K. N. Reddy, *Modern Electrochemistry 1 & 2*, Plenum Press, New York, NY, USA, 1998.
- [47] A. J. Appleby and J. Marie, "Kinetics of oxygen reduction on carbon materials in alkaline solution," *Electrochimica Acta*, vol. 24, no. 2, pp. 195–202, 1979.
- [48] A. Damjanovic, A. Dey, and J. O'M. Bockris, "Electrode kinetics of oxygen reduction on oxide-free platinum electrodes," *Electrochimica Acta*, vol. 12, no. 6, pp. 615–628, 1967.
- [49] A. Damjanovic and V. Brusić, "Oxygen reduction at Pt-Au and Pd-Au alloy electrodes in acid solution," *Electrochimica Acta*, vol. 12, no. 9, pp. 1171–1184, 1967.
- [50] A. Damjanovic, M. A. Genshaw, and J. O'M. Bockris, "The role of hydrogen peroxide in oxygen reduction at platinum in H₂SO₄ solution," *Journal of The Electrochemical Society*, vol. 114, pp. 466–472, 1967.
- [51] T. Hurlen, Y. L. Sandler, and E. A. Pantier, "Reactions of oxygen and hydrogen peroxide at silver electrodes in alkaline solutions," *Electrochimica Acta*, vol. 11, no. 10, pp. 1463–1473, 1966.
- [52] L. Qi, X. Qian, and J. Li, "Kinetics of congruent vaporization of ZnO islands," *Physical Review Letters*, vol. 107, no. 14, Article ID 146101, 4 pages, 2011.

Review Article

Recent Developments of Nanostructured Electrodes for Bioelectrocatalysis of Dioxygen Reduction

Marcin Opallo¹ and Renata Bilewicz²

¹ *Institute of Physical Chemistry, Polish Academy of Sciences, Kasprzaka 44/52, 01-224 Warszawa, Poland*

² *Faculty of Chemistry, University of Warsaw, Pasteura 1, 02-093 Warsaw, Poland*

Correspondence should be addressed to Marcin Opallo, mopallo@ichf.edu.pl

Received 29 April 2011; Accepted 28 June 2011

Academic Editor: Milan M. Jaksic

Copyright © 2011 M. Opallo and R. Bilewicz. This is an open access article distributed under the Creative Commons Attribution License, which permits unrestricted use, distribution, and reproduction in any medium, provided the original work is properly cited.

The recent development of nanostructured electrodes for bioelectrocatalytic dioxygen reduction catalysed by two copper oxidoreductases, laccase and bilirubin oxidase, is reviewed. Carbon-based nanomaterials as carbon nanotubes or carbon nanoparticles are frequently used for electrode modification, whereas there are only few examples of biocathodes modified with metal or metal oxide nanoparticles. These nanomaterials are adsorbed on the electrode surface or embedded in multicomponent film. The nano-objects deposited act as electron shuttles between the enzyme and the electrode substrate providing favourable conditions for mediatorless bioelectrocatalysis.

1. Introduction

Although the first report on a dioxygen-glucose biofuel cell working at neutral pH was published in the early 60's [6], construction of electrodes suitable for this device became challenging research area in the late 90's. Similar to the conventional fuel cell dioxygen remains the oxidant in biofuel cells, because of its ubiquity, in particular its presence in the air and body fluids of mammals. Contrary to inorganic catalysts, enzymes allow for significant decrease of the dioxygen reduction overpotential also at neutral pH. This aspect is important if the biofuel cell is prepared to generate electricity in human body. Among the enzymes two types of copper oxidoreductases as high potential laccases and bilirubin oxidase [7–9] are superior, and electrodes modified by these proteins are the subject of almost all studies of prospective biocathodes. Although electrodes modified by high potential laccases allow for the larger decrease of the dioxygen reduction overpotential, bilirubin oxidase is more active at pH close to neutral as in physiological fluids [2, 10]. This property together with the fact that it retains its activity in the presence of chloride ions makes bilirubin oxidase modified electrode prospective biocathode working at physiological conditions without membrane separator.

However, the problem of its deactivation in the presence of other species such as urates [11] is still needed to be solved.

Both laccase and bilirubin oxidase contain two separate active sites embedded in polypeptide chains being close enough for electron transfer between them. Three-copper ion cluster is responsible for the binding of dioxygen and a separate copper ion responsible for electron transfer with the exterior substrate [22, 23]. Establishing direct electronic communication between the latter and the electrode surface becomes of central interest for enzyme-based mediatorless electrocatalysis. T1 center of laccase or bilirubin oxidase (Figure 1) is hidden in hydrophobic pocket of the protein, and it is accessible for electrons from electrode as it is for organic mediator. It has been shown that attachment of polyaromatic functionalities provides favourable conditions for efficient electron transfer to the acceptor site of the enzyme [1, 24–26]. However, the catalytic current density obtained on these electrodes is limited by the low coverage of the electrode with the enzyme. The use of conductive nanomaterials like carbon nanotubes or various nanoparticles for biocathode modification provides an alternative and frequently used option. Due to the similar sizes of the flexible enzyme and the rigid nanoparticles (or other nanoobjects), the electron transfer distance can be decreased without

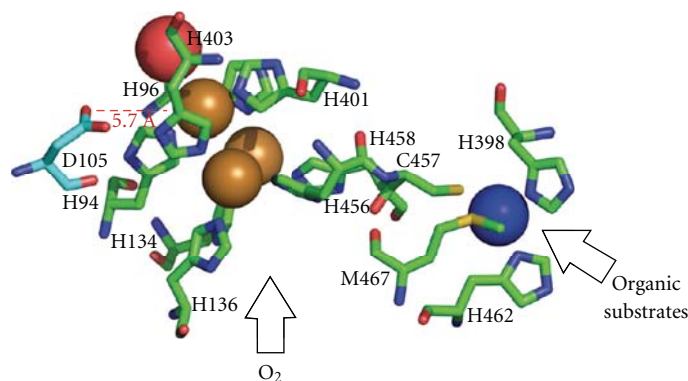


FIGURE 1: Three-dimensional representation of the copper binding sites of bilirubin oxidase from *Myrothecium verrucaria*. The copper centers of T2/T3 type are represented by brown spheres, whereas the T1 copper is represented by blue sphere. Red sphere represents O_2 bound to the trinuclear cluster (from [1]).

deterioration of enzyme activity [27, 28]. The increase of the electroactive surface after modification with nanomaterials is another important advantage. Reconstitution of the enzyme may also bring conductive nanoparticles close to the active site of the enzyme [29, 30] possibly accelerating bioelectrocatalytic process.

Early papers from the Tarasevich group [36, 37] are often cited as the first example of mediatorless catalysis with laccase adsorbed on carbon black. Indeed the high current density of dioxygen reduction reported on these materials may be connected with their specific nanosized features allowing for favourable orientation of the adsorbed enzyme. However, in the first few years of the 21st century the majority of research was oriented towards mediated bioelectrocatalysis following the concept of “wiring” the enzyme to osmium redox polymers [38–41]. Later when the application of nanomaterials for electrode modification became increasingly popular, it was found that nanostructured electrodes further modified by copper oxidoreductases are suitable materials for mediatorless bioelectrocatalysis of dioxygen reduction [2, 42–44]. Not only carbon nanoparticulate materials and carbon nanotubes but also films consisting of graphenes, metal or metal oxide nanoparticles were successfully applied for mediatorless dioxygen bioelectrocatalysis. This paper reviews the recent efforts to construct nanoparticulate biocathodes.

2. Electrodes Modified with Nanoparticulate Carbon Materials

Almost 30 years passed from the first observation of mediatorless bioelectrocatalysis at laccase adsorbed on carbon black [36, 37] until a well-defined carbon-based nanomaterial was used for this purpose. The Kano group prepared a carbon aerogel (22 nm average pore size) poly(vinylidene fluoride) film on glassy carbon with adsorbed laccase or bilirubin oxidase [2]. The use of a copper-oxidoreductase-modified carbon nanostructured material resulted in a significant overpotential decrease compared with Pt electrodes.

The electrocatalytic activity of these electrodes resulted in a dioxygen reduction current density of ca. 4 mA cm^{-2} as measured at rotating disc electrode (Figure 2).

More importantly similar current densities were obtained in quiescent conditions when Toray carbon paper was used as support for the carbon aerogel [3] (Figure 3).

This indicates that not only the structure and composition of the nanostructured film electrode but also the support material affect efficiency of the bioelectrocatalytic process. The extremely high current density (20 mA cm^{-2}) was obtained in quiescent conditions with a polytetrafluoroethylene-Ketjen black composite deposited on carbon paper in contact with air [45]. However, in these experiments another copper oxidoreductase—copper efflux oxidase—was used for modification of the air breathing cathode. Although very high current densities and remarkable stability can be obtained with this enzyme on mesoporous carbon supports [46], its dioxygen reduction overpotential is too large to be applied in a biofuel cell.

Another commercially available carbon black—Vulcan XC72R—embedded in a Nafion film with bilirubin oxidase provides a rather modest 0.05 mA cm^{-2} catalytic current determined by cyclic voltammetry at 0.003 V s^{-1} in quiescent O_2 -saturated solution [47]. Gas-diffusion electrodes with immobilised bilirubin oxidase [48] or laccases [4] were prepared with the same carbon material hydrophobized with Teflon. With the first enzyme catalytic current density above 0.1 mA cm^{-2} was determined by cyclic voltammetry at 0.02 V s^{-1} and up to 0.35 mA cm^{-2} at 0.5 V versus Ag/AgCl from polarisation curve [48]. Polarisation curves also show a three times increase of the current as compared with aqueous dioxygen supply. Even larger current densities and excellent stability was observed for a similar laccase-modified electrode with significant difference between tree and fungal laccases (Figure 4) [4].

Based on a similar principle, “floating,” air diffusion biocathode prepared from hydrophobic carbon black modified with *Trametes Hirsuta* laccase exhibits a current density up to 0.5 mA cm^{-2} on a dioxygen saturated buffer solution

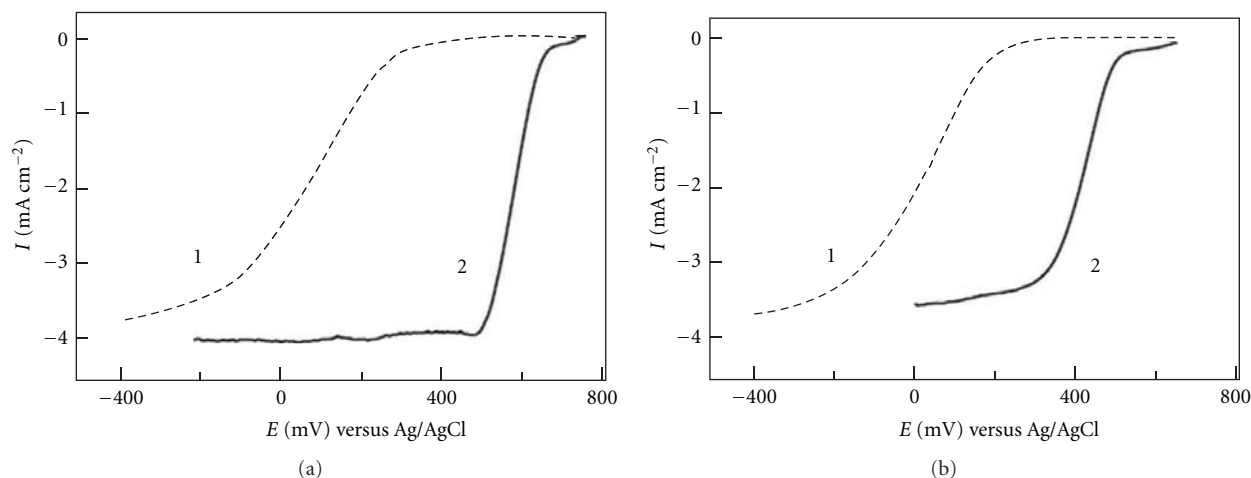


FIGURE 2: Linear sweep voltammograms of (a) Pt (1) and laccase-adsorbed carbon aerogel electrode (2) in pH 5 McIlvaine buffer and (b) bilirubin oxidase-adsorbed carbon aerogel electrode (2) in pH 7 phosphate buffer at 25°C. The measurements were done in O₂-saturated solution at 1000 rpm at scan rate 0.02 V s⁻¹ (from [2]).

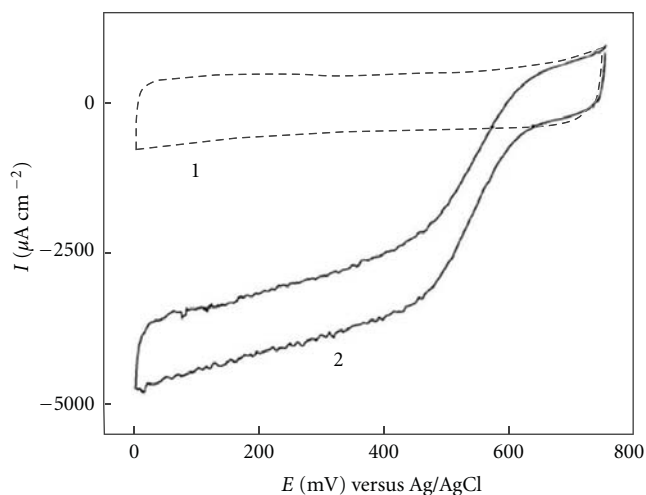


FIGURE 3: Cyclic voltammograms obtained on laccase adsorbed on carbon-aerogel-modified carbon paper electrode in pH 5 McIlvaine buffer under (1) anaerobic and (2) dioxxygen-saturated conditions. Enzyme concentration 5.5×10^{-6} mol dm⁻³. Scan rate 0.02 V s⁻¹ (from [3]).

(pH 4.5) [49]. Importantly this electrode is reported to lose only 5% of its initial activity after 1 month of operation at low current density (0.02 mA cm^{-2}) [49].

One of our groups proposed commercially available hydrophilic carbon nanoparticles functionalised with phenyl sulphate groups (known as Emperor2000) as biocathode material [50]. The film electrode consisting of these nanoparticles encapsulated into a hydrophilic sol-gel-processed silicate and further modified with adsorbed laccase exhibited mediatorless catalysis with ca. 0.1 mA cm^{-2} current density obtained by slow scan (0.001 V s^{-1}) cyclic voltammetry in quite conditions. Current density in a similar range was obtained with adsorbed bilirubin oxidase on the same nanoparticles embedded in hydrophobic silicate film functionalised

with methyl [5] or imidazolium [51]. It is worth noting that the addition of hydrophilic carbon nanoparticles to hydrophobic silicate-carbon microparticles composite material (carbon ceramic electrode) leads to an increase in the catalytic current density to 0.2 mA cm^{-2} as measured by cyclic voltammetry with scan rate 0.001 V s^{-1} in air-saturated solution [5] (Figure 5).

Scanning electrochemical microscopy studies revealed significant deaggregation of laccase [50] and bilirubin oxidase [5] by the presence of carbon micro- or nanoparticles in the electrode material (Figure 6). However some enzyme aggregates can be found by atomic force microscopy.

Employment of imidazolium functionalised silicate sub-microparticles [12, 52] or Au nanoparticles [53] as linkers of phenyl sulphate functionalised carbon nanoparticles in layer-by-layer procedure allows for the preparation of nanostructured 3-dimensional film electrodes (Figure 7).

With functionalised silicate sub-microparticles the stable film is obtained due to electrostatic interactions between particles of opposite sign, and electronic conduction is secured due to the formation of percolation paths by the carbon nanoparticles (Figure 8).

By increase of the number of alternate immersion and withdrawal steps of the substrate into nanoparticles suspensions a larger amount of material is deposited (Figure 7). With adsorbed laccase or bilirubin oxidase these films exhibit mediatorless bioelectrocatalytic activity towards dioxxygen reduction, and it is controlled by the number of immersion and withdrawal steps [12, 52] (Figure 9). With adsorbed bilirubin oxidase a catalytic activity above 0.3 mA cm^{-2} (measured by cyclic voltammetry with scan rate 0.001 V s^{-1} in dioxxygen saturated buffer) is attained.

This is due to an increase of the electroactive surface where a larger amount of enzyme molecules can be adsorbed. Interestingly the bioelectrocatalytic activity of these electrodes is significantly larger than that prepared with functionalised sol-gel-processed silicate as a linker (electrode

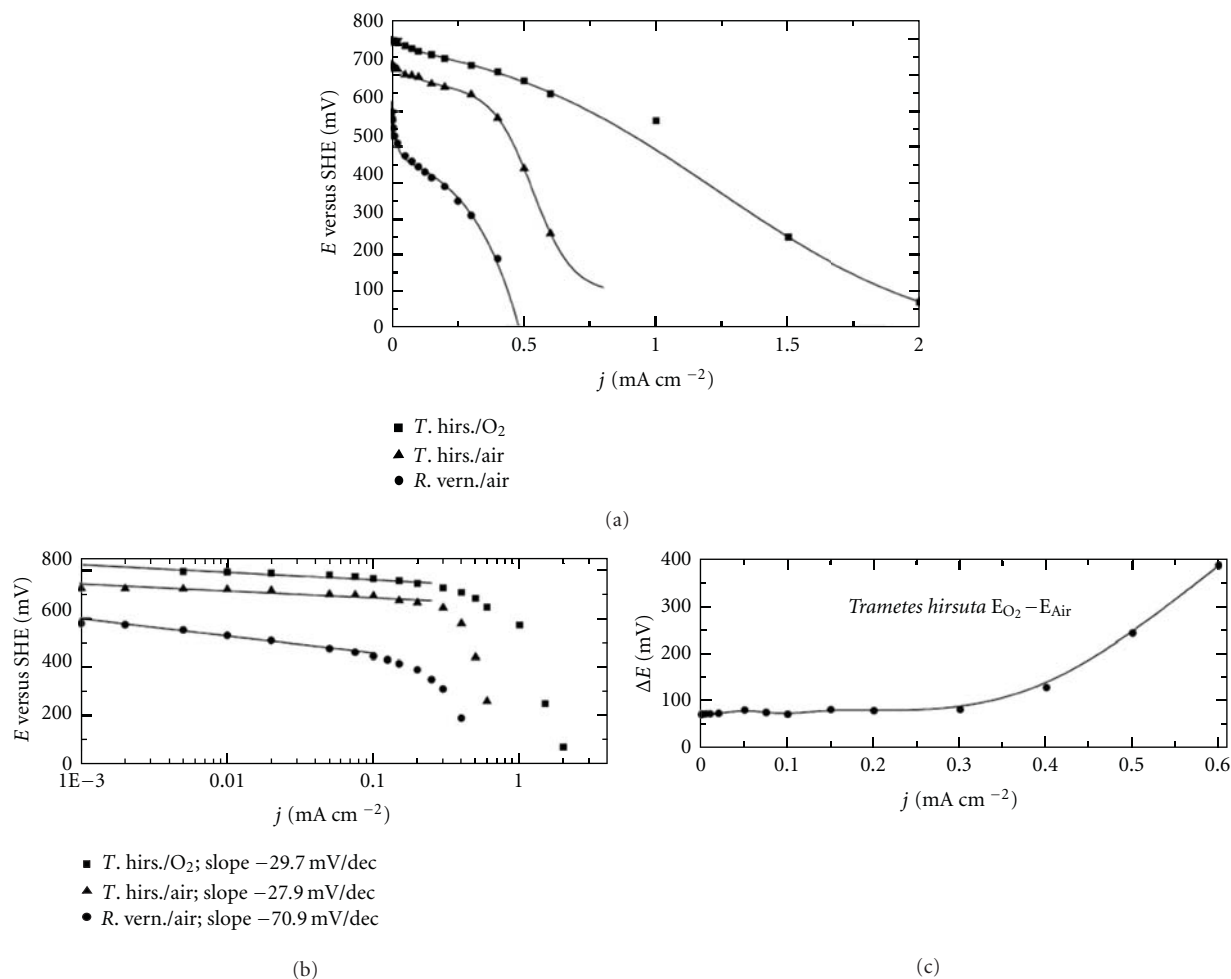


FIGURE 4: (a) Current-voltage behaviour of fungal (squares, triangles) and tree (circles) laccase-based gas diffusion cathodes. Influence of oxygen on the polarisation curve obtained for fungal laccase in air (triangles) and oxygen (squares) stream conditions. (b) Tafel plots obtained from polarisation data for fungal (squares, triangles) and tree (circles) laccase. (c) The difference between potentials obtained in oxygen and air as a function of current density (from [4]).

1 in Figure 8) [52, 54]. This is perhaps due to the porous structure of the film obtained entirely from particles allowing for adsorption of the enzyme and relatively easy access of the substrate. However, chronoamperometric experiments show initial decrease of the current by ca. 50% [52].

The same concept was used to prepare nanoparticulate films composed of negatively charged carbon nanoparticles with phenylsulphonate functionalities and positively charged ones with sulphonamide-linked ammonium functionalities (Figure 10) [13].

Also these electrodes exhibit mediatorless bioelectrocatalysis of dioxygen reduction after adsorption of bilirubin oxidase and the magnitude of the catalytic current depends on the amount of material deposited on the ITO surface (Figure 11).

To summarize, the maximal catalytic current density obtained at film electrodes consisting of functionalised hydrophilic carbon nanoparticles by slow scan (0.001 V s^{-1}) voltammetry under dioxygen saturation is in the range of $0.1\text{--}0.4 \text{ mA cm}^{-2}$.

Another carbon-based material with nanosized pores—mesoporous carbon was also used as support for laccase-modified biocathode [55]. It exhibits catalytic current in the range of $0.1\text{--}0.3 \text{ mA cm}^{-2}$ as measured by slow scan (0.001 V s^{-1}) voltammetry at pH 6.

Quite remarkable results were recently reported for bilirubin oxidase adsorbed on micro/macrocylular foams [56]. These porous materials can be obtained in a somewhat controlled process, and their pore size ranges from tens of nanometers to tens of micrometers. With this material, the catalytic current density measured at 1000 rpm with scan rate 0.005 V s^{-1} in O_2 -saturated solution of pH 7.2 achieves 2 mA cm^{-2} .

3. Electrodes Modified with Carbon Nanotubes and Graphenes

Not surprisingly carbon nanotubes are the most frequently used nanomaterials for biocathode modification. They can

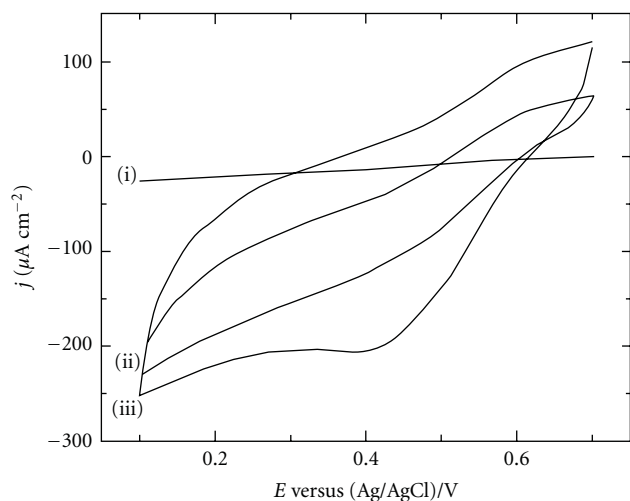


FIGURE 5: Cyclic voltammograms (second scan) obtained with bilirubin oxidase modified carbon ceramic electrode in air saturated 0.1 mol dm^{-3} phosphate buffer (pH 5). Electrode material contained (i) 0%, (ii) 10% and (iii) 20% carbon nanoparticles (from [5]).

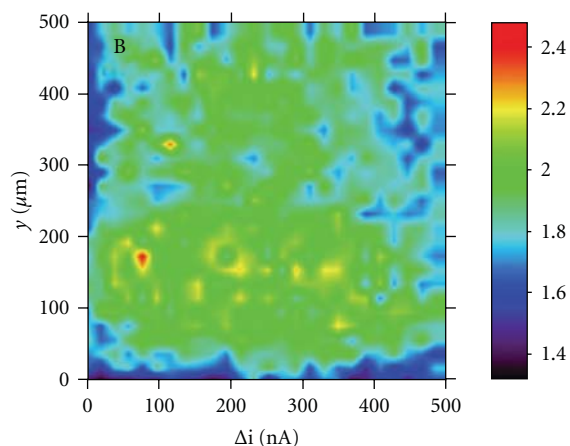


FIGURE 6: Scanning electrochemical microscopy visualisation of the lateral activity distribution of bilirubin-oxidase-modified carbon ceramic electrode in air-saturated 0.1 mol dm^{-3} phosphate buffer (pH 5). Electrode material contained 10% of 20% carbon nanoparticles (from [5]).

be used for building extended conducting networks with large effective surface area providing good electronic communication with the active site of the enzyme without decreasing its activity [8, 9, 57–60]. In addition, they can be easily functionalized through covalent bonding at the edges and defect sites or sidewalls of the carbon nanotube or noncovalently at the sidewalls [61, 62]. Chemical modification of the nanotubes sidewalls or its terminus is generally needed to control their dispersion and is crucial for the construction of devices [63–65]. In biosensing applications, functionalization can provide biocompatibility and specific interactions with biological molecules in solution [66, 67].

If mediators are employed to transfer electrons between the electrode and T1 center of oxygen by laccase or bilirubin oxidase, their leaching to the solution, and as a result a fast decrease of catalytic currents, as well as side reactions with the enzymes or other components of the biocathode or bioanode (in biofuel cells) are the adverse effects. This stimulates research on their immobilization, most frequently of ABTS^{2-} (2,2'-azino-bis(3-ethylbenzthiazoline-6-sulfonate), on carbon nanotubes or graphenes [15, 16, 65, 68–73].

Carbon-nanotubes-based biocathodes employing ABTS^{2-} as the mediator dissolved in solution were constructed from multiwalled carbon nanotubes (MWCNTs) functionalized with chitosan and laccase [74]. MWCNTs-ionic liquid gel and laccase [75] or single-walled carbon nanotubes (SWCNTs) and bilirubin oxidase were encapsulated in silicate matrix [76]. However these materials require the presence of a mediator in the oxygen-saturated catholyte. Therefore, membrane had to be employed to separate the glucose oxidase and SWCNT-modified anode from the catholyte [74, 76, 77]. This is not necessary when ABTS^{2-} is immobilised on the electrode surface, for example, attached to the walls or ends of SWCNTs [14, 65, 68, 78, 79]. This approach leads to the dioxygen reduction current density to 0.4 mA/cm^2 for electrodes covered with SWCNT-amine-ABTS and 0.2 mA/cm^2 for SWCNT-ABTS-side and Nafion layer containing laccase (Figure 12) [80].

Three ways of covalent modification of SWCNTs with ABTS^{2-} have been recently proposed (Figure 12). Their purity was evaluated by TGA (Table 1), because impurities or unintended functionalization may give rise to catalytic behavior [81]. Moreover, TGA allows for the determination of the degree of nanotube modification expressed as the ratio of the number of moles of substituent to mole of carbon (Table 1) [14, 78–80].

Raman spectroscopy allows determining the SWCNTs surface properties [82, 83] and is another method to verify their functionalization with redox mediators or other reagents decreasing their aggregation when immobilized on electrode surface [14, 15, 21, 79, 80] (Table 2).

For pristine SWCNTs, four main peaks should be present in the Raman spectrum: D , G , G' and a low frequency peak ($\omega_{\text{RBM}} < 300 \text{ cm}^{-1}$), called radial breathing mode (RBM) (Figure 13).

RBM corresponds to the symmetric in-phase displacements of all carbon atoms in SWCNT in the radial direction and its frequency is related to the nanotube diameter [15]. The multicomponent tangential G band is derived from the in-plane Raman-active mode in graphite. The RBM and multi- G -band are the first-order Raman features, which are characteristic only for SWCNTs. The last two main bands present in SWCNTs Raman spectrum are the disorder-induced D band (at $\omega_D \sim 1350 \text{ cm}^{-1}$) and its overtone, the harmonic G' band, at a frequency equal to $\sim 2\omega_D$. The dispersive D mode is observed when the symmetry of hexagonal sp^2 bonded lattice is destroyed, so it is related to the presence of the defects in the nanotube structure or amorphous carbon material in the tested sample. The intensities of all observed modes in Raman spectra can

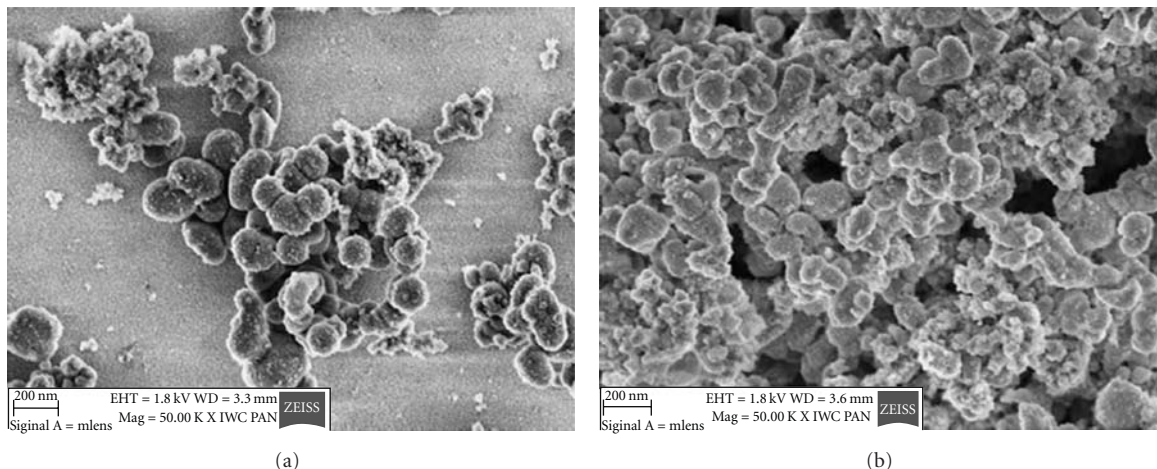


FIGURE 7: Scanning electron microscopy images of ITO electrode coated by one (a) and three (b) immersion and withdrawal steps to cationic silicate particles and carbon nanoparticles suspension alternatively (from [12]).



FIGURE 8: Scheme of the structure of carbon nanoparticulate film electrodes with (1) imidazolium-appended silicate and (2) imidazolium-appended silicate submicroparticles.

change and the frequency of modes can be shifted due to chemical modification (Figure 13). The relative intensity ratios of Raman bands for pristine and modified SWCNTs also change. Commonly, the direct I_D/I_G intensity ratios are utilized to monitor the purity of the nanotubes and functionalization of the CNTs (Table 2), and I_D and I_G intensities are measured relative to the intensity of the two-phonon G' mode, $I_{G'}$. The latter is decreased when uniformity of the sample decreases due to impurities or large distribution of nanotube sizes. Interestingly, the D peak is not observed to increase as a result of adsorption of, for example, hydronium ions or surfactants on the nanotube sidewalls, thus it allows for distinguishing covalent from noncovalent modification.

For nanotubes modified with azobenzene and anthraquinone, the frequency shifts of the observed bands were negligible; however the intensity of the D band increased

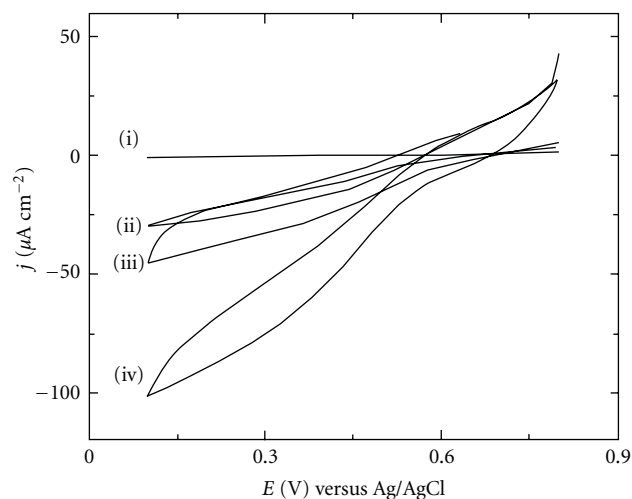


FIGURE 9: Cyclic voltammograms (second scan) obtained with ITO electrode coated by (i) one, (ii) six, (iii) twelve, and (iv) twenty-four immersion and withdrawal steps followed by laccase adsorption. Experiments were performed in dioxygen-saturated 0.1 mol dm^{-3} phosphate buffer (pH 4.8). Scan rate 0.001 V s^{-1} (from [12]).

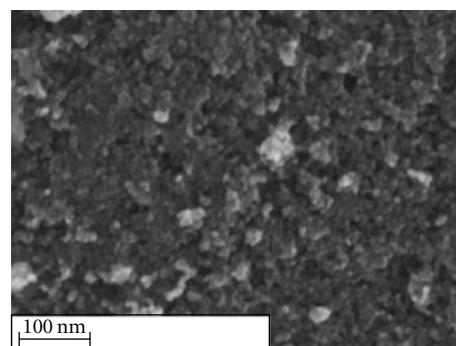


FIGURE 10: immersion and withdrawal steps alternatively into cationic and anionic carbon nanoparticles suspensions (from [13]).

TABLE 1: TGA characterization of ABTS-modified carbon nanotubes [14, 78, 79, 81].

Sample	Mass loss below 200°C (%)	Mass loss in the range of 200–420°C (%)	Estimated percentage of SWCNT (%)	Mol of moiety/mol of carbon	Assumed m.w. of detached moiety
Pristine SWCNT	0	0	100	—	—
SWCNT-ABTS-side	0	10	90	$2.2 \cdot 10^{-3}$	597
SWCNT-ABTS-end	2	5	92	$1.1 \cdot 10^{-3}$	583
SWCNT-amine ABTS	7	10	50	$4.4 \cdot 10^{-3}$	540

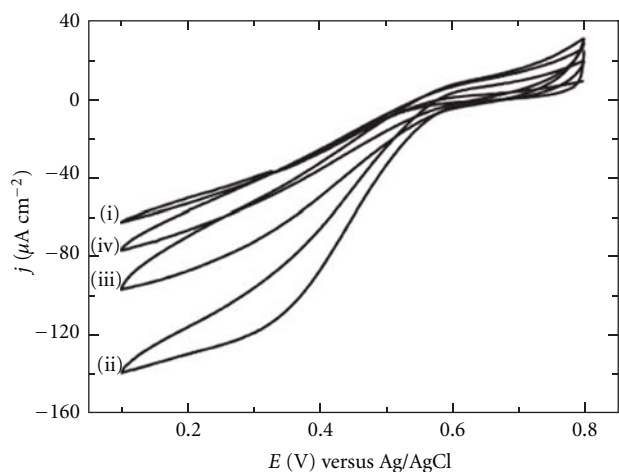


FIGURE 11: Cyclic voltammograms (second scan) obtained with ITO electrode coated by (i) one, (ii) three, (iii) six, and (iv) nine immersion and withdrawal steps alternatively into suspension of negatively and positively charged carbon nanoparticles, followed by bilirubin oxidase adsorption. Experiments were performed in dioxygen-saturated 0.1 mol dm^{-3} phosphate buffer (pH 4.8). Scan rate 0.001 V s^{-1} (from [13]).

strongly (Figure 13) as compared to the pristine nanotubes. Comparing the I_D/I_G ratio, which is 0.12 for pristine SWCNTs, 0.26 for SWCNT-anthraquinone, 0.67 for SWCNT-azobenzene, and 0.34 for SWCNT-ABTS (Table 2), we can find that the disorder is enhanced after modification. Additionally, grafting of the moieties to the nanotube sidewalls leads to changes of strength and frequency of RBM mode [15]. Anthraquinone-derivatized SWCNTs produced a significant spectral shift of the radial breathing modes from 269 to 380 cm^{-1} . This is a strong indication of sidewall functionalization and disruption of the radial breathing motion due to the added functionality.

The assessment of carbon nanotubes modification by Raman spectroscopy is extremely important when functionalities are not electroactive. This is the case of pyrene with hydrophilic functional groups, adsorbed on SWCNTs due to π - π interactions [21]. After modification characteristic bands partially overlapping with the SWCNTs G-band and additional band at 1230 cm^{-1} from adsorbed pyrene can be seen. Additionally the ratio of D/G bands increases compared to that of pristine nanotubes confirming large extent of pyrene functionalization [21, 84].

SWCNTs with covalently attached ABTS^{2-} moieties were used for preparation of biocathodes [14, 79]. The

TABLE 2: Relative intensity ratios of Raman bands for pristine and modified SWCNTs [81].

Sample	I_D/I_G	I_G/I_D	I_G/I_G
Pristine SWCNT	0.12	2.78	0.32
SWCNT- CH_2CN	0.40	0.79	0.31
SWCNT- $\text{CH}_2\text{-COOH}$	0.60	0.39	0.23
SWCNT-ABTS-side	0.34	0.96	0.32
SWCNT-ABTS	0.34	0.92	0.31

voltammogram of glassy carbon electrode modified with SWCNTs-ABTS and SWCNTs-ABTS-side and covered with lipid liquid crystalline cubic phase film containing laccase exhibits pair of peaks characteristic of mediator redox process [14, 79] (Figure 14). In the presence of oxygen both electrodes show mediated bioelectrocatalysis with end modified SWCNTs more efficient (0.6 mA cm^{-2} compared to 0.4 mA cm^{-2}) (Figure 14). These values are much higher than those obtained for similar electrodes with SWCNTs modified by adsorbed ABTS^{2-} (0.09 mA cm^{-2}) or with the same mediator in solution (0.02 mA cm^{-2}).

The redox activity of the mediator also helps in the determination of the degree of SWNTs modification from the magnitude of cyclic voltammetry signal. For electrodes modified with MWCNTs encapsulated in silicate sol-gel-processed film and then modified with adsorbed ABTS^{2-} less than 10% of the surface is covered by mediator molecules [68]. These electrodes exhibit catalytic current density below 0.1 mA cm^{-2} as measured by slow scan (0.001 V s^{-1}) voltammetry in dioxygen-saturated solution, ten times larger than in the absence of adsorbed mediator [68]. Slightly larger current density was obtained with the same ABTS^{2-} functionalized carbon nanotubes stabilized with Nafion [65]. Larger signal is observed from SWCNT-ABTS-side as compared to SWCNT-ABTS encapsulated in Nafion film together with laccase (Table 3). Also catalytic current density of this electrode is larger [79, 80] (Table 3). Interestingly the catalytic efficiency per mediator molecule is significantly larger when mediator is attached to the end of carbon nanotube (Table 3). On the other hand, the total current density is larger when modification takes place at the sidewalls since the number of functional groups is larger. Modification of the electrodes with ABTS^{2-} functionalized SWCNTs allows to obtain catalytic current density up to 0.5 mA cm^{-2} and to decrease the onset potential of dioxygen reduction to 0.5 V versus Ag/AgCl making these biocathodes suitable for biofuel cells.

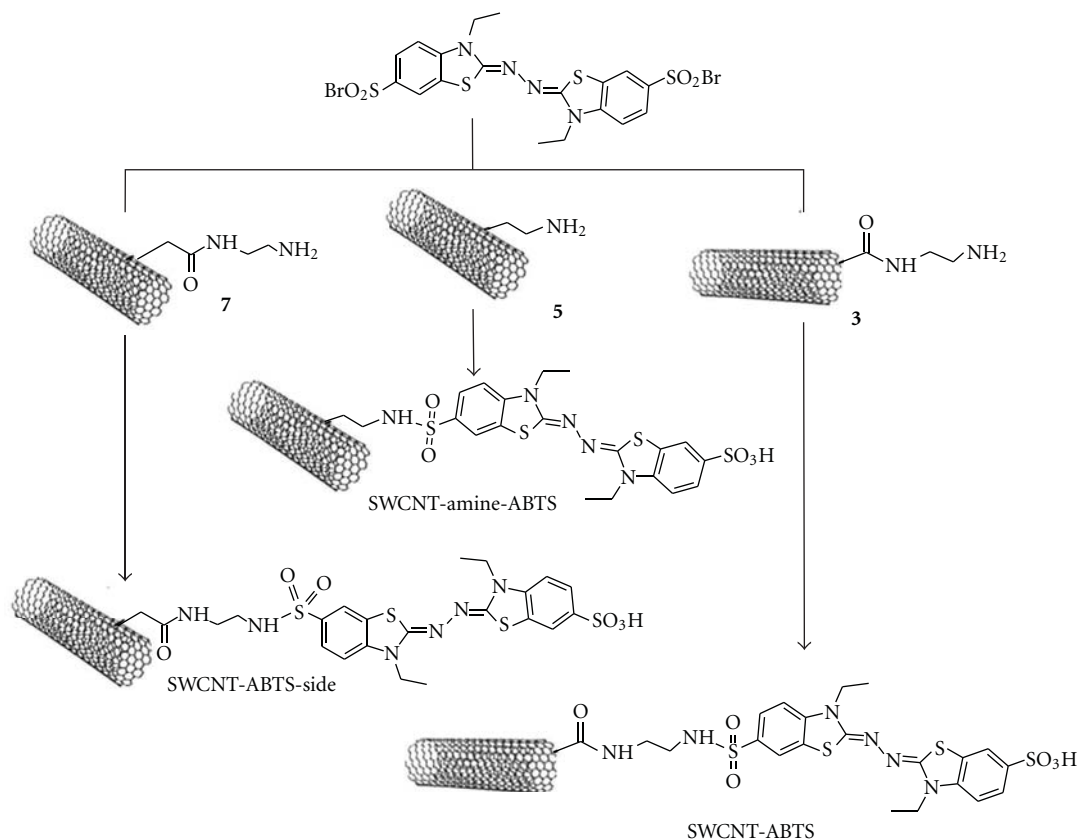


FIGURE 12: Three routes for covalent modification of SWCNTs with ABTS functionalities (from [14]).

TABLE 3: Catalytic current of oxygen reduction in McIlvaine buffer solution (pH 5.2) recorded at GCE electrodes covered with SWCNTs modified covalently with redox mediator ABTS²⁻ and Nafion layer containing laccase. Scan rate 0.001 V s⁻¹ [81].

GCE-Nafion film modification	j_{cat} (mA/cm ²) ^a (at 0.2 V versus SCE)	Q_{ABTS} (mC/cm ^{2a})	$j_{\text{cat}}/\Gamma_{\text{ABTS}}$ (mA/nmol)
SWCNT with laccase	-0.186		
SWCNT-ABTS-side with laccase	-0.199	6.863	5.6
SWCNT-ABTS-end with laccase	-0.066	0.199	54.7
SWCNT-amine-ABTS with laccase	-421.5	7.062	11.5

^a Average of 5 experiments.

Carbon nanotubes can be organized perpendicularly to the electrode surface, which allows utilization of their extended surface and takes advantage of the fast electron transfer along their main axis [85]. Very recently vertically aligned MWCNTs were used for biocathode preparation [16]. These electrodes were prepared by a CNT-transfer technique attaching the as-grown carbon nanotubes to ITO substrate with a glue prepared from MWCNTs and epoxy. ABTS²⁻ and laccase immobilization produce a not-very-efficient catalytic system with the current density not exceeding 0.1 mA cm⁻² as measured by voltammetry with scan rate 0.001 V s⁻¹ (Figure 15). Replacement of ABTS²⁻ with syringaldazine increases catalytic current eight times. However, the onset potential of the catalytic current is not as positive as in case of ABTS²⁻ due to the lower redox potential of syringaldazine.

The application of buckypaper-based electrodes prepared from MWCNTs and exhibiting apparent electrical conductivities up to 2500 S m⁻¹ as biocathodes was recently reported [86]. This material was further impregnated with ABTS²⁻ salt, Nafion, and bilirubin oxidase, and it allows obtaining catalytic current ca. 0.2 mA cm⁻².

Remarkable stability of the enzyme was obtained with screen printed electrodes with MWCNTs, laccase, and ABTS²⁻ salt as ink component [87]. Although the current density was not larger than 0.02 mA cm⁻², this way of nanoparticulate modification of cathode may become important in the future, because of the cost-effective manufacturing.

Another way of ABTS²⁻ immobilization on SWCNTs-modified electrode is based on their combination with layered double hydroxides to entrap and electrically connect

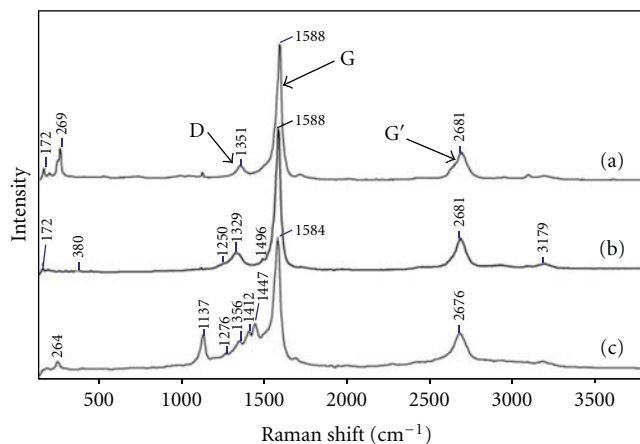


FIGURE 13: Comparison of Raman spectrum of pristine SWCNTs (a) and SWCNTs with walls functionalized with anthraquinone (b) and azobenzene (c) moieties (from [15]).

laccase [88]. The coating was based on electrostatic interactions between hydroxyl and carboxylic groups of chemically oxidized carbon nanotubes with the positively charged layered double hydroxides. Although the bioelectrocatalysis of dioxygen reduction with wired laccase was demonstrated, the current densities reported were relatively low [88].

Although few ways of carbon nanotube modification with mediator were proposed, the majority of research with this material is oriented towards mediatorless bioelectrocatalysis of dioxygen reduction. Non-functionalized MWCNTs in silicate matrix with laccase exhibits current densities below 0.01 mA cm^{-2} measured by cyclic voltammetry with scan rate 0.001 V s^{-1} in dioxygen-saturated phosphate buffer pH 5.2 [69], whereas similar material impregnated with polyethylene glycol and bilirubin oxidase provides catalytic current above 0.1 mA cm^{-2} [89]. A current density of ca. 0.06 mA cm^{-2} , measured at scan rate 0.005 V s^{-1} , was obtained when the MWCNTs suspension in chloroform was casted on glassy carbon electrode and allowed to dry. In the second step, laccase was coadsorbed on this nanostructured surface and again left to dry [90]. Non-functionalized SWCNTs with laccase provide ca. 0.04 mA cm^{-2} measured by cyclic voltammetry with scan rate 0.001 V s^{-1} in dioxygen-saturated phosphate buffer, pH 6 [91]. Cross-linked bilirubin oxidase on similar electrodes provides 0.1 mA cm^{-2} at pH 7 [42]. More importantly the catalytic current density increased more than five times when SWCNTs and cross-linked laccase were immobilized on a $7 \mu\text{m}$ diameter carbon fibre [92]. This improvement is clearly due to specific geometry of the system, namely, enhanced mass transport, because of radial substrate diffusion. The replacement of laccase with bilirubin oxidase doubles catalytic efficiency of this micro-biocathode (Figure 16) [17]. Modification of biocathode of similar geometry consisting of carbon nanotubes assembled on carbon nanofibers with osmium polymer and bilirubin oxidase results in the current density ca. 1.6 mA cm^{-2} as measured with scan rate 0.005 V s^{-1} in phosphate saline buffer [93]. This highly porous material in

a form of microwire provides large contribution of radial diffusion not present at nanoparticulate flat film electrode.

Recently, a comparative study of bioelectrocatalytic dioxygen reduction on different carbon-based materials was published [18]. Laccase adsorbed on graphite felt, porous carbon tubes, carbon nanofibers as well as SWCNTs and MWCNTs was characterised under comparable experimental conditions as half-cell electrodes using current density-cathode potential plots. Obviously, open circuit potential of all materials was significantly increased by laccase adsorption, indicating mediatorless catalysis. It was concluded that deterioration performance of these materials in the absence of mediator is due to electrode-material-dependent parameters, for example, oxygen diffusion within porous electrodes, enzyme adsorption or its orientation at the electrode surface. Among the investigated materials, MWCNTs show the best performance in terms of volume-normalized current density. However, the study also revealed that carbon nanotubes and porous carbon tubes exhibit dramatically lower current densities when normalized to BET surface area (Figure 17). This was ascribed to either material-dependent rate of direct electron transfer or limitations due to agglomeration of the nanotubes. Anyway, it also confirms that it is difficult to attain catalytic current density larger than 0.1 mA cm^{-2} (referred to as geometric area) with flat electrodes modified by nonfunctionalised carbon nanotubes and copper oxidoreductase.

The attempts to increase the efficiency of carbon nanotube biocathodes by preparing three-dimensional structures on the electrode surface have to be noted [19, 73, 94]. In some experiment multilayered film composed of polylysine, MWCNTs, and laccase was prepared [19, 94]. A controlled amount of nanotubes and enzyme was immobilised using layer-by-layer technique (Figure 18(A)). Efficient bioelectrocatalysis with current density over 0.5 mA cm^{-2} (Figure 18(B)) allowed for the use of this biocathode in a glucose- O_2 biofuel cell [19] and as a self powered biosensor [94].

A three-dimensional carbon nanotube-hydroxyapatite nanocomposite film was also used as a biocathode material; however, rather low catalytic efficiency was achieved [73].

Very impressive catalytic efficiency was achieved with biocathodes made of directly grown SWCNTs [20]. Laccase was immobilized on carbon nanotube forest by liquid-induced shrinkage (Figure 19), and a catalytic current density up to 4 mA cm^{-2} was obtained.

There are many reports exploring modification of carbon nanotubes to prevent their aggregation and promote direct electron transport to immobilised copper oxidoreductase and therefore mediatorless bioelectrocatalysis. SWCNTs non-covalently functionalized with 1-pyrene derivatives and immobilized in hydrophilic (obtained from tetramethoxysilane) and hydrophobic (obtained from methyltrimethoxysilane) silicate matrix were used to enhance direct electron transfer to enzyme laccase [69] and bilirubin oxidase [21]. The enzymes were either adsorbed from the solution or co-immobilized with the nanotubes. In the former case the charge of the functionalized nanotubes was decisive for the efficiency of bioelectrocatalytic reduction of oxygen. It was

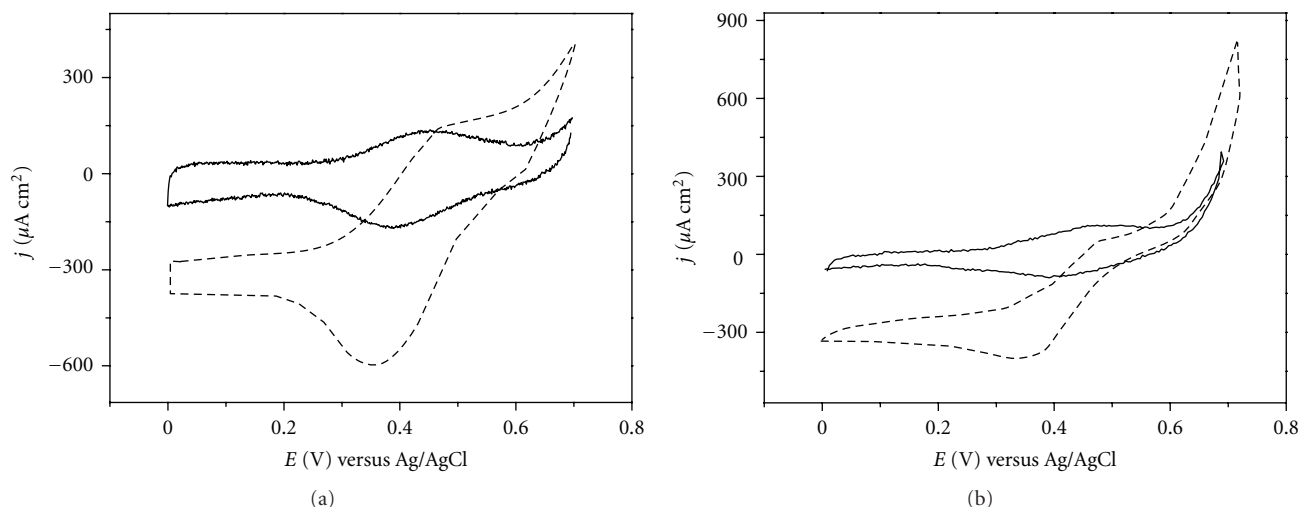


FIGURE 14: Biocatalytic oxygen reduction at (a) GC/SWCNTs-ABTS and (b) GC/SWCNTs-ABTS-side modified with cubic phase with incorporated laccase, McIlvaine buffer, pH 5.2. Scan rate 1 mV s^{-1} (from [14]).

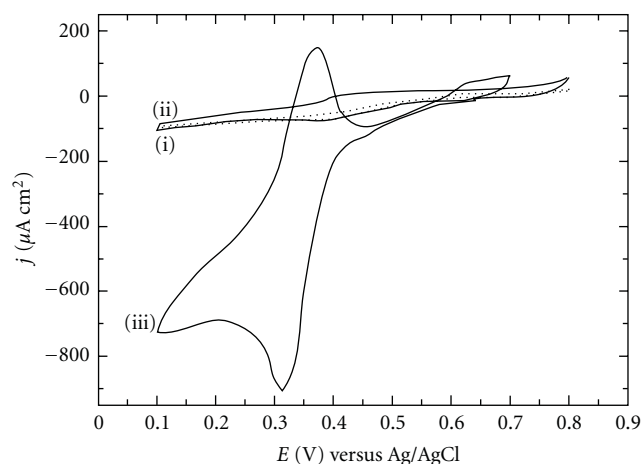


FIGURE 15: Voltammograms obtained at electrodes modified with vertically aligned MWCNTs and (i) adsorbed ABTS^{2-} and laccase, (ii) adsorbed ABTS^{2-} and laccase encapsulated in hydrophobic silicate film, and (iii) adsorbed syringaldazine and laccase encapsulated in hydrophobic silicate film, dioxygen-saturated McIlvaine buffer, pH 4.8. Scan-rate 1 mV s^{-1} (from [16]).

also shown that the functional group of adsorbed pyrene affects the magnitude of catalytic current, and the use of 1-pyrene sulfonate is most favourable for bilirubin oxidase modified electrode (Figure 20). The importance of electrode functional groups and superiority of sulfonate was also found in fundamental studies of bioelectrocatalytic dioxygen reduction on gold [26, 95]. Interestingly for laccase-modified electrodes four times larger catalytic current is observed for vertically aligned MWCNTs modified with 1-pyrene sulfonate [16] indicating importance of film geometry. These electrodes prepared were used as cathode zinc-dioxygen batteries [16, 21].

SWCNTs with attached nonelectroactive aromatic groups either on the side or at the ends of the carbon nanotubes

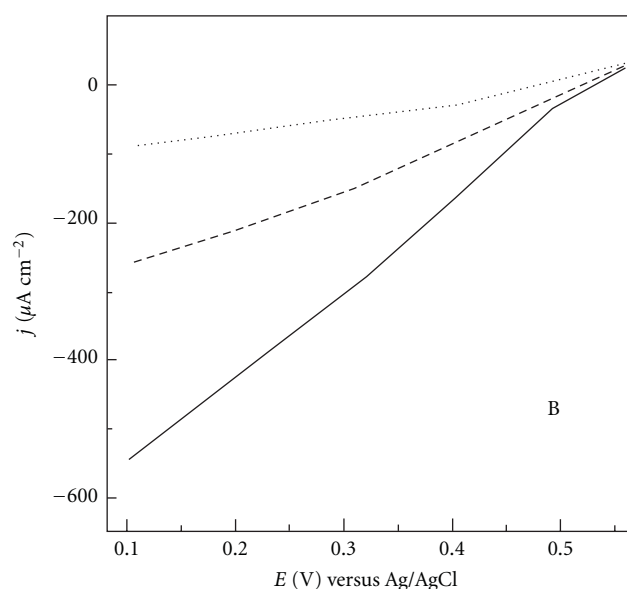


FIGURE 16: Polarisation curves obtained for carbon fiber microelectrode modified with SWCNTs and bilirubin oxidase immersed in 0.1 mol dm^{-3} phosphate buffer saturated with N_2 (dotted), ambient air (dashed), and O_2 (solid). Scan rate 0.001 V s^{-1} (from [17]).

(Figures 21 and 22) were explored for biocathode modification [31]. Aryl functionalized nanotubes were expected to enter the hydrophobic pocket of the T1 centre of copper oxidoreductases. The approach of Sosna et al. [26] allows binding anthracene and anthraquinone to the electrode by deprotecting amine linkers organized in a monolayer; however, the population of laccase molecules bound this way to the monolayer modified electrode is very small. Nanostructuring the electrode with SWCNTs covalently modified with anthraquinone or anthracene leads to a visible increase of the oxygen catalytic current since it allows much more

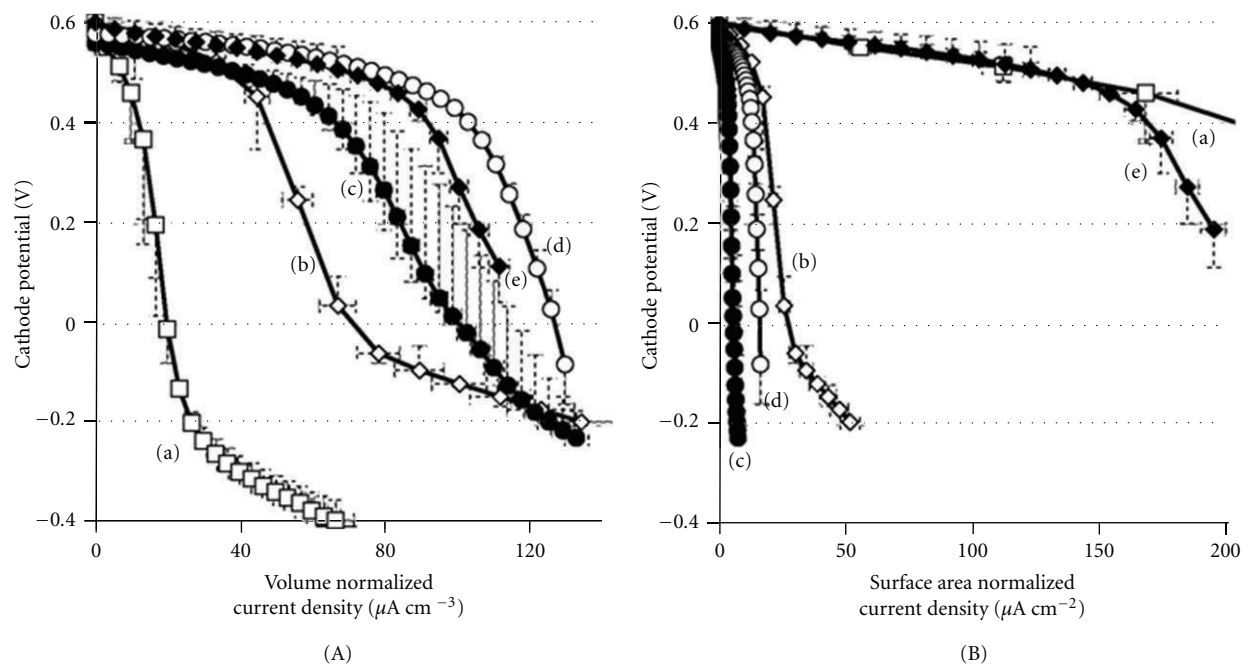


FIGURE 17: Current density-cathode potential plots for the electrodes with laccase adsorbed on the following materials: graphite felt (a), porous carbon tubes (b), single-walled carbon nanotubes (c), multiwalled carbon nanotubes (d), and carbon nanofibers (e). (A) Comparison of cathode performance with a current density normalized to volume. (B) Comparison of cathode performance with a current density normalized to BET surface area. Reproduced with permission (from [18]).

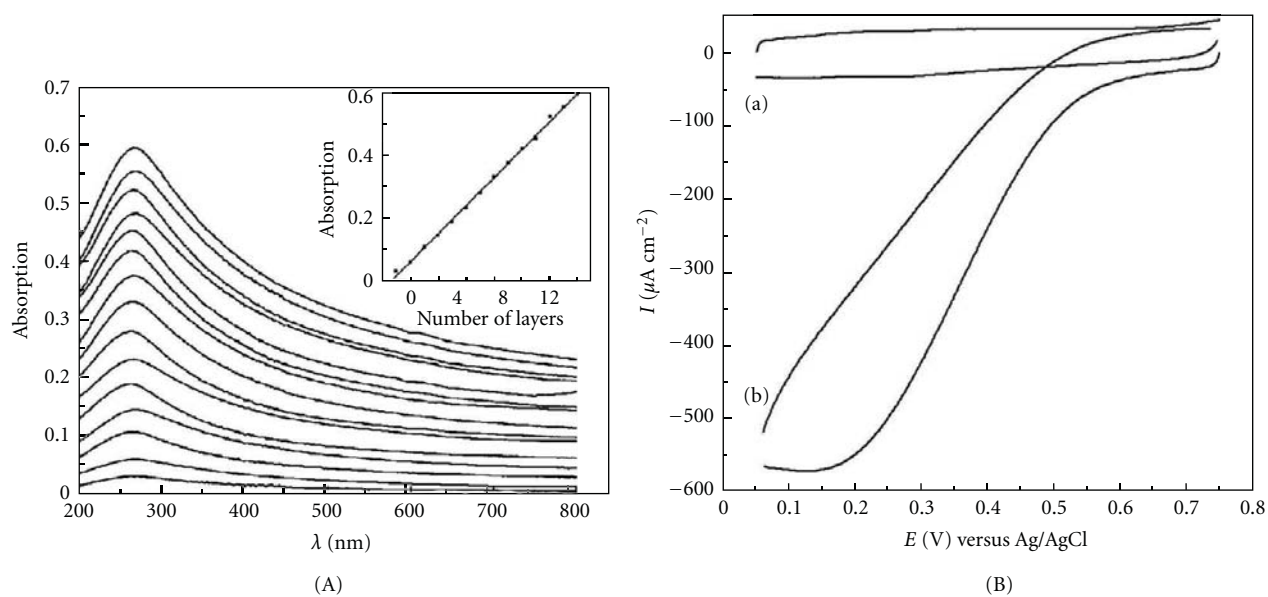


FIGURE 18: (A) UV-vis absorption spectra of multilayer on quartz substrate (laccase as the outmost layer) with different numbers of layers: 1–15 (curves from bottom to top). The inset shows the absorbance at 267 nm as a function of the number of layers. (B) Cyclic voltammograms of the (MWCNT/polylysine/laccase)₁₅-modified ITO electrodes in 0.1 mol dm⁻³ PBS (pH 6.0), under (a) N₂-saturated condition and (b) air-saturated conditions, respectively. Scan rate 0.05 V s⁻¹ (from [19]).

laccase to be hydrophobically bound to the electrode surface. The 2D type of binding is transformed this way into a 3D assembly connected electrically [31]. Anthraquinone-modified SWCNTs were obtained from acid chloride functionalized nanotubes (Figure 21). This functionality reacts with amine substituted anthraquinone.

Synthesis of SWCNTs arylated on side walls was carried out by free radical reaction. The first step involves generation of diazonium compounds from aromatic amines. This intermediate was thermally decomposed in the presence of carbon nanotubes under permanent sonication at elevated temperature (60–65°C) (Figure 20).

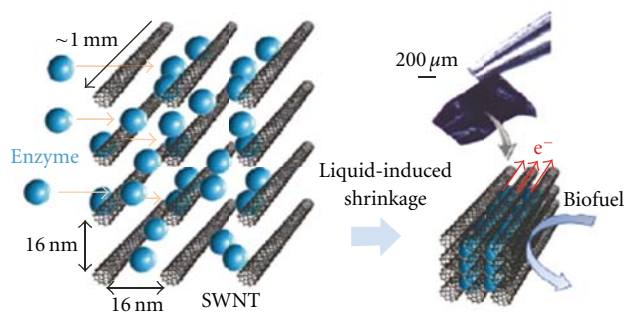


FIGURE 19: Schematic diagram of enzyme entrapment inside a carbon nanotube forest by liquid-induced shrinkage. The photograph in the right upper corner shows a free-standing enzyme carbon nanotube forest ensemble film that can be manipulated with tweezers (from [20]).

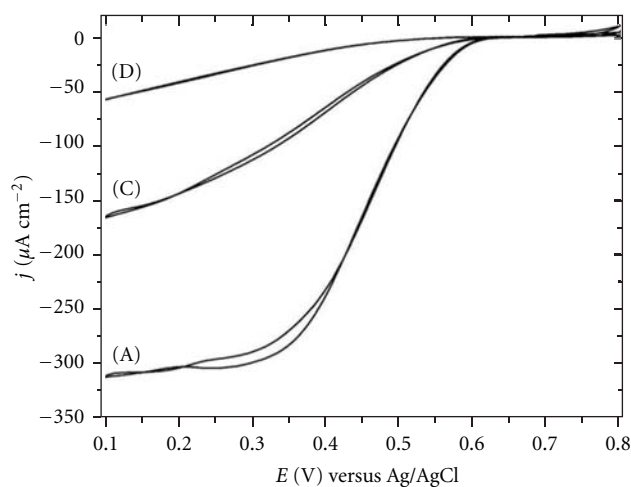


FIGURE 20: Voltammograms obtained at electrodes modified with SWCNTs functionalized with (A) 1-pyrene sulfonate, (C) 1-pyrene butyrate, and (D) pyrene methylamine and laccase encapsulated in hydrophobic silicate film in dioxygen-saturated McIlvaine buffer, pH 4.8. Scan rate 0.001 V s^{-1} (from [21]).

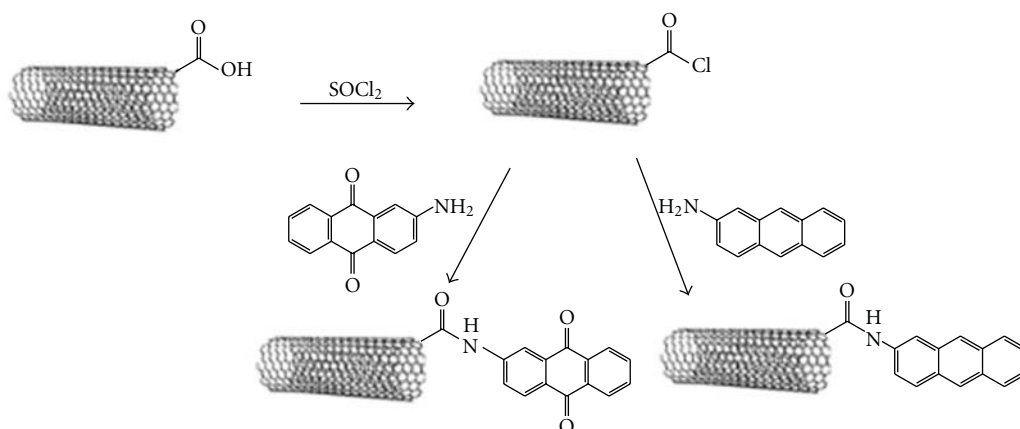


FIGURE 21: Synthesis of anthraquinone-modified SWCNTs.

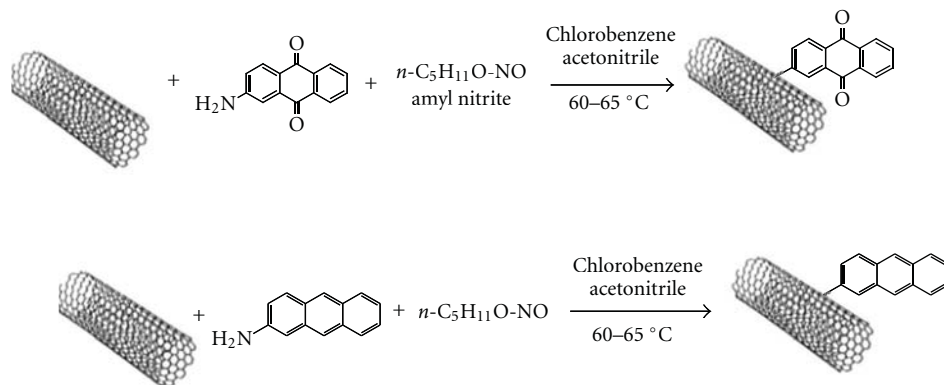


FIGURE 22: Synthesis of SWCNTs arylated on side walls.

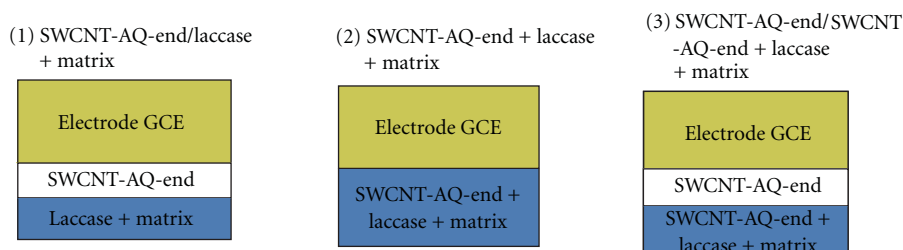


FIGURE 23: Scheme of preparation of electrodes modified with arylated SWCNTs (from [31]).

Arylated SWCNTs were deposited on glassy carbon surface in three ways (Figure 23). This affects catalytic current density: the highest is observed for the electrodes first modified with a layer of arylated SWCNTs casted on the GC surface and then covered with the matrix, for example Nafion, lecithin, chitosan, or lipid liquid crystalline cubic phase, containing laccase and the same arylated SWCNTs [14, 31, 78, 79].

The type of functional group also affects catalytic current density (Table 4), and its largest value was obtained with terphenyl functionalized SWCNTs. On the other hand, for all these electrodes showing DET, the onset potential is close to the formal potential of laccase T1 site. (Figure 24) [32]. These electrodes were also successfully applied as cathodes in a hybrid biofuel cell with a Zn anode [32].

Wrapping SWCNTs with single-stranded DNA was shown to decrease the shear stress between the enzymes and SWCNTs [96, 97].

Enzymatic functionalization of nanotubes as well as graphene nanosheets would allow appropriate orientation of the enzyme molecule and efficient electrical connection. The use of these materials provides also greater surface area for anchoring enzymes and improving kinetics of the enzyme [98]. Indeed, covalent linking of multicopper oxidases to well dispersed conductive carbon nanotubes represent alternative strategy to facilitate direct electron transfer and efficient bioelectrocatalytic oxygen reduction [33, 34, 70, 99–101].

Irreversible adsorption of pyrene moieties on carbon nanotubes and their functionalization with copper oxidoreductase was explored [33, 99]. Linking laccase or bilirubin oxidase to MWCNTs via the molecular tethering reagent 1-pyrenebutanoic acid, succinimidyl ester, results in a catalytic current efficiency in the range of 0.3–0.4 mAcm⁻² [99]. Similar way of laccase bonding based on reaction of 1-aminopyrene with glutaraldehyde was proposed (Figure 25) [33]. Although the catalytic efficiency of this system is not very impressive, the authors report that after one week the electrode retains 85% of its initial activity, which is much better than for analogous electrode with adsorbed enzyme.

Schubert et al. [34] immobilized bilirubin oxidase on gold by means of thiol-modified MWCNTs fixed on the gold electrode. The enzyme was covalently bonded to the other end of carbon nanotube (Figure 26). The direct electron transfer process led to remarkably high bioelectrocatalytic oxygen reduction current (50 $\mu\text{A cm}^{-2}$ measured by cyclic voltammetry at 0.01 V s⁻¹ in air-saturated buffer, pH 7) and rate constant of enzymatic reaction equal to 80–100 s⁻¹. In an earlier study the selection of interlayer compound for direct electronic communication of the enzyme with the electrode was emphasized. This indicates the importance of the linkage for electrodes stability, and indeed these electrodes retain 50% of their activity after 16 days of storage.

Not surprisingly several examples of the application of graphene sheets for biocathode construction have been reported recently [70, 102–104].

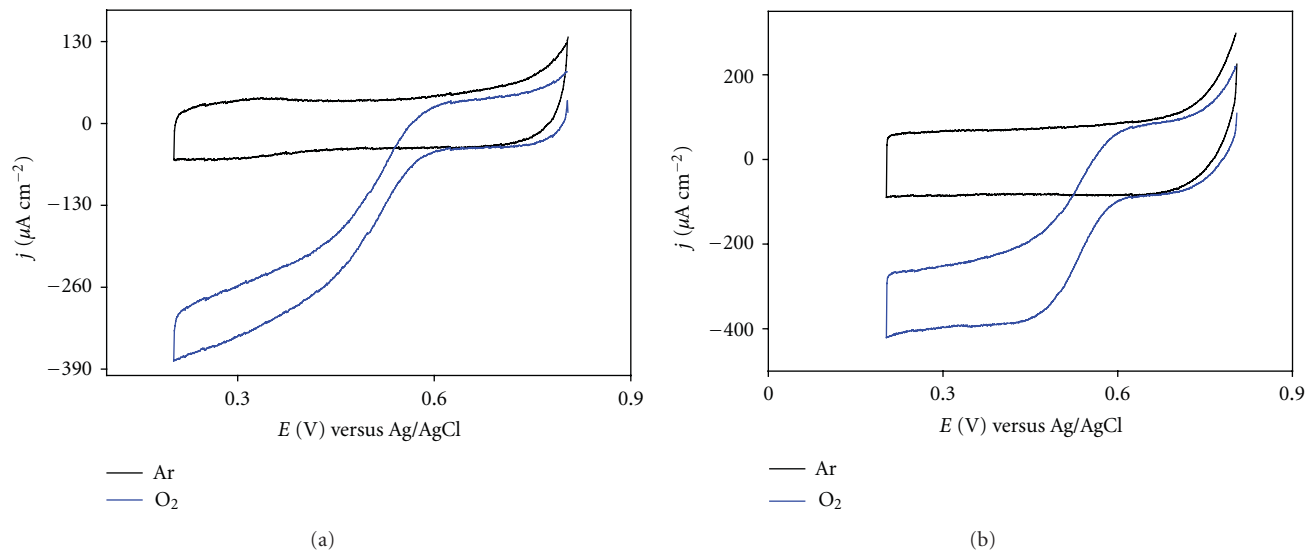


FIGURE 24: Voltammograms for laccase catalyzed reduction of oxygen obtained at GC electrodes modified with (a) naphthalene and (b) terphenyl side-derivatized SWCNTs. Scan rate 0.001V/s, McIlvaine buffer solution, pH 5.2/0.2NaNO₃ (from [32]).

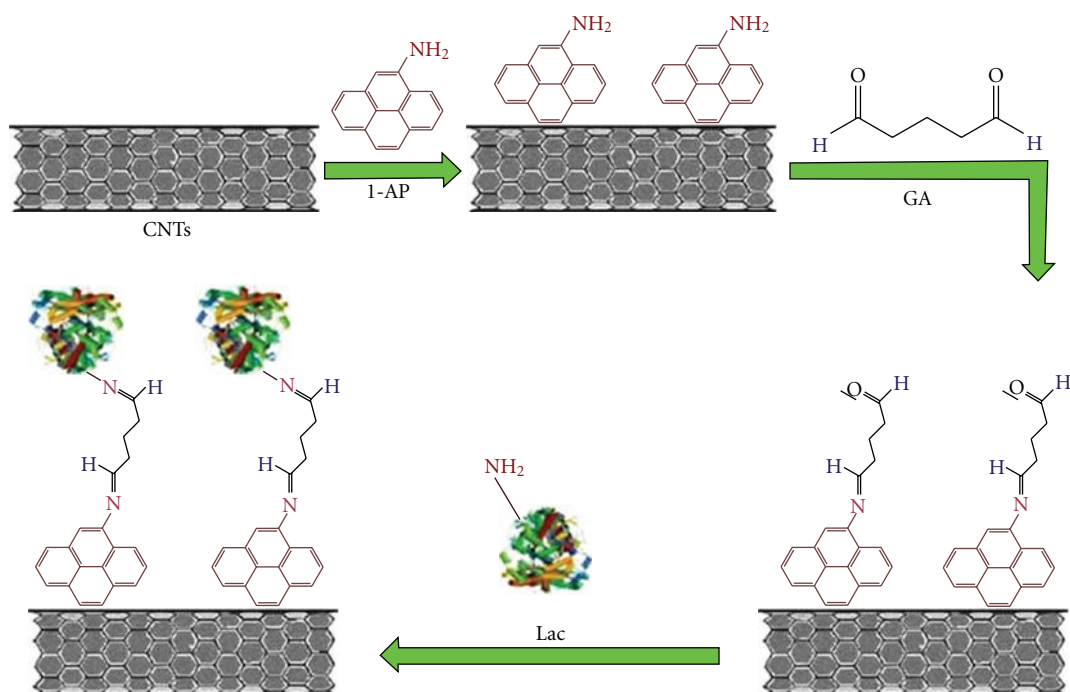


FIGURE 25: Schematic diagram for the immobilization of laccase on 1-AP functionalized CNTs (from [33]).

TABLE 4: Background and dioxygen reduction current densities (j_{bcg} and j_{cat}) recorded at GC electrodes covered with Nafion films containing SWCNTs covalently modified with different functional groups. Scan rate 0.001 V/s, McIlvaine buffer solution, pH 5.2/0.2 NaNO₃ (from [32]).

GCE modification	j_{bcg} (mA/cm ²)	j_{cat} (mA/cm ²)	$j_{cat} - j_{bcg}$ (mA/cm ²)
SWCNT/laccase + Nafion	-0.065 ± 0.011	-0.187 ± 0.018	-0.121 ± 0.026
SWCNT-amine-ABTS-side/laccase + Nafion	-0.038 ± 0.005	-0.421 ± 0.007	-0.380 ± 0.012
SWCNT-AQ-end/SWCNT-AQ-end + laccase + Nafion	-0.067 ± 0.004	-0.246 ± 0.002	-0.178 ± 0.006
SWCNT-anthracene side/laccase + Nafion	-0.022 ± 0.005	-0.238 ± 0.032	-0.215 ± 0.033
SWCNT-naphthalene side/laccase + Nafion	-0.014 ± 0.006	-0.230 ± 0.006	-0.211 ± 0.012
SWCNT-terphenyl side/laccase + Nafion	-0.071 ± 0.005	-0.424 ± 0.006	-0.354 ± 0.006

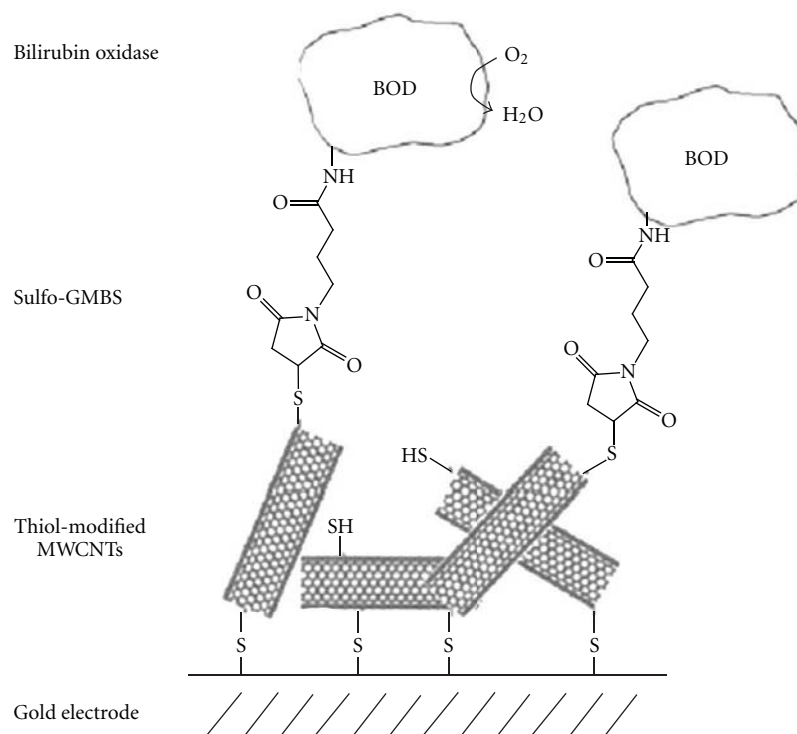


FIGURE 26: Bilirubin oxidase covalently bound to MWCNT-modified gold electrode (from [34]).

Biocathode consists of a gold substrate on which bilirubin oxidase, graphene were coimmobilized using silica sol and gel matrix [102]. The catalytic efficiency of this electrode in the presence, ABTS^{2-} salt in solution was not very high; however, authors emphasize the importance of graphene in the enhancement of stability of the constructed biofuel cell. Some improvement was seen with similar electrode based on a polypyrrole matrix [70].

Electrode system based on graphene integrated with laccase and ABTS^{2-} was developed for detection of the extracellular oxygen released from human erythrocytes [103]. Similar to the case of carbon-nanotubes-modified electrodes [65, 68] strong π - π interactions were employed for mediator immobilization on the graphene sheets, whereas immobilization of laccase involves electrostatic interactions [103]. This electrode exhibits mediated electrocatalysis, and the use of graphene increases electrocatalytic activity of the glassy carbon electrode 5 times. In the absence of mediator no bioelectrocatalysis was observed. The use of graphene nanoplatelets for laccase-modified biocathode was reported but this electrode shows only mediated catalysis with ABTS^{2-} salt in solution [104].

At the moment no advantage of the replacement of carbon nanotubes with graphene for biocathode construction is seen. Interestingly current research has also not shown any clear advantages of this material in the case of electrochemical biosensors [59].

4. Electrodes Modified with Metal and Metal Oxide Nanoparticles

There are not so many examples of metallic nanostructured films used for biocathode preparation in comparison with carbon-based materials. In the case of gold this may be due to unfavourable orientation of copper oxidoreductase on this material [105].

Nanoporous gold electrodes with a pore size in the range of 10–100 nm with adsorbed laccase exhibit enzyme direct voltammetry and modest bioelectrocatalytic activity. Catalytic current equal to 0.03 mA cm^{-2} was recorded by cyclic voltammetry with scan rate 0.1 V s^{-1} in air-saturated buffer solution (pH 4.4). Further studies of this material revealed that a larger pore size promotes adsorption of a larger amount of the enzyme. Interestingly from the point of view of stability, physical adsorption of laccase was found to be a superior immobilisation method, better than covalent binding or electrostatic attraction.

The study of glassy carbon electrode modified with citrate-stabilised Au nanoparticles (average diameter 50 nm) and laccase also reveals low (0.01 mA cm^{-2}) catalytic current density determined by slow voltammetry (at 0.001 V s^{-1}). However, contrary to other studies involving nanostructured metal electrodes the redox signal of the enzyme can be seen. This study also shows that electron transfer rate between T1 site of laccase and gold is similar to that obtained at carbon

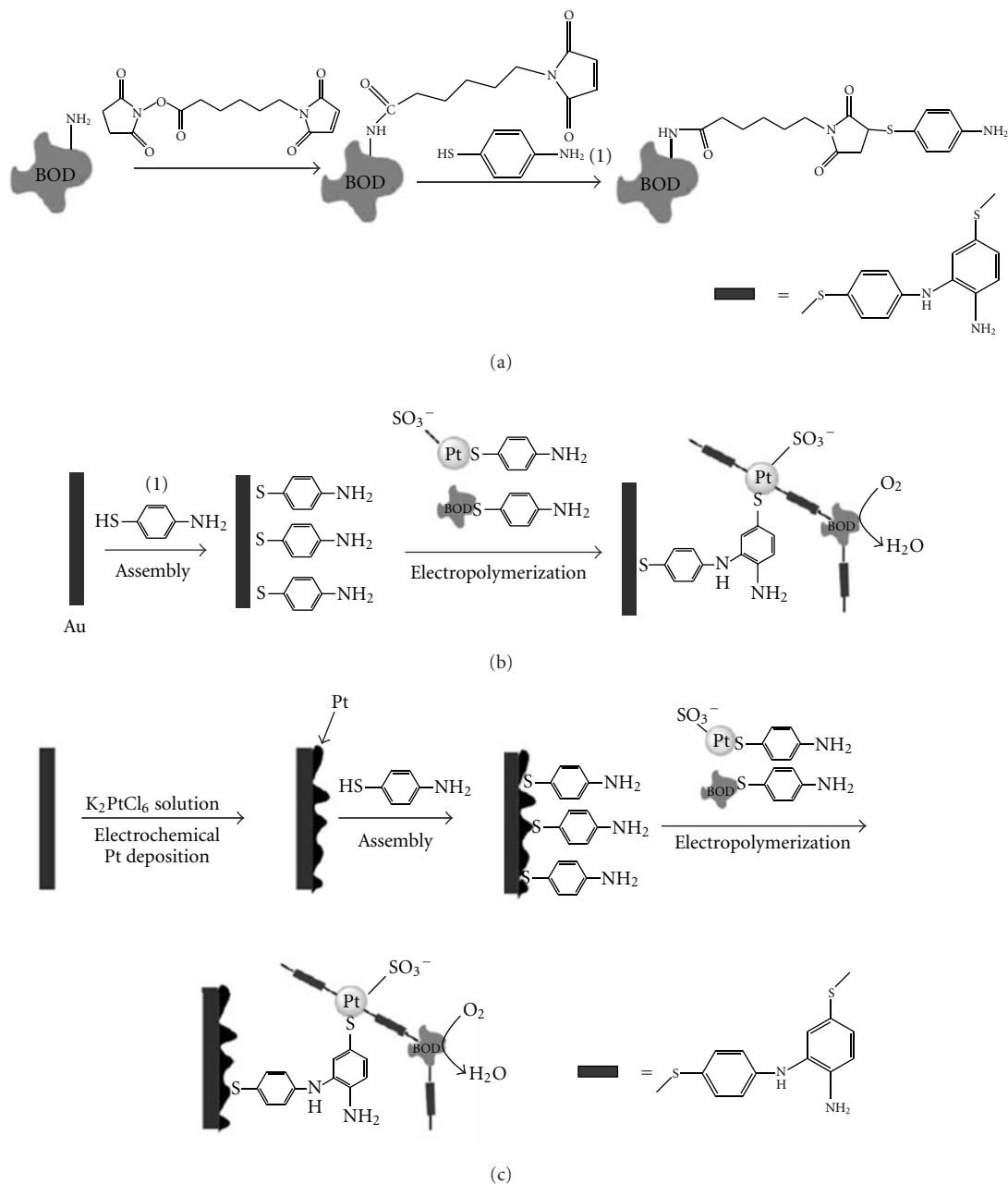


FIGURE 27: (a) Modification of bilirubin oxidase with polymerizable thioaniline functionality. (b) Synthesis of the 3D oligoaniline cross-linked Pt nanoparticles/bilirubin oxidase composite by electropolymerisation of the thioaniline-modified Pt nanoparticles and thioaniline modified bilirubin oxidase on the thioaniline monolayer functionalised Au electrode (from [35]).

materials. Interestingly the authors showed that the presence of Au nanoparticles decreases laccase activity.

Three-dimensional gold nanoparticulate electrodes can be also obtained by casting 15 nm Au nanoparticles suspension on polycrystalline Au electrode [106]. This procedure is followed by modification of the resulted film with 1-propanethiol and adsorption of bilirubin oxidase. On such electrode a catalytic current density 0.5 mA cm^{-2} (as measured by cyclic voltammetry at 0.01 V s^{-1}) is reported in quiescent O_2 -saturated solution at pH 7. The catalytic current is also

a function of the functional group of the adsorbed thiol (COOH , NH_2 , OH , and CH_3) with carboxylate group having superior effect. Activity of these electrodes is perhaps the largest observed for metallic support, and they exhibit also that remarkable stability and a further substantial increase of the current can be achieved with the application of carbon paper as support.

Mediatorless bioelectrocatalysis of dioxygen reduction was recently reported on Au nanoparticles immobilised in a film composed of partially sulfonated (3-mercaptopropyl)-

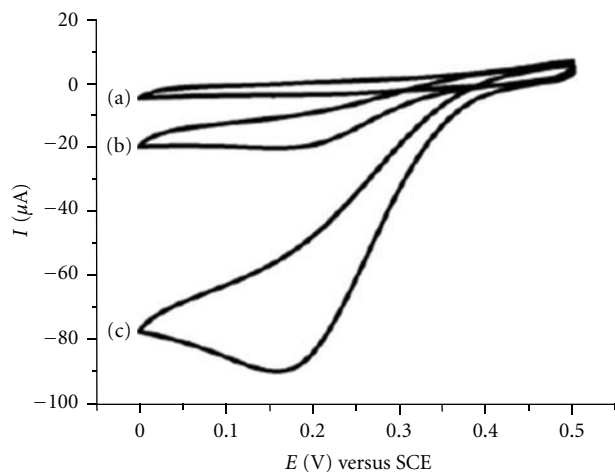


FIGURE 28: (a) Cyclic voltammograms of the Pt nanoparticles/bilirubin oxidase Pt-film-modified Au electrode under (a) Ar-, (b) air-, and (c) O_2 -saturated electrolyte. The electrode was prepared using 1:1 molar ratio of Pt nanoparticles and bilirubin oxidase mixture using 50 electropolymerisation cycles. Data recorded in 0.1 mol dm^{-3} phosphate buffer (pH 7.0) at scan rate 0.005 V s^{-1} (from [35]).

trimethoxysilane sol-gel-processed silicate, chitosan, and laccase [107]. This material immobilised on carbon felt provides extremely high current density up to 4 mA cm^{-2} . This biocathode was applied in biofuel cell powered by alcoholic beverages.

Sophisticated approach employing Pt nanoparticles (2 nm) for biocathode construction was recently reported by Willner group [35, 108]. It is based on the modification of bilirubin oxidase by a polymerizable thioaniline monomer (Figure 27). This procedure affects enzyme activity only to very small extent and allows for preparation of a bioelectrocatalytic polymeric film at thioaniline-modified Au or Pt black surfaces. This is done electrochemically in the presence of thioaniline-appended bilirubin oxidase and thioaniline-capped Pt nanoparticles.

Such modification allows to obtain catalytic current density in the range of $0.5\text{--}0.8 \text{ mA cm}^{-2}$. Most importantly this value is ca. 10 times higher than that obtained in electropolymerised film with encapsulated non functionalised enzyme (Figure 28).

According to the authors the enzyme functionalisation establishes better electrical contact between the Pt nanoparticles and partially unfolded enzyme or enables cooperative action of both species [35]. This paper shows one of the possible research paths to increase the efficiency of the bioelectrocatalytic process.

Recently nanoparticulate electrodes consisting of metal oxides were tested for dioxygen reduction bioelectrocatalysis with adsorbed bilirubin oxidase [109]. The modest catalytic effect was observed for nanocrystalline hematite ($\alpha\text{-Fe}_2\text{O}_3$) due to proline residue binding affinity. Generation of photocurrent is also possible in the presence of dioxygen under illumination conditions. This effect is not seen

with nanocrystalline TiO_2 or WO_3 [109]. O_2 reduction electrocatalysis with a current density above 0.1 mA cm^{-2} as measured by cyclic voltammetry at 0.001 V s^{-1} is also seen with a film electrode prepared from 10 nm diameter ITO nanoparticles [110]. Interestingly, 0.015 mA cm^{-2} current is seen on bare ITO without any surface modification. This is perhaps due to the inherent nanostructure of ITO film on glass which can be seen under scanning electron microscopy. Additionally ITO substrate is more favourable materials than $\alpha\text{-Fe}_2\text{O}_3$ from the point of view of overpotential decrease.

5. Conclusions

In the last few years we have observed a great research effort to develop nanoparticulate biocathodes. This is due to the significant development of nanotechnology and the requirements of elimination of mediators from biofuel cells and electrochemical biosensors. Many systems based on electrodes modified with nanoobjects and biocatalysts of dioxygen reduction exhibit direct electron transfer and therefore mediatorless bioelectrocatalysis.

One may argue that, although the electron shuttle molecule is eliminated, a new, larger element (nanoparticle, nanotube) is introduced to the system. However, in the latter case a different mechanism of electron transfer is operative, based on electronic conductivity and not on the redox processes of the mediator. The notable advantage of such mechanism is that it does not affect the stability of the nanoobjects to any significant degree. On the other hand, the possibility of aggregation of the nanoparticles and restructuring of the film has to be taken into account.

Many nanoparticulate film biocathodes exhibit mediatorless bioelectrocatalysis and current densities competitive with those achieved using osmium polymers. There are few examples of particularly high current densities (up to 4 mA cm^{-2} in quiescent conditions) [17, 20, 107]. This may be achieved by means of specific film structure [20] or specific geometry of the electrode, for example, using microwire [17] or carbon felt support [107]. The majority of nanoparticulate biocathodes exhibit current densities in the range of 0.05 to 0.5 mA cm^{-2} , and we believe that there is still room for improvement. The development of new electrode preparation procedures resulting in novel architectures represents important outcome of the research on biocathodes.

Unfortunately, in most cases a significant decrease of the current is seen during the first hour of biocathode operation. This is due to not only decrease of the copper oxidoreductase stability and/or their weak bonding to the electrodes but also restricted access of dioxygen to the active sites located in the film pores. This difficulty can be at least partially overcome by the preparation of films with larger pores [56]. Another approach is to design electrodes which provide direct access of gaseous dioxygen to the active sites of the biocathode. Therefore, very recently we could witness the development of "air breathing," gas-diffusion biocathodes [4, 45, 48, 49, 111].

Acknowledgments

M. Opallo acknowledges support by the European Union within European Regional Development Fund, through grant Innovative Economy (POIG.01.01.02-00-008/08). R. Bilewicz acknowledges support by the Polish Ministry of Sciences and Higher Education, grant no. 05-0017-10/2010 (PBR-11). The critical reading of the paper by dr. Martin Jonsson-Niedziolka is gratefully acknowledged.

References

- [1] L. dos Santos, V. Climent, C. F. Blanford, and F. A. Armstrong, "Mechanistic studies of the "blue" Cu enzyme, bilirubin oxidase, as a highly efficient electrocatalyst for the oxygen reduction reaction," *Physical Chemistry Chemical Physics*, vol. 12, no. 42, pp. 13962–13974, 2010.
- [2] S. Tsujimura, Y. Kamitaka, and K. Kano, "Diffusion-controlled oxygen reduction on multi-copper oxidase-adsorbed carbon aerogel electrodes without mediator," *Fuel Cells*, vol. 7, no. 6, pp. 463–469, 2007.
- [3] Y. Kamitaka, S. Tsujimura, N. Setoyama, T. Kajino, and K. Kano, "Fructose/dioxygen biofuel cell based on direct electron transfer-type bioelectrocatalysis," *Physical Chemistry Chemical Physics*, vol. 9, no. 15, pp. 1793–1801, 2007.
- [4] G. Gupta, C. Lau, B. Branch, V. Rajendran, D. Ivniński, and P. Atanassov, "Direct bio-electrocatalysis by multi-copper oxidases: gas-diffusion laccase-catalyzed cathodes for biofuel cells," *Electrochimica Acta*. In press.
- [5] W. Nogala, A. Celebanska, K. Szot, G. Wittstock, and M. Opallo, "Bioelectrocatalytic mediatorless dioxygen reduction at carbon ceramic electrodes modified with bilirubin oxidase," *Electrochimica Acta*, vol. 55, no. 20, pp. 5719–5724, 2010.
- [6] A. T. Yahiro, S. M. Lee, and D. O. Kimble, "Bioelectrochemistry. I. Enzyme utilizing bio-fuel cell studies," *Biochimica Biophysica Acta*, vol. 88, no. 2, pp. 375–383, 1964.
- [7] E. I. Solomon, U. M. Sundaram, and T. E. Machonkin, "Multicopper oxidases and oxygenases," *Chemical Reviews*, vol. 96, no. 7, pp. 2563–2605, 1996.
- [8] F. A. Armstrong, "The importance of enzymes: benchmarks for electrocatalysis," in *Fuel Cells. Theory, Fundamentals and Electrocatalysis*, A. Wieckowski, Ed., pp. 237–257, John Wiley & Sons, Hoboken, NJ, USA, 2010.
- [9] R. Bilewicz and M. Opallo, "Biocathodes for dioxygen reduction in biofuel cells," in *Fuel Cells. Theory, Fundamentals and Electrocatalysis*, A. Wieckowski, Ed., pp. 169–215, John Wiley & Sons, Hoboken, NJ, USA, 2010.
- [10] R. A. Bullen, T. C. Arnot, J. B. Lakeman, and F. C. Walsh, "Biofuel cells and their development," *Biosensors & Bioelectronics*, vol. 21, no. 11, pp. 2015–2045, 2006.
- [11] H. Shin, C. Kang, and A. Heller, "Irreversible and reversible deactivation of bilirubin oxidase by urate," *Electroanalysis*, vol. 19, no. 6, pp. 638–643, 2007.
- [12] A. Lesniewski, J. Niedziolka-Jonsson, C. Rizzi, L. Gaillon, J. Rogalski, and M. Opallo, "Carbon ceramic nanoparticulate film electrode prepared from oppositely charged particles by layer-by-layer approach," *Electrochemistry Communications*, vol. 12, no. 1, pp. 83–85, 2010.
- [13] K. Szot, J. D. Watkins, S. D. Bull, F. Marken, and M. Opallo, "Three dimensional film electrode prepared from oppositely charged carbon nanoparticles as efficient enzyme host," *Electrochemistry Communications*, vol. 12, no. 6, pp. 737–739, 2010.
- [14] E. Nazaruk, K. Sadowska, K. Madrak, J. F. Biernat, J. Rogalski, and R. Bilewicz, "Composite bioelectrodes based on lipidic cubic phase with carbon nanotube network," *Electroanalysis*, vol. 21, no. 3-5, pp. 507–511, 2009.
- [15] K. Sadowska, K. P. Roberts, R. Wiser, J. F. Biernat, E. Jablonowska, and R. Bilewicz, "Synthesis, characterization, and electrochemical testing of carbon nanotubes derivatized with azobenzene and anthraquinone," *Carbon*, vol. 47, no. 6, pp. 1501–1510, 2009.
- [16] A. Zloczewska, M. Jönsson-Niedziolka, J. Rogalski, and M. Opallo, "Vertically aligned carbon nanotube film electrodes for bioelectrocatalytic dioxygen reduction," *Electrochimica Acta*, vol. 56, no. 11, pp. 3947–3953, 2011.
- [17] X. Li, L. Zhang, L. Su, T. Ohsaka, and L. Mao, "A miniature glucose/O₂ biofuel cell with a high tolerance against ascorbic acid," *Fuel Cells*, vol. 9, no. 1, pp. 85–91, 2009.
- [18] S. Rubenwolf, O. Strohmeier, A. Kloke, S. Kerzenmacher, R. Zengerle, and F. von Stetten, "Carbon electrodes for direct electron transfer type laccase cathodes investigated by current density-cathode potential behavior," *Biosensors & Bioelectronics*, vol. 26, no. 2, pp. 841–845, 2010.
- [19] L. Deng, L. Shang, Y. Wang, T. Wang, H. Chen, and S. Dong, "Multilayer structured carbon nanotubes/poly-L-lysine/laccase composite cathode for glucose/O₂ biofuel cell," *Electrochemistry Communications*, vol. 10, no. 7, pp. 1012–1015, 2008.
- [20] T. Miyake, S. Yoshino, T. Yamada, K. Hata, and M. Nishizawa, "Self-regulating enzyme-nanotube ensemble films and their application as flexible electrodes for biofuel cells," *Journal of the American Chemical Society*, vol. 133, no. 13, pp. 5129–5134, 2011.
- [21] M. Jönsson-Niedziolka, A. Kaminska, and M. Opallo, "Pyrene-functionalised single-walled carbon nanotubes for mediatorless dioxygen bioelectrocatalysis," *Electrochimica Acta*, vol. 55, no. 28, pp. 8744–8750, 2010.
- [22] A. V. Lyashenko, I. Bento, V. N. Zaitsev et al., "X-ray structural studies of the fungal laccase from *Cerrena maxima*," *Journal of Biological Inorganic Chemistry*, vol. 11, no. 8, pp. 963–973, 2006.
- [23] K. Mizutani, M. Toyoda, K. Sagara et al., "X-ray analysis of bilirubin oxidase from *Myrothecium verrucaria* at 2.3 Å resolution using a twinned crystal," *Acta Crystallographica Section F*, vol. 66, no. 7, pp. 765–770, 2010.
- [24] C. F. Blanford, C. E. Foster, R. S. Heath, and F. A. Armstrong, "Efficient electrocatalytic oxygen reduction by the "blue" copper oxidase, laccase, directly attached to chemically modified carbons," *Faraday Discussions*, vol. 140, pp. 319–335, 2008.
- [25] C. F. Blanford, R. S. Heath, and F. A. Armstrong, "A stable electrode for high-potential, electrocatalytic O₂ reduction based on rational attachment of a blue copper oxidase to a graphite surface," *Chemical Communications*, no. 17, pp. 1710–1712, 2007.
- [26] M. Sosna, J. M. Chrétien, J. D. Kilburn, and P. N. Bartlett, "Monolayer anthracene and anthraquinone modified electrodes as platforms for *Trametes hirsuta* laccase immobilisation," *Physical Chemistry Chemical Physics*, vol. 12, no. 34, pp. 10018–10026, 2010.
- [27] O. Lazarus, T. W. Woolerton, A. Parkin et al., "Water-gas shift reaction catalyzed by redox enzymes on conducting graphite

- platelets," *Journal of the American Chemical Society*, vol. 131, no. 40, pp. 14154–14155, 2009.
- [28] K. A. Vincent, X. Li, C. F. Blanford, N. A. Belsey, J. H. Weiner, and F. A. Armstrong, "Enzymatic catalysis on conducting graphite particles," *Nature Chemical Biology*, vol. 3, no. 12, pp. 761–762, 2007.
- [29] Y. Xiao, F. Patolsky, E. Katz, J. F. Hainfeld, and I. Willner, "Plugging into enzymes: nanowiring of redox enzymes by a gold nanoparticle," *Science*, vol. 299, no. 5614, pp. 1877–1881, 2003.
- [30] R. Tel-Vered, H. B. Yildiz, Y. M. Yan, and I. Willner, "Plugging into enzymes with light: photonic "wiring" of enzymes with electrodes for photobiofuel cells," *Small*, vol. 6, no. 15, pp. 1593–1597, 2010.
- [31] K. Stolarczyk, M. Sepelowska, D. Lyp et al., "Hybrid biofuel cell based on arylated carbon nanotubes," submitted to *Bioelectrochemistry*.
- [32] K. Stolarczyk, K. Zelechowska, J. Rogalski, J. F. Biernat, and R. Bilewicz, "Arylated carbon nanotubes for biocatalytic reduction of dioxygen," submitted to *Electrochimica Acta*.
- [33] H. L. Pang, J. Liu, D. Hu, X. H. Zhang, and J. H. Chen, "Immobilization of laccase onto 1-aminopyrene functionalized carbon nanotubes and their electrocatalytic activity for oxygen reduction," *Electrochimica Acta*, vol. 55, no. 22, pp. 6611–6616, 2010.
- [34] K. Schubert, G. Goebel, and F. Lisdat, "Bilirubin oxidase bound to multi-walled carbon nanotube-modified gold," *Electrochimica Acta*, vol. 54, no. 11, pp. 3033–3038, 2009.
- [35] Y. M. Yan, I. Baravik, R. Tel-Vered, and I. Willner, "An ethanol/O₂ biofuel cell based on an electropolymerized bilirubin oxidase/Pt nanoparticle bioelectrocatalytic O₂-reduction cathode," *Advanced Materials*, vol. 21, no. 42, pp. 4275–4279, 2009.
- [36] M. R. Tarasevich, A. I. Yaropolov, V. A. Bogdanovskaya, and S. D. Varfolomev, "Ways of using enzymes for acceleration of electrochemical reactions," *Bioelectrochemistry Bioenergetics*, vol. 6, no. 4, pp. 587–597, 1979.
- [37] I. V. Berezin, V. A. Bogdanovskaya, S. D. Varfolomeev, M. R. Tarasevich, and A. I. Yaropolov, "Bioelectrocatalysis. The oxygen reduction potential in the presence of laccase," *Doklady Akademii Nauk SSSR*, vol. 240, no. 3, pp. 615–618, 1978.
- [38] N. Mano, H. H. Kim, and A. Heller, "On the relationship between the characteristics of bilirubin oxidases and O₂ cathodes based on their "wiring"," *Journal of Physical Chemistry B*, vol. 106, no. 34, pp. 8842–8848, 2002.
- [39] S. C. Barton, H. H. Kim, G. Binyamin, Y. Zhang, and A. Heller, "Electroreduction of O₂ to water on the "wired" laccase cathode," *Journal of Physical Chemistry B*, vol. 105, no. 47, pp. 11917–11921, 2001.
- [40] S. C. Barton, H. H. Kim, G. Binyamin, Y. Zhang, and A. Heller, "The "wired" laccase cathode: high current density electroreduction of O₂ to water at +0.7 V (NHE) at pH 5," *Journal of the American Chemical Society*, vol. 123, no. 24, pp. 5802–5803, 2001.
- [41] S. Tsujimura, K. Kano, and T. Ikeda, "Glucose/O₂ biofuel cell operating at physiological conditions," *Electrochemistry*, vol. 70, no. 12, pp. 940–942, 2002.
- [42] F. Gao, Y. Yan, L. Su, L. Wang, and L. Mao, "An enzymatic glucose/O₂ biofuel cell: preparation, characterization and performance in serum," *Electrochemistry Communications*, vol. 9, no. 5, pp. 989–996, 2007.
- [43] M. C. Weigel, E. Tritscher, and F. Lisdat, "Direct electrochemical conversion of bilirubin oxidase at carbon nanotube-modified glassy carbon electrodes," *Electrochemistry Communications*, vol. 9, no. 4, pp. 689–693, 2007.
- [44] W. Zheng, Q. Li, L. Su, Y. Yan, J. Zhang, and L. Mao, "Direct electrochemistry of multi-copper oxidases at carbon nanotubes noncovalently functionalized with cellulose derivatives," *Electroanalysis*, vol. 18, no. 6, pp. 587–594, 2006.
- [45] R. Kontani, S. Tsujimura, and K. Kano, "Air diffusion biocathode with CueO as electrocatalyst adsorbed on carbon particle-modified electrodes," *Bioelectrochemistry*, vol. 76, no. 1-2, pp. 10–13, 2009.
- [46] S. Tsujimura, Y. Miura, and K. Kano, "CueO-immobilized porous carbon electrode exhibiting improved performance of electrochemical reduction of dioxygen to water," *Electrochimica Acta*, vol. 53, no. 18, pp. 5716–5720, 2008.
- [47] A. Habrioux, T. Napporn, K. Servat, S. Tingry, and K. B. Kokoh, "Electrochemical characterization of adsorbed bilirubin oxidase on Vulcan XC 72R for the biocathode preparation in a glucose/O₂ biofuel cell," *Electrochimica Acta*, vol. 55, no. 26, pp. 7701–7705, 2010.
- [48] G. Gupta, C. Lau, V. Rajendran et al., "Direct electron transfer catalyzed by bilirubin oxidase for air breathing gas-diffusion electrodes," *Electrochemistry Communications*, vol. 13, no. 3, pp. 247–249, 2011.
- [49] S. Shleev, G. Shumakovich, O. Morozova, and A. Yaropolov, "Stable "floating" air diffusion biocathode based on direct electron transfer reactions between carbon particles and high redox potential laccase," *Fuel Cells*, vol. 10, no. 4, pp. 726–733, 2010.
- [50] K. Szot, W. Nogala, J. Niedziolka-Jönsson et al., "Hydrophilic carbon nanoparticle-laccase thin film electrode for mediatorless dioxygen reduction. SECM activity mapping and application in zinc-dioxygen battery," *Electrochimica Acta*, vol. 54, no. 20, pp. 4620–4625, 2009.
- [51] J. Niedziolka-Jönsson, M. Jönsson-Niedziolka, W. Nogala, and B. Palys, "Electrosynthesis of thin sol-gel films at a three-phase junction," *Electrochimica Acta*, vol. 56, no. 9, pp. 3311–3316, 2011.
- [52] K. Szot, R. P. Lynch, A. Lesniewski et al., "The effect of linker of electrodes prepared from sol-gel ionic liquid precursor and carbon nanoparticles on dioxygen electroreduction bioelectrocatalysis," *Electrochimica Acta*. In press.
- [53] A. Lesniewski, M. Paszewski, and M. Opallo, "Gold-carbon three dimensional film electrode prepared from oppositely charged conductive nanoparticles by layer-by-layer approach," *Electrochemistry Communications*, vol. 12, no. 3, pp. 435–437, 2010.
- [54] K. Szot, J. Niedziolka, J. Rogalski, F. Marken, and M. Opallo, "Bioelectrocatalytic dioxygen reduction at hybrid silicate-polyallylamine film with encapsulated laccase," *Journal of Electroanalytical Chemistry*, vol. 612, no. 1, pp. 1–8, 2008.
- [55] M. Zhou, L. Deng, D. Wen, L. Shang, L. Jin, and S. Dong, "Highly ordered mesoporous carbons-based glucose/O₂ biofuel cell," *Biosensors & Bioelectronics*, vol. 24, no. 9, pp. 2904–2908, 2009.
- [56] V. Flexer, N. Brun, O. Courjean, R. Backov, and N. Mano, "Porous mediator-free enzyme carbonaceous electrodes obtained through integrative chemistry for biofuel cells," *Energy & Environmental Science*, vol. 4, no. 6, pp. 2097–2106, 2011.
- [57] P. F. Harris, *Carbon Nanotube Science*, Cambridge Publishers, 2009.

- [58] C. Ménard-Moyon, K. Kostarelos, M. Prato, and A. Bianco, "Functionalized carbon nanotubes for probing and modulating molecular functions," *Chemistry and Biology*, vol. 17, no. 2, pp. 107–115, 2010.
- [59] M. H. Osman, A. A. Shah, and F. C. Walsh, "Recent progress and continuing challenges in bio-fuel cells. Part I: enzymatic cells," *Biosensors & Bioelectronics*, vol. 26, no. 7, pp. 3087–3102, 2011.
- [60] W. Yang, K. R. Ratinac, S. R. Ringer, P. Thordarson, J. J. Gooding, and F. Braet, "Carbon nanomaterials in biosensors: should you use nanotubes or graphene," *Angewandte Chemie International Edition*, vol. 49, no. 12, pp. 2114–2138, 2010.
- [61] P. J. Britto, K. S. V. Santhanam, A. Rubio, J. A. Alonso, and P. M. Ajayan, "Improved charge transfer at carbon nanotube electrodes," *Advanced Materials*, vol. 11, no. 2, pp. 154–157, 1999.
- [62] A. Hirsch, "Functionalization of single-walled carbon nanotubes," *Angewandte Chemie International Edition*, vol. 41, no. 11, pp. 1853–1859, 2002.
- [63] C. A. Mitchell, J. L. Bahr, S. Arepalli, J. M. Tour, and R. Krishnamoorti, "Dispersion of functionalized carbon nanotubes in polystyrene," *Macromolecules*, vol. 35, no. 23, pp. 8825–8830, 2002.
- [64] S. Banerjee, T. Hemraj-Benny, and S. S. Wong, "Covalent surface chemistry of single-walled carbon nanotubes," *Advanced Materials*, vol. 17, no. 1, pp. 17–29, 2005.
- [65] K. Karnicka, K. Miecznikowski, B. Kowalewska et al., "ABTS-modified multiwalled carbon nanotubes as an effective mediating system for bioelectrocatalytic reduction of oxygen," *Analytical Chemistry*, vol. 80, no. 19, pp. 7643–7648, 2008.
- [66] M. Shim, N. W. S. Kam, R. J. Chen, Y. Li, and H. Dai, "Functionalization of carbon nanotubes for biocompatibility and biomolecular recognition," *Nano Letters*, vol. 2, no. 4, pp. 285–288, 2002.
- [67] R. J. Chen, S. Bangsaruntip, K. A. Drouvalakis et al., "Non-covalent functionalization of carbon nanotubes for highly specific electronic biosensors," *Proceedings of the National Academy of Sciences of the United States of America*, vol. 100, no. 9, pp. 4984–4989, 2003.
- [68] M. Jönsson, K. Szot, J. Niedziolka et al., "Adsorption of 2,2'-azino-bis(3-ethylbenzothiazoline6-sulfonate) on multi-walled carbon nanotubessilicate film: application to bioelectrocatalytic dioxygen reduction," *Journal of Nanoscience and Nanotechnology*, vol. 9, no. 4, pp. 2346–2352, 2009.
- [69] M. Jönsson-Niedziolka, K. Szot, J. Rogalski, and M. Opallo, "Pyrene sulfonate functionalised single-walled carbon nanotubes for mediatorless dioxygen bioelectrocatalysis," *Electrochemistry Communications*, vol. 11, no. 5, pp. 1042–1044, 2009.
- [70] C. Liu, Z. Chen, and C.-Z. Li, "Surface engineering of graphene-enzyme nanocomposites for miniaturized biofuel cell," *IEEE Transactions on Nanotechnology*, vol. 10, no. 1, pp. 59–62, 2011.
- [71] E. Nazaruk, S. Smoliński, M. Swatko-Ossor et al., "Enzymatic biofuel cell based on electrodes modified with lipid liquid-crystalline cubic phases," *Journal of Power Sources*, vol. 183, no. 2, pp. 533–538, 2008.
- [72] K. Sadowska, E. Jabłonowska, K. Stolarczyk et al., "Chemically modified carbon nanotubes: synthesis and implementation," *Polish Journal of Chemistry*, vol. 82, no. 6, pp. 1309–1313, 2008.
- [73] H. Y. Zhao, H. M. Zhou, J. X. Zhang, W. Zheng, and Y. F. Zheng, "Carbon nanotube-hydroxyapatite nanocomposite: a novel platform for glucose/O₂ biofuel cell," *Biosensors & Bioelectronics*, vol. 25, no. 2, pp. 463–468, 2009.
- [74] Y. Liu, M. Wang, F. Zhao, B. Liu, and S. Dong, "A low-cost biofuel cell with pH-dependent power output based on porous carbon as matrix," *Chemistry: A European Journal*, vol. 11, no. 17, pp. 4970–4974, 2005.
- [75] Y. Liu, L. Huang, and S. Dong, "Electrochemical catalysis and thermal stability characterization of laccase-carbon nanotubes-ionic liquid nanocomposite modified graphite electrode," *Biosensors & Bioelectronics*, vol. 23, no. 1, pp. 35–41, 2007.
- [76] J. Lim, P. Malati, F. Bonet, and B. Dunn, "Nanostructured sol-gel electrodes for biofuel cells," *Journal of the Electrochemical Society*, vol. 154, no. 2, pp. A140–A145, 2007.
- [77] Y. Liu and S. Dong, "A biofuel cell with enhanced power output by grape juice," *Electrochemistry Communications*, vol. 9, no. 7, pp. 1423–1427, 2007.
- [78] R. Bilewicz, K. Stolarczyk, K. Sadowska, J. Rogalski, and J. F. Biernat, "Carbon nanotubes derivatized with mediators for laccase catalyzed oxygen reduction," *ECS Transactions*, vol. 19, no. 6, pp. 27–36, 2009.
- [79] E. Nazaruk, K. Sadowska, J. F. Biernat, J. Rogalski, G. Ginalska, and R. Bilewicz, "Enzymatic electrodes nanostructured with functionalized carbon nanotubes for biofuel cell applications," *Analytical and Bioanalytical Chemistry*, vol. 398, no. 4, pp. 1651–1660, 2010.
- [80] K. Sadowska, K. Stolarczyk, J. F. Biernat, K. P. Roberts, J. Rogalski, and R. Bilewicz, "Derivatization of single-walled carbon nanotubes with redox mediator for biocatalytic oxygen electrodes," *Bioelectrochemistry*, vol. 80, no. 1, pp. 73–80, 2010.
- [81] C. E. Banks, A. Crossley, C. Salter, S. J. Wilkins, and R. G. Compton, "Carbon nanotubes contain metal impurities which are responsible for the "electrocatalysis" seen at some nanotube-modified electrodes," *Angewandte Chemie International Edition*, vol. 45, no. 16, pp. 2533–2537, 2006.
- [82] M. S. Dresselhaus, G. Dresselhaus, and A. Jorio, "Raman spectroscopy of carbon nanotubes in 1997 and 2007," *Journal of Physical Chemistry C*, vol. 111, no. 48, pp. 17887–17893, 2007.
- [83] M. S. Dresselhaus, G. Dresselhaus, R. Saito, and A. Jorio, "Raman spectroscopy of carbon nanotubes," *Physics Reports*, vol. 409, no. 2, pp. 47–99, 2005.
- [84] Y. Zhang, S. Yuan, W. Zhou, J. Xu, and Y. Li, "Spectroscopic evidence and molecular simulation investigation of the π - π interaction between pyrene molecules and carbon nanotubes," *Journal of Nanoscience and Nanotechnology*, vol. 7, no. 7, pp. 2366–2375, 2007.
- [85] J. Liu, A. Chou, W. Rahmat, M. N. Paddon-Row, and J. J. Gooding, "Achieving direct electrical connection to glucose oxidase using aligned single walled carbon nanotube arrays," *Electroanalysis*, vol. 17, no. 1, pp. 38–46, 2005.
- [86] L. Hussein, G. Urban, and M. Krüger, "Fabrication and characterization of buckypaper-based nanostructured electrodes as a novel material for biofuel cell applications," *Physical Chemistry Chemical Physics*, vol. 13, no. 13, pp. 5831–5839, 2011.
- [87] M. Smolander, H. Boer, M. Valkiainen et al., "Development of a printable laccase-based biocathode for fuel cell applications," *Enzyme and Microbial Technology*, vol. 43, no. 2, pp. 93–102, 2008.
- [88] S. N. Ding, M. Holzinger, C. Mousty, and S. Cosnier, "Laccase electrodes based on the combination of single-walled carbon

- nanotubes and redox layered double hydroxides: towards the development of biocathode for biofuel cells," *Journal of Power Sources*, vol. 195, no. 15, pp. 4714–4717, 2010.
- [89] J. Lim, N. Cirigliano, J. Wang, and B. Dunn, "Direct electron transfer in nanostructured sol-gel electrodes containing bilirubin oxidase," *Physical Chemistry Chemical Physics*, vol. 9, no. 15, pp. 1809–1814, 2007.
- [90] K. Stolarczyk, E. Nazaruk, J. Rogalski, and R. Bilewicz, "Nanostructured carbon electrodes for laccase-catalyzed oxygen reduction without added mediators," *Electrochimica Acta*, vol. 53, no. 11, pp. 3983–3990, 2008.
- [91] Y. Yan, W. Zheng, L. Su, and L. Mao, "Carbon-nanotube-based glucose/O₂ biofuel cells," *Advanced Materials*, vol. 18, no. 19, pp. 2639–2643, 2006.
- [92] X. Li, H. Zhou, P. Yu, L. Su, T. Ohsaka, and L. Mao, "A Miniature glucose/O₂ biofuel cell with single-walled carbon nanotubes-modified carbon fiber microelectrodes as the substrate," *Electrochemistry Communications*, vol. 10, no. 6, pp. 851–854, 2008.
- [93] F. Gao, L. Viry, M. Maugey, P. Poulin, and N. Mano, "Engineering hybrid nanotube wires for high-power biofuel cells," *Nature Communications*, vol. 1, no. 1, article 2, 2010.
- [94] L. Deng, C. Chen, M. Zhou, S. Guo, E. Wang, and S. Dong, "Integrated self-powered microchip biosensor for endogenous biological cyanide," *Analytical Chemistry*, vol. 82, no. 10, pp. 4283–4287, 2010.
- [95] M. Tominaga, M. Ohtani, and I. Taniguchi, "Gold single-crystal electrode surface modified with self-assembled monolayers for electron tunneling with bilirubin oxidase," *Physical Chemistry Chemical Physics*, vol. 10, no. 46, pp. 6928–6934, 2008.
- [96] J. Y. Lee, H. Y. Shin, S. W. Kang, C. Park, and S. W. Kim, "Application of an enzyme-based biofuel cell containing a bioelectrode modified with deoxyribonucleic acid-wrapped single-walled carbon nanotubes to serum," *Enzyme and Microbial Technology*, vol. 48, no. 1, pp. 80–84, 2011.
- [97] J. Y. Lee, H. Y. Shin, S. W. Kang, C. Park, and S. W. Kim, "Use of bioelectrode containing DNA-wrapped single-walled carbon nanotubes for enzyme-based biofuel cell," *Journal of Power Sources*, vol. 195, no. 3, pp. 750–755, 2010.
- [98] J. Kim, H. Jia, and P. Wang, "Challenges in biocatalysis for enzyme-based biofuel cells," *Biotechnology Advances*, vol. 24, no. 3, pp. 296–308, 2006.
- [99] R. P. Ramasamy, H. R. Luckarift, D. M. Ivnitski, P. B. Atanassov, and G. R. Johnson, "High electrocatalytic activity of tethered multicopper oxidase-carbon nanotube conjugates," *Chemical Communications*, vol. 46, no. 33, pp. 6045–6047, 2010.
- [100] C. Tanne, G. Göbel, and F. Lisdat, "Development of a (PQQ)-GDH-anode based on MWCNT-modified gold and its application in a glucose/O₂-biofuel cell," *Biosensors & Bioelectronics*, vol. 26, no. 2, pp. 530–535, 2010.
- [101] G. Göbel, T. Dietz, and F. Lisdat, "Bienenzyme sensor based on an oxygen reducing bilirubin oxidase electrode," *Electroanalysis*, vol. 22, no. 14, pp. 1581–1585, 2010.
- [102] C. Liu, S. Alwarappan, Z. Chen, X. Kong, and C. Z. Li, "Membraneless enzymatic biofuel cells based on graphene nanosheets," *Biosensors & bioelectronics*, vol. 25, no. 7, pp. 1829–1833, 2010.
- [103] X. Wu, Y. Hu, J. Jin et al., "Electrochemical approach for detection of extracellular oxygen released from erythrocytes based on graphene film integrated with laccase and 2,2-azino-bis(3-ethylbenzothiazoline-6-sulfonic acid)," *Analytical Chemistry*, vol. 82, no. 9, pp. 3588–3596, 2010.
- [104] W. Zheng, H. Y. Zhao, J. X. Zhang et al., "A glucose/O₂ biofuel cell base on nanographene platelet-modified electrodes," *Electrochemistry Communications*, vol. 12, no. 7, pp. 869–871, 2010.
- [105] S. Shleev, J. Tkac, A. Christenson et al., "Direct electron transfer between copper-containing proteins and electrodes," *Biosensors & Bioelectronics*, vol. 20, no. 12, pp. 2517–2554, 2005.
- [106] K. Murata, K. Kajiya, N. Nakamura, and H. Ohno, "Direct electrochemistry of bilirubin oxidase on three-dimensional gold nanoparticle electrodes and its application in a biofuel cell," *Energy & Environmental Science*, vol. 2, no. 12, pp. 1280–1285, 2009.
- [107] L. Deng, L. Shang, D. Wen, J. Zhai, and S. Dong, "A membraneless biofuel cell powered by ethanol and alcoholic beverage," *Biosensors & Bioelectronics*, vol. 26, no. 1, pp. 70–73, 2010.
- [108] R. Tel-Vered and I. Willner, "Bis-aniline-crosslinked enzyme-metal nanoparticle composites on electrodes for bioelectronic applications," *Israel Journal of Chemistry*, vol. 50, no. 3, pp. 321–332, 2010.
- [109] R. Nakamura, K. Kamiya, and K. Hashimoto, "Direct electron-transfer conduits constructed at the interface between multicopper oxidase and nanocrystalline semiconductive Fe oxides," *Chemical Physics Letters*, vol. 498, no. 4-6, pp. 307–311, 2010.
- [110] E. Rozniecka, M. Jonsson-Niedziolka, J. W. Sobczak, and M. Opallo, "Mediatorless bioelectrocatalysis of dioxygen reduction at ITO and ITO nanoparticulate film electrodes," *Electrochimica Acta*, vol. 56, no. 24, pp. 8739–8745, 2011.
- [111] W. Nogala, A. Celebanska, G. Wittstock, and M. Opallo, "Bioelectrocatalytic carbon ceramic gas electrode for reduction of dioxygen and its application in a zinc-dioxygen cell," *Fuel Cells*, vol. 10, no. 6, pp. 1157–1163, 2010.

Research Article

FeCr₂O₄ Nanoparticles as Anode Catalyst for Ethane Proton Conducting Fuel Cell Reactors to Coproduce Ethylene and Electricity

Jian-Hui Li, Xian-Zhu Fu, Gui-Hua Zhou, Jing-Li Luo, Karl T. Chuang, and Alan R. Sanger

Department of Chemical and Materials Engineering, University of Alberta, Edmonton, AB, Canada T6G 2G6

Correspondence should be addressed to Jing-Li Luo, jingli.luo@ualberta.ca

Received 15 May 2011; Accepted 22 July 2011

Academic Editor: Milan M. Jaksic

Copyright © 2011 Jian-Hui Li et al. This is an open access article distributed under the Creative Commons Attribution License, which permits unrestricted use, distribution, and reproduction in any medium, provided the original work is properly cited.

Ethylene and electrical power are cogenerated in fuel cell reactors with FeCr₂O₄ nanoparticles as anode catalyst, La_{0.7}Sr_{0.3}FeO_{3-δ} (LSF) as cathode material, and BaCe_{0.7}Zr_{0.1}Y_{0.2}O_{3-δ} (BCZY) perovskite oxide as proton-conducting ceramic electrolyte. FeCr₂O₄, BCZY and LSF are synthesized by a sol-gel combustion method. The power density increases from 70 to 240 mW cm⁻², and the ethylene yield increases from about 14.1% to 39.7% when the operating temperature of the proton-conducting fuel cell reactor increases from 650°C to 750°C. The FeCr₂O₄ anode catalyst exhibits better catalytic performance than nanosized Cr₂O₃ anode catalyst.

1. Introduction

Solid oxide fuel cells (SOFC) are promising as clean power sources having high energy conversion efficiency and excellent fuel flexibility. Typically, SOFC are based on an oxygen-ion-conducting electrolyte, which usually requires high operating temperature. In the last few years, an ever-growing interest has been directed toward proton-conducting electrolytes for intermediate or low-temperature SOFC applications [1]. Among these, the most investigated proton-conducting electrolytes are doped perovskite oxides (ABO₃), in which the A sites are occupied by alkaline earth elements such as Ba, Sr, and Ca, and B sites are occupied by tetravalent elements (usually Ce or Zr), and these perovskites are doped with trivalent ions such as Y, Nd, Sm, Yb, and In to increase the density of oxide ion vacancies required for ion conductivity. Among these electrolytes Y-doped barium cerate (BCY) stands out for its high proton conductivity but it has insufficiently high chemical stability as, for example, it reacts readily with CO₂ or SO₂. On the other hand, Y-doped barium zirconate (BZY) shows good chemical stability but suffers from insufficient proton conductivity. When codoped with Y and Zr, barium cerate (BCZY) has balanced

conductivity and chemical stability in reactive environments [2, 3].

Ethylene is an important feedstock in the petrochemical industry, and its demand is expected to increase significantly in the near future [4, 5]. Currently, ethylene is produced mainly by steam cracking of naphtha or ethane, FCC (fluid catalytic cracking), and catalytic dehydrogenation of ethane. However, when steam cracking is operated at high temperature the process consumes much energy and has a low selectivity to ethylene and unavoidable coke formation. Recently, ethane-fueled proton-conducting ceramic fuel cell reactors have been developed to cogenerate ethylene and electrical energy with high efficiency [6–11]. This reaction system has several specific advantages including high selectivity to ethylene and low impact on the environment, as there are very little or no greenhouse gas (CO₂) emissions. In a proton-conducting fuel cell reactor, the dehydrogenation of ethane to ethylene and hydrogen (forming protons) is conducted over the anode catalyst, while the protons are conducted through the proton conducting electrolyte to the cathode side and reacted with oxygen to form water. Electrons are conducted through an external circuit during this reaction.

Catalysts are needed to achieve more efficient power production and utilization of ethane resources and higher activity and selectivity to ethylene of reaction at the anode. Recently, nanosized Cr_2O_3 particles prepared by a sol-gel combustion method were proven to be effective and stable anode catalysts for the process [6]. Such metal oxides, especially in the form of solid solutions, are interesting solids due to their surface acid-base properties and oxidation-reduction potentials. Chromium iron oxide catalysts, in particular, have been explored for the last two decades for their superior catalytic activity in processes such as the water-gas-shift (WGS) reaction [12, 13], conversion of methanol [14], Fischer Tropsch synthesis [15], when compared with the corresponding Fe- or Cr-alone catalysts. Now precipitated Fe,Cr-containing oxide catalysts are used commercially for the high-temperature WGS reaction.

In previous studies Pt often was used as both anode and cathode catalysts. However, Pt is expensive and easily poisoned by carbon deposition at fuel cell operating temperature. Herein, we report the fabricating and testing of electrolyte-supported fuel cells using chromium iron oxide nanoparticles (FeCr_2O_4) as anode catalyst, $\text{La}_{0.7}\text{Sr}_{0.3}\text{FeO}_{3-\delta}$ as cathode material, and $\text{BaCe}_{0.7}\text{Zr}_{0.1}\text{Y}_{0.2}\text{O}_{3-\delta}$ as electrolyte for coproduction of ethylene and electrical power. The catalytic performance, electrical performance, and resistance of the fuel cell also are described.

2. Experimental

2.1. Materials Preparation and Characterization. FeCr_2O_4 nanopowders were prepared using a sol-gel method [16, 17]. $\text{Cr}(\text{NO}_3)_3 \cdot 6\text{H}_2\text{O}$, and $\text{Fe}(\text{NO}_3)_3 \cdot 6\text{H}_2\text{O}$ were first dissolved in deionized water. Subsequently, citric acid as chelating agent was added in 2 : 1 molar ratio to metal ions. The resulting solution was adjusted to about pH 8 with ammonium hydroxide, then heated on a hot plate to evaporate water at 90°C until it formed a gel which then was dried. The dry gel was calcined at 500°C for 4 h.

$\text{BaCe}_{0.7}\text{Zr}_{0.1}\text{Y}_{0.2}\text{O}_{3-\delta}$ (BCZY) perovskite nanopowders were prepared using a citric acid-nitrate combustion method. $\text{Ba}(\text{NO}_3)_2$, $\text{Ce}(\text{NO}_3)_3 \cdot 6\text{H}_2\text{O}$, $\text{ZrO}(\text{NO}_3)_2 \cdot 2.6\text{H}_2\text{O}$, and $\text{Y}(\text{NO}_3)_3 \cdot 6\text{H}_2\text{O}$ were first dissolved in deionized water. Subsequently, citric acid as chelating agent and NH_4NO_3 as oxidant agent were added in molar ratio of citric acid: total metal ions: NH_4NO_3 of 1.5 : 1 : 3. The resulting solution was adjusted to about pH 8 with ammonium hydroxide and heated on a hot plate to evaporate water until it changed into brown foam and then ignited. After combustion, the obtained ash was calcined at 1000°C in air for 6 h to obtain BCZY powders.

The $\text{La}_{0.7}\text{Sr}_{0.3}\text{FeO}_{3-\delta}$ (LSF) perovskite nanopowders were synthesized using the same method used for BCZY, described above. $\text{La}(\text{NO}_3)_3 \cdot 6\text{H}_2\text{O}$, $\text{Sr}(\text{NO}_3)_2 \cdot 6\text{H}_2\text{O}$, and $\text{Fe}(\text{NO}_3)_3 \cdot 9\text{H}_2\text{O}$ were the reactants. The obtained ash was calcined at 800°C in air for 5 h to obtain LSF powders.

The phase structures of materials were identified using a Rigaku Rotaflex X-ray diffractometer (XRD) with $\text{Co K}\alpha$ radiation. The morphology of sintered BCZY disc cross

sections was determined using a Hitachi S-2700 scanning electron microscope (SEM).

2.2. Fuel Cell Reactor Fabrication. Dense BCZY electrolyte pellets were fabricated via a pressing method. The nanosized powder was first pressed at 5 tonnes in a stainless-steel die with 1.86 cm ID to form a substrate disc, which was sintered at 1500°C for 10 h to obtain a nonporous, dense BCZY thick film. An intimate mixture comprising similar weights of FeCr_2O_4 , Cu powder, and BCZY was dispersed in terpineol mixed with 10% polyethylene glycol (PEG) as screen printing binder to form a paste. This paste was screen painted onto one side of the electrolyte and dried under infrared light to form the anode. A mixture of 50% LSF and 50% BCZY was pasted onto the opposite side to form the cathode. The cell then was heated at 950°C for 4 h in air to achieve strong bonding between the electrolyte and electrode materials.

2.3. Fuel Cell Reactor System Fabrication and Test. The fuel cell reactor setup and the testing system were as described previously [6]. The fuel cell reactor was set up by securing the MEA (membrane electrode assembly) between coaxial pairs of alumina tubes and sealed using ceramic sealant, which was cured by heating in a vertical Thermolyne F79300 tubular furnace. Au paste and mesh were used to make the current collector at both electrodes. 10% H_2 (balance with He) was fed into the anode chamber as the temperature was increased from room temperature to 750°C at $1^\circ\text{C}/\text{min}$. Then, ethane was fed into the anode chamber to replace the 10% H_2 feed. The cathode feed was oxygen.

The electrochemical performance of fuel cell reactors was measured using a Solartron 1287 electrochemical interface together with 1255B frequency response analysis instrumentation. The outlet gases from the anode chamber were analyzed using a Hewlett-Packard model HP5890 GC equipped with a packed bed column (OD: 1/8"; length: 2 m; packing: Poropak QS) operated at 80°C and equipped with a thermal conductivity detector. The ethane conversion and ethylene selectivity were calculated according to the previously reported method [9].

3. Results and Discussion

3.1. Textural and Structural Properties. The phases of the electrode and electrolyte materials were determined using X-ray diffraction (XRD). Figure 1(a) shows the XRD patterns of the $\text{La}_{0.7}\text{Sr}_{0.3}\text{FeO}_{3-\delta}$ cathode and the $\text{BaCe}_{0.7}\text{Zr}_{0.1}\text{Y}_{0.2}\text{O}_{3-\delta}$ electrolyte after firing. It can be seen that all samples were a single perovskite phase, without detectable amounts of any impurities. Figure 1(b) compares the XRD spectra of fresh and reduced Fe,Cr-based anode catalyst. XRD confirmed that pure FeCr_2O_4 phase (JCPDS Card No. 34-0140) was formed after calcination of the Fe,Cr-citrate complex gel at 500°C for 4 h in air. When this material was reduced in H_2 at 750°C for 4 h, some iron ions were reduced to metallic iron nanoparticles. However, the remaining ions remained present as the FeCr_2O_4 phase.

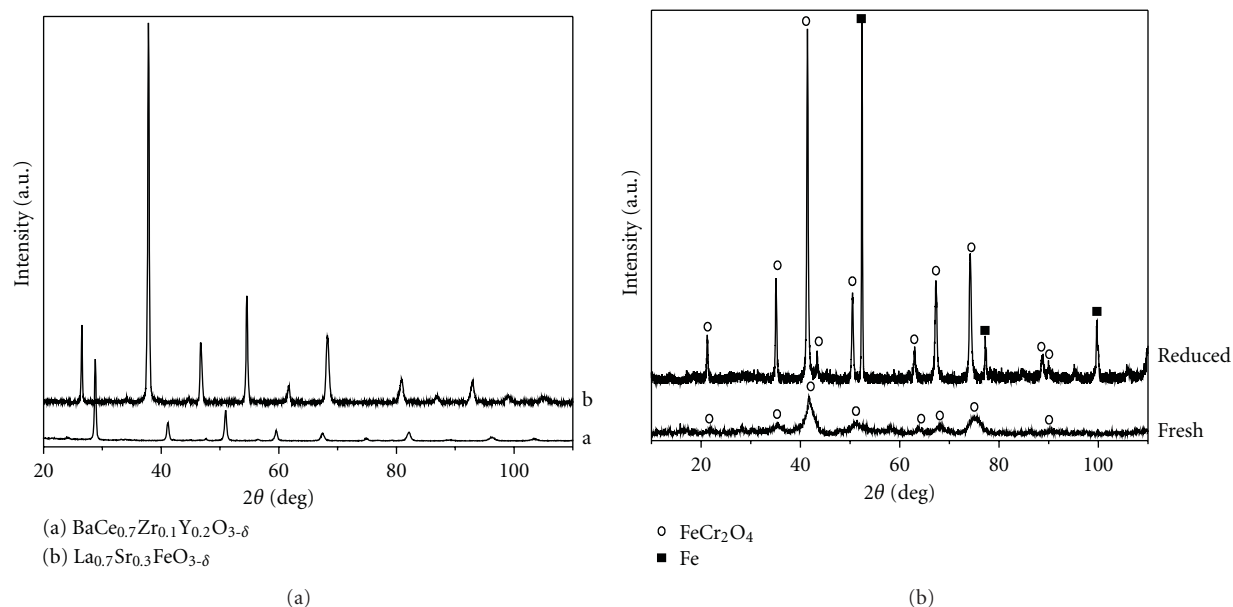


FIGURE 1: XRD patterns for: (a) $\text{La}_{0.7}\text{Sr}_{0.3}\text{FeO}_{3-\delta}$ and $\text{BaCe}_{0.7}\text{Zr}_{0.1}\text{Y}_{0.2}\text{O}_{3-\delta}$, and (b) FeCr_2O_4 catalysts before and after being reduced by H_2 .

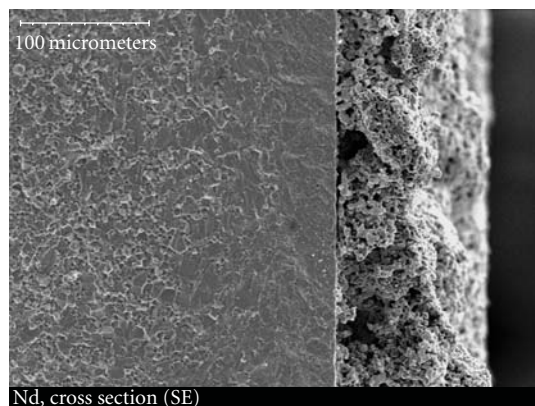


FIGURE 2: SEM image of a cross section of the BCZY electrolyte-supported cell with FeCr_2O_4 catalyst.

The XRD peaks of fresh FeCr_2O_4 phase were broadened due to the small crystalline size. From the line broadening of the diffraction peak at 42° , the average crystallite sizes of the catalysts were calculated using the Scherrer Formula ($T = 0.89 \lambda / \beta \cos \theta$). The fresh catalyst crystallites averaged only 4.2 nm. Thus, using citrate as a chelating agent provided good distribution of Fe and Cr ions throughout the dry gel, generated a large amount of gas during the citrate-nitrate gel combustion and decomposition, and so the combination of these effects resulted in the formation of very fine particles. When the catalysts were reduced in H_2 at high temperature of 750°C for 4 h, the crystallite size increased to 33.6 nm.

Figure 2 shows a typical scanning electron microscopy (SEM) image of the electrolyte supported fuel cell. The BCZY electrolyte was dense, thus it separates the anode and cathode feeds very well. The image also shows the typical porous microstructure of the electrodes, required to achieve good

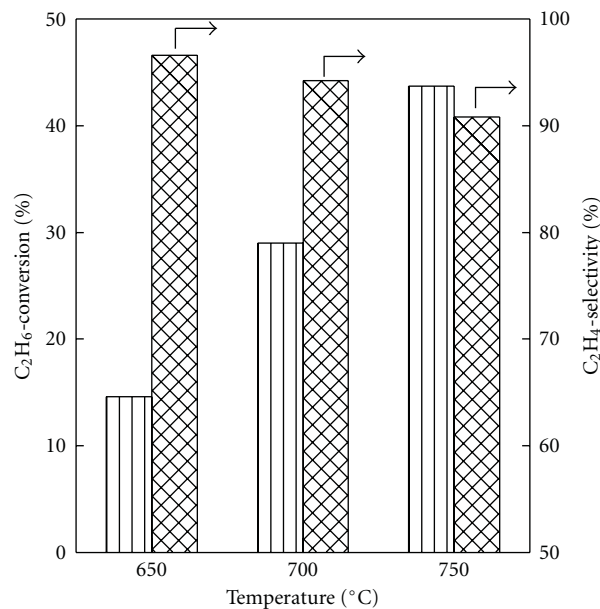


FIGURE 3: Ethane conversion and ethylene selectivity for a FeCr_2O_4 -BCZY|BCZY|LSF-BCZY single cell as a function of temperature. The flow rates of ethane and oxygen are each 150 mL/min.

diffusion of feed to the electrochemically active triple phase boundary sites (TPB).

3.2. Catalytic Performance. At elevated temperatures the main reaction in the anode chamber was dehydrogenation of ethane to ethylene with high selectivity, with cogeneration of electricity. Figure 3 shows the ethane conversion and ethylene selectivity at different reaction temperatures. The conversion of ethane increased from 14.6% to 29% and 43.7% whilst

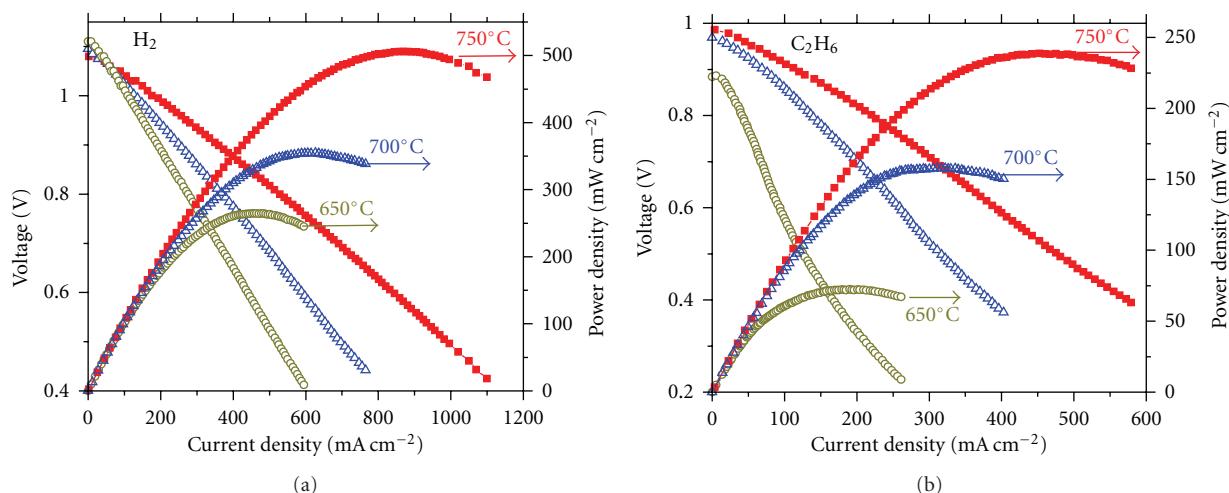


FIGURE 4: I–V curves and power density output of the $\text{FeCr}_2\text{O}_4\text{-BCZY|BCZY|LSF-BCZY}$ single cell at different temperatures with (a) hydrogen and (b) ethane as the fuel.

the selectivity to ethylene decreased from 96.6% to 94.2% and 90.8% as the operating temperature increased from 650°C to 700°C and then 750°C. The ethane conversions over this nanosized FeCr_2O_4 catalyst were higher than the values over Cr_2O_3 catalysts under the same conditions, described in our previous study [6]. In that study, conversion of ethane increased from 8.5% to 35.3% whilst the selectivity of ethylene decreased from 98.6% to 88.2% as the operating temperature increased from 650 to 750°C. Cr_2O_3 is widely used as an excellent dehydrogenation catalyst, and so dehydrogenation of ethane to ethylene occurred readily [18]. However, the present FeCr_2O_4 catalyst showed even better catalytic performance than Cr_2O_3 nanoparticles.

The differences between GC analyses of the anode feed and effluent showed the formation of small but increasing amounts of methane and hydrogen and traces of carbon oxides, as the rate of dehydrogenation of ethane increased with temperature. The hydrogen in the anode outlet was attributable to either or both of the gas phase cracking of ethane and the more rapid catalytic production of H_2 than could be accommodated by conduction of protons through the thick electrolyte membrane used in this study. Methane was produced from the thermal cracking of ethane which, as expected, was more favoured at the higher temperature, so that ethylene selectivity decreased while methane selectivity increased with temperature. The amounts of CO_2 formed were traces. The proton-conducting ceramic electrolyte membrane prevented contact with any oxygen source other than the oxide materials themselves and the very small amount of oxide conductivity in the electrolyte, as the proton ceramic electrolyte membrane conducted the protons to the cathode to react with oxygen and form water, thus providing the thermodynamic driving force and removing equilibrium limitation of the dehydrogenation reaction.

3.3. Electrochemical Performance. To investigate the electrochemical performance of the FeCr_2O_4 anode under fuel cell

operating conditions a single cell based on BCZY electrolyte was tested in the range from 650°C to 750°C using different types of fuel. Figure 4 shows the I–V and power density curves (after manual compensation) of the single cell using pure hydrogen (Figure 4(a)) or ethane (Figure 4(b)) as fuel. The open-circuit voltages (OCVs) of 1.04, 1.07, and 1.1 V for H_2 fuel and 0.98, 0.95, and 0.88 V for C_2H_6 fuel at 750, 700, and 650°C, respectively, indicated that the BCZY electrolyte was dense and impermeable. The OCV value decreased as the temperature increased for the tests with H_2 as fuel. In contrast, the trend was the inverse when C_2H_6 was used as fuel. The OCV for C_2H_6 fuel was lower than that when using H_2 as fuel. These trends suggest that the dissolution rate of a proton generated from C_2H_6 fuel into the electrolyte bulk was slower than that of a proton generated from H_2 as fuel, probably as a consequence of the relative rates of generation of protons from the respective feeds. The maximum power densities were 510, 360, and 250 mW cm^{-2} for H_2 fuel and 240, 160, and 70 mW/cm^{-2} for C_2H_6 fuel at 750, 700, and 650°C, respectively. The high power density values indicated that the FeCr_2O_4 material is a suitable candidate as an anode catalyst for proton-conducting SOFC. The high performance of the cell is attributable mainly to the high activity of H_2 on the FeCr_2O_4 surface and the Fe metallic sites. Comparison of these power density values suggested that the FeCr_2O_4 -based anode had higher catalytic activity for the electrochemical oxidation of H_2 than for that of C_2H_6 .

In order to further compare the different contributions to the total resistance with H_2 or C_2H_6 as fuel in the single cell test, electrochemical impedance spectroscopy measurements were performed under open-circuit conditions at different temperatures, as shown in Figure 5. The intercept with the real axis at high frequency represented the ohmic resistance (R_{ohm}) of the cell which, reasonably, was usually taken as the overall electrolyte resistance of the cell. The difference between the high-frequency and low-frequency intercepts with the real axis represented the total interfacial polarization resistance (R_p) of the cell. The overall electrolyte

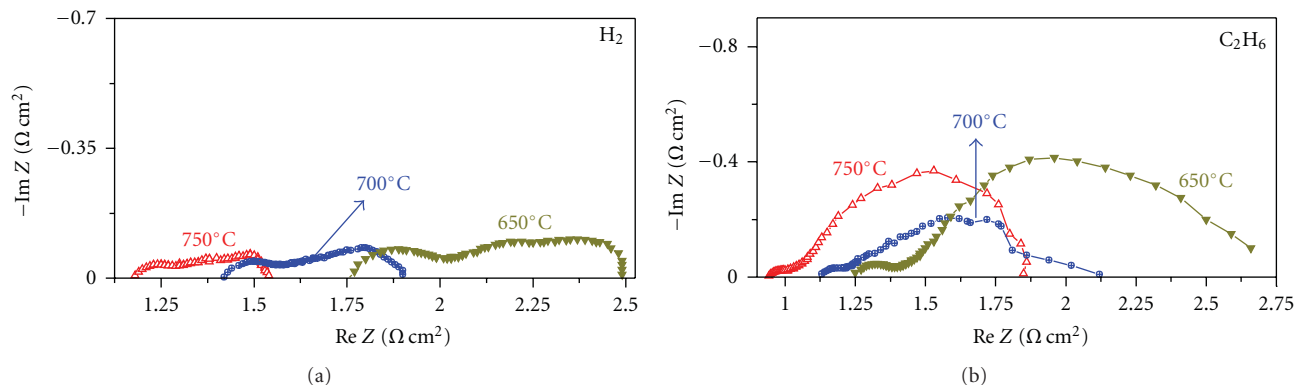


FIGURE 5: Electrochemical impedance spectra of the $\text{FeCr}_2\text{O}_4\text{-BCZY|BCZY|LSF-BCZY}$ single cell at different temperatures, with (a) hydrogen and (b) ethane as the fuel.

resistances of the cell were 1.19, 1.42, and 1.75 $\Omega\text{ cm}^2$ for H_2 fuel and 0.94, 1.12, and 1.24 $\Omega\text{ cm}^2$ for C_2H_6 fuel at 750, 700, and 650°C, respectively. The corresponding polarization resistances (R_E) of the cell were 0.35, 0.48, and 0.78 $\Omega\text{ cm}^2$ for H_2 fuel and 0.91, 1.02 and 1.44 $\Omega\text{ cm}^2$ for C_2H_6 fuel. Apparently, as the operating temperature was decreased, R_{ohm} and R_p , the two specific contributions to the total resistance, both increased dramatically. R_{ohm} was predominant for the test using H_2 as fuel, while R_{ohm} and R_p had comparable values for the tests using C_2H_6 as fuel. The impedance arcs for both the H_2 fuel and C_2H_6 fuel decreased significantly with the increase in temperature. It is interesting that the impedance responses of the ethane fuel tests became clearly separated at high frequencies. This indicated that the H_2 oxidation reaction on FeCr_2O_4 anodes was controlled by at least two distinct electrode processes. In addition, it is obvious that the R_{ohm} in C_2H_6 fuel is a little lower than that in H_2 fuel. A similar phenomenon was observed for the Cu-Ce-YSZ fuel cell fed by hydrogen and *n*-butane [19]. It has been reported that the value of R_{ohm} of Cu-Ni alloy cermets decreased with time after long-time exposure to methane [20]. It was suggested that deposition of hydrocarbons in the anode improves the connectivity between catalyst particles and decreases the ohmic resistance [19, 20].

In each of the fuel cell tests the activation polarization was very similar in value, which meant that the activation ability of FeCr_2O_4 catalysts for H_2 and C_2H_6 varied little with temperature. Overall, the plots (Figure 5) each consisted of a small higher-frequency depressed arc and a large lower-frequency arc, the sizes of both of which increased with decreasing temperature, as typically observed for electrochemical processes such as charge transfer or surface diffusion. However, in each case the arcs were envelopes of a series of overlapping arcs. The overlapping arcs may arise from the presence of both nano-Fe particles and FeCr_2O_4 in the anode catalyst (Figure 1). While it is not possible to unequivocally determine this from the present data and further investigation is required, it is known that Fe particles are active catalysts for alkane dehydrogenation, including isobutane to isobutene [21].

The high values of the ohmic resistance were attributable to the overall configuration of the single cell, in particular the large thickness of the BCZY electrolyte (about 0.9 mm), suggesting that higher performance should be attainable from cells with much thinner electrolyte layers.

4. Conclusions

An electrolyte-supported proton-conducting SOFC fabricated using FeCr_2O_4 as the anode catalyst, and LSF as the cathode has high performance for conversion of ethane to cogenerate ethylene and electrical power. The fuel cell reactor provides high selectivity, over 90%, for ethane dehydrogenation and ethylene yields of 14.1, 27.3 and 39.7%, while co-generating 70, 160, and 240 mW cm^{-2} power densities at 650, 700, and 750°C, respectively. The ethane conversions over this nanosized FeCr_2O_4 catalyst are notably higher than the values over previously described Cr_2O_3 catalysts.

Acknowledgments

This work was supported by the Natural Sciences and Engineering Research Council of Canada/NOVA Chemicals CRD Grant, the Alberta Energy Research Institute, and the Micro Systems Technology Research Institute. The authors thank Dr. Juri Melnik for very helpful discussions.

References

- [1] E. Fabbri, D. Pergolesi, and E. Traversa, "Electrode materials: a challenge for the exploitation of protonic solid oxide fuel cells," *Science and Technology of Advanced Materials*, vol. 11, no. 4, article 044301, 2010.
- [2] K. Katahira, Y. Kohchi, T. Shimura, and H. Iwahara, "Protonic conduction in Zr-substituted BaCeO_3 ," *Solid State Ionics*, vol. 138, no. 1-2, pp. 91-98, 2000.
- [3] Y. Guo, Y. Lin, R. Ran, and Z. Shao, "Zirconium doping effect on the performance of proton-conducting $\text{BaZr}_y\text{Ce}_{0.8-y}\text{Y}_{0.2}\text{O}_{3-\delta}$ ($0.0 \leq y \leq 0.8$) for fuel cell applications," *Journal of Power Sources*, vol. 193, no. 2, pp. 400-407, 2009.

- [4] F. Cavani, N. Ballarini, and A. Cericola, "Oxidative dehydrogenation of ethane and propane: how far from commercial implementation?" *Catalysis Today*, vol. 127, no. 1–4, pp. 113–131, 2007.
- [5] D. Akporiaye, S. F. Jensen, U. Olsbye et al., "A novel, highly efficient catalyst for propane dehydrogenation," *Industrial and Engineering Chemistry Research*, vol. 40, no. 22, pp. 4741–4748, 2001.
- [6] X. Z. Fu, X. X. Luo, J. L. Luo, K. T. Chuang, A. R. Sanger, and A. Krzywicki, "Ethane dehydrogenation over nano-Cr₂O₃ anode catalyst in proton ceramic fuel cell reactors to co-produce ethylene and electricity," *Journal of Power Sources*, vol. 196, no. 3, pp. 1036–1041, 2011.
- [7] C. K. Cheng, J. L. Luo, K. T. Chuang, and A. R. Sanger, "Propane fuel cells using phosphoric-acid-doped polybenzimidazole membranes," *Journal of Physical Chemistry B*, vol. 109, no. 26, pp. 13036–13042, 2005.
- [8] W. S. Li, D. S. Lu, J. L. Luo, and K. T. Chuang, "Chemicals and energy co-generation from direct hydrocarbons/oxygen proton exchange membrane fuel cell," *Journal of Power Sources*, vol. 145, no. 2, pp. 376–382, 2005.
- [9] S. Wang, J. L. Luo, A. R. Sanger, and K. T. Chuang, "Performance of ethane/oxygen fuel cells using yttrium-doped barium cerate as electrolyte at intermediate temperatures," *Journal of Physical Chemistry C*, vol. 111, no. 13, pp. 5069–5074, 2007.
- [10] Z. Shi, J. L. Luo, S. Wang, A. R. Sanger, and K. T. Chuang, "Protonic membrane for fuel cell for co-generation of power and ethylene," *Journal of Power Sources*, vol. 176, no. 1, pp. 122–127, 2008.
- [11] X. Z. Fu, J. L. Luo, A. R. Sanger, Z. R. Xu, and K. T. Chuang, "Fabrication of bi-layered proton conducting membrane for hydrocarbon solid oxide fuel cell reactors," *Electrochimica Acta*, vol. 55, no. 3, pp. 1145–1149, 2009.
- [12] Y. Lei, N. W. Cant, and D. L. Trimm, "Kinetics of the water-gas shift reaction over a rhodium-promoted iron-chromium oxide catalyst," *Chemical Engineering Journal*, vol. 114, no. 1–3, pp. 81–85, 2005.
- [13] BASF, vol. German Offen 254572, 1911.
- [14] A. Khaleel, I. Shehadi, and M. Al-Shamisi, "Nanostructured chromium-iron mixed oxides: physicochemical properties and catalytic activity," *Colloids and Surfaces A*, vol. 355, no. 1–3, pp. 75–82, 2010.
- [15] A. A. Khassin, A. G. Sipatrov, M. P. Demeshkina, and T. P. Minyukova, "Partially hydrated iron-chromium oxide catalyst for the Fischer-Tropsch synthesis," *Reaction Kinetics and Catalysis Letters*, vol. 97, no. 2, pp. 371–379, 2009.
- [16] J. Livage, "Sol-gel processes," *Current Opinion in Solid State and Materials Science*, vol. 2, no. 2, pp. 132–138, 1997.
- [17] J. D. Mackenzie and E. P. Bescher, "Chemical routes in the synthesis of nanomaterials using the sol-gel process," *Accounts of Chemical Research*, vol. 40, no. 9, pp. 810–818, 2007.
- [18] B. M. Weckhuysen and R. A. Schoonheydt, "Alkane dehydrogenation over supported chromium oxide catalysts," *Catalysis Today*, vol. 51, no. 2, pp. 223–232, 1999.
- [19] S. McIntosh, J. M. Vohs, and R. J. Gorte, "Role of hydrocarbon deposits in the enhanced performance of direct-oxidation SOFCs," *Journal of the Electrochemical Society*, vol. 150, no. 4, pp. A470–A476, 2003.
- [20] H. Kim, C. Lu, W. L. Worrell, J. M. Vohs, and R. J. Gorte, "Cu-Ni cermet anodes for direct oxidation of methane in solid-oxide fuel cells," *Journal of the Electrochemical Society*, vol. 149, no. 3, pp. A247–A250, 2002.
- [21] H. Shimada, T. Akazawa, N. O. Ikenaga, and T. Suzuki, "Dehydrogenation of isobutane to isobutene with iron-loaded activated carbon catalyst," *Applied Catalysis A*, vol. 168, no. 2, pp. 243–250, 1998.

Review Article

Nanoporous PdCo Catalyst for Microfuel Cells: Electrodeposition and Dealloying

Satoshi Tominaka¹ and Tetsuya Osaka²

¹International Center for Materials Nanoarchitectonics, National Institute for Materials Science, Ibaraki 305-0044, Japan

²Nano-Science and Engineering, Applied Chemistry, Graduate School of Advanced Science and Engineering, Waseda University, Tokyo 169-8555, Japan

Correspondence should be addressed to Satoshi Tominaka, tominaka.satoshi@nims.go.jp

Received 5 May 2011; Accepted 17 June 2011

Academic Editor: Milan M. Jaksic

Copyright © 2011 S. Tominaka and T. Osaka. This is an open access article distributed under the Creative Commons Attribution License, which permits unrestricted use, distribution, and reproduction in any medium, provided the original work is properly cited.

PdCo alloy is a promising catalyst for oxygen reduction reaction of direct methanol fuel cells because of its high activity and the tolerance to methanol. We have applied this catalyst in order to realize on-chip fuel cell which is a membraneless design. The novel design made the fuel cells to be flexible and integratable with other microdevices. Here, we summarize our recent research on the synthesis of nanostructured PdCo catalyst by electrochemical methods, which enable us to deposit the alloy onto microelectrodes of the on-chip fuel cells. First, the electrodeposition of PdCo is discussed in detail, and then, dealloying for introducing nanopores into the electrodeposits is described. Finally, electrochemical response and activities are fully discussed.

1. Introduction

Recent progress in microelectrochemical devices, for example, on-chip fuel cells [1–6], microbatteries [7, 8], and on-chip sensors [9, 10], inevitably requires developments of both electrode materials with a large surface area and processes for depositing such materials precisely onto the tiny current collectors. For such selective deposition, we regard that electrodeposition is attractive, because this technique enables us to selectively synthesize metals onto conductive materials, even onto microelectrodes and to directly synthesize alloys without thermal treatment [11–13]. Moreover, its possible control of morphology by tuning applied current densities appears applicable to the synthesis of nanostructured materials [12–14]. Thus, electrodeposition is an important technique for synthesizing electrode materials for microelectrochemical devices. In view of this, we electrodeposited electrocatalysts for on-chip fuel cells, for example, Pt black, PtRu alloy, and PdCo alloy [1, 2, 11, 15].

In order to increase surface area of electrode of interest, nanostructured materials, for example, nanoparticles, have been widely used. Moreover, since each of the devices

needs electrode with a different porosity appropriate to its own requirements for reactant and product transportations, synthesis of nanoporous structures with defined porosity is beneficial. For example, nanoporous Pt electrodes synthesized using soft or hard templates [16–19]. Though such templating processes are useful for synthesizing well-organized nano- and microstructures, they are generally time consuming and need hazardous chemicals to remove the templates. Therefore, we considered that more versatile methods for synthesizing nanostructured electrodes for microelectrochemical devices need to be developed.

Contrary to such templating methods, the dealloying method can form metals with sponge-like nanoporous structures without any templates [20, 21]. Dealloying refers to the selective dissolution of one or more components out of an alloy. The unique porous structure is formed by a competition of two processes: dissolution of less-noble component (i.e., pore formation) and surface diffusion of more noble component to aggregate into two-dimensional clusters (i.e., surface passivation) [20–24]. Their surface area can reach a value comparable to those of nanoparticles when the pore size is a nanoscale [25].

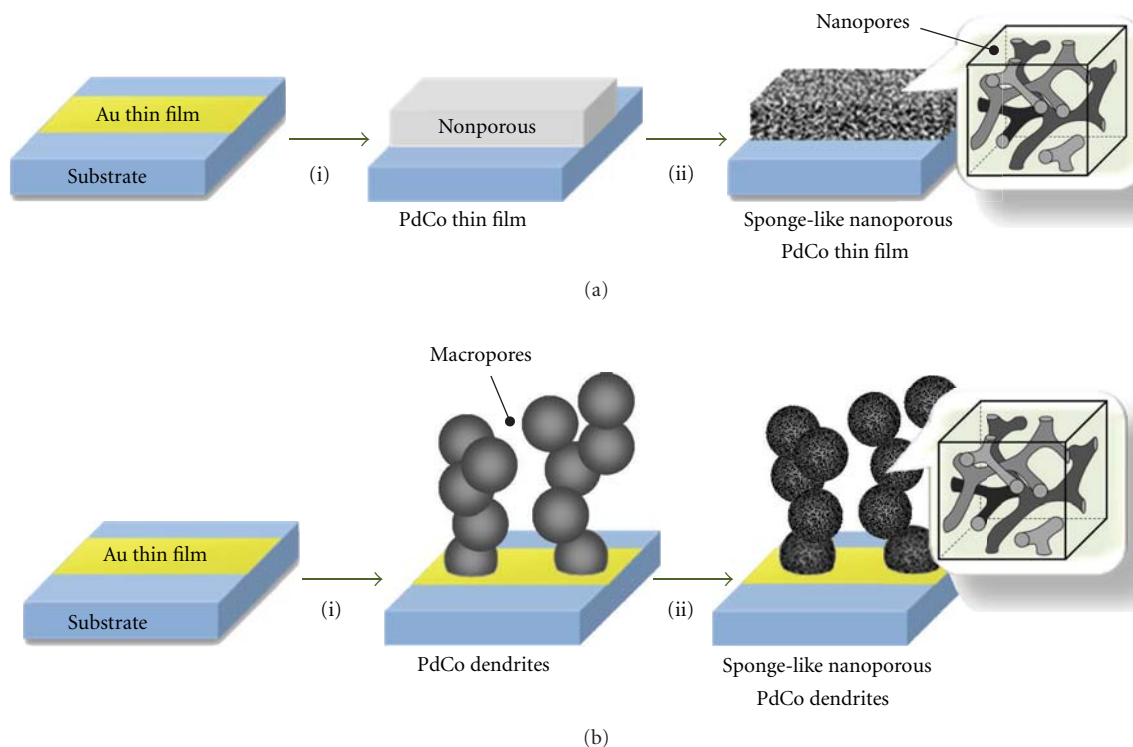


FIGURE 1: Electrochemical synthesis of nanostructured PdCo catalyst selectively on Au layer by (i) electrodeposition and (ii) dealloying. (a) Sponge-like nanoporous thin film and (b) nanoporous dendrites. Such three-dimensional porosity is beneficial in terms of diffusion inside.

Here, we summarize our recent research on the synthesis of nanostructured PdCo catalyst by electrochemical methods, which enable us to deposit the alloy onto micro-electrodes of the on-chip fuel cells [1]. We have used the combination of electrodeposition and dealloying in order to synthesize sponge-like nanoporous thin films [26–28] and coral-reef-like nanostructures [29] selectively onto current collectors as illustrated in Figure 1.

Pd-based alloys such as PdCo are attractive as oxygen reduction reaction (ORR) catalysts for direct methanol fuel cells (DMFCs) because of its high activity comparable to Pt catalyst and its high tolerance to methanol [30–35]. Based on the latter property, we have used this catalyst for realizing a tiny on-chip DMFC of a membraneless design [1]. Since Pd-based catalyst may not be sufficiently stable in acidic media at such a positive potential for oxygen reduction reaction for practical use [36], we have tested the use of neutral pH atmosphere for the on-chip fuel cell system [1, 3]. For the reasonable comparison with data reported by others, we used sulfuric acid as the supporting electrolyte for evaluating catalytic activity in this paper.

Figure 2 is a phase diagram of PdCo alloy with an indication of composition range enhancing ORR ($\text{Pd}_x\text{Co}_{1-x}$, $x = 0.7 - 0.9$) [30–35, 37–41]. This alloy system mainly forms solid solution phase, but in some composition range, ordered phases of intermetallic compounds such as L_{12} phase (i.e., Pd_3Co_1) and L_{10} phase (i.e., Pd_1Co_1) can be formed [42, 43]. In the potential range where high ORR activities were obtained, L_{12} type Pd_3Co_1 phase may exist. Since those

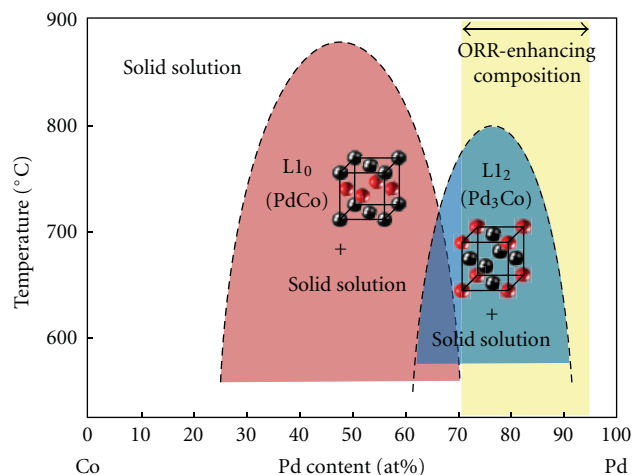


FIGURE 2: Phase diagram of PdCo system showing the composition range where oxygen reduction reaction is enhanced. The diagram was based on the figure reported in the literature [43]. Mainly, the phase is an fcc solid solution. In specific composition range, the alloy contains ordered fcc phase (L_{12} type) or ordered face-centered tetragonal phase (L_{10} type).

ordered phases were detectable only by electron diffraction, we have to be careful on such. The surface composition was reported to be Pd-rich after reduction in H_2 and Co-rich after oxidation. This surface segregation is typical for this

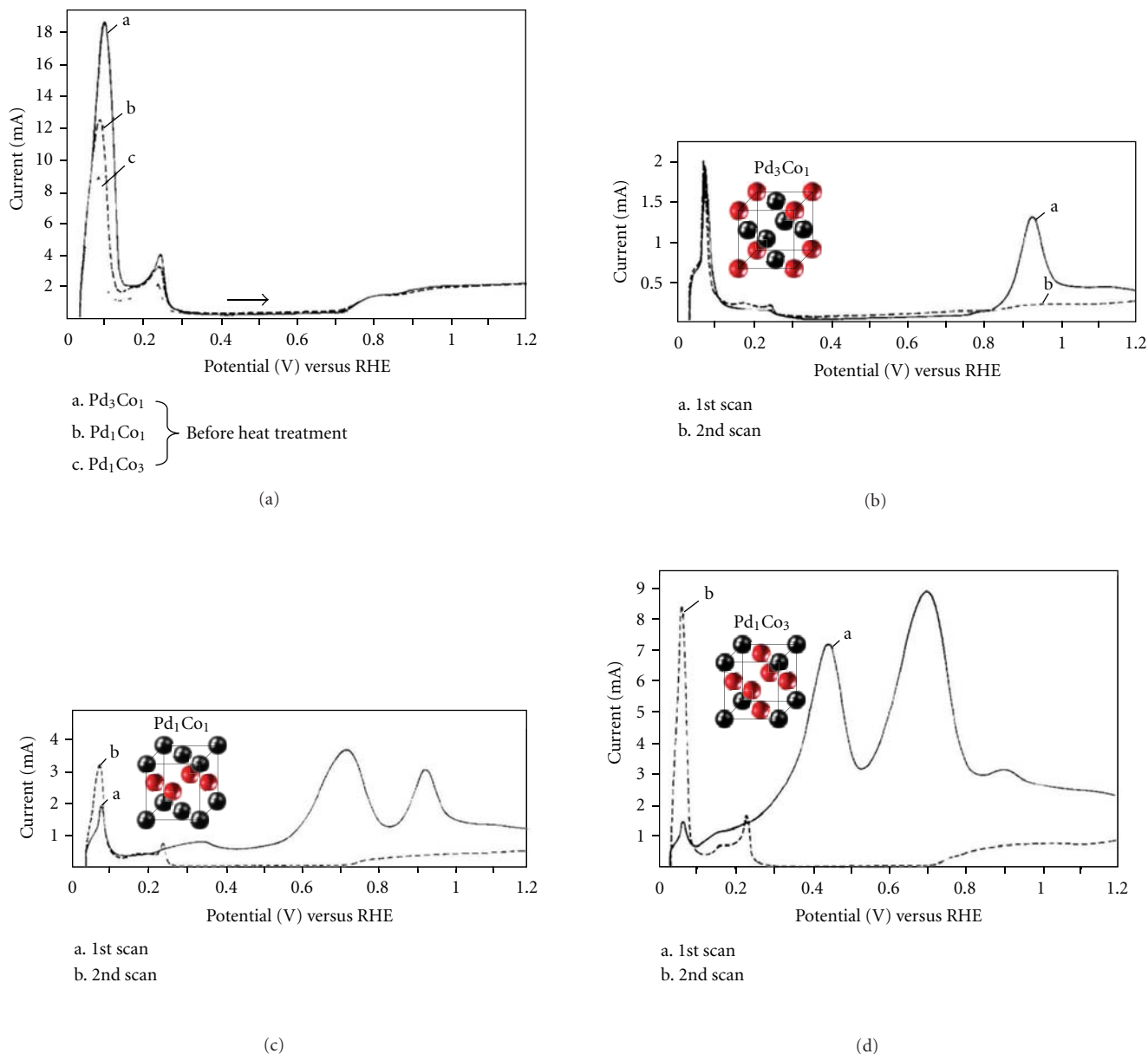


FIGURE 3: Linear sweep voltammograms of PdCo powders (positive scans) in nitrogen-saturated 0.5 M sulfuric acid solution: (a) Before heat treatment: Curve (a) Pd_3Co_1 , curve (b) Pd_1Co_1 , and curve (c) Pd_1Co_3 . (b–d) After heat treatment at 500°C: Curve (a) first sweep and curve (b) second sweep after reduction with hydrogen. Reproduced with permission from [42]. Copyright 1986, Elsevier.

type of alloys as supported by the alloy segregation theory [44].

In order to use PdCo catalyst for fuel cells, understanding of electrochemistry is needed. Mallet et al. reported linear sweep voltammograms of PdCo alloys scanned in acidic solution [42]. Figure 3(a) shows that the disordered phases did not exhibit any anodic current associated with Co dissolution, but this does not mean high stability of them, because the authors reported that these samples lost some portion of Co atoms just after dipping into the solution. It is reasonable that the redox potential of Co is more negative than the hydrogen evolution potential in the acid solution.

The removal of Co atoms probably resulted in the formation of a passive Pd layer.

Since, from the viewpoint of thermodynamics, Co atoms in the ordered phases are considered more stable than those in disordered phases, the Pd-rich ordered phases of $L1_2$ type are considered the most stable in acidic media. Anodic current attributable to Co dissolution was observed for an ordered phase of Pd_3Co_1 above ~ 0.8 V, which is more negative than fuel cell cathode potential. This result indicates the stability may not be sufficient even for this phase. Considering that the charge associated with the dissolution was roughly in the same level as oxide formation current and

that such dissolution was observed only in the first scan, only the surface Co atoms were considered to be dissolved. The same thing holds true for the other ordered phases. These results indicate that the surface of PdCo alloys is stabilized in the fuel cell condition by the formation of Pd skin layer.

2. Synthesis of PdCo Alloys by Electrodeposition

Electrodeposition of PdCo alloys was investigated by Abys et al. [45], and their aqueous bath was in a mixed ligand system. The first ligand, that is, ammonia, forms strong complexes with palladium and weak complexes with cobalt. The second ligand, that is, an organic molecule containing carboxylic acid group(s), forms strong complexes with cobalt, because cobalt complexes (octahedral with coordination number 6 [46]) bind favorably to oxygen containing ligands rather than to nitrogen containing ligands. These complex formations bring the deposition potentials of Pd and Co closer. Moreover, pH control of the solution (<10.58) is important to obtain a stable bath. They investigated numerous ligands consisting of mono-, di-, and tetracarboxylic acid.

Figure 4 shows typical scanning electron microscope images of PdCo alloy synthesized by electrodeposition. By applying a low current density, a flat film with granular surface with ca. 10-nm particles was obtained (Figure 4(a)), while dendritic deposits with ca. 50-nm particles were obtained by applying a high current density (Figure 4(b)). The pores between dendritic deposits were expected to make the entire surface readily accessible by the reactants. The deposition condition and the solution were adjusted to obtain active catalyst for ORR (details are available in Section 6) [11]. The particle size is quite large compared to that of typical fuel cell catalysts, that is, <10 nm, reasonably leading to the conclusion that further improvement in nanostructure is needed for fuel cell applications. Thus, the surface was modified with additional PdCo deposits with smaller particles, which were deposited at a similar condition as the flat PdCo film. As shown in Figure 4(c), the surface of the dendrites was successfully covered with small particles in the 5–10 nm range. This treatment increased the surface area by ca. 30% as summarized in Table 1.

The dendritic one was a substitutional solid solution of Pd₇₅Co₂₅, which is in the composition range active in the ORR [11] (cf. Figure 2). The X-ray photoelectron spectroscopy (XPS) results (Figure 5) indicate that the surface Pd and Co were metallic, not oxide, by comparing the binding energies of the deposits (Pd 3d_{5/2}: 334.7 eV, Co 2p_{3/2}: 777.4 eV) to those of a metallic Pd and a metallic Co reported in the literature (Pd 3d_{5/2}: 335.1 eV, Co 2p_{3/2}: 778.3 eV [47]). The spectra also suggest that the surface composition was apparently Pd-rich by comparing the peak intensities with taking the sensitivity factors into consideration (the factor of Pd 3d is ~1.5 times larger than Co 2p [47]). That is, Pd-skin was formed as often reported for Pt alloy catalysts of fuel cells [48, 49]. The skin was probably formed by the dissolution of surface Co by air or Pd ions in the solution.

Figure 6 shows the electrochemical response of the PdCo film in an acid solution, compared with that of a pure Pd film. The cyclic voltammogram (CV) of PdCo is similar

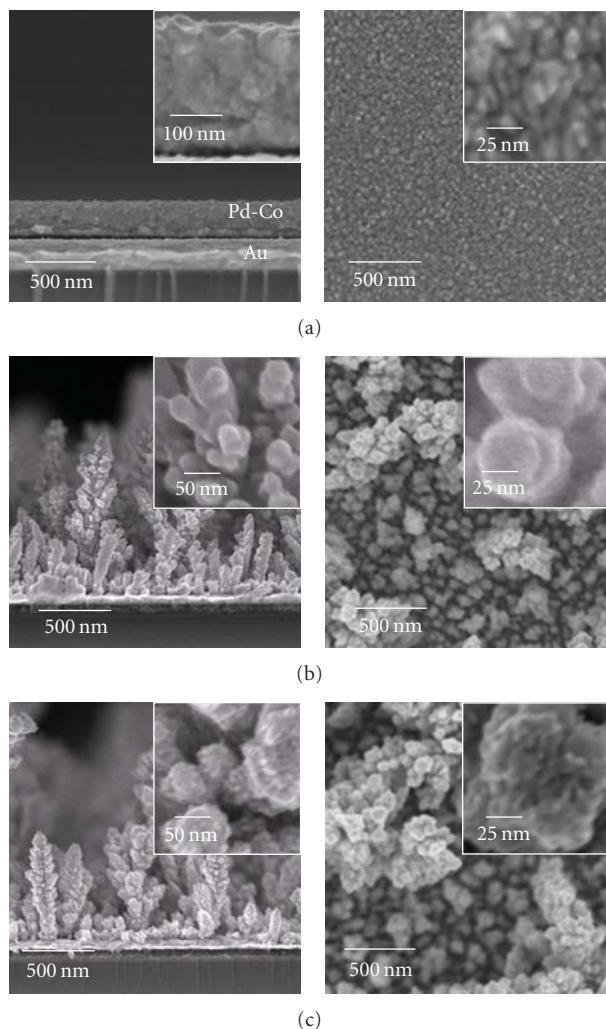


FIGURE 4: SEM images of PdCo alloys synthesized by electrodeposition: (a) at a low current density, (b) at a high current density, and (c) modification of the sample “b” by additional deposition. Left: cross-sectional view. Right: plan view. Reproduced with permission from [15]. Copyright 2007, The Electrochemical Society.

to that of Pd, except for the sharp peaks obtained in the hydrogen region (−0.2 to +0.1 V). Since this CV trace of the PdCo film is similar to that of a nanostructured Pd (Pd-black), we assigned the peaks located in the hydrogen region in accordance with a report on nanostructured Pd [50]:

- (i) Peak 1 (0.05 V): hydrogen adsorption/desorption for the surface Pd (strongly bound),
- (ii) Peak 2 (−0.05 V): hydrogen absorption/desorption for the subsurface Pd (α and β phases),
- (iii) Peak 3 (−0.2 V): hydrogen adsorption/desorption for the surface Pd or hydrogen evolution/oxidation reactions (less-strongly bound).

From this identification, it is found that the sharp peaks of PdCo (Peaks 1 and 3) strongly indicate the presence of Pd-skin. Compared with pure Pd, the hydrogen absorption was found to be prevented by alloying with Co.

TABLE 1: Oxygen reduction reaction characteristics of the PdCo catalysts evaluated in 0.5 M H₂SO₄ compared with those of Pt electrode and Pd electrode.

	Onset potential ^a /V	Electrode performance ^b /mA cm ⁻²		Specific activity ^c /μA cm ⁻²		Tafel slope/mV decade ⁻¹	Roughness factor/-	Ref.
		0.65 V versus Ag/AgCl	0.60 V versus Ag/AgCl	0.65 V versus Ag/AgCl	0.60 V versus Ag/AgCl			
Pt electrode ^f	0.72	3.5×10^{-2}	1.1×10^{-1}	8.4	2.7×10^1	71 ^c , 116 ^d	4.2	[60]
Pd thin film ^g	0.58	1.0×10^{-4h}	5.8×10^{-4h}	3.4×10^{-2h}	1.9×10^{-1h}	67	3.1	[11]
PdCo thin film ^f	0.66	2.4×10^{-2}	2.6×10^{-1}	1.5	1.6×10^1	44	16	[60]
PdCo dendrite ^g	0.68	5.7×10^{-2}	6.2×10^{-1h}	4.4	4.7×10^{1h}	48	13	[15]
Modified PdCo dendrite ^g	0.71	1.9×10^{-1}	1.6 ^h	1.1×10^1	9.2×10^{1h}	55	17	[15]
Nanoporous PdCo thin film ^f	0.69	3.5×10^{-1}	2.5	8.6	6.2×10^1	43	41	[60]
Nanoporous PdCo dendrite ^g	0.72	3.9×10^{-1i}	—	1.3 ⁱ	—	—	290	[29]

^a at the current density of 1 μA cm⁻² (electrochemically active surface area). ^b based on the geometrical surface area. ^c 0.7–0.75 V. ^d 0.55–0.65 V. ^e based on the electrochemically active surface area. ^f measured by hydrodynamic voltammetry at room temperature (22°C). ^g measured by linear sweep voltammetry at (30°C). ^h estimated by extrapolating the Tafel slope. ⁱ with a slight mass-transfer limitation.

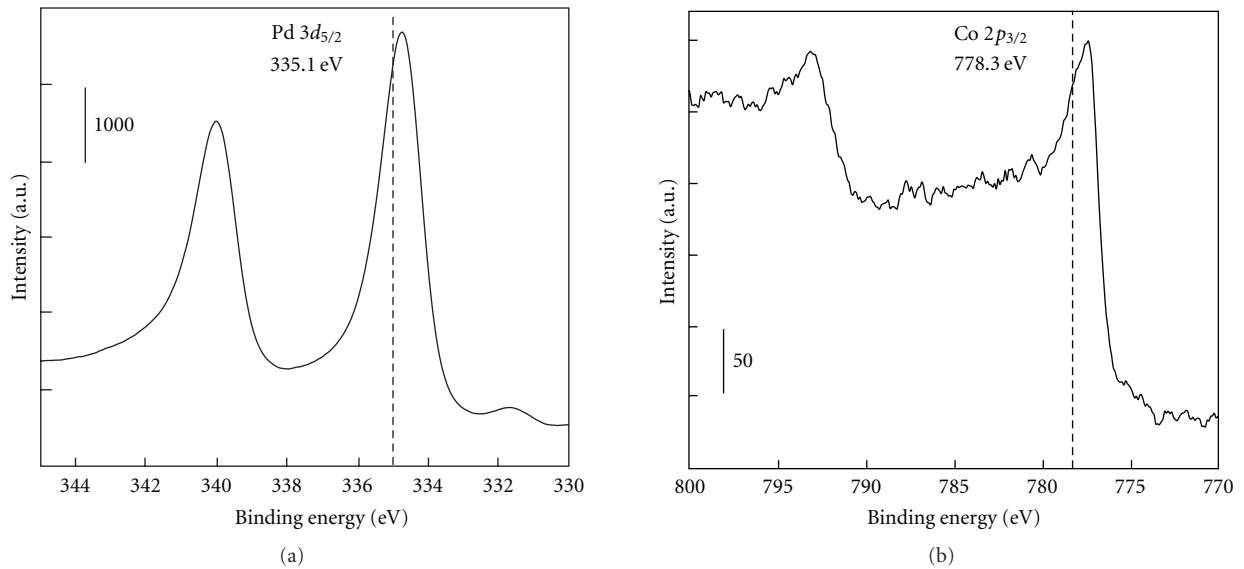


FIGURE 5: Core-level XPS of PdCo thin film of Pd 3d and Co 2p. The vertical dotted lines refer to Pd 3d_{5/2} of pure Pd and Co 2p_{3/2} of pure Co. The data of PdCo dendrites is consistent with this data. Reproduced with permission from [11]. Copyright 1986, Elsevier.

In the oxide region, the current densities from the PdCo are almost the same as that from the Pd, this meaning that the amount of sites binding with oxygen atoms is the same. However, the potential of oxide formation/deformation of the PdCo alloy was shifted to more negative potential, and this means that the Pd-skin is easily oxidized compared with pure Pd. This tendency was reported also by other groups [31]. Interestingly, this effect of the alloying on the oxide region is opposite to that of Pt alloys [51, 52] and to the prediction based on the shift of *d*-band center to a larger binding energy and the result of first-principle consideration [31, 53]. Since the CV behavior in the potential region was dominated by adsorption of oxygenated species and desorption of sulfate anions, we speculate that the apparent

negative shift of oxidation potential was probably due to the negative shift of sulfate desorption potential.

The current densities of the CVs were based on electrochemically active area (A_{ec}). Such area of Pt electrode has been calculated on the basis of hydrogen adsorption charge [54, 55], and that of Au electrode has been calculated on the basis of oxide reduction charge [55, 56]; however, on Pd electrode, hydrogen absorption in hydrogen region and Pd dissolution in the oxide region make such charges unclear [36, 57]. In view of this, we assumed that the double-layer capacitance (C_{dl}) per A_{ec} for Pd was the same as that for Pt. This assumption is acceptable, because the adsorbed-sulfate structure on a Pd electrode is similar to a Pt electrode. In detail, the adsorbed-sulfate structure was reported to be the

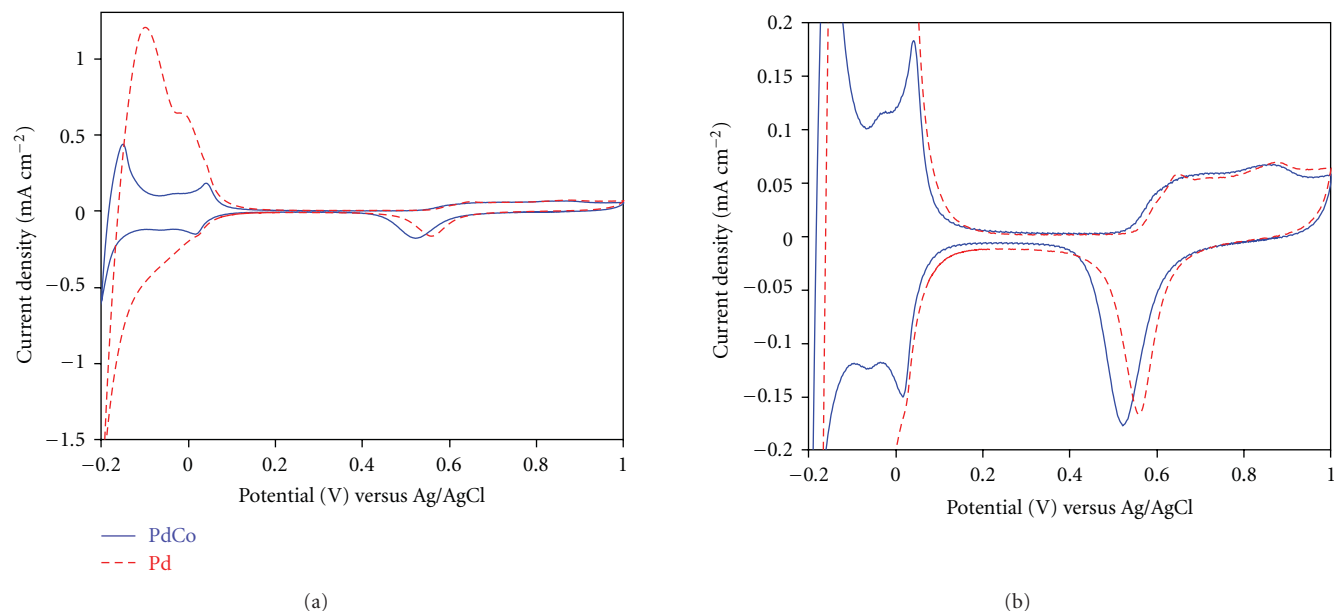


FIGURE 6: Cyclic voltammograms of the electrodeposited PdCo catalyst scanned at 50 mV s^{-1} in $0.5 \text{ M H}_2\text{SO}_4$ deaerated with N_2 at lower (a) and at higher (b) expansion of current axis scale. The dotted line is a voltammogram of the electrodeposited Pd. The current density is normalized by electrochemical surface areas. Reproduced with permission from [11]. Copyright 1986, Elsevier.

same on (111) surface and slightly different on (100) surface [58, 59]. We measured such capacitance for Pt by cyclic voltammetry, and a value of $86 \mu\text{F cm}^{-2}$ was obtained. Using this value, the electrochemically active surface areas of PdCo alloys were calculated.

For the successful improvement of microfuel cell performance, large surface area of catalyst is needed [5]. General direct methanol fuel cells require Pt loading of about 2.5 mg cm^{-2} . This loading is translated into a roughness factor (a ratio of actual electrode surface area divided by geometrical one) of 2000 ($80 \text{ m}^2 \text{ g}^{-1}$) [39]. The value of the PdCo dendrite described above was 13.3. Even though longer deposition time was used, the value was limited to less than 100. This large gap is because the particles of the electrodeposited dendrites were more than ten times as big as the nanoparticles generally used for fuel cells. Thus, in order to increase the surface area of such electrodeposits, we have introduced nanopores into the electrodeposits by dealloying.

3. Electrochemical Dealloying for Introducing Nanopores into Electrodeposits

In order to increase the surface area of electrodeposited PdCo catalyst, we used dealloying technique as illustrated in Figure 1(a). First, a Co-rich PdCo alloy was electrodeposited, and then, the deposit was partially dealloyed by applying more positive potential in a sulfuric acid solution. A thin film of nanoporous PdCo catalyst was thus synthesized. Figure 7 shows that the dealloyed PdCo thin film was highly porous sponge-like film with $<50\text{-nm}$ thick ligaments. The TEM images show crystalline ligaments whose lattice spacing was observed to be ca. 0.22 nm , which is close to that of Pd(111)

plane (0.226 nm). Interestingly, Figure 7(D) indicates that the ligament was formed by large crystal domains; namely, the ligaments were not composed of small particles, but of a long single crystal domain.

The as-deposited PdCo alloy of a nonporous fcc $\text{Pd}_{30}\text{Co}_{70}$ film became the sponge-like nanoporous $\text{Pd}_{93}\text{Co}_7$. In accordance with Vegard's law, since the peak angles of XRD pattern were shifted to higher angles [60], the crystal domains of the dealloyed PdCo alloy were found to be a substitutional solid solution of $\text{Pd}_{92}\text{Co}_8$. This degree of lattice contraction seems of great promise as ORR catalyst, because such a 8% lattice contraction was reported to endow Pd alloys with a high ORR activity [53].

The XPS results (Figure 8) show that the surface of this dealloyed thin film was Pd-rich, suggesting the formation of a Pd-skin layer as those of electrodeposited PdCo catalyst. The presence of Pd-skin was confirmed by CV measurement as shown in Figure 11. Compared with those of electrodeposited PdCo catalyst (Figure 5) and the as-deposited one (Figure 8), the dealloyed one had the Pd $3d_{5/2}$ peak located at a slightly higher energy. Since the Pd $3d_{5/2}$ peak energy located at 335.5 eV is close to that of a metallic Pd (335.1 eV) rather than those of Pd oxides (PdO at 336.3 eV and PdO_2 at 337.9 eV) [47], the Pd skin of the dealloyed one was still metallic. The slight shift toward higher energy probably suggested that the lattice of the Pd skin layer was contracted by the presence of subsurface PdCo alloy.

Since there was a concern about that, for use as an electrode for fuel cells, reactant transports seem hampered by their small and tortuous pores. On this point, we conceived that the macropores between dendrites formed by electrodeposition can compensate for the limitation. In

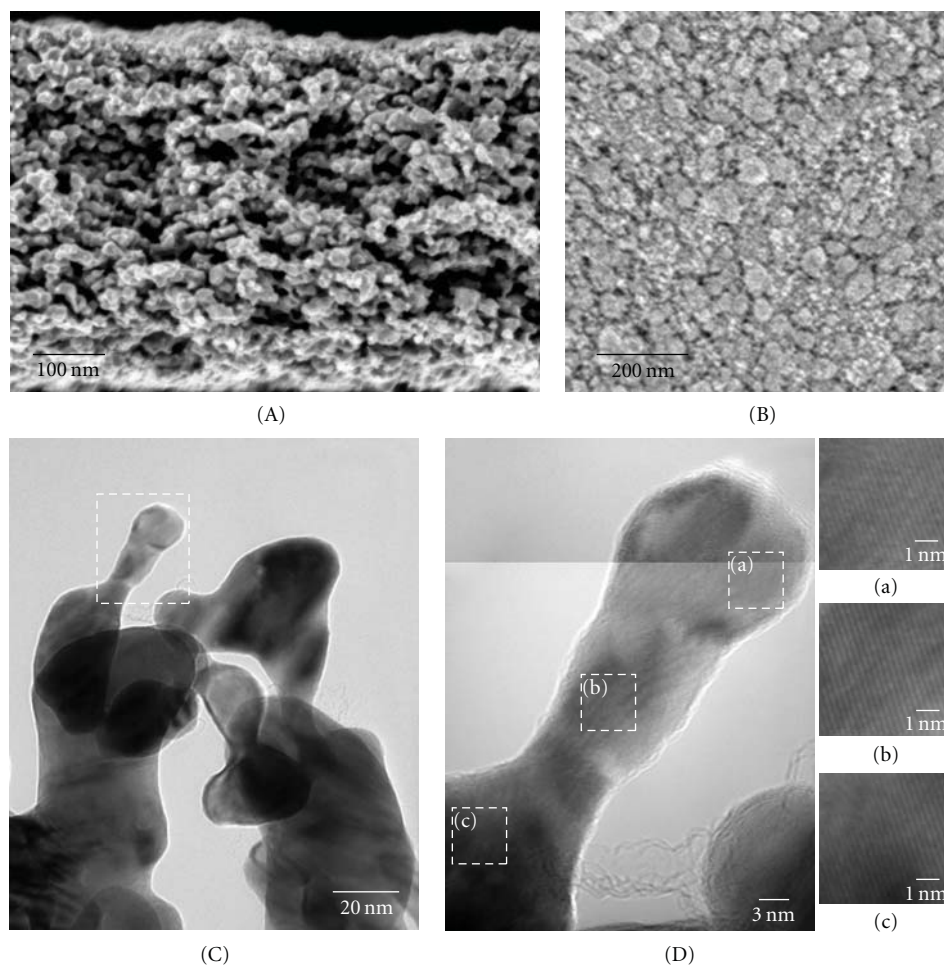


FIGURE 7: Electron micrographs of the dealloyed PdCo film. Cross-sectional (A) and (B) plan-view SEM images. (C, D) TEM images. (a-c) High-resolution images of lattice fringes with a lattice distance of 2.2 Å. Reproduced with permission from [27]. Copyright 2010, RSC.

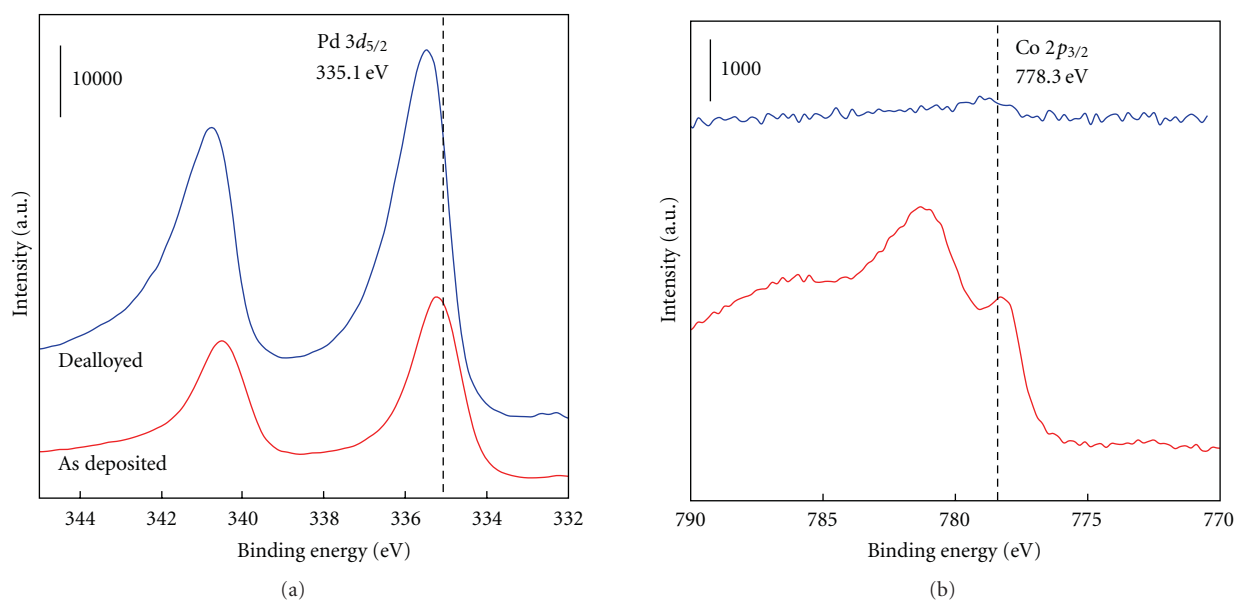


FIGURE 8: Core-level XPS of the nanoporous PdCo thin film of Pd $3d$ and Co $2p$. The vertical dotted lines refer to Pd $3d_{5/2}$ of pure Pd and Co $2p_{3/2}$ of pure Co. Reproduced with permission from [27]. Copyright 2010, RSC.

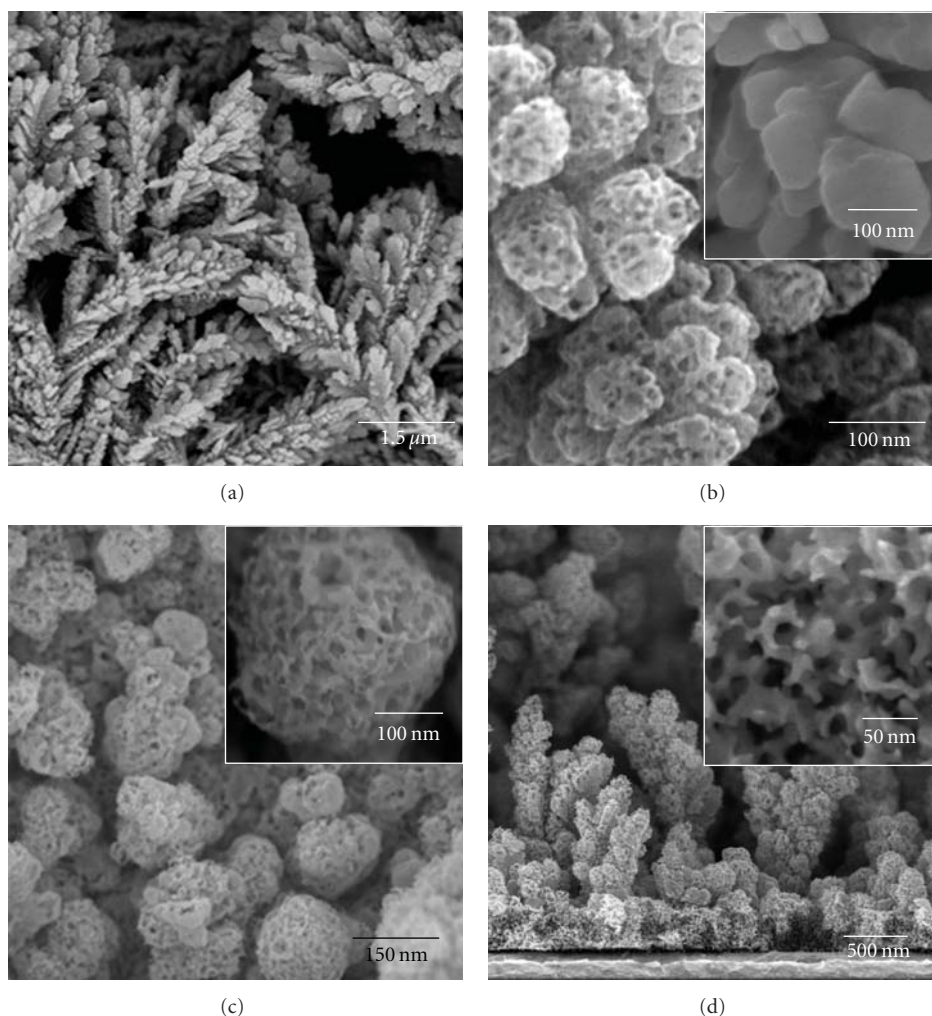


FIGURE 9: SEM images of nanoporous PdCo dendrites: (a–c) plan view, and (d) cross-sectional. The sample shown in “a” and “b” was electrodeposited at a constant current of -50 mA cm^{-2} for 600 s followed by the immersion in an air-saturated 0.5 M sulfuric acid solution for $\sim 15 \text{ h}$ at 60°C . The sample shown in “c” and “d” was prepared by galvanic pulse deposition and dealloying. Reproduced with permission from [29]. Copyright 2010, Elsevier.

this view, we proposed a simple method to synthesize a unique nanostructure with both a hierarchical porosity and a large surface area, that is nanoporous dendrites, which have macropores between dendrites formed by electrodeposition and nanopores formed by dealloying (Figure 1(b)).

Likewise, the dealloying of dendritic structures resulted in the nanoporous dendrites as shown in Figures 9 and 10. Compared with as-deposited ones, the nanopores were found to be formed without changing the macroscopic morphology of dendrites (Figure 9(b)). The dendrites consisted of 100–300 nm nanoparticles having $\sim 10 \text{ nm}$ nanopores. The sponge-like porous structure is typical for the metal architecture prepared by dealloying. Since the lattice fringes were observed to be aligned over nanopores (Figure 10(c)), the crystallites were found to be larger than the ligaments. The whole deposited layer was thin enough ($4\text{--}5 \mu\text{m}$) for use as a catalyst for on-chip fuel cells [1]. The macropores between the deposits are expected to make the entire surface of the dendrites readily accessible by oxygen.

The bulk composition and crystal structure were changed from amorphous $\text{Pd}_{24}\text{Co}_{76}$ (as-deposited one) to a polycrystalline fcc crystals of $\text{Pd}_{79}\text{Co}_{21}$, whose XRD pattern was well consistent with that of a pure fcc Pd. The surface composition was determined to be nearly pure metallic Pd by XPS, which corresponds to the results shown in Figure 5. This layer probably protected the residual Co atoms in the subsurface alloy phases from leaching out. As we described above, Pd atoms in some easily dissolvable phases, for example, solid solutions and intermetallic compounds of PdCo_3 (L1_2 phase) [42], probably resulted in thick Pd skin layers that incorporated some relatively stable phases, for example, fcc Pd_3Co (L1_2 phase) and fct Pd_1Co_1 (L1_0 phase).

Electron diffraction (Figure 10(d)) reveals such presence of alloy domains. The diffraction pattern is assignable to a face-centered tetragonal structure with lattice parameters of $a = 4.9 \text{ \AA}$ and $c = 2.5 \text{ \AA}$, or a hexagonal close packing (hcp) structure with lattice parameters of $a = 2.8 \text{ \AA}$ and $c = 4.1 \text{ \AA}$, observed at [111] direction (for determining details,

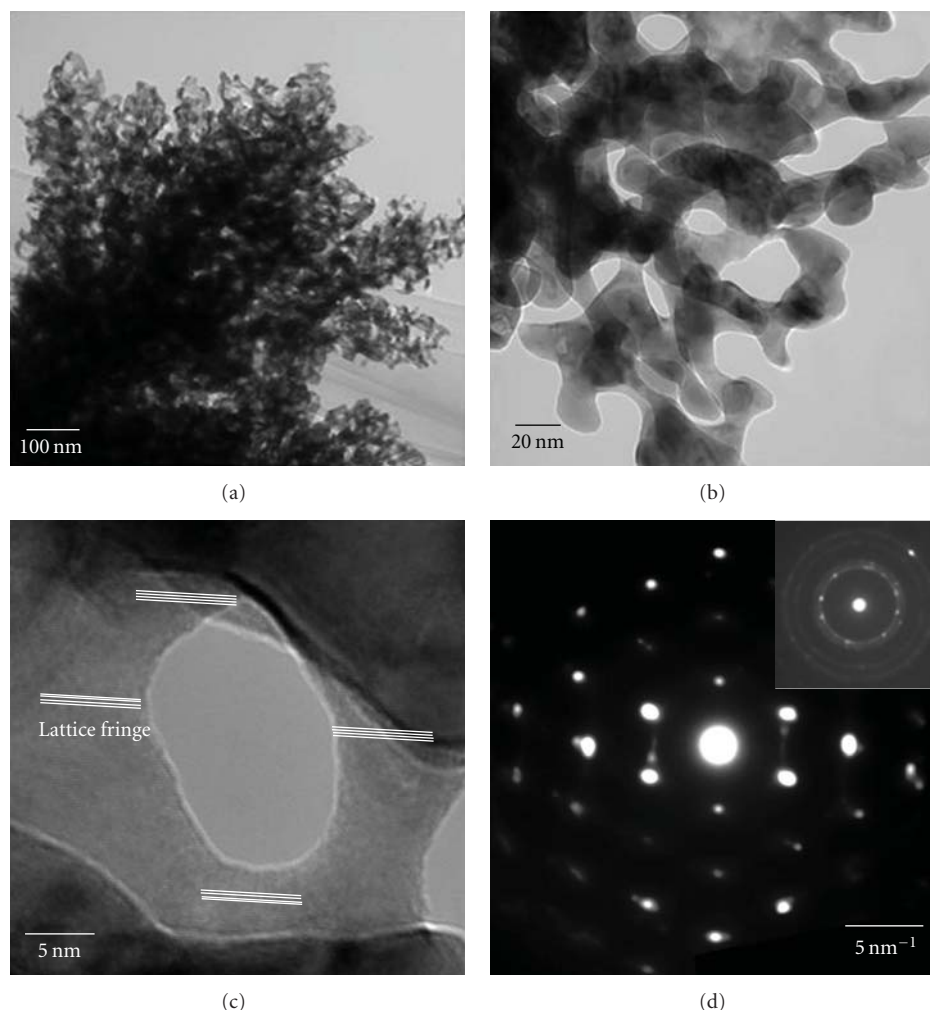


FIGURE 10: TEM images (a–c) and selected-area electron diffraction pattern (d) of nanoporous PdCo dendrites synthesized by the combination of electrodeposition and dealloying. The parallel lines in “c” show the direction of lattice fringes. The diffraction pattern was collected at 200 kV with a camera length of 1.0 m. The inset in “d” is another diffraction pattern. Reproduced with permission from [29]. Copyright 2010, RSC.

further investigation is needed). Compared with fcc Pd ($a = 3.90 \text{ \AA}$), fcc Co ($a = 3.54 \text{ \AA}$) and hcp Co ($a = 2.51 \text{ \AA}$ and $c = 4.09 \text{ \AA}$), whichever, this pattern can be assignable to an alloy phase. In addition, we could obtain weak polycrystalline fcc ED pattern as shown in the inset, this might be assignable to the surface Pd skin layer, considering the fact that a fcc pattern was obtained by XRD. Thus, we can conclude that the nanoporous dendrites contained both crystalline pure Pd skin layer and fct or hcp PdCo alloy phase.

4. Comparison as Catalyst Layers for Microfuel Cells

Figure 11 compares CVs of the PdCo catalysts synthesized. Electrochemical response of the nanoporous dendrite was apparently larger than nanoporous thin film and nonporous dendrite. The roughness factor of the nanoporous dendrite was determined to be ca. 290. This value is more than twentyfold of the value of the PdCo dendrite without nanopores

(ca. 13), indicating a positive effect of the formation of nanopores even though the nanoporous one is a few times thicker than the nonporous one (ca. $1.5 \mu\text{m}$). This quite large surface area is expected to improve the electrode performance. The roughness factors were compared also in Table 1.

ORR activities of the PdCo catalysts synthesized are compared in Table 1. Apparently, the electrode performances of the nanoporous catalysts are higher than those of nonporous ones, and the nanoporous dendrite exhibited the best performance. This is simply because of its large surface area. The onset potentials were $\sim 0.7 \text{ V}$ versus Ag/AgCl, which is by 0.1 V more positive than pure Pd catalyst and comparable to pure Pt catalyst. In terms of specific activity, most of PdCo alloys were comparable to Pt catalyst at 0.65 V and became better at 0.60 V. Thus, we confirmed positive effect of alloying.

The activity of nanoporous PdCo thin film was ~ 200 times higher than that of pure Pd catalyst and still a few times

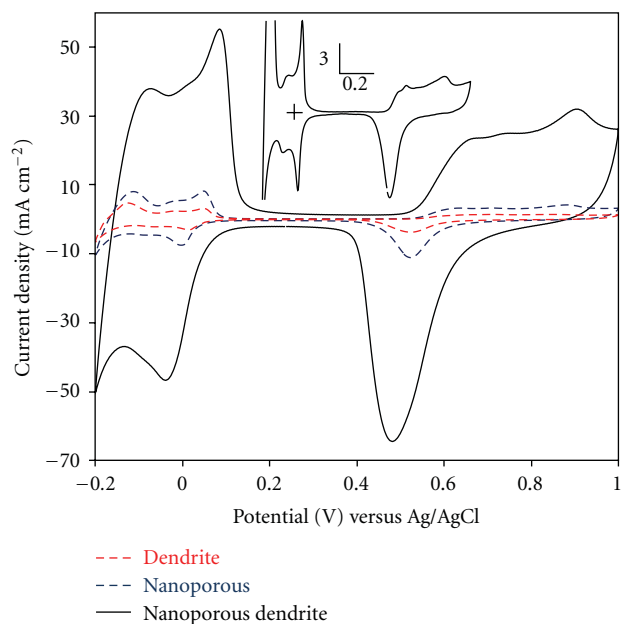


FIGURE 11: Comparison of cyclic voltammograms of the PdCo dendrite (dashed red line), nanoporous PdCo thin film (dotted blue line), and nanoporous PdCo dendrite (black solid line) scanned in 0.5 M H_2SO_4 deaerated with N_2 at 50 mV s^{-1} . The inset shows voltammogram of the nanoporous dendrite scanned at 5 mV s^{-1} .

higher than the PdCo alloys which did not exhibit the apparent peak shift of Pd $3d$ XPS (i.e., PdCo dendrite, PdCo thin film and nanoporous PdCo dendrite). Therefore, we conclude that the lattice contraction of the surface Pd-skin is the most important, and the nanoporous PdCo thus obtained had an active surface as well as the large surface area.

The higher activity than Pt catalyst is because of the preferably small Tafel slope, which indicates that the rate-determining step of ORR on the nanoporous PdCo thin film was different from Pt catalyst. As discussed previously [60], all of the PdCo catalysts synthesized by electrochemical methods had small Tafel slopes as shown in Table 1. Those values are apparently smaller than those of PdCo catalysts synthesized by other techniques ($60\text{--}70 \text{ mV decade}^{-1}$). This unique property of such PdCo catalysts synthesized by electrochemical techniques is of significant importance for developing effective catalysts.

5. Conclusions

We have synthesized PdCo catalysts for microfuel cells by electrodeposition and electrochemical dealloying. The former technique successfully synthesized PdCo alloys selectively onto conductive Au substrates, and by changing the potential applied, morphologies of the deposits were tuned into thin films or dendrites. The latter technique successfully increased the electrochemically active surface area by roughly ten times. Thus, such combination of electrodeposition and dealloying was proved effective for synthesizing high-performance electrodes for microsystems.

In terms of fuel cell catalyst, the PdCo nanostructures exhibited better activity for oxygen reduction reaction than

Pt catalyst, especially in the potential range of interest for actual fuel cell operation (0.8 V versus NHE). This is because of the smaller Tafel slope value of our PdCo catalysts. We believe that detailed analyses on such unique Tafel slope values, which have been obtained only for such PdCo catalysts synthesized by electrochemical methods, are needed and of quite importance for developing effective fuel cell catalysts.

6. Experimental

6.1. Synthesis. PdCo thin film was electrodeposited at -10 mA cm^{-2} for 60 s, and PdCo dendrite was deposited at -200 mA cm^{-2} for 5 s. The dendrite was modified by further deposition at -0.75 V versus Ag/AgCl for 10 s. This potential was consistent with the deposition potential of the PdCo thin film at -10 mA cm^{-2} . The deposition bath contained 76 mM $[\text{Pd}(\text{NH}_3)_4]\text{Cl}_2$, 34 mM CoCl_2 , 78 mM NH_4Cl and 120 mM malonic acid ($\text{pH} = 9.1$, adjusted by NH_4OH).

Nanoporous PdCo flat film was synthesized as follows. First, Co-rich PdCo thin film was electrodeposited at -0.9 V versus Ag/AgCl for 10 min in a solution containing 34 mM $[\text{Pd}(\text{NH}_3)_4]\text{Cl}_2$, 76 mM CoCl_2 , 76 mM NH_4Cl and 268 mM malonic acid at $14 \pm 2^\circ\text{C}$. This solution was prepared by mixing (i) a Pd solution containing 68 mM $[\text{Pd}(\text{NH}_3)_4]\text{Cl}_2$ and 152 mM NH_4Cl ($\text{pH} = 10$ adjusted by NH_4OH) and (ii) a Co solution containing 152 mM CoCl_2 and 536 mM malonic acid ($\text{pH} = 10$ adjusted by NH_4OH), in a volume ratio of 1 : 1. Then, the solution was aged for 3 days at 14°C . The PdCo film thus obtained was electrochemically dealloyed for 6 h at 0.6 V in 0.5 M H_2SO_4 deaerated with N_2 ($\sim 22^\circ\text{C}$).

Nanoporous PdCo dendrites with hierarchical porosity were synthesized as follows. First, Co-rich PdCo dendrites were electrodeposited by applying a galvanic pulse (on: -40 mA cm^{-2} for 1 s; off: 2 s; 500 cycles) in a bath of the same composition for synthesizing nanoporous thin film but without the aging treatment. Then, the electrodeposits were dealloyed by immersing in an air-saturated 0.5 M H_2SO_4 at 60°C overnight ($\sim 15 \text{ h}$).

For these deposition experiments, a conventional three-electrode cell was used. The reference and the counter electrodes were a Ag/AgCl (KCl-saturated) electrode and a Pt coil, respectively. The working electrode was a flat Au thin film (200 nm thick), which was deposited on silicon substrate with 20-nm Ti adhesion layer by electron-beam evaporation [11].

6.2. Characterization. The morphology was observed using a high-resolution scanning electron microscope (HR-SEM) (S-5500, Hitachi). The composition was determined by energy dispersive X-ray fluorescence spectroscopy or by inductively coupled plasma atomic emission spectroscopy. The surface composition and the surface elemental state were evaluated by X-ray photoelectron spectroscopy (XPS) using an Mg target. The crystal structure was examined by means of X-ray diffractometry (XRD) using a $\text{Cu K}\alpha$ radiation.

The surfaces of the synthesized catalysts were electrochemically cleaned by scanning in a 0.5 M H_2SO_4 solution deaerated with N_2 in the potential range of $+0.2$ to 1.0 V versus Ag/AgCl at 50 mV s^{-1} . The electrochemical response

was evaluated by cyclic voltammetry (CV) in a 0.5 M H₂SO₄ deaerated with N₂ in the potential range of -0.2 to +1.0 V versus Ag/AgCl at 50 mV s⁻¹. The roughness factor was calculated based on the double-layer capacitance in the CVs (8.6 mF cm⁻²) [11]. The activity for the oxygen reduction reaction was evaluated by linear sweep voltammetry (LSV) in an oxygen-saturated 0.5 M H₂SO₄ solution from the open circuit potential.

Acknowledgments

This work was partly supported by Grant-in-Aid for Specially Promoted Research "Establishment of Electrochemical Device Engineering" and by the Global COE program "Practical Chemical Wisdom" from the Ministry of Education, Culture, Sports, Science, and Technology (MEXT), Japan. S. Tominaka acknowledges Grant-in-Aid for Young Scientists B (22750174) and World Premier International Research Center Initiative (WPI Initiative) on "Materials Nanoarchitectonics", MEXT, Japan.

References

- [1] S. Tominaka, S. Ohta, H. Obata, T. Momma, and T. Osaka, "On-chip fuel cell: micro direct methanol fuel cell of an air-breathing, membraneless, and monolithic design," *Journal of the American Chemical Society*, vol. 130, no. 32, pp. 10456–10457, 2008.
- [2] S. Motokawa, M. Mohamedi, T. Momma, S. Shoji, and T. Osaka, "MEMS-based design and fabrication of a new concept micro direct methanol fuel cell (μ -DMFC)," *Electrochemistry Communications*, vol. 6, no. 6, pp. 562–565, 2004.
- [3] S. Tominaka, H. Nishizeko, S. Ohta, and T. Osaka, "On-chip fuel cells for safe and high-power operation: investigation of alcohol fuel solutions," *Energy and Environmental Science*, vol. 2, no. 8, pp. 849–852, 2009.
- [4] S. Tominaka, H. Obata, and T. Osaka, "On-chip direct methanol fuel cells of a monolithic design: consideration on validity of active-type system," *Energy and Environmental Science*, vol. 2, no. 8, pp. 845–848, 2009.
- [5] S. Tominaka, S. Ohta, T. Osaka, and R. Alkire, "Prospects of on-chip fuel cell performance: improvement based on numerical simulation," *Energy and Environmental Science*, vol. 4, no. 1, pp. 162–171, 2011.
- [6] S. Tominaka, H. Nishizeko, J. Mizuno, and T. Osaka, "Bendable fuel cells: on-chip fuel cell on a flexible polymer substrate," *Energy and Environmental Science*, vol. 2, no. 10, pp. 1074–1077, 2009.
- [7] H. Nakano, K. Dokko, J. I. Sugaya, T. Yasukawa, T. Matsue, and K. Kanamura, "All-solid-state micro lithium-ion batteries fabricated by using dry polymer electrolyte with micro-phase separation structure," *Electrochemistry Communications*, vol. 9, no. 8, pp. 2013–2017, 2007.
- [8] D. Golodnitsky, V. Yufit, M. Nathan et al., "Advanced materials for the 3D microbattery," *Journal of Power Sources*, vol. 153, no. 2, pp. 281–287, 2006.
- [9] D. Niwa, K. Omichi, N. Motohashi, T. Homma, and T. Osaka, "Organosilane self-assembled monolayer-modified field effect transistors for on-chip ion and biomolecule sensing," *Sensors and Actuators*, vol. 108, no. 1–2, pp. 721–726, 2005.
- [10] R. Popovtzer, T. Neufeld, D. Biran, E. Z. Ron, J. Rishpon, and Y. Shacham-Diamand, "Novel integrated electrochemical nanobiochip for toxicity detection in water," *Nano Letters*, vol. 5, no. 6, pp. 1023–1027, 2005.
- [11] S. Tominaka, T. Momma, and T. Osaka, "Electrodeposited Pd-Co catalyst for direct methanol fuel cell electrodes: preparation and characterization," *Electrochimica Acta*, vol. 53, no. 14, pp. 4679–4686, 2008.
- [12] T. Osaka, H. Iida, S. Tominaka, and T. Hachisu, "New trends in nanoparticles: syntheses and their applications to fuel cells, health care, and magnetic storage," *Israel Journal of Chemistry*, vol. 48, no. 3–4, pp. 333–347, 2008.
- [13] M. Paunovic and M. Schlesinger, *Fundamentals of Electrochemical Deposition*, John Wiley & Sons, Hoboken, NJ, USA, 2006.
- [14] R. M. Penner, "Hybrid electrochemical/chemical synthesis of quantum dots," *Accounts of Chemical Research*, vol. 33, no. 2, pp. 78–86, 2000.
- [15] S. Tominaka, S. Ohta, T. Momma, and T. Osaka, "An electrodeposited Pd-Co cathode catalyst for a microfabricated direct methanol fuel cell," in *Proceedings of the 212th ECS Meeting*, vol. 11, pp. 1369–1377, Washington, DC, USA, October 2007.
- [16] Y. Yamauchi, H. Kitoh, T. Momma, T. Osaka, and K. Kuroda, "Development of microfabrication process of mesoporous Pt via "Solvent-Evaporation-Mediated Direct Physical Casting": selective deposition into sloped microchannels," *Science and Technology of Advanced Materials*, vol. 7, no. 5, pp. 438–445, 2006.
- [17] G. S. Attard, P. N. Bartlett, N. R. B. Coleman, J. M. Elliott, J. R. Owen, and J. H. Wang, "Mesoporous platinum films from lyotropic liquid crystalline phases," *Science*, vol. 278, no. 5339, pp. 838–840, 1997.
- [18] S. Tominaka, C. W. Wu, T. Momma, K. Kuroda, and T. Osaka, "Perpendicular mesoporous Pt thin films: electrodeposition from titania nanopillars and their electrochemical properties," *Chemical Communications*, no. 25, pp. 2888–2890, 2008.
- [19] Y. Yamauchi and K. Kuroda, "Rational design of mesoporous metals and related nanomaterials by a soft-template approach," *Chemistry*, vol. 3, no. 4, pp. 664–676, 2008.
- [20] J. Erlebacher, M. J. Aziz, A. Karma, N. Dimitrov, and K. Sieradzki, "Evolution of nanoporosity in dealloying," *Nature*, vol. 410, no. 6827, pp. 450–453, 2001.
- [21] J. Rugolo, J. Erlebacher, and K. Sieradzki, "Length scales in alloy dissolution and measurement of absolute interfacial free energy," *Nature Materials*, vol. 5, no. 12, pp. 946–949, 2006.
- [22] K. Wagner, S. R. Brankovic, N. Dimitrov, and K. Sieradzki, "Dealloying below the critical potential," *Journal of the Electrochemical Society*, vol. 144, no. 10, pp. 3545–3555, 1997.
- [23] K. Sieradzki, N. Dimitrov, D. Movrin, C. McCall, N. Vasiljevic, and J. Erlebacher, "The dealloying critical potential," *Journal of the Electrochemical Society*, vol. 149, no. 8, pp. B370–B377, 2002.
- [24] J. Erlebacher, "An atomistic description of dealloying porosity evolution, the critical potential, and rate-limiting behavior," *Journal of the Electrochemical Society*, vol. 151, no. 10, pp. C614–C626, 2004.
- [25] Y. Ding, M. Chen, and J. Erlebacher, "Metallic mesoporous nanocomposites for electrocatalysis," *Journal of the American Chemical Society*, vol. 126, no. 22, pp. 6876–6877, 2004.
- [26] S. Tominaka, T. Hayashi, Y. Nakamura, and T. Osaka, "Mesoporous PdCo sponge-like nanostructure synthesized by electrodeposition and dealloying for oxygen reduction reaction," *Journal of Materials Chemistry*, vol. 20, no. 34, pp. 7175–7182, 2010.
- [27] S. Tominaka, "Facile synthesis of nanostructured gold for microsystems by the combination of electrodeposition and dealloying," *Journal of Materials Chemistry*, vol. 21, pp. 9725–9730, 2011.

- [28] S. Tominaka, M. Shigeto, H. Nishizeko, and T. Osaka, "Synthesis of mesoporous PtCu film modified with Ru submonolayer as catalyst for methanol electrooxidation," *Chemical Communications*, vol. 46, no. 47, pp. 8989–8991, 2010.
- [29] S. Tominaka, Y. Nakamura, and T. Osaka, "Nanostructured catalyst with hierarchical porosity and large surface area for on-chip fuel cells," *Journal of Power Sources*, vol. 195, no. 4, pp. 1054–1058, 2010.
- [30] J. L. Fernández, V. Raghuvver, A. Manthiram, and A. J. Bard, "Pd-Ti and Pd-Co-Au electrocatalysts as a replacement for platinum for oxygen reduction in proton exchange membrane fuel cells," *Journal of the American Chemical Society*, vol. 127, no. 38, pp. 13100–13101, 2005.
- [31] K. Lee, O. Savadogo, A. Ishihara, S. Mitsushima, N. Kamiya, and K. I. Ota, "Methanol-tolerant oxygen reduction electrocatalysts based on Pd-3D transition metal alloys for direct methanol fuel cells," *Journal of the Electrochemical Society*, vol. 153, no. 1, pp. A20–A24, 2006.
- [32] W. E. Mustain, K. Kepler, and J. Prakash, "Investigations of carbon-supported CoPd₃ catalysts as oxygen cathodes in PEM fuel cells," *Electrochemistry Communications*, vol. 8, no. 3, pp. 406–410, 2006.
- [33] W. E. Mustain, K. Kepler, and J. Prakash, "CoPd_x oxygen reduction electrocatalysts for polymer electrolyte membrane and direct methanol fuel cells," *Electrochimica Acta*, vol. 52, no. 5, pp. 2102–2108, 2007.
- [34] V. Raghuvver, A. Manthiram, and A. J. Bard, "Pd-Co-Mo electrocatalyst for the oxygen reduction reaction in proton exchange membrane fuel cells," *Journal of Physical Chemistry B*, vol. 109, no. 48, pp. 22909–22912, 2005.
- [35] O. Savadogo, K. Lee, K. Oishi, S. Mitsushima, N. Kamiya, and K. -I. Ota, "New palladium alloys catalyst for the oxygen reduction reaction in an acid medium," *Electrochemistry Communications*, vol. 6, no. 2, pp. 105–109, 2004.
- [36] M. Grden, M. Lukaszewski, G. Jerkiewicz, and A. Czerwinski, "Electrochemical behaviour of palladium electrode: oxidation, electrodisolution and ionic absorption," *Electrochimica Acta*, vol. 53, pp. 7583–7598, 2008.
- [37] J. L. Fernández, D. A. Walsh, and A. J. Bard, "Thermodynamic guidelines for the design of bimetallic catalysts for oxygen electroreduction and rapid screening by scanning electrochemical microscopy. M-Co (M: Pd, Ag, Au)," *Journal of the American Chemical Society*, vol. 127, no. 1, pp. 357–365, 2005.
- [38] V. Raghuvver, P. J. Ferreira, and A. Manthiram, "Comparison of Pd-Co-Au electrocatalysts prepared by conventional borohydride and microemulsion methods for oxygen reduction in fuel cells," *Electrochemistry Communications*, vol. 8, no. 5, pp. 807–814, 2006.
- [39] M. H. Shao, T. Huang, P. Liu et al., "Palladium monolayer and palladium alloy electrocatalysts for oxygen reduction," *Langmuir*, vol. 22, no. 25, pp. 10409–10415, 2006.
- [40] Y. Wang and P. B. Balbuena, "Design of oxygen reduction bimetallic catalysts: ab-initio-derived thermodynamic guidelines," *Journal of Physical Chemistry B*, vol. 109, no. 40, pp. 18902–18906, 2005.
- [41] L. Zhang, K. Lee, and J. Zhang, "The effect of heat treatment on nanoparticle size and ORR activity for carbon-supported Pd-Co alloy electrocatalysts," *Electrochimica Acta*, vol. 52, no. 9, pp. 3088–3094, 2007.
- [42] T. Mallát, J. Petró, S. Szabó, and L. Marcziš, "Investigation of Pd + Co alloys by the linear potential sweep method," *Journal of Electroanalytical Chemistry*, vol. 208, no. 1, pp. 169–173, 1986.
- [43] Y. Matsuo, "Ordered alloys in the cobalt-palladium system," *Journal of the Physical Society of Japan*, vol. 32, no. 4, pp. 972–978, 1972.
- [44] F. L. Williams and D. Nason, "Binary alloy surface compositions from bulk alloy thermodynamic data," *Surface Science*, vol. 45, no. 2, pp. 377–408, 1974.
- [45] J. A. Abys, I. Boguslavsky, and H. K. Straschil, "Composition for electroplating palladium alloys and electroplating process using that composition," in *US Patent*, 1999.
- [46] Y. Q. Zheng and H. Z. Xie, "Two malonato coordination polymers: syntheses and crystal structures of M(H₂O)₂(C₃H₂O₄) with M = Co and Ni, C₃H₄O₄ = malonic acid," *Journal of Coordination Chemistry*, vol. 57, no. 17–18, pp. 1537–1543, 2004.
- [47] J. F. Moulder, W. F. Stickle, P. E. Sobol, and K. D. Bomben, *Handbook of X-ray Photoelectron Spectroscopy*, Physical Electronics, Eden Prairie, Minn, USA, 1992.
- [48] T. Toda, H. Igarashi, and M. Watanabe, "Role of electronic property of Pt and Pt alloys on electrocatalytic reduction of oxygen," *Journal of the Electrochemical Society*, vol. 145, no. 12, pp. 4185–4188, 1998.
- [49] T. Toda, H. Igarashi, and M. Watanabe, "Enhancement of the electrocatalytic O₂ reduction on Pt-Fe alloys," *Journal of Electroanalytical Chemistry*, vol. 460, no. 1–2, pp. 258–262, 1999.
- [50] J. P. Chevillot, J. Farcy, C. Hinnen, and A. Rousseau, "Electrochemical study of hydrogen interaction with palladium and platinum," *Journal of Electroanalytical Chemistry*, vol. 64, no. 1, pp. 39–62, 1975.
- [51] J. F. Drillet, A. Ee, J. Friedemann, R. Kötz, B. Schnyder, and V. M. Schmidt, "Oxygen reduction at Pt and Pt70Ni30 in H₂SO₄/CH₃OH solution," *Electrochimica Acta*, vol. 47, no. 12, pp. 1983–1988, 2002.
- [52] R. K. Raman, G. Murgia, and A. K. Shukla, "A solid-polymer electrolyte direct methanol fuel cell with a methanol-tolerant cathode and its mathematical modelling," *Journal of Applied Electrochemistry*, vol. 34, no. 10, pp. 1029–1038, 2004.
- [53] Y. Suo, L. Zhuang, and J. Lu, "First-principles considerations in the design of Pd-alloy catalysts for oxygen reduction," *Angewandte Chemie*, vol. 46, no. 16, pp. 2862–2864, 2007.
- [54] T. Biegler, D. A. J. Rand, and R. Woods, "Limiting oxygen coverage on platinized platinum; relevance to determination of real platinum area by hydrogen adsorption," *Journal of Electroanalytical Chemistry*, vol. 29, no. 2, pp. 269–277, 1971.
- [55] S. Trasatti and A. Petrii, "Real surface area measurements in electrochemistry," *Pure and Applied Chemistry*, vol. 63, no. 5, pp. 711–734, 1991.
- [56] H. Angerstein-Kozłowska, B. E. Conway, A. Hamelin, and L. Stoicoviciu, "Elementary steps of electrochemical oxidation of single-crystal planes of Au Part II. A chemical and structural basis of oxidation of the (111) plane," *Journal of Electroanalytical Chemistry*, vol. 228, no. 1–2, pp. 429–453, 1987.
- [57] M. Baldauf and D. M. Kolb, "A hydrogen adsorption and absorption study with ultrathin Pd overlayers on Au(111) and Au(100)," *Electrochimica Acta*, vol. 38, no. 15, pp. 2145–2153, 1993.
- [58] L. J. Wan, T. Suzuki, K. Sashikata, J. Okada, J. Inukai, and K. Itaya, "In situ scanning tunneling microscopy of adsorbed sulfate on well-defined Pd(111) in sulfuric acid solution," *Journal of Electroanalytical Chemistry*, vol. 484, no. 2, pp. 189–193, 2000.

- [59] N. Hoshi, M. Kuroda, O. Koga, and Y. Hori, "Infrared reflection absorption spectroscopy of the sulfuric acid anion on low and high index planes of palladium," *Journal of Physical Chemistry B*, vol. 106, no. 35, pp. 9107–9113, 2002.
- [60] S. Tominaka, T. Hayashi, Y. Nakamura, and T. Osaka, "Mesoporous PdCo sponge-like nanostructure synthesized by electrodeposition and dealloying for oxygen reduction reaction," *Journal of Materials Chemistry*, vol. 20, no. 34, pp. 7175–7182, 2010.

Research Article

Hydrogen Adsorption on Palladium and Platinum Overlayers: DFT Study

Igor A. Pašti,¹ Nemanja M. Gavrilov,¹ and Slavko V. Mentus^{1,2}

¹ Faculty of Physical Chemistry, University of Belgrade, Studentski trg 12-16, 11158 Belgrade, Serbia

² Serbian Academy of Sciences and Arts, Knez Mihajlova 35, 11185 Belgrade, Serbia

Correspondence should be addressed to Igor A. Pašti, igor@ffh.bg.ac.rs

Received 15 February 2011; Accepted 13 May 2011

Academic Editor: Milan M. Jaksic

Copyright © 2011 Igor A. Pašti et al. This is an open access article distributed under the Creative Commons Attribution License, which permits unrestricted use, distribution, and reproduction in any medium, provided the original work is properly cited.

Hydrogen adsorption on twenty different palladium and platinum overlayer surfaces with (111) crystallographic orientation was studied by means of periodic DFT calculations on the GGA-PBE level. Palladium and platinum overlayers here denote either the Pd and Pt mono- and bilayers deposited over (111) crystallographic plane of Pd, Pt, Cu, and Au monocrystals or the (111) crystallographic plane of Pd and Pt monocrystals with inserted one-atom-thick surface underlayer of Pd, Pt, Cu, and Au. The attention was focused on the bond lengths, hydrogen adsorption energetics, mobility of adsorbed hydrogen, and surface reactivity toward hydrogen electrode reactions. Both the ligand and strain effects were considered, found to lead to a significant modification of the electronic structure of Pd and Pt overlayers, described through the position of the d-band center, and tuning of the hydrogen adsorption energy in the range that covers approximately 120 kJ mol^{-1} . Mobility of hydrogen adsorbed on studied overlayers was found to be determined by hydrogen-metal binding energy. Obtained results regarding Pd layers on Pt(111) and Au(111) surfaces, in conjunction with some of the recent experimental data, were used to explain its electrocatalytic activity towards hydrogen evolution reaction.

1. Introduction

Hydrogen evolution/oxidation reaction (*her/hor*) is one of the most important electrochemical reactions from both theoretical and practical aspects. The search for new efficient electrocatalysts is motivated by the high price of platinum, which is known as the most efficient metal for *her/hor* [1]. This search necessary involves the investigation of *her/hor* on well-defined surfaces which was identified as essential in order to link the atomic-/molecular-level properties of the electrochemical interface to the macroscopic kinetic parameters.

The first insights in structural sensitivity of *her/hor* on Pt(hkl) were provided by Marković et al. [2, 3] and Barber et al. [4, 5]. The modification of known electrocatalyst surfaces was often undertaken to improve their catalytic activity. For instance, well-defined Pt surfaces, modified by palladium monolayers, have been used as model systems in electrocatalysis by Marković et al. [6]. They demonstrated that Pd_{ML}/Pt(111) surface was more active than the Pt(111)

surface. Baldauf and Kolb [7] found that palladium grows pseudoisomorphically on Au(111) surface, while Kibler [8] recently demonstrated that catalytic performance of Pd-modified Au(111) electrodes depends on the number of deposited Pd layers. Kibler et al. [9] investigated the activity of several Pd-monolayer-modified surfaces demonstrating the linear relationship between the hydrogen desorption potential and the shift of the d-band center. The activity of platinum overlayers has been extensively studied primarily with respect to oxygen reduction reaction, and there is a lot of experimental data available in the literature [10, 11].

Greeley and Mavrikakis [12] emphasized the importance of the detailed knowledge of hydrogen chemistry of different surfaces, related closely to the practical importance of hydrogen. The authors screened promising solid catalysts by means of computational approach and reported the existence of the class of surfaces with low hydrogen binding energies and low barriers for hydrogen dissociation. Among the computational studies of hydrogen adsorption on well-defined surfaces, the work of Roudgar and Groß [13, 14] offers

a deep insight into hydrogen chemisorption on Pd-modified Au(111) and Au(100) surfaces. The authors invoked both electronic structure of surfaces and geometrical effect in order to analyze adsorption and applied the obtained results to rationalize the reactivity of palladium nanoparticles supported by Au(111) surface, studied by Meier et al. [15]. Significant amount of theoretical results regarding electrocatalytic activity of well-defined surfaces was published recently by Schmickler and coworkers [16, 17]. For example, Santos et al. [17] reported the study of electrocatalytic activity of various Pd monolayers on different M(111) substrates and identified the main factors determining the electrocatalytic activity of the studied surfaces. They pointed out that catalytic performance of a particular nanostructure can be very different for oxidation versus reduction direction of any electrode reaction.

In the present work, we investigated systematically the hydrogen adsorption on 20 different palladium and platinum overlayer surfaces with a common (111) crystallographic orientation. Since the published experimental investigations indicate that, on platinum metals surfaces, *her* proceeds usually at high-coverage of strongly adsorbed hydrogen (underpotential deposited hydrogen, H_{upd}) [1, 18], we focused the attention on the high-coverage states, $\theta = 1$ ML. Finally, for selected surfaces, we discussed the correlation of calculated hydrogen adsorption energies to the experimentally determined catalytic activities.

2. Computational Details

The DFT calculations have been performed using PWscf code of the quantum ESPRESSO distribution [19]. Ultrasoft pseudopotentials have been generated on the GGA-PBE level of approximation [20]. Basis set has been approximated by a set of plane waves with kinetic energy less than 435 eV, while charge density cutoff was 10 times higher. Equilibrium lattice parameters (a_0) of clean metals considered in this study were obtained by fitting $E_{\text{tot}} = f(a)$ curve, where E_{tot} is the total energy of bulk metal unit cell. Infinite surface has been obtained using periodic boundary conditions.

The (111) type surfaces have been modeled using (1×1) hexagonal supercell geometry with seven metal layers and 20 Å thick vacuum layer separating periodic images along the z -direction of the cell. First 2D Brillouin zone has been sampled by $7 \times 7 \times 1$ set of k points generated through the general Monkhorst-Pack scheme [21]. Hydrogen adsorption was allowed on the both sides of the slab in order to prevent electrostatic coupling of the periodic images. Both the slab and the adsorbate layer have been fully relaxed until the forces acting on atoms were below 0.05 eV \AA^{-1} . The adsorption was analyzed at four distinct adsorption sites: fcc and hcp (threefold sites), bridge (twofold site) and atop (single-fold site). The energy of adsorption (E_{ads}) was calculated using the following equation:

$$E_{\text{ads}} = \frac{1}{2}(E_{\text{slab}+2\text{H}} - (E_{\text{slab}} + E_{\text{H}_2})), \quad (1)$$

where $E_{\text{slab}+2\text{H}}$, E_{slab} , and E_{H_2} are the total energy of the slab with one hydrogen atom adsorbed on each side of the slab,

the total energy of the isolated slab, and the total energy of the isolated H_2 molecule, respectively.

As previously discussed by Conway and Jerkiewicz [18], the presence of water has negligible effect on the H-Pt bond energy. Therefore, the water molecules were not included in the presented calculations. Strictly speaking, the described results correspond to the gas-phase adsorption of hydrogen, but we extended the results to hydrogen adsorption on metal-solution interface in order to discuss the catalytic performance of some of the surfaces included in this study (Section 3.3). The procedure described here is, however, common practice in computational studies of the problems related to electrochemistry [23].

3. Results and Discussions

3.1. Adsorption Trends: Equilibrium Geometries and Energetics. In this section, the dissociative hydrogen adsorption on transition and noble metal surfaces (Cu, Au, Pt, or Pd), modified by palladium and platinum overlayers, was analyzed. The obtained equilibrium lattice parameters, used throughout the present work, were 3.63 Å for Cu, 4.00 Å for Pd, 4.01 Å for Pt, and 4.17 Å for Au. The Pd and Pt monolayers on other (111) metal surfaces are denoted here as $\text{Pd}_{\text{ML}}/\text{M}(111)$ or $\text{Pt}_{\text{ML}}/\text{M}(111)$. Depending on the lattice mismatch, these surfaces subject either compressive or tensile strain. The effects of strain on the electronic structure of the surfaces are already well documented in the literature [24]. However, electronic structure of surface atoms is inevitably modified by the presence of M atoms in the second layer. This is known as the ligand effect [25], which can be estimated separately from the strain effect by inserting a monolayer of other metal, M_{und} , under the first surface layer of the analyzed metal surface. This class of systems is denoted here as $\text{M}_{\text{und}}/\text{Pd}(111)$ or $\text{M}_{\text{und}}/\text{Pt}(111)$ (subscript “und” stands for underlayer; for such systems Greeley and Mavrikakis [12] used the term subsurface alloys). In order to observe the strain effects only, Mavrikakis et al. [26] proposed to introduce the lateral expansion or compression of the lattice. In the present study, the surfaces with double monolayers of palladium or platinum ($(\text{Pd}_{\text{ML}})_2/\text{M}(111)$ or $(\text{Pt}_{\text{ML}})_2/\text{M}(111)$) were used in order to analyze the strain effects separated from the ligand effect, rather than applying the expansion of the metal lattice parallel to the surface. This is the way to make the obtained results comparable to the experimental data.

Table 1 summarizes the results relating to the electronic structure of studied surfaces (expressed through the position of the d-band center [27]), preferential adsorption sites, and hydrogen adsorption energy (the last one was calculated by means of (1)).

The stability of the structure of the studied surfaces is a rather important issue, having in mind that surface electronic structure and their catalytic activity may vary with the variation of structural parameters. We address these problems to the studies available in the literature [12, 28]. While some of the systems included in the present study are well known and could be easily realized experimentally,

TABLE 1: The d-band centers ($E_{d\text{-band}}$), the preferential adsorption sites for H adsorption, and the energies of hydrogen adsorption (E_{ads}) on studied surfaces. Both palladium and platinum surfaces are divided by bolded lines in three groups, depending on their exposition to the compressive strain (the first group), the absence of the surface strain (the second group), or the presence of the tensile strain (the third group).

Palladium surface				Platinum surfaces			
Label	$E_{d\text{-band}}/\text{eV}$	Adsorption site	E_{ads}/eV	Label	$E_{d\text{-band}}/\text{eV}$	Adsorption site	E_{ads}/eV
Pd _{ML} /Cu(111)	-2.42	hcp	0.10	Pt _{ML} /Cu(111)	-2.82	atop	0.40
(Pd _{ML}) ₂ /Cu(111)	-2.09	fcc	-0.16	(Pt _{ML}) ₂ /Cu(111)	-2.62	atop	-0.05
Pd(111)	-1.71	fcc	-0.48	Pt _{ML} /Pd(111)	-2.15	fcc	-0.38
Cu _{und} /Pd(111)	-1.76	fcc	-0.40	(Pt _{ML}) ₂ /Pd(111)	-2.42	fcc	-0.39
Pt _{und} /Pd(111)	-1.81	fcc	-0.49	Pt(111)	-2.13	fcc	-0.43
Au _{und} /Pd(111)	-1.63	fcc	-0.46	Cu _{und} /Pt(111)	-2.14	fcc	-0.18
Pd _{ML} /Pt(111)	-1.80	fcc	-0.51	Pd _{und} /Pt(111)	-2.10	fcc	-0.41
(Pd _{ML}) ₂ /Pt(111)	-1.68	fcc	-0.51	Au _{und} /Pt(111)	-1.91	fcc	-0.39
Pd _{ML} /Au(111)	-1.37	fcc	-0.60	Pt _{ML} /Au(111)	-1.75	fcc	-0.60
(Pd _{ML}) ₂ /Au(111)	-1.50	fcc	-0.62	(Pt _{ML}) ₂ /Au(111)	-2.02	fcc	-0.58

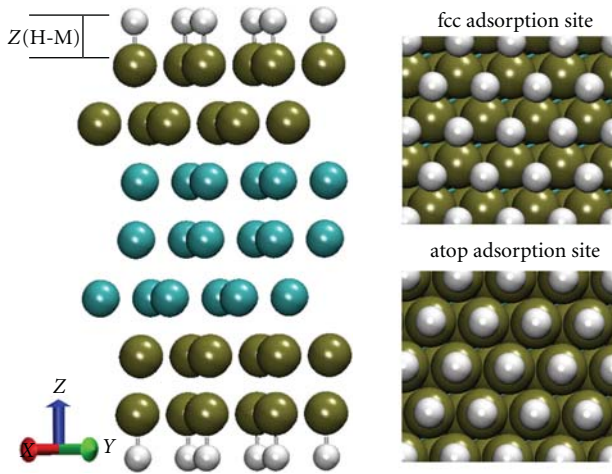


FIGURE 1: A side view of the metal slabs applied for hydrogen adsorption analysis and a perpendicular view of the surface covered with hydrogen adsorbed on fcc and atop site. For graphical representations, Visual Molecular Dynamics was used [22].

some of them, such as $M_{\text{und}}/\text{Pd}(111)$ and $M_{\text{und}}/\text{Pt}(111)$, are supposed only theoretically, for the purpose of analysis of the effects of electronic structure on the catalytic activity and on adsorption trends.

The vertical displacement between the centers of the adsorbed hydrogen atoms and the metal atoms in the first surface layer was used to characterize equilibrium geometry of adsorbed hydrogen on a given surface (adsorption height, as defined by Roudgar and Groß [13], $Z(\text{H-M})$, Figure 1). The parameter $Z(\text{H-M})$ was found to be the smallest for the adsorption on threefold sites, medium on the bridge sites, and largest for the adsorption on the atop sites. The other equilibrium structure parameter is the metal-hydrogen bond length ($d(\text{H-M})$). The trend in bond lengths is opposite

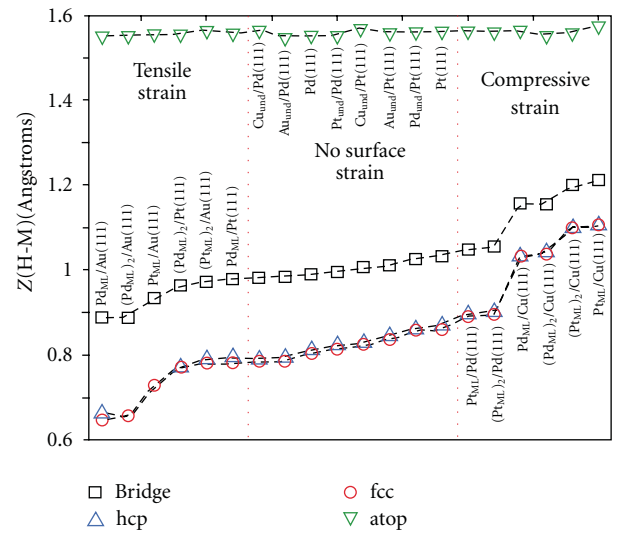


FIGURE 2: Calculated values of $Z(\text{H-M})$ on fcc (circles), hcp (up triangles), atop (down triangles), and bridge sites (squares).

to the trend in $Z(\text{H-M})$ distances. The bond length is the smallest for the atop adsorption (when the equation $Z(\text{H-M}) = d(\text{H-M})$ holds) while the largest one is for the adsorption on threefold sites. The interesting trends in calculated $Z(\text{H-M})$ values were found observing the effects of surface strain on the equilibrium geometries (Figure 2). Namely, the $Z(\text{H-M})$ values of H atoms adsorbed on an atop site was found to be invariant to the type of the surface, with the relative variation not exceeding 0.5%. Furthermore, the surfaces exposed to a tensile strain were found to have the smallest $Z(\text{H-M})$ distance. On the other hand, the surfaces exposed to a compressive strain have the highest $Z(\text{H-M})$. Between these two types of surfaces are the surfaces with no surface strain. The rationale for observed trends can be found in the work

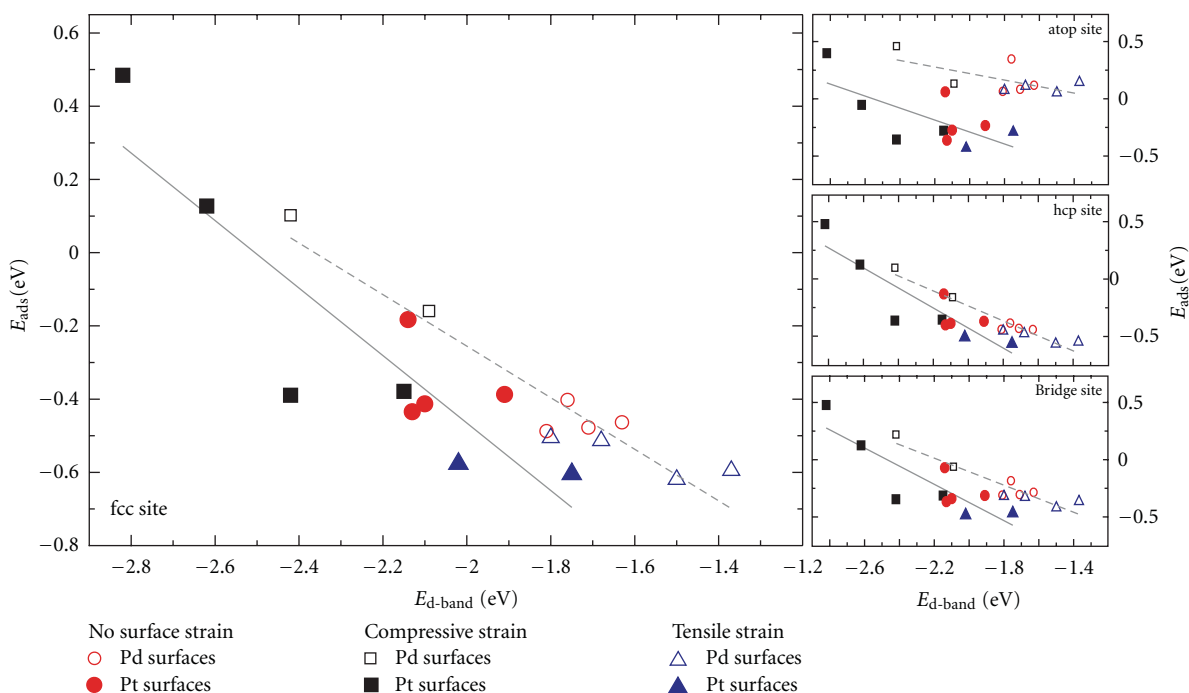


FIGURE 3: The energies of adsorption (E_{ads}) plotted versus the position of the d-band center ($E_{\text{d-band}}$) for the studied surfaces. The surfaces with compressive strain are marked by squares; the surfaces with no strain are represented by circles, while the surfaces with tensile strain are marked by triangles. The empty symbols relate to Pd surfaces, while the full symbols relate to Pt surfaces. The best linear fits for platinum surfaces are given by solid lines, while the best linear fits for palladium surfaces are given by dashed lines. Positive values of E_{ads} mean the endothermic dissociative adsorption of H_2 and vice versa.

of Roudgar and Groß [13]. These authors demonstrated, for Pd layers on Au surfaces, that the expansion of the crystal lattice parallel to the observed surface causes the decrease of $Z(\text{H-Pd})$, to preserve an ideal H-Pd bond length related closely to the coordination of adsorbed H atom. Indeed, the site-dependent metal-hydrogen bond lengths calculated in the present study are almost identical for all studied surfaces. The average values of $d(\text{H-M})$ are 1.834 Å for fcc site, 1.836 Å for hcp site, 1.739 Å for bridge site, and 1.558 Å for atop site. The relative variation of $d(\text{H-M})$ over the entire group of studied surfaces (both Pd and Pt overlayer surfaces), for any of four adsorption sites, did not exceed 1%. The differences in calculated $Z(\text{H-M})$ of the hydrogen atom adsorbed at different adsorption sites justify the fact that the ideal H-M bond distance depends on the coordination of adsorbed H atom. Results presented here unambiguously confirm these reasoning for a wide range of surfaces. Location of the adsorbed hydrogen atom with respect to the surface might have some important consequences on the mobility of adatoms and catalytic performance of the particular surface, as will be discussed later.

Hydrogen adsorption energies are closely related to the catalytic activity of solid surfaces toward *hor/her*. Parsons demonstrated volcano type of dependence having the maximum around $\Delta G^0 = 0$, when logarithm of exchange current density for *her* was plotted versus standard Gibbs free energy of adsorption of H (ΔG^0) [29]. This topic was reviewed in detail by Trasatti [30, 31]. Hydrogen adsorption energies

on surfaces studied in this paper cover a range of about 120 kJ mol^{-1} , which is the result of substantial modification of electronic structure of studied surfaces ($E_{\text{d-band}}$, Table 1). Following the work of Hammer and Nørskov [27], the correlation between the adsorption energy and the position of the d-band center of the surface atoms is expected. Namely, the interaction of the adsorbate states with the metal d-states can be considered as a perturbation of the main adsorbate-substrate states, that is the interaction of adsorbate states with the substrate sp-states. The strength of the perturbation depends on (a) the fractional filling of substrate d-states (f , $f(\text{Pt}) < f(\text{Pd})$ [24]), (b) matrix elements for the interaction with the substrate (V_{ad}^2 , $V_{\text{ad}}^2(\text{Pt}) > V_{\text{ad}}^2(\text{Pd})$ [24]), and (c) the difference between the position of the adsorbate states and the substrate d-band center. As Pt and Pd atoms have different d-band fractional fillings and different matrix elements for interaction with adsorbates, Pd and Pt surfaces are not expected to fall onto the same E_{ads} versus $E_{\text{d-band}}$ line. In the cases of multicoordinated sites, good correlations between E_{ads} and $E_{\text{d-band}}$ were observed, with R^2 close to 0.75, while more pronounced scattering was evidenced in the case of atop adsorption site (Figure 3). As the theory of Hammer and Nørskov [27] does not treat all the factors able to contribute to the adsorbate-substrate bonding (e.g., the effects of the d-band widths are not considered), certain deviation from the linear relationship appears to be reasonable. It is interesting to note that adsorption parameters display higher sensitivity to the modification of

surface electronic structure in the case of Pt overlayers than in the case of Pd overlayers. This may be explained by the fact that the slope of the dependence E_{ads} versus $E_{\text{d-band}}$ should be proportional to $(1-f)V_{\text{ad}}^2$ [27], which is higher for platinum than for palladium.

Similarly to the equilibrium geometries, the surface activities depend strongly on the surface strain. The tensile strain shifts the d-band center towards the Fermi level, which is accompanied by negative shift in E_{ads} . The compressive strain lowers the position of d-band center and reduces the reactivity on the studied surfaces. Surfaces with no lateral strain display intermediate reactivity. Kibler [8] identified an upshift of 0.35 eV of the d-band center of the first Pd layer in Pd_{ML}/Au(111) as the main reason of enhanced reactivity in comparison to the Pd(111) surface. Our calculation gave the up-shift of 0.34 eV. It is noteworthy (Table 1) that the introduction of the Au underlayer in Pd(111) surface causes destabilization (upshift) of palladium d-band center. Even more pronounced effect is observed in the case of Pt_{ML}/Au(111) and Au_{und}/Pt(111) surfaces (Table 1).

Connected to the results presented here, Inderwildi et al. [32] analyzed modification of transition metal d-states in transition metal-coinage metal alloys surfaces in the case of Rh-Ag alloys and attributed an increased reactivity of the surfaces to the buildup of Rh d-states below the Fermi energy. Michaelides [33] pointed out possible importance of transition metal-coinage metal alloys in view of the fact that this class of materials can provide high surface reactivity and superior catalytic performance by subtle modification of surface composition.

3.2. Mobility of Adsorbed Hydrogen. As explained by Nilekar and coworkers [34], mobility of adsorbed species on transition metal surfaces, which is the function of E_{ads} , might play a key role in the transport of species during the catalytic reactions, growth of the surface nanostructures, and many other important processes. Roudgar and Groß [13] reported that the absolute values of E_{ads} are sensitive, but the adsorption trends on (111) surfaces are almost insensitive toward the change of surface coverage, allowing the analysis given below. To be more precise, although the absolute values of adsorption energies are expected to be affected by surface coverage, relative differences among different adsorption sites are expected to remain unaffected, as well as relative differences among different surfaces. Nevertheless, this is an interesting subject that should be subjected to detailed calculations. Following the work of Nilekar et al. [34], we found a linear relationship between the binding energy of initial/final state ($BE_{\text{IS}}/BE_{\text{FS}}$) for surface diffusion and the binding energy of the transition state for surface diffusion (BE_{TS} , Figure 4). As the initial states preferential adsorption sites were taken to identify transition state, first plausible diffusion paths connecting high-symmetry sites on studied surfaces were established, and transition state was chosen to be the lowest adsorption site on the path connecting the initial and the final state. The final states are chosen to be adsorption sites located after the transition state along the diffusion path with a condition to be energetically more favorable than

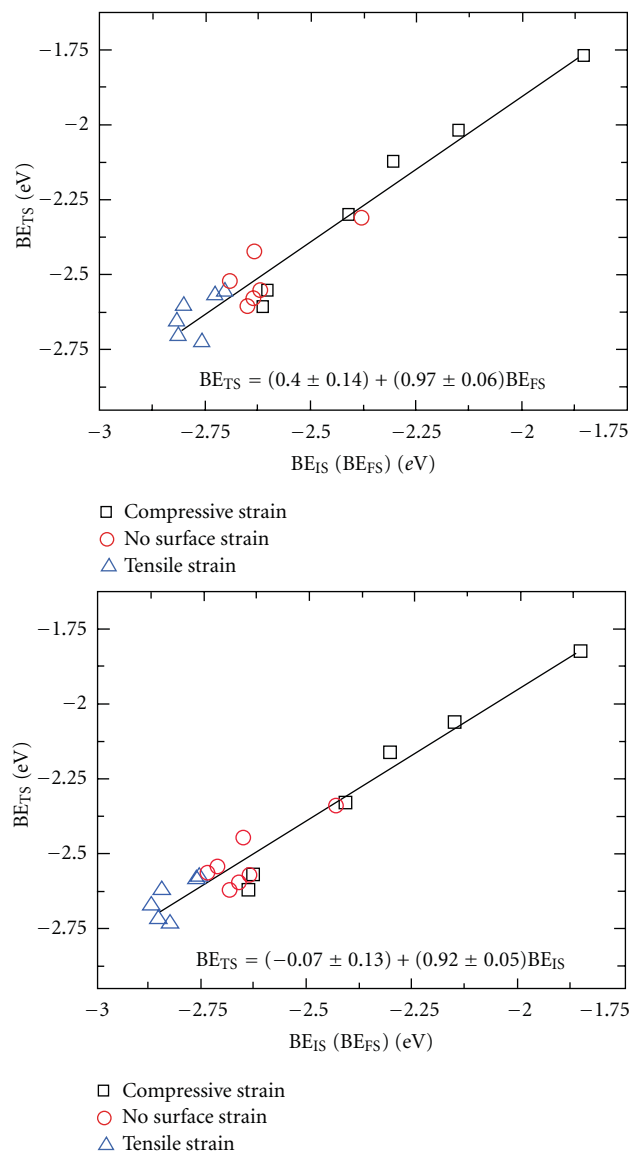


FIGURE 4: Lower pane: the binding energy of transition state for H diffusion (BE_{TS}) plotted versus the binding energy of initial state (BE_{IS}); upper pane: the binding energy of transition state for H diffusion (BE_{TS}) plotted versus the binding energy of final state (BE_{FS}). In order to calculate hydrogen binding energies we refer adsorbed state to the isolated H atom. Binding energy of H_2 molecule was estimated here to amount to 4.50 eV.

transition state [35]. For most of the studied surfaces, the path runs from the fcc site (initial state), through the bridge site (transition state), to the neighboring hcp site (final state).

The results presented here for hydrogen mobility on palladium and platinum surfaces agree very well with results published by Nilekar et al. [34] for clean transition metal surfaces and seven adsorbates in either atomic or molecular state (25 substrate/adsorbate systems in total). This sounds with the finding of Nilekar et al. that potential energy barriers (calculated as $BE_{\text{TS}} - BE_{\text{IS}}$) for surface diffusion can be estimated as approximately one-tenth of binding energy of the initial state (BE_{IS}) for surface diffusion (more precisely,

12% of BE_{IS}) [34]. Furthermore, detailed calculations of vibrational entropy of the initial and transition states for surface diffusion [34] showed that for the diffusion on transition metal surfaces there is no compensation between the activation energy and the preexponential factor. The authors showed that the preexponential factor for surface diffusion, proposed to amount to 10^{13} s^{-1} , may be considered as a constant. Nevertheless, experimentally determined values may differ from this value by several orders of magnitude. To reconcile these opposing results, one may say that preexponential factors for surface diffusion are similar on different transition metals, without specifying its value, and that the potential energy barrier is what actually determines adsorbate mobility. These calculations, in general, indicate that the strength of adsorbate-substrate interaction determines the mobility of adsorbed species.

One may expect that the geometrical effects should display the impact on the mobility of adsorbed phase and contribute to certain scatter of diffusion energy barrier obtained by strict calculations based on the above-proposed scheme. Hence, the presented estimation of the potential energy barriers should be considered as a useful rule of thumb, as emphasized by Nilekar et al. [34]. Nevertheless, the range of hydrogen binding energies (Figure 4) indicates that the average diffusion barrier is approximately 25 kJmol^{-1} (for the sake of comparison, the experimentally determined value for Pt(111) is 30 kJmol^{-1} [36]). This exceeds the thermal energy at room temperature by one order of magnitude and indicates reduced 2D mobility of adsorbed hydrogen. This is further supported by a large negative change of standard molar entropy accompanying the hydrogen adsorption on Pt surface [37].

Figure 4 demonstrates another important consequence of the surface strain. Namely, potential energy surface for hydrogen-surface interaction is expected to be rather rough, and the compressive strain makes it smooth. In connection with the $Z(\text{H-M})$ changes (Section 3.1, Figure 2), one may conclude that the applied tensile strain results in deep potential wells of stable adsorption sites and location of adsorbed hydrogen rather in the surface than on the surface. On contrary, compressive strain, smoothing the potential energy surface for hydrogen-metal interaction, squeezes out the adsorbed hydrogen (and exposes it to the solution phase, if one deals with the metal-solution interface).

3.3. Catalytic Performance of Selected Surfaces. Here we would like to make some correlation of presented results with the available experimental data relating to the catalytic behavior of precious metal surfaces toward the *her/hor*. As reviewed by Marković and Ross [1], $\text{Pd}_{\text{ML}}/\text{Pt}(111)$ surface provides unique reactivity for *her* [6], being found at the apex of the volcano curve. Activation energy for *her* on this surface was found to be 9 kJmol^{-1} , which is half of the activation energy on clean Pt(111) surface, indicating that kinetics of *her* is significantly enhanced on $\text{Pd}_{\text{ML}}/\text{Pt}(111)$. Compared to Pt(111) surface, on which *her* proceeds at $\theta = 0.67 \text{ ML}$ of underpotentially adsorbed hydrogen (H_{upd}) on $\text{Pd}_{\text{ML}}/\text{Pt}(111)$, *her* proceeds at $\theta = 1 \text{ ML}$ of H_{upd} [1].

Considering H_{upd} as an inhibitor species of the kinetics of *her*, Marković and Ross [1] emphasized the importance of hydrogen adsorption energetics for understanding of catalytic activity and suggested that this (paradoxical) activity of $\text{Pd}_{\text{ML}}/\text{Pt}(111)$ surface can be explained by a strong ($\text{Pd}_{\text{ML}}/\text{Pt}(111)$)- H_{upd} interaction and/or weaker H_{upd} - H_{upd} interaction, compared to Pt(111) surface. The authors also stated that some amount of H_{upd} might sit in deeper potential wells of the threefold hollow sites, being more in the surface than on the surface. Our results suggest that the adsorption of H on $\text{Pd}_{\text{ML}}/\text{Pt}(111)$ surface is favored by 8 kJmol^{-1} compared to the clean Pt(111) surface, which is close to the change of the activation energy for *her* and supports the findings that the coverage of H_{upd} at Nernst potential is higher on $\text{Pd}_{\text{ML}}/\text{Pt}(111)$ surface. The distance of adsorbed H atoms from the surface was found to be less in the case of $\text{Pd}_{\text{ML}}/\text{Pt}(111)$ surface than in the case of Pt(111) surface (Figure 2). In addition, the reduced mobility of adsorbed H (Section 3.2) unambiguously confirms that adsorbed hydrogen sits in deeper potential wells (of fcc sites) on $\text{Pd}_{\text{ML}}/\text{Pt}(111)$ surface than on Pt(111) surface. The strongly adsorbed H (H_{upd}) on $\text{Pd}_{\text{ML}}/\text{Pt}(111)$ leaves the atop sites available for the formation of weakly bound overpotentially deposited hydrogen (H_{opd}), which is considered as an intermediate for *her* [1, 18]. In contrast to $\text{Pd}_{\text{ML}}/\text{Pt}(111)$ surface, clean Pt(111) surface has empty sites for H_{opd} formation, and in this case, H_{upd} and H_{opd} are only formally distinguished by the potential range in which deposition occurs and not by the type of adsorption site [18]. Following the discussion given by Conway and Jerkiewicz [16], one may conclude that the high coverage of H_{upd} on $\text{Pd}_{\text{ML}}/\text{Pt}(111)$ results in the shift of (kinetically relevant) ΔG^0 of adsorbed H toward the theoretically significant $\Delta G^0 = 0$ condition proposed by Parsons [29]. This is, namely, the consequence of the fact that H_{upd} and H_{opd} occupy different adsorption sites.

The results presented here for Pd-modified Au(111) surface are in excellent agreement with the ones reported by Roudgar and Groß [13] for flat palladium nanoparticles on Au(111) surfaces [15]. Our results, together with the ones by Roudgar and Groß [13], suggest that hydrogen adsorption energy increases when going from both the Pd(111) and $\text{Pd}_{\text{ML}}/\text{Au}(111)$ surfaces toward the $(\text{Pd}_{\text{ML}})_2/\text{Au}(111)$ surface. Recently, Kibler [8] reported the activity of different number of Pd layers deposited on Au(111) surface toward *her*. All, Pd(111), $\text{Pd}_{\text{ML}}/\text{Au}(111)$, and $(\text{Pd}_{\text{ML}})_2/\text{Au}(111)$ surfaces, display strong interaction with hydrogen and lie on one branch of the volcano curve [8, Figure 1]. This indicates that desorption of H_2 is rate-determining step for *her*. Namely, the Heyrowsky reaction is known to be the rate-determining step on palladium [38] and can be reasonably assumed to hold for Pd-modified Au(111) surfaces. Qualitatively, the trends in exchange current densities of *her* on these three surfaces could be rationalized when the logarithm of exchange current density is plotted versus hydrogen chemisorption energy, referred to isolated H_2 molecule (this value may be easily converted to H-metal bond energy using H_2 bond energy). We found here linear relationship between calculated E_{ads} and experimentally determined $\log(j_0)$ values for *her* on the mentioned three surfaces (Figure 5). The decrease of the rate

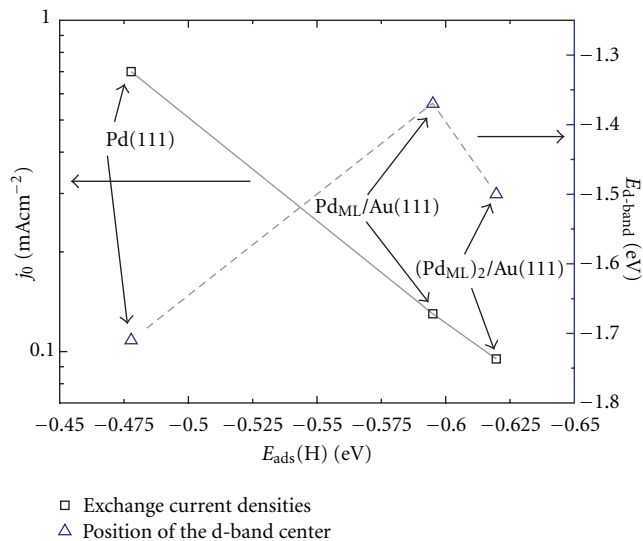


FIGURE 5: The literature data for standard exchange current densities (j_0) for *her* on Pd(111) and Pd-modified Au(111) surfaces (squares) [8], and calculated positions of $E_{d\text{-band}}$ (triangles) plotted versus calculated hydrogen adsorption energies.

of *her* may be correlated to strong H-metal interaction, which limits the rate of H_2 desorption. In Figure 5, also the position of $E_{d\text{-band}}$ is presented as the function of E_{ads} . Although $E_{d\text{-band}}$ was in certain cases demonstrated as a valuable tool for establishing the electrocatalytic trends [39], this example demonstrates that one should be reserved in generalizations of this kind.

4. Conclusions

In the present study, the hydrogen adsorption on different palladium and platinum overlayer surfaces was studied by DFT method, from the aspects of the equilibrium geometries, the surface mobility, and the rate of electrode reactions. The effects of the surface strain and the electronic environment of surface layer (ligand effect) on the equilibrium geometries and adsorption energetics were estimated. It was shown that the mobility of adsorbed H may be directly correlated to the strength of adsorbate-substrate interaction. Presented results can be appended to the results of Nilekar and coworkers [34], showing that the relationship between the adsorption energies and the mobility of adsorbate holds not only for clean transition metal surfaces, but also for metal overlayers and subsurface alloys. In view of the previously evidenced absence of the compensation effect for surface diffusion on the transition metal surfaces [34], the mobility of adatoms may be considered to be completely determined by the strength of substrate-adsorbate interaction. In addition, the obtained results were used to analyze reactivity of $Pd_{ML}/Pt(111)$ and Pd-modified Au(111) surfaces toward the *her/hor*. For the explanation of the reactivity of $Pd_{ML}/Pt(111)$ surface, one has to take into account the adsorption energetics and the shape of the potential energy surface for the $(Pd_{ML}/Pt(111))\text{-H}$ interaction. The increase in coverage

of H_{upd} shifts the kinetically relevant ΔG^0 for H adsorption toward the theoretically significant $\Delta G^0 = 0$ condition, proposed for *her* by Parsons [29]. This is considered as a consequence of the difference in the adsorption sites occupied by H_{upd} and H_{opd} . However, for a rough explanation of the reactivity of Pd-modified Au(111) surfaces, the adsorption energetics was found to be sufficient, through the finding that linear relationship exists between the E_{ads} and the $\log(j_0)$. This linear dependence may be considered as a part of a branch of general volcano curve that correlates exchange current density for *her* to the hydrogen adsorption energy.

Acknowledgments

The authors are indebted to the Ministry of Science and Technological Development, Serbia, for the financial support under the Contract no. III45014. S.V. Mentus also acknowledges the support provided by the Serbian Academy of Science and Arts through the project "Electrocatalysis in the contemporary processes of energy conversion".

References

- [1] N. M. Marković and P. N. Ross Jr., "Surface science studies of model fuel cell electrocatalysts," *Surface Science Reports*, vol. 45, no. 4–6, pp. 117–229, 2002.
- [2] N. M. Marković, B. N. Grgur, and P. N. Ross Jr., "Temperature-dependent hydrogen electrochemistry on platinum low-index single-crystal surfaces in acid solutions," *Journal of Physical Chemistry B*, vol. 101, no. 27, pp. 5405–5413, 1997.
- [3] N. M. Marković, S. T. Sarraf, H. A. Gasteiger, and P. N. Ross, "Hydrogen electrochemistry on platinum low-index single-crystal surfaces in alkaline solution," *Journal of the Chemical Society*, vol. 92, no. 20, pp. 3719–3725, 1996.
- [4] J. Barber, S. Morin, and B. E. Conway, "Specificity of the kinetics of H_2 evolution to the structure of single-crystal Pt surfaces, and the relation between *opd* and *upd* H," *Journal of Electroanalytical Chemistry*, vol. 446, no. 1–2, pp. 125–138, 1998.
- [5] J. H. Barber and B. E. Conway, "Structural specificity of the kinetics of the hydrogen evolution reaction on the low-index surfaces of Pt single-crystal electrodes in 0.5 M dm^{-3} NaOH," *Journal of Electroanalytical Chemistry*, vol. 461, no. 1–2, pp. 80–89, 1999.
- [6] N. M. Marković, C. A. Lucas, V. Climent, V. Stamenković, and P. N. Ross, "Surface electrochemistry on an epitaxial palladium film on Pt(111): surface microstructure and hydrogen electrode kinetics," *Surface Science*, vol. 465, no. 1–2, pp. 103–114, 2000.
- [7] M. Baldauf and D. M. Kolb, "A hydrogen adsorption and absorption study with ultrathin Pd overlayers on Au(111) and Au(100)," *Electrochimica Acta*, vol. 38, no. 15, pp. 2145–2153, 1993.
- [8] L. A. Kibler, "Dependence of electrocatalytic activity on film thickness for the hydrogen evolution reaction of Pd overlayers on Au(111)," *Electrochimica Acta*, vol. 53, no. 23, pp. 6824–6828, 2008.
- [9] L. A. Kibler, A. M. El-Aziz, R. Hoyer, and D. M. Kolb, "Tuning reaction rates by lateral strain in a palladium monolayer," *Angewandte Chemie—International Edition*, vol. 44, no. 14, pp. 2080–2084, 2005.

- [10] J. Zhang, M. B. Vukmirovic, K. Sasaki, A. U. Nilekar, M. Mavrikakis, and R. R. Adzic, "Mixed-metal Pt monolayer electrocatalysts for enhanced oxygen reduction kinetics," *Journal of the American Chemical Society*, vol. 127, no. 36, pp. 12480–12481, 2005.
- [11] V. Stamenković, T. J. Schmidt, P. N. Ross, and N. M. Marković, "Surface composition effects in electrocatalysis: Kinetics of oxygen reduction on well-defined Pt₃Ni and Pt₃Co alloy surfaces," *Journal of Physical Chemistry B*, vol. 106, no. 46, pp. 11970–11979, 2002.
- [12] J. Greeley and M. Mavrikakis, "Alloy catalysts designed from first principles," *Nature Materials*, vol. 3, no. 11, pp. 810–815, 2004.
- [13] A. Roudgar and A. Groß, "Local reactivity of thin Pd overlayers on Au single crystals," *Journal of Electroanalytical Chemistry*, vol. 548, pp. 121–130, 2003.
- [14] A. Roudgar and A. Groß, "Local reactivity of metal overlayers: density functional theory calculations of Pd on Au," *Physical Review B*, vol. 67, no. 3, Article ID 033409, 4 pages, 2003.
- [15] J. Meier, K. A. Friedrich, and U. Stimming, "Novel method for the investigation of single nanoparticle reactivity," *Faraday Discussions*, vol. 121, pp. 365–372, 2002.
- [16] E. Santos, P. Quaino, P. F. Hindelang, and W. Schmickler, "Hydrogen evolution on a pseudomorphic Cu-layer on Ni(1 1 1)—a theoretical study," *Journal of Electroanalytical Chemistry*, vol. 649, no. 1-2, pp. 149–152.
- [17] E. Santos, P. Quaino, and W. Schmickler, "On the electrocatalysis of nanostructures: monolayers of a foreign atom (Pd) on different substrates M(1 1 1)," *Electrochimica Acta*, vol. 55, no. 14, pp. 4346–4352, 2010.
- [18] B. E. Conway and G. Jerkiewicz, "Relation of energies and coverages of underpotential and overpotential deposited H at Pt and other metals to the "volcano curve" for cathodic H₂ evolution kinetics," *Electrochimica Acta*, vol. 45, no. 25-26, pp. 4075–4083, 2000.
- [19] P. Giannozzi, S. Baroni, N. Bonini et al., "QUANTUM ESPRESSO: a modular and open-source software project for quantum simulations of materials," *Journal of Physics Condensed Matter*, vol. 21, no. 39, Article ID 395502, 2009.
- [20] J. P. Perdew, K. Burke, and M. Ernzerhof, "Generalized gradient approximation made simple," *Physical Review Letters*, vol. 77, no. 18, pp. 3865–3868, 1996.
- [21] H. J. Monkhorst and J. D. Pack, "Special points for Brillouin-zone integrations," *Physical Review B*, vol. 13, no. 12, pp. 5188–5192, 1976.
- [22] W. Humphrey, A. Dalke, and K. Schulten, "VMD: visual molecular dynamics," *Journal of Molecular Graphics*, vol. 14, no. 1, pp. 33–38, 1996.
- [23] M. T. M. Koper, "Ab initio quantum-chemical calculations in electrochemistry," in *Modern Aspects of Electrochemistry*, Number 36, C. G. Vayenas, B. E. Conway, and R. E. White, Eds., chapter 2, Kluwer Academic/Plenum Publishers, New York, NY, USA, 2003.
- [24] A. Ruban, B. Hammer, P. Stoltze, H. L. Skriver, and J. K. Nørskov, "Surface electronic structure and reactivity of transition and noble metals," *Journal of Molecular Catalysis A*, vol. 115, no. 3, pp. 421–429, 1997.
- [25] J. R. Kitchin, J. K. Nørskov, M. A. Barteau, and J. G. Chen, "Role of strain and ligand effects in the modification of the electronic and chemical Properties of bimetallic surfaces," *Physical Review Letters*, vol. 93, no. 15, pp. 156801–4, 2004.
- [26] M. Mavrikakis, B. Hammer, and J. K. Nørskov, "Effect of strain on the reactivity of metal surfaces," *Physical Review Letters*, vol. 81, no. 13, pp. 2819–2822, 1998.
- [27] B. Hammer and J. K. Nørskov, "Electronic factors determining the reactivity of metal surfaces," *Surface Science*, vol. 343, no. 3, pp. 211–220, 1995.
- [28] Y. Ma and P. B. Balbuena, "Pt surface segregation in bimetallic Pt₃M alloys: a density functional theory study," *Surface Science*, vol. 602, no. 1, pp. 107–113, 2008.
- [29] R. Parsons, "The rate of electrolytic hydrogen evolution and the heat of adsorption of hydrogen," *Transactions of the Faraday Society*, vol. 54, pp. 1053–1063, 1958.
- [30] S. Trasatti, "The work function in electrochemistry," *Advances in Electrochemical Science and Engineering*, vol. 10, pp. 213–321, 1977.
- [31] S. Trasatti, in *Handbook of Fuel Cells—Fundamentals, Technology and Applications*, W. Vielstich, A. Lamm, and H. A. Gasteiger, Eds., vol. 2, p. 88, John Wiley & Sons, Chichester, NY, USA, 2003.
- [32] O. R. Inderwildi, S. J. Jenkins, and D. A. King, "When adding an unreactive metal enhances catalytic activity: NO_x decomposition over silver-rhodium bimetallic surfaces," *Surface Science*, vol. 601, no. 17, pp. L103–L108, 2007.
- [33] A. Michaelides, "The unhappy marriage of transition and noble metal atoms: a new way to enhance catalytic activity? (A perspective on: "when adding an unreactive metal enhances catalytic activity: NO_x decomposition over silver-rhodium bimetallic surfaces" by O.R. Inderwildi, S.J. Jenkins, D.A. King)," *Surface Science*, vol. 601, no. 17, pp. 3529–3531, 2007.
- [34] A. U. Nilekar, J. Greeley, and M. Mavrikakis, "A simple rule of thumb for diffusion on transition-metal surfaces," *Angewandte Chemie—International Edition*, vol. 45, no. 42, pp. 7046–7049, 2006.
- [35] D. C. Ford, Y. Xu, and M. Mavrikakis, "Atomic and molecular adsorption on Pt(1 1 1)," *Surface Science*, vol. 587, no. 3, pp. 159–174, 2005.
- [36] E. G. Seebauer and L. D. Schmidt, "Surface diffusion of hydrogen on Pt(111): laser-induced thermal desorption studies," *Chemical Physics Letters*, vol. 123, no. 1-2, pp. 129–133, 1986.
- [37] B. E. Conway, H. Angerstein-Kozłowska, and W. B. A. Sharp, "Temperature and pressure effects on surface processes at noble metal electrodes. Part 1—entropy of chemisorption of H at Pt surfaces," *Journal of the Chemical Society, Faraday Transactions 1*, vol. 74, pp. 1373–1389, 1978.
- [38] W. Schmickler and S. Trasatti, "Comment on "trends in the exchange current for hydrogen evolution" [J. Electrochem. Soc., 152, J23 (2005)]," *Journal of the Electrochemical Society*, vol. 153, no. 12, Article ID 053612JES, pp. L31–L32, 2006.
- [39] V. R. Stamenkovic, B. S. Mun, M. Arenz et al., "Trends in electrocatalysis on extended and nanoscale Pt-bimetallic alloy surfaces," *Nature Materials*, vol. 6, no. 3, pp. 241–247, 2007.

Research Article

Synthesis, Characterization, and Electrochemical Study of Tetradentate Ruthenium-Schiff Base Complexes: Dioxygen Activation with a Cytochrome P450 Model Using 1- or 2-Methylimidazole as Axial Bases

Ali Ourari,¹ Mostefa Khelafi,¹ Djouhra Aggoun,¹ Gilles Bouet,² and Mustayeen A. Khan²

¹Laboratoire d'Électrochimie, d'Ingénierie Moléculaire et de Catalyse Rédox (LEIMCR), Faculté des Sciences de l'Ingénieur, Université Ferhat Abbas, Sétif 19000, Algeria

²SONAS, EA 921, Faculté de Pharmacie, Université d'Angers 16 Boulevard Daviers, 49045 Angers Cedex 01, France

Correspondence should be addressed to Ali Ourari, alourari@yahoo.fr

Received 18 September 2010; Revised 21 December 2010; Accepted 22 March 2011

Academic Editor: Milan M. Jaksic

Copyright © 2011 Ali Ourari et al. This is an open access article distributed under the Creative Commons Attribution License, which permits unrestricted use, distribution, and reproduction in any medium, provided the original work is properly cited.

Salicylaldehyde, 2-hydroxyacetophenone, and 3,5-dichlorosalicylaldehyde react with 1,2-diaminoethane to give three symmetrical Schiff bases H_2L^1 , H_2L^2 , and H_2L^3 , respectively. With Ru(III) ions, these ligands lead to three complexes: Ru(III)CIL¹ (**1**), Ru(III)CIL² (**2**), and Ru(III)CIL³ (**3**). The purity of these compounds was estimated by TLC technique and microanalysis while their structures were supported by the usual spectroscopic methods such as NMR, infrared, and electronic spectra. The cyclic voltammetry in acetonitrile showed irreversible waves for all three ligands. Under the same experimental conditions, it was proved that the ruthenium is coordinated in the three complexes **1**, **2**, and **3** showing quasireversible redox systems. The behavior of these complexes and their comparison with cytochrome P450 are investigated using them as catalysts in the presence of molecular oxygen with an apical nitrogen base: 1- or 2-methylimidazole.

1. Introduction

During the last decade, the tetradentate Schiff base complexes of transition metals have been extensively studied mainly with manganese, iron, cobalt, copper, and nickel [1–5] while those of ruthenium are relatively less studied [6]. Thus, it was demonstrated that such materials might be involved in several applications such as in catalysis [7] or electrocatalysis [8] by activating many small molecules like carbon dioxide [9] or molecular oxygen [10]. Here, we focus on the electrochemical study and the activation of molecular oxygen using the tetradentate ruthenium-Schiff base complexes, in order to substantially reduce its reduction potential, leading to electrocatalytic systems operating at lower potential values. So, the metabolic role of cytochrome P450 is well known [11] and its metabolic cycle is established [12]. In some steps, molecular dioxygen fixation, water elimination, and peroxo high oxidation state metal (i.e.,

Fe^{IV}) and so forth, are involved. In all cases, the active form of the coordinated iron ion is axially linked to a sulfur protein. Therefore, a large number of cytochrome P450 oxocomplexes, including the nonporphyrinic ligands such as Schiff base complexes, have been tested for their catalytic activity [13–17] and their electrocatalytic properties [8, 17–26]. Thus, new catalysts deriving from symmetrical tetradentate ruthenium-Schiff base complexes seem to be more and more attractive and efficient in catalysis [27, 28]. These new electrocatalytic systems have been less studied than those currently applied in catalysis [6].

Manganese(III), iron(III), cobalt(II), and ruthenium(III)-Schiff base complexes are mainly used in indirect electroreductions of halohydrocarbons [29, 30] or molecular oxygen [31–36] in order to epoxide olefins or to oxidize hydrocarbons. These reactions using electrocatalytic systems could be performed in homogeneous as well as in heterogeneous catalysis. This second case concerns the elaboration

of modified electrodes (ME) by covalent grafting of pyrrole or thiophene moieties via the etherification [37] or esterification [38] reactions involving a phenolic group. These materials for electrodes may also be used as amperometric sensors to detect various species: molecular dioxygen [39–42] and biomolecules like glucose [43–45]. Several studies have demonstrated the high efficiency of these electrocatalytic systems when operating in heterogeneous catalysis in a chemical-electrochemical pathway using modified electrodes based mainly upon organic polymer films containing the complex species covalently grafted as catalyst [35, 38, 46].

In this work, three complexes with ruthenium(III) ions are synthesized (Scheme 1) and characterized. Our main aim is to study these complexes as catalysts by cyclic voltammetry in the presence of molecular oxygen and of two axial bases; 1-methylimidazole and its position isomer 2-methylimidazole. Thus, the electrophile character on the metallic center increases when the basicity of the axial base is higher leading to a prompt reaction between oxygen and metal. This electrocatalytic system model of cytochrome P450 is mainly studied in the activation of small molecules among them the molecular oxygen. This study might also be supported by further applications such as epoxidation of olefins or oxidation of hydrocarbons or for other applications.

2. Experimental

2.1. Physical Measurements. The ^1H NMR spectra of the ligands were recorded with a Bruker AC 300 at 25°C in $\text{DMSO-}D_6$ as solvent. All chemical shifts are given in ppm using tetramethylsilane (TMS) as internal reference. The IR spectra were recorded using a Perkin-Elmer 1000-FTIR Spectrometer (KBr discs). The UV-visible spectra were obtained with a Unicam UV-300 Spectrophotometer. The microanalysis was performed on “Microanalyseur Flash EA1112CHNS Thermoelectron” (Laboratoire des Sciences Chimiques, Rennes-1 University, France). Cyclic voltammograms were performed with a Tacussel PJT Potentiostat Galvanostat, driven by Pilovit-Num. All measurements were carried out in a 5 mL Metrohm monocompartment cell equipped with a conventional three-electrodes system. The electrodes were polished with diamond paste and rinsed with large amounts of acetone and finally with the solvent. The working electrode was a disc of glassy carbon (5 mm diameter), the counter electrode was a platinum wire, and the reference electrode was a saturated calomel electrode (SCE), and all results are given versus SCE. The solvent was acetonitrile with a $10^{-3}\text{ mol}\cdot\text{L}^{-1}$ concentration for the studied complexes, and the ionic strength was maintained at $0.1\text{ mol}\cdot\text{L}^{-1}$ with tetra-*n*-butylammonium perchlorate (TBAP).

2.2. Chemicals. Organic chemicals, solvents, and ruthenium chloride $\text{RuCl}_3\cdot x\text{H}_2\text{O}$ were analytical grade, purchased from Aldrich France and used as received without any further purification except benzoic anhydride because it contains traces of benzoic acid. It was washed with aqueous solution (10%, w/w), a sodium hydrogencarbonate, and recrystallized from a toluene-petroleum ether by dropwise adding of

petroleum ether to toluene solution until a neat trouble. Then, the product was left overnight in refrigerator and the solid was recovered by filtration and washed with petroleum ether.

2.3. Syntheses of the Ligands. The ligands were prepared as previously reported in the literature [1, 22–25]. 60 mg (1 mmol) of diaminoethane in EtOH (8 cm^3) was added dropwise to 244 mg (2 mmol) of salicylaldehyde or its derivatives (EtOH, 12 cm^3). The mixture was stirred under argon atmosphere at room temperature for 2 hours. In the case of 2-hydroxyacetophenone the reaction was carried out under refluxing conditions for the same time. The resulting product was kept overnight at *ca.* 4°C . The solid was filtered, washed several times with diethyloxide, and its purity was checked by TLC using a mixture of $\text{CH}_2\text{Cl}_2/\text{MeOH}$ (9/1, v/v) as solvents.

Ligand H_2L^1 ($\text{R}_1 = \text{H}$, $\text{R}_2 = \text{H}$): solid with yellow color, R_f (0.64), yield (70%), ^1H nmr: $2\text{CH}_2\text{-N}$ (4H, s = 3.87), $2\text{N}=\text{CH}$ (2H, s = 8.60), $\text{H}_{\text{arom.}}$ (8H, m = 7.21), $\text{OH}_{\text{phenol}}$ (2H, s = 13.36).

Ligand H_2L^2 ($\text{R}_1 = \text{CH}_3$, $\text{R}_2 = \text{H}$): solid with yellow color, R_f (0.28), yield (77%), ^1H nmr: $2\text{CH}_2\text{-N}$ (4H, s = 3.90), $2\text{N}=\text{C}(\text{CH}_3)$ (6H, s = 2.40), $\text{H}_{\text{arom.}}$ (8H, m = 7.26), $\text{OH}_{\text{phenol}}$ (2H, s = 16.10).

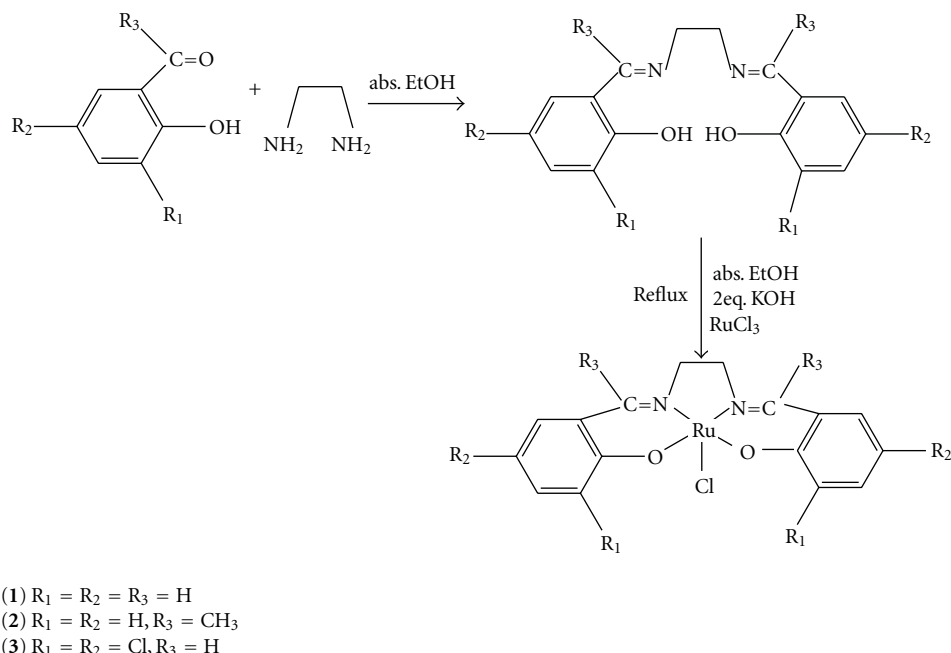
Ligand H_2L^3 ($\text{R}_1 = \text{H}$, $\text{R}_2 = \text{Cl}$): solid with yellow color, R_f (0.20), yield (90%), C, ^1H nmr: $2\text{CH}_2\text{-N}$ (4H, t = 4.00), $2\text{N}=\text{CH}$ (2H, s = 8.57), $\text{H}_{\text{arom.}}$ (4H, m = 6.91), $\text{OH}_{\text{phenol}}$ (2H, s = 12.71).

2.4. Preparation of the Complexes. The complexes were prepared as described in the literature [47] with a slight modification. A solution of the ligand H_2L^n ($n = 1, 2, 3$) in absolute EtOH (0.5 mmol, 10 cm^3), containing two molar equivalents of KOH, was added quickly to the ruthenium chloride, 0.5 mmol dissolved in 5 cm^3 of absolute EtOH. The mixture was heated for at least 12 h under argon atmosphere and kept overnight at 4°C . The complex was filtered, washed several times with a $\text{MeOH}/\text{H}_2\text{O}$ (1 : 1, v/v) mixture previously bubbled with Ar for 20–30 min (in order to avoid the oxygenation of the complex). Moreover, this operation was done as soon as possible in glove box under argon atmosphere for the same reasons. The purity of these complexes was checked by TLC under the same conditions as for the ligands.

3. Results and Discussion

The main analytical data for the complexes are given in Table 1.

3.1. Molecular Formulae. The elemental analysis (Table 1) indicated that the molecular formulae of our three complexes 1, 2, and 3 contain the potassium chloride (KCl). These results are similar to those obtained by Taqui Khan et al. [47] because the experimental procedure is almost the same. For the mass spectroscopy analysis, it has only given some fragments without the expected molecular peaks as it was mentioned in the literature [48, 49].



SCHEME 1: Complexes obtained according the reactions pathway.

TABLE 1: Analytical data for the complexes.

Compound	No.	Color	R_f^a	Yield (%) ^b	Analysis calc. (found)		
					C (%)	H (%)	N (%)
Ru(III)ClL ¹	1	Green	0.69	42	40.25 (40.56)	2.90 (3.09)	5.87 (6.09)
Ru(III)ClL ²	2	Green	0.70	40	42.77 (43.10)	3.56 (3.85)	5.54 (5.83)
Ru(III)ClL ³	3	Green	0.78	45	31.22 (31.48)	1.62 (1.78)	4.55 (4.79)

^aRetarding factor; noted R_f (TLC), ^bbased on mol number of starting material diaminoethane

TABLE 2: Spectroscopic data FT-IR and UV-Visible of the complexes.

Compound	Infrared (cm^{-1})			UV-vis λ (nm) [ϵ] ($M \cdot cm^{-1}$)					
	ν (O–H)	ν (C=N)	ν (C–O)	ν	ν	ν	ν	ν	ν
H ₂ L ¹	3090	1630	1293	252	[3714]			316	[1856]
Ru(III)ClL ¹		1610	1313	257	[916]	280	[500]	407	[250]
H ₂ L ²	3196	1623	1277	300	[1072]	350	[600]	398	[473]
Ru(III)ClL ²		1605	1345	300	[650]	388	[327]	467	[218]
H ₂ L ³	3380	1665	1274	254	[931]	325	[343]	382	[218]
Ru(III)ClL ³		1601	1274	250	[1249]	325	[315]	425	[500]

All compounds were obtained with the ligand dianion corresponding to the deprotonation of the two phenolic groups. Thus, these complexes of ruthenium appear to be cationic species with chloride anion as counter ion. So, the complexes formulae are supported by the elemental analysis, the spectroscopic data as IR, UV-Vis, and their electrochemical characteristics.

3.2. Infrared Spectra. The main vibration bands observed in the infrared spectra of the ligands and their ruthenium complexes are those of phenol, azomethine, and phenoxy groups (Table 2). For the ligands, a vibration band appearing as a broad one in the 3300–3400 cm^{-1} range indicates the presence of hydroxyl groups with hydrogen bonds. This band disappears in the cases of the corresponding complexes,

suggesting the coordination of the metal ion through the O phenolic atoms. The stretching vibration bands of the azomethine group is shifted to lower wavenumbers, indicating that the nitrogen atoms are involved in the coordination [14–16, 50–53] leading to OONN tetradentate ligands. On the opposite side, a shift to higher values of the $\nu(\text{C}-\text{O})$ vibration bands of phenoxy groups was observed, corresponding to the simultaneous strengthening of the electronic density of these bonds and coordination of the oxygen atoms to the metallic center. These results are in good agreement with those reported for similar structures [54, 55].

3.3. Electronic Spectra. The electronic spectrum of the unsubstituted H_2Salen , in DMSO, showed two absorption bands at 252 and 316 nm while those of the both remaining ligands H_2L^2 and H_2L^3 exhibit three absorption bands between 254 and 398 nm (Table 2). These bands were attributed to the $\pi-\pi^*$ and $n-\pi^*$ transitions. These free ligands show other absorption bands assigned to the $n-\pi^*$ and $n-\sigma^*$ transitions, respectively [56, 57]. The electronic spectra of the ruthenium(III) complexes showed new absorption bands due to the coordination of the ruthenium ion. This coordination is accompanied by an hypsochromic effect showing that the bands appearing in the 407–467 nm region, assigned to the $d-\pi^*$ charge transfer transitions, are overlapping with $\pi-\pi^*$ or $n-\pi^*$ transitions of the free ligands. These modifications in positions and intensities of the absorption bands confirm the coordination mode. As well, the molar extinction coefficients maxima ϵ_{max} is higher only for the tetrachlorinated complex **3** due to the huge electronic delocalisation caused by the presence of the metallic center bridging the two phenolic moieties comforted by the chlorine atoms as mentioned in the literature [56–59].

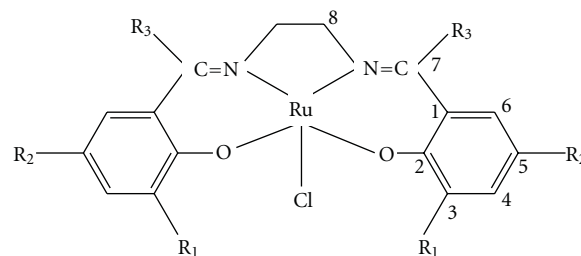
4. Electrochemical Study

In this study, we have, firstly, recorded the voltammograms of the complexes **1**, **2**, and **3** under nitrogen atmosphere using two axial bases 1- and 2-methylimidazole. Secondly, the same cyclic voltammetry studies were carried out under oxygen atmosphere.

4.1. Under Nitrogen Atmosphere. The cyclic voltammetry experiments were performed as described using acetonitrile solutions ($10^{-3} \text{ mol}\cdot\text{L}^{-1}$) and $10^{-1} \text{ mol}\cdot\text{L}^{-1}$ TBAP, 1- or 2-methylimidazole (1-Me-im or 2-Me-im $10^{-2} \text{ mol}\cdot\text{L}^{-1}$). In this case, the voltammograms were recorded under nitrogen atmosphere at various sweep rates.

4.1.1. Complexes. The carbon atoms in our three ruthenium (III)-complexes were numbered according to the structure illustrated by Scheme 2.

The voltamperograms of the complexes **1**, **2**, and **3** were recorded in the -1000 to $+100$ mV range. Each of them shows a redox system at the cathodic potentials appearing before -0.75 V corresponding to the redox system of molecular oxygen [60]. In this case, we have only studied



SCHEME 2: Numbering of carbon atoms of Ru(III)-complex.

the Ru(III)/Ru(II) redox system according to the following equation:



Where L^n : L^1 , L^2 , and L^3 . E and C are respectively electrochemical and chemical steps.

The electrochemical characteristics of these complexes such as $E_{1/2}$ values are -0.622 (**1**), -0.565 (**2**), and -0.507 V/SCE (**3**). These half-wave potentials ($E_{1/2} = (E_{\text{pa}} - E_{\text{pc}})/2$), involve E_{pa} and E_{pc} as potential values of oxidation and reduction waves of a redox couple. These $E_{1/2}$ values show an obvious shifting to the anodic potentials, caused by the substituents of the H_2Salen . Thus, the complex **2** is dimethylated at (C_7 , $\text{C}_{7'}$) positions while the third one **3** is rather tetrachlorinated at (C_3 , $\text{C}_{3'}$) and (C_5 , $\text{C}_{5'}$) positions. So, its complex **3**, exhibits a withdrawing electronic effect, inducing an $E_{1/2} = -0.507$ V which is significantly shifted to more anodic potentials as usually expected. The corresponding $\Delta E_p = (E_{\text{pa}} - E_{\text{pc}})$ values are stable around 65–75 mV for all three complexes. Their $I_{\text{pa}}/I_{\text{pc}}$ ratios increase with increasing sweep rate, converging to 1, suggesting quasireversible redox systems [61, 62] (Table 3). These results are consistent with the electronic effects due to the substituents such as methyl and chlorine grafted on the H_2Salen [22–25, 47].

4.1.2. Complexes with 1- or 2-Methylimidazole. The addition of an amount of 10^{-2} M of a nitrogen base like 1- or 2-Me-im., acting as an axial ligand bound to the metal center 10^{-3} M, leads to a well-defined redox system without any significant shift of $E_{1/2}$ values. An enhancement of the current peaks I_{pa} and I_{pc} is observed as previously mentioned for iron [63] or manganese complexes [22–25].

4.2. Under Oxygen Atmosphere

4.2.1. Complexes without Axial Base. In this case, the reduction wave of the Ru(III)/Ru(II) redox couple appears as two successive waves E_{pc1} and E_{pc2} indicating the electroreduction of two species. This may be explained by the following equations:

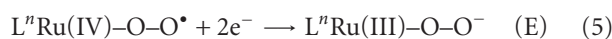
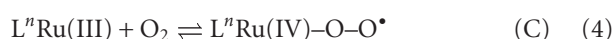
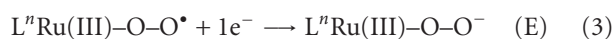
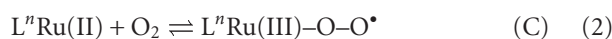


TABLE 3: Cyclic voltammetry data of the Ru(III)-complexes under nitrogen and oxygen atmosphere.

Complex	Electrochemical characteristics of the Ru(III)-complexes							
	Under nitrogen				Under oxygen			
	E_{pc} (V)	E_{pa} (V)	$E_{1/2}$ (V) ^a	I_{pa}/I_{pc}	E_{pc1} (V)	E_{pc2} (V)	I_{pc} (μ A) ^b	$I_{pc}(O_2)/I_{pc}(N_2)$
1	0.660	0.585	0.622	0.80	0.580	0.720	09.60	1.60
2	0.600	0.530	0.565	0.80	0.520	0.700	14.40	2.57
3	0.540	0.475	0.507	0.86	0.500	0.620	14.80	1.76

^a $E_{1/2} = (E_{pa} - E_{pc})/2$; values obtained under nitrogen.

^b $I_{pc} = (I_{pc1} + I_{pc2})$; values between brackets are obtained under oxygen.

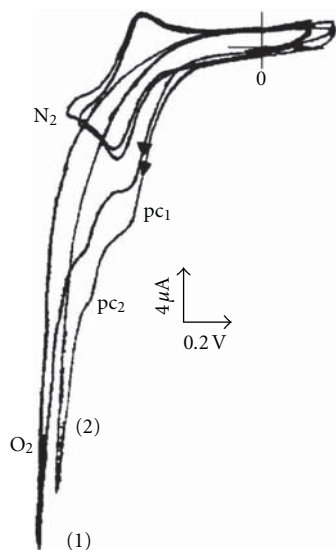


FIGURE 1: Voltammograms of complex 3; 10^{-3} M in CH_3CN with TBAP 10^{-1} M obtained at scan rate 25 $mV s^{-1}$. (1) Under nitrogen without 1-methylimidazole and then with oxygen; (2) under nitrogen in presence of 1-methylimidazole and then with oxygen.

The chemical steps involving the reversible reactions with oxygen are (2) and (4) whereas the electrochemical ones such as the reduction waves E_{pc1} and E_{pc2} may result from electroreduction of two different species as represented by (3) for E_{pc1} (Figure 5, way (a)) and (5) for E_{pc2} (Figure 5, way (b)). The second one E_{pc2} , appearing at more cathodic potentials, was assigned to the bielectronic transfer on the metallic center of $L^nRu(IV)-O-O^*$ (5) giving the $L^nRu(III)-O-O^-$ species, which are simultaneously produced by (3) according a monoelectronic transfer.

When the $L^nRu(II)$ species are coordinated to 2-methylimidazole, they exhibit a greater reactivity towards oxygen causing the disappearance of E_{pc2} to the benefit of E_{pc1} as illustrated by Figure 3.

However, for this reason, it is worth noting that such M^{II} -oxygenated species are often usually reduced at the same potential of their formation [18, 21–25, 63] leading to the superoxo moieties. Similarly, the oxygenated $Ru(IV)-O-O^-$ species, resulting from (4), are also reduced at the same potential value, giving the same result $L^nRu(III)-O-O^-$ obtained from (5) (Figure 1). The peak-to-peak separation potentials (ΔE_p) between these two reduction waves (E_{pc1} , E_{pc2}) were estimated to be about 100 mV. Therefore, this

behaviour shows a particular reactivity for the Ru(III)-complexes when they are compared to their analogous such as Mn(III)-, Fe(III)-, and Co(III)-complexes. So, this excess of reactivity involving an easy reaction of the Ru(III) species with molecular oxygen was not observed seeing that, to our knowledge, only the divalent form M(II) of these complexes is known as the more reactive species towards the oxygen.

In this case, the redox systems of all these complexes appear always before those of oxygen but their $E_{1/2}$ values are very slightly shifted to the more cathodic potentials by about 33–55 mV. For example, the nearer $E_{1/2}$ value is that of the complex 1 which is observed at -0.660 instead of -0.622 V under nitrogen atmosphere. So, under the same experimental conditions and under oxygen atmosphere, the superoxide species are exclusively produced as reported by Sawyer et al. [60]. For this reason, all the complexes 1, 2, and 3 (Table 1: $E_{1/2} < -750$ mV) may be considered as catalysts activating the molecular oxygen like P450 cytochrome [18]. The shape of the voltammograms obtained from these Ru(III)-complexes is represented in Figure 1.

On these voltammograms, it was observed that the half-wave potential values remain stable under nitrogen or oxygen atmosphere noting that the electroreduction of the metal-superoxo species occurred at the same potential of their formation as it was already indicated. When varying the scan rate, the cathodic peak currents (I_{pc}) decrease at low sweep rates leading to the lower $I_{pc}(O_2)/I_{pc}(N_2)$ ratios 1.60 (1), 2.57 (2) and 1.76 (3) at 10 $mV s^{-1}$ while, at scan rates moderately higher (100 $mV s^{-1}$), they are 3.06, 3.27, and 3.48, respectively. Considering the reversibility of oxygenation reaction for these species, this behavior may be approached to their corresponding manganese(III)-superoxo species [22–25].

4.2.2. Complexes with 1-Methylimidazole. First, under nitrogen atmosphere, the addition of 10^{-2} M of nitrogen base like 1-Me-im., acting as an axial ligand, leads to a well-defined redox system without any significant displacement of $E_{1/2}$ values. There is, also, a neat enhancement of the peak currents I_{pa} and I_{pc} after the addition of a nitrogen base as 1-methylimidazole [63]. This nitrogen base coordinated to the central metal ion enhances the coordination number and produces an improvement of the electrophilic character on the metal center, and its further reaction with molecular oxygen becomes easier.

Under oxygen atmosphere, the shape of the voltammograms is quite similar to those obtained without 1-methylimidazole except some differences in their wave intensities

exhibiting a relative high reactivity of the ruthenium(III)-complexes towards oxygen molecules as illustrated in Figures 1 and 3. Thus, the E_{pc1} wave enhancement (3) was noted when comparing these voltammograms with those recorded in the same experimental conditions without nitrogen base. This enhancement involving the reaction of the Ru(II) species with oxygen (3) was estimated to be 10–13% according to the nature of the complex. This behavior is also accompanied by the diminishing of the E_{pc2} wave up to 28–37% suggesting an accelerating of the chemical reaction between Ru(II) species and oxygen (Figure 5, way (a)) when their coordination number is increased by an addition of an amount of 1-methylimidazole (10 equivalents).

The electrocatalytic currents of these three complexes were represented by the ratio I_{pcO_2}/I_{pcN_2} values and are 1.75 (1), 2.42 (2), and 1.90 (3). It should be noted that these ratios were calculated by summing the I_{pc} cathodic current ($I_{pc1} + I_{pc2}$) values obtained in the presence of 1-methylimidazole under oxygen atmosphere. The greater ratios are mainly obtained from an excess of redox properties induced by the σ donor effect of substituents on the metal centre such as those of the two methyl groups, symmetrically grafted on the complex (2) Ru(III)-[7,7'-(Me)₂Salen].

Under these experimental conditions (Figure 2) and Table 3, all the voltammograms of the complexes give almost similar results. Thus, the redox system of the metallic center Ru(II)/Ru(III) was studied and the electrochemical characteristics obtained as peak-to-peak separation potential ΔE_p values, $I_{pc}/f(v^{1/2})$ and I_{pa}/I_{pc} ratio are consistent with a quasireversible redox couple [61, 62].

4.2.3. Complexes with 2-Methylimidazole. The addition of 10^{-2} M of 2-methylimidazole to the Ru(III) complex 10^{-3} M, acting as an axial ligand, induces the same effects as 1-methylimidazole but with a higher speed of the chemical reaction (3) and the disappearance of E_{pc2} reduction wave (5) to the benefit of E_{pc1} reduction wave (3) as shown in Figure 3.

This expresses the relative high reactivity of the ruthenium(II) complex molecules towards oxygen when 1-methylimidazole is replaced with 2-methylimidazole. This result is observed with all our Ru(III)-complexes. This relative reactivity induced by the use of 1- or 2-methylimidazole as apical bases indicates a higher electrophilic character on the metal center leading to a greater accelerating of the oxygen consumption by the Ru(II) species (2). To our knowledge, these results were not reported in the literature, seeing that these complexes were not studied by cyclic voltammetry in the presence of different nitrogen bases. In this case, when adding 1- or 2-Me-im., the speed of formation of the superoxo or peroxy species (peroxidase form) is significantly increased as expressed by the ratios $I_{pc}(O_2)/I_{pc}(N_2)$ in Table 4. Finally, it must be noted that these oxygenation reactions of ruthenium complexes are reversible when the solutions are bubbled in argon or nitrogen atmosphere, as reported in the literature [22–25, 63].

These results may be connected with the high relative basicity of 1- and 2-methylimidazole as previously reported in literature [17]. Moreover, we have also determined the number of electrons that are involved in these electrochem-

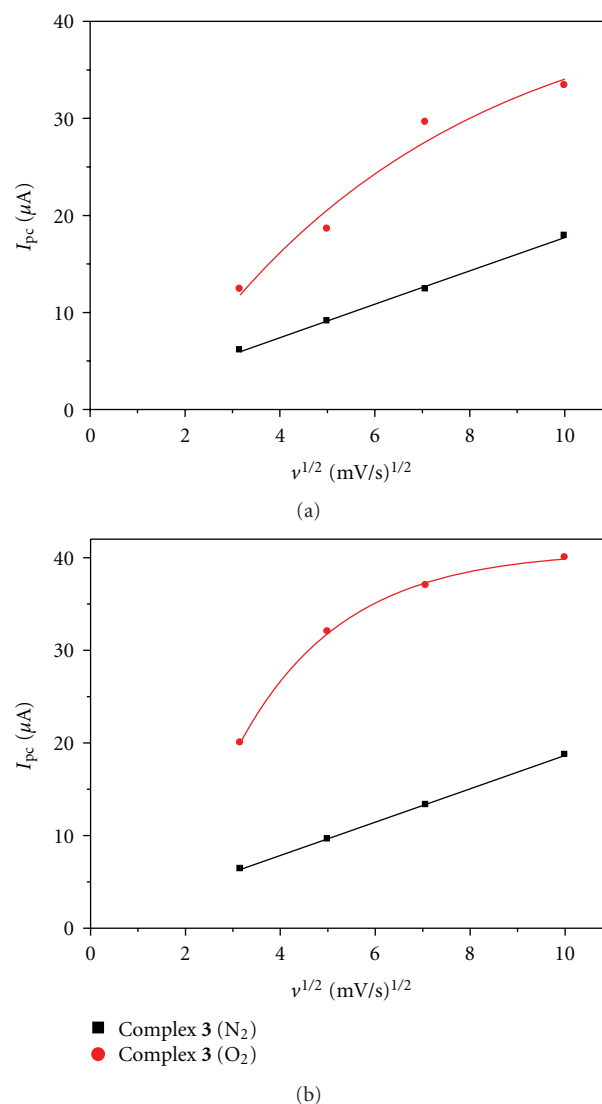


FIGURE 2: Curves $I_{pc} = f(v^{1/2})$ of complex 3; 10^{-3} M in CH₃CN solutions 10^{-1} M TBAP. (a) 1-methylimidazole; (b) 2-methylimidazole.

ical reactions. There are few reports in the literature on these reactions with molecular oxygen, reduced to hydrogen peroxide or water via a two- or four-electron transfer on chemically modified electrodes. The main papers were published by Horwitz et al. [21] and Taqui Khan et al. [47], Anson et al. [64–66], and Chang et al. [67–69]. Here, we have determined the number of electrons for our ruthenium complexes using coulometry after electrolysis under oxygen atmosphere.

4.3. Coulometry Study. For this study, we have proceeded as reported in the literature [47]. Thus, our three complexes were electrolyzed at controlled potentials in a three-compartment cell (acetonitrile solution) in presence of 1-methylimidazole as an apical base. Before each experiment, a pre-electrolysis was achieved for at least one half hour under nitrogen atmosphere in order to eliminate any electroactive

TABLE 4: Electrochemical characteristics of the Ru(III)-complexes 1, 2, and 3 in presence of 1- and 2-methylimidazole under N₂ then under O₂ atmosphere.

Complex	$E_{1/2}$ (mV) ^a	ΔE_p (mV)	I_{pc1} (μ A)	I_{pc2} (μ A)	I_{pa}/I_{pc}	$I_{pc(O_2)}/I_{pc(N_2)}$ ^b
Electrochemical characteristics of the Ru(III)-complexes						
With 1-methylimidazole						
1	580 (622)	70 (70)	6.4 (10.0)	— (1.2)	0.75	1.75
2	520 (565)	75 (75)	5.6 (11.6)	— (2.0)	0.82	2.42
3	500 (507)	65 (65)	8.8 (14.8)	— (2.0)	0.86	1.90
With 2-methylimidazole						
1	580 (622)	70 (70)	6.6 (16.6)	— (0.0)	0.80	2.51
2	520 (565)	70 (70)	6.4 (20.9)	— (0.0)	0.82	3.26
3	500 (507)	75 (75)	9.6 (32.5)	— (0.0)	0.88	2.45

^a $E_{1/2}$; values obtained under nitrogen.

^b $I_{pc} = (I_{pc1} + I_{pc2})$; values given between brackets are obtained under oxygen.

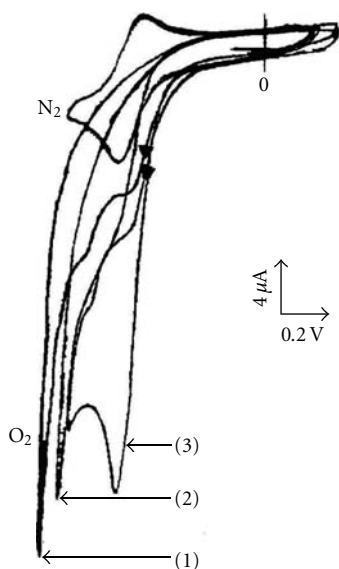


FIGURE 3: Voltammograms of complex 3; 10^{-3} M in CH₃CN with TBAP 10^{-1} M obtained at scan rate 25 mV s^{-1} : (1) Under nitrogen and then oxygen; (2) in presence of 1-methylimidazole under oxygen; (3) in presence of 2-methylimidazole under oxygen atmosphere.

impurities. The number of electrons was finally calculated from the following Faraday equation:

$$n = \frac{Q}{(m/M) \cdot F}, \quad (6)$$

where n is the number of electrons involved in the reaction, and Q the amount of electricity, m , and M are, respectively, the mass of the complex and its molar mass. The results are given in Table 5.

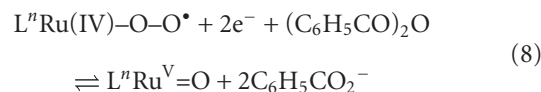
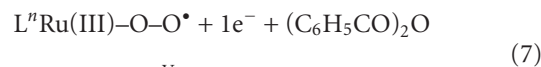
These results suggest that the major part of the compound (75%) was electroreduced according to the first reduction wave E_{pc1} and only 25% were electrolyzed following the second reduction wave E_{pc2} . When the 2-methylimidazole is used as an apical base, the complex is exclusively electrolyzed according to the first reduction wave E_{pc1}

TABLE 5: Number of electrons involved in the electrolyses of Ru(III)-complexes under oxygen atmosphere in presence of 1-methylimidazole.

Determination of number of electrons for waves E_{pc1} and E_{pc2}		
Complex	Number of electrons E_{pc1}	Number of electrons E_{pc2}
1	1.50	0.44
2	1.60	0.36
3	1.50	0.46

with high reactivity of the Ru(II) species towards dioxygen molecules which were subsequently electroreduced by a mono-electronic transfer process (3). At this level, it seems us important to note this particular behavior, characterizing the high reactivity of Ru(III)-Schiff base complexes when they are compared to their analogs such as the iron(III)-[63] and Mn(III)-complexes [22–25] with which the metal-oxo ($M=O$) species are almost exclusively formed from the electroreduced M(II)-species.

4.4. Complexes with 1- or 2-Methylimidazole and Benzoic Anhydride. Benzoic anhydride reacts with superoxo intermediates, giving an oxo compound with elimination of one oxygen atom according to the following equation [6, 21, 36, 47]:



When benzoic anhydride is added to the acetonitrile solution of a complex and Me-im, we note a significant enhancement of the cathodic peak current I_{pc} . In the mean time, the anodic peak current is clearly diminishing, showing a loss of reversibility of the Ru(III)/Ru(II) redox system. This is due to an important consumption of the two superoxo species ($L^n\text{Ru(III)-O-O}^\bullet + 1e^-$ and $L^n\text{Ru(IV)-O-O}^\bullet + 2e^-$)

TABLE 6: Electrochemical characteristics giving the electrocatalytic currents $I_{pc}(O_2)/I_{pc}(N_2)$.

Complex	ν (mVs^{-1})	$-E_{pc1}$ (mV/SCE)	$I_{pc}(O_2)$ (μA)	$I_{pc}(N_2)$ (μA)	$I_{pc}(O_2)/I_{pc}(N_2)$
Electrochemical characteristics of the Ru(III)-complexes					
With 1-methylimidazole					
2	10	680	080.00 ^a	03.50	22.85
	100	710	086.00 ^a	12.00	07.16
3	10	600	060.00 ^a	06.00	10.00
	100	660	067.00 ^a	16.00	04.20
With 2-methylimidazole					
2	10	680	140.00	03.80	36.84
	100	710	136.00	12.80	10.62
3	10	600	075.00	06.40	11.72
	100	660	073.00	18.70	04.00

^a $I_{pc} = (I_{pc1} + I_{pc2})$.

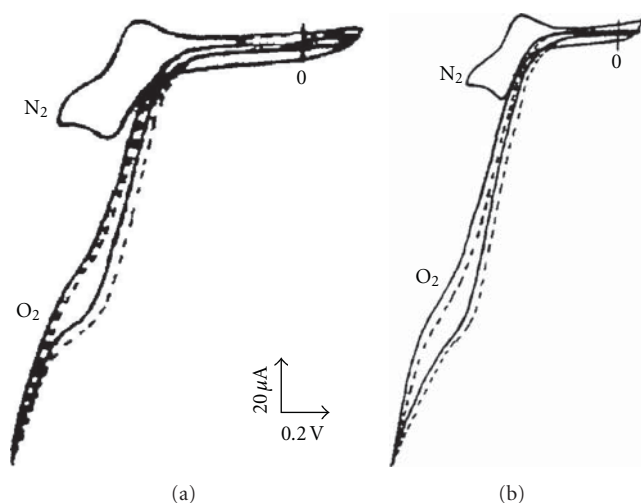


FIGURE 4: Voltammograms of complex 2; 10^{-3} M in CH_3CN with TBAP 10^{-1} M obtained in presence of nitrogen base 10^{-2} M and benzoic anhydride 10^{-1} M under nitrogen and then oxygen atmosphere at scan rate $25 mVs^{-1}$. (a) 1-methylimidazole; (b) 2-methylimidazole, (full line: with pure benzoic anhydride; dotted line: with benzoic anhydride containing 2-3% of its acid).

according to (7) and (8) where they are transformed to the corresponding metal-oxo species. As soon as these superoxo species are produced, the electrophilic intermediates (i.e., $C_6H_5-CO^+$) react faster to produce the metal-oxo species [6, 21, 47]. Of course, an important enhancement of the two cathodic peak currents $I_{pc}(O_2)$ was observed at each one of the both reduction waves E_{pc1} and E_{pc2} as previously indicated. These two waves explain the formation of the ruthenium-oxo species, which could be further involved in the epoxidation of olefins or oxidation of hydrocarbons (Figure 4).

These ruthenium-oxo species are formed at the same potential values than the corresponding superoxo species (E_{pc1} and E_{pc2}). At this important step, the ruthenium-oxo species could transfer their oxygen atom to the substrate

leading to an efficient electrocatalytic cycle or they are simply electrochemically reduced to recover their initial form of the ruthenium(III)-complex giving an inefficient electrocatalytic cycle as illustrated in Figure 5 [21–25].

The enhancement of the cathodic peak current $I_{pc}(O_2)$ expresses a catalytic activity towards oxygen as given by the $I_{pc}(O_2)/I_{pc}(N_2)$ ratio. Figure 4 showed clearly that the $I_{pc}(O_2)$ is not influenced by the traces of benzoic acid as observed for their corresponding Manganese(III)-complexes where the electrocatalytic efficiency was seriously affected [22–25]. The I_{pc} values plotted versus the square root of sweep rates (Figure 6) shows also higher ratios of $I_{pc}(O_2)/I_{pc}(N_2)$ at lower scan rates, suggesting more time to achieve the chemical reaction with oxygen as illustrated in Figure 6.

Their shapes are typical of a high electrocatalytic activity towards the reaction with oxygen, to produce the metal-oxo derivatives which might transfer their oxygen atom to a substrate in the oxidation reactions of hydrocarbons. Thus, as it can be observed in Table 6, showing systematically higher values for the $I_{pc}(O_2)/I_{pc}(N_2)$ ratios, mainly with 2-Melm. or 1-Me-im. (10^{-2} M) in the presence of benzoic anhydride (10^{-1} M) as activator, expressing the formation of ruthenium-oxo species from the superoxo ones.

Under these experimental conditions and with 1-Melm. or 2-Melm., the cathodic peak current ratios $I_{pc}(O_2)/I_{pc}(N_2)$ are remarkably increased particularly at lower scan rates ($10 mVs^{-1}$). This improvement at lower scan rates ($10 mVs^{-1}$) implies a sufficient time to achieve the chemical reaction between ruthenium species and oxygen. These results allow to conclude that the best electrocatalytic currents are obtained, as well, at lower scan rates ($10 mVs^{-1}$) 22.85 (1-Melm.) and 36.84 (2-Melm.) for the complex (2). These current ratios $I_{pc}(O_2)/I_{pc}(N_2)$ are fairly higher without any comparison to those obtained with their analogous of manganese, iron, and cobalt already mentioned. Regarding the complex 3, it shows current ratios $I_{pc}(O_2)/I_{pc}(N_2)$ relatively lower, but they should be more efficient towards olefins epoxidation for their robustness, acquired by the chlorine atoms grafted on the ligand as yet reported in the

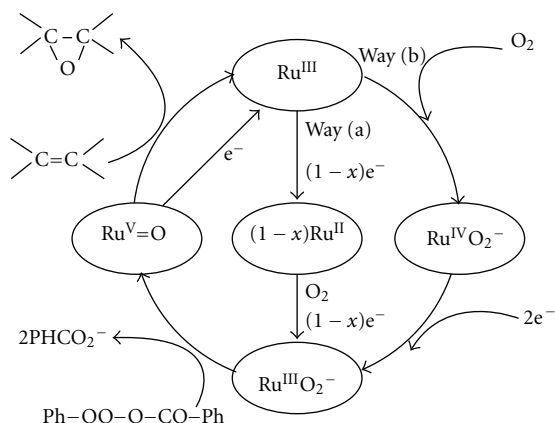


FIGURE 5: Proposed scheme for the electrocatalytic epoxidation of olefins or oxidation of hydrocarbons.

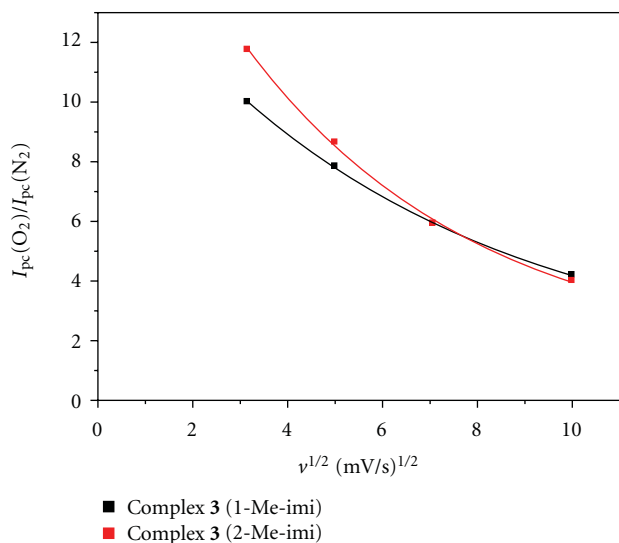


FIGURE 6: $I_{pc}(O_2)/I_{pc}(N_2) = f(v^{1/2})$ Curves for complex 3; (10^{-3} M, acetonitrile). (a) 1-methylimidazole, (b) 2-methylimidazole.

literature for the polyhalogenated Schiff base [22–25, 63] or porphyrinic complexes [70, 71]. Thus, the Ru(III) and Ru(II) species may develop an important and particular reactivity towards molecular oxygen as in the diverse systems of P450 cytochrome [72].

5. Conclusion

In this work, we have showed that the Ru(III)-species develop a particular reactivity towards molecular oxygen in comparison to their corresponding analogs species of manganese(III), iron(III), and cobalt(III). These latter complexes exhibit a reactivity quite similar towards oxygen when they are in their divalent form M(II). In this case, it was also revealed that the formation of byproducts such as μ -oxodimers are advantageously avoided with the Ru(III)-complexes. In the presence of benzoic anhydride, the electrocatalytic currents $I_{pc}(O_2)/I_{pc}(N_2)$ are remarkably exalted

particularly when 2-methylimidazole is used and they are seven times greater than their Mn(III)Cl-Salen analogs. Therefore, these Ru(III)-complexes can work as good catalysts in biomimetic oxidation or as oxygen sensors operating with high sensitivity.

References

- [1] H. S. Schiff, "Sur quelques d eriv es ph eniques des ald ehydes," *Ann. Chim. (Paris)*, vol. 131, p. 118, 1864.
- [2] L. Canali and D. C. Sherrington, "Utilisation of homogeneous and supported chiral metal(salen) complexes in asymmetric catalysis," *Chemical Society Reviews*, vol. 28, no. 2, pp. 85–93, 1999.
- [3] E. N. Jacobsen, "Asymmetric catalysis of epoxide ring-opening reactions," *Accounts of Chemical Research*, vol. 33, no. 6, pp. 421–431, 2000.
- [4] T. Katsuki, "Catalytic asymmetric oxidations using optically active (salen) manganese (III) complexes as catalysts," *Coordination Chemistry Reviews*, vol. 140, pp. 189–214, 1995.
- [5] D. A. Atwood and M. J. Harvey, "Group 13 compounds incorporating Salen ligands," *Chemical Reviews*, vol. 101, no. 1, pp. 37–52, 2001.
- [6] M. M. T. Khan, S. H. Mehta, A. P. Rao, and K. N. Bhatt, "Electrocatalytic oxidation of organic substrates with oxygen using ruthenium-Schiff base complex," *Journal of Molecular Catalysis*, vol. 75, no. 3, pp. 245–251, 1992.
- [7] W. H. Leung and C. M. Che, "Oxidation chemistry of ruthenium-salen complexes," *Inorganic Chemistry*, vol. 28, no. 26, pp. 4619–4622, 1989.
- [8] S. E. Creager, S. A. Raybuck, and R. W. Murray, "An efficient electrocatalytic model cytochrome P-450 epoxidation cycle," *Journal of the American Chemical Society*, vol. 108, no. 14, pp. 4225–4227, 1986.
- [9] A. A. Isse, A. Gennaro, E. Vianello, and C. Floriani, "Electrochemical reduction of carbon dioxide catalyzed by [Co^I(salophen)Li] ," *Journal of Molecular Catalysis*, vol. 70, no. 2, pp. 197–208, 1991.
- [10] S. F. Tan, P. H. Leung, and W. C. Sin, "Catalytic autooxidation of p-anisaldehyde and styrene by a cobalt bis-schiff base complex," *Transition Metal Chemistry*, vol. 16, no. 5, pp. 542–545, 1991.
- [11] J. P. Collman, T. R. Halbert, K. S. Suslick, and T. Spiro, Eds., *Metal Ion Activation of Dioxygen*, Wiley Interscience, New York, NY, USA, 1980.
- [12] I. G. Denisov, T. M. Makris, S. G. Sligar, and I. Schlichting, "Structure and chemistry of cytochrome P450," *Chemical Reviews*, vol. 105, no. 6, pp. 2253–2277, 2005.
- [13] I. C. Gunsalus, T. C. Pederson, and S. G. Sligar, "Oxygenase-catalyzed biological hydroxylations," *Annual Review of Biochemistry*, vol. 44, pp. 377–407, 1975.
- [14] R. I. Kureshy, N. H. Khan, S. H. R. Abdi, and P. Iyer, "Chiral Ru(III) metal complex-catalyzed aerobic enantioselective epoxidation of styrene derivatives with co-oxidation of aldehyde," *Journal of Molecular Catalysis A*, vol. 124, no. 2-3, pp. 91–97, 1997.
- [15] W. H. Leung and C. M. Che, "Oxidation chemistry of ruthenium-salen complexes," *Inorganic Chemistry*, vol. 28, no. 26, pp. 4619–4622, 1989.
- [16] A. M. El-Hendawy, A. H. Alkubaisi, A. E. G. El-Kourashy, and M. M. Shanab, "Ruthenium(II) Complexes of O,N-donor Schiff base ligands and their use as catalytic organic oxidants," *Polyhedron*, vol. 12, no. 19, pp. 2343–2350, 1993.

- [17] L. Salmon, C. Bied-Charreton, A. Gaudemer, P. Moisy, F. Bedioui, and J. Devynck, "Structural studies of metalloporphyrins. 9. "Looping-over" cobalt porphyrins: coordinating properties and application to dioxygen fixation and activation," *Inorganic Chemistry*, vol. 29, no. 15, pp. 2734–2740, 1990.
- [18] L. Gaillon, N. Sajot, F. Bedioui, J. Devynck, and K. J. Balkus, "Electrochemistry of zeolite-encapsulated complexes. Part 3. Characterization of iron and manganese SALEN entrapped in Y faujasite type zeolite," *Journal of Electroanalytical Chemistry*, vol. 345, no. 1-2, pp. 157–167, 1993.
- [19] H. Nishihara, K. Pressprich, R. W. Murray, and J. P. Collman, "Electrochemical olefin epoxidation with manganese meso-tetraphenylporphyrin catalyst and hydrogen peroxide generation at polymer-coated electrodes," *Inorganic Chemistry*, vol. 29, no. 5, pp. 1000–1006, 1990.
- [20] S. F. Tan, P. H. Leung, and W. C. Sin, "Catalytic autooxidation of p-anisaldehyde and styrene by a cobalt bis-schiff base complex," *Transition Metal Chemistry*, vol. 16, no. 5, pp. 542–545, 1991.
- [21] C. P. Horwitz, S. E. Creager, and R. W. Murray, "Electrocatalytic olefin epoxidation using manganese Schiff-base complexes and dioxygen," *Inorganic Chemistry*, vol. 29, no. 5, pp. 1006–1011, 1990.
- [22] J. C. Moutet and A. Ourari, "Electrocatalytic epoxidation and oxidation with dioxygen using manganese(III) Schiff-base complexes," *Electrochimica Acta*, vol. 42, no. 16, pp. 2525–2531, 1997.
- [23] "Etude de deux réactions d'électrocatalyse: Hydrogénation électrocatalytique sur des films de polymères contenant des microparticules de métaux nobles et activation de l'oxygène moléculaire par des complexes de bases de Schiff," Ph.D. thesis, Joseph Fourier University, Grenoble, France, 1995.
- [24] A. Pui, I. Berdan, I. Morgenstern-Badarau, A. Gref, and M. Perrée-Fauvet, "Electrochemical and spectroscopic characterization of new cobalt(II) complexes. Catalytic activity in oxidation reactions by molecular oxygen," *Inorganica Chimica Acta*, vol. 320, no. 1-2, pp. 167–171, 2001.
- [25] J. H. Cameron and S. C. Turner, "Electrochemically controlled dissociation of dioxygen from a μ -peroxo cobalt(III) dimer," *Journal of the Chemical Society, Dalton Transactions*, no. 23, pp. 3285–3289, 1992.
- [26] M. M. T. Khan, S. H. Mehta, A. P. Rao, and K. N. Bhatt, "Electrocatalytic oxidation of organic substrates with oxygen using ruthenium-Schiff base complex," *Journal of Molecular Catalysis*, vol. 75, no. 3, pp. 245–251, 1992.
- [27] R. M. Wang, C. J. Hao, Y. P. Wang, and S. B. Li, "Amino acid Schiff base complex catalyst for effective oxidation of olefins with molecular oxygen," *Journal of Molecular Catalysis A*, vol. 147, no. 1-2, pp. 173–178, 1999.
- [28] E. Kwiatkowski, G. Romanowski, W. Nowicki, M. Kwiatkowski, and K. Suwińska, "Dioxovanadium(V) Schiff base complexes of N-methyl-1,2-diaminoethane and 2-methyl-1,2-diaminopropane with aromatic o-hydroxyaldehydes and o-hydroxyketones: synthesis, characterisation, catalytic properties and structure," *Polyhedron*, vol. 22, no. 7, pp. 1009–1018, 2003.
- [29] D. D. Agarwal, R. P. Bhatnagar, R. Jain, and S. Srivastava, "Epoxidation of olefins catalysed by Fe(III) Schiff base complexes as catalyst," *Journal of Molecular Catalysis*, vol. 59, no. 3, pp. 385–395, 1990.
- [30] B. Fisher and R. Eisenberg, "Electrocatalytic reduction of carbon dioxide by using macrocycles of nickel and cobalt," *Journal of the American Chemical Society*, vol. 102, no. 24, pp. 7361–7363, 1980.
- [31] C. E. Dahm and D. G. Peters, "Catalytic reduction of iodoethane and 2-iodopropane at carbon electrodes coated with anodically polymerized films of nickel(II) salen," *Analytical Chemistry*, vol. 66, no. 19, pp. 3117–3123, 1994.
- [32] C. E. Dahm and D. G. Peters, "Catalytic reduction of α,ω -dihaloalkanes with nickel(I) salen as a homogeneous-phase and polymer-bound mediator," *Journal of Electroanalytical Chemistry*, vol. 406, no. 1-2, pp. 119–129, 1996.
- [33] R. Zhang, J. Ma, W. Wang, B. Wang, and R. Li, "Zeolite-encapsulated M(Co, Fe, Mn)(SALEN) complexes modified glassy carbon electrodes and their application in oxygen reduction," *Journal of Electroanalytical Chemistry*, vol. 643, no. 1-2, pp. 31–38, 2010.
- [34] B. Tyagi, B. Shaik, and H. C. Bajaj, "Epoxidation of styrene with sulfated Y-ZrO₂ based solid catalysts," *Applied Catalysis A*, vol. 383, no. 1-2, pp. 161–168, 2010.
- [35] P. Guo and K. Y. Wong, "Enantioselective electrocatalytic epoxidation of olefins by chiral manganese Schiff-base complexes," *Electrochemistry Communications*, vol. 1, no. 11, pp. 559–563, 1999.
- [36] F. Bedioui, E. De Boysson, J. Devynck, and K. J. Balkus, "Electrochemistry of zeolite-encapsulated cobalt salen complexes in acetonitrile and dimethyl sulphoxide solutions," *Journal of the Chemical Society, Faraday Transactions*, vol. 87, no. 24, pp. 3831–3834, 1991.
- [37] G. N. Vyas and N. M. Shah, "Quinacetophenone monomethyl ether," *Organic Syntheses, Coll.*, vol. 4, p. 886, 1963.
- [38] A. Anthonysamy and S. Balasubramanian, "Synthesis, spectral, thermal and electrochemical studies of nickel (II) complexes with NO donor ligands," *Inorganic Chemistry Communications*, vol. 8, no. 10, pp. 908–911, 2005.
- [39] M. Yuasa, T. Nagaiwa, M. Kato, I. Sekine, and S. Hayashi, "Electrochemical properties of metalloporphyrin-clay complex-modified electrode systems: investigation as oxygen sensors," *Journal of the Electrochemical Society*, vol. 142, no. 8, pp. 2612–2617, 1995.
- [40] I. Sasaki, D. Pujol, and A. Gaudemer, "Non-symmetric Schiff base Co(II) complexes. Synthesis and catalytic activity in the oxidation of 2,6-Di-tert-butylphenol by molecular oxygen," *Inorganica Chimica Acta*, vol. 134, no. 1, pp. 53–57, 1987.
- [41] Y. W. Liou and C. M. Wang, "Peroxidase mimicking: Fe(Salen)Cl modified electrodes, fundamental properties and applications for biosensing," *Journal of Electroanalytical Chemistry*, vol. 481, no. 1, pp. 102–109, 2000.
- [42] J. Losada, I. del Peso, L. Beyer, J. Hartung, V. Fernández, and M. Möbius, "Electrocatalytic reduction of O and CO with electropolymerized films of polypyrrole cobalt(II) Schiff-base complexes," *Journal of Electroanalytical Chemistry*, vol. 398, no. 1-2, pp. 89–93, 1995.
- [43] P. N. Barlett and J. M. Cooper, "A review of the immobilization of enzymes in electropolymerized films," *Journal of Electroanalytical Chemistry*, vol. 362, no. 1-2, pp. 1–12, 1993.
- [44] W. Schuhmann, "Conducting polymer based amperometric enzyme electrodes," *Mikrochimica Acta*, vol. 121, no. 1–4, pp. 1–29, 1995.
- [45] S. Cosnier, A. Lepellec, B. Guidetti, and I. Rico-Lattes, "Enhancement of biosensor sensitivity in aqueous and organic solvents using a combination of poly(pyrrole-ammonium) and poly(pyrrole-lactobionamide) films as host matrices," *Journal of Electroanalytical Chemistry*, vol. 449, no. 1-2, pp. 165–171, 1998.
- [46] G. Cauquis, S. Cosnier, A. Deronzier et al., "Poly(pyrrole-manganese porphyrin): a catalytic electrode material as a model system for olefin epoxidation and drug metabolism

- with molecular oxygen," *Journal of Electroanalytical Chemistry*, vol. 352, no. 1-2, pp. 181-195, 1993.
- [47] M. M. Taqui Khan, N. H. Khan, R. I. Kureshy, A. B. Boricha, and Z. A. Shaikh, "Synthesis, characterisation, oxygenation and carbonylation of ruthenium(III) schiff base complexes," *Inorganica Chimica Acta*, vol. 170, no. 2, pp. 213-223, 1990.
- [48] T. Katsuki, "Some recent advances in metallosalen chemistry," *Synlett*, no. 3, pp. 281-297, 2003.
- [49] P. G. Cozzi, "Metal-Salen Schiff base complexes in catalysis: practical aspects," *Chemical Society Reviews*, vol. 33, no. 7, pp. 410-421, 2004.
- [50] J. Sanmartín, M. R. Bermejo, A. M. Garía-Deibe, M. Maneiro, C. Lage, and A. J. Costa-Filho, "Mono- and polynuclear complexes of Fe(II), Co(II), Ni(II), Cu(II), Zn(II) and Cd(II) with N,N'-bis(3-hydroxysalicylidene)-1,3-diamino-2-propanol," *Polyhedron*, vol. 19, no. 2, pp. 185-192, 2000.
- [51] P. Gili, M. G. Martín Reyes, P. Martín Zarza et al., "Synthesis, spectroscopic, magnetic and electrochemical properties of Cu(II) and Fe(III) complexes with the new ligand N,N'-[1,1'-dithiobis (phenyl)]bis (5'-methoxysalicylaldimine)," *Inorganica Chimica Acta*, vol. 244, no. 1, pp. 25-36, 1996.
- [52] L. J. Bellamy, *The Infrared Spectra of Complex Molecules*, Chapman and Hall, London, UK, 3rd edition, 1975.
- [53] P. Gili, M. G. Martín Reyes, P. Martín Zarza, M. F. C. Guedes Da Silva, Y. Y. Tong, and A. J. L. Pombeiro, "Complexes of Mn(II) and Mn(III) with the Schiff base N-[2-(3-ethylindole)]pyridoxaldimine. Electrochemical study of these and related Ni(II) and Cu(II) complexes," *Inorganica Chimica Acta*, vol. 255, no. 2, pp. 279-288, 1997.
- [54] A. Vogt, S. Wołowiec, R. L. Prasad, A. Gupta, and J. Skarzewski, "Synthesis and characterization of nickel(II), copper(II), manganese(III) and iron(III) complexes with new chiral salen-type ligand N,N'-bis(3,5-di-tert-butylsalicylidene)-(1R,3S)-1,3-diamine-1,2,2-trimethylcyclopentane," *Polyhedron*, vol. 17, no. 8, pp. 1231-1240, 1998.
- [55] Z. Cimerman, N. Galic, and B. Bosner, "The Schiff bases of salicylaldehyde and aminopyridines as highly sensitive analytical reagents," *Analytica Chimica Acta*, vol. 343, no. 1-2, pp. 145-153, 1997.
- [56] A. B. P. Lever, *Inorganic Electronic Spectroscopy*, Elsevier, London, UK, 2nd edition, 1992.
- [57] S. Djebbar-Sid, O. Benali-Baitich, and J. P. Deloume, "Synthesis, characterization and electrochemical behaviour of cobalt(II) and cobalt(III):O complexes, respectively, with linear and tripodal tetradentate ligands derived from Schiff bases," *Journal of Molecular Structure*, vol. 569, no. 1-3, pp. 121-128, 2001.
- [58] T. W. Hambley, C. J. Hawkins, and T. A. Kabanos, "Synthetic, structural, and physical studies of tris(2,4-pentanedionato)vanadium(IV) hexachloroantimonate(V) and tris(1-phenyl-1,3-butanedionato)vanadium(IV) hexachloro-antimonate(V)," *Inorganic Chemistry*, vol. 26, no. 22, pp. 3740-3745, 1987.
- [59] C. J. Hawkins and T. A. Kabanos, "Synthesis and characterization of (catecholato)bis(β -diketonato)vanadium(IV) complexes," *Inorganic Chemistry*, vol. 28, no. 6, pp. 1084-1087, 1989.
- [60] D. T. Sawyer, M. J. Gibian, M. M. Morrison, and E. T. Seo, "On the chemical reactivity of superoxide ion," *Journal of the American Chemical Society*, vol. 100, no. 2, pp. 627-628, 1978.
- [61] R. S. Nicholson and I. Shain, "Theory of stationary electrode polarography single scan and cyclic methods applied to reversible, irreversible, and kinetic systems," *Analytical Chemistry*, vol. 36, no. 4, pp. 706-723, 1964.
- [62] C. Evans, G. J. Harfoot, J. S. McIndoe et al., "The preparation and characterisation of monomeric and linked metal carbonyl clusters containing the closo-SiCo pseudo-octahedral core," *Journal of the Chemical Society. Dalton Transactions*, no. 24, pp. 4678-4683, 2002.
- [63] A. Ourari, K. Ouari, M. A. Khan, and G. Bouet, "Dioxygen activation with a cytochrome P450 model. Characterization and electrochemical study of new unsymmetrical tetradentate Schiff-base complexes with iron(III) and cobalt(II)," *Journal of Coordination Chemistry*, vol. 61, no. 23, pp. 3846-3859, 2008.
- [64] J. P. Collman, M. Marrocco, P. Denisevich, C. Koval, and F. C. Anson, "Potent catalysis of the electroreduction of oxygen to water by dicobalt porphyrin dimers adsorbed on graphite electrodes," *Journal of Electroanalytical Chemistry*, vol. 101, no. 1, pp. 117-122, 1979.
- [65] J. P. Collman, P. Denisevich, Y. Konai, M. Marrocco, C. Koval, and F. C. Anson, "Electrode catalysis of the four-electron reduction of oxygen to water by dicobalt face-to-face porphyrins," *Journal of the American Chemical Society*, vol. 102, no. 19, pp. 6027-6036, 1980.
- [66] R. R. Durand, C. S. Bencosme, J. P. Collman, and F. C. Anson, "Mechanistic aspects of the catalytic reduction of dioxygen by cofacial metalloporphyrins," *Journal of the American Chemical Society*, vol. 105, no. 9, pp. 2710-2718, 1983.
- [67] H. Y. Liu, I. Abdalmuhdi, C. K. Chang, and F. C. Anson, "Catalysis of the electroreduction of dioxygen and hydrogen peroxide by an anthracene-linked dimeric cobalt porphyrin," *Journal of Physical Chemistry*, vol. 89, no. 4, pp. 665-670, 1985.
- [68] H. Y. Liu, M. J. Weaver, C. B. Wang, and C. K. Chang, "Dependence of electrocatalysis for oxygen reduction by adsorbed dicobalt cofacial porphyrins upon catalyst structure," *Journal of Electroanalytical Chemistry*, vol. 145, no. 2, pp. 439-447, 1983.
- [69] C. K. Chang, H. Y. Liu, and I. Abdalmuhdi, "Electroreduction of oxygen by pillared cobalt cofacial diporphyrin catalysts," *Journal of the American Chemical Society*, vol. 106, no. 9, pp. 2725-2726, 1984.
- [70] K. M. Kadish, C. Araullo-McAdams, B. C. Han, and M. M. Franzen, "Syntheses and spectroscopic characterization of (T(P-MeN)FPP)H and (7(p-MeN)FPP)M where 7(p-MeN)FPP is the dianion of meso-tetrakis(o,o,w,w-tetrafluoro-p-(dimethylamino)phenyl)-porphyrin and M = Co(II), Cu(II), or Ni(II)," *Journal of the American Chemical Society*, vol. 112, no. 23, pp. 8364-8368, 1990.
- [71] T. G. Traylor, Y. S. Byun, P. S. Traylor, P. Battioni, and D. Mansuy, "Polymeric polyhalogenated metalloporphyrin catalysts for hydroxylation of alkanes and epoxidation of alkenes," *Journal of the American Chemical Society*, vol. 113, no. 20, pp. 7821-7823, 1991.
- [72] P. K. S. Tsang and D. T. Sawyer, "Electron-transfer thermodynamics and bonding for the superoxide (O⁻), dioxygen (O₂), and hydroxyl (OH) adducts of (tetrakis(2,6-dichlorophenyl)porphinato)iron, -manganese, and -cobalt in dimethylformamide," *Inorganic Chemistry*, vol. 29, no. 15, pp. 2848-2855, 1990.

Review Article

Recent Progress in Hydrogen Electrocatalysis

P. Quaino,^{1,2} E. Santos,^{1,3} G. Soldano,¹ and W. Schmickler¹

¹Institute of Theoretical Chemistry, Ulm University, 89069 Ulm, Germany

²PRELINE, Universidad Nacional del Litoral, 3000 Santa Fe, Argentina

³Facultad de Matemáticas, Astronomía y Física, IFEG-CONICET, Universidad Nacional de Córdoba, Córdoba, Argentina

Correspondence should be addressed to P. Quaino, paola.quaino@uni-ulm.de

Received 15 February 2011; Accepted 25 March 2011

Academic Editor: Milan M. Jaksic

Copyright © 2011 P. Quaino et al. This is an open access article distributed under the Creative Commons Attribution License, which permits unrestricted use, distribution, and reproduction in any medium, provided the original work is properly cited.

Recently, we have proposed a unified model for electrochemical electron transfer reactions which explicitly accounts for the electronic structure of the electrode. It provides a framework describing the whole course of bond-breaking electron transfer, which explains catalytic effects caused by the presence of surface d bands. In application on real systems, the parameters of this model—interaction strengths, densities of states, and energies of reorganization—are obtained from density functional theory (DFT). In this opportunity, we review our main achievements in applying the theory of electrocatalysis. Particularly, we have focused on the electrochemical adsorption of a proton from the solution—the Volmer reaction—on a variety of systems of technological interest, such as bare single crystals and nanostructured surfaces. We discuss in detail the interaction of the surface metal d band with the valence orbital of the reactant and its effect on the catalytic activity as well as other aspects that influence the surface-electrode reactivity such as strain and chemical factors.

1. Introduction

The increasing demand for electrical energy and the issues related to environmental pollution have contributed to the development of new technologies for the generation and storage of electrical energy. These technologies focus the attention on the electrochemical devices because of their known advantages (no contamination, usage of renewable resources, low-temperature operation, etc.). In this context, the fuel cell is a promising alternative for the development of new methods of production, conversion, and storage of clean energy. This technology enables direct conversion of chemical energy into electricity; it employs a device in which hydrogen, through reaction with oxygen, produces water and heat as the only products. However, there are still many problems to be solved to ensure that *hydrogen-based systems* become a competitive force.

For decades, a great number of groups worldwide have investigated the hydrogen electrode reaction (HER) experimentally and theoretically in order to improve the electrocatalytic properties of electrode materials and contribute to the general understanding of the hydrogen reaction. For

instance, the role of the electrolyte and the electrode material and the behavior of the reaction intermediate, among others, are the most studied topics.

In this sense, our group has investigated the HER in the framework of a theory for electrocatalysis proposed by two of us (E. Santos and W. Schmickler) [1, 2]. This theory is based on a model Hamiltonian for electrochemical bond breaking reactions [3, 4], which combines ideas of Marcus theory, the Anderson-Newns model [5, 6], and density functional theory (DFT). Hence, realistic calculations for an electrochemical environment can be performed, and the interaction of the valence orbital of the reactant and the d band of the electrocatalyst, when either fluctuations of the solvent or the applied potential shift their relative positions, can be understood.

On the basis of this Hamiltonian, E. Santos and W. Schmickler have proposed a mechanism [1, 2] by which a metal d band interacting strongly with the valence level of the reactant may broaden the latter's density of states (DOSs) as it passes the Fermi level and, thereby, enhance the reaction rate. First applications of this idea explained well the trends in the hydrogen electrocatalysis in terms of the position of the metal d band and its coupling to the hydrogen orbital [7–9].

In this paper, we paper the main contributions we have achieved applying our theory of electrocatalysis. Particularly, we have investigated the hydrogen electrode reaction on several single-crystal surfaces as well as on various nanostructures (clusters, monolayers, nanowires, etc.) on different substrates. We also discuss in detail the role of the position of the metal d band and its interaction with the $1s$ hydrogen orbital on the catalytic activity, and finally, we shall explain in detail the contribution of different aspects, such as strain and chemical interactions, on the reactivity of the electrode materials.

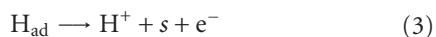
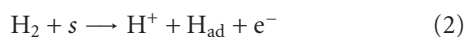
2. Mechanism of Electrocatalysis

In order to describe the catalysis mechanism proposed by us (a detailed description of the model can be found in [9]) and the role played by the solvent, we employ an ideal system consisting of the superposition of a wide sp band with a thin d band. Two different reactions concerning bond breaking and electron transfer—a reduction and an oxidation reaction—are considered. In both reactions, the bonding orbital of the molecule lies below the Fermi level at the initial state and is filled (Figure 1). In order for the reactions to occur, a thermal fluctuation in the configuration of the solvent must move up (down) the bonding (antibonding) orbital to the Fermi level, so that an electron can be transferred from (to) the reactant to (from) the metal for the oxidation (reduction) process. The resulting ion interacts strongly with the solvent, the solvation shell relaxes towards equilibrium, and, in the final state the bonding (antibonding) orbital lies well above (below) the Fermi level. The most important properties of the metal catalyst that determine their effectivity are the position of the d band and its coupling strength to the molecular orbitals: a good catalyst usually has a d band extending across the Fermi level, which interacts strongly with the reactant. When the interaction is weak, the level is just broadened, and when the interaction is strong, the level is split into a bonding and an antibonding orbitals but in this case with respect to the metal. When the overall reaction is in equilibrium, the orbital is half-filled at the transition state and the part of the density of states that lies below the Fermi level reduces the energy of activation. Figure 1 illustrates the described mechanism for the case when $A \rightarrow A^+ + e^-$.

In addition, it is important to remark that the same mechanism also operates in other electron transfer reactions.

3. Hydrogen Reaction on Single-Crystal Surfaces

It is well known that the hydrogen electrode reaction (HER) consists of the following elementary steps, Tafel (1), Heyrovsky (2), and Volmer (3), respectively:



Therefore the reaction evolves through an adsorbed intermediate (H_{ad}) on an active site (s) on the metal

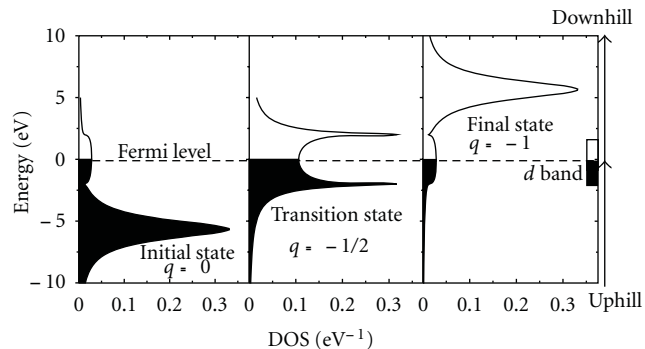


FIGURE 1: Mechanism of electrocatalysis by a d band near the Fermi level for the following reaction: $A \rightarrow A^+ + e^-$ on a good metal catalyst: (a) initial, (b) transition, and (c) final states. The Fermi level has been taken as the energy zero.

TABLE 1: Energies of activation for hydrogen adsorption (Volmer step) on various metals [11].

Metal	Cd	Cu	Ag	Au	Pt
ΔG_{act} (eV)	0.93	0.71	0.71	0.70	0.30

electrode; and although this is one of the most fundamental reactions in electrochemistry and during the last decades much effort has been spent to clarify the mechanism of electrocatalysis, the behavior of the adsorbed intermediate, the effect of the electrode potential on the adsorbate, the role of the electrolyte, and so forth, there is still a lack of knowledge in understanding the nature of the hydrogen electrocatalysis.

As discussed previously (Sections 1 and 2), a good catalyst has a metal d band situated at the Fermi level that interacts strongly with the adsorbate and broadens its valence orbital and, thereby, decrease the activation energy. Accordingly, first applications of our theory (for detailed information, see [8, 10, 11]) on the electrochemical adsorption of a proton from the solution onto the surface-Volmer reaction (3)—on good (Pt), mediocre (Au, Ag, Cu), and bad catalysts (Cd) show, as expected, a high activation energy for Cd, medium values for the coin metals, and the lowest one on Pt. The free energy surfaces for the Volmer reaction for four of these metals are shown in Figure 2; the energies of activation are shown in Table 1, and to facilitate the interpretation, the densities of states of the d bands are given in Figure 3. In all the free energy surfaces, the valley near $q = -1$ corresponds to a solvated proton close to the metal surface; the minimum near $q = 0$ represents the adsorbed hydrogen atom. The two minima are separated by a barrier with a saddle point of ΔG_{act} height.

In accord with experimental findings, the activation barrier is highest for Cd, because its d band lies well below the Fermi level to affect the activation energy; therefore it has no catalytic effect and the reaction is mostly dominated by the sp band. On the coin metals Cu, Ag, and Au, the reaction has the same activation energies. This is due to a compensation effect: the interaction with the d band increases down the column of the periodic table, which lowers the energy of

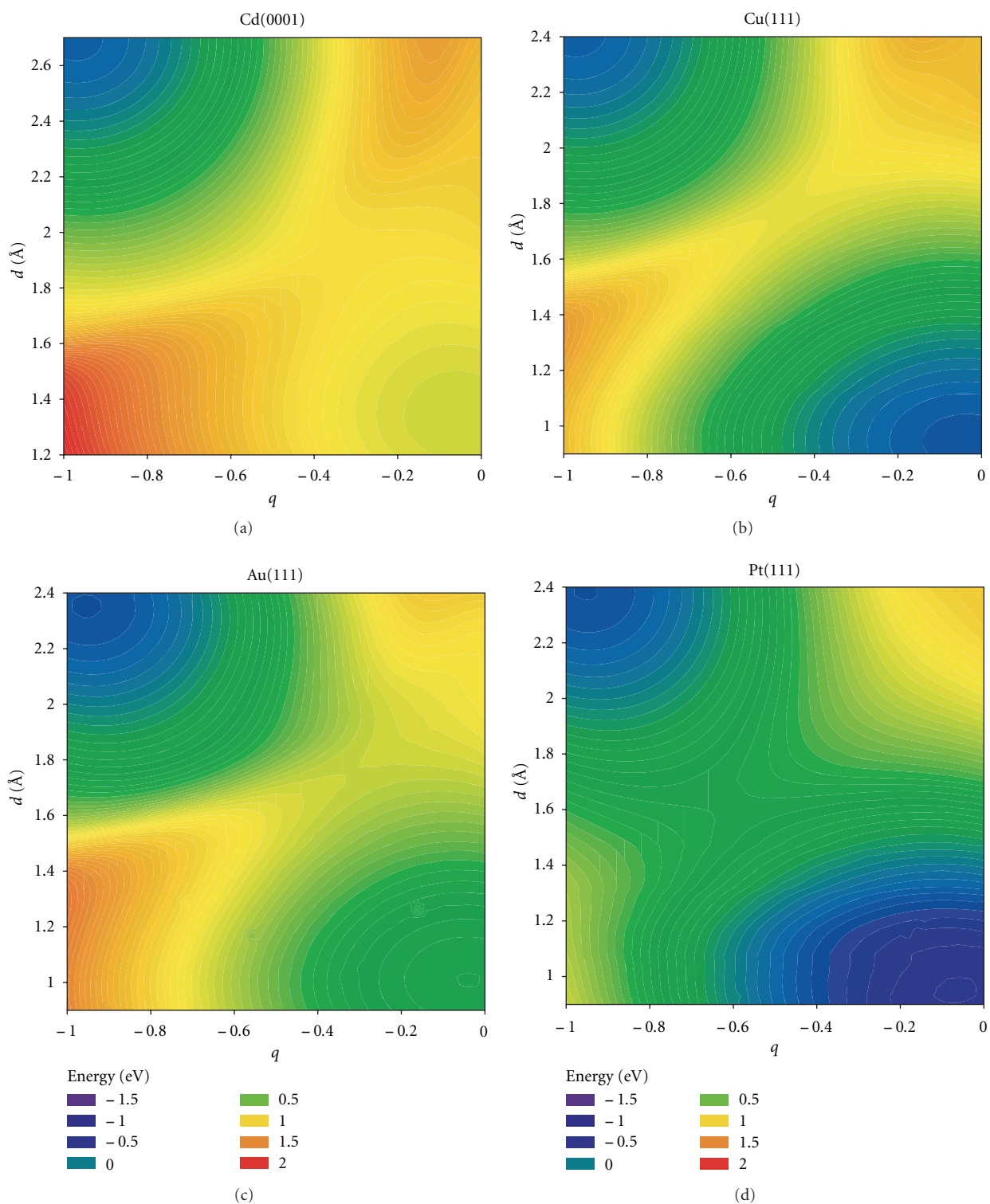


FIGURE 2: Free energy surfaces for hydrogen adsorption at Cd(0001), Cu(111), Au(111), and Pt(111).

activation. On the other hand, the energy of the adsorbed hydrogen increases in the same order therefore; the reaction free energy for the adsorption rises, which in turn raises the activation energy. On all the three coin metals, the d band lies well below the Fermi level and both the bonding and

the antibonding parts of the hydrogen DOS caused by the interaction with the d band are filled, so that the d band does not contribute much to the adsorption bond which is dominated by the interaction with the sp band. Of all the metals considered, Pt is the only one whose d band extends

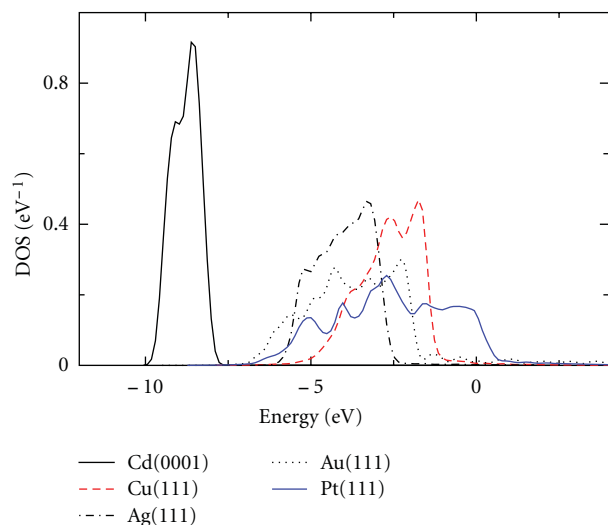


FIGURE 3: Surface d band DOS of the metals considered. The Fermi level has been taken as the energy zero.

over the Fermi level. Its interaction with H is strong, and therefore, it has by far the lowest activation energy. At the equilibrium electrode potential, the energy of the adsorbed hydrogen is lower than that of the solvated proton. Therefore, adsorption sets in at potentials above the hydrogen evolution, so that one speaks of strongly adsorbed hydrogen (H_{upd}). However, there is convincing experimental evidence that this is not the species that takes part in hydrogen evolution [12], but the intermediate is a more weakly adsorbed species. So, our calculations correspond to the deposition of strongly adsorbed hydrogen. Experimentally, this reaction is so fast that it has not been possible to measure its rate. This is in line with the very low energy of activation that we reported.

So far, we have shown that explicit model calculations performed for the densest crystal surfaces reproduced well the observed experimental trends and, even, gave a good estimate for the reaction rates [11, 13], but for long time, it has been known that the rate of hydrogen evolution depends strongly on the electrode material. When well-defined single-crystal electrodes became available, an important question was whether the rate depends only on the nature of the electrode or on the crystal face as well. Experiments on silver [14, 15] and copper [16] showed that, in both cases, the (111) surface was the better catalyst. The differences in the rate constants between various facets of Ag and Cu are not large and, as yet, unexplained. Hence, we have also investigated the hydrogen evolution on silver and copper on open crystal faces, such as (100) surfaces, and compared our results with the (111) surfaces [17].

To begin with, we have calculated the free energies of adsorption of hydrogen on the four surfaces that we consider. On both metals, the adsorption energy is less favourable on the (100) than on the (111) surface (Table 2) and the lowest energy is associated with the four- and threefold hollow sites, respectively.

To understand the effect of the metal d band on the H-metal bond, an analysis of the surface d band DOS is

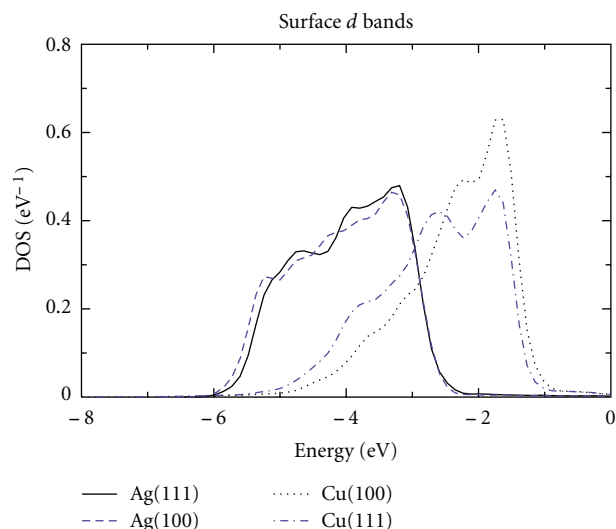


FIGURE 4: Surface density of states of the d bands. The Fermi level has been taken as the energy zero.

TABLE 2: Reaction free energy and free energy of activation for the Volmer reaction on the hydrogen scale [17].

Metal	Ag(111)	Ag(100)	Cu(111)	Cu(100)
ΔG_{ad} (eV)	0.39	0.48	0.10	0.14
ΔG_{act} (eV)	0.71	0.81	0.71	0.79

helpful. Figure 4 shows the d band structure for each system. As it can be seen, all the d bands lie below the Fermi level indicating that they are mediocre catalysts. The hydrogen-metal interaction splits the $1s$ hydrogen orbital in a bonding and an antibonding part. Since both parts are located well below the Fermi level, they are filled and no bonding results. Thus, the hydrogen adsorption is purely due to the hydrogen- sp band interaction. Because silver and copper d bands are filled and they do not contribute to the bonding, the Pauli repulsion becomes important, probably inducing a weaker adsorption on these open surfaces.

In the framework of our theory, we have investigated the Volmer reaction (the first step in hydrogen evolution) as described in [11, 17]. The resulting free energy surfaces for a variable energy of reorganization λ and the standard hydrogen potential are shown in Figure 5. In all the surfaces, the minimum the upper left corner, at $q = 1$, corresponds to the initial state, the solvated proton, and the minimum at the bottom right corner, $q = 0$, to the final state, the adsorbed hydrogen atom. In all cases the final state has higher free energies, which are the values given in Table 2. These two states are separated by an energy barrier; the energy of the saddle point gives the free energy of activation of the Volmer reaction, which is also given in the table. For both metals, the energy of activation is higher for the surface with the higher free energy of adsorption, as may have been expected. Thus, in agreement with experimental data, we find higher activation energies and, hence, lower rate constants, for the (100) than for the (111) surfaces. The main cause is the

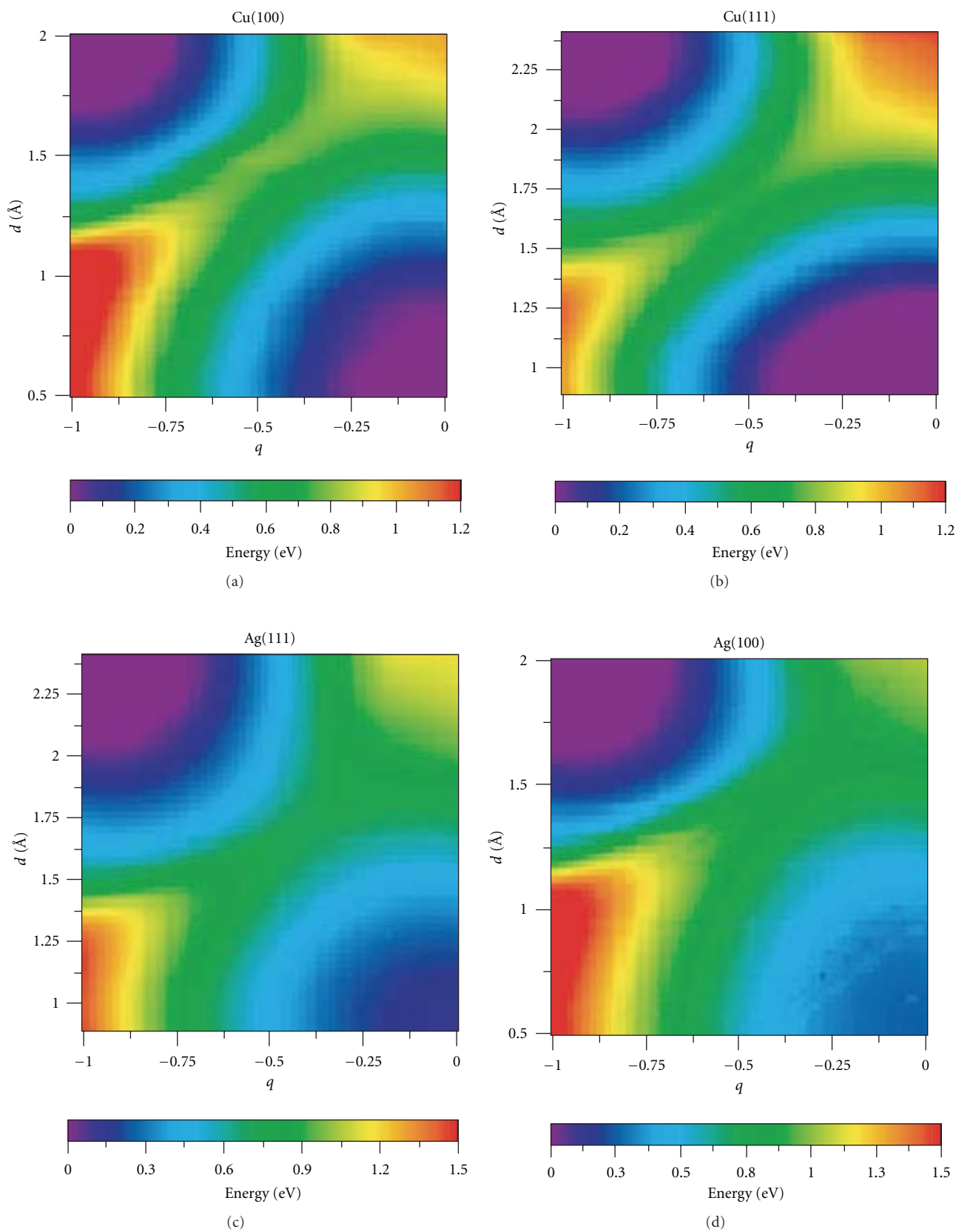


FIGURE 5: Free energy surfaces for hydrogen adsorption on single-crystal surfaces of copper and silver.

more endergonic adsorption energy on the open surfaces. For silver, both theory and experiments [14] suggest that the second step is the electrochemical desorption of the hydrogen atoms. On copper, the same mechanism is likely to operate, though we cannot rule out at what low absolute values of the overpotential chemical recombination may occur. Thus, electrochemical desorption seems to be more prevalent than previously thought [12, 18], and there is a need for a theoretical description of this process. Corresponding work is in progress in our group.

4. Electrocatalytic Properties of Nanostructures

4.1. Intrinsic Chemical Nature and Strain Effect: Monolayers of Pd on (111) Substrates. Electrochemical nanostructures have gained a great interest in the last decade because of the large variation of their reactivity in comparison with bulk material [19–25]. An interesting aspect is the possibility to design at the nano scale materials with specific properties in order to improve the electrocatalytic properties of electrodes. In this sense, electrochemistry offers convenient techniques for the synthesis of nanostructures such as metal overlayers, steps decorated by adatoms, or even monoatomic nanowires [26, 27]. One of the main features of nanomaterials is that their properties can be controlled by their electrochemical potential, a variable that is not available in vacuum or in air. This makes electrochemical nanostructures versatile. The big scientific challenge is to understand how the structure affects the chemical and physical properties of the materials and how this in turn influences their reactivity [28]. However, the implementation of these nanostructures is difficult because of the lack of understanding of the fundamental aspects and mechanisms which determine their stability, reactivity, and dynamics.

In the framework of our theory, we have examined the reactivity of various nanostructures on which much attention has been focused recently. Particularly, the role of the geometry and chemistry of the substrate on the electrocatalytic activity was investigated.

Monolayers of foreign atoms deposited on different metallic substrates have been extensively studied from an experimental point of view. We have systematically investigated monolayers of Pd at different substrates $M(111)$, $M = \text{Pt, Au, Ni, Cu, Ru, Pd}$.

Figure 6 shows the contour plots of the potential energy surfaces calculated by employing parameters which correspond to the hydrogen oxidation reaction. To analyse the catalytic activity of the systems, we focus on the region corresponding to the transition state, where the bond of the molecule starts to break and the electrons are being transferred to the electrode. In accord with experiments [19–21], a monolayer of Pd on Au(111) shows the best catalytic property, while the activity of the deposit on Cu(111) is the lowest. All the cases are compared with Pd(111). Pd on Ru(111) shows a similar behaviour as Pd on Cu(111), while Pd on Pt(111) is slightly less active than Pd(111).

As we explained in detail [29], there exists different factors which can affect the reaction. Frequently, these changes on the catalytic reactivity are explained in terms of

strains in the lattice of the deposited monolayer resulting in a shift of the d band center to higher or lower energies. Since the overlap of metal d states at neighbouring sites is affected, the band width is also simultaneously modified. Thus, the interaction with the reactants also changes [30].

We have systematically studied a palladium monolayer at different substrates having either larger or smaller lattice constants (a_0). Figure 7 illustrates the strain effect mentioned above for two extreme cases: when Pd is deposited on Au(111), the monolayer is expanded with respect to the bulk Pd ($a_0^{\text{Pd}} < a_0^{\text{Au}}$), consequently the distance between nearest neighbours increases. In contrast, when it is deposited on Cu(111), it is compressed ($a_0^{\text{Pd}} > a_0^{\text{Cu}}$) and the distortions produce changes in the electronic properties.

Particularly, the density of states of the d band shows important alterations. However, these changes are too complex to be explained only by a modification of the geometrical arrangements. Specific chemical interactions between the substrate and the monolayer should also play an important role.

To clarify the strain effect and the influence of the substrate on the reactivity, a set of theoretical systems have been investigated by us [29]. We have replaced the value of the lattice constant of Pd by that corresponding to the different substrates employed for the deposit and calculated the density of states for the surface of Pd(111) with this fixed value. Obviously, these are not *real* systems but their electronic behaviors allow us to distinguish between the strain effect and the role played by the chemical interactions between the foreign atom and the substrate. Figure 8 shows the comparison of the electronic properties, specifically on the shapes and position of the d bands. The lattice constants decrease from top to bottom. The distribution of electronic states for the bare (111) surfaces of the different substrates is shown on Figure 8(a). Here, the effect of the lattice constant does not produce a systematic change because of other effects that are also involved. There exists a combination of two factors: going from left to right in the periodic table, the number of d electrons increases, and thus the position of the d band relative to the Fermi level shifts to lower energies, and going from top to bottom the orbitals are more extended in space producing a higher overlap, and thus the bands are wider.

The effect of the lattice constant can be observed in the middle part of Figure 8(b) for the *artificial* systems obtained for Pd(111) with the lattice constants of the other metals. Here, the number of electrons is constant and the spatial extension of the orbitals is the same. When the lattice constant decreases, the delocalization of the orbitals increases producing the extension of the d band into lower energies. The distribution of the electronic states of the d band of a monolayer of Pd deposited on different substrates is shown on the right side of Figure 8(c). Here, the structure of the d band is the result of the combination of all the effects mentioned above. In general, one observes a widening of the d band with the decrease of the lattice constant of the substrate, whose orbitals are located at different energies depending on its chemical nature (see Figure 8(a)). The density of states decreases slightly at the Fermi level in all the cases, but it appears to be more localized at lower energies.

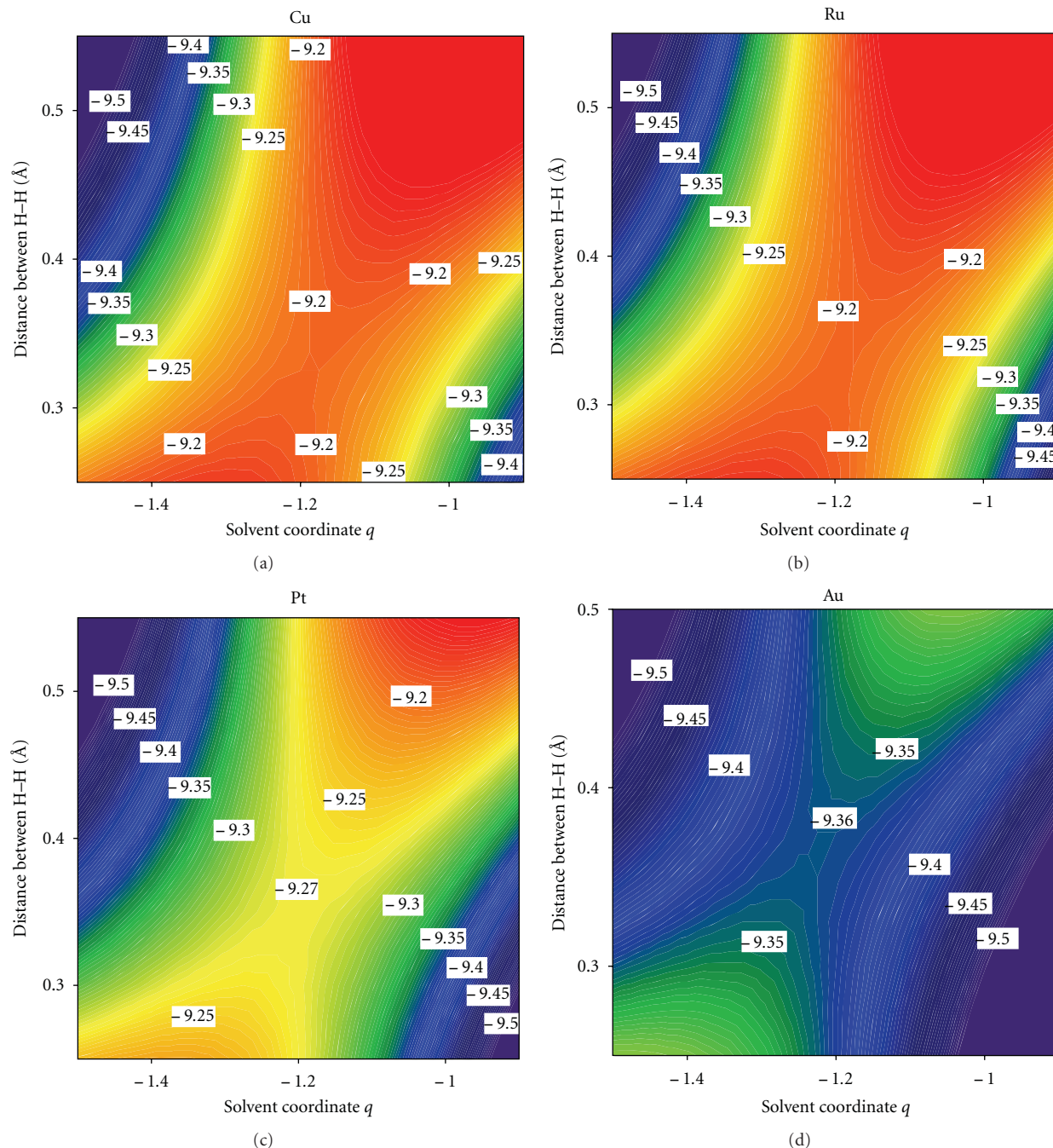


FIGURE 6: Contour plots of the potential energy surfaces showing the saddle point of the reaction path for the hydrogen oxidation at a monolayer of Pd deposited on different substrates M(111). The projections are done on the plane of the solvent coordinate q and the distance between both hydrogen atoms relative to the equilibrium in the molecule.

This effect is especially noticeable by the monolayer of Pd deposited on Au(111), where a sharp peak is observed at about -0.5 eV below the Fermi level.

Thus, in order to predict the catalytic activities of these systems, it is not enough to make estimations considering the strain produced by the different lattice constants of the substrates; it is necessary to make a more detailed analysis taking into account specific chemical interactions with the substrate.

4.2. Intrinsic Chemical Nature and Geometrical Effect: Noble Metal Nanowires Supported on Graphite Edges. Due to their unique properties, nanowires are employed in many applications and electrochemistry is one of them. In a recent communication, we have investigated the catalytic properties of isolated monoatomic wires. Cu and Au free-standing wires were predicted to be promising catalysts for the hydrogen reaction [31]. However, it is known that isolated wires are impractical as electrocatalysts. Therefore, we focus in more

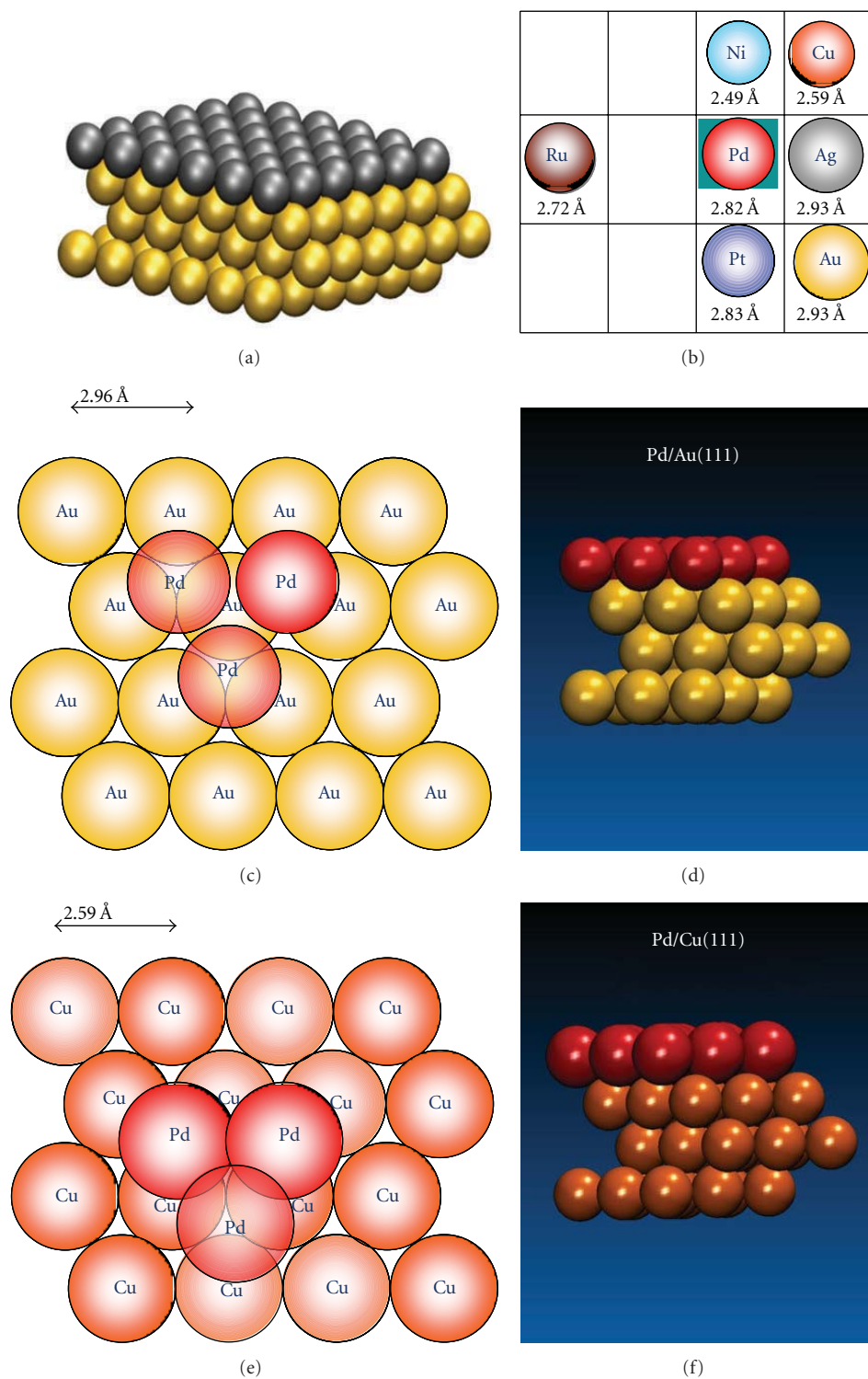


FIGURE 7: Monolayer of Pd on different substrates: M(111) (a). Distances to the next neighbours for the different substrates in comparison with Pd bulk (b). Expanded (c, d) and compressed (e, f) structures of the monolayer when the substrate atoms are larger and smaller than Pd, respectively.

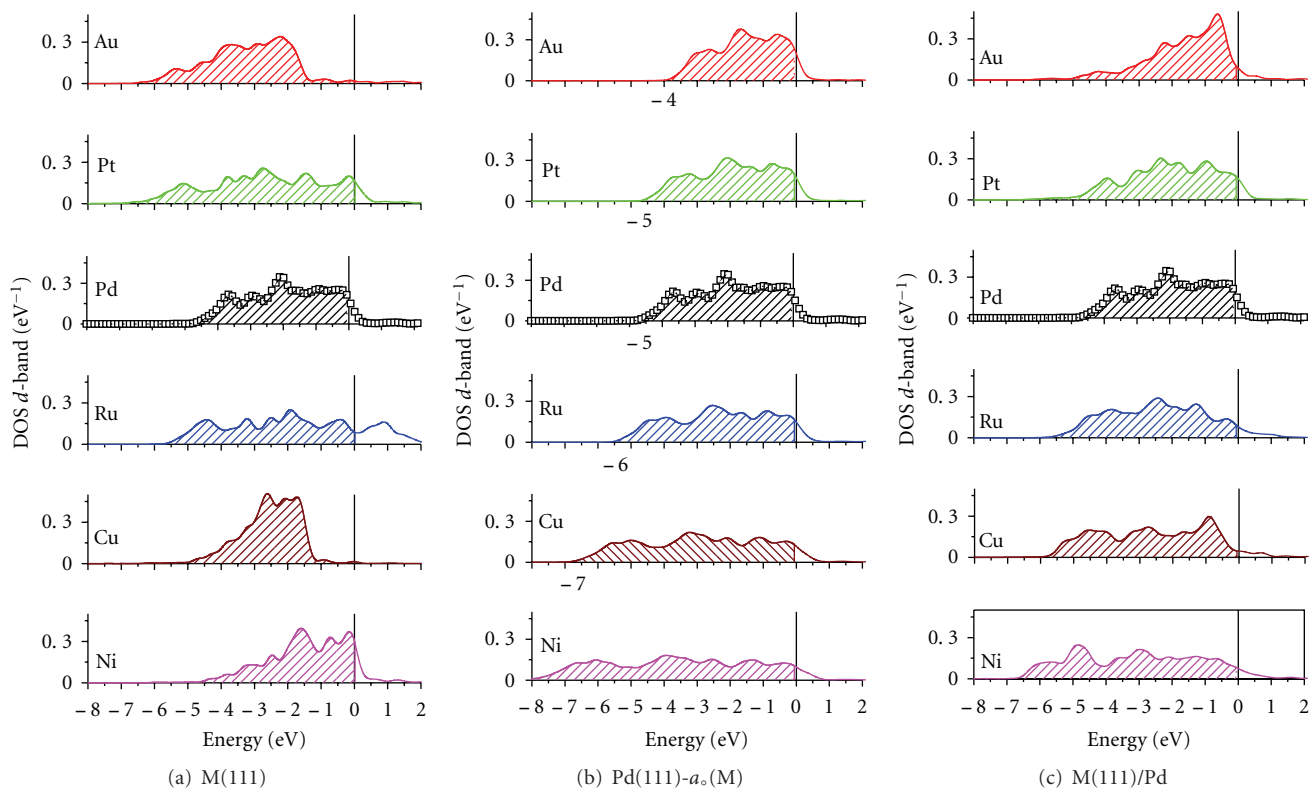


FIGURE 8: Density of states projected on the d bands for three different systems: (a) atoms at the surface (111) for different metals M , (b) atoms at the surface of Pd(111), where the lattice constant a_0 of palladium has been *artificially* changed by that of different metals M ; (c) atoms of the monolayer of Pd deposited on different metallic substrates $M(111)$. The vertical lines indicate the position of the Fermi level.

realistic systems, where these nanowires are supported on inert substrates to examine their stability and the influence of their chemical properties on the electrocatalytic activity (for details, see [32]).

Specifically, we considered Pt and Au monoatomic wires attached to monoatomic steps on the basal planes of graphite, the so-called graphite-supported wires (GSW). Considering the sp^2 hybridization of the carbon orbitals and the distance between two unsaturated carbon atoms (2.46 Å), which fits quite well the bond distances of the bare wires (≈ 2.50 Å), the zigzag arrangement was taken as the initial configuration. The system is shown in Figure 9—more detailed information can be found in [32].

The chain of metal atoms shows a corrugation along the z -axis forming an angle θ , which, in these commensurate structures is induced by the graphite lattice. The binding energy of the systems per metal atom is given in Table 4.

As it can be concluded from the adsorption energies, both metals adsorb exothermically, but the wire-graphite bond is much stronger for Pt. This fact can be revealed by a detailed analysis of the projected density of states (PDOSs) of the orbitals involved in the graphite-wire bond (Figure 10).

In the systems under study, the overlapping orbitals are sp_y^2 of the carbon atoms C_{edge} and $d_{x^2-y^2}$ of each metal. Before the adsorption process, sp_y^2 of C_{edge} is centered at the Fermi level; $d_{x^2-y^2}$ of the metals is below the Fermi level in Au-GSW and above it in Pt-GSW. During the

adsorption process, sp_y^2 of C_{edge} and $d_{x^2-y^2}$ of the metals overlaps and splits into a bonding and an antibonding parts. The bonding contribution appears below the Fermi level for both metals (Figure 10). The antibonding contribution is below the Fermi level only in Au-GSW, and this is the reason for the differences in the binding energy: the binding of Pt on graphite is stronger because the antibonding is unoccupied.

In the search for a good electrocatalyst for the hydrogen reaction, the hydrogen-GSWs adsorption was also investigated. The hydrogen adsorption process can occur on the attached wires at several positions and also directly on the graphite, cleaving one wire-graphite bond. Both situations were considered, and the most stable configurations for the adsorption are shown in Figure 11 together with their energies of adsorption.

To clarify the behavior of these systems, we must analyze the bond formation and the adsorption energies of hydrogen (Table 4). In Figure 12, the DOSs of the metal states overlapping with hydrogen are plotted and compared with the same orbitals in the absence of hydrogen. The adsorbate overlaps not only with d but with p states. On surfaces, p orbitals form a wide band spanning the Fermi level; this delocalization of the p band occurs on all metals.

In BW and GSW, only the p orbital along the axis of the wire is delocalized (p_x in our case) and the others are empty. p_y is empty in GSW; therefore, its DOS appears above the Fermi level for Au and Pt (In Figure 12, top). However,

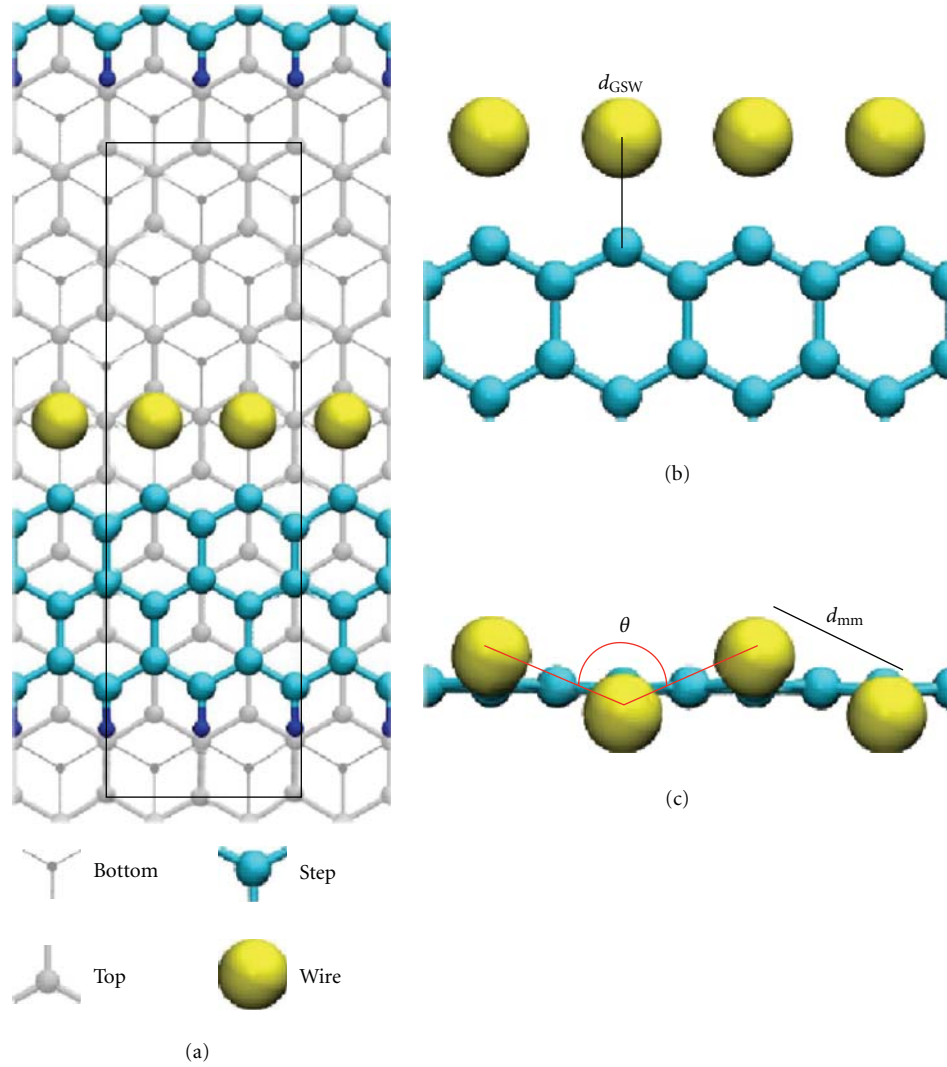


FIGURE 9: (a) The system (GSW—graphite supported wires) is formed by two layers (black and cyan), one step (blue), and the wire (yellow). The unit cell is indicated with red dash lines. (b) Metal-metal distance (d_{GSW}). (c) Corrugation angle of the wire (θ).

TABLE 3: Binding energy (E_{bin}), wire-graphite bond distance (d_{GSW}), metal-metal distance of bare wire ($d_{\text{mm(BW)}}$) and graphite-supported wires ($d_{\text{mm(GSW)}}$), the zigzag angle (θ) is shown in Figure 9(c).

Wires	E_{bin} (eV)	d_{GSW} (Å)	$d_{\text{mm(GSW)}}$ (Å)	$d_{\text{mm(BW)}}$ (Å)	θ (°)
Au	-1.78	2.08	2.68	2.61	133.2
Pt	-3.29	1.95	2.54	2.39	151.1

TABLE 4: Hydrogen adsorption energies on fcc(111) surfaces, bare wires [31] and wires of GSW.

E_{ads} (eV)	Au	Pt
fcc(111)	0.17	-0.49
BW	-0.751	-0.573
GSW	-0.548	0.055

after the adsorption of hydrogen, the p_y of both metals lie below the Fermi level and strongly overlap with hydrogen. Besides the overlap with p_y , hydrogen overlaps with d states:

for geometric reasons, with d_{z^2} in the case of Pt and with $d_{x^2-y^2}$ in the case of Au. p_y and d_{z^2} in platinum wire have almost the same profile, which indicates a hybridization between these two states; the resulting orbital overlaps with hydrogen. In contrast, p_y and $d_{x^2-y^2}$ of gold overlap separately with hydrogen. As can be noticed, hydrogen bonds similarly on both metals. The difference in the adsorption energies is because Au-GSW is more reactive than Pt-GSW due to the Au-graphite weaker bond.

As mention previously, the adsorption of hydrogen on graphite was also studied. In this case, the adsorption energy is lower than on wires for Au-GSW but almost the same for

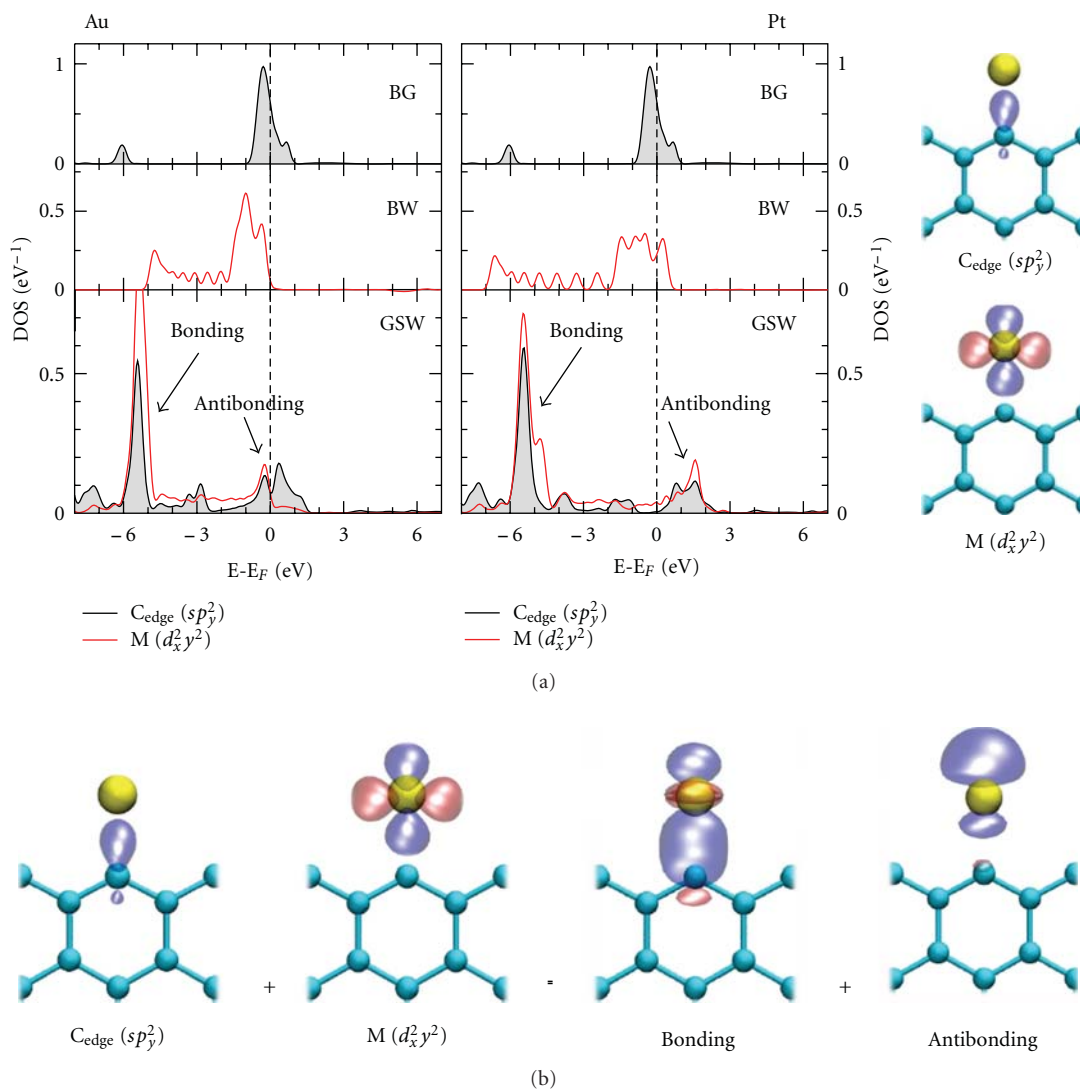


FIGURE 10: (a) PDOS of the sp_y^2 of C_{edge} and the $d_{x^2-y^2}$ of the metal for BG (bare graphite), BWs (bare wires) and GSWs (graphite supported wires) of gold and platinum. (b) Bonding and antibonding orbitals of the wire-graphite bond. The antibonding orbital is occupied only in the case of Au.

Pt-GSW (Figure 11). A cleavage of the wire-graphite bond is observed on Au-GSW, and a single bond of hydrogen with C_{edge} is formed. However, in the case of Pt-GSW, the adsorption process does not imply bond breaking and a simple bond with C_{edge} is formed. These results suggest that in the presence of hydrogen, gold wires may desorb from graphite, which may not be the case for platinum.

On the platinum wires, hydrogen adsorption is isoenergetic, because the platinum-graphite bond is weakened. However, hydrogen adsorption on the wire and on graphite is almost the same, and it does not imply desorption of the wire. Finally, hydrogen adsorption on the supported gold wires is more favorable than at Au(111) surfaces, and at 0 V SHE and pH 0, such a gold wire would be covered with a layer of strongly adsorbed hydrogen. Thus, these wires also promise to be good catalysts, just like the bare gold wires, but for a definite conclusion, more studies are needed.

5. Outlook

The results presented in this paper have been mostly oriented to investigate the hydrogen reaction on pure single-crystal surfaces and monolayers of a foreign metal on a variety of (111) substrates, in good agreement with experimental data reported in the literature. In addition and to the best of our knowledge, this is the first explanation of the hydrogen electrocatalysis founded on a theory and not on a correlation.

In the last few years, the searching for a better catalyst was centered on pure and modified single-crystals. However, the hope for the future advances in electrochemistry focuses no longer on such surfaces but on nanostructures, due to the fact that they are cheaper, more versatile, and efficient [33].

Dealing with nanomaterials is a challenge for both experiments and theory. Hence, our goal is to combine DFT and our theory to elucidate the electronic structure and predict

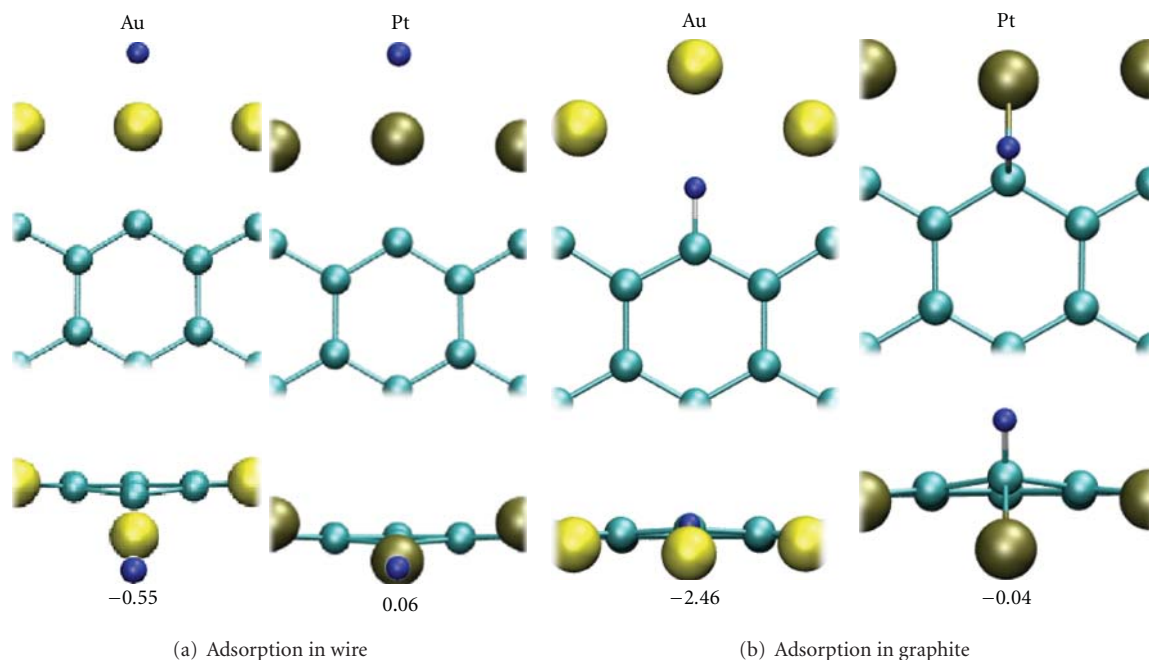


FIGURE 11: Configuration of the most stable adsorption of hydrogen (blue) on the wire (a) and at the edge of graphite (b) of GSW. The corresponding energies in eV are shown below. On the wire, for both metals, the adsorption is on top. On the graphite edge, the adsorption is in the same plane in the case of gold and above it in the case of platinum.

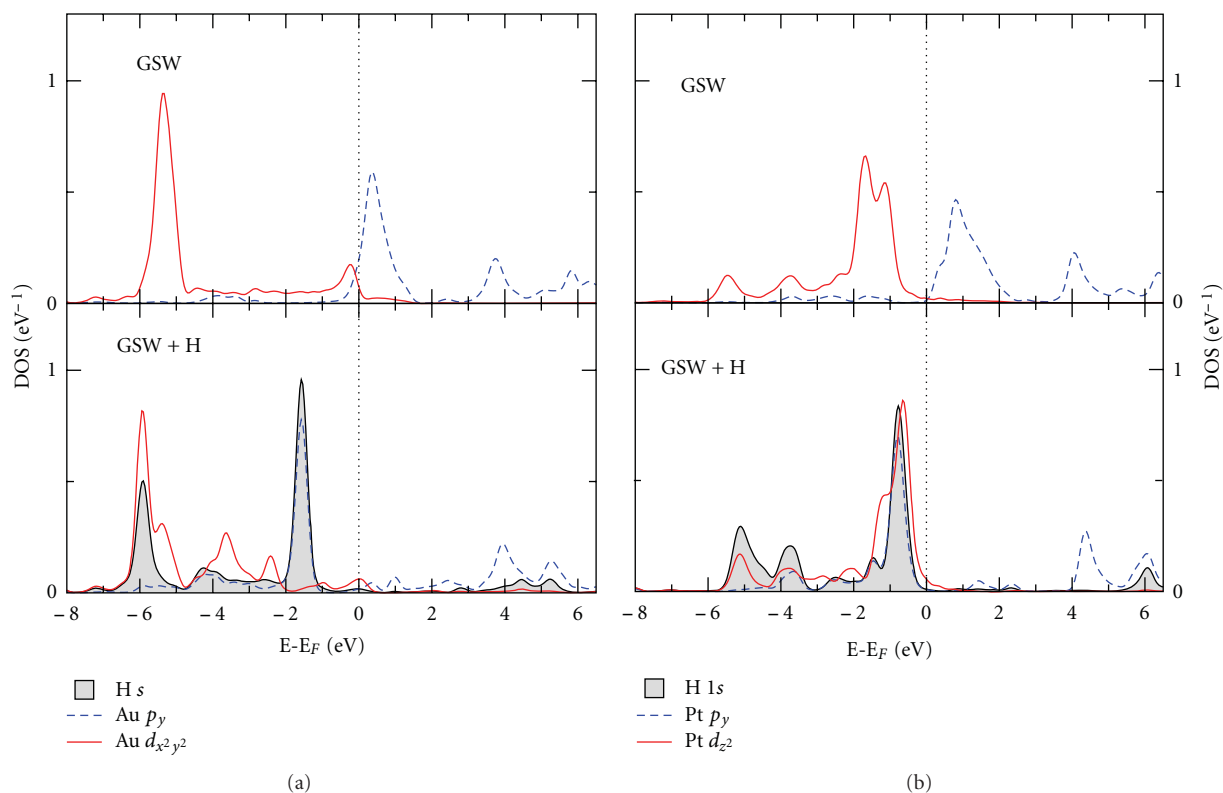


FIGURE 12: DOS of $d_{x^2-y^2}$ and p_y of the metals for Au-GSW; d_{z^2} and p_y for Pt-GSW with and without H. p_y of the metals is empty in the absence of hydrogen, and becomes occupied when hydrogen adsorbs.

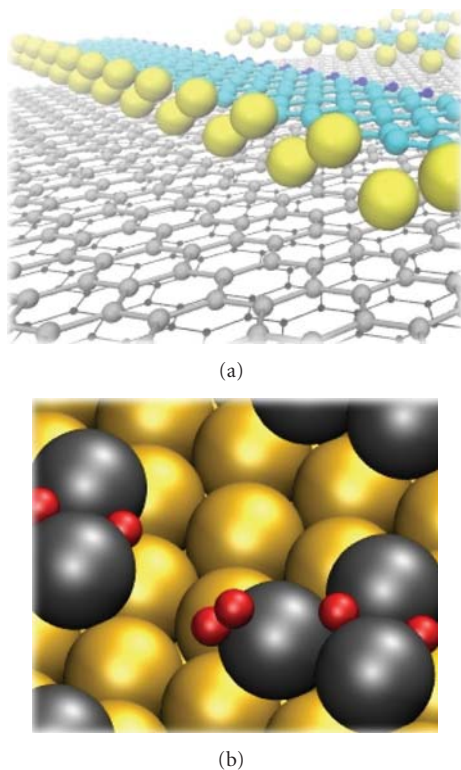


FIGURE 13: (a) Wire Adsorption on Graphite steps. (b) Hydrogen adsorption on Pd nanoclusters on Au(111).

their catalytic activity. In this context, Pd submonolayers on Au substrates and graphite-supported wires (Figure 13) are being investigated in our group.

Acknowledgments

Financial support by the Deutsche Forschungsgemeinschaft under Schm 344/40-1, Sa 1770-1,2 and FOR1376, Mincyt-BMBF, CONICET, the European Union under ELCAT, PICT-2008-0737 (ANPCyT), and a generous grant of computing time from the Baden-Württemberg grid is gratefully acknowledged. E. Santos, P. Quaino, W. Schmickler thank CONICET for continued support.

References

- [1] E. Santos and W. Schmickler, "d-band catalysis in electrochemistry," *ChemPhysChem*, vol. 7, no. 11, pp. 2282–2285, 2006.
- [2] E. Santos and W. Schmickler, "Fundamental aspects of electrocatalysis," *Chemical Physics*, vol. 332, no. 1, pp. 39–47, 2007.
- [3] E. Santos, M. T. M. Koper, and W. Schmickler, "A model for bond-breaking electron transfer at metal electrodes," *Chemical Physics Letters*, vol. 419, no. 4–6, pp. 421–425, 2006.
- [4] E. Santos, M. T. M. Koper, and W. Schmickler, "Bond-breaking electron transfer of diatomic reactants at metal electrodes," *Chemical Physics*, vol. 344, no. 1-2, pp. 195–201, 2008.
- [5] P. W. Anderson and A. T. Ramsey, "Localized magnetic states in metals," *Physical Review*, vol. 124, p. 41, 1961.
- [6] D. M. Newns, "Self-consistent model of hydrogen chemisorption," *Physical Review*, vol. 178, no. 3, pp. 1123–1135, 1969.
- [7] E. Santos and W. Schmickler, "Electrocatalysis of hydrogen oxidation—theoretical foundations," *Angewandte Chemie*, vol. 46, no. 43, pp. 8262–8265, 2007.
- [8] E. Santos, K. Pötting, and W. Schmickler, "On the catalysis of the hydrogen oxidation," *Faraday Discussions*, vol. 140, pp. 209–218, 2008.
- [9] E. Santos and W. Schmickler, "Electronic interactions decreasing the activation barrier for the hydrogen electro-oxidation reaction," *Electrochimica Acta*, vol. 53, no. 21, pp. 6149–6156, 2008.
- [10] E. Santos, A. Lundin, K. Pötting, P. Quaino, and W. Schmickler, "Hydrogen evolution and oxidation—a prototype for an electrocatalytic reaction," *Journal of Solid State Electrochemistry*, vol. 13, no. 7, pp. 1101–1109, 2009.
- [11] E. Santos, A. Lundin, K. Pötting, P. Quaino, and W. Schmickler, "Model for the electrocatalysis of hydrogen evolution," *Physical Review B*, vol. 79, no. 23, Article ID 235436, 2009.
- [12] E. Santos and W. Schmickler, *Interfacial Electrochemistry*, Springer, London, UK, 2nd edition, 2010.
- [13] E. Santos and W. Schmickler, *Electrocatalysis; From Fundamental Aspects to Fuel Cells*, 2010.
- [14] D. Eberhardt, E. Santos, and W. Schmickler, "Hydrogen evolution on silver single crystal electrodes—first results," *Journal of Electroanalytical Chemistry*, vol. 461, no. 1-2, pp. 76–79, 1999.
- [15] L. M. Doubova and S. Trasatti, "Effect of the crystallographic orientation of Ag single crystal face electrodes on the kinetics of proton discharge," *Journal of Electroanalytical Chemistry*, vol. 467, no. 1, pp. 164–176, 1999.
- [16] V. V. Batrakov, Y. Dittikh, and A. N. Popov, "Influence of the surface structure on the overpotential for hydrogen evolution in acid solutions," *Elektrokhimiya*, vol. 8, p. 640, 1972.
- [17] E. Santos, K. Pötting, A. Lundin, P. Quaino, and W. Schmickler, "Hydrogen evolution on single-crystal copper and silver: a theoretical study," *ChemPhysChem*, vol. 11, no. 7, pp. 1491–1495, 2010.
- [18] W. Vielstich, C. H. Hamann, and A. Hamnett, *Electrochemistry*, Wiley-VCH, Cambridge, UK, 2007.
- [19] S. Pandelov and U. Stimming, "Reactivity of monolayers and nano-islands of palladium on Au(1 1 1) with respect to proton reduction," *Electrochimica Acta*, vol. 52, no. 18, pp. 5548–5555, 2007.
- [20] H. Wolfschmidt, R. Bussar, and U. Stimming, "Charge transfer reactions at nanostructured Au(111) surfaces: influence of the substrate material on electrocatalytic activity," *Journal of Physics Condensed Matter*, vol. 20, no. 37, Article ID 374127, 2008.
- [21] L. A. Kibler, "Hydrogen electrocatalysis," *ChemPhysChem*, vol. 7, no. 5, pp. 985–991, 2006.
- [22] F. Hernandez and H. Baltruschat, "Hydrogen evolution and Cu UPD at stepped gold single crystals modified with Pd," *Journal of Solid State Electrochemistry*, vol. 11, no. 7, pp. 877–885, 2007.
- [23] H. Baltruschat, R. Bussar, S. Ernst, and F. Hernandez, *In-Situ Spectroscopic Studies of Adsorption at the Electrode and Electrocatalysis*, Elsevier, 2007.
- [24] R. R. Adzic, A. V. Tripkovic, and V. B. Vessovic, "Structural effects in electrocatalysis: oxidation of formic acid and hydrogen adsorption on platinum single-crystal stepped surfaces," *Journal of Electroanalytical Chemistry*, vol. 204, no. 1-2, pp. 329–341, 1986.

- [25] G. Garcia and M. T. M. Koper, "Stripping voltammetry of carbon monoxide oxidation on stepped platinum single-crystal electrodes in alkaline solution," *Physical Chemistry Chemical Physics*, vol. 10, no. 25, pp. 3802–3811, 2008.
- [26] C. Z. Li, A. Bogozi, W. Huang, and N. J. Tao, "Fabrication of stable metallic nanowires with quantized conductance," *Nanotechnology*, vol. 10, no. 2, pp. 221–223, 1999.
- [27] H. X. He, S. Boussaad, B. Q. Xu, C. Z. Li, and N. J. Tao, "Electrochemical fabrication of atomically thin metallic wires and electrodes separated with molecular-scale gaps," *Journal of Electroanalytical Chemistry*, vol. 522, no. 2, pp. 167–172, 2002.
- [28] A. Gross, "Adsorption at nanostructured surfaces," in *Handbook of Theoretical and Computational Nanotechnology*, chapter 89, American Scientific Publishers, 2006.
- [29] E. Santos, P. Quaino, and W. Schmickler, "On the electrocatalysis of nanostructures: monolayers of a foreign atom (Pd) on different substrates $M(1\ 1\ 1)$," *Electrochimica Acta*, vol. 55, no. 14, pp. 4346–4352, 2010.
- [30] B. Hammer and J. K. Nørskov, "Theoretical surface science and catalysis—calculations and concepts," *Advances in Catalysis*, vol. 45, pp. 71–129, 2000.
- [31] E. Santos, P. Quaino, G. Soldano, and W. Schmickler, "Electrochemical reactivity and fractional conductance of nanowires," *Electrochemistry Communications*, vol. 11, no. 9, pp. 1764–1767, 2009.
- [32] G. J. Soldano, P. Quaino, E. Santos, and W. Schmickler, "Stability of gold and platinum nanowires on graphite edges," *ChemPhysChem*, vol. 11, no. 11, pp. 2361–2366, 2010.
- [33] P. Quaino, E. Santos, H. Wolfschmidt, M. Montero, and U. Stimming, "Theory meets experiment: electrocatalysis of hydrogen oxidation/evolution at Pd-Au Nanostructures," *Catalysis Today*. In Press.